ITS UCDAVIS
INSTITUTE OF TRANSPORTATION STUDIES

Research Report – UCD-ITS-RR-12-49

Human Control of a Bicycle

September 2012

Jason Moore

Institute of Transportation Studies ◦ University of California, Davis
1605 Tilia Street ◦ Davis, California 95616
PHONE (530) 752-6548 ◦ FAX (530) 752-6572
www.its.ucdavis.edu

Human Control of a Bicycle

By

JASON KEITH MOORE
B.S. (Old Dominion University) 2004
M.S. (University of California at Davis) 2007

DISSERTATION

Submitted in partial satisfaction of the requirements for the degree of

DOCTOR OF PHILOSOPHY

in

Mechanical and Aerospace Engineering

in the

OFFICE OF GRADUATE STUDIES

of the

UNIVERSITY OF CALIFORNIA

DAVIS

Approved:

Mont Hubbard, Chair

Ronald A. Hess

Arend L. Schwab

Committee in charge

2012

Human Control of a Bicycle

Jason K. Moore

August 2012

ABSTRACT

For the non-nonsensical it may be best to skip to the last section...

Unlike the plethora of scientific opuses that reveal how the average *Ursidae* (bear) can balance on a bicycle, little has been garnered about how *Homo sapiens* is able to accomplish this feat. When the rider's normal locomotion instruments for continual balance are replaced by two in-line wheels connected to one another by a manipulatable semi-vertical revolute joint the rider is then forced to direct his mental energy to observing the additional states of the bicycle's configuration and the proper actuation of his arms to maintain vertical equilibrium. It was found that this "simpler" task is well suited for manual control theoretic dissection and postulation.

I herein present the findings of the seventh age of my tenure as a doctoral candidate in the prefecture of Mechanical and Aerospace Engineering at the Davis campus of the University of California. These describe our experimental procedure which involved strapping the untamed and aggressive *Homo sapiens* to a velocipede of extraordinary measurement capabilities. We perturbed the beasts as they tried with all their mental and physical might to stay upright, constrained as they were. Following more than seven hundred trials with three hand-picked quality specimens, the clouds of data have shaped into more than distant blurs. The control and identification tools of Bode, Evans, and Ljung combined with the modern day data management tools of van Rossum, Moler, and Torvalds have shed light on the details of the sensory feedback mechanisms present in the neurological pathways connecting the *Homo sapien*'s senses to his actuators. To the bear's dismay, this has in turn revealed that the highly regarded 1899 bicycle model of Whipple is sorely lacking and that the control theoretic hypothesis of McRuer for the great aeroplane pilots of yesteryear does, in fact, apply to the human control of a machine as simply complex as the bicycle.

The dissertation will provide the reader with a glimpse into the reductio complexio of the physiological system of the greater *Homo sapiens* by forced travel on the automatic velocipede with highlights of manual control theories, inertial investigations, data wrangling, and of course demonstrations of the magical-like auto stability of the bicycle.

The sensical...

For those of you who'd rather read a more traditional abstract here is a quick explanation of the above in plain modern Engineering English:

The bicycle, a simple toy to many, turns out to be an excellent platform to study the intricacies of vehicle dynamics, human-machine interaction, and human operator control for both academic and economical reasons. The bicycle is inherently unstable at low speeds and the human generally actuates the non-minimum phase system, and thus balances, only by means of rotating the handlebars. This dissertation describes a multi-year multi-person effort to better understand the dynamics of the bicycle, the biomechanics of the rider, and the rider's internal control system through theory and extensive experimentation.

The chapters herein focus on the development of open loop bicycle models, some of which include the rider's biomechanics, the resulting predicted motion and model characteristics, the accurate measurement and estimation of both the bicycle and rider's physical parameters, observation of a rider's control motions, the development of experimental bicycles capable of measuring kinematics and forces, control theory including that of the human operator, and finally the identification of the both the plant and controller of the bicycle-rider system.

The work has revealed a number of interesting conclusions including the primary biomechanic actuators used by the human in control, effects of the rider's motion and constraints on bicycle stability, the inadequacy of the Whipple bicycle model, and the ability of a simple multi-output control system based on the classical crossover model to describe the human's control efforts while being externally perturbed. These findings have implications in both single track vehicle design and human-machine interaction theory. Future applications may be able to utilize the methods and results to help objectively design bicycles with improved handling, stability, and controllability whereas human operator research may be able to build on the validated crossover model theory of manual control.

FOREWORD

On rare occasion in life one must halt everything in order to focus on one monumental task of great importance. Few really comprehend the inordinate amount of time, effort and sacrifice that goes into a dissertation. This paper was such an endeavor.

Around the world millions of people ride their bikes daily, yet the secrets that make the magic of bicycling possible have never been fully understood or entirely quantified. This work brings us closer to that goal. The melding of man and machine that allows for transportation and gratification has always been somewhat of a mystery. This compilation delves into the foundations of bicycling and investigates why it's possible.

These principles, when fully understood, will greatly enhance our understanding and perhaps change the world as we know it… at least the bicycling world.

Jan Phillip Wright
8. 13. 2012
University of California, Davis

ACKNOWLEDGEMENTS

On the road to a higher degree, there are always many people who assist in the process, from one's professors to librarians, but there are always some very special folks to thank. Jonathan Eisen, a professor at Davis, pointed out once during a talk that he thought the acknowledgement sections of papers were the most under-utilized sections in scientific literature. I agree with him and can only hope that I can give my gratitude to all who have helped me during my tenure as a graduate student.

This first person I'd like to recognize is Mont Hubbard. He has been my adviser since I took his multi-body dynamics course during the Winter of 2006. Along the way he has always been there for me academically in every way possible and I'm grateful for his dedication to working closely with his students and his willingness to more than share his time. I don't explicitly name him much in the dissertation, but his thoughts, ideas, and support permeate all of the content. We've also become great friends and have worked together on many projects both inside and out of our academic lives. His search for Luke and my preliminary exams through a mound of trash is a typical example of his devoted care for his students. Secondly, I owe much to my long time lab mate and great friend Luke Peterson. We've been working on understanding the same bicycle stuff for years now and if I didn't have him to bounce ideas off and his deep nerdiness to keep my work in check I'm not sure where I'd be with all this. Next, I owe my wonderful Fulbright experience to my advisor Arend Schwab and colleague Jodi Kooijman in the Netherlands. I'd like to thank them for giving me so many great opportunities and allowing me to see the research world from the viewpoint of another culture. I'd also like to thank my co-advisor Ron Hess at UC Davis who has worked closely with me these past couple of years on the human control and identification portions of my research. His expertise allowed us to stand on a strong foundation and get to the solutions much more quickly than we would have on our own.

We've had several graduate student interns who have played important roles in the project. Both Danique Fintelman and Peter de Lange were able to do their TU Delft Master's internships with us. Danique helped up sort out our early design ideas for data collection and Peter enlightened us about system identification, eventually using some of the data collected here in his excellent Master's thesis [DL11]. Chris Dembia worked with us one summer, impressing us with his excellent software work. Gilbert Gede helped with the mechanical design and construction of the instrumented bicycle and Garry Negroni documented the electrical system.

We also had quite a few undergrads work with us on the instrumented bicycle designs and the physical parameter measurements: Steven Yen, Mohammed Osman, Joe Rinek, Eric Chan, Chet Corcos, Steven Brendel, and Derek Pell all contributed to the work herein.

The experimental work couldn't be done without many folks help: Jan Wright, Tai Stillwater, Alvin Yu, Andrew Kickertz, Zach Sabato, Elliot Marshall, and Ziqi Yin all helped run the experiments. I'm also grateful to the experimental subjects for sitting through long hours on uncomfortable bicycles riding the same line over and over again: Charlie Persson, Victor Alhm, and Luke Peterson.

Dr. Knoek van Soest allowed us to use the large treadmill at the Vrije Universiteit in Amsterdam and Richard Casius ran the motion capture equipment for us. At Davis, Dr. James Jones and George Crocker graciously allowed us to use the horse treadmill facility in off hours.

Several players in the bicycle dynamics world have come to my aid or given great insight over the years, in particular

Jim Papadopoulos, Andy Ruina, Karl Åström, and Chet Kyle. Also the folks on the single track vehicle dynamics email list have always been a great help.

Both Batavus and Amped Bikes donated equipment for the projects. Both Dave Scurti at Pacific Medical Prosthetics and Orthotics and Renee Vondelft at Anchor Orthotics and Prosthetics helped out and donated materials for the body harnesses.

I made use of many software packages to analyze data, make plots, and build this dissertation, most of which are open source. I'd like to thank all the thousands of people involved in developing all the open source software tools that I use. And in particular, I'd like to thank Matthias Troffaes for helping me get his sphinx bibtex extension working with my bibliographic data in the final weeks.

On that note, I'd also like to thank the thousands of researchers that I've based my work on. If it weren't for the available reports[1] of years and years of research successes and failures, I would have been in a much different position at this point. The ideas herein are an amalgamation of many people that I've read and interacted with over the years. I thank you all.

I'd like to thank the Fulbright program. The experiences I gained through it are invaluable and have affected my life in so many ways. Programs like these are essential for promoting understanding among cultures and building bonds among the countries of the world.

The UCD librarians have found virtually every obscure article that I've asked them for. In particular, I'd like to thank Bob Heyer-Gray for all his work.

Thanks to my UC Davis qualifying exam committee: Dr. Ron A. Hess (Chair), Dr. Fidelis O. Eke, Dr. Donald L. Margolis, Dr. Keith R. Williams, and Dr. Michael R. Hill.

The NSF grant we received really gave us the freedom to explore this somewhat obscure topic and I'm grateful that we have a country that supports the sciences like it does. Their official disclaimer follows:

This material is partially based upon work supported by the National Science Foundation under Grant No. 0928339. Any opinions, findings, and conclusions or recommendations expressed in this material are those of the author(s) and do not necessarily reflect the views of the National Science Foundation.

Finally, I'd like to thank my friends and family for their support over the years. My parents, Cindy and Mark, have given me unconditional love and support through all of my schooling and I'm grateful to have such caring parents. My girlfriend, Yumi, has been by my side for the last two and half years where we have both been working to finish our doctoral degrees. Her love and support have helped kept me going through the high stress of getting all this done. She also drew the wonderful studying bear drawing for my cover page.

[1] Actually all papers aren't always available and are often extremely difficult or not possible to obtain. Open access has to become the de facto norm in science if we expect to make greater strides than in the past.

CONTENTS

LIST OF FIGURES

LIST OF TABLES

CHAPTER

ONE

PREFACE

1.1 Introduction

The typical conversation with someone I've met over the past years that I've been a graduate student inevitably comes to this: "So what do you do in graduate school?". My reply is "I study how people balance on bicycles". This is a great conversation starter as almost everyone recalls learning how to ride a bicycle. It is something we weren't born to do and we almost always remember the feeling of learning the skill. It is typically quite a momentous occasion in most folks' lives. Usually everyone thinks the research is cool and can identify with it, but the next question (as with most research), is "What application is that good for?". As an engineer, we are trained to be application minded. It is certainly what drove me to start down this path in the first place. There is an answer to this second question, but over the years I've gotten less enthusiastic about trying to justify why I'm working on this project with respect to an immediate application. In many ways this is simply the reality for the growing scientist. It becomes obvious that basic science simply needs to be performed, without regard to what it may or may not accomplish. The benefits down the road are inevitable and there is a large body of evidence to support that. But nonetheless my initial curiosity about bicycle dynamics is rooted in application and it still is in many ways. But I'm content with understanding difficult problems for basic progression in learning and science.

My first inquiries about bicycle dynamics came from my attempts to design a recumbent bicycle frame for my senior design project at Old Dominion University. Recumbents are notorious for not being that easy to ride and we were building one for the annual ASME Human Powered Vehicle challenge which would be especially unusual with an extremely low center of gravity. It needed to be suitable for novice riders to control. I found myself in the design process where one needs to choose the wheel sizes, front end geometry and location and seating position of the rider. As a young engineer is taught, I went looking for technical guidelines to choose these parameters for our bicycle design. But all I came back with were many conflicting ideas from various bicycle fabricators and the book Bicycling Science 2nd Ed [WW82] which gave a synopsis of Jones' [Jon70] conclusions from his famous study on the stability of bicycles. I studied this in detail and designed my bicycle geometry to be exactly what was specified as good handling by Jones.[1] The bicycle turned out to be rideable (after lots of practice), but this was probably the first time I realized in my engineering career that there isn't a formula for everything.

These particulars fell onto the back burner as I finished my work at the Langley Full Scale Tunnel and did not re-emerge until a few classes at UC Davis brought these concepts back into my picture. In particular, I attempted to derive the equations of motion of the bicycle in Mont Hubbard's multi-body dynamics class at the beginning of 2006 and the power to potentially properly answer the questions I had back at Old Dominion seemed to be at my finger tips. Little did I realize that those answers simply introduced more difficult questions and a research project was born.

This dissertation documents most of the work I've done and my thoughts on bicycle dynamics, control, and handling at UC Davis and TU Delft since around December 2006.

[1] It was not untill after welding the bicycle frame together that I realized that I'd cut a tube too long and the geometry was very different than I'd planned.

1.2 Reproducibility

Over the past few years, I've begun realize how reproducibility is crucial for science to improve and grow rapidly, all the while building a deeply intact and strong foundation for future researchers and that it may not be as reproducible as we may all think. With that in mind, I have put a great deal of effort into making my work more accessible, reusable, and ultimately reproducible, which is the cornerstone of all scientific understanding. For the type of work presented here, the majority is computational and the computer along with software have enabled our generation to make the work reproducible without too much extra effort. My intention is provide enough information in the form of data, source code, and writing, that others will have a *relatively* easy time reproducing my work. This has been mostly possible in the time frame that I've had to complete the thesis, but there are some holes in particular with respect to the work done in the earlier years of the project.

1.2.1 Literature

I really enjoy reading older dissertations and technical reports because they typically have so much detail, much more than any journal paper will ever have. I find these details to be invaluable for developing new research plans and understanding. This is especially true when the null science is reported, which gives a much better idea of what not to do. My dissertation is modeled after these longer documents and I've attempted to include as much detail in the decision making processes, methods, and results as possible.

This dissertation is partly original work that has not been published in any form and partly based on several journal and conference papers that I have written or co-authored over the years. I've given an outline below of the papers which have been subsumed into this thesis.

[FMPM06] This is an internal report done with two other students in my modern controls class. We developed several controllers for a simple bicycle model. Some elements of this paper influenced Chapter *Control*.

[Moo06] This is the internal report which described my first effort at deriving the equations of motion of the bicycle[2], estimating the physical parameters of the bicycle/rider, and running a numerical parameter study.

[MPH07] Luke Peterson and I wrote this short paper for the 11th International Symposium on Computer Simulation in Biomechanics in Tainan, Taiwan. We presented a basic rider biomechanic extension to the Whipple model which I had developed in [Moo06]. This contributes directly to Chapter *Extensions of the Whipple Model*.

[MH08] This is the polished and corrected version of [Moo06] which was submitted to the 2008 International Sports Engineering Conference in Biarritz, France. The model derivation is written out thoroughly in Chapter *Bicycle Equations Of Motion*, the physical parameter estimation in Chapter *Physical Parameters*, and the parameter studies in Chapter *Parameter Studies*.

[KS08] Jodi Kooijman presented this paper at a conference in Hungary not long after I had been in the Netherlands. It contained the results from the experimental studies we did during my first few months in Delft.

[MKS09] I presented this paper at the 2009 Multibody Dynamics conference in Warsaw, Poland. This work focused on the motion identification experiments we did early in 2009.

[MKHS09] This paper presented a combination of the bicycle measurement technique used in [Koo06] and an improved version of the human inertia estimation technique developed in [Moo06]. I presented it at the 2009 ASME conference in San Diego, CA.[3]

[KSM09] This is a polished version of [KS08]. Jodi Kooijman presented it at the 2009 ASME conference. This work is presented in Chapter *Delft Instrumented Bicycle*.

[2] The equations derived here are slightly incorrect.

[3] I remember this being a poor presentation on my part. I arrived in San Diego after living for a year in the Netherlands. My mind was lost in experiencing everything I missed about my home country and I couldn't focus on properly preparing for the presentation.

[MHP+10] This is a report on the work I did in the last few months I spent in Delft in which I used a modified technique from [Koo06] to more accurately measure the physical parameters of a variety of bicycles. I presented it as a poster at the first Bicycle and Motorcycle Dynamics Conference in 2010.

[MHS+10] Jodi Kooijman presented this paper for me at the International Sports Engineering Conference in 2010. It was about simple statistical analyses of the data we collected in [MKHS09]. This work can be found in Chapter *Motion Capture*.

[PMFH10] Dr. Hubbard presented this paper for us at the ISEA conference in 2010. It gave a preliminary look at the instrumented/robot bicycle we were developing.

[MKSH11] The paper written for the conference in Warsaw, [MKS09], was accepted to be published in Multibody System Dynamics. It is a polished version of [MKS09] and is presented in Chapter *Motion Capture*.

[HMH12] This work was originally presented at the Bicycle and Motorcycle Dynamics conference in 2010 and eventually published by IEEE in 2012. The work is expanded on and detailed in Chapter *Control*.

1.2.2 Source Code

It is very possible to code every computation that an engineer does and in many ways the most preferable method to record it. It is not only a record of the working computation that contains all of the details needed but an executable source that can be reused. But this doesn't mean one can simply drop all of their undocumented scripts into a folder, publish it to the web and expect anyone to ever be able to decipher it and actually use it. It takes much more effort to document the source code and to put it into a usable form. These techniques are very rarely, if at all, taught to engineers. Once I got a taste of the development methods of software engineers and computer scientists I couldn't believe how poorly we engineers execute our code. Not only does creating usable and well documented code help others to use it, but it helps you to know what it is and be able to reuse it yourself. It is documented proof of working methods. I have no idea how much code "waste" is on my hard drive that I will never have the time to decipher again and make use of it.

I have several layers of code that supports this document. In general, all of the figures and tables are generated by scripts in the *src* directory included with the source to this dissertation. These scripts access a variety packages in my software stack with most of them being open source packages that I or some of my collaborators have written. The following gives a list of the packages we've developed:

AutolevToolKit (https://github.com/moorepants/AutolevToolKit) (Python) A collection of tools which parse Autolev (http://www.autolev.com) output for extracting the equations of motion and some basic tool to convert them to LaTeX. It has a prototype of a numerical dynamic system class with accompanying linear dynamic system class to make basic analysis quick and painless.

BicycleDAQ (https://github.com/moorepants/BicycleDAQ) (Matlab) A GUI tool that collects time series and meta data from the instrumented bicycle via the NI USB-6218 data acquisition board and the VectorNav VN-100. It has tools for also collecting calibration data for the various sensors.

BicycleDataProcessor (https://github.com/moorepants/BicycleDataProcessor) (Python) A tool that stores all of the data collected from the instrumented bicycle in a database for easy retrieval and manipulation. It also processes the raw data into the variables of interest, so you can directly compare it with models.

BicycleID (https://github.com/moorepants/BicycleID) (Python A GTK GUI for visualizing the bicycle model identification data.

BicycleParameters (http://pypi.python.org/pypi/BicycleParameters) (Python) [Moo11] A program that generates the physical parameters of a bicycle and rider from experimental measurements. It also allows for basic manipulation and analysis with some widely used models.

BicycleSystemID (https://github.com/moorepants/BicycleSystemID) (Matlab & Python) A set of tools for interacting with the Matlab System ID toolbox. It has functions built around the grey and black box identification of several bicycle, rider and control models.

CanonicalBicycleID (https://github.com/moorepants/CanonicalBicycleID) (Python) A module for identifying a 4th order bicycle model from the canonical form.

DelftBicycleDataViewer (https://github.com/moorepants/DelftBicycleDataViewer) (Matlab) A prototype video and data viewer for the Delft instrumented bicycle data.

DynamicistToolKit (https://github.com/moorepants/DynamicistToolKit) (Python) A clearing house for all the generic functions and classes that I write that may be useful across all the work I do.

HumanControl (https://github.com/moorepants/HumanControl) (Matlab) An implementation of our bicycle human control model from [HMH12] and Chapter *Control*. It computes the controller parameters for most bicycles and most speeds, simulates the model during lane changes, and computes a handling quality metric.

MotionCapture (https://github.com/moorepants/DynamicistToolKit) (Python & Matlab) A Matlab GUI tool for interactively exploring the data from the bicycle motion capture experiments and python tools for basic statistics.

Yeadon (http://pypi.python.org/pypi/yeadon) (Python) [Dem11] A program that computes the inertia of a human using the method from [Yea90b].

This software stack is built upon several languages and software packages including: Python (http://www.python.org), NumPy (http://www.numpy.org), SciPy (http://www.scipy.org), Matplotlib (http://matplotlib.sourceforge.net/), PyTables (http://www.pytables.org), Pandas (http://pandas.pydata.org/), Uncertainties (http://pypi.python.org/pypi/uncertainties/), SymPy (http://www.sympy.org), Autolev (http://www.autolev.com), Matlab (http://www.mathworks.com/products/matlab/). Each software package will have a git tag called `dissertation` to pin it to the version used to generate all the results in the text.

1.2.3 Data

During the experimental studies, I've collected a fair amount of data and have worked to provide at least the raw data from the experimental studies with enough meta data for it to be reusable. Also, the data is used directly with the software packages above. All of the data described below is accessible through the bicycle data page on our lab website: http://biosport.ucdavis.edu/research-projects/bicycle/data.

Physical Parameters The physical parameter data consists of measured values, such as geometry and mass, of both the bicycles and the riders.

Delft Instrumented Bicycle This data is in the form of comma separated text files with the time histories of the sensors and accompanying meta data in the header of each file. The various treadmill experiments with two riders are included. This includes video data for each of the runs.

Motion Capture This data set includes Matlab mat files for each run for several days of experimenting with several riders on the treadmill. There is also video data for a good portion of the runs.

Steer Torque Experiments There is video data for each run and also the manually derived comma separated value text file with the torque values determined from the video.

Identification Experiments This data is available both as raw data mat files with included meta data for each run and as a single HDF5 database which stores the time histories of the sensors in multiple arrays and the meta data in tables. Video data of all the runs were also recorded.

Photos I've taken extensive photo documentation of the instrumentation construction and the experiments. The albums are divided into ones of the work done at UC Davis (http://picasaweb.google.com/moorepants/BicycleDynamics) and the work done at TU Delft (http://picasaweb.google.com/moorepants/BicycleDynamicsTUDelft).

1.3 Dissertation website

I decided to publish my dissertation publicly on the internet from the day I started writing it. The first reason for this is that I want to take full advantage of the ability the web offers for conveying ideas and information, whether it be a video or an interactive program. Paper-based publication is a thing of the past and is an unbelievably limited form of sharing, especially in science. Secondly, I want the process of writing my dissertation to be in the open with the ability for anyone to offer comments, suggestions and edits. Dissertations are traditionally considered to be the work of a single individual, but that is never true. All the research we do as scientists is built upon the works of others and rarely does anyone produce their work without the help of others. Dissertations in the USA are typically very individualistically oriented but I've begun to believe that we should strive to move away from the idea that some work is only due to one person and embrace the fact that we need help from many people to complete something like a dissertation for a doctoral degree. So it is best to be collaborative from the beginning with a sufficient mechanism to provide credit where credit is due. I also want this work to be the best it can be, and if others are interested in helping me make it that way then an interactive website is a platform that is capable of promoting this.

I desired to follow these basic rules when writing my dissertation:

- The content should be written presentation format neutral.
- The primary presentation view is through a web browser, but a static PDF version is also available to suit UCD's archaic submission rules.
- The source code for all the figures, animations, and interactive bits should be included with the dissertation.
- The experimentally collected data should all be available for download and use by others.
- Software tools should be developed if at all possible, instead of disconnected scripts.

Based on these goals, I choose the Sphinx (http://sphinx.pocoo.org/) publishing platform for my dissertation. The text source, which is written in reStructuredText, is available along with the source code for the figures at https://github.com/moorepants/dissertation. The HTML version can be viewed and the PDF version downloaded at http://moorepants.github.com/dissertation

1.4 Writing Style

I generally find scientific writing in my field to be extremely dry. We've developed a collective style that removes any material that isn't technical from the articles and this in turn causes us to gloss over the fact that people are behind all of the reported research. These people have ideas, struggles, mishaps, revelations, and sometimes even fun. But these things weren't always hidden. Early engineering articles ended with lengthy personal conversations between the reviewers and the authors ([Wil51], [Kon55]) and include much more artistic and beautiful illustrations. Page limits in journal and conference articles force today's writer to make their writing as dry as possible to maximize the amount of technical content. I'm no writing ace, but have decided to inject some of the humanism that comes along with a project than spans seven years of ones life into this text. I mostly corralled these ramblings in the prefaces and footnotes of the chapters, but some has sneaked into the drier areas too. I hope that these asides give some idea of how all of this work developed and who to attribute the ideas and labor to along with breaking up the monotony of the technical parts of the text. I figured that a dissertation will be one of the few writings in my career that provides a chance to do this.

1.5 Attribution

As a child, I was programmed to think that any form of plagiarism was evil: you shouldn't copy anything. But how would we ever make any progress if we didn't copy and improve on what others have done in the past? The work presented here is mostly based on the work that I have done in the past several years, but there are many other people's work that is wrapped up in it. Their writings and thoughts will inevitably be present in this text. I do not claim these as

my own, but they will be required to tell the story of the research. I will do my best to acknowledge everyone's work in this thesis, but there will surely be some that I have forgotten. Please let me know if that is so, and I will remedy it.

1.6 Notation

I attempt to keep notation consistent throughout each chapter, with much of the notation being consistent throughout the dissertation. The extensions chapter has different notation for each model. The notation for the Chapter is given at the end of each Chapter. There are ultimately two notations forms for the bicycle: mine which follows a Kane-like syntax and the one adapted from [MPRS07].

1.7 License

CHAPTER

TWO

INTRODUCTION

2.1 Preface

The bicycle is indeed a curious contraption that has greatly affected the lives of human's since the early 19th century. There are probably more bicycles in the world than any other kind of vehicle. The bicycle has a notable history and it helped pave the way for the industrial revolution, the automobile, the airplane and even played a role in the emancipation of western women. Yet it is often an overlooked item in this day and age, especially in the United States of America, where the automobile is the dominant form of transportation and the bicycle is mostly considered a child's toy. But in other parts of the world the bicycle can be viewed as a person's stepping stone to progress or the most convenient way to get around. And what may be even more special about the bicycle is that in its elegant simplicity it still embodies the solutions to many of the world's transportation problems, whether it be on the congested 12 lane freeways of Los Angeles or in a rural African village.

In my life, I have become an ever stronger proponent of the use of the bicycle as an appropriate mode of transportation. It is the most energy efficient way for a human to travel [WP04]. It has crept into all parts of my life with much of my time being spent thinking about different aspects of bicycles and bicycling. But this dissertation is concerned with how we actually balance on the blasted thing. Balancing, in general, may seem like a trivial task because we can all do it without consciously thinking about it, but the fact that the best engineers in the world are still baffled by the intricacies of balancing human-like robots give an idea of the difficulty of the subject. And to muddle it even more, humans are capable of much more advanced balancing acts like tight rope walking in which we invoke our *very* active control. Riding a bicycle falls somewhere between simply standing and these more extreme acts. The bicycle effectively disconnects us from the ground and forces us to use different control strategies to stay upright. The bicycle's complex dynamics, the difficulty of the task, limited control actuation methods, and the ubiquity of the machine make the bicycle an ideal candidate platform for human control studies.

2.2 The Bicycle and Rider as a Dynamic System

The bicycle can be classified as a lightweight single track vehicle that is fundamentally made up of four components: two wheels, a front frame, and a rear frame. The wheels are connected to the respective frames by revolute joints and the two frames are connected to one another by a revolute joint such that the wheels are in-line with one another. This revolute joint between the two frames is necessary for balance and directional control of the vehicle. It is easy to show that locking the steering on a bicycle almost completely removes its ability to balance or be balanced, and certainly to be guided in a desired direction, no matter how the rider moves their body.

The bicycle has been studied by many scientists over the years. It is a rich dynamic system that is difficult to model accurately. [MPRS07] did an excellent job of sorting through 140 years of bicycle dynamics papers and providing a benchmarked bicycle model that finally verified the correct linearized equations of motion of the basic model, usually attributed as the Whipple Model [Whi99]. The model is able to predict both the non-minimum phase behavior and speed dependent stability and is now considered the foundation to all more detailed models.

I'll briefly mention some of the common bicycle models and do so by dividing them into two main categories: models that do not exhibit open loop stability and models that do. All of these models can be extended by adding additional dynamics such as tire-road interactions, frame flexibility, and human biomechanics. These extensions can have effects on the stability and control of the complete system.

2.2.1 Simple Models

Typically a one degree of freedom model that produces a roll equation of motion is used to model a bicycle in its most basic form. This model has been derived and analyzed by many including, but not limited to, [TY48], [Kar04], and [ASKL05]. These models do not have great fidelity with regard to predicting the bicycle's open-loop, speed-dependent stability but they are able to predict the non-minimum phase behavior. This situates them to be good candidates for basic control studies ([Get94], [CHA96], [Kar04], [ASKL05], [LS06]) as they predict the necessity of steering into the roll for stabilization and control. Controllers based on these models have also been successfully implemented on actual experimental control models [STW02] with some success. Beyond this paragraph, I will not be discussing these low order models any further.

2.2.2 Whipple Model

The lowest order model that has had some reasonable experimental validation [KSM08] is one which is able to predict speed dependent stability, and includes a complete physical description of the four basic rigid bodies that constitute a bicycle. The model is now typically referred to as the "Whipple Model". This is in honor of Francis J. W. Whipple, the first author to publish a correct derivation of the linear equations of motion of this particular bicycle model [Whi99]. This model will be used as the basis for all further studies proposed in this dissertation. Many researchers over the past century have attempted to derive and analyze this model but very few have been successful. [MPRS07] give a complete historical review of uncontrolled bicycle research which made use of the historical comparisons in the thesis by [Han88]. [MPRS07] also benchmarked the Whipple Model by deriving the linearized equations of motion by using four independent methods (two independent pen and paper calculations and two different dynamic software packages). Furthermore, [BMCP07] benchmarked various torque-free circular motions in the non-linear case with two additional independent derivations of the equations of motion. There has been a series of recent validation attempts ([Koo06], [KSM08], [KS09], [Ste09], [ER10], [ER11]) for the Whipple model in particular and the evidence for it's ability to describe the motion of the bicycle with no rider around the stable speed range is strong. This is important because it may be the lowest order model with the ability to predict the dynamics. In this dissertation, I make use of both the [MPRS07] model and my own derivation of the Whipple Model.

2.2.3 Complex Models

With modern dynamic tools it is relatively easy to add more degrees of freedom, flexible bodies, and more detailed forcing functions to the Whipple model with the intent of pushing the model's ability to accurately predict bicycle and motorcycle motion. For example, the typical motorcycle is modeled with more realistic empirically derived tire-road interactions and a full suspension.

The most cited models typically have some reference to the model developed by Robin S. Sharp [Sha71]. This model extends the Whipple model concepts to include tire compliance and side slip. The model has been refined over the years to improve accuracy by adding frame flexibility, rider models and improving the tire models [SLG99] , [SL01], [SEL04] with Pacejka-style [Pac06] tire models being a popular choice. Sharp was also the first to give names to the eigenmodes of the Whipple Model [Sha75]. He and David Limebeer give a review of bicycle and motorcycle modeling in [LS06] covering much of their work. Other notable studies include ones developed by [Koe83] and the Italian group lead by Vittore Cossalter [CL02].

The motorcycle researchers have more experimental data validation of their models than in bicycle studies, and their more complicated models in general do a very good job of predicting the high speed motorcycle dynamics[1]. This is

[1] For example, [BBCL03] is great example.

due to the fact that more work has been done to understand and measure the phenomena, that the high speed dynamics are easier to predict, and that the human's biomechanical motions play a smaller role in the vehicle motion.

2.3 Conclusion

Albert Einstein once said "Any intelligent fool can make things bigger, more complex, and more violent. It takes a touch of genius - and a lot of courage - to move in the opposite direction." With the wide variety of models available, I've generally taken the approach of trying to use the simplest models possible to predict the measured motion in my experiments rather than adding great complexity. In my case, this model is often the Whipple model[2] with or without various rider biomechanical models which attempt to account for the large affect the rider's freedom of movement can contribute to the system dynamics.

[2] Not to say that the Whipple Model is not complex, au contraire.

CHAPTER

THREE

BICYCLE EQUATIONS OF MOTION

3.1 Preface

Attempting to derive the equations of motion of the Whipple bicycle model was the trigger which solidified my graduate research topic. I attempted the derivation for my class project in Mont Hubbard's winter 2006 multi-body dynamics class and struggled with it well into the summer before finally getting a mostly correct answer. After the fact, I realized much of my pain was caused by a single missing apostrophe in my Autolev source code[1]. Luckily another student in the class, Thomas Englehardt, had also derived the equations and helped me debug by sharing his code and going over his methods. Even then, it turned out that my original equations weren't "exactly" correct and it wasn't until Luke Peterson joined our lab and got the bicycle dynamics itch did I get the bugs sorted out in my derivation with his help. Conversations and collaboration with Luke have improved the derivation significantly and influence much of what follows. Luke has also continued to improve the derivation with the goal of printing the first compact symbolic result. With careful parameterization and selection of generalized speeds, the non-linear equations may be able to be put into human readable form.

3.2 Non-linear Equations of Motion

The Whipple Model is the foundation of all the models presented in this dissertation. This section details derivation of the non-linear equations of motion using Kane's method [KL85][2]. The non-linear equations of motion are algebraically unwieldy and no one so far has publicly printed them in a form compact enough to print on reasonably sized paper, and certainly not in a form suitable for any in-depth analytical understanding as pointed out in [MPRS07]. My methodology relies heavily on computer aided algebra to do the bookkeeping in the derivation, so I will only describe the necessary details to correctly derive the equations, leaving the algebra, trigonometry and calculus to the computer. The symbolic equations of motion herein were originally developed using Autolev [KL00], a proprietary and now defunct software package for symbolically deriving equations of motion for multi-body systems. I've since used the open source software SymPy (http://sympy.org) to derive the equations with the help of the included `mechanics` package which was developed in our lab to provide a software package suitable for academia with capabilities similar to Autolev[3]. The input code for both software packages are available in the `src/eom` directory of the dissertation source files.

[1] These programming growing pangs were especially harsh with Autolev. The program is unfortunately missing virtually all of the useful tools and paradigms found in full-featured programming languages.

[2] Kane himself has done work on bicycle and motorcycle models and made use of his method to derive the equations of motion [Kan75], [Kan77a], [Kan77b], [Kan78], [MK79]. Furthermore, [VZ75] derived linear equations of motion of the bicycle and models developed with AutoSim also employ Kane's method [Say90], [SLG99].

[3] Luke and I have dreamed of developing an open source version of Autolev for years and that has finally culminated through primarily Luke and Gilbert Gede's efforts in the creation of sympy.physics.mechanics (http://www.sympy.org).

3.2.1 Model Description

The *Whipple Bicycle Model* [Whi99] is defined by this set of assumptions:

- The model is made up of four rigid bodies: the rear frame (the main bicycle frame which may or may not include a rigid rider), the front frame (typically the fork and handlebar assembly), and two wheels.
- The bodies are connected to each other by frictionless revolute joints.
- The wheels have knife edges and contact the ground under pure rolling with no side-slip.
- The complete bicycle is assumed to be laterally symmetric.
- The bicycle rolls on flat ground.

[ASKL05], [LS06], and [MPRS07] all provide excellent overviews of the model, its history, and its features.

Unfortunately the word "model" is often ambiguous. I will attempt to be as precise as possible with my wording. For this chapter, I consider a dynamic model, such as the *Whipple Bicycle Model*, to be equivalent to another dynamic model if at least the minimal set of equations of motions are the same (i.e. they give the same result when evaluated at a particular configuration and state of interest). This implies that the Whipple Bicycle Model linearized about the nominal configuration is a different model than the non-linear *Whipple Bicycle Model*. I will try to be explicit when discussing the various models.

I will use the following terminology and labels for the four rigid bodies, see *Figure 3.2*:

Rear Frame, C The main bicycle frame which may include parts or all of the rider.

Rear Wheel, D The rear wheel of the bicycle.

Front Frame, E The fork and handlebar assembly.

Front Wheel, F The front wheel of the bicycle.

3.2.2 Parameterization

The benchmark derivation of the linear Whipple model [MPRS07] about the nominal configuration uses a non-minimal set of parameters based on typical geometric parameters and inertia definitions using an inertially fixed reference frame in which the x axis points forward and the z axis points down, *Figure 3.1*. The *nominal configuration* is defined as the configuration when the steering angle is zero and the bicycle is upright with respect to gravity and the ground plane. The parameters presented in [MPRS07] are not necessarily the best choice of parameters, especially when looking at the model from a non-linear perspective, as they are not the simplest set nor a minimal set. For example, the benchmark parameters can be reduced in number by making use of gyrostats, see [Sha08] for an implementation. Choosing a minimum, constant set of parameters can certainly reduce the complexity of the resulting non-linear equations. In this derivation, I use a parameterization with different geometry and inertial definitions to facilitate a more intuitive non-linear derivation, but do not make use of gyrostats to reduce the number of parameters.

3.2.3 Geometry

The geometry of the Whipple model can be parameterized in an infinite number of ways. It is typical and often natural to define the geometry with respect to the descriptions of bicycle geometry used in the bicycle fabrication industry, such as wheel diameter, head tube angle, trail and or rake, *Figure 3.1*. Choices of parameterizations like these create unnecessary complications when developing the non-linear equations of motion because they are typically defined with respect to only the nominal configuration of the bicycle and are not constant with respect to the system configuration.

With that in mind and after trying various parameterizations, I use geometric formulation presented by [Psi79][4]. The wheels are described by their radius ($r_{F,R} \geq 0$) and the remaining geometry is defined by three distances, all of which

[4] The coordinates are also used by [FSR90], among others.

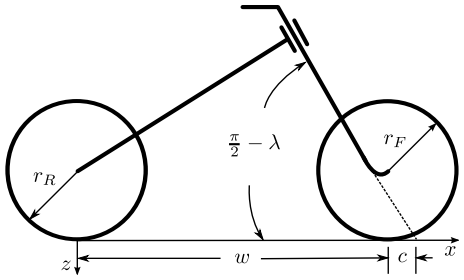

Figure 3.1: The typical parameterization of the fundamental bicycle's geometry given in [MPRS07]. The wheelbase w, trail c, steer axis tilt λ, front wheel radius r_F, and rear wheel radius r_R are shown.

are configuration invariant. The distance d_1 is the offset to the center of the rear wheel from the steer axis and d_3 is the offset of the front wheel from the steering axis. d_2 is then the distance between the wheel centers as measured along the steer axis. *Figure 3.2* gives a complete visual description of the bodies and the geometry.

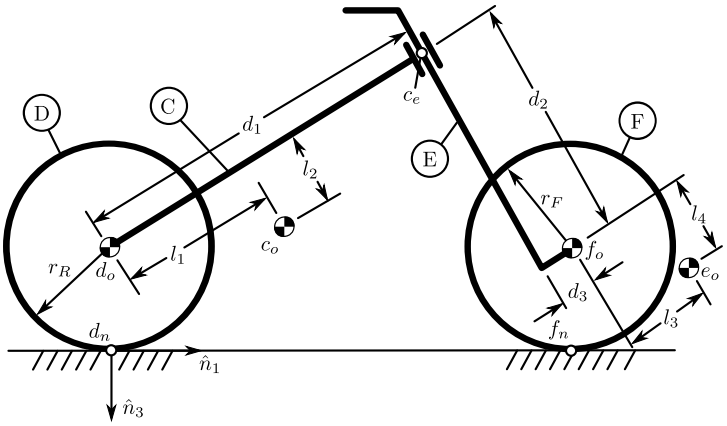

Figure 3.2: The bicycle in the nominal configuration. The rigid bodies are the rear frame C, rear wheel D, front frame E, and front wheel F. The geometric parameters and important points are also shown.

3.2.4 Generalized Coordinates

The bicycle is completely configured in a Newtonian reference frame by nine generalized coordinates: six coordinates locate and orient the rear frame in space and three additional coordinates are needed for the three revolute joints connecting the front frame and wheels to the rear frame. I made use of the SAE vehicle dynamics reference frame standard and all rotations are are defined as positive right-handed which makes the configuration identical to that in [MPRS07][5]. The rotation matrices are defined as

$$^a\bar{v} = {}^N\mathbf{R}^A\, {}^n\bar{v} \tag{3.1}$$

where $^n\bar{v}$ is a vector expressed in the N frame and $^a\bar{v}$ is the same vector expressed in the A frame.

To configure the bicycle, begin by locating the point that follows the rear wheel contact in the ground plane of the Newtonian reference frame, N, with longitudinal and lateral coordinates q_1 and q_2, respectively, see *Figure 3.3*. Then orient the rear frame, C, with respect to the Newtonian reference frame through a body-fixed 3-1-2 rotation defining

[5] I don't necessarily agree that this is a great standard to follow, because it creates much unessary confusion when defining and mapping between parameterizations. The three axis pointing upward would be less error prone because a bicycle is never below the ground plane, except maybe in an academic.

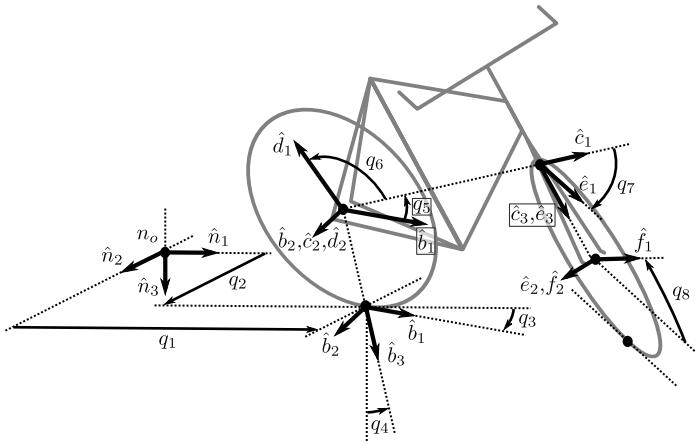

Figure 3.3: The bicycle in a general configuration showing each of the eight generalized coordinates.

the yaw angle, q_3, the roll angle, q_4, and the pitch angle, q_5. The intermediate frames yaw, A, and roll, B, are implicitly generated. The rotation matrix of C relative to N is then

$$
{}^N\mathbf{R}^C = \begin{bmatrix} c_3c_5 - s_3s_4s_5 & s_4s_5c_3 + s_3c_5 & -s_5c_4 \\ -s_3c_4 & c_3c_4 & s_4 \\ s_5c_3 + s_3s_4c_5 & s_3s_5 - s_4c_3c_5 & c_4c_5 \end{bmatrix} \tag{3.2}
$$

where the notation $s_i = \sin(q_i)$ and $c_i = \cos(q_i)$ in (3.2) and also all subsequent equations in this chapter.

The rear wheel, D, rotates with respect to the rear frame about the $\hat{c}_2$ axis through q_6.

$$
{}^C\mathbf{R}^D = \begin{bmatrix} c_6 & 0 & -s_6 \\ 0 & 1 & 0 \\ s_6 & 0 & c_6 \end{bmatrix} \tag{3.3}
$$

The front frame, E, rotates with respect to the rear frame about the $\hat{c}_3$ axis through the steering angle, q_7.

$$
{}^C\mathbf{R}^E = \begin{bmatrix} c_7 & s_7 & 0 \\ -s_7 & c_7 & 0 \\ 0 & 0 & 1 \end{bmatrix} \tag{3.4}
$$

Finally, the front wheel, F, rotates with respect to the front frame through q_8 about the $\hat{e}_2$ axis.

$$
{}^E\mathbf{R}^F = \begin{bmatrix} c_8 & 0 & -s_8 \\ 0 & 1 & 0 \\ s_8 & 0 & c_8 \end{bmatrix} \tag{3.5}
$$

The first two coordinates locate the rear wheel contact point in the Newtonian reference frame and the remaining six coordinates orient the four rigid bodies within the Newtonian reference frame.

The positions of the various points on the bicycle must be defined with respect to the Newtonian reference frame. There are six primary points of interest: the four mass centers, d_o, c_o, e_o, f_o, and the two points fixed on the wheels which are instantaneously in contact with the ground, d_n, f_n[6].

The mass center of the rear wheel, d_o, is assumed to be at the center of the wheel and is located by

$$
\bar{r}^{d_o/n_o} = q_1\hat{n}_1 + q_2\hat{n}_2 - r_R\hat{b}_3 \tag{3.6}
$$

[6] The bicycle wheels' points of contact are abstract points in dynamics. At any instant there are two coincident points at the contact location: one on the wheel and one on the ground. If no-slip rolling is assumed, both of these points are motionless, i.e. their velocities are zero. These points are distinctly different from the points that trace out the path on the ground of the wheel contact locations through time. Those points are not motionless and therefore do have a velocity.

The rear frame mass center, c_o, is located by two additional parameters

$$\bar{r}^{c_o/d_o} = l_1\hat{c}_1 + l_2\hat{c}_3 \tag{3.7}$$

For convenience, define an additional point on the steer axis, c_e, such that

$$\bar{r}^{c_e/d_o} = d_1\hat{c}_1 \tag{3.8}$$

The mass center of the front wheel, f_o, is then located by:

$$\bar{r}^{f_o/c_e} = d_2\hat{c}_3 + d_3\hat{e}_1 \tag{3.9}$$

The front frame mass center, e_o, is located by two more additional parameters:

$$\bar{r}^{e_o/f_o} = l_3\hat{e}_1 + l_4\hat{e}_3 \tag{3.10}$$

The location of the point on the rear wheel instantaneously in contact with the ground in the Newtonian frame is then defined by

$$\bar{r}^{d_n/d_o} = r_F\hat{b}_3 \tag{3.11}$$

The location of the front wheel contact point is less trivial. The vector from the front wheel center to the contact point is defined as

$$\bar{r}^{f_n/f_o} = r_F\left(\frac{(\hat{e}_2 \times \hat{a}_3) \times \hat{e}_2}{||(\hat{e}_2 \times \hat{a}_3) \times \hat{e}_2||}\right) \tag{3.12}$$

$$\bar{r}^{f_n/f_o} = r_F(s_4s_7 - s_5c_4c_7)/(c_4^2c_5^2 + (s_4s_7 - s_5c_4c_7)^2)^{1/2}\hat{e}_1 + r_Fc_4c_5/(c_4^2c_5^2 + (s_4s_7 - s_5c_4c_7)^2)^{1/2}\hat{e}_3$$

Here the triple cross product divided by its magnitude represents the unit vector pointing from the front wheel center to the point on the front wheel instantaneously in contact with the ground. [BMCP07] give a good explanation and diagram. Another description of this vector is in terms of dot products, i.e. subtract the $\hat{n}_3$ component of $\hat{e}_2$ from $\hat{n}_3$ to get a vector that points from the front wheel center to the contact point.

$$\bar{r}^{f_n/f_o} = r_F\left(\frac{\hat{a}_3 - (\hat{e}_2 \cdot \hat{a}_3)\hat{e}_2}{||\hat{a}_3 - (\hat{e}_2 \cdot \hat{a}_3)\hat{e}_2||}\right) \tag{3.13}$$

This is easily shown to be equivalent to (3.12) by writing the triple cross product as sum of dot products.

3.2.5 Holonomic Constraints

Two holonomic configuration constraints, arising from the fact that both wheels must touch the ground, complicate the model derivation. The first holonomic equation is obviated by definition of the rear wheel center (3.6). This enforces that the rear wheel contact point cannot have an displacement in the $\hat{n}_3$ direction[7]. The second holonomic constraint is enforced by requiring the front wheel to touch the ground plane. The constraint is characterized by a non-linear relationship between the roll angle q_4, steer angle q_7 and pitch angle q_5.

$$\begin{aligned}\bar{r}^{f_n/d_n} \cdot \hat{a}_3 =& d_2c_4c_5 - d_1s_5c_4 + r_Rc_4 + r_Fc_4^2c_5^2/(c_4^2c_5^2 + (s_4s_7 - s_5c_4c_7)^2)^{1/2} - \\ & (s_4s_7 - s_5c_4c_7)(d_3 + r_F(s_4s_7 - s_5c_4c_7)/(c_4^2c_5^2 + (s_4s_7 - s_5c_4c_7)^2)^{1/2}) = 0\end{aligned} \tag{3.14}$$

In this equation, pitch, q_6, is defined as the dependent coordinate. The choice of pitch has to do with the fact that for "normal" bicycle configurations, pitch is practically constant. This is not universal and it may be smart to choose the dependent coordinate differently for other cases. The constraint equation can actually be formulated into a quartic in the sine of the pitch ([Psi79], [PH08a]) which does have an analytic, albeit lengthy, solution. I do not opt for the analytical solution, so care is needed when simulating and linearizing to properly choose the proper roots associated with this dependent coordinate.

[7] This constraint can readily be modified to accomodate a non-flat ground.

3.2.6 Kinematical Differential Equations

The choice of generalized speeds can significantly reduce the length of the equations of motion [MK96]. This is beneficial for both working with the analytical forms of the equations of motion and the efficiency in computation. Even though this is true, little effort was spent in selecting optimal generalized speeds, as the analytical form of the equations of motion of this system would be difficult to interpret regardless of the choice and because computational speed was of little concern. For $i = 1, \ldots, 8$ simply choose the generalized speeds to be equal to the time derivatives of the generalized coordinates

$$u_i = \dot{q}_i \tag{3.15}$$

3.2.7 Velocity

The angular and linear velocities of each rigid body are required for computing the partial velocities and accelerations used in Kane's method. Also, the velocities of the points on the wheels at the ground contact points are needed for the development of the nonholomic constraints. The angular velocity of the rear frame, C, in N is

$${}^N\bar{\omega}^C = (c_5u_4 - s_5c_4u_3)\hat{c}_1 + (u_5 + s_4u_3)\hat{c}_2 + (s_5u_4 + c_4c_5u_3)\hat{c}_3 \tag{3.16}$$

Both the front frame and the rear wheel are connected to the bicycle rear frame by simple revolute joints, so the angular velocities are simply

$${}^C\bar{\omega}^D = u_6\hat{c}_2 \tag{3.17}$$

and

$${}^C\bar{\omega}^E = u_7\hat{c}_3 \tag{3.18}$$

The front wheel has angular velocity relative to the front frame

$${}^E\bar{\omega}^F = u_8\hat{e}_2 \tag{3.19}$$

The angular velocity of any of the bodies can now be computed with respect to the Newtonian reference frame. For example,

$${}^N\bar{\omega}^F = {}^N\bar{\omega}^C + {}^C\bar{\omega}^E + {}^E\bar{\omega}^F \tag{3.20}$$

which expands to

$$\begin{aligned} {}^N\bar{\omega}^F =& (s_7c_8u_5 - s_8u_7 - (s_5s_8 - c_5c_7c_8)u_4 - (s_8c_4c_5 - c_8(s_4s_7 - s_5c_4c_7))u_3)\hat{f}_1 + \\ & (u_8 + c_7u_5 + (s_4c_7 + s_5s_7c_4)u_3 - s_7c_5u_4)\hat{f}_2 + \\ & (c_8u_7 + s_7s_8u_5 + (s_5c_8 + s_8c_5c_7)u_4 + (c_4c_5c_8 + s_8(s_4s_7 - s_5c_4c_7))u_3)\hat{f}_3 \end{aligned} \tag{3.21}$$

Using the angular velocities and the position vectors, the velocities of the mass centers can be computed. Starting with mass center of the rear wheel

$${}^N\bar{v}^{d_o} = \frac{d}{dt}\left(\bar{r}^{d_o/n_o}\right) = u_1\hat{n}_1 + u_2\hat{n}_2 - r_Rs_4u_3\hat{b}_1 + r_Ru_4\hat{b}_2 \tag{3.22}$$

The remaining velocities can be computed by taking advantage of the fact that various pairs of points are fixed on the same rigid body. The mass centers of the rear wheel, d_o and the rear frame, c_o, and the steer axis point, c_e, (*Figure 3.2*) all lie on the rear frame.

$${}^N\bar{v}^{c_o} = {}^N\bar{v}^{d_o} + {}^N\bar{\omega}^C \times \bar{r}^{c_o/d_o} \tag{3.23}$$

where

$${}^N\bar{\omega}^C \times \bar{r}^{c_o/d_o} = l_2(u_5 + s_4u_3)\hat{c}_1 + (l_1(s_5u_4 + c_4c_5u_3) - l_2(c_5u_4 - s_5c_4u_3))\hat{c}_2 - l_1(u_5 + s_4u_3)\hat{c}_3$$

and

$$^N\bar{v}^{c_e} = {}^N\bar{v}^{d_o} + {}^N\bar{\omega}^C \times \bar{r}^{c_e/d_o} \tag{3.24}$$

where

$$^N\bar{\omega}^C \times \bar{r}^{c_e/d_o} = d_1(s_5u_4 + c_4c_5u_3)\hat{c}_2 - d_1(u_5 + s_4u_3)\hat{c}_3$$

The velocity of the front wheel mass center is computed with respect to the steer axis point as they both lie on the front frame

$$^N\bar{v}^{f_o} = {}^N\bar{v}^{c_e} + {}^N\bar{\omega}^E \times \bar{r}^{f_o/c_e} \tag{3.25}$$

where

$$\begin{aligned}^N\bar{\omega}^E \times \bar{r}^{f_o/c_e} =& - d_2(s_7c_5u_4 - c_7u_5 - (s_4c_7 + s_5s_7c_4)u_3)\hat{e}_1 + \\ & (d_3(u_7 + s_5u_4 + c_4c_5u_3) - d_2(s_7u_5 + c_5c_7u_4 + (s_4s_7 - s_5c_4c_7)u_3))\hat{e}_2 + \\ & d_3(s_7c_5u_4 - c_7u_5 - (s_4c_7 + s_5s_7c_4)u_3)\hat{e}_3\end{aligned}$$

Then the velocity of the front frame mass center is similarly

$$^N\bar{v}^{e_o} = {}^N\bar{v}^{f_o} + {}^N\bar{\omega}^E \times \bar{r}^{e_o/f_o} \tag{3.26}$$

where

$$\begin{aligned}^N\bar{\omega}^E \times \bar{r}^{e_o/f_o} =& - l_4(s_7c_5u_4 - c_7u_5 - (s_4c_7 + s_5s_7c_4)u_3)\hat{e}_1 + \\ & (l_3(u_7 + s_5u_4 + c_4c_5u_3) - l_4(s_7u_5 + c_5c_7u_4 + (s_4s_7 - s_5c_4c_7)u_3))\hat{e}_2 + \\ & l_3(s_7c_5u_4 - c_7u_5 - (s_4c_7 + s_5s_7c_4)u_3)\hat{e}_3\end{aligned}$$

The velocity of the contact points on the wheel are needed to enforce the no-slip condition and can be computed with respect to the rear and front wheel centers. The rear contact point is

$$^N\bar{v}^{d_n} = {}^N\bar{v}^{d_o} + {}^N\bar{\omega}^D \times \bar{r}^{d_n/d_o} \tag{3.27}$$

where

$$^N\bar{\omega}^D \times \bar{r}^{d_n/d_o} = r_R(u_5 + u_6 + s_4u_3)\hat{b}_1 - r_Ru_4\hat{b}_2$$

which simplifies to

$$^N\bar{v}^{d_n} = r_R(u_5 + u_6)\hat{b}_1 + u_1\hat{n}_1 + u_2\hat{n}_2 \tag{3.28}$$

The front wheel contact velocity is

$$^N\bar{v}^{f_n} = {}^N\bar{v}^{f_o} + {}^N\bar{\omega}^F \times \bar{r}^{f_n/f_o} \tag{3.29}$$

where

$$\begin{aligned}^N\bar{\omega}^F \times \bar{r}^{f_n/f_o} =& r_F/(c_4^2c_5^2 + (s_4s_7 - s_5c_4c_7)^2)^{1/2} \\ & [-c_4c_5(s_7c_5u_4 - u_8 - c_7u_5 - (s_4c_7 + s_5s_7c_4)u_3)\hat{e}_1 - \\ & (c_4c_7u_4 + s_7c_4c_5u_5 - s_4s_5s_7u_4 - (s_4s_7 - s_5c_4c_7)u_7)\hat{e}_2 + \\ & (s_4s_7 - s_5c_4c_7)(s_7c_5u_4 - u_8 - c_7u_5 - (s_4c_7 + s_5s_7c_4)u_3)\hat{e}_3]\end{aligned}$$

3.2.8 Acceleration

The angular acceleration of each body along with the linear acceleration of each mass center are required to form F_r^* in Kane's equations. The angular acceleration of the rear frame, C, in N is

$$\begin{aligned}{}^N\bar{\alpha}^C =&(s_4s_5u_3u_4 + c_5\dot{u}_4 - s_5u_4u_5 - c_4c_5u_3u_5 - s_5c_4\dot{u}_3)\hat{c}_1+\\ &(c_4u_3u_4 + \dot{u}_5 + s_4\dot{u}_3)\hat{c}_2+\\ &(c_5u_4u_5 + s_5\dot{u}_4 + c_4c_5\dot{u}_3 - s_4c_5u_3u_4 - s_5c_4u_3u_5)\hat{c}_3\end{aligned} \tag{3.30}$$

The remaining bodies' angular accelerations follow from simple rotations

$${}^C\bar{\alpha}^D = \dot{u}_6\hat{c}_2 \tag{3.31}$$

$${}^C\bar{\alpha}^E = \dot{u}_7\hat{c}_3 \tag{3.32}$$

$${}^E\bar{\alpha}^F = \dot{u}_8\hat{e}_2 \tag{3.33}$$

The linear acceleration of each mass center can then be computed. The acceleration of the rear wheel center of mass is

$${}^N\bar{a}^{d_o} = \frac{d}{dt}\left({}^N\bar{v}^{d_o}\right) \tag{3.34}$$

$${}^N\bar{a}^{d_o} = \dot{u}_1\hat{n}_1 + \dot{u}_2\hat{n}_2 - r_Rs_4u_3^2\hat{a}_2 - r_R(2c_4u_3u_4 + s_4\dot{u}_3)\hat{b}_1 + r_R\dot{u}_4\hat{b}_2 + r_Ru_4^2\hat{b}_3$$

The remaining accelerations are computed using the analogous two point relationship utilized for the velocities. The acceleration of the rear frame center of mass is

$${}^N\bar{a}^{c_o} = {}^N\bar{a}^{d_o} + {}^N\bar{\omega}^C \times ({}^N\bar{\omega}^C \times \bar{r}^{c_o/d_o}) + {}^N\bar{\alpha}^C \times \bar{r}^{c_o/d_o} \tag{3.35}$$

where

$$\begin{aligned}{}^N\bar{\omega}^C \times ({}^N\bar{\omega}^C \times \bar{r}^{c_o/d_o}) =&(-l_1(u_5 + s_4u_3)^2 - (s_5u_4 + c_4c_5u_3)(l_1(s_5u_4 + c_4c_5u_3)-\\ &l_2(c_5u_4 - s_5c_4u_3)))\hat{c}_1+\\ &(u_5 + s_4u_3)(l_2(s_5u_4 + c_4c_5u_3) + l_1(c_5u_4 - s_5c_4u_3))\hat{c}_2+\\ &((c_5u_4 - s_5c_4u_3)(l_1(s_5u_4 + c_4c_5u_3) - l_2(c_5u_4 - s_5c_4u_3))-\\ &l_2(u_5 + s_4u_3)^2)\hat{c}_3\end{aligned}$$

and

$$\begin{aligned}{}^N\bar{\alpha}^C \times \bar{r}^{c_o/d_o} =&l_2(c_4u_3u_4 + \dot{u}_5 + s_4\dot{u}_3)\hat{c}_1+\\ &(-l_1(s_4c_5u_3u_4 + s_5c_4u_3u_5 - c_5u_4u_5 - s_5\dot{u}_4 - c_4c_5\dot{u}_3)-\\ &l_2(s_4s_5u_3u_4 + c_5\dot{u}_4 - s_5u_4u_5 - c_4c_5u_3u_5 - s_5c_4\dot{u}_3))\hat{c}_2-\\ &l_1(c_4u_3u_4 + \dot{u}_5 + s_4\dot{u}_3)\hat{c}_3\end{aligned}$$

The acceleration of the steer axis point is

$${}^N\bar{a}^{c_e} = {}^N\bar{a}^{d_o} + {}^N\bar{\omega}^C \times ({}^N\bar{\omega}^C \times \bar{r}^{c_e/d_o}) + {}^N\bar{\alpha}^C \times \bar{r}^{c_e/d_o} \tag{3.36}$$

where

$$\begin{aligned}{}^N\bar{\omega}^C \times ({}^N\bar{\omega}^C \times \bar{r}^{c_e/d_o}) =& - d_1((u_5 + s_4u_3)^2 + (s_5u_4 + c_4c_5u_3)^2)\hat{c}_1+\\ &d_1(u_5 + s_4u_3)(c_5u_4 - s_5c_4u_3)\hat{c}_2+\\ &d_1(s_5u_4 + c_4c_5u_3)(c_5u_4 - s_5c_4u_3)\hat{c}_3\end{aligned}$$

and

$$
\begin{aligned}
{}^N\bar{\alpha}^C \times \bar{r}^{c_e/d_o} = &- d_1(s_4c_5u_3u_4 + s_5c_4u_3u_5 - c_5u_4u_5 - s_5\dot{u}_4 - c_4c_5\dot{u}_3)\hat{c}_2 - \\
&d_1(c_4u_3u_4 + \dot{u}_5 + s_4\dot{u}_3)\hat{c}_3
\end{aligned}
$$

The acceleration of the front wheel center of mass is

$$
{}^N\bar{a}^{f_o} = {}^N\bar{a}^{c_e} + {}^N\bar{\omega}^E \times ({}^N\bar{\omega}^E \times \bar{r}^{f_o/c_e}) + {}^N\bar{\alpha}^E \times \bar{r}^{f_o/c_e} \tag{3.37}
$$

where

$$
\begin{aligned}
{}^N\bar{\omega}^E \times ({}^N\bar{\omega}^E \times \bar{r}^{f_o/c_e}) = &(-d_3(s_7c_5u_4 - c_7u_5 - (s_4c_7 + s_5s_7c_4)u_3)^2 - \\
&(u_7 + s_5u_4 + c_4c_5u_3)(d_3(u_7 + s_5u_4 + c_4c_5u_3) - \\
&d_2(s_7u_5 + c_5c_7u_4 + (s_4s_7 - s_5c_4c_7)u_3)))\hat{e}_1 - \\
&(s_7c_5u_4 - c_7u_5 - (s_4c_7 + s_5s_7c_4)u_3)(d_2(u_7 + s_5u_4 + c_4c_5u_3) + \\
&d_3(s_7u_5 + c_5c_7u_4 + (s_4s_7 - s_5c_4c_7)u_3))\hat{e}_2 + \\
&((s_7u_5 + c_5c_7u_4 + (s_4s_7 - s_5c_4c_7)u_3)(d_3(u_7 + s_5u_4 + c_4c_5u_3) - \\
&d_2(s_7u_5 + c_5c_7u_4 + (s_4s_7 - s_5c_4c_7)u_3)) - \\
&d_2(s_7c_5u_4 - c_7u_5 - (s_4c_7 + s_5s_7c_4)u_3)^2)\hat{e}_3
\end{aligned}
$$

and

$$
\begin{aligned}
{}^N\bar{\alpha}^E \times \bar{r}^{f_o/c_e} = &- d_2(s_7u_5u_7 + c_5c_7u_4u_7 + u_3(s_4s_7u_7 + s_4s_5s_7u_4 - c_4c_7u_4 - s_5c_4c_7u_7 - s_7c_4c_5u_5) + \\
&s_7c_5\dot{u}_4 - s_5s_7u_4u_5 - c_7\dot{u}_5 - (s_4c_7 + s_5s_7c_4)\dot{u}_3)\hat{e}_1 + \\
&(d_2(s_5c_7u_4u_5 + s_7c_5u_4u_7 - c_7u_5u_7 - u_3(s_4c_7u_7 + s_7c_4u_4 + s_4s_5c_7u_4 + s_5s_7c_4u_7 - \\
&c_4c_5c_7u_5) - s_7\dot{u}_5 - c_5c_7\dot{u}_4 - (s_4s_7 - s_5c_4c_7)\dot{u}_3) - \\
&d_3(s_4c_5u_3u_4 + s_5c_4u_3u_5 - c_5u_4u_5 - \dot{u}_7 - s_5\dot{u}_4 - c_4c_5\dot{u}_3))\hat{e}_2 + \\
&d_3(s_7u_5u_7 + c_5c_7u_4u_7 + u_3(s_4s_7u_7 + s_4s_5s_7u_4 - c_4c_7u_4 - s_5c_4c_7u_7 - s_7c_4c_5u_5) + \\
&s_7c_5\dot{u}_4 - s_5s_7u_4u_5 - c_7\dot{u}_5 - (s_4c_7 + s_5s_7c_4)\dot{u}_3)\hat{e}_3
\end{aligned}
$$

The acceleration of the front frame center of mass is

$$
{}^N\bar{a}^{e_o} = {}^N\bar{a}^{f_o} + {}^N\bar{\omega}^E \times ({}^N\bar{\omega}^E \times \bar{r}^{e_o/f_o}) + {}^N\bar{\alpha}^E \times \bar{r}^{e_o/f_o} \tag{3.38}
$$

where

$$
\begin{aligned}
{}^N\bar{\omega}^E \times ({}^N\bar{\omega}^E \times \bar{r}^{e_o/f_o}) = &(-(d_3 + l_3)(s_7c_5u_4 - c_7u_5 - (s_4c_7 + s_5s_7c_4)u_3)^2 - \\
&(u_7 + s_5u_4 + c_4c_5u_3)((d_3 + l_3)(u_7 + s_5u_4 + c_4c_5u_3) - \\
&d_2(s_7u_5 + c_5c_7u_4 + (s_4s_7 - s_5c_4c_7)u_3) - \\
&l_4(s_7u_5 + c_5c_7u_4 + (s_4s_7 - s_5c_4c_7)u_3)))\hat{e}_1 - \\
&(s_7c_5u_4 - c_7u_5 - (s_4c_7 + s_5s_7c_4)u_3)((d_2 + l_4)(u_7 + s_5u_4 + c_4c_5u_3) + \\
&(d_3 + l_3)(s_7u_5 + c_5c_7u_4 + (s_4s_7 - s_5c_4c_7)u_3))\hat{e}_2 + \\
&((s_7u_5 + c_5c_7u_4 + (s_4s_7 - s_5c_4c_7)u_3)((d_3 + l_3)(u_7 + s_5u_4 + c_4c_5u_3) - \\
&d_2(s_7u_5 + c_5c_7u_4 + (s_4s_7 - s_5c_4c_7)u_3) - \\
&l_4(s_7u_5 + c_5c_7u_4 + (s_4s_7 - s_5c_4c_7)u_3)) - \\
&(d_2 + l_4)(s_7c_5u_4 - c_7u_5 - (s_4c_7 + s_5s_7c_4)u_3)^2)\hat{e}_3
\end{aligned}
$$

and

$$
\begin{aligned}
{}^N\bar{\alpha}^E \times \bar{r}^{e_o/f_o} = &-(d_2+l_4)(s_7u_5u_7 + c_5c_7u_4u_7 + u_3(s_4s_7u_7 + s_4s_5s_7u_4 - c_4c_7u_4 - s_5c_4c_7u_7 - \\
&s_7c_4c_5u_5) + s_7c_5\dot{u}_4 - s_5s_7u_4u_5 - c_7\dot{u}_5 - (s_4c_7 + s_5s_7c_4)\dot{u}_3)\hat{e}_1 + \\
&(d_2(s_5c_7u_4u_5 + s_7c_5u_4u_7 - c_7u_5u_7 - u_3(s_4c_7u_7 + s_7c_4u_4 + s_4s_5c_7u_4 + s_5s_7c_4u_7 - \\
&c_4c_5c_7u_5) - s_7\dot{u}_5 - c_5c_7\dot{u}_4 - (s_4s_7 - s_5c_4c_7)\dot{u}_3) + l_4(s_5c_7u_4u_5 + s_7c_5u_4u_7 - c_7u_5u_7 - \\
&u_3(s_4c_7u_7 + s_7c_4u_4 + s_4s_5c_7u_4 + s_5s_7c_4u_7 - c_4c_5c_7u_5) - s_7\dot{u}_5 - \\
&c_5c_7\dot{u}_4 - (s_4s_7 - s_5c_4c_7)\dot{u}_3) - (d_3+l_3)(s_4c_5u_3u_4 + s_5c_4u_3u_5 - c_5u_4u_5 - \\
&\dot{u}_7 - s_5\dot{u}_4 - c_4c_5\dot{u}_3))\hat{e}_2 + \\
&(d_3+l_3)(s_7u_5u_7 + c_5c_7u_4u_7 + u_3(s_4s_7u_7 + s_4s_5s_7u_4 - c_4c_7u_4 - s_5c_4c_7u_7 - \\
&s_7c_4c_5u_5) + s_7c_5\dot{u}_4 - s_5s_7u_4u_5 - c_7\dot{u}_5 - (s_4c_7 + s_5s_7c_4)\dot{u}_3)\hat{e}_3
\end{aligned}
$$

3.2.9 Motion Constraints

Motion constraints reduce the dimensions of the locally achievable configuration space from nine to three. The first four constraints are introduced to enforce the pure rolling, no side-slip, contact of the knife-edge wheels with the ground plane and are nonholonomic. This sets the components of velocity of the contact points on the wheels in the $\hat{a}_1$ and $\hat{a}_2$ directions equal to zero, producing the following relationships

$$
{}^N\bar{v}^{d_n} \cdot \hat{a}_1 = s_3u_2 + c_3u_1 + r_R(u_5 + u_6) = 0 \tag{3.39}
$$

$$
{}^N\bar{v}^{d_n} \cdot \hat{a}_2 = c_3u_2 - s_3u_1 = 0 \tag{3.40}
$$

$$
\begin{aligned}
{}^N\bar{v}^{f_n} \cdot \hat{a}_1 = &s_3u_2 + c_3u_1 + d_2c_5u_5 + d_2s_4c_5u_3 - r_Rs_4u_3 - d_3s_7c_4u_3 - d_1s_5(u_5 + s_4u_3) \\
&r_Fc_4c_7(u_8 + c_7u_5 + (s_4c_7 + s_5s_7c_4)u_3)/(c_4^2c_5^2 + (s_4s_7 - s_5c_4c_7)^2)^{1/2} - \\
&s_7c_5(d_3u_7 - r_F(s_7c_4c_5u_5 - (s_4s_7 - s_5c_4c_7)u_7)/(c_4^2c_5^2 + (s_4s_7 - s_5c_4c_7)^2)^{1/2}) - \\
&s_5(d_3c_7(u_5 + s_4u_3) + r_Fs_4s_7(u_8 + c_7u_5 + (s_4c_7 + s_5s_7c_4)u_3)/(c_4^2c_5^2 + \\
&(s_4s_7 - s_5c_4c_7)^2)^{1/2}) = 0
\end{aligned} \tag{3.41}
$$

$$
\begin{aligned}
{}^N\bar{v}^{f_n} \cdot \hat{a}_2 = &c_3u_2 + d_1c_5u_3 + r_Rc_4u_4 + d_1s_4c_5u_5 + d_1s_5c_4u_4 + \\
&(c_4c_7 - s_4s_5s_7)(d_3(u_7 + s_5u_4 + c_4c_5u_3) - \\
&d_2(s_7u_5 + c_5c_7u_4 + (s_4s_7 - s_5c_4c_7)u_3) - r_F(c_4c_7u_4 + s_7c_4c_5u_5 - s_4s_5s_7u_4 - \\
&(s_4s_7 - s_5c_4c_7)u_7)/(c_4^2c_5^2 + (s_4s_7 - s_5c_4c_7)^2)^{1/2}) - \\
&s_3u_1 - (s_7c_4 + s_4s_5c_7)(d_2(s_7c_5u_4 - c_7u_5 - (s_4c_7 + s_5s_7c_4)u_3) + \\
&r_Fc_4c_5(s_7c_5u_4 - u_8 - c_7u_5 - (s_4c_7 + s_5s_7c_4)u_3)/(c_4^2c_5^2 + (s_4s_7 - s_5c_4c_7)^2)^{1/2}) - \\
&s_4c_5(d_3(s_7c_5u_4 - c_7u_5 - (s_4c_7 + s_5s_7c_4)u_3) + \\
&r_F(s_4s_7 - s_5c_4c_7)(s_7c_5u_4 - u_8 - c_7u_5 - \\
&(s_4c_7 + s_5s_7c_4)u_3)/(c_4^2c_5^2 + (s_4s_7 - s_5c_4c_7)^2)^{1/2}) = 0
\end{aligned} \tag{3.42}
$$

The fifth motion constraint is used to enforce the constraint on the velocities imposed by the holonomic constraint, Equation (3.14). This is strictly introduced to ease numerical integration and linearization. By differentiating the holonomic constraint equation we arrive at an equation that is linear in the generalized speeds and can be treated as

any other motion constraint

$$\begin{aligned}\frac{d}{dt}(\bar{r}^{G_n/d_n}\cdot\hat{a}_3) =& r_R s_4 u_4 + d_1 s_4 s_5 u_4 + (d_3 + r_F(s_4 s_7 - s_5 c_4 c_7)/(c_4^2 c_5^2 + (s_4 s_7 - s_5 c_4 c_7)^2)^{1/2})\\ & (s_4 c_7 u_7 + s_7 c_4 u_4 + s_4 s_5 c_7 u_4 + s_5 s_7 c_4 u_7 - c_4 c_5 c_7 u_5) - d_1 c_4 c_5 u_5 -\\ & d_2 s_4 c_5 u_4 - d_2 s_5 c_4 u_5 - r_F c_4 c_5 (s_4 c_4^2 c_5^3 u_4 + s_5 c_4^3 c_5^2 u_5 +\\ & (s_4 s_7 - s_5 c_4 c_7)^2 (s_4 c_5 u_4 + s_5 c_4 u_5))/(c_4^2 c_5^2 + (s_4 s_7 - s_5 c_4 c_7)^2)^{1.5} = 0\end{aligned} \tag{3.43}$$

These five equations are linear in the eight generalized speeds. Following convention, I choose the roll rate, u_4, the rear wheel rate, u_6, and steer rate, u_7, as independent generalized speeds.

Now we calculate the dependent speeds as functions of the independent speeds by solving the linear system of equations and differentiating the resulting equations to find the dependent $\dot{u}$'s. The dependent speeds take the form

$$\begin{aligned} u_1 &= f(u_4, u_6, u_7, q_3, \ldots, q_8)\\ u_2 &= f(u_4, u_6, u_7, q_3, \ldots, q_8)\\ u_3 &= f(u_4, u_6, u_7, q_4, \ldots, q_8)\\ u_5 &= f(u_4, u_7, q_4, \ldots, q_8)\\ u_8 &= f(u_4, u_6, u_7, q_4, \ldots, q_8)\end{aligned} \tag{3.44}$$

At this point, the equations become analytically long and it is not necessarily trivial to reduce the length of the equations. A smarter choice of generalized speeds could certainly help, but no effort was spent searching for a good set. From this point on in the derivation, the analytical results of the equations of motion will not be shown. I will only outline the remainder of the theory, as all of the kinematical building blocks are in place to derive the equations with Kane's method (or any other method). I highly recommend the use of computer aided algebra to continue on, but the die-hard could certainly write them by hand.

3.2.10 Generalized Active Forces

The three expressions for the nonholomonic generalized active forces, $\tilde{F}_r$ can now be formed. For the four body system with three degrees of freedom $(r = 4, 6, 7)$ they take the form

$$\begin{aligned}\tilde{F}_r &= (\tilde{F}_r)_C + (\tilde{F}_r)_D + (\tilde{F}_r)_E + (\tilde{F}_r)_F\\ (\bar{F}_r)_X &= {}^N\bar{V}_r^{x_o}\cdot\bar{R}^{x_o} + {}^N\bar{\omega}_r^X\cdot\bar{T}^X\end{aligned} \tag{3.45}$$

where ${}^N\bar{V}_r^{x_o}$ is the r$^{\text{th}}$ partial velocity of the mass center corresponding to the generalized speed u_r, $\bar{R}^{x_o}$ is the resultant force on the mass center (excluding non-contributing forces), ${}^N\bar{\omega}_r^X$ is the r$^{\text{th}}$ partial angular velocity of the body corresponding to the generalized speed u_r, and $\bar{T}^X$ is the resultant torques on the body where X is one of the four bodies. The partial velocities are simply the partial derivative of the velocities in question with respect to the generalized speeds and can be found systematically [KL85]. We assume that the only contributing force acting on the system is the gravitational force, g. The resultant forces are

$$\begin{aligned}\bar{R}^{c_o} &= m_C g\hat{n}_3\\ \bar{R}^{d_o} &= m_D g\hat{n}_3\\ \bar{R}^{e_o} &= m_E g\hat{n}_3\\ \bar{R}^{f_o} &= m_F g\hat{n}_3\end{aligned} \tag{3.46}$$

We also assume that three generalized active torques act on the system which correspond to the three independent generalized speeds found in Section *Motion Constraints*.

The roll torque, T_4, acts between the rear frame and the Newtonian frame about $\hat{a}_1$. The rear wheel torque, T_6, acts between the rear frame and the rear wheel about $\hat{c}_2$ and the steer torque, T_7, acts between the rear frame and the front

frame about $\hat{c}_3$.

$$\begin{aligned} \bar{T}^C &= T_4\hat{a}_1 - T_6\hat{c}_2 - T_7\hat{c}_3 \\ \bar{T}^D &= T_6\hat{c}_2 \\ \bar{T}^E &= T_7\hat{c}_3 \\ \bar{T}^F &= 0 \end{aligned} \tag{3.47}$$

3.2.11 Generalized Inertia Forces

The nonholonomic generalized inertia forces, $\tilde{F}_r^*$, are formed using the accelerations and the inertial properties of the bodies.

$$\begin{aligned} \tilde{F}_r^* &= (\tilde{F}_r^*)_C + (\tilde{F}_r^*)_D + (\tilde{F}_r^*)_E + (\tilde{F}_r^*)_F \\ (\bar{F}_r^*)_X &= {}^N\bar{V}_r^{X_o} \cdot \bar{R}_{X_o}^* + {}^N\bar{\omega}_r^X \cdot \bar{T}_X^* \end{aligned} \tag{3.48}$$

where ${}^N\bar{V}_r^{x_o}$ is once again the r[th] partial velocity of the mass center with corresponding to the generalized speed u_r, $\bar{R}_{x_o}^*$ is the inertia force for body X in frame N and is defined as

$$\bar{R}_{x_o}^* = -m_X \, {}^N\bar{a}^{x_o} \tag{3.49}$$

where the mass of each rigid body is a constant (m_C, m_D, m_E and m_F) which is multiplied by the acceleration of the body's center of mass. ${}^N\bar{\omega}_r^X$ is the partial angular velocity of the body corresponding to u_r, and $\bar{T}_X^*$ is the inertia torque on the body and is defined as

$$\bar{T}_X^* = -({}^N\bar{\alpha}^X \cdot I_X + {}^N\bar{\omega}^X \times I_X \cdot \bar{\omega}^X) \tag{3.50}$$

where I_X is the central inertia dyadic for the body in question which corresponds to the following tensor definitions for the inertia of each rigid body. The inertia tensor for each body is defined with respect to the mass center and the body's local reference frame. The bicycle wheels are assumed to be symmetric about both their 1-3 and 1-2 planes.

$$\mathbf{I}_D = \begin{bmatrix} I_{D11} & 0 & 0 \\ 0 & I_{D22} & 0 \\ 0 & 0 & I_{D11} \end{bmatrix} \tag{3.51}$$

$$\mathbf{I}_F = \begin{bmatrix} I_{F11} & 0 & 0 \\ 0 & I_{F22} & 0 \\ 0 & 0 & I_{F11} \end{bmatrix} \tag{3.52}$$

The rear frame and front frame are assumed to be symmetric about their 1-3 planes.

$$\mathbf{I}_C = \begin{bmatrix} I_{C11} & 0 & I_{C13} \\ 0 & I_{C22} & 0 \\ I_{C13} & 0 & I_{C33} \end{bmatrix} \tag{3.53}$$

$$\mathbf{I}_E = \begin{bmatrix} I_{E11} & 0 & I_{E13} \\ 0 & I_{E22} & 0 \\ I_{E13} & 0 & I_{E33} \end{bmatrix} \tag{3.54}$$

3.2.12 Dynamical Equations of Motion

Kane's equations are

$$\tilde{F}_r + \tilde{F}_r^* = 0 \qquad r = 4, 6, 7$$

and are a vector function of three coupled equations which are linear in the roll, steer, and rear wheel accelerations. The linear system can be solved to give the first order equations for $\dot{u}_r$, where $r = 4, 6, 7$. These can then be paired with the essential kinematical differential equations to form the complete set of dynamic equations of motion in the form

$$\dot{u}_i = f_i(u_4, u_6, u_7, q_4, q_5, q_7)$$
$$\dot{q}_j = u_j$$

where $i = 4, 6, 7$ and $j = 4, 5, 6, 7$. Keep in mind that the pitch angle, q_5, is in fact a dependent coordinate, $q_5 = f(q_4, q_7)$, selected when dealing with the holonomic constraint, (3.14). Special attention during simulation and linearization will have to be paid to accommodate the coordinate and will be described in the following sections.

3.2.13 Model discussion

[ASKL05], [MPRS07], [BMCP07], [LS06], and others do excellent jobs describing the essential nature of both the non-linear Whipple model and various linearized models. Notable concepts include the fact that many of the coordinates are *ignorable*, that is they do not show up in the essential dynamical equations of motion. These are typically the location of the ground contact point, q_1 and q_2, the yaw angle, q_3, and the wheel angles, q_6 and q_8. The model is also energy conserving, because the contact points do no work. The model has many equilibrium points and when linearized about the nominal configuration at constant forward speed the open loop model (i.e. with no inputs) can exhibit stability within various speed regimes. The system exhibits non-minimum phase behavior and this is clearly identified in the linear models by the right half plane zeros in various transfer functions. The previously mentioned references are recommended for a more detailed description of the model.

3.2.14 Simulation

The non-linear model can be simulated with various initial conditions. In the presented formulation all initial conditions can be set independently except for the roll, steer, and pitch angles. Once two of the three are chosen, the third is determined. Typically one chooses a steer and roll angle and then solves the holonomic constraint equation numerically for the pitch angle, q_5, to provide the correct initial condition. *Figure 3.4* is an example open loop simulation of the non-linear model.

3.2.15 Non-linear Validation

It is often difficult to validate that two independently derived multibody dynamical systems are equivalent. This due to mostly to the complexity of large analytical expressions which can be derived by different methodologies. A common method of validation is to evaluate the symbolic equations numerically for non-trivial inputs and compare the results to high precision. These type of numerical benchmarks are invaluable. They provide a baseline for model comparison allowing for scientific reproducibility and error checking.

[BMCP07] present the non-linear Whipple model derived with both the Newton-Euler and Lagrange methods, along with a numerical benchmark. Table 1 in their paper gives the derivatives of all the coordinates and speeds to high precision for both of their derivations at a single state. They claim that if one can compute the values to machine precision to ~10 significant figures then the models can be concluded to be the same[8].

[8] The very first model I developed in 2006 would not have held up to this test. I owe the validity of my model to my lab mate, Luke, as his persistence and interest in minute detail helped me bring my model up to par. Several issues plagued both of our derivations. The first was an simple

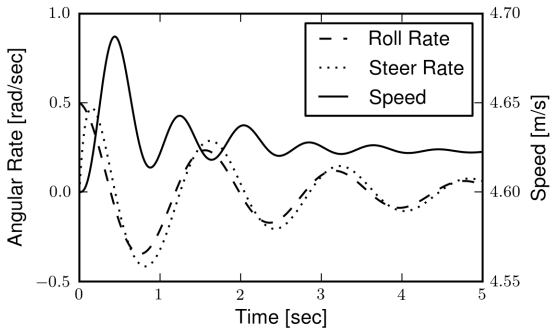

Figure 3.4: A reproduction of Figure 4 from [MPRS07]. For these initial conditions the model demonstrates stability. It also shows the energy conserving nature of the non-linear model (i.e. the forward speed settles to a higher value than the initial speed as the energy associated with lateral motion is transferred to the forward speed). Generated by *src/eom/nonlinear_simulation.py*.

The Basu-Mandal et al. derivations are based on different coordinates than those used here, but regardless of the coordinates they provide numerical values which can be benchmarked if the correct coordinate transformations are applied[9]. In *Table 3.1*[10] I present the values computed from the present model in comparison to the values presented in [BMCP07]. I've presented the same number of significant digits as provided by Basu-Mandall for each variable[11]. My model produces the same result to at least eleven significant figures, thus verifying the derivation is correct.

missing apostrophe in my Autolev code, the second was that we had defined our rear wheel rotation with respec to the B frame instead of the C frame, the third was incorrect parameter conversions from the [MPRS07] paper to our parameters, and the fourth was a bug in my original code that I never found, with an entire code rewrite finally giving me matching eigenvalues.

[9] The conversion equations from the [BMCP07] coordinates to the present set and vice versa can be found in the source code for the DynamicistToolKit bicycle module.

[10] The variable names correspond to the convention provided in [BMCP07]. This table is generated with `src/eom/basu_comparison.py`.

[11] Basu-Mandall presents varying significant digits from 10 to 14.

Table 3.1: Nonlinear Whipple Model Comparision

Variable	Basu-Mandal	Moore
β_f	0	0
$\dot{\beta}_f$	8.0133620584155	8.0133620584154
$\ddot{\beta}_f$	2.454807290455	2.454807290455
β_r	0	0
$\dot{\beta}_r$	8.912989661489	8.912989661489
$\ddot{\beta}_r$	1.8472554144217	1.8472554144220
ϕ	3.1257073014894	3.1257073014894
$\dot{\phi}$	-1.19185528069e-02	-1.19185528069e-02
$\ddot{\phi}$	1.205543897884e-01	1.205543897886e-01
ψ	9.501292851472e-01	9.501292851472e-01
$\dot{\psi}$	6.068425835418e-01	6.068425835418e-01
$\ddot{\psi}$	-7.8555281128244	-7.8555281128245
ψ_f	2.311385135743e-01	2.311385135743e-01
$\dot{\psi}_f$	4.859824687093e-01	4.859824687093e-01
$\ddot{\psi}_f$	-4.6198904039403	-4.6198904039394
θ	0	0
$\dot{\theta}$	7.830033527065e-01	7.830033527065e-01
$\ddot{\theta}$	8.353281706379e-01	8.353281706377e-01
x	0	0
$\dot{x}$	-2.8069345714545	-2.8069345714545
$\ddot{x}$	-5.041626315047e-01	-5.041626315048e-01
y	0	0
$\dot{y}$	-1.480982396001e-01	-1.480982396001e-01
$\ddot{y}$	-3.449706619454e-01	-3.449706619455e-01
z	2.440472102925e-01	2.440472102925e-01
$\dot{z}$	1.058778746261e-01	1.058778746261e-01
$\ddot{z}$	-1.460452833298	-1.460452833298

3.3 Linearized Equations of Motion

The non-linear equations of motion can be linearized about various equilibrium points. The obvious one is about the nominal configuration [MPRS07] but there are are an infinity of other associated with steady turns [BMCP07]. The equations can be linearized by computing the Taylor series expansion of the non-linear equations of motion about the equilibrium point of interest and disregarding the terms higher than first order. For the nominal configuration, this amounts to calculating the Jacobian of the system of equations with respect to the coordinates, speeds, and inputs to obtain the state matrix, $\mathbf{A}$, and the input matrix, $\mathbf{B}$. Output, $\mathbf{C}$, and feed-forward, $\mathbf{D}$, matrices are computed in the same fashion from the non-linear equations of the desired outputs. The partial derivatives of each equation were evaluated at the following fixed point: $q_i = 0$ where $i = 4, 5, 7$, $u_i = 0$ where $i = 4, 7$, and $u_5 = -v/r_R$ where v is the magnitude of the component of velocity of the rear wheel center in the direction of travel. Care has to be taken when linearizing as q_5 is a dependent coordinate which still appears on the right hand side of the equations. In general, the chain rule applies, but for the nominal configuration, the terms due to the implicit definition of pitch equal zero. The linearization transforms the system into four linear first order differential equations in the form

$$\begin{bmatrix} \dot{q}_4 \\ \dot{q}_7 \\ \dot{u}_4 \\ \dot{u}_7 \end{bmatrix} = \mathbf{A} \begin{bmatrix} q_4 \\ q_7 \\ u_4 \\ u_7 \end{bmatrix} + \mathbf{B} \begin{bmatrix} T_4 \\ T_7 \end{bmatrix} \tag{3.55}$$

I calculate the equations symbolically to reach the same results presented in [MPRS07], but my equations are much lengthier because the simplification routines available in Autolev and SymPy where not that effective. [MPRS07] assumes linearity in their derivation from the start of the derivation and avoids many of the simplification issues. The accuracy of the linearized model was checked by comparing the numerical results to the benchmark bicycle in two ways. First the linearized equations of motion, Equation (3.55), were rearranged into two second order differential equations in the canonical form (Equation (3.56)) presented in [MPRS07]. They present the values for the coefficient matrices ($\mathbf{M}$, $\mathbf{C}_1$, $\mathbf{K}_0$ and $\mathbf{K}_2$) for the benchmark parameter set to at least 13 significant figures and the linearization presented here matched all of the significant figures. [MPRS07] also provide the eigenvalues of the state matrix at various speeds. *Table 3.2*[12] shows the eigenvalues computed at 5 m/s compared to the values in Table 2 of [MPRS07]. These match to at least 13 significant figures.

$$\mathbf{M}\ddot{\bar{q}} + v\mathbf{C}_1\dot{\bar{q}} + \left[g\mathbf{K}_0 + v^2\mathbf{K}_2\right]\bar{q} = 0 \tag{3.56}$$
$$\bar{q} = [\phi \quad \delta]^T = [q_4 \quad q_7]^T$$

Table 3.2: Linear Whipple Model Comparision

Model	Caster	Weave Real	Capsize	Weave Imaginary
Meijaard	-1.407838969279822e+01	-7.7534188219585e-01	-3.2286642900409e-01	4.46486771378823e+00
Moore	-1.407838969279825e+01	-7.7534188219584e-01	-3.2286642900409e-01	4.46486771378822e+00

The lateral dynamics of this linear model are remarkably similar to the non-linear model especially around the regime of a typical bicycle's operating point. *Figure 3.5* gives an example simulation with the same initial conditions as the *Figure 3.4*. Notice that the lateral dynamics, steer and roll, are almost identical, but that the constant forward speed equilibrium condition destroys the conservative property demonstrated in the non-linear model.

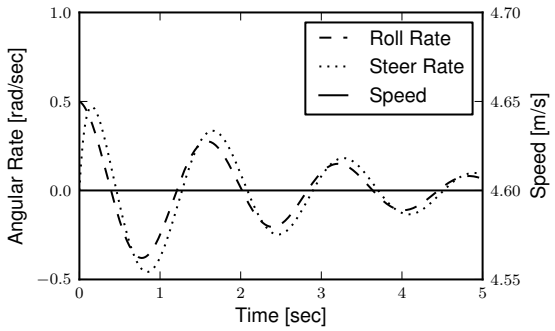

Figure 3.5: Simulation of the linear model given the same initial conditions as *Figure 3.4*. Generated by `src/eom/linear_comparison.py`.

It turns out that speed has profound effect on the lateral dynamics of the bicycle. It is useful to plot the root locus, *Figure 3.6*, of the characteristic equation with respect to the change in the equilibrium forward speed to visualize the time constants, damping, frequency, and stability of each of the modes of motion. The modes can be clearly identified along with the speed dependent stability.

Another useful and popular way to visualize the root locus is by plotting the real and imaginary eigenvalue components separately versus forward speed, *Figure 3.7*. This view gives a clearer view of the stable speed range.

The behavior of the modes of motion can be visualized by plotting the eigenvector components in the complex plane for various speeds. For the speeds shown in the root locus plots, there are four distinct speed ranges of interest: below the weave bifurcation, between the weave bifurcation and the weave critical speed, the stable speed range, and above the capsize critical speed. At a forward speed of 0.5 m/s, all eigenvalues are real, with two unstable and two stable. In *Figure 3.8*, notice that the unstable eigenvalues predict two modes where the roll and steer states exponentially

[12] This table is generated with `src/eom/linear_comparison.py`.

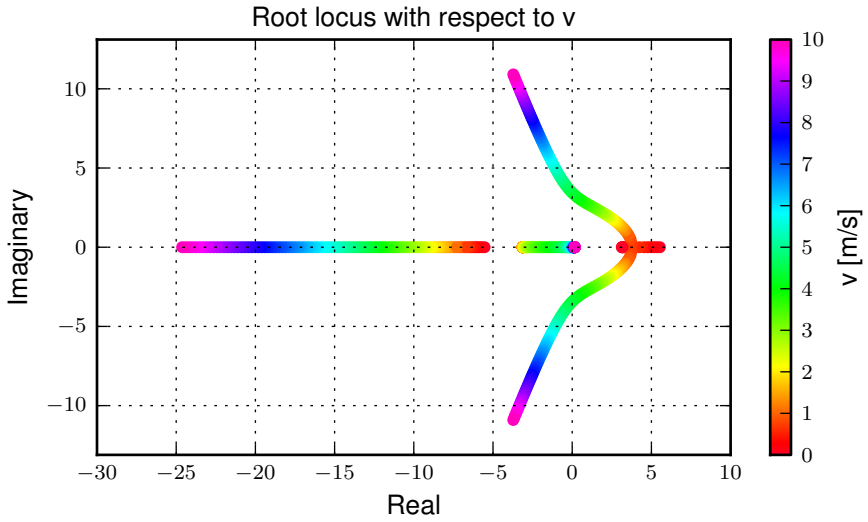

Figure 3.6: The root locus with respect to forward speed. The color variation signifies speed as shown in the right side color bar. Two eigenvalues are real, one being stable but increasingly fast and the other slowing to a marginally unstable location at high speed. The other two are initially real and unstable, but these coalesce into a complex pair and eventually become stable, at a higher moderately well damped frequency. Generated by *src/eom/linear_comparison.py*.

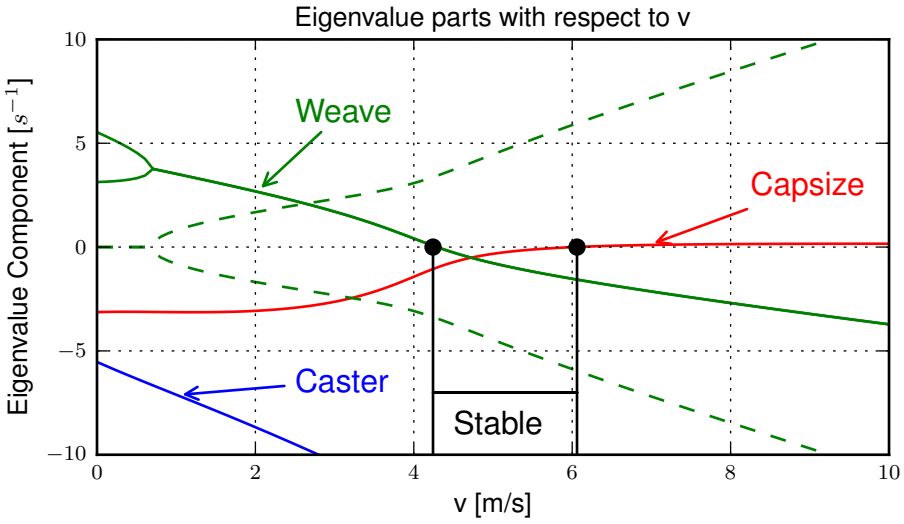

Figure 3.7: The real (solid) and imaginary (dashed) eigenvalue components versus speed for an example parameter set. The four modes of motion are identified. *Caster* is stable and real for all positive values of speed. It describes the tendency for the front wheel to right itself in forward motion. *Capsize* is always real and stable at low speeds but becomes marginally unstable at a higher speed. It describes the roll of the rear frame. *Weave* is real at very low speeds and describes an inverted pendulum-like motion i.e. the bicycle falls over. As speed increases the eigenvalues coalesce into a complex conjugate pair at the weave bifurcation that describes an exponentially increasing sinusoidal motion of roll and steer, with steer lagging the roll. This mode becomes stable at a higher speed. The weave and capsize critical speeds bound the stable speed range. Generated by *src/eom/linear_comparison.py*.

increase and with roll and steer 180 degrees out of phase. These modes describes a simple unstable inverted pendulum motion.

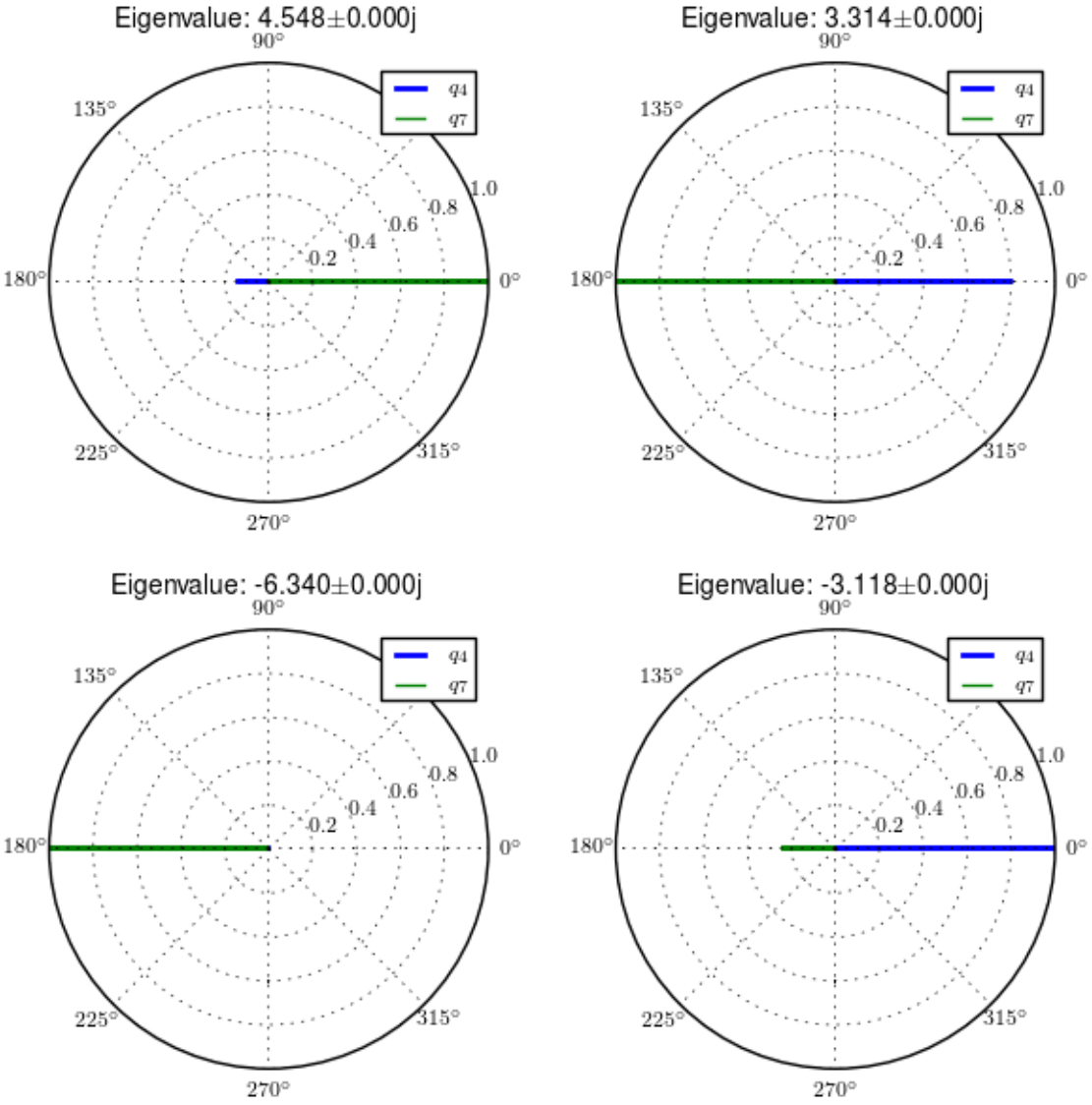

Figure 3.8: Normalized eigenvector components plotted in the real/imaginary plane for each mode at 5.0 m/s. Only the roll angle, q_4, and steer angle, q_7, components are shown. Generated by `src/eom/plot_eigenvectors.py`.

For speeds above the weave bifurcation speed, this linear model exhibits three distinct modes of motion, which have been named *weave*, *capsize*, and *caster*. As the bicycle is brought up to a speed of 3 m/s the two unstable eigenvalues coalesce into a complex pair. In *Figure 3.9*, the left-most graph depicts the caster mode which simply shows a rapidly decaying steer angle. The unstable weave mode eigenvector components show that the steer amplitude is about 25% larger than the roll amplitude and roll angle leads the steer angle by about 50 degrees. Finally, the capsize mode is a decays in roll and steer, with the roll at about twice the amplitude as steer.

At 5 m/s all modes are stable with the weave mode showing that the roll now only leads the steer by about 10 degrees. The caster and capsize are similar to 3 m/s.

Finally, at 7 m/s the capsize mode becomes unstable, with a slow exponential increase primarily in roll.

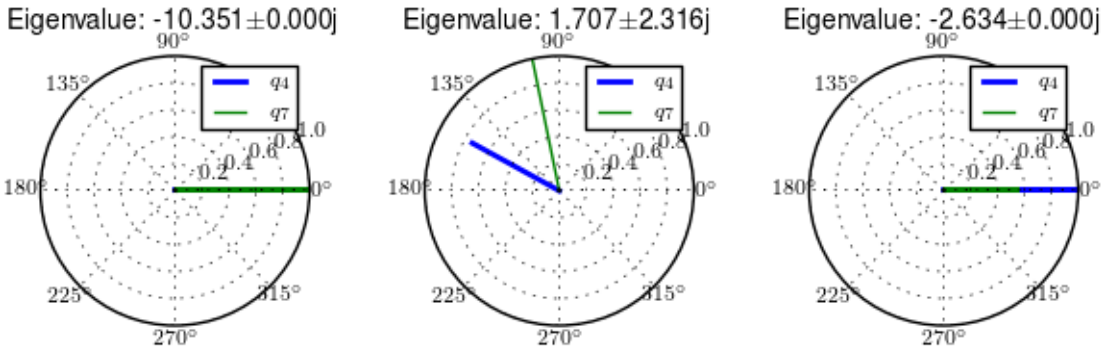

Figure 3.9: Normalized eigenvector components plotted in the real/imaginary plane for each mode at 3.0 m/s. Only the roll angle, q_4, and steer angle, q_7, components are shown. Generated by `src/eom/plot_eigenvectors.py`

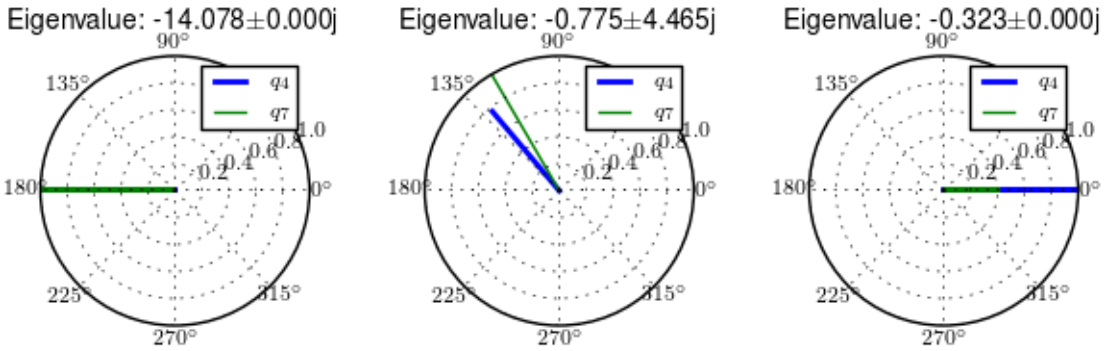

Figure 3.10: Normalized eigenvector components plotted in the real/imaginary plane for each mode at 5.0 m/s. Only the roll angle, q_4, and steer angle, q_7, components are shown. Generated by `src/eom/plot_eigenvectors.py`

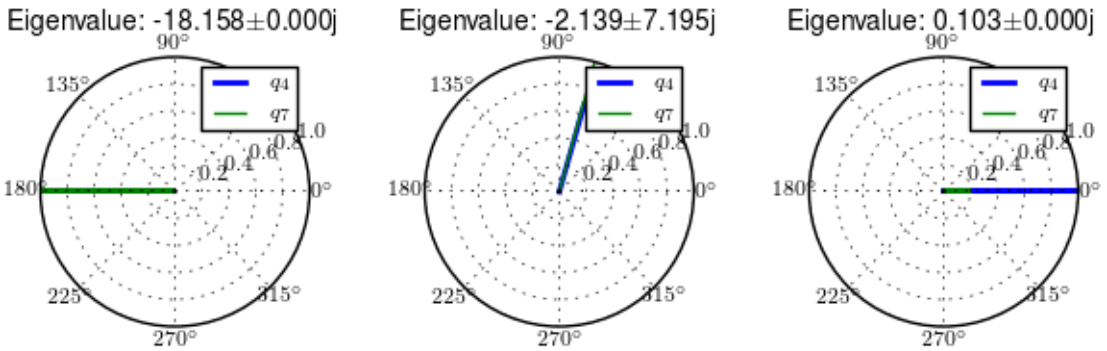

Figure 3.11: Normalized eigenvector components plotted in the real/imaginary plane for each mode at 7.0 m/s. Only the roll angle, q_4, and steer angle, q_7, components are shown. Generated by `src/eom/plot_eigenvectors.py`

The eigenvalues and eigenvectors describe the complete motion of the linear bicycle model where the motion from each mode is sum to gather the whole motion at a given speed. Typical diamond frame bicycle designs with an average sized rigid rider exhibit this basic behavior, but even small variations in some of the parameters can change the system behavior drastically, especially with regards to stability.

3.4 Parameter Conversion

This section details the conversion from the benchmark parameter set in [MPRS07] to the presented parameter set, *Figure 3.2*. As mentioned earlier, the Meijaard parameters are not a good choice when working with the non-linear derivation because most are not constant with respect to configuration. So the parameters must be converted to a configuration independent set. When the bicycle is in the nominal configuration the parameters can be converted with the following relationships.

Starting with the geometry, the wheel radii are defined the same, but the remaining geometry is calculated as

$$\begin{aligned} d_1 &= \cos(\lambda)(c + w - r_R \tan(\lambda)) \\ d_3 &= -\cos(\lambda)(c - r_F \tan(\lambda)) \\ d_2 &= \frac{(r_R + d_1 \sin(\lambda) - r_F + d_3 \sin(\lambda))}{\cos(\lambda)} \end{aligned} \tag{3.57}$$

The mass center locations are

$$\begin{aligned} l_1 &= x_B \cos(\lambda) - z_B \sin(\lambda) - r_R \sin(\lambda) \\ l_2 &= x_B \sin(\lambda) + z_B \cos(\lambda) + r_R \cos(\lambda) \\ l_4 &= (z_H + r_F) \cos(\lambda) + (x_H - w) \sin(\lambda) \\ l_3 &= \frac{x_H - w - l_4 \sin(\lambda)}{\cos(\lambda)} \end{aligned} \tag{3.58}$$

The masses are equivalently defined. Here the left side gives the present variables and the right gives the benchmark variables.

$$\begin{aligned} m_C &= m_B \\ m_D &= m_R \\ m_E &= m_H \\ m_F &= m_F \end{aligned} \tag{3.59}$$

The moments of inertia of the wheels are also equivalently defined.

$$\begin{aligned} \mathbf{I}_D = \begin{bmatrix} I_{D11} & 0 & 0 \\ 0 & I_{D22} & 0 \\ 0 & 0 & I_{D11} \end{bmatrix} = \mathbf{I}_R = \begin{bmatrix} I_{Rxx} & 0 & 0 \\ 0 & I_{Ryy} & 0 \\ 0 & 0 & I_{Rxx} \end{bmatrix} \\ \mathbf{I}_F = \begin{bmatrix} I_{F11} & 0 & 0 \\ 0 & I_{F22} & 0 \\ 0 & 0 & I_{F11} \end{bmatrix} = \mathbf{I}_F = \begin{bmatrix} I_{Fxx} & 0 & 0 \\ 0 & I_{Fyy} & 0 \\ 0 & 0 & I_{Fxx} \end{bmatrix} \end{aligned} \tag{3.60}$$

The moments and products of inertia for the frame and fork require the direction cosine matrix with respect to rotation through the steer axis tilt, λ.

$$\mathbf{R} = \begin{bmatrix} c_\lambda & 0 & -s_\lambda \\ 0 & 1 & 0 \\ s_\lambda & 0 & c_\lambda \end{bmatrix} \tag{3.61}$$

$$\mathbf{I}_B = \begin{bmatrix} I_{Bxx} & 0 & I_{Bxz} \\ 0 & I_{Byy} & 0 \\ I_{Bxz} & 0 & I_{Bzz} \end{bmatrix} \tag{3.62}$$
$$\mathbf{I}_C = \mathbf{R}\mathbf{I}_B\mathbf{R}^T$$

$$\mathbf{I}_H = \begin{bmatrix} I_{Hxx} & 0 & I_{Hxz} \\ 0 & I_{Hyy} & 0 \\ I_{Hxz} & 0 & I_{Hzz} \end{bmatrix} \tag{3.63}$$
$$\mathbf{I}_E = \mathbf{R}\mathbf{I}_H\mathbf{R}^T$$

3.5 Notation

A, B, C, D, E, F Reference frames and/or rigid bodies.

d_1, d_2, d_3 Distances that describe the rear and front frame essential geometry.

l_1, l_2, l_3, l_4 In plane distances to the rear and front frame centers of mass.

m_C, m_D, m_E, m_F Mass of each rigid body.

$\mathbf{I}_C, \mathbf{I}_D, \mathbf{I}_E, \mathbf{I}_F$ Local inertia tensor of each rigid body.

${}^Y\mathbf{R}^X$ Rotation matrix of body or reference frame X with respect to body or reference frame Y.

q_i Generalized coordinates.

u_i Generalized speeds.

$\hat{x}_1, \hat{x}_2, \hat{x}_3$ Three orthogonal unit vectors in reference frame X.

x_o Mass center of body X.

c_e Point on the steer axis in both bodies C and E.

d_n, f_n Points fixed in the rear and front wheels which are instantaneously in contact with the ground.

$\bar{r}^{y_o/x_o}$ Vector from point x_o to point y_o.

${}^X\bar{\omega}^Y$ Angular velocity of frame Y in frame X.

${}^Y\bar{v}^{x_o}$ Velocity of point x_o in reference frame Y.

${}^X\bar{\alpha}^Y$ Angular acceleration of frame Y in frame X.

${}^Y\bar{a}^{x_o}$ Acceleration of point x_o in reference frame Y.

s_1, c_1 Shorthand notation for $\sin q_1$ and $\cos q_1$.

s_λ, c_λ Shorthand notation for $\sin \lambda$ and $\cos \lambda$.

$\tilde{F}_r$ Nonholonomic generalized active forces. The subscript r denotes one of the independent generalized speeds.

${}^N\bar{V}_r^{x_o}$ r$^{\text{th}}$ partial velocity of point x_o in reference frame N with respect to the independent generalized speed, u_r.

$\bar{R}^{x_o}$ Resultant forces on the point x_o.

${}^N\bar{\omega}_r^C$ r$^{\text{th}}$ partial angular velocity of reference frame C in reference frame N with respect to the independent generalized speed, u_r.

$\bar{T}^C$ Resultant torques acting on body C.

$\tilde{F}_r^*$ Nonholonomic generalized inertia forces. The subscript r denotes one of the independent generalized speeds.

$\bar{R}_{x_o}^*$ Generalized inertia force of point x_o.

$\bar{T}_X^*$ Generalized inertia torque of body X.

I_X Central inertia dyadic of body X.

$\mathbf{A}, \mathbf{B}, \mathbf{C}, \mathbf{D}$ The state, input, output and feed-forward matrices.

The following benchmark parameters are all defined in [MPRS07].

λ Steer axis tilt.

c Trail.

w Wheelbase.

r_F, r_R Front and rear wheel radii.

x_B, z_B, x_H, z_H Mass center locations of the rear frame and front frame.

B, R, H, F Rigid bodies as defined in.

m_B, m_R, m_H, m_F Mass of each rigid body.

$\mathbf{I}_B, \mathbf{I}_R, \mathbf{I}_H, \mathbf{I}_F$ Inertia tensor of each rigid body.

v Forward speed of the linear bicycle model.

$\mathbf{M}, \mathbf{C}_1, \mathbf{K}_0, \mathbf{K}_2$ Velocity and gravity independent mass, damping, and stiffness matrices of the linearized Whipple model.

$\bar{q}$ Essential coordinates.

CHAPTER

FOUR

EXTENSIONS OF THE WHIPPLE MODEL

4.1 Preface

After I had derived the Whipple model, it was natural to start thinking about extending it to understand various other phenomena. It turned out that one of Mont's former students, David de Lorenzo, had worked on adding rider biomechanical degrees of freedom to the Whipple model in the early 90's, submitted the work to Vehicle System Dynamics but never resubmitted after the first round of reviews, and the work was still sitting dormant in Mont's files. Luke and I had just finished our preliminary exams and decided to try to write a paper for the 2007 International Symposium on Computer Simulation in Biomechanics. de Lorenzo's work inspired us to explore a model with more realistic rider motion, which we based on this dormant model. This was the first of several model extensions I developed for various reasons over the years. Others included variations on the rider biomechanics and models of unusual bicycle products such as the Swing Bike and Gyro Bike. This chapter details the findings from some of the models.

4.2 Introduction

The Whipple model is an ideal basic model and platform from which to explore more realistic models of both the bicycle and the rider. It has been demonstrated that the linear Whipple model can reliably predict the motion of a riderless uncontrolled bicycle [Koo06], [KSM08], [KS09], [Ste09], [ER11] for speeds in and around the stable speed range. But the Whipple model may certainly be limited in it's ability to predict the motion of the bicycle and rider as an integrated system. A person's body keeps its shape through passive joint forces, unconscious active control and conscious active control. Assuming no active control and lumping the unconscious control with the passive control one can potentially model the rider as flexible assembly of many bodies. Secondly, the rider's weight is typically 80 to 90 percent of the entire system, which potentially invalidates the knife edge wheel assumptions employed in the Whipple model. Here I present several bicycle models that attempt to explain some of the rider's passive dynamics and also a model with a passive stability augmentation device. The models are all based on the basic formulation of the Whipple model in Chapter *Bicycle Equations Of Motion* and make use of the variables defined therein. Various combinations of these model extensions are used in the later Chapters for analysis of more complicated systems.

4.3 Notation

Each model presented in this chapter makes use of the notation defined in Chapter *Bicycle Equations Of Motion* otherwise each model in each section is treated independently and may use the same notation of the other models.

4.4 Lateral Force Input

The Whipple model is typically defined with three inputs: roll torque T_4, rear wheel torque T_6, and steer torque T_7. These ideal inputs are not necessarily easy to map to the actual inputs to the system. In particular, it is generally not possible to execute a pure roll torque, but a lateral force from the environment is much easier. This type of input has long been used and modeled, e.g. [Rol73] uses a lateral perturbation in modeling and experimentation of a motorcycle.

Here I add a fourth input, a lateral force F_{c_l}, which acts at a point on the rear frame, c_l. The force is defined such that it is always in the $\hat{n}_2$ direction and acts on the point located in the mid-plane of the bicycle frame. The $\hat{n}_2$ direction is chosen instead of the yaw frame's $\hat{a}_2$ direction because it better models the impulsive forces applied in the experiments detailed in Chapter *System Identification*. The force can describe a person walking beside a bicycle and simply pushing laterally on the rear frame. One can even think of it as a simplified version of the resultant force from lateral wind gust, although a gust would also apply a force to the front frame.

The vector from the rear wheel center to the lateral force point is

$$\bar{r}^{c_l/d_o} = d_4\hat{c}_1 + d_5\hat{c}_3 \tag{4.1}$$

The velocity of the point is

$$^N\bar{v}^{c_l} = {}^N\bar{v}^{d_o} + {}^N\bar{\omega}^C \times \bar{r}^{c_l/d_o} \tag{4.2}$$

where

$$^N\bar{\omega}^C \times \bar{r}^{c_l/d_o} = d_5(u_5 + s_4u_3)\hat{c}_1 + (d_4(s_5u_4 + c_4c_5u_3) - d_5(c_5u_4 - s_5c_4u_3))\hat{c}_2 - d_4(u_5 + s_4u_3)\hat{c}_3$$

To form the equations of motion, an additional generalized active force dot multiplied with the partial velocities of the point is required. The generalized active force is simply

$$\bar{R}^{c_l} = F_{c_l}\hat{n}_2 \tag{4.3}$$

The non-linear and linear models are computed in the same fashion as described in Chapter *Bicycle Equations Of Motion*, with an additional column in both the input, $\mathbf{B}$, and feed-forward, $\mathbf{D}$, matrices corresponding to the new input force. Unlike a pure roll torque this force can effectively contribute to both the roll and steer torques. The location of the point determines the contribution.

Figure 4.1 compares the impulse response for roll torque to that of a lateral force at the seat for a particular bicycle within its stable speed range. Notice that the lateral force input does not excite the system with as large amplitudes but that the response is similar. The amplitude is a function of where the force is applied. If the force is applied directly above the rear wheel contact at a height of unity from the ground, the response will be identical.

Figure 4.2 shows the frequency response in a similar fashion as the impulse response. The responses for both input types are very similar for this frequency range, with the difference in magnitudes a function of the distance the lateral force is from the rear wheel contact point.

This model is used extensively in the later chapters for modeling and simulation of lateral perturbation experiments.

4.4.1 Notation

c_l The point at which the lateral force is applied.

d_4, d_5 The distances which locate the lateral force point c_l.

F_{cl} The magnitude of the lateral force.

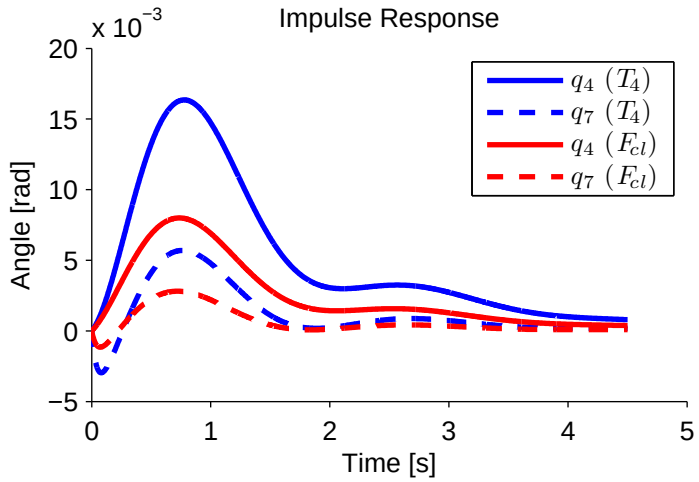

Figure 4.1: Impulse responses for the roll angle, q_4, and steer angle, q_7, for a roll torque input (blue) and the lateral force input at a point just below the seat (red). The numerical parameters were generated from the data of Jason on the Davis instrumented bicycle and the equations were linearized at a forward speed of 7 m/s. Plot generated by *src/extensions/lateral/lateral_force.m*‘.

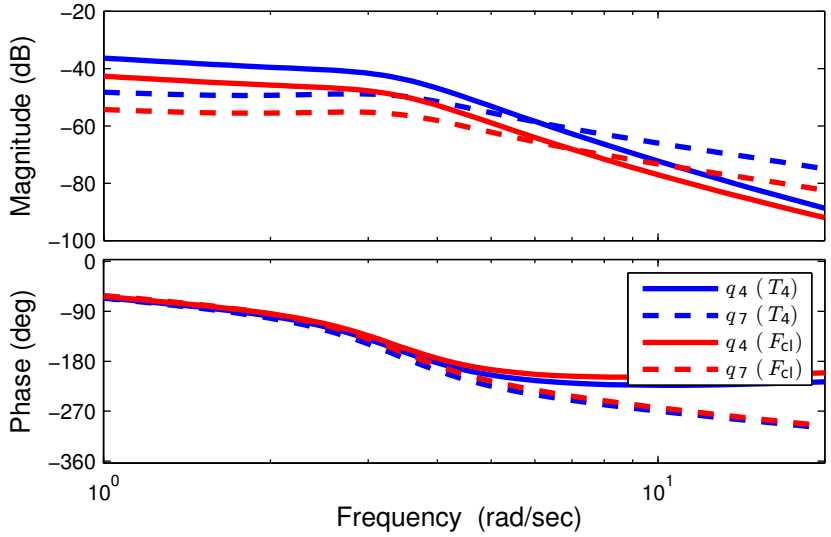

Figure 4.2: Frequency responses for the roll angle, q_4, and steer angle, q_7, for a roll torque input (blue) and the lateral force input at a point just below the seat (red). The numerical parameters were generated from the data of Jason on the Davis instrumented bicycle and the equations were linearized at a forward speed of 7 m/s. Plot generated by `src/extensions/lateral/lateral_force.m`.

4.5 Rider Arms

[SK10b] and [SMK12] has shown that the addition of the inertial effects of the arms can significantly alter the open loop dynamics of the bicycle-rider system, and most importantly, that a typical bicycle and rider may not have a stable speed range. As will be described in Chapter *Davis Instrumented Bicycle*, we rigidified the rider's torso and legs with respect to the rear frame of the bicycle. The rider was then only able to make use of their arms to control the bicycle. The Whipple model does not take into account the dynamic motion of the arms and certainly not the fact that steer torques are actually generated from the muscle contraction and flexion in the riders arms. Being that our riders were able to move their arms and the motion can have significant effect on the open loop dynamics, we developed a similar model as the upright flexed arm model found in [SK10b] and [SMK12].

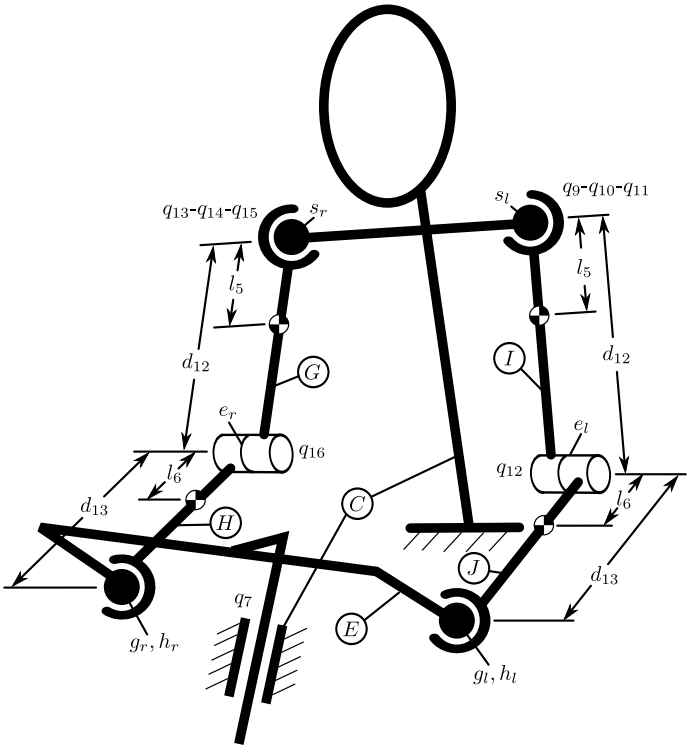

Figure 4.3: Diagram of the additional arm bodies. Only the upper portion of the system is shown. The rider's torso, neck, and head are assumed to be part of the rear frame rigid body, C.

In most bicycle models, the front frame is externally forced to move with respect to the rear frame through a torque applied between the rear frame and the front frame. A more realistic model with arms would force the front frame motion through joint torques in the arms. For simplicity's sake and without loss of generality we keep the steer torque, T_4, as the driving torque but retain the associated motion of the arms. The inertial effects of the arms can then be captured by adding four additional rigid bodies to the Whipple model for the left and right upper and lower arm segments and introducing enough constraints such that the additional degrees of freedom are removed *Figure 4.3*. The arms are assumed to symmetric with respect to the sagittal plane when in the nominal configuration. The four new bodies are defined as:

G**:** right upper arm

H**:** right lower arm

I**:** left upper arm

J**:** left lower arm

The right and left upper arms are each oriented through body fixed 1-2-3 rotations through the abduction, elevation and rotation angles q_9, q_{10}, q_{11} and q_{13}, q_{14}, q_{15} for the right and left arms respectively.

$$
{}^{C}\mathbf{R}^{G} = \begin{bmatrix} c_{10}c_{11} & -c_{10}s_{11} & s_{10} \\ s_9 s_{10} c_{11} + s_{11} c_9 & -s_9 s_{10} s_{11} + c_{11} c_9 & -s_9 c_{10} \\ -c_9 s_{10} c_{11} + s_{11} s_9 & c_9 s_{10} s_{11} + c_{11} s_9 & c_9 c_{10} \end{bmatrix} \tag{4.4}
$$

$$
{}^{C}\mathbf{R}^{I} = \begin{bmatrix} c_{14}c_{15} & -c_{14}s_{15} & s_{14} \\ s_{13} s_{14} c_{15} + s_{15} c_{13} & -s_{13} s_{14} s_{15} + c_{15} c_{13} & -s_{13} c_{14} \\ -c_{13} s_{14} c_{15} + s_{15} s_{13} & c_{13} s_{14} s_{15} + c_{15} s_{13} & c_{13} c_{14} \end{bmatrix} \tag{4.5}
$$

The right and left lower arms are oriented through simple rotations through q_{12} and q_{16} with respect to the upper arms at the elbow joint.

$$
{}^{G}\mathbf{R}^{H} = \begin{bmatrix} c_{12} & 0 & -s_{12} \\ 0 & 1 & 0 \\ s_{12} & 0 & c_{12} \end{bmatrix} \tag{4.6}
$$

$$
{}^{I}\mathbf{R}^{J} = \begin{bmatrix} c_{16} & 0 & -s_{16} \\ 0 & 1 & 0 \\ s_{16} & 0 & c_{16} \end{bmatrix} \tag{4.7}
$$

This definition differs from [SK10b] and will allow full non-linear unlocked motion of the arms. Schwab's joint configuration limits the model to be valid only in and around the linear equilibrium point presented therein.

The right and left shoulders are located in the rear frame by

$$
\begin{aligned} \bar{r}^{s_r/d_o} &= d_6 \hat{c}_1 + d_7 \hat{c}_2 + d_8 \hat{c}_3 \\ \bar{r}^{s_l/d_o} &= d_6 \hat{c}_1 - d_7 \hat{c}_2 + d_8 \hat{c}_3 \end{aligned} \tag{4.8}
$$

The right and left elbows are located by

$$
\begin{aligned} \bar{r}^{e_r/s_r} &= d_{12} \hat{g}_3 \\ \bar{r}^{e_l/s_l} &= d_{12} \hat{i}_3 \end{aligned} \tag{4.9}
$$

The upper and lower arm mass centers are located by

$$
\begin{aligned} \bar{r}^{g_o/s_r} &= l_5 \hat{g}_3 \\ \bar{r}^{h_o/e_r} &= l_6 \hat{i}_3 \\ \bar{r}^{i_o/s_l} &= l_5 \hat{i}_3 \\ \bar{r}^{j_o/e_l} &= l_6 \hat{j}_3 \end{aligned} \tag{4.10}
$$

The hands are located by

$$
\begin{aligned} \bar{r}^{h_r/e_r} &= d_{13} \hat{h}_3 \\ \bar{r}^{h_l/e_l} &= d_{13} \hat{j}_3 \end{aligned}
$$

The handlebar grips are located by

$$
\begin{aligned} \bar{r}^{g_r/f_o} &= d_9 \hat{e}_1 + d_{10} \hat{e}_2 + d_{11} \hat{e}_3 \\ \bar{r}^{g_l/f_o} &= d_9 \hat{e}_1 - d_{10} \hat{e}_2 + d_{11} \hat{e}_3 \end{aligned} \tag{4.11}
$$

To enforce that the hands remain on the grips, I first introduce six holonomic constraints embodied in

$$\bar{r}^{h_r/s_r} - \bar{r}^{g_r/s_r} = 0$$
$$\bar{r}^{h_l/s_l} - \bar{r}^{g_l/s_l} = 0 \tag{4.12}$$

After forcing the hands to be at the grips this leaves two degrees of freedom, one for each arm. The free motion is such that the arms can rotate about the lines connecting the shoulders to the grips. I choose to eliminate these two degrees of freedom by forcing the arms to always "hang down" relative to the rear frame, i.e. that the vector aligned with the elbow has no component in the downward direction of the roll frame, B.

$$\hat{g}_2 \cdot \hat{b}_3 = 0$$
$$\hat{i}_2 \cdot \hat{b}_3 = 0 \tag{4.13}$$

This assumption is limited in validity to small pitch angles, as a large pitch angles would cause the riders arms to rotate in odd positions. A better constraint would be to dot with a vector in the C frame which is aligned with $\hat{b}_3$ when the bicycle is not pitched, but this definition would require a new geometric parameter so I chose the former, i.e. Equation (4.13).

With these eight holonomic constraints, the model now has three degrees of freedom which are the same number as the Whipple model, but with the added inertial effects of the arms. The expressions for the velocities and accelerations of the mass centers of the four new bodies needed to form the equations of motion are lengthy and they are omitted here. Please refer to the source code for the equations: `src/extensions/arms/Arms.al`.

The generalized active forces remain the same as described in Chapter *Bicycle Equations Of Motion* with the addition of the lateral force described in the previous section. The generalized inertia forces must be modified to include the accelerations of the mass centers along with the mass and inertia of the new bodies. The masses are simply defined as m_g, m_h, m_i and m_j. The arms segments are assumed to be symmetric about their associated 3 axes, thus $I_{11} = I_{22}$.

$$\mathbf{I}_G = \begin{bmatrix} I_{G11} & 0 & 0 \\ 0 & I_{G11} & 0 \\ 0 & 0 & I_{G33} \end{bmatrix} = \mathbf{I}_I = \begin{bmatrix} I_{I11} & 0 & 0 \\ 0 & I_{I11} & 0 \\ 0 & 0 & I_{I33} \end{bmatrix} \tag{4.14}$$

$$\mathbf{I}_H = \begin{bmatrix} I_{H11} & 0 & 0 \\ 0 & I_{H11} & 0 \\ 0 & 0 & I_{H33} \end{bmatrix} = \mathbf{I}_J = \begin{bmatrix} I_{J11} & 0 & 0 \\ 0 & I_{J11} & 0 \\ 0 & 0 & I_{J33} \end{bmatrix} \tag{4.15}$$

With this information the equations of motion can be formed with Kane's method as described in Chapter *Bicycle Equations Of Motion*. Special care must be taken when linearizing the equations of motion due to the eight holonomic constraints. The additional generalized coordinates, q_9 through q_{16}, are dependent coordinates and are ultimately functions of the pitch and steer angles. The chain rule must be properly applied or the independent coordinates must be solved for when expanding the Taylor series and forming the Jacobian matrices.

Figures *4.4* and *4.5* show how the eigenvalues vary with speed with respect to the nominal configuration equilibrium point. There are three distinct modes for all speeds shown, two of which are real and one that is complex. The oscillatory mode is always stable, unlike the weave mode in the Whipple model. Secondly, one real mode is always unstable and the other is always stable. The addition of the arms' inertial effects causes the system to not have a stable speed range unlike the prediction of the Whipple model.

One may be quick to parallel the three modes of motion to the weave, capsize, and caster modes of the Whipple model, but closer examination of the eigenvectors reveals that the motions are not quite the same. Figures *4.6*, *4.7*, *4.8*, and *4.9* are phasor plots of the eigenvector components at various speeds which correspond to the ones given in previous chapter for the Whipple model.

The phasor diagrams show that the most negative real eigenmode is not as nearly as fast as the caster mode and it is no longer dominated by steer angle. The mode decays in both roll and steer with roll dominant at low speeds and steer at high speeds. The unstable real eigenmode is dominant in roll angle and slows with increasing speed like the Whipple model, but is unstable for the given speeds. The stable oscillatory mode is dominant in steer at low speeds and roll at high speeds. The 0.5 m/s case is interesting in that the mode is primarily a stable oscillation in steer angle around 0.3 hertz. As the speed increases the larger roll angle magnitude is different in behavior than the Whipple weave mode.

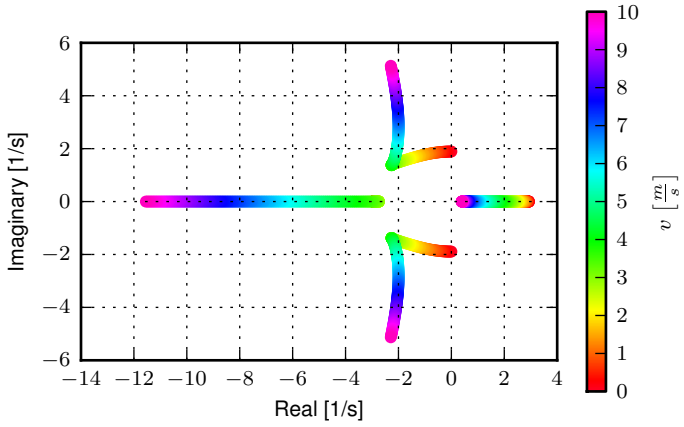

Figure 4.4: The root locus with respect to speed of the Whipple model with arms for the parameter set associated with Jason seated on the Davis instrumented bicycle calculated with the Yeadon method. Generated with `src/extensions/arms/plot_eig.py`.

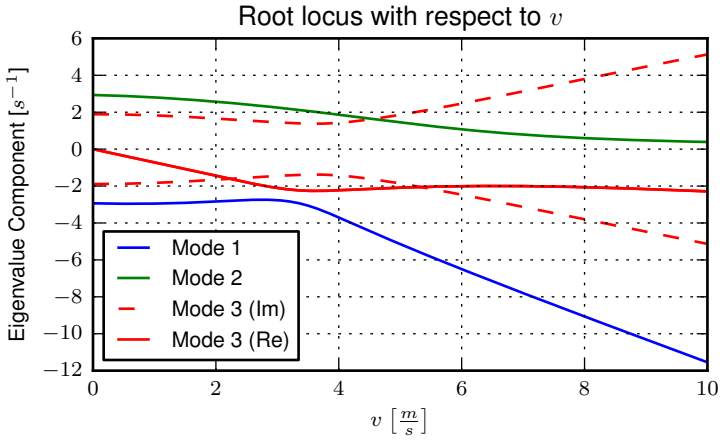

Figure 4.5: The components of the eigenvalues with respect to speed of the Whipple model with arms for the parameter set associated with Jason seated on the Davis instrumented bicycle calculated with the Yeadon method. This plot shares similar characteristics as the one presented in [SK10b]. Generated with `src/extensions/arms/plot_eig.py`.

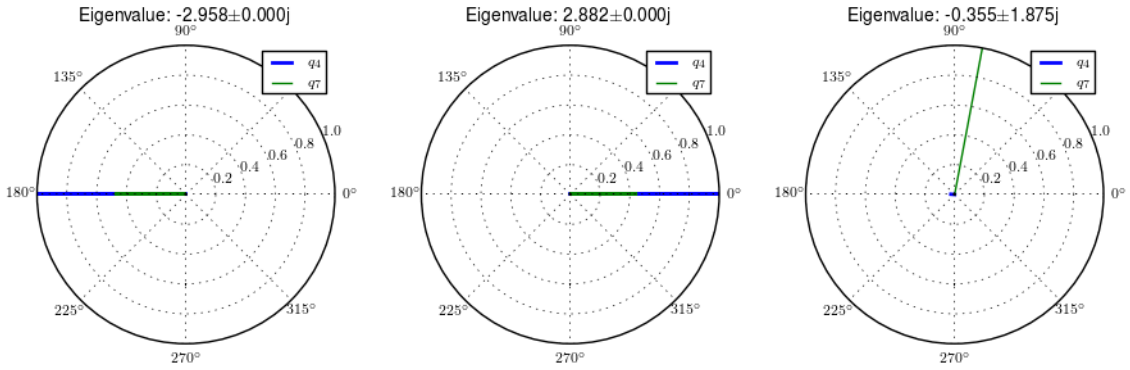

Figure 4.6: Normalized eigenvector components plotted in the real/imaginary plane for each mode at a forward speed of 0.5 m/s. Only the roll angle, q_4, and steer angle, q_7, components are shown. Generated with `src/extensions/arms/plot_eig.py`.

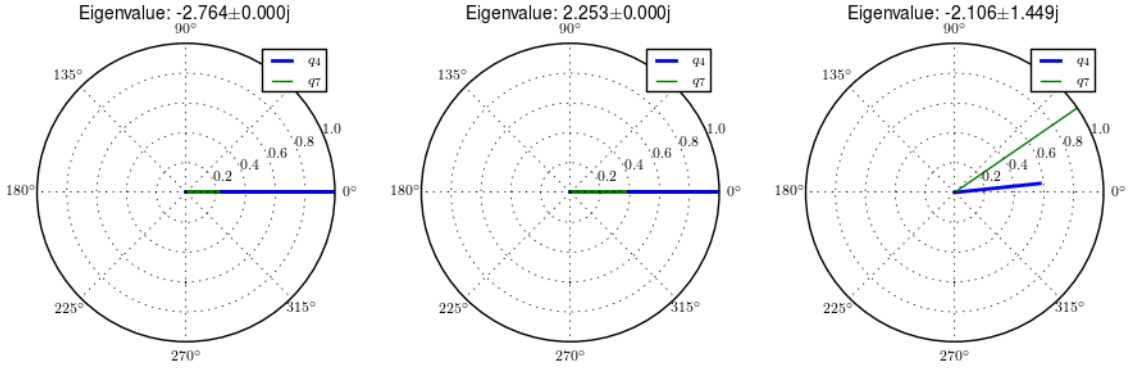

Figure 4.7: Normalized eigenvector components plotted in the real/imaginary plane for each mode at a forward speed of 3.0 m/s. Only the roll angle, q_4, and steer angle, q_7, components are shown. Generated with `src/extensions/arms/plot_eig.py`.

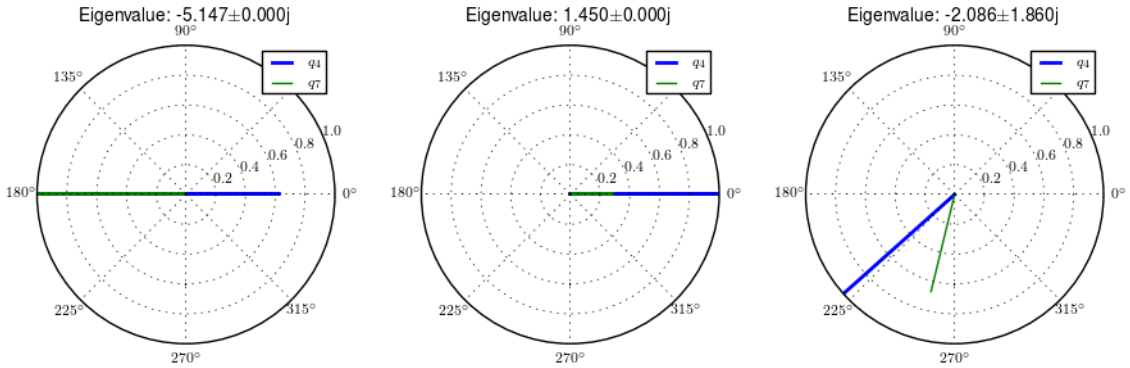

Figure 4.8: Normalized eigenvector components plotted in the real/imaginary plane for each mode at a forward speed of 5.0 m/s. Only the roll angle, q_4, and steer angle, q_7, components are shown. Generated with `src/extensions/arms/plot_eig.py`.

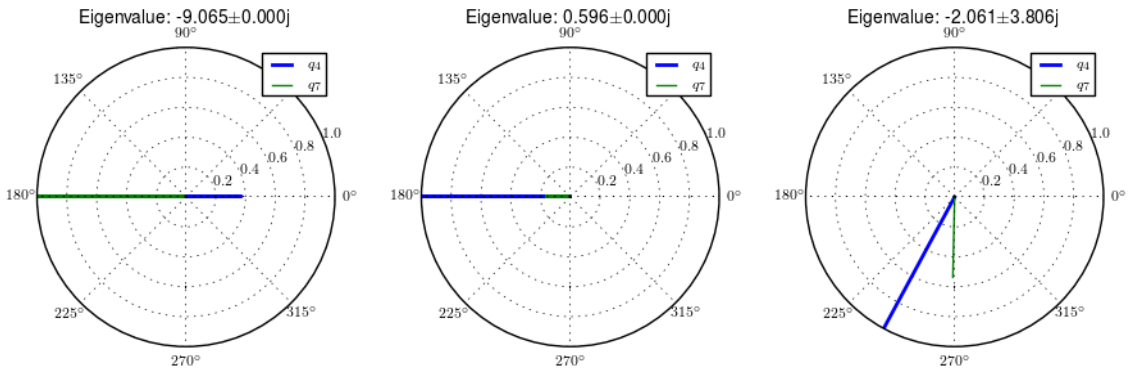

Figure 4.9: Normalized eigenvector components plotted in the real/imaginary plane for each mode at a forward speed of 8.0 m/s. Only the roll angle, q_4, and steer angle, q_7, components are shown. Generated with `src/extensions/arms/plot_eig.py`.

4.5.1 Notation

G, J, I, J The arm rigid bodies.

d_6-d_{13} Geometric distances to locate the arm joints.

$s_r, e_r, h_r, g_r, s_l, e_l, h_l, g_l$ Points on the arms and handlebars: (s)houlder, (e)lbow, (h)and, and (g)rip. Subscripts: (l)eft and (r)ight.

m_g, m_h, m_i, m_j The masses of the arm rigid bodies.

$\mathbf{I}_G, \mathbf{I}_H, \mathbf{I}_I, \mathbf{I}_J$ The inertia tensors of the arm rigid bodies defined about the mass center and with respect to the local reference frame.

4.6 Front wheel flywheel

Another model extension of interest involves addition of an extra rotating wheel coincident with the front wheel. It is well known that that increasing the angular momentum of the front wheel via change in inertia ([ASKL05], [FSR90]) or rotational speed, has a strong effect on the stability of the Whipple model. For the benchmark bicycle [MPRS07], independently increasing the moment of inertia of the front wheel, decreases both the weave and capsize speeds. A low weave speed may provide open loop stability advantages to riders at low speed, with the reasoning that a stable bicycle may require less rider control. Conversely, it has also been shown both that a bicycle without gyroscopic effects can be stable [KMP+11] and that humans can ride them [Jon70] with little difficulty. The idea that gyroscopic action can stabilize a moving two wheeled vehicle has been demonstrated as early as the dawn of the 20th century, with the invention of the gyro monorail and the gyro car ([Wik12a], [Wik12b]) which made use of control servos to gyros to applied roll righting torques to the single track vehicles. Of more recent interest, several engineering students at Dartmouth University applied this theory to a compact flywheel mounted within the spokes of a children's bicycle wheel [War06] taking advantage of the fact that the flywheel imparts torques such that the bicycle steers into the fall. This has since been developed into a commercially available product, the GyroBike, that claims to allow children to learn to ride more easily, due to the bicycle's increased stability at low speeds. I was given an article about the bicycle from the Dartmouth alumni magazine, subsequently met the woman who created the startup company around the idea in San Francisco, was able to test ride the full scale prototype, and eventually purchased a 12" version of the bicycle. The bicycle alone stays very stable even to extremely low speeds, but when I, as an experienced rider, tried to ride and control it the steering felt less responsive than one would generally prefer.

Using the Whipple model presented in Chapter *Bicycle Equations Of Motion* as a base, the flywheel's effect can be modeled by adding an additional symmetric rigid body, G with mass m_g to the system which rotates about the front

wheel axis though a new generalized coordinate, q_9. The angular velocity and acceleration of the new body are defined with the simple kinematical differential equation

$$^F\omega^G = \dot{q}_9\hat{e}_2 = u_9\hat{e}_2 \tag{4.16}$$

where

$$^F\alpha^G = \dot{u}_9\hat{e}_2 \tag{4.17}$$

The location of the flywheel center of mass is at the same point as the front wheel center of mass, making the linear velocities and accelerations the same as the front wheel

$$^N\bar{v}^{g_o} = {}^N\bar{v}^{f_o} \tag{4.18}$$

$$^N\bar{a}^{g_o} = {}^N\bar{a}^{f_o} \tag{4.19}$$

An additional torque, T_9, is required to drive the flywheel relative to the front wheel

$$\begin{aligned}\bar{T}^F &= -T_9\hat{e}_2 \\ \bar{T}^G &= T_9\hat{e}_2\end{aligned} \tag{4.20}$$

At this point, $\tilde{F}_r$, can be formed with an additional equation for the new degree of freedom.

The generalized inertia force, $\tilde{F}_r^*$ is formed by taking into account the mass, m_g, and inertia of the new body

$$\mathbf{I}_G = \begin{bmatrix} I_{G11} & 0 & 0 \\ 0 & I_{G22} & 0 \\ 0 & 0 & I_{G11} \end{bmatrix} \tag{4.21}$$

The equations of motion are formed and linearized with respect to the nominal equilibrium point and a nominal angular velocity of the flywheel. Figures *4.10*, *4.11*, *4.12*, and *4.13* show how adjusting the flywheel angular velocity can affect the stability of the bicycle which may be beneficial for people learning to ride a bicycle. All of the plots were generated using parameters measured from a production GyroBike and the rider's parameters were generated by scaling the Yeadon geometry of an adult, Charlie, to child-size proportions which are detailed in Chapter *Physical Parameters*.

Figure 4.10 depicts similar dynamics as one would expect from a riderless bicycle with a relatively low weave critical speed (~2.25 m/s). *Figure 4.11* then shows that the very unstable system at low speeds can certainly be made stable by increasing the angular velocity of the flywheel. In particular the bicycle becomes stable around 1000 rpm but it is also interesting to note that increasing the velocity too much (> 3500 rpm) results in an unstable system. The actual Gyrobike flywheel spins at speeds up to 2000 rpm and riderless stability can clearly be observed.

Figure 4.12 shows that the weave critical speed with a rider is only about 1 m/s greater than without a rider. *Figure 4.13* shows that if a child-sized rider is rigidly added to the rear frame that the flywheel must spin up to 3500 rpm for the system to be stable and the time constant of the unstable eigenvalue does not decrease significantly until the flywheel spins at 2000 rpm. Also as with the riderless case, the system can be destabilized if the wheel spins at a high enough rate; in this case about 7000 rpm.

Figure 4.14 shows the resulting time history of the non-linear model traveling at a very slow speed with the flywheel spinning fast enough to stabilize the bicycle. The gyroscopic torques cause the steer angle to decay rapidly in a steer into the fall. The conservative nature of the system causes the forward speed to increase slightly. This is reflected as a decrease in the flywheel rotational speed because it is defined with respect to the front wheel.

This model and these examples give credence to the effectiveness of increasing the angular momentum of the front wheel in stabilizing the bicycle. The gyroscopic forces may not be necessary for stability but they have great power in stabilizing even very unstable systems. This assistance does come a cost though, both in the flywheel weight and the need to spin the flywheel at high speeds. When the child rider's inertia is accounted for, very high spin speeds are needed to stabilize the system. And interestingly, increasing the flywheel speed too much can destabilize the system, albeit only marginally.

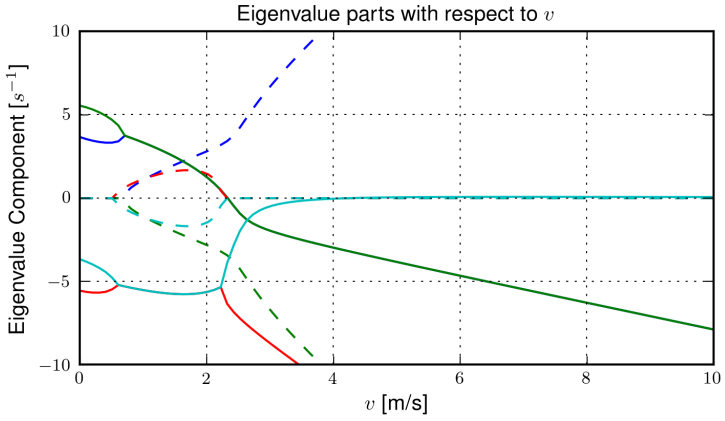

Figure 4.10: The magnitudes of the eigenvalue components with respect to the forward speed when the flywheel is fixed to the front wheel (i.e. has the same angular velocity as the front wheel). The solid lines show the real parts and the dotted lines show the imaginary parts, with color matching the parts for a given eigenvalue. Generated by `src/extensions/gyro/gyrobike_linear.py`.

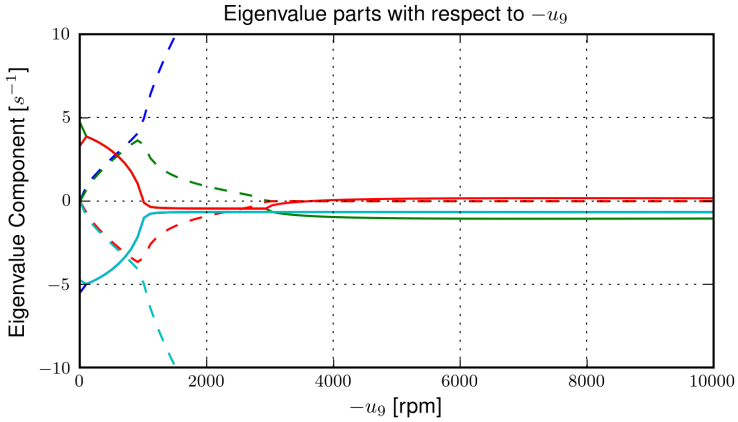

Figure 4.11: The magnitudes of the eigenvalue components with respect to the flywheel angular speed when the forward velocity is 0.5 m/s. The solid lines show the real parts and the dotted lines show the imaginary parts, with color matching the parts for a given eigenvalue. Generated by `src/extensions/gyro/gyrobike_linear.py`.

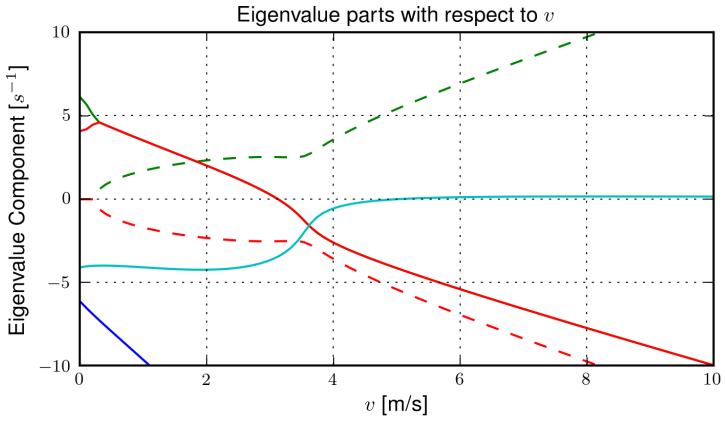

Figure 4.12: The magnitudes of the eigenvalue components with respect to the forward speed when the flywheel is fixed to the front wheel (i.e. has the same angular velocity as the front wheel) and a rigid child is seated on the bicycle. The solid lines show the real parts and the dotted lines show the imaginary parts, with color matching the parts for a given eigenvalue. Generated by `src/extensions/gyro/gyrobike_linear.py`.

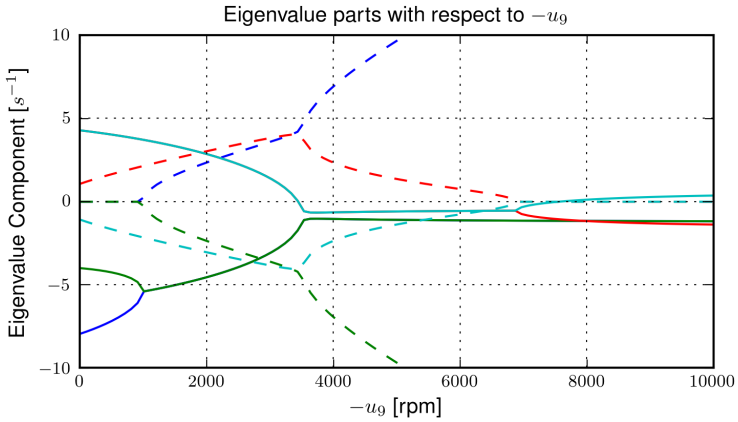

Figure 4.13: The magnitudes of the eigenvalue components with respect to the flywheel angular speed when the forward velocity is 0.5 m/s and a rigid child is seated on the bicycle. The solid lines show the real parts and the dotted lines show the imaginary parts, with color matching the parts for a given eigenvalue. Generated by `src/extensions/gyro/gyrobike_linear.py`.

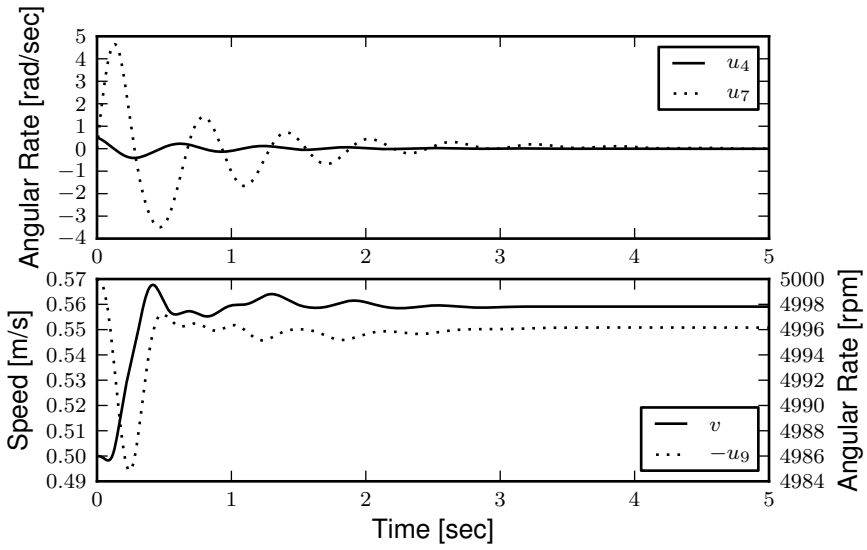

Figure 4.14: The open loop non-linear simulation of the gyro bicycle given the initial conditions: $u_4 = 0.5$ rad/s, $u_6 = -v/r_R$ where $v = 0.5$ m/s, $u_9 = -5000$ rpm.

4.6.1 Notation

G The flywheel rigid body.

m_g Mass of the flywheel.

q_9 Angle of the flywheel with respect to the front wheel.

u_9 Angular rate of the flywheel with respect to the front wheel.

g_o Flywheel mass center.

T_9 Torque acting between the front wheel and the flywheel.

$\mathbf{I}_G$ Inertia tensor of the flywheel.

v The forward speed of the bicycle: $v = -r_R u_6$.

4.7 Leaning rider extension

A common assumption regarding how a person biomechanically controls a bicycle with minimal or no input via the handlebars is that the rider can lean their body relative to the bicycle rear frame. This assumption is more often than not drawn from observing no-hands riding during which the rider seems to lean relative to the bicycle frame. A simple leaning rider can be modeled by adding an additional rider upper body as an inverted pendulum atop the bicycle. This introduces an additional lean degree of freedom, q_9, and can be accompanied by a rider lean torque, T_9 which models the rider's ability to apply forces between the upper torso and the rear frame.

Many have created variations of this model in the past including [VLS67], [RL72], [Wei72], [VZ75], [Nag83], etc. but, as [RL72] points out, the roll torque is the more realistic control input as opposed to roll angle as many of the other authors tend to prefer. Weir et al. notes the fact that lean control has much less authority than steer control, and that the rider more or less leans equal and opposite to the vehicles roll angle [WZT79]. The inverted pendulum with a roll torque has now been widely adopted and more recent works focus on understanding these types of models

([Sha07a], [Sha08], [SKM08], [PH08b], etc.), with the hypothesis that control by roll torque is much less effective than steer torque being confirmed in all these studies.

To build the same model, we define the upper body hinge as a horizontal line at a distance d_4 below the rear wheel center when the bicycle is in the nominal configuration. The direction cosine matrix relating the upper body to the rear frame is

$$
{}^{C}\mathbf{R}^{G} = \begin{bmatrix} c_\lambda & 0 & s_\lambda \\ -s_\lambda s_9 & c_9 & c_\lambda s_9 \\ -s_\lambda c_9 & -s_9 & c_\lambda c_9 \end{bmatrix} \tag{4.22}
$$

A point, c_g, on the hinge is then defined as

$$
\bar{R}^{c_g/d_o} = -d_4 s_\lambda \hat{c}_1 + d_4 c_\lambda \hat{c}_3 \tag{4.23}
$$

where λ is the steer axis tilt and is a function of d_1, d_2, and d_3 as described in *Bicycle Equations Of Motion*.

The mass center is located by

$$
\bar{R}^{g_o/c_g} = l_5 \hat{g}_1 + l_6 \hat{g}_3 \tag{4.24}
$$

The angular velocity and angular acceleration of the upper body in the bicycle frame is defined as

$$
{}^{C}\bar{\omega}^{G} = u_9 \hat{g}_1 \tag{4.25}
$$

$$
{}^{C}\bar{\alpha}^{G} = \dot{u}_9 \hat{g}_1 \tag{4.26}
$$

with $u_9 = \dot{q}_9$. The linear velocities of the hinge point and the upper body center of mass are

$$
{}^{N}\bar{v}^{c_g} = {}^{N}\bar{v}^{d_o} + {}^{N}\bar{\omega}^{C} \times \bar{r}^{c_g/d_o} \tag{4.27}
$$

where

$$
\begin{aligned}
{}^{N}\bar{\omega}^{C} \times \bar{r}^{c_g/d_o} =& d_4 c_\lambda (u_5 + s_4 u_3)\hat{c}_1 - \\
& d_4 (s_\lambda (s_5 u_4 + c_4 c_5 u_3) + c_\lambda (c_5 u_4 - s_5 c_4 u_3))\hat{c}_2 + \\
& d_4 s_\lambda (u_5 + s_4 u_3)\hat{c}_3
\end{aligned}
$$

and

$$
{}^{N}\bar{v}^{g_o} = {}^{N}\bar{v}^{c_g} + {}^{N}\bar{\omega}^{G} \times \bar{r}^{g_o/c_g} \tag{4.28}
$$

where

$$
\begin{aligned}
{}^{N}\bar{\omega}^{G} \times \bar{r}^{g_o/c_g} =& -l_6 (s_9 s_{\lambda-5} u_4 - c_9 u_5 - (s_4 c_9 + s_9 c_4 c_{\lambda-5}) u_3)\hat{g}_1 + \\
& (-l_6 (u_9 + c_{\lambda-5} u_4 + c_4 s_{\lambda-5} u_3) - l_5 (s_9 u_5 + c_9 s_{\lambda-5} u_4 + (s_4 s_9 - c_4 c_9 c_{\lambda-5}) u_3))\hat{g}_2 + \\
& l_5 (s_9 s_{\lambda-5} u_4 - c_9 u_5 - (s_4 c_9 + s_9 c_4 c_{\lambda-5}) u_3)\hat{g}_3
\end{aligned}
$$

The linear accelerations of the hinge point and the upper body center of mass are as follows

$$
{}^{N}\bar{a}^{c_g} = {}^{N}\bar{a}^{d_o} + {}^{N}\omega^{C} \times ({}^{N}\omega^{C} \times \bar{r}^{c_g/d_o}) + {}^{N}\bar{\alpha}^{C} \times \bar{r}^{c_g/d_o} \tag{4.29}
$$

where

$$
\begin{aligned}
{}^{N}\omega^{C} \times ({}^{N}\omega^{C} \times \bar{r}^{c_g/d_o}) =& d_4 (s_\lambda (u_5 + s_4 u_3)^2 + (s_5 u_4 + c_4 c_5 u_3)(s_\lambda (s_5 u_4 + c_4 c_5 u_3) + \\
& c_\lambda (c_5 u_4 - s_5 c_4 u_3)))\hat{c}_1 + \\
& d_4 (u_5 + s_4 u_3)(c_\lambda (s_5 u_4 + c_4 c_5 u_3) - s_\lambda (c_5 u_4 - s_5 c_4 u_3))\hat{c}_2 - \\
& d_4 (c_\lambda (u_5 + s_4 u_3)^2 + (c_5 u_4 - s_5 c_4 u_3)(s_\lambda (s_5 u_4 + c_4 c_5 u_3) + \\
& c_\lambda (c_5 u_4 - s_5 c_4 u_3)))\hat{c}_3
\end{aligned}
$$

and

$$\begin{aligned}{}^N\bar{\alpha}^C \times \bar{r}^{c_g/d_o} =& d_4 c_\lambda (c_4 u_3 u_4 + \dot{u}_5 + s_4 \dot{u}_3)\hat{c}_1 + \\ & d_4 (s_\lambda (s_4 c_5 u_3 u_4 + s_5 c_4 u_3 u_5 - c_5 u_4 u_5 - s_5 \dot{u}_4 - c_4 c_5 \dot{u}_3) - \\ & c_\lambda (s_4 s_5 u_3 u_4 + c_5 \dot{u}_4 - s_5 u_4 u_5 - c_4 c_5 u_3 u_5 - s_5 c_4 \dot{u}_3))\hat{c}_2 + \\ & d_4 s_\lambda (c_4 u_3 u_4 + \dot{u}_5 + s_4 \dot{u}_3)\hat{c}_3\end{aligned}$$

and

$${}^N\bar{a}^{g_o} = {}^N\bar{a}^{c_g} + {}^N\omega^G \times ({}^N\omega^G \times \bar{r}^{g_o/c_g}) + {}^N\bar{\alpha}^G \times \bar{r}^{g_o/c_g} \tag{4.30}$$

where

$$\begin{aligned}{}^N\omega^G \times ({}^N\omega^G \times \bar{r}^{g_o/c_g}) =& (-l_5(s_9 s_{\lambda-5} u_4 - c_9 u_5 - (s_4 c_9 + s_9 c_4 c_{\lambda-5})u_3)^2 - \\ & (s_9 u_5 + c_9 s_{\lambda-5} u_4 + (s_4 s_9 - \\ & c_4 c_9 c_{\lambda-5})u_3)(l_6(u_9 + c_{\lambda-5} u_4 + c_4 s_{\lambda-5} u_3) + \\ & l_5(s_9 u_5 + c_9 s_{\lambda-5} u_4 + (s_4 s_9 - c_4 c_9 c_{\lambda-5})u_3)))\hat{g}_1 - \\ & (s_9 s_{\lambda-5} u_4 - c_9 u_5 - (s_4 c_9 + s_9 c_4 c_{\lambda-5})u_3)(l_5(u_9 + c_{\lambda-5} u_4 + c_4 s_{\lambda-5} u_3) - \\ & l_6(s_9 u_5 + c_9 s_{\lambda-5} u_4 + (s_4 s_9 - c_4 c_9 c_{\lambda-5})u_3))\hat{g}_2 + \\ & (-l_6(s_9 s_{\lambda-5} u_4 - c_9 u_5 - (s_4 c_9 + s_9 c_4 c_{\lambda-5})u_3)^2 - \\ & (u_9 + c_{\lambda-5} u_4 + c_4 s_{\lambda-5} u_3)(l_6(u_9 + c_{\lambda-5} u_4 + \\ & c_4 s_{\lambda-5} u_3) + l_5(s_9 u_5 + c_9 s_{\lambda-5} u_4 + (s_4 s_9 - c_4 c_9 c_{\lambda-5})u_3)))\hat{g}_3\end{aligned}$$

where

$$\begin{aligned}{}^N\bar{\alpha}^G \times \bar{r}^{g_o/c_g} =& -l_6(s_9 u_5 u_9 + c_9 s_{\lambda-5} u_4 u_9 + u_3(s_4 s_9 u_9 + s_4 s_9 c_{\lambda-5} u_4 - c_4 c_9 u_4 - s_9 c_4 s_{\lambda-5} u_5 - \\ & c_4 c_9 c_{\lambda-5} u_9) + s_9 s_{\lambda-5} \dot{u}_4 - s_9 c_{\lambda-5} u_4 u_5 - c_9 \dot{u}_5 - (s_4 c_9 + s_9 c_4 c_{\lambda-5})\dot{u}_3)\hat{g}_1 + \\ & (l_6(s_4 s_{\lambda-5} u_3 u_4 + c_4 c_{\lambda-5} u_3 u_5 - s_{\lambda-5} u_4 u_5 - \dot{u}_9 - c_{\lambda-5}\dot{u}_4 - c_4 s_{\lambda-5}\dot{u}_3) + \\ & l_5(s_9 s_{\lambda-5} u_4 u_9 + c_9 c_{\lambda-5} u_4 u_5 - c_9 u_5 u_9 - u_3(s_4 c_9 u_9 + s_9 c_4 u_4 + s_4 c_9 c_{\lambda-5} u_4 + \\ & s_9 c_4 c_{\lambda-5} u_9 - c_4 c_9 s_{\lambda-5} u_5) - s_9 \dot{u}_5 - c_9 s_{\lambda-5}\dot{u}_4 - (s_4 s_9 - c_4 c_9 c_{\lambda-5})\dot{u}_3))\hat{g}_2 + \\ & l_5(s_9 u_5 u_9 + c_9 s_{\lambda-5} u_4 u_9 + u_3(s_4 s_9 u_9 + s_4 s_9 c_{\lambda-5} u_4 - c_4 c_9 u_4 - s_9 c_4 s_{\lambda-5} u_5 - \\ & c_4 c_9 c_{\lambda-5} u_9) + s_9 s_{\lambda-5}\dot{u}_4 - s_9 c_{\lambda-5} u_4 u_5 - c_9 \dot{u}_5 - (s_4 c_9 + s_9 c_4 c_{\lambda-5})\dot{u}_3)\hat{g}_3\end{aligned}$$

We introduce two additional torques. The first is an input torque between the rear frame and the rider's upper body, T_9. This can be considered as the active torque contribution which the rider's control system would provide. The second torque is defined as

$$T_9^p = -c_9 u_9 - k_9 q_9 \tag{4.31}$$

where c_9 and k_9 are damping and stiffness coefficients which are provided as way to characterize the passive torques generated by the tissue, ligament, tendon, and bone structures. A free lean joint without this passive torque is far from realistic as large active torques would be required to keep the body upright. These are equivalent to simple proportional and derivative negative feedback on the roll angle and could be defined as such equivalently.

The additional generalized force is

$$\bar{R}^{g_o} = m_G g \hat{n}_3 \tag{4.32}$$

and the generalized torques are modified to include the new torques

$$\begin{aligned}\bar{T}^C &= T_4 \hat{a}_1 - T_6 \hat{c}_2 - T_7 \hat{c}_3 + (k_9 q_9 + c_9 u_9 - T_9)\hat{g}_1 \\ \bar{T}^G &= -(k_9 q_9 + c_9 u_9 - T_9)\hat{g}_1\end{aligned} \tag{4.33}$$

The mass of the upper body is m_g and it is assumed to by symmetric about its sagittal plane

$$\mathbf{I}_G = \begin{bmatrix} I_{G11} & 0 & I_{G13} \\ 0 & I_{G22} & 0 \\ I_{G13} & 0 & I_{G33} \end{bmatrix} \tag{4.34}$$

The equations of motion are again formed using Kane's method and linearized as described in Chapter *Bicycle Equations Of Motion*. This linear model has been explicitly explored by both [SKM08] and [PH08b] with parameter values estimated by proportioning the benchmark parameter set from [MPRS07]. The following plot, *Figure 4.15*, uses more realistic rider parameters which are generated with methods described in Chapter *Physical Parameters* and the passive lean torque coefficients are set to zero to demonstrate the nature of the system with no passive stiffness and damping. Notice that the largest eigenvalue is much larger than those reported in Schwab and Peterson with a time to double of about a tenth of a second. We found that root difficult to stabilize when employing a manual control model based on the one presented in Chapter *Control*, which suggests the need and existence for some additional passive stabilization.

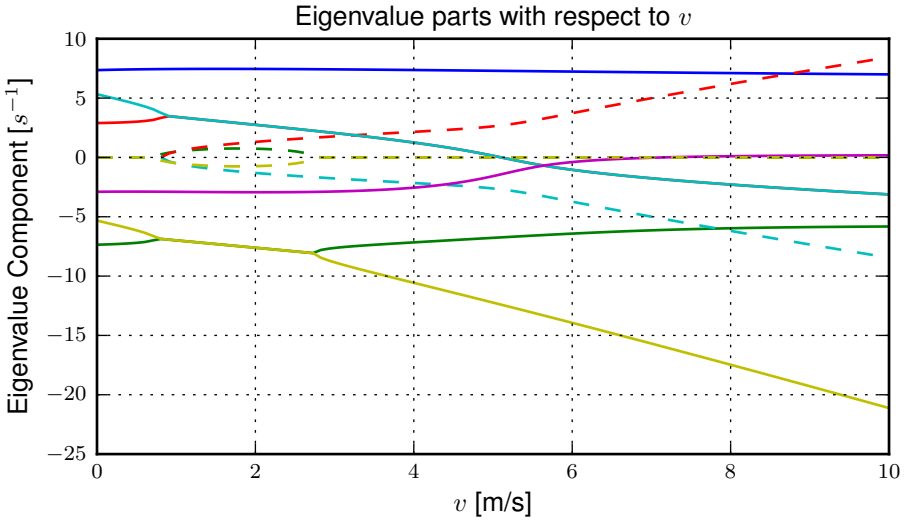

Figure 4.15: The magnitudes of the eigenvalue components with respect to the forward speed for the leaning rider model. The solid lines show the real parts and the dotted lines show the imaginary parts, with color matching the parts for a given eigenvalue. Generated by `src/extensions/lean/riderlean.py`.

The damping and stiffness coefficients can be selected such that the highly unstable rider mode is stabilized and the stable speed range observed in the Whipple model is restored, *Figure 4.16*. It is likely that control strategies that work with the Whipple model can be applied to this model with appropriate stiffness and damping selections. The parameters used are taken from [DLH96], which he estimated to be, $k_9 = 128$ N-m/rad and $c_9 = 50$ N-m/rad/s.

The leaning rider model exhibits a very fast, unstable eigenmode which is constant with respect to speed when the upper body is treated as a simple inverted pendulum. In general, rider lean degrees of freedom have a de-stabilizing effect to the Whipple model. A combination of the rider's active and passive postural control most likely stabilizes this mode in the real system, but it is debatable whether the passive control alone completely stabilizes the mode.

4.7.1 Notation

d_4 The distance to the torso hinge.

l_5, l_6 Distances to locate the upper body mass center.

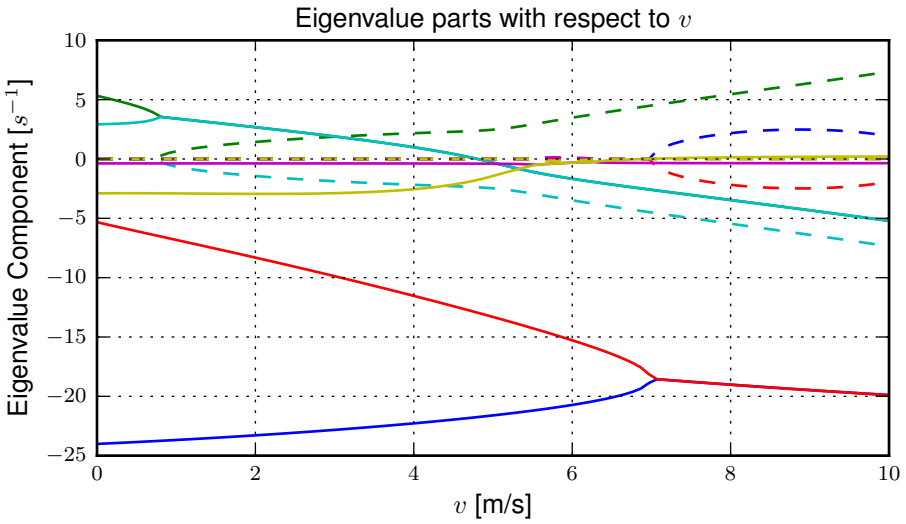

Figure 4.16: The magnitudes of the eigenvalue components with respect to the forward speed for the leaning rider model. The solid lines show the real parts and the dotted lines show the imaginary parts, with color matching the parts for a given eigenvalue. Generated by `src/extensions/lean/riderlean.py`.

$s_{\lambda-5}$, $c_{\lambda-5}$ Shorthand for $\sin(\lambda - q_5)$ and $\sin(\lambda - q_5)$.

c_g Rider hinge point.

c_9, k_9 The passive stiffness and damping coefficients.

m_g Mass of the upper body (torso, arms, neck, and head).

$\mathbf{I}_g$ Inertia of the upper body.

T_9 The active torque acting between the rider's upper body and the rear frame.

T_9^p The passive torque acting between the rider's upper body and the rear frame.

4.8 David de Lorenzo extension

4.8.1 Preface

To expand on the ideas presented in the previous section, I'd like to share some findings from a short conference paper that Luke Peterson and I put together for the 11th International Symposium on Computer Simulation in Biomechanics [MPH07]. I have included it here almost verbatim but have updated the writings to tie it better into the dissertation and make it less dated. I have not updated the derivation of the equations of motion to reflect the parameters and methodology presented in this dissertation, so I will leave those out but they can be found in the source code. Nonetheless the model can be systematically derived in the same fashion as the previous sections. The initial interest in this model was based on an unpublished paper by de Lorenzo and Hubbard [DLH96] which explored parameter studies of a model similar to the one that is presented. Here we pursue the effects that passive springs and dampers at the biomechanical joints have on the stability of the bicycle, in much the same way as in the previous section but with a more complex rider model.

4.8.2 Introduction

We build on the Whipple model by adding biomechanical degrees of freedom that capture the dominant rider's motion and the flexible coupling to the rear frame. The rationale for doing so is that the mass and inertia of a rider is much larger than that of the bicycle, and the coupling between the rider and the bicycle is certainly not rigid. Rider modeling has been approached in the motorcycle literature [LS06] but typically does not address the smaller vehicle inertial properties and the possible difference in the coupling constants. For example, when riding a bicycle, it is easy to observe that the frame yaw and roll motions differ from the rider yaw and roll motions. Modeling the rider and frame as a single rigid body ignores this flexible coupling. In this analysis, we seek to understand the effect of the addition of these new degrees of freedom on the stable speed ranges of the bicycle. We examine the additional modes associated with the new degrees of freedom and how they impact the weave, capsize, and caster modes seen in the Whipple model.

4.8.3 Methods

Beginning with the Whipple model, the bicycle/rider rigid body is divided into three separate bodies; the bicycle rear frame, the rider lower body and the rider upper body. The lower body includes the legs and hips while the upper body includes the torso, arms, and head. Three additional generalized coordinates are used to configure the rider rigid bodies with respect to the frame and to each other. The first two are the lateral rotation of the lower body about a pivot point at the feet and lateral rotation of the upper body with respect to the lower body, both about horizontal axes parallel to the forward axis of the bicycle frame. The lower body is connected to the frame at the foot pivot by a revolute joint and at the seat by a linear spring and damper in parallel. The third coordinate is the twist of the upper body relative to the lower body about a nominally vertical axis. Both upper body lean and twist motions are resisted by linear torsional springs and dampers, also in parallel. These rider degrees of freedom are detailed in *Figure 4.17* and are similar to the motorcycle rider model constructed by Katayama, et al. [KAN88] with the exception of the rider twist. The lateral linear spring and damper represents the connection between the rider's crotch and the seat[1]. The spring and damper constants are influenced by the seat and the properties of the skeletal muscle tissue of the inner thighs and/or buttocks. The torsional springs and dampers represent the musculoskeletal stiffness and damping at the hips.

This six-rigid-body model has eleven generalized coordinates. One generalized coordinate (frame pitch) is eliminated by the holonomic configuration constraints requiring that both wheels touch the ground. This leaves ten generalized speeds, of which four are eliminated due to the nonholonomic constraints for the purely rolling wheels. The nonlinear equations of motion were linearized numerically about the nominal upright, constant velocity configuration using a central differencing method with an optimum perturbation size. The linear system is tenth order in frame roll, steer, lower body lean, upper body lean, and upper body twist.

The physical parameters are adapted from [MPRS07] with exception of the rider pivot point locations and the spring and damper constants. The pivot point locations were measured and the spring and damper constants were taken from [DLH96], which he estimated. All of the physical parameters were chosen in such a way that, if the rider degrees of freedom are locked, the model reduces to the benchmark Whipple model, similar to the later work done by [PH08b] and [SKM08].

4.8.4 Results and Discussion

In order to understand how the eigenvalues impact each state variable of our system, it is essential to examine the components of each eigenvector corresponding to each generalized coordinate. By detailed examination, we are able to determine how each eigenvalue contributes to each generalized coordinate, across the range of speeds examined.

Figure 4.18 shows the real parts of the identified eigenvalues of the flexible rider model and *Figure 4.19*. By comparison to the Whipple model, it can be seen that the modes are greatly affected by the additional rider states. The weave mode has become unstable for all velocities and no stable speed range is present. Additionally, the rider modes are all complex at all speeds.

[1] We got a kick out of "crotch stiffness" i.e. the stiffness of the crotch spring, and tried to encourage Mont to use the terminology when he presented this for us in Taiwan.

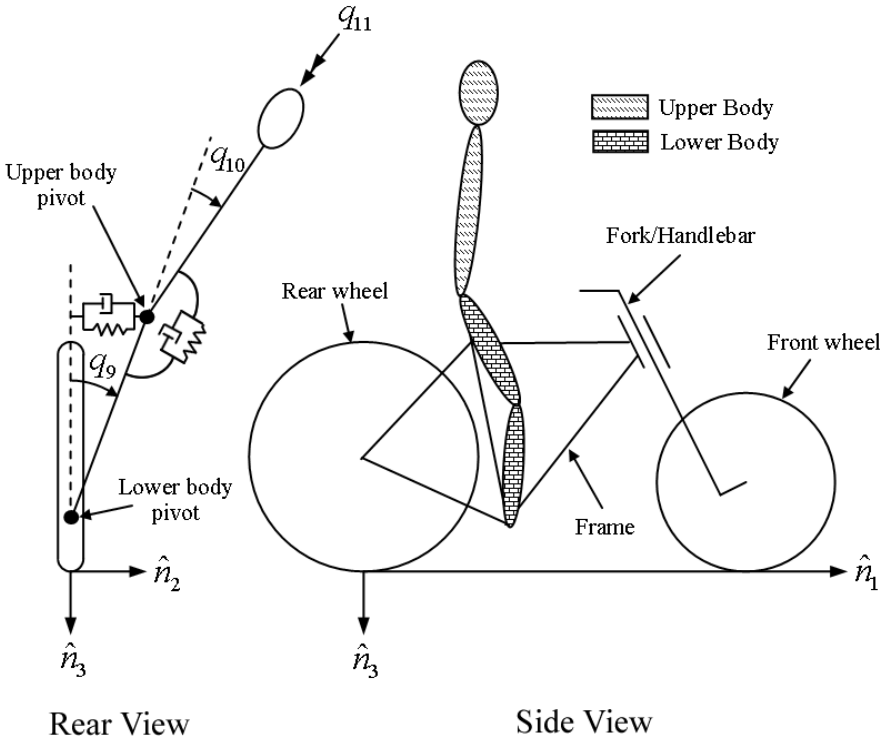

Figure 4.17: Pictorial description of (a) the additional rider degrees of freedom and (b) the six rigid bodies.

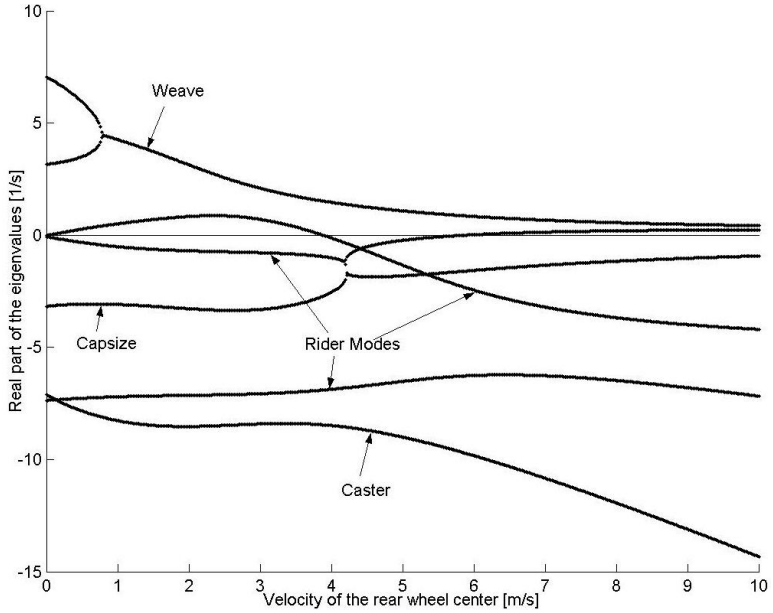

Figure 4.18: Real parts of the eigenvalues as a function of forward speed with the stiffness and damping terms set to realistic values.

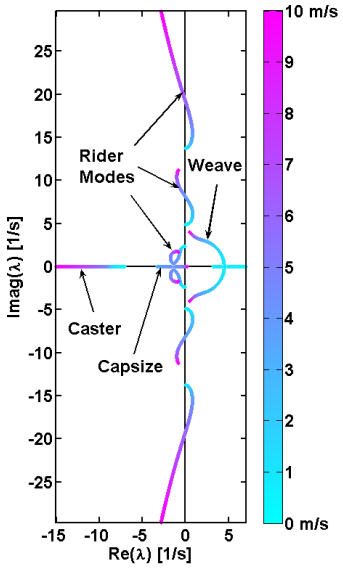

Figure 4.19: Root locus of the eigenvalues with respect to speed, a different view of *Figure 4.18*.

Examining the eigenvector of the weave mode at different velocities, we find that at low speeds the weave mode is dominated by frame roll and steer, while at high speeds the weave is dominated by upper body lean and twist about the body's long axis, *Figure 20*. This phenomenon was also observed by Limebeer and Sharp [LS06]. Furthermore, another unstable oscillatory eigenvalue pair is present at velocities below about 4 m/s for this parameter set.

As the stiffness and damping coefficients for the rider/frame coupling are increased (by factors of about 10^3 and 30 respectively), the eigenvalues begin to match those of the Whipple model, and a stable speed range reappears. However, the values of stiffness and damping for which a stable speed range did exist are unrealistically high *Figure 21*.

4.8.5 Conclusion

The notion that the bicycle-rider system can be stable during hands-free riding with no active control from the rider seems to be not necessarily true when the rider's biomechanics are modeled more realistically. For the particular set of estimated parameters, the weave mode is unstable for the entire range of speeds investigated when realistic flexible rider dynamics are included. While the Whipple model provides many insights into the dynamics and control of the bicycle, it lacks the complexity to capture the essential dynamics that are present in open-loop hands-free riding. In particular, it is highly likely that bicycle rider must always use active control to keep the bicycle upright and self-stabilization is not guaranteed. Parameters studies that show the dependence of stability across a range of speeds for ranges of stiffness and damping at the biomechanical joints can shed more light on the system for more conclusive results.

4.9 No Hands

I've ended up thinking a great deal about the actual biomechanical motion one uses to balance a bicycle when riding no handed and I've learned much about it by talking with colleagues such as Jim Papadopoulos, Jodi Kooijman, Arend Schwab, and others. For the final studies in this dissertation I had intended to do a thorough study of the dynamics of balancing with no hands by more carefully modeling the actual biomechanics we employ during the task. Understanding hands free balancing can also shed light into how we use our body when we also have our hands on the

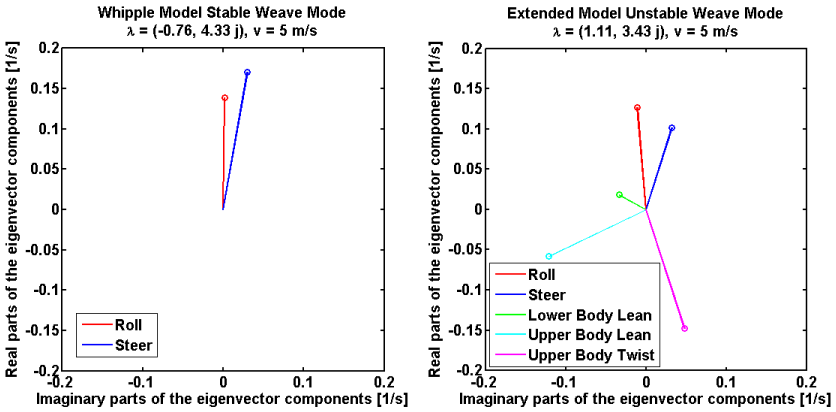

Figure 4.20: Weave mode eigenvector components for the Whipple model (left) and the de Lorenzo model (right) at 5.0 m/s.

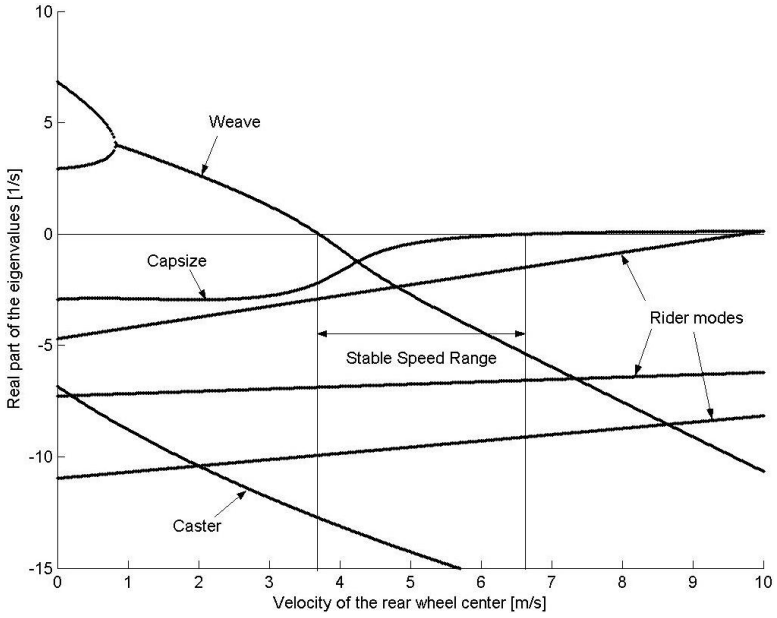

Figure 4.21: Real parts of the eigenvalues as a function of forward speed with the stiffness and damping terms set to unrealistically high values.

bars, albeit with much smaller body motions because steer is almost always the optimal control input to the bicycle. Steer provides much more control authority.

It is relatively easy to learn to ride without using ones hands and many people that know how to ride a bicycle can do so. Some can even navigate roads and obstacles reasonably well. Without being able to directly affect the steering angle for control purposes, one must somehow affect the roll angle, which in turn is coupled to steering. Driving the roll angle drives the steer angle which points the bicycle in the desired direction. In the purely mechanical sense one can imagine that a rider could "lean" relative to the rear frame, thus inducing the counter reaction causing the frame to roll the opposite direction of the lean. Models are often the chosen with this theory in mind [VZ75], [PH08b], [SKM08], [Sha08], etc. They are the most intuitive and simple model but the idea of leaning may in fact be too simplistic to describe the actual biomechanical coupling a rider has with a bicycle[2].

The rider's upper body is typically more than three times the mass of the bicycle and it takes proportionally more force to move it. The studies that will be presented in Chapters *Delft Instrumented Bicycle* and *Motion Capture* show that the rider's upper body both moves little relative to the rear frame and leans little with with respect to inertial space[3]. In contrast the bicycle can quickly roll relative to the relatively inertially "fixed" rider. With that in mind, it is possible to imagine rolling the bicycle frame underneath the body using leg and buttock muscles. The fact that during hands-free riding one feels the seat moving back and forth under between one's legs, gives some evidence that the coupling at the seat is important. Another interesting thing to note is that it is virtually impossible to control a bicycle without both hands *and* both feet placed on the grips and pedals, respectively. Removing ones feet from the pedals removes the ability to apply forces from the rider's body to the bicycle frame, which can contribute to control of the bicycle roll angle. Secondly, it is also noteworthy that the roll angle of the bicycle can be commanded much easier when the rider is up off the seat (i.e. the rider contacts the bicycle only with hands and feet). This leads me to hypothesize that no-hand-control is dependent on the rider's ability to roll the bicycle frame using the lower extremity muscles which are critically dependent on the leg.

If that is true, then there is may be a simple model that can capture the relative motion of the bicycle rear frame with respect to the lower extremities and pelvis. To help confirm this I examined the data from the motion capture experiments (Chapter *Motion Capture*) of a no-hand run with the rider pedaling. *Figure 22* plots the motion of the coccyx and pelvis markers in the rear frame reference frame from the perspective of looking at the rider's torso from the front for a single run. This plot was shows that the coccyx moves laterally with respect to bike frame, but more prevalent are the curves that the pelvis follows. This gives indication that the pelvis basically rotates about an axis just below the seat that runs longitudinally with respect to the bicycle.

Gilbert Gede and I began devising a harness that would both constrain the rider's motion to the motion observed in *Figure 22* and allows us to measure the forces and the kinematics involved. We created a video (http://www.youtube.com/embed/FcAp-DbHp9M) shot from behind and shows me balancing no-handed on a treadmill. We taped three sticks to my back: one across the shoulders, the second to the upper portion of my spine, and the third to the lower portion of my spine to visualize the dominant motion of the rider with respect to the bicycle frame and how the spine moved. I chose the stick locations based on the motion capture studies we did. This video confirmed that the spine bend could probably be described by a single joint in the middle of the spine and that the pelvis rolls about the seat (i.e. a longitudinal axis just below the seat).

At this point, we constructed a mock-up of a harness that would both measure these motions and limit the rider to the observed motions.

The model to describe this motion would have a revolute joint just below the seat such that the riders pelvis can roll about a longitudinal revolute joint just below the seat. The legs would be constrained such that the feet locked into the foot pegs and the knee angles would be dependent on the pelvis roll angle. Finally, the spine would be stiffened with a back brace and a single revolute joint for back lean relative to the pelvis would be measured.

We intended to develop a harness and pair it with a force measuring seat post and foot pegs which measure the downward force applied by the feet to the bicycle. The goal would have been to characterize the both the kinematic

[2] A model for leaning on a motorcycle makes more sense as the mass of the motorcycle is comparable to or more than the mass of the riders upper body.

[3] [WZT79] points out this with respect to motorcycles, in that the rider's upper body mostly stays still and rider's lean angle is nearly equal and opposite to the motorcycle.

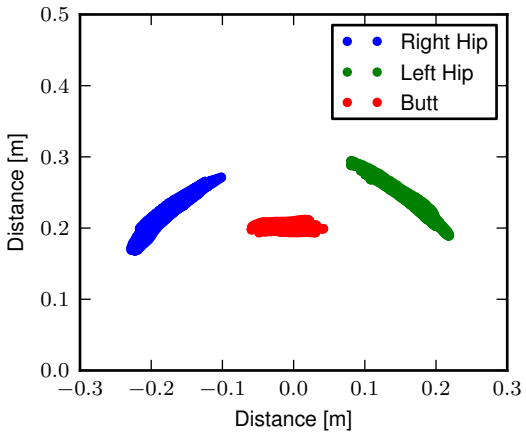

Figure 4.22: The hip trace from run # 3104. This plots the position of the two hip markers and the coccyx marker relative to the bicycle's rear frame in space over time. View the video (http://www.youtube.com/7KXQPUsA3ds).

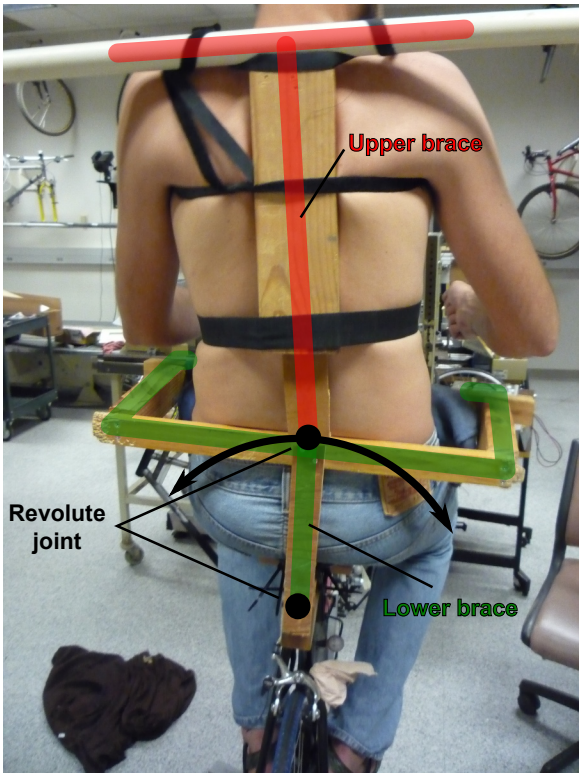

Figure 4.23: A mock-up of a harness to measure the dominant motions of the rider's pelvis roll angle relative to the bicycle rear frame and the lean angle relative to the pelvis. The lower brace (green) is affixed the rider's pelvis and rotates relative to the bicycle frame. The second joint allows the rider's torso to lean relative to the pelvis.

and kinetic coupling between the rider and the bicycle which causes the bicycle to roll. I included this section to simply document the thoughts and effort, but none of this was ever executed in a proper experiment.

4.10 Conclusions

Several extensions to the Whipple model have been presented. The details are not exhaustive but provide some useful conclusions for the coming chapters. I showed that the lateral force input we used in the control experiments must be properly accounted for and not simply assumed to be characterized by a pure roll torque. This force contributes to both the roll and steer degrees of freedom which is a function of the location of the force application. Secondly, the addition of the inertial affects of the arms change the bicycle system dynamics significantly. In this particular case, it eliminates any possibility for stability and the capsize mode becomes very unstable. This model will play a role in the data analysis presented in Chapter *System Identification* because it more realistically models our test subjects' motion. In the third section, I show how adding a flywheel to the front wheel of a bicycle can radically change it's stable speed regime and can make the model stable at very low speeds, even slower than average walking. But if the inertial effects of the rider are taken into account, the flywheel may have to spin at very high speeds for any significant change in dynamics. Next, I show that adding various rider degrees of freedom generally creates an unstable system, but passive forces acting on the new joints can potentially stabilize the new modes. It is likely that the rider must make use of a combination of both passive and active control to keep the bicycle/rider system stable. Finally, I've presented some ideas and thoughts on developing a slightly different biomechanical model of the rider that may be a more realistic way of characterizing the motion used for hands-free control of the bicycle.

CHAPTER

FIVE

PHYSICAL PARAMETERS

5.1 Preface

My first concern with the physical parameters of the bicycle and rider occurred in my multi-body dynamics class project [Moo06]. There I developed a method of estimating the parameter values using simply the geometry and mass of the bicycle and rider. It was eventually presented as part of a paper at the 2008 ISEA conference in Biarritz, France [MH08]. This method served me well until more accurate estimates of the parameters were needed for the first instrumented bicycle I helped build at TU Delft, see Chapter *Delft Instrumented Bicycle*. I signed on to the task of measuring the bike's physical parameters using the equipment and procedures developed in [Koo06] and to combine the results with my basic human model from [MH08] for the estimation of the complete system parameters of the Whipple model. These first measurements and the details of the human model were eventually presented in [MKHS09]. During this work, Dr. Hubbard encouraged me to think about the accuracy of the measurements in more detail, as some of the practices we were using were not as accurate as they could be. With that in mind and the fact that there was very little complete data available on the physical parameters of real bicycles, I decided to measure an assortment of bicycles we had available around the lab in Delft [MHP+10]. From this tedious task a rich data set was created and the measurement methodology tightened up considerably. Once I was back in Davis, we setup almost identical equipment to measure the two new bicycles we were constructing, see Chatper *Davis Instrumented Bicycle*. Danique Fintelman helped us come up with a more accurate geometry measurement. Steven Yen also used the equipment to measure a children's bicycle with a gyro wheel. With one last improvement, we updated the human parameter estimates when Chris Dembia implemented Yeadon's human inertia model and it was combined with the accurate bicycle measurements. These final methods for both bicycle and rider are implemented in two open source software packages.

5.2 Bicycle Parameters

Accurate measurements of a bicycle's physical parameters are required for realistic dynamic simulation and analysis. The most basic models require the geometry, mass, mass location, and mass distributions for the rigid bodies. More complex models require estimates of tire characteristics, human body segment inertial characteristics, friction, stiffness, damping, etc. In this chapter I present the measurement of the minimal bicycle/rider parameters required for the benchmark Whipple bicycle model presented in [MPRS07]. This model is composed of four rigid bodies, has ideal rolling and frictionless joints, and is laterally symmetric. A set of 25 parameters describes the geometry, mass, mass location and mass distribution of each of the rigid bodies. The experimental methods used to estimate the parameters described herein are based primarily on the work done in [Koo06], [KSM08] and [MKHS09] but have been refined for improved accuracy and methodology.

Koojiman's work was preceded by that of several others. Roland and Massing [RM71] measured the physical parameters of a bicycle in much the same way as is presented, including calculations of uncertainty from the indirect measurement techniques. [VZ75] measured the inertial parameters of his robotic bicycle with a swing pendulum and a stop watch. Patterson [Pat04b] used a swing to measure the roll inertia of recumbent bicycles with a rider. [Con09]

and [Ste09] used a computer aided design package to estimate the parameters. [ER10] measured a bicycle for his bicycle dynamics class in Spain. Also, some notable motorcycle and scooter measurements include [Doh53], [Doh55], [SG71], [Eat73b], [RR73], and [Sha97].

Here is documented the indirect measurement of ten real bicycles' physical parameters. We improve upon previous methods by both increasing and reporting the accuracies of the measurements and by measuring the complete moments of inertia of the laterally symmetric frame and fork needed for analysis of the nonlinear model. Furthermore, very little data exists on the physical parameters of different types of bicycles and this work aims to provide a small sample of bicycles.

We measured the physical characteristics of eleven different bicycles, three of which were set up in two different configurations. The first six bicycles, chosen for both variety and convenience, are as follows: *Batavus Browser*, a Dutch style city bicycle measured with and without instrumentation as described in [KSM09]; *Batavus Stratos Deluxe*, a Dutch style sporty city bicycle; *Batavus Crescendo Deluxe* a Dutch style city bicycle with a suspended fork; *Gary Fisher Mountain Bike*, a hard-tail mountain bicycle; *Bianchi Pista*, a modern steel frame track racing bicycle; and *Yellow Bicycle*, a stripped down aluminum frame road bicycle measured in two configurations, the second with the fork rotated in the head tube 180 degrees for larger trail. The last two bicycles were measured in Davis: the instrumented bicycle presented in chapter *Davis Instrumented Bicycle* and a children's bicycle with a stabilizing flywheel called the GyroBike.

These eleven different parameter sets can be used with, but are not limited to, the benchmark bicycle model. The accuracy of all the measurements are presented. The accuracies are based measurement inaccuracies and the proper use of error propagation theory with correlations taken into account.

5.2.1 Parameters

Of primarily concern was measuring and estimating the 25 parameters associated with the benchmark Whipple bicycle model which is derived and described in [MPRS07]. The unforced two degree-of-freedom, $\mathbf{q} = [\delta \quad \phi]^T$ model takes the form:

$$\mathbf{M}\ddot{\mathbf{q}} + v\mathbf{C}_1\dot{\mathbf{q}} + \left[g\mathbf{K}_0 + v^2\mathbf{K}_2\right]\mathbf{q} = 0 \tag{5.1}$$

where the entries of the $\mathbf{M}$, $\mathbf{C}_1$, $\mathbf{K}_0$ and $\mathbf{K}_2$ matrices are combinations of 25 bicycle physical parameters that include the geometry, mass, mass location and mass distribution of the four rigid bodies. The 25 parameters presented in [MPRS07] are not necessarily a minimum set for the Whipple model, as shown in [Sha08], but are useful none-theless as they represent intuitively measurable quantities and have become become standard due to the nature of the benchmark. They are also not parameters used in directly in the derivation in Chapter *Bicycle Equations Of Motion* but can easily be converted, as was shown. The 25 parameters can be measured using many techniques. In general, I attempted to measure the benchmark parameter as directly as possible to improve the accuracy.

5.2.2 Bicycle Descriptions

We measured a total of eight bicycles in eleven configurations, *Figure 5.1*. The three Batavus bicycles were donated by the manufacturer. We asked for a bicycle that they considered stable and one that they did not. They offered the Browser as a "stable" bicycle and the Stratos as "nervous". The Crescendo was considered average handling. We measured an instrumented version of the Browser that was used in the experiments described in Chapter *Delft Instrumented Bicycle*. The Fisher and the Pista were chosen to provide some variety, a mountain and road bike. The yellow bike is used to demonstrate bicycle stability and the forked is reversed to provide better stability when perturbed with no rider. The Davis instrumented bicycle is an instrumented bicycle described in Chapter *Davis Instrumented Bicycle* and we measured the frame in configurations for different rider seating positions. The child's bicycle has the GyroWheel product installed in the front wheel. The first six of these bicycles were measured in Delft and will hereafter be referred to as the *Delft Bicycles*. The remaining two bicycles were measure in Davis and will be referred to as the *Davis Bicycles*.

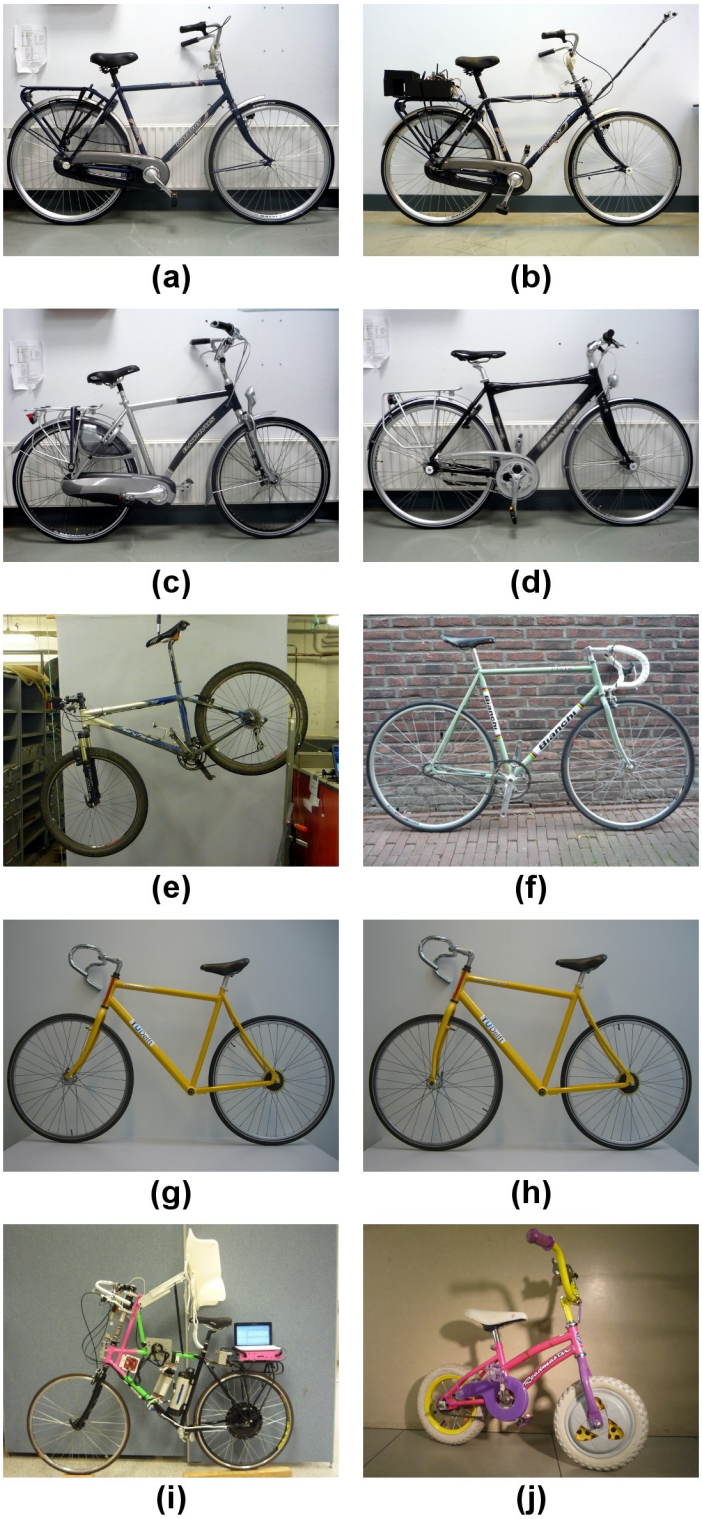

Figure 5.1: The ten measured bicycles: (a) Batavus Browser, (b) Instrumented Batavus Browser, (c) Batavus Crescendo Deluxe, (d) Batavus Stratos Deluxe, (e) Gary Fisher, (f) Bianchi Pista, (g) Yellow Bicycle, (h) Yellow Bicycle with reversed fork, (i) Davis Instrumented Bicycle, (j) Gyro Bicycle. The Davis Instrumented Bicycle was measured twice each with the body cast and seat height in different positions. The first "Rigid" was set up for Jason and the second "Rigidcl" was set up for Luke and Charlie. Only one image of the Rigid bicycle is shown, even though it was measured in two slightly different configurations.

5.2.3 Accuracy

We here analyze the accuracy of the measurements of the parameters. Following the lead of [RM71] error propagation theory was used to calculate accuracy of the 25 benchmark parameters. This begins by estimating the standard deviation of the actual measurements taken, see Section *Bicycle Measured Parameters*. The measurement error was chosen based on the measuring tool and methods used. If x is a parameter and is a function of the measurements, $u, v, \ldots$, which are Gaussian random variables then x is also a Gaussian random variable defined as $x = f(u, v, \ldots)$. The sample variance of x is defined as

$$s_x^2 = \frac{1}{N-1}\sum_{i=1}^{N}\left[(u_i - \bar{u})^2\left(\frac{\partial x}{\partial u}\right)^2 + (v_i - \bar{v})^2\left(\frac{\partial x}{\partial v}\right)^2 + 2(u_i - \bar{u})(v_i - \bar{v})\left(\frac{\partial x}{\partial u}\right)\left(\frac{\partial x}{\partial v}\right) + \ldots\right] \tag{5.2}$$

Using the definitions for variance and covariance, Equation (5.2) can be simplified to

$$s_x^2 = s_u^2\left(\frac{\partial x}{\partial u}\right)^2 + s_v^2\left(\frac{\partial x}{\partial v}\right)^2 + 2s_{uv}\left(\frac{\partial x}{\partial u}\right)\left(\frac{\partial x}{\partial v}\right) + \ldots \tag{5.3}$$

If u and v are uncorrelated then $s_{uv} = 0$. Most of the calculations hereafter have uncorrelated variables but a few do not and the covariance has to be taken into account. Equation (5.3) can be used to calculate the variance of all types of functions. I made use of the Python package uncertainties (http://pypi.python.org/pypi/uncertainties/) [Leb10] to simplify the book keeping of the correlations and variance calculations, thus some of the equations for the error are not shown in the following sections.

5.2.4 Geometry

The geometry measurements of the Delft bicycles focused on measuring the benchmark parameters: trail, wheelbase, and steer axis tilt as directly as possible. I also present an alternative method for the geometry used with the Davis bicycles that attempts to measure the distances in my model derivation, Chapter *Bicycle Equations Of Motion*, which improves the accuracy of the parameters. Keep in mind, that I assumed that the frame did not flex and that the wheel radii do not change with rider weight when taking geometric measurements.

Wheel Radii

The radii of the front r_F and rear r_R wheels were estimated by measuring the linear distance traversed along the ground through at least ten rotations of the wheel. Each wheel traversal was measured separately and the measurements were taken with rider seated on the bicycle, except for the gyro bicycle which had no rider. A 72 kg rider sat on the Delft bicycles and an 84 kg rider on the Davis instrumented bicycle [1]. A 30 meter tape measure (resolution: 2mm) was pulled tight and taped on a flat level smooth floor for the Delft bicycles and for the Davis bicycles we marked a 68 foot length on the floor and used a 1/16 inch resolution ruler to measure the 6 to 15 inch distance past the 68 foot mark where the rotation stopped. The tire was marked and aligned with the tape measure *Figure 5.2*. The accuracy of the distance measurement is approximately ± 0.01 meter. The tires were pumped to the recommended inflation pressure before the measurements. The wheel radius is calculated by

$$r \pm \sigma_r = \frac{d}{2\pi n} \pm \left(\frac{\sigma_d}{2\pi n}\right) \tag{5.4}$$

where r is the wheel radius, d, is the traversal distance, n, is the number of rotations and σ is the respective standard deviation of the subscripted variable. I use subscripts F and R from front and rear wheels, respectively, in the measurement tables in Section *Bicycle Measured Parameters*.

[1] This is actually the same rider: I gained some weight after drinking all that good beer in the Netherlands!

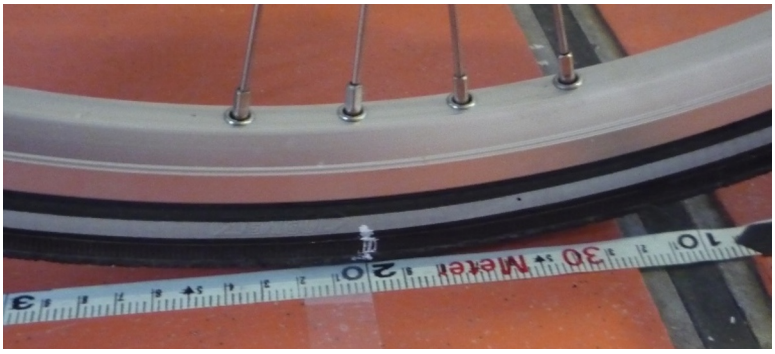

Figure 5.2: Wheel and tire with chalk mark aligned to the tape measure.

Head Tube Angle

For the Delft Bicycles, the head tube angle was measured directly using an electronic level, *Figure 5.3*. The bicycle frame was fixed perpendicular to the ground, the steering angle was set to the nominal position, tire pressures were at recommended levels, and the bicycle was unloaded. The steer axis tilt λ is the complement to the head tube angle, γ.

$$\lambda \pm \sigma_\lambda = \frac{\pi}{180°}(90° - \gamma) \pm \left(\frac{\pi}{180°}\right)\sigma_\gamma \tag{5.5}$$

Figure 5.3: The digital level set against the Yellow Bicycle's head tube.

Trail

The idealized trail is difficult to measure directly due to the fact that the tire has a contact patch and there is no distinct contact point. Instead I chose to measure the fork offset, f_o, and compute the ideal trail. The fork offset was measured by clamping the steer tube of the front fork into a v-block on a flat table, *Figure 5.4*. For the Delft bicycles, a ruler

was used to measure the height of the center of the head tube and the height of the center of the axle axis, and for the Davis bicycles we made use of more accurate height gages. The fork blades were aligned such that the axle axis was parallel to the table surface.

$$c = \frac{r_\mathrm{F} \sin\lambda - f_o}{\cos\lambda} \tag{5.6}$$

$$\sigma_c^2 = \sigma_{r_\mathrm{F}}^2 \tan^2\lambda - \sigma_{f_o}^2 \sec^2\lambda + \sigma_\lambda^2 \left(r_\mathrm{F} \sec^2\lambda - f_o \sec\lambda \tan\lambda\right)^2 \tag{5.7}$$

Figure 5.4: The fork of the Davis Bicycle setup for measuring the fork offset.

Wheelbase

I measured the wheelbase directly with the bicycle in nominal configuration described in Section *Head Tube Angle*. We used a tape measure to measure the distance from one wheel axle center to the other.

5.2.5 Alternative Geometry Measurement Method

The geometry for the bicycle model presented in Chapter:*eom* can almost be measured directly. I used this method for the Davis Bicycles. The bicycle frame is set on a granite measurement table such that the head tube is in a v-block and parallel to the table surface and the bicycle frame is situated such that the frame is perpendicular to the table surface, *Figure 5*. The fork is rotated in the head tube such that the fork blades curve upwards. Two dummy axles are fit into the front and rear dropouts and the axles are ensured to be parallel to the table surface. The height from the table surface to the top of each axle are recorded with a height gage and the diameters of the axles are measured with a micrometer or caliper.

These measurements can then be converted to the three essential bicycle dimensions, d_1, d_2, d_3 described in Chapter *Bicycle Equations Of Motion*.

$$d_1 = h_1 + h_2 - h_3 + \frac{\hat{d}_1 - \hat{d}_2}{2} \tag{5.8}$$

$$d_3 = h_4 - h_5 + \frac{\hat{d}_4 - \hat{d}_3}{2} \tag{5.9}$$

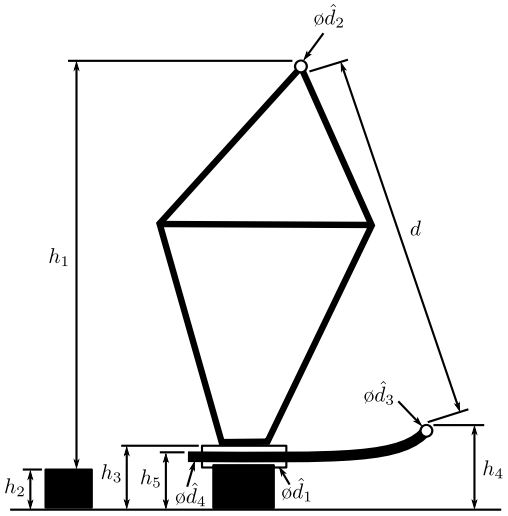

Figure 5.5: The actual measurements taken to compute the basic bicycle geometry.

$$d_2 = \sqrt{\left(d + \frac{\hat{d}_2 + \hat{d}_3}{2}\right)^2 - (d_1 - d_2)^2} \tag{5.10}$$

The traditional [MPRS07] parameters can then be calculated. If r_F does not equal r_R then the steer axis tilt cannot be computed analytically as Equation (5.11) holds.

$$\sin(\lambda) = \frac{r_F - r_R + d_2 \cos(\lambda)}{d_1 + d_3} \tag{5.11}$$

It is trivial to find the solution to Equation (5.11) numerically. If $r_F = r_R$, the solution for λ is analytic.

$$\lambda = \arctan\left(\frac{d_2}{d_1 + d_3}\right) \tag{5.12}$$

The wheelbase is

$$w = (d_1 + d_3)\cos(\lambda) + d_2 \sin(\lambda) \tag{5.13}$$

and trail is then computed with Equation (5.6), realizing $f_o = d_3$:

$$c = \frac{r_F \sin(\lambda) - d_3}{\cos(\lambda)} \tag{5.14}$$

5.2.6 Mass

For the Delft bicycles, each of the four bicycle parts were measured using a Molen 20 kilogram scale with a resolution of 20 grams, *Figure 5.6*. The accuracy was conservatively assumed to also be ± 20 grams. Also, the total mass was measured using a spring scale with a resolution of 100 grams. The total mass was only used for comparison purposes, as it was not very accurate. The masses of the parts of the Davis bicycles were measured with a digital scale with a resolution of 50 grams (A & D FV-150k Industrial Scale).

Figure 5.6: The scale used to measure the mass of each Delft bicycles' components.

5.2.7 Center of Mass

Wheels

The centers of mass of the wheels were assumed to be at their geometrical centers to comply with the Whipple model. This was also assumed for the flywheel in the gyro bike.

Rear Frame

The rear frame bicycle configuration was hung in at least three orientations through the assumed lateral plane of symmetry. I assumed that the frame was laterally symmetric, complying with the Whipple model, thus reducing the need to use a more complex three dimensional measurement setup. The frame could rotate about a joint such that gravity aligned the center of mass with the support rod axis. The orientation angle of the steer axis, α_{B}, see *Figure 5.7*, relative to the earth was measured using a digital level ($\pm 0.2^{\circ}$ accuracy), *Figure 5.8*. A thin string was aligned with the pendulum axis which passed by the frame. The horizontal distance a_{B} between the rear axle and the string was measured by aligning a 1 mm resolution ruler perpendicular to the string *Figure 5.9*. The distance a_{B} was negative if the string fell to the right of the rear axle and positive if it fell to the left of the rear axle, when viewing the bicycle from the right side. These measurements allow for the calculation of the center of mass location in the global reference frame.

The frame rotation angle β_{B} is defined as rotation of the frame in the nominal benchmark configuration to the hanging orientation, rotated about the Y axis.

$$\begin{aligned} \beta_{\mathrm{B}} &= \lambda - \alpha_{\mathrm{B}} \\ \sigma_{\beta}^2 &= \sigma_{\lambda}^2 + \sigma_{\alpha}^2 \end{aligned} \tag{5.15}$$

The center of mass can be found by realizing that the pendulum axis X_P is simply a line in the nominal bicycle reference frame with a slope m and a z-intercept b where the i subscript corresponds to the different frame orientations,

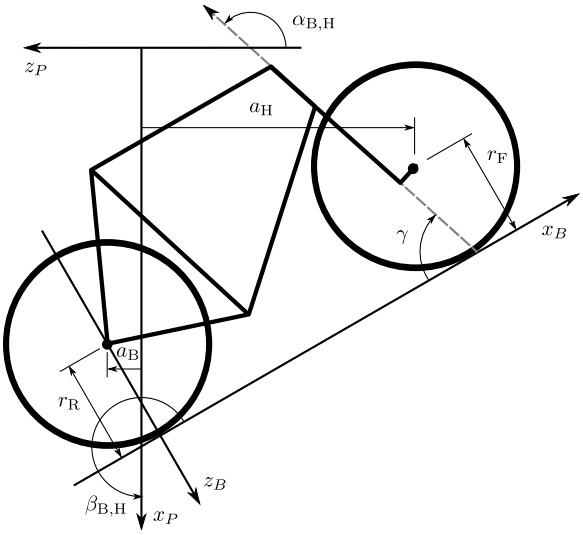

Figure 5.7: Pictorial description of the angles and dimensions that related the nominal bicycle reference frame XYZ_B with the pendulum reference frame XYZ_P.

Figure 5.8: The digital level was mounted to a straight edge aligned with the head tube of the bicycle frame. This was done without allowing the straight edge to touch the frame. The frame was not absolutely stationary so this was difficult. The light frame oscillations could be damped out by submerging a low hanging area of the frame into a bucket of water to decrease the oscillation.

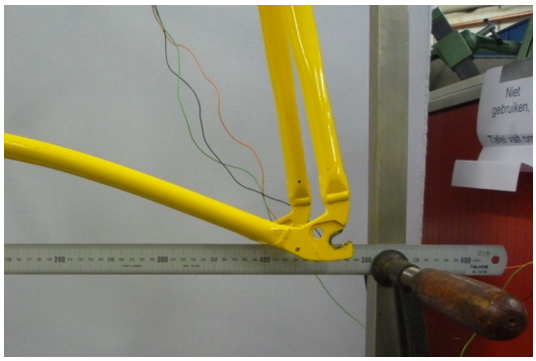

Figure 5.9: Measuring the distance from the pendulum axis to the rear wheel axle using a level ruler.

see *Figure 5.10*. The slope can be shown to be

$$
\begin{aligned}
m_{\mathrm{B}} &= -\tan\beta_{\mathrm{B}} \\
\sigma_m^2 &= \sigma_\beta^2 \sec^4\beta
\end{aligned}
\tag{5.16}
$$

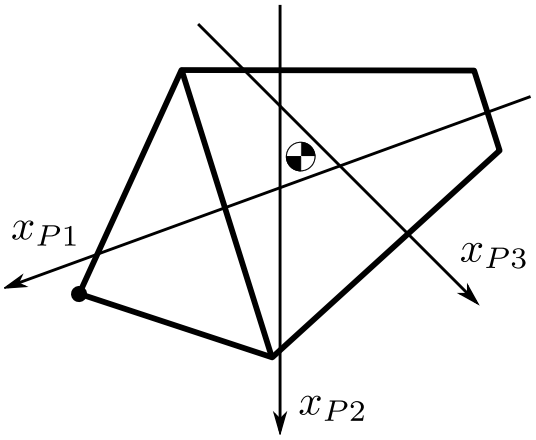

Figure 5.10: Exaggerated intersection of the three pendulum axes and the location of the center of mass.

The z-intercept can be shown to be

$$
\begin{aligned}
b_{\mathrm{B}i} &= -\left(\frac{a_{\mathrm{B}i}}{\cos\beta_{\mathrm{B}i}} + r_{\mathrm{R}}\right) \\
\sigma_b^2 &= \sigma_a^2 \sec^2\beta + \sigma_{r_{\mathrm{R}}}^2 + \sigma_\beta^2 a^2 \sec^2\beta \tan^2\beta
\end{aligned}
\tag{5.17}
$$

Theoretically, the center of mass lies on each line but due to experimental error, if there are more than two lines, the lines do not all cross at the same point. Only two lines are required to calculate the center of mass of the laterally symmetric frame, but more orientations increase the center of mass measurement accuracy. The three lines are defined as

$$
z_{\mathrm{B}i}(x) = m_{\mathrm{B}i} x + b_{\mathrm{B}i} \tag{5.18}
$$

The mass center location can be calculated by finding the intersection of pairs of these three lines. Two approaches were used used to calculate the center of mass. Intuition leads one to think that the center of mass may be the centroid

of the triangle made by the three intersecting lines. The centroid can be found by calculating the intersection point of each pair of lines and then averaging the three intersection points[2].

$$\begin{bmatrix} x_a \\ z_a \end{bmatrix} = \begin{bmatrix} -m_1 & 1 \\ -m_2 & 1 \end{bmatrix}^{-1} \begin{bmatrix} b_1 \\ b_2 \end{bmatrix} \tag{5.19}$$
$$\begin{bmatrix} x_b \\ z_b \end{bmatrix} = \begin{bmatrix} -m_1 & 1 \\ -m_3 & 1 \end{bmatrix}^{-1} \begin{bmatrix} b_1 \\ b_3 \end{bmatrix}$$
$$\begin{bmatrix} x_c \\ z_c \end{bmatrix} = \begin{bmatrix} -m_2 & 1 \\ -m_3 & 1 \end{bmatrix}^{-1} \begin{bmatrix} b_2 \\ b_3 \end{bmatrix}$$

$$x_{\mathrm{B}} = \frac{x_a + x_b + x_c}{3} \tag{5.20}$$

$$z_{\mathrm{B}} = \frac{z_a + z_b + z_c}{3} \tag{5.21}$$

Fork and Handlebar

The fork and handlebars are generally a bit trickier to hang in three different orientations, *Figure 5.11*. Typically two angles can be obtained by clamping to the steer tube at the top and the bottom. The third angle can be obtained by clamping to the stem. The center of mass of the fork is calculated in the same fashion as the frame. The slope of the line in the benchmark reference frame is the same as for the rear frame but the z-intercept is different

$$b_{\mathrm{H}i} = w \tan \beta_{\mathrm{H}i} - r_{\mathrm{F}} - \frac{a}{\cos \beta_{\mathrm{H}i}} \tag{5.22}$$
$$\sigma_b^2 = \sigma_w^2 \tan^2 \beta + \sigma_\beta^2 \left(w \sec^2 \beta - a \sec \beta \tan \beta \right)^2 + \sigma_{r_{\mathrm{F}}}^2 + \sigma_a^2 \sec^2 \beta$$

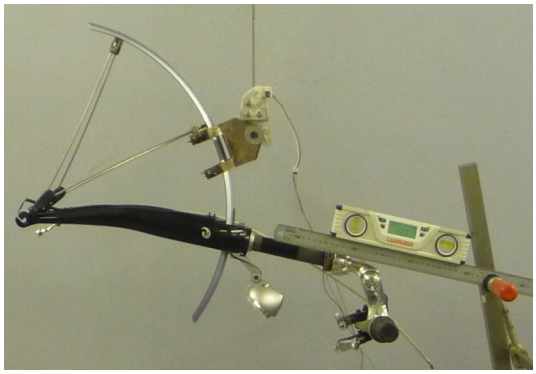

Figure 5.11: The Stratos fork and handlebar assembly hung as a torsional pendulum.

The fork of the Davis instrumented bicycle was connected to the handlebars by a steer torque sensor with universal joint. Due to the fact that the sensor and joint were not designed to support the weight of the adjacent components and the fact that we needed the inertia of the portion above the torque sensor for proper estimation of the steer torque applied by the rider[3], we opted to measure the center of mass and inertia of the fork and handlebar separately. The fork was measured as previously described, with the universal joint locked in its nominal position. The handlebar was measured in a similar fashion making use of small clamps to hang it in different orientations, *Figure 5.12*.

[2] Alternatively, the three lines can be treated as an over determined linear system and the least squares method used to find a unique solution. This solution is not the same as the triangle centroid method. The solution with the higher accuracy would be the preferred one.

[3] See Chapter *Davis Instrumented Bicycle*.

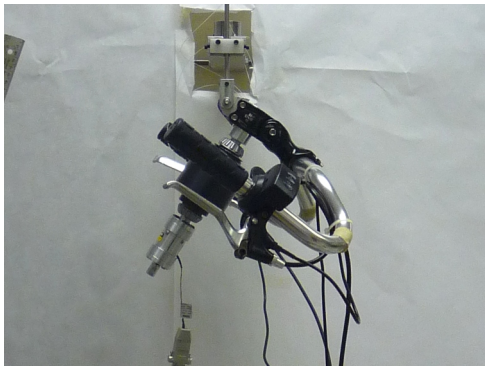

Figure 5.12: The handlebar mounted as a torsional pendulum.

I choose the center of the stem clamp bolt to be the reference point (as were the front and rear wheel centers for the front and rear frames). The location of this point relative to the front wheel center was measured as shown in *Figure 5.13*.

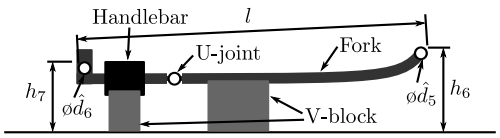

Figure 5.13: A diagram of how the handlebar reference point was located with respect to the front wheel center. These were the raw measurements taken.

The distances along and perpendicular to the steer axis from the front wheel center to the handlebar reference point are as follows

$$l_1 = h_7 - h_6 + \frac{\hat{d}_5 - \hat{d}_6}{2} \tag{5.23}$$
$$l_2 = \left(l - \frac{]hatd_5 + \hat{d}_6}{2}\right) \cos\left[\arcsin\left(\frac{l_1}{l - \frac{\hat{d}_5 + \hat{d}_6}{2}}\right)\right]$$

The distance from the front wheel center to the handlebar reference point in the global bicycle reference frame are

$$u_1 = l_2 \sin(\lambda) - l_1 \cos(\lambda) \tag{5.24}$$
$$u_2 = \frac{u_1}{\tan(\lambda)} + \frac{l_1}{\sin(\lambda)}$$

The center of mass is computed with respect to the handlebar reference point and u_1 and *u_2* locate the reference point of the handlebar to the front wheel center and thus the global origin.

5.2.8 Inertia

The moments of inertia of the wheels, rear frame, and fork (and handlebar) were measured both by taking advantage of the assumed symmetry of the parts and by hanging the parts as both compound and torsional pendulums while measuring their periods of oscillation when perturbed at small angles. The rate of oscillation was measured using a Silicon Sensing CRS03 100 deg/s rate gyro (http://www.siliconsensing.com/CRS03) for the Delft bicycles and a Silicon Sensing CRS04 200 deg/s rate gyro (http://www.siliconsensing.com/CRS04) for the Davis bicycles. The rate gyros were sampled at 1000 hz with a National Instruments USB-6008 12 bit data acquisition unit (http://sine.ni.com/nips/cds/view/p/lang/en/nid/14604) and at 500 hz with a National Instruments USB-6218 16 bit

data acquisition unit (http://sine.ni.com/nips/cds/view/p/lang/en/nid/203092), respectively, and the Matlab data acquisition toolbox. The measurement durations were between 15 and 30 secs and each moment of inertia measurement was performed at least three times. No extra care was taken to calibrate the rate gyro, maintain a constant power source (i.e. the battery drains slowly), or account for drift because I was only concerned with the period. The raw voltage signal was used to determine the period of oscillation which is needed for the moment of inertia calculations, *Figure 5.14*.

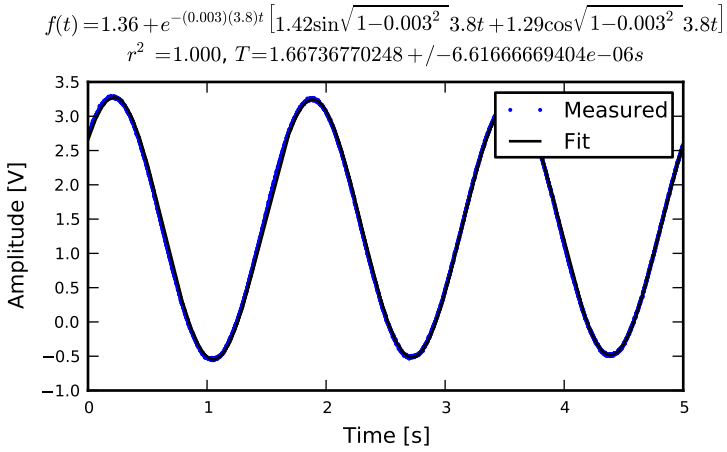

Figure 5.14: Example portion of the raw voltage data taken during a 30 second measurement of the oscillation of the Browser rear frame as a compound pendulum.

The function Equation (5.25) was fit to the data using the least squares method for each experiment to determine the quantities A, B, C, ζ, and ω.

$$f(t) = A + e^{-\zeta\omega t}\left[B\sin\sqrt{1-\zeta^2}\omega t + C\cos\sqrt{1-\zeta^2}\omega t\right] \tag{5.25}$$

Most of the data fit the damped oscillation function well with very light (and potentially ignorable) damping. There were several instances in the Delft experiments of beating-like phenomena for some of the parts at particular orientations. Roland and Massing, [RM71], also encountered this problem and used a bearing to prevent the torsional pendulum from swinging. *Figure 5.15* shows an example of the beating like phenomena. I used Roland and Massing's solution to prevent this in the Davis measurements.

The physical phenomenon observed corresponding to data sets such as these occurred when the bicycle frame or fork was perturbed torsionally. After being set into motion, the torsional motion damped and a longitudinal swinging motion increased. The motions alternated back and forth with neither ever reaching zero. The frequencies of these motions were very close to one another and it was not apparent how to dissect the two. We explored fitting to a function such as

$$y(t) = A\sin(\omega_1 t) + B\sin(\omega_2 t + \phi) + C \tag{5.26}$$

But the fit predicts that ω_1 and ω_2 are very similar frequencies. There was no easy way to choose which of the two ω's was the one associated with the torsional oscillation. Some work was done to model the torsional pendulum as a laterally flexible beam to determine this, but we ended up assuming that the accuracy of the period calculation would not improve enough for the effort required. The later experiments simply prevented the swinging motion of the pendulum without damping the torsional motion.

The period for a damped oscillation is

$$T = \frac{2\pi}{\sqrt{1-\zeta^2}\omega_n} \tag{5.27}$$

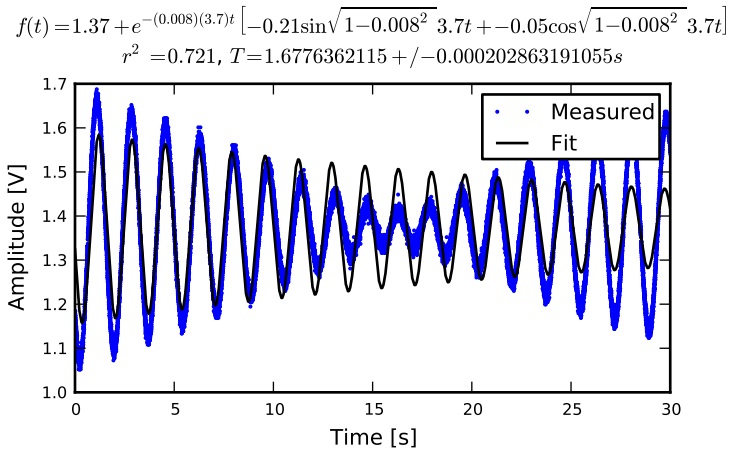

Figure 5.15: An example of the beating-like phenomena observed during less than 5% of the Delft trials.

The uncertainty in the period, T, can be determined from the fit. First, the variance of the fit is calculated

$$\sigma_y^2 = \frac{1}{N-5}\sum_{i=1}^{N}(y_{mi} - \bar{y}_m)^2 - (y_{pi} - \bar{y}_m)^2 \tag{5.28}$$

The covariance matrix of the fit function can be formed

$$\mathbf{U} = \sigma_y^2 \mathbf{H}^{-1} \tag{5.29}$$

where $\mathbf{H}$ is the Hessian [Hubbard1989b] of the fit function, (5.25). $\mathbf{U}$ is a 5×5 matrix with the variances of each of the five fit parameters along the diagonal. The variance of T can be computed using the variance of ζ and ω. It is important to note that the uncertainties in the period are very low ($< 1e-4$) due to the high sample rate, even for the fits with low r^2 values.

Torsional Pendulum

A torsional pendulum was used to measure all moments of inertia about axes in the laterally symmetric plane of each of the wheels, fork and frame. The pendulum is made up of a rigid mount, an upper clamp, a torsion rod, and various lower clamps, *Figure 5.16* .

A mild steel rod was used as the torsion spring. Lightweight, relatively low moment of inertia clamps were constructed that could fix the torsional rod to the various bicycle parts. The moments of inertia of the clamps were neglected [4].

The torsional pendulum was calibrated using a rod with an easily computed, i.e. "known", moment of inertia *Figure 5.17*[5]. A torsional pendulum almost identical to the one used in [Koo06] was used to measure the average period $\overline{T}_i$ of oscillation of the rear frame at three different orientation angles β_i, where $i = 1, 2, 3$, as shown in *Figure 5.10*. The parts were perturbed slightly, around 1 degree, and allowed to oscillate about the pendulum axis through several periods. This was repeated at least three times for each frame and the recorded periods were averaged.

Wheels

Estimating the full inertia tensors of the wheels is less complex because the wheels are assumed symmetric about three orthogonal planes making all products of inertia zero. The $I_{xx} = I_{zz}$ moments of inertia were calculated by

[4] The Davis clamp was a bit larger relative to forks with no handlebars. This may have decreased the accuracy of the related measurements.
[5] A different rod was used for the Delft and Davis Bicycles.

Figure 5.16: The rigid pendulum fixture from the Delft experiments mounted to a concrete column.

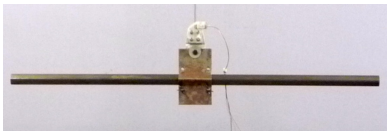

Figure 5.17: The steel calibration rod. The moment of inertia of the rod, $I_P = \frac{m_P}{12}(3r_P^2 + l_P^2)$, can be used to estimate the stiffness of the torsional pendulum, $k = \frac{4I_P\pi^2}{\bar{T_P}^2}$.

measuring the averaged period of oscillation about an axis in the XZ_B-plane using the torsional pendulum setup and Equation (5.32). The wheels are also assumed to be laterally symmetric about any radial axis. Thus only two moments of inertia are required for the set of benchmark parameters [MPRS07]. The moment of inertia about the axle was measured by hanging the wheel as a compound pendulum, *Figure 5.18*. The wheel was hung on a horizontal rod and perturbed to oscillate about the axis of the rod. The rate gyro was attached to the spokes near the hub[6] and oriented mostly along the axle axis. The wheels for the Delft bicycles would rotate at the rod contact point about the vertical axis which added a very low frequency component of rate along the vertical radial axis, but this should have little effect on the period estimation about the compound pendulum axis. A fixture was designed for the Davis bicycles that prevented undesired rotation. The pendulum length is the distance from the rod/rim contact point to the mass center of the wheel[7]. The inner diameter of the rim was measured and divided by two to get $l_{\mathrm{F,R}}$. The moment of inertia about the axle is calculated from

$$I_{\mathrm{F,R}yy} = \left(\frac{\bar{T}_{\mathrm{F,R}}}{2\pi}\right)^2 m_{\mathrm{F,R}} g l_{\mathrm{F,R}} - m_{\mathrm{F,R}} l_{\mathrm{F,R}}^2 \tag{5.30}$$

The radial moment of inertia was measured by hanging the wheel as a torsional pendulum, *Figure 5.19*. The wheel was first hung freely such that the center of mass aligned with the torsional pendulum axis and then the clamp secured. The wheel was then perturbed and oscillated about the vertical pendulum axis. The radial moment of inertia can be calculated with

$$I_{\mathrm{F,R}xx} = \frac{k\bar{T}_{\mathrm{F,R}}^2}{4\pi^2} \tag{5.31}$$

[6] The gyro should have been attached as close to the pivot point as possible to minimize additional inertia, but the weight of the gyro is still quite negligible.

[7] I should have used a edge rather than a rod for the pivot, as the period for a pendulum about a point contact edge is different than that about a rod of non-negligble diameter. The radius of this rod was about 3 mm which is neglible to the pendulum length of about 300 mm.

Figure 5.18: A wheel hung as a compound pendulum.

Figure 5.19: The front wheel of the Crescendo hung as a torsional pendulum.

Frame

At least three measurements were made to estimate the locally level moments and products of inertia ($I_{\mathrm{B}xx}$, $I_{\mathrm{B}xz}$, and $I_{\mathrm{B}zz}$) of the rear frame in the nominal configuration. The rear frame was typically hung from either the three main tubes (seat tube, down tube, and top tube), the seat post, or a small fixture mounted to the brake mounts *Figure 5.8*. The rear fender prevented easy connection to the seat tube on some of the bikes and the clamp was attached to the fender. The fender was less rigid than the frame tube. For best accuracy with only three orientation angles, the frame should be hung at three angles that are 120° apart. Attaching by the three tubes on the frame generally provide that the orientation angles were spread evenly at about 120°. Furthermore, taking data at more orientation angles improved the accuracy and was generally possible with standard diamond frame bicycles.

Three moments of inertia $J_{\mathrm{B}i}$ about the pendulum axes were calculated using

$$J_{\mathrm{B}i} = \frac{k\overline{T}_{\mathrm{B}i}^2}{4\pi^2} \tag{5.32}$$

The moments and products of inertia of the rear frame and handlebar/fork assembly with reference to the benchmark coordinate system were calculated by formulating the relationship between the rotated inertial frames

$$\mathbf{J}_{\mathrm{B}i} = \mathbf{R}_i \mathbf{I}_{\mathrm{B}} \mathbf{R}_i^T \tag{5.33}$$

where $\mathbf{J}_{\mathrm{B}i}$ is the inertia tensor about the pendulum reference frame, $\mathbf{I}_{\mathrm{B}}$ is the inertia tensor in the locally level reference frame, and $\mathbf{R}_{\mathrm{B}i}$ is the rotation matrix relating the two frames, *Figure 5.7*. The planar inertia tensor is defined as

$$\mathbf{I}_{\mathrm{B}} = \begin{bmatrix} I_{\mathrm{B}xx} & I_{\mathrm{B}xz} \\ I_{\mathrm{B}xz} & I_{\mathrm{B}zz} \end{bmatrix} \tag{5.34}$$

The inertia tensor can be reduced to a 2×2 matrix because the frame is assumed to be laterally symmetric and the Y axis of the pendulum reference is the same as the Y axis of the benchmark reference frame. The simple rotation matrix about the Y-axis can similarly be reduced to a 2×2 matrix where $s_{\beta i}$ and $c_{\beta i}$ are defined as $\sin\beta_i$ and $\cos\beta_i$, respectively.

$$\mathbf{R} = \begin{bmatrix} c_{\beta i} & -s_{\beta i} \\ s_{\beta i} & c_{\beta i} \end{bmatrix} \tag{5.35}$$

The first entry of $\mathbf{J}_{\mathrm{B}i}$ in Equation (5.33) is the moment of inertia about the pendulum axis and is written explicitly as

$$J_{\mathrm{B}i} = c_{\beta i}^2 I_{\mathrm{B}xx} - 2 s_{\beta i} c_{\beta i} I_{\mathrm{B}xz} + s_{\beta i}^2 I_{\mathrm{B}zz} \tag{5.36}$$

Similarly, calculating all three, or more, $J_{\mathrm{B}i}$ allows one to form

$$\begin{bmatrix} J_{\mathrm{B}1} \\ J_{\mathrm{B}2} \\ J_{\mathrm{B}3} \\ \vdots \end{bmatrix} = \begin{bmatrix} c_{\beta 1}^2 & -2 s_{\beta 1} c_{\beta 1} & s_{\beta 1}^2 \\ c_{\beta 2}^2 & -2 s_{\beta 2} c_{\beta 2} & s_{\beta 2}^2 \\ c_{\beta 3}^2 & -2 s_{\beta 3} c_{\beta 3} & s_{\beta 3}^2 \\ \vdots & \vdots & \vdots \end{bmatrix} \begin{bmatrix} I_{\mathrm{B}xx} \\ I_{\mathrm{B}xz} \\ I_{\mathrm{B}zz} \end{bmatrix} \tag{5.37}$$

and the moments of inertia can be solved as a linear system or with least squares if it is over determined. The inertia of the frame about an axis normal to the plane of symmetry was estimated by hanging the frame as a compound pendulum about the wheel axis, *Figure 5.20*. Equation (5.30) is used but with the mass of the frame and the frame pendulum length.

$$l_B = \sqrt{x_B^2 + (z_B + r_R)^2} \tag{5.38}$$

Figure 5.20: The yellow bicycle rear frame hung as a compound pendulum about the wheel axis (the wheel is fixed in place).

Fork and handlebar

The inertia of the fork and handlebar is calculated in the same way as the frame. The fork is hung as both a torsional pendulum, *Figure 5.11*, and as a compound pendulum, *Figure 5.21*. The fork provides fewer mounting options to obtain at least three equally spaced orientation angles, especially if there is no fender. We designed a connection to the brake mounts for the Davis bicycles to remedy that. The torsional calculations follow equations (5.32) through (5.37) and the compound pendulum calculations is calculated with Equation (5.30). The fork pendulum length is calculated using

$$l_H = \sqrt{(x_H - w)^2 + (z_H + r_F)^2} \tag{5.39}$$

5.2.9 Notation

The notation used in the bicycle parameter estimation.

v Forward speed of the linear bicycle model.

g Acceleration due to gravity.

$\mathbf{M}, \mathbf{C}_1, \mathbf{K}_0, \mathbf{K}_2$ Velocity and gravity independent mass, damping, and stiffness matrices of the linearized Whipple model from [MPRS07].

$\mathbf{q}$ Essential coordinates from [MPRS07].

ϕ Roll angle.

δ Steer angle.

σ Standard deviation. The subscript corresponds to the associated nominal variable.

$r_{(F,R)} \pm \sigma_{r(F,R)}$ Front F and rear wheel R radii and their respective standard deviations.

Figure 5.21: Browser fork hung as a compound pendulum.

$d_{(F,R)} \pm \sigma_{d(F,R)}$ The traversed distance of each wheel.

$n_{(F,R)}$ The number of wheel rotations.

$\gamma \pm \sigma_\gamma$ The head tube angle and standard deviation.

$\lambda \pm \sigma_\lambda$ The steer axis tilt and standard deviation.

f_o Fork offset.

$c \pm \sigma_c$ Trail and its standard deviation.

d_1, d_2, d_3 Fundamental bicycle geometry from Chapter *Bicycle Equations Of Motion*.

d_1, d_2, d_3 Fundamental bicycle geometry from Chapter *Bicycle Equations Of Motion*.

d Inner dimension between the axles from the alternative geometry method.

$\hat{d}_1, \hat{d}_2, \hat{d}_3, \hat{d}_4$ Measured diameters from the alternative geometry method.

h_1, h_2, h_3, h_4, h_5 Measured heights from the table surface in the alternative geometry method.

i Indices for each orientation of the front and rear frames in the pendulum.

$\alpha_{\mathrm{H,B}i}$ Angle of the steer axis relative to horizontal when the front frame and rear frame are hung as a pendulum.

$a_{\mathrm{H,B}i}$ Horizontal distance from the front or rear axle to the pendulum axis when the front and rear frames are hung as a pendulum.

XYZ_P Pendulum reference frame.

XYZ_B Global bicycle reference frame from [MPRS07].

$\beta_{\mathrm{H,B}i}$ Angle of the pendulum axis relative to the bicycle's reference frame.

$m_{\mathrm{H,B}i}$ Slope of the pendulum axis in the bicycle reference frame.

$b_{\mathrm{H,B}i}$ Z intercept of the pendulum axis in the bicycle reference frame.

$z_{\mathrm{B}i}(x)$ Function describing the pendulum axis line in the XZ_B plane.

$\hat{d}_5, \hat{d}_6$ Handlebar and front wheel axle diameters.

l The outer distance from the front wheel axle to the handlebar reference point.

l_1, l_2 The distances along and perpendicular to the steer axis from the front wheel center to the handlebar reference point.

u_1, u_2 The distances from the front wheel center to the handlebar reference point in the global bicycle reference frame.

A, B, C The offset, sin amplitude, and cosine amplitude in the oscillations.

ω, ζ The frequency and damping ratio in the oscillations.

T Period of oscillation.

σ_y The standard deviation of the measured voltage about the best fit curve.

y_{mi} The measured voltage at each time.

$\bar{y}_m$ The mean of the measured voltage across all time.

y_{pi} The predicted voltage value at each time.

$\mathbf{U}$ Covariance matrix of the fit function parameters.

$\mathbf{H}$ Hessian of the fit function parameters.

$\overline{T}_i$ Average period at orientation i.

I_P Inertia of the calibration rod about the pendulum axis.

k Stiffness of the torsional pendulum.

m_P Mass of the calibration rod.

r_P Radius of the calibration rod.

l_P Length of the calibration rod.

T_P Oscillation period of the calibration rod.

$l_{\mathrm{F,R}}$ Front and rear wheel compound pendulum length.

I_{Fyy}, I_{Ryy} Moment of inertia of the front and rear wheels about the axle.

$I_{\mathrm{F,R}xx}$ Moment of inertia of the front and rear wheels about the radii.

$I_{\mathrm{B}xx}, I_{\mathrm{B}xz}, I_{\mathrm{B}zz}$ Moments and products of inertia of the rear fame with reference to the bicycle reference frame and the center of mass.

$\mathbf{I}_{\mathrm{H,B}}$ The inertia tensor of the front and rear frame with reference to the bicycle reference frame and the center of mass.

$\mathbf{J}_{\mathrm{H,B}i}$ The inertia tensor of the front and rear frame with reference to the pendulum reference frame and the center of mass for each orientation.

$\mathbf{R}_i$ The rotation matrix relating the pendulum and bicycle reference frames.

$s_{\beta i}, c_{\beta i}$ Shorthand for $\sin\beta_i$ and $\cos\beta_i$.

x_B, z_B The X and Z coordinates of the rear frame center of mass.

l_B The rear frame pendulum length.

x_H, z_H The X and Z coordinates of the front frame center of mass.

l_H The front frame pendulum length.

5.3 Human Parameters

To properly model the bicycle rider system it is necessary to estimate the physical parameters of the bicycle rider. The measurement of the physical properties of a human is more difficult than for a bicycle because the human body parts are not as easily described as rigid bodes with defined joints and due to flexible geometry, daily varying mass, wobbly mass, etc.

Human mass, center of mass, and inertial properties have been measured and estimated in a multitude of ways. Each method has its advantages and disadvantages. Many methods exist including cadaver measurements ([Dem55], [CMY69], [CCM+75]), photogrammetry, ray scanning techniques ([ZS83], [ZSC90]), water displacement ([PKP99]), rotating platforms ([GWS05]), and geometrical estimation of the body segments ([Yea90a]). [Doh53], [Eat73b], and [Pat04b] measured the moments of inertia and centers of mass of a combined rider and vehicle, but this is not always practical especially if the properties of multiple riders are desired.

I approached the human parameter estimation in a more analytical fashion based primarily on geometric measurements much like Yeadon. Both methods that were used were based on estimating the inertial parameters from mass and geometry measurement along with a human body density estimate. With the first method, I estimated the physical properties of the rider in a seated position using a simple mathematical geometrical estimation similar in idea to [Yea90a] in combination with mass data from [Dem55]. The second method substitutes Yeadon's more robust model with my previous one.

5.3.1 Simple Geometry Method

This method calculates the center of mass and inertia of a simplified model of the ten major human body parts: head, torso, upper and lower arms, and upper and lower legs, in a general configuration for sitting on typical bicycles. The mass of the rider was measured along with fourteen anthropometric measurements of the body. These measurements in combination with the geometrical bicycle measurements taken in the previous section (*Bicycle Parameters*) and several additional bicycle geometrical measurements are used to define a model of the rider made up of simple geometrical shapes (*Figure 5.22*). The legs and arms are represented by cylinders, the torso by a cuboid and the head by a sphere. The feet are positioned at the center of the bottom bracket axis to maintain symmetry about the XZ-plane.

All but one of the anthropomorphic measurements are taken when the rider was standing casually on flat ground. The lower leg length l_{ll} is the distance from the floor to the knee joint. The upper leg length l_{ul} is the distance from the knee joint to the hip joint. The length from hip to hip l_{hh} and shoulder to shoulder l_{ss} are the distances between the two hip joints and two shoulder joints, respectively. The torso length l_{to} is the distance between hip joints and shoulder joints. The upper arm length l_{ua} is the distance between the shoulder and elbow joints. The lower arm length l_{al} is the distance from the elbow joint to the center of the hand when the arm is outstretched. The circumferences are taken at the cross section of maximum circumference (e.g. around the bicep, around the brow, over the nipples for the chest). The final dimension is taken while the rider is seated on the bicycle in a normal riding position. The forward lean angle λ_{fl} is the approximate angle made between the floor (XY-plane) and the line connecting the center of the rider's head and the top of the seat. This was estimated by taking a side profile photograph of the rider on the bicycle and scribing a line from the center of the head to the top of the seat. The measurements were made as accurately as possible with basic tools but no special attention is given further to the accuracy of the calculations due to the fact that modeling the human as basic geometric shapes already introduces an unknown error.

I measured twelve additional geometric values (only five of which are needed for this setup[8]) to assist in configuring the rider to the be seated on the bicycle, *Figure 5.23*.

h_{bb}**, Bottom Bracket Height** The distance from the ground to the bottom bracket when the bicycle is in the nominal configuration.

l_{cs}**, Chain stay length** Not the true chain stay length, but the distance from the center of the bottom bracket to the center of the rear wheel.

[8] These dimensions are not necessary for the provided methods, but are necessary to build the grid point system. Early on they were used to analytically estimate the inertia of the bicycle frame. See [MH08]

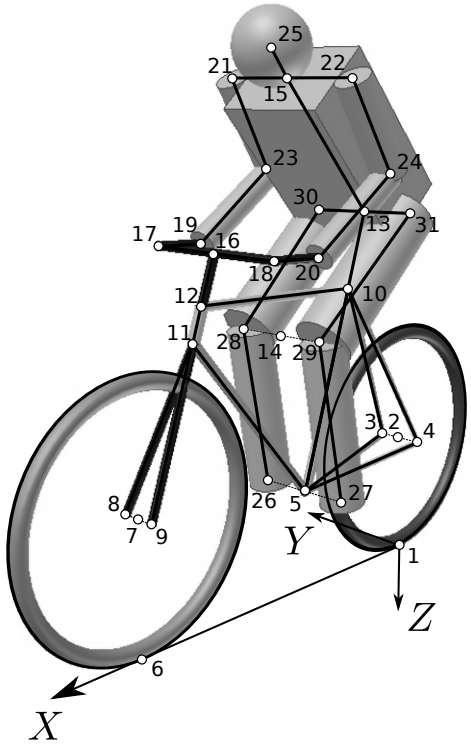

Figure 5.22: Locations of grid points and simple geometric shapes of the simple geometric inertia model.

l_{sp}**, Seat post length** The distance from the intersection of a horizontal top tube and the seat tube to the top of the seat. Measured along the center line of the seat post.

l_{st}**, Seat tube length** The distance from the bottom bracket to the point at which a horizontal top tube would intersect the seat tube.

λ_{st}**, Seat tube angle** The acute angle between the ground and the seat tube.

l_f**, fork length**[8] The distance from the center of the front wheel to the intersection of the head tube and the down tube.

w_{fh}**, front hub width**[8] The distance between the front dropouts.

w_{hb}**, handlebar width**[8] The distance between the handlebar grips.

l_{hb}**, handlebar length**[8] The horizontal distance from the steer axis to the handlebar grips.

λ_{ht}**, head tube angle**[8] The angle between the ground and the head tube.

w_{rh}**, rear hub width**[8] The distance between the rear dropouts.

l_s**, stem length**[8] The distance from the intersection of the top tube and the head tube to the level of the handlebar grips.

The masses of each segment (*Table 5.1*) were defined as a proportion of the total mass of the rider m_{Br} using data from cadaver studies by [Dem55].

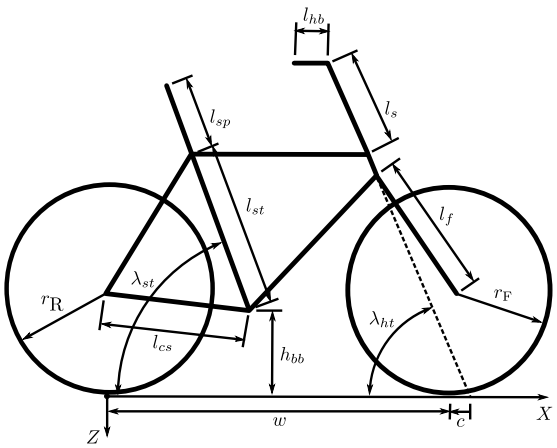

Figure 5.23: The dimensions need to construct the grid point system in the simple inertia method.

Table 5.1: Body mass and segment masses.

Segment	Symbol	Equation
body	m_{B_r}	m_{B_r}
head	m_h	$0.068 \cdot m_{B_r}$
lower arm	m_{la}	$0.022 \cdot m_{B_r}$
lower leg	m_{ll}	$0.061 \cdot m_{B_r}$
torso	m_{to}	$0.510 \cdot m_{B_r}$
upper arm	m_{ua}	$0.028 \cdot m_{B_r}$
upper leg	m_{ul}	$0.100 \cdot m_{B_r}$

The geometrical and anthropomorphic measurements are converted into a set of thirty one grid points in three dimensional space that map the skeleton of the rider and bicycle (*Figure 5.22*). The position vectors to these grid points are listed in *Table 5.2*. Several intermediate variables used in the grid point equations are listed in *Table 5.3* where f_o is the fork offset and the rest arise due to multiple solutions to the location of the elbow and knee joints and have to be solved numerically. The correct solutions are the ones that force the arms and legs to bend in a natural fashion. The grid points mark the center of the sphere and the end points of the cylinders and cuboid. The segments are aligned along lines connecting the appropriate grid points.

Table 5.2: Skeleton grid points with respect to the global frame.

Description	Equation
rear contact point	$\mathbf{r}_1 = [0 \quad 0 \quad 0]$
rear wheel center	$\mathbf{r}_2 = [0 \quad 0 \quad -r_{\mathrm{R}}]$
right rear hub center	$\mathbf{r}_3 = \mathbf{r}_2 + [0 \quad \frac{w_{rh}}{2} \quad 0]$
left rear hub center	$\mathbf{r}_4 = \mathbf{r}_2 + [0 \quad -\frac{w_{rh}}{2} \quad 0]$
bottom bracket center	$\mathbf{r}_5 = \left[\sqrt{l_{cs}^2 - (r_{\mathrm{R}} - h_{bb})^2} \quad 0 \quad -h_{bb}\right]$
front wheel contact point	$\mathbf{r}_6 = [w \quad 0 \quad 0]$
front wheel center	$\mathbf{r}_7 = \mathbf{r}_6 + [0 \quad 0 \quad -r_{\mathrm{F}}]$
right front hub center	$\mathbf{r}_8 = \mathbf{r}_7 + [0 \quad \frac{w_{fh}}{2} \quad 0]$
left front hub center	$\mathbf{r}_9 = \mathbf{r}_7 + [0 \quad -\frac{w_{fh}}{2} \quad 0]$
top of seat tube	$\mathbf{r}_{10} = \mathbf{r}_5 + [-l_{st}\cos\lambda_{st} \quad 0 \quad -l_{st}\sin\lambda_{st}]$
fork crown	$\mathbf{r}_{11} = \mathbf{r}_7 + \left[-f_o\sin\lambda_{ht} - \cos\lambda_{ht}\sqrt{l_f^2 - f_o^2} \quad 0 \quad f_o\cos\lambda_{ht} - \sin\lambda_{ht}\sqrt{l_f^2 - f_o^2}\right]$

Continued on next page

Table 5.2 – continued from previous page

top of head tube	$\mathbf{r}_{12} = \begin{bmatrix} r_{X11} - \frac{r_{Z11} - r_{Z10}}{\tan \lambda_{ht}} & 0 & r_{Z10} \end{bmatrix}$
top of seat	$\mathbf{r}_{13} = \mathbf{r}_{10} + \begin{bmatrix} -l_{sp} \cos \lambda_{st} & 0 & -l_{sp} \sin \lambda_{st} \end{bmatrix}$
center of knees	$\mathbf{r}_{14} = \mathbf{r}_5 + \begin{bmatrix} s & 0 & -t \end{bmatrix}$
shoulder midpoint	$\mathbf{r}_{15} = \mathbf{r}_{13} + \begin{bmatrix} l_{to} \cos \lambda_{fl} & 0 & -l_{to} \sin \lambda_{fl} \end{bmatrix}$
top of stem	$\mathbf{r}_{16} = \mathbf{r}_{12} + \begin{bmatrix} -l_s \cos \lambda_{ht} & 0 & -l_s \sin \lambda_{ht} \end{bmatrix}$
right handlebar	$\mathbf{r}_{17} = \mathbf{r}_{16} + \begin{bmatrix} 0 & \frac{l_{ss}}{2} & 0 \end{bmatrix}$
left handlebar	$\mathbf{r}_{18} = \mathbf{r}_{16} + \begin{bmatrix} 0 & -\frac{l_{ss}}{2} & 0 \end{bmatrix}$
right hand	$\mathbf{r}_{19} = \mathbf{r}_{17} + \begin{bmatrix} -l_{hb} & 0 & 0 \end{bmatrix}$
left hand	$\mathbf{r}_{20} = \mathbf{r}_{18} + \begin{bmatrix} -l_{hb} & 0 & 0 \end{bmatrix}$
right shoulder	$\mathbf{r}_{21} = \mathbf{r}_{15} + \begin{bmatrix} 0 & \frac{l_{ss}}{2} & 0 \end{bmatrix}$
left shoulder	$\mathbf{r}_{22} = \mathbf{r}_{15} + \begin{bmatrix} 0 & -\frac{l_{ss}}{2} & 0 \end{bmatrix}$
right elbow	$\mathbf{r}_{23} = \mathbf{r}_{19} + \begin{bmatrix} -u & \frac{l_{ss}}{2} & -v \end{bmatrix}$
left elbow	$\mathbf{r}_{24} = \mathbf{r}_{23} + \begin{bmatrix} 0 & -l_{ss} & 0 \end{bmatrix}$
center of head	$\mathbf{r}_{25} = \mathbf{r}_{15} + \begin{bmatrix} \frac{c_h}{2\pi} \cos \lambda_{fl} & 0 & -\frac{c_h}{2\pi} \sin \lambda_{fl} \end{bmatrix}$
right foot	$\mathbf{r}_{26} = \mathbf{r}_5 + \begin{bmatrix} 0 & \frac{l_{hh}}{2} & 0 \end{bmatrix}$
left foot	$\mathbf{r}_{27} = \mathbf{r}_5 + \begin{bmatrix} 0 & -\frac{l_{hh}}{2} & 0 \end{bmatrix}$
right knee	$\mathbf{r}_{28} = \mathbf{r}_{14} + \begin{bmatrix} 0 & \frac{l_{hh}}{2} & 0 \end{bmatrix}$
left knee	$\mathbf{r}_{29} = \mathbf{r}_{14} + \begin{bmatrix} 0 & -\frac{l_{hh}}{2} & 0 \end{bmatrix}$
right hip	$\mathbf{r}_{30} = \mathbf{r}_{13} + \begin{bmatrix} 0 & \frac{l_{hh}}{2} & 0 \end{bmatrix}$
left hip	$\mathbf{r}_{31} = \mathbf{r}_{13} + \begin{bmatrix} 0 & -\frac{l_{hh}}{2} & 0 \end{bmatrix}$

Table 5.3: Grid point intermediate variables.

Symbol	Equation
f_o	$r_{\mathrm{F}} \cos \lambda_{ht} - c \sin \lambda_{ht}$
s	$0 = l_{ul}^2 - l_{ll}^2 - (r_{Z13} - r_{Z5})^2 - (r_{X5} - r_{X13})^2 - 2(r_{Z13} - r_{Z5})\sqrt{(l_{ll}^2 - s^2)} - 2s(r_{X5} - r_{X13})$
t	$\sqrt{l_{ll}^2 - s^2}$
u	$0 = l_{la}^2 - l_{ua}^2 + (r_{Z21} - r_{Z19})^2 + (r_{X19} - r_{X21})^2 + 2(r_{Z21} - r_{Z19})\sqrt{(l_{la}^2 - u^2)} - 2u(r_{X19} - r_{X21})$
v	$\sqrt{l_{la}^2 - u^2}$

The segments are assumed to have uniform density so the centers of mass are taken to be at the geometrical centers. The midpoint formula can then be used to calculate the local centers of mass for each segment in the global reference frame. The total body center of mass can be found from the standard formula

$$\mathbf{r}_{\mathrm{B}r} = \frac{\sum m_i \mathbf{r}_i}{m_{\mathrm{B}r}} \tag{5.40}$$

where $\mathbf{r}_i$ is the position vector to the centroid of each segment and m_i is the mass of each segment. The local moments of inertia of each segment are determined using the ideal definitions of inertia for each segment type (*Table 5.4*).

Table 5.4: Segment inertia tensors defined in their local reference frames.

Segment	Inertia
cuboid	$\frac{1}{12} m \begin{bmatrix} l_y^2 + l_z^2 & 0 & 0 \\ 0 & l_x^2 + l_z^2 & 0 \\ 0 & 0 & l_x^2 + l_y^2 \end{bmatrix}$
cylinder	$I_x, I_y = \frac{1}{12} m \left(\frac{3c^2}{4\pi^2} + l^2 \right), I_z = \frac{mc^2}{8\pi^2}$
sphere	$I_x, I_y, I_z = \frac{mc^2}{10\pi^2}$

The width of the cuboid representing the torso l_y is defined by the shoulder width and upper arm circumference.

$$l_y = l_{ss} - \frac{c_{ua}}{\pi} \tag{5.41}$$

The cuboid thickness was estimated using the chest circumference measurement assuming that the cross section of the chest is similar to a stadium shape.

$$l_x = \frac{c_{ch} - 2l_y}{\pi - 2} \tag{5.42}$$

The local $\hat{\mathbf{z}}_i$ unit vector for the segments was defined along the line connecting the associated grid points from the lower numbered grid point to the higher numbered grid point. The local unit vector in the y direction was set equal to the global $\hat{\mathbf{Y}}$ unit vector with the $\hat{\mathbf{x}}_i$ unit vector following from the right hand rule. The rotation matrix needed to rotate each of the moments of inertia to the global reference frame can be calculated by dotting the global unit vectors $\hat{\mathbf{X}}$, $\hat{\mathbf{Y}}$, $\hat{\mathbf{Z}}$ with the local unit vectors $\hat{\mathbf{x}}_i$, $\hat{\mathbf{y}}_i$, $\hat{\mathbf{z}}_i$ for each segment.

$$\mathbf{R}_i = \begin{bmatrix} \hat{\mathbf{X}} \cdot \hat{\mathbf{x}}_i & \hat{\mathbf{X}} \cdot \hat{\mathbf{y}}_i & \hat{\mathbf{X}} \cdot \hat{\mathbf{z}}_i \\ \hat{\mathbf{Y}} \cdot \hat{\mathbf{x}}_i & \hat{\mathbf{Y}} \cdot \hat{\mathbf{y}}_i & \hat{\mathbf{Y}} \cdot \hat{\mathbf{z}}_i \\ \hat{\mathbf{Z}} \cdot \hat{\mathbf{x}}_i & \hat{\mathbf{Z}} \cdot \hat{\mathbf{y}}_i & \hat{\mathbf{Z}} \cdot \hat{\mathbf{z}}_i \end{bmatrix} \tag{5.43}$$

The local inertia matrices are then rotated to the global reference frame with

$$\mathbf{I}_i = \mathbf{R}_i \mathbf{J}_i \mathbf{R}_i^T \tag{5.44}$$

The local moments of inertia can then be translated to the center of mass of the entire body using the parallel axis theorem

$$\mathbf{I}_i^* = \mathbf{I}_i + m_i \begin{bmatrix} d_y^2 + d_z^2 & -d_x d_y & -d_x d_z \\ -d_x d_y & d_z^2 + d_x^2 & -d_y d_z \\ -d_x d_z & -d_y d_z & d_x^2 + d_y^2 \end{bmatrix} \tag{5.45}$$

where d_x, d_y and d_z are the distances along the X, Y and Z axes, respectively, from the local center of mass to the global center of mass. Finally, the local translated and rotated moments of inertia are summed to give the total moment of inertia of the rider.

$$\mathbf{I}_{\mathrm{B}r} = \sum \mathbf{I}_i^* \tag{5.46}$$

The results of measuring the riders are presented in Chapter *Delft Instrumented Bicycle*, *Motion Capture*, and [MKHS09].

5.3.2 Yeadon method

The [Yea90a] human inertial model was developed for estimating the inertial parameters needed to describe a human model for complex gymnastic maneuvers. It is essentially a more complete and accurate method than the one previously presented. There are 95 geometrical measurements of the human and a single mass measurement for scaling the body part densities. Yeadon makes use of stadium solids and a single semi-ellipse to more accurately model the human geometry. Two apparent deficiencies are the fact that too much detail is taken for body parts that have less inertia (i.e. the hands/feet) and at large configuration angles for some joints, the inertia is poorly modeled (e.g. the buttocks disappears when the human in a seated position). The model also does not have full freedom at each joint. Refer to [Yea90a] for a complete description of the model.

Once the inertia of each segment in the Yeadon model is computed, the joint angles must be set. We set the somersault angle to match the forward lean angle as described in the previous section. We then measure three additional bicycle dimensions to assist in the configuration of the rider. They are as follows:

w_{hb}**, Handlebar width** The lateral distance between the points the hands hold the handlebars.

l_{hbR}**, Rear hub to handlebar.** The distance from the center of the rear hub to the point on the handlebar where the hand grips.

l_{hbF}**, Front hub to handlebar.** The distance from the center of the front hub to the point on the handlebar where the hand grips.

We locate the hip center (Ls0) at the top of the bicycle seat and the somersault joint angle is set such that the torso (P, T, C) aligned by the forward lean angle λ_{fl}.

The basic process for setting the elbow elevation angle is to find the distance between the shoulder (La0, Lb0) and the handlebar grip. The handlebar grip location is at the point at which the lateral line with length $\frac{w_{hb}}{2}$ intersects the circle formed by the intersection of the two spheres which are centered at the front and rear wheel centers with radii l_{hbF} and l_{hbR}, respectively. The elevation angle of the elbow then is defined as the angle at which the distance from the shoulder (La0, Lb0) to the knuckle (La6, Lb6) is equal to the distance from the shoulder (La0, Lb0) to the handlebar grip. We then assume that the shoulder rotation angle is zero and find the shoulder elevation and abduction angles which force the vector from the shoulder to the knuckle to equal the vector from the shoulder to the handlebar grip.

The thigh and knee elevation angles are set such that the center of the heel level (Lj6, Lk6) is aligned with the bottom bracket axis and that both the thigh abduction and rotation angles are zero. We assume that the foot peg is located at the bottom bracket center and is the same lateral distance from the sagittal plane as the hip centers. The knee and thigh elevation angles are then found in the same fashion as the elbow and shoulder angles, which the lesser restriction that the thigh abduction angle is zero.

Figure 5.24 shows a visualization of the Yeadon model when configured to sit on a bicycle. The details of the calculations and all of the data is included with the Yeadon [Dem11] and BicycleParameters [Moo11] software packages.

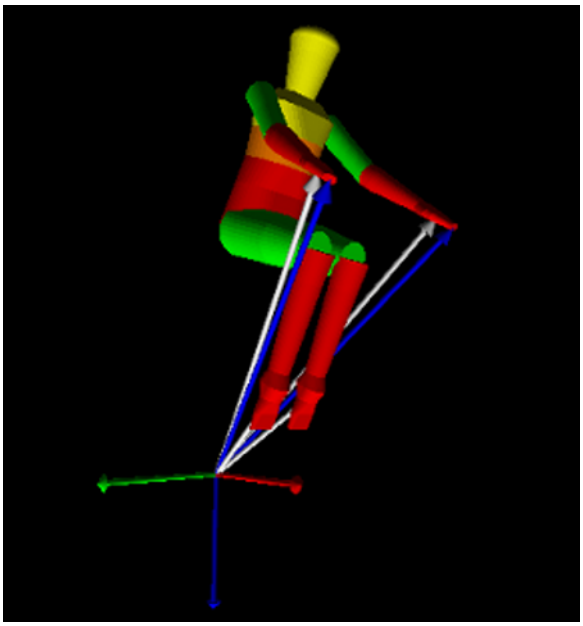

Figure 5.24: A visualization of the Yeadon inertia model configured to sit on a bicycle. Output is from the BicycleParameters software package.

5.4 Bicycle-Rider Parameters

Once both the bicycle and rider parameters are known, the parameter for various systems can be extracted. The simplest is that the rider is rigidly attached to the frame. The parallel axis theorem allows one to calculate the combined

inertia of the bicycle frame and the rigid rider. Both of the rider formulations also allow one to segment the body for more complex rider models with multiple degrees of freedom. For example, the inertia for a leaning rider's upper body can be determined separately and the legs can be fixed in the bicycle frame. We make use of this for the different rider biomechanical models presented in Chapter *Extensions of the Whipple Model*.

5.5 Software Implementation

The bicycle parameter calculation and the Yeadon method have been implemented in two open source software packages written in the Python language, called yeadon (http://pypi.python.org/pypi/yeadon) [Dem11] and BicycleParameters (http://pypi.python.org/pypi/BicycleParameters) [Moo11]. The Yeadon package uses geometric measurements and joint configuration angles to output the total inertia properties of the human in an arbitrary reference frame. It also can provide inertial properties of individual body segments or combinations of body segments. It is suitable for a wide variety of human dynamic models. The BicycleParameters package accepts either the raw measurements described in Section *Bicycle Parameters* or the benchmark parameterization [MPRS07] and computes the benchmark bicycle parameters. It makes use of the Yeadon package to allow one to configure riders in a seated position on the bicycle and outputs the inertial properties of the bicycle/rider system. Overall it allows one to provide values and uncertainties for all of the raw measurements as described in both the Bicycle and Yeadon parameter sections and compute the parameters for the Whipple Bicycle model. Details of use of the software can be found in the documentation for each of the packages: http://packages.python.org/yeadon, http://packages.python.org/BicycleParameters.

5.6 Parameter Tables

The tabulated values for the both the raw measurements (Tables *5.5* to *5.8*) and the computed physical parameters (Tables *5.9* to *5.12*) of the ten bicycles are given in the following tables.

5.6.1 Bicycle Measured Parameters

Table 5.5: Raw measurements and their estimated uncertainty.

	Browser		**Browserins**		**Stratos**	
Variable	v	σ	v	σ	v	σ
a_{B1}	0.098	0.003	-0.018	0.003	0.249	0.003
a_{B2}	0.169	0.003	-0.355	0.003	-0.267	0.003
a_{B3}	-0.294	0.003	-0.242	0.003	-0.071	0.003
a_{H1}	0.474	0.003	0.474	0.003	0.329	0.003
a_{H2}	0.383	0.003	0.383	0.003	-0.038	0.003
a_{H3}	0.215	0.003	0.215	0.003	0.400	0.003
α_{B1}	3.4	0.2	154.1	0.2	128.9	0.2
α_{B2}	138.7	0.2	230.8	0.2	221.6	0.2
α_{B3}	229.8	0.2	286.9	0.2	184.5	0.2
α_{H1}	346.7	0.2	346.7	0.2	36.0	0.2
α_{H2}	28.1	0.2	28.1	0.2	94.0	0.2
α_{H3}	287.0	0.2	287.0	0.2	347.3	0.2
d_F	28.06	0.01	27.98	0.01	27.77	0.01
d_P	0.0300	0.0001	0.0300	0.0001	0.0300	0.0001
d_R	27.85	0.01	27.84	0.01	29.77	0.01
f	0.070	0.001	0.070	0.001	0.045	0.001

Continued on next page

Table 5.5 – continued from previous page

	Browser		**Browserins**		**Stratos**	
g	9.81	0.01	9.81	0.01	9.81	0.01
γ	67.1	0.2	67.1	0.2	73.1	0.2
h_{bb}	0.295	NA	0.295	NA	0.29	NA
λ_{st}	1.195550538	NA	1.195550538	NA	1.308996939	NA
l_{cs}	0.46	NA	0.46	NA	0.445	NA
l_F	0.293	0.001	0.293	0.001	0.297	0.001
l_{hbF}	0.893	NA	0.893	NA	0.6552	NA
l_{hbR}	0.9213	NA	0.9213	NA	1.1014	NA
l_P	1.050	0.001	1.050	0.001	1.050	0.001
l_R	0.293	0.001	0.293	0.001	0.296	0.001
l_{sp}	0.24	NA	0.24	NA	0.195	NA
l_{st}	0.53	NA	0.53	NA	0.48	NA
m_B	9.86	0.02	14.71	0.02	7.22	0.02
m_F	2.02	0.02	2.02	0.02	3.33	0.02
m_H	3.22	0.02	3.22	0.02	3.04	0.02
m_P	5.56	0.02	5.56	0.02	5.56	0.02
m_R	3.11	0.02	3.11	0.02	3.96	0.02
n_F	13.0	NA	13.0	NA	13.0	NA
n_R	13.0	NA	13.0	NA	14.0	NA
T^c_{B1}	1.717307	0.000005	1.811022	0.000007	1.598802	0.000006
T^c_{F1}	1.481127	0.000007	1.481127	0.000007	1.353666	0.000005
T^c_{H1}	1.601851	0.000007	1.601851	0.000007	1.45407	0.00002
T^c_{R1}	1.361090	0.000004	1.361090	0.000004	1.312177	0.000007
T^t_{B1}	2.09957	0.00008	3.36393	0.00004	1.81595	0.00001
T^t_{B2}	2.37672	0.00002	2.81391	0.00007	1.585198	0.000009
T^t_{B3}	1.83977	0.00001	3.57185	0.00009	1.660199	0.000008
T^t_{F1}	0.787577	0.000001	0.787577	0.000001	0.801625	0.000001
T^t_{H1}	1.368796	0.000006	1.368796	0.000006	1.011494	0.000004
T^t_{H2}	1.295272	0.000006	1.295272	0.000006	0.525351	0.000002
T^t_{H3}	0.760951	0.000003	0.760951	0.000003	1.086037	0.000006
T^t_{P1}	1.893993	0.000006	1.893993	0.000006	1.893993	0.000006
T^t_{R1}	0.796565	0.000001	0.796565	0.000001	0.8116623	0.0000009
w	1.121	0.002	1.121	0.002	1.037	0.002
w_{hb}	0.58	NA	0.58	NA	0.58	NA

Table 5.6: Raw measurements and their estimated uncertainty.

	Crescendo		**Fisher**		**Pista**	
Variable	v	σ	v	σ	v	σ
a_{B1}	0.248	0.003	0.304	0.003	0.329	0.003
a_{B2}	0.075	0.003	0.395	0.003	0.293	0.003
a_{B3}	-0.289	0.003	-0.107	0.003	-0.267	0.003
a_{H1}	0.496	0.003	0.341	0.003	0.337	0.003
a_{H2}	0.466	0.003	0.277	0.003	0.400	0.003
a_{H3}	0.301	0.003	-0.008	0.003	-0.063	0.003
α_{B1}	127.6	0.2	125.9	0.2	120.2	0.2
α_{B2}	158.0	0.2	75.7	0.2	40.7	0.2
α_{B3}	223.9	0.2	190.8	0.2	215.9	0.2
α_{H1}	358.4	0.2	35.3	0.2	38.8	0.2

Continued on next page

Table 5.6 – continued from previous page

	Crescendo		**Fisher**		**Pista**	
α_{H2}	20.6	0.2	50.0	0.2	12.4	0.2
α_{H3}	303.8	0.2	93.8	0.2	102.2	0.2
d_F	27.98	0.01	29.04	0.01	29.37	0.01
d_P	0.0300	0.0001	0.0300	0.0001	0.0300	0.0001
d_R	27.77	0.01	29.79	0.01	29.21	0.01
f	0.045	0.001	0.038	0.001	0.032	0.001
g	9.81	0.01	9.81	0.01	9.81	0.01
γ	69.0	0.2	71.1	0.2	74.2	0.2
h_{bb}	0.29	NA	NA	NA	NA	NA
λ_{st}	1.23569311041	NA	NA	NA	NA	NA
l_{cs}	0.465	NA	NA	NA	NA	NA
l_F	0.301	0.001	0.264	0.001	0.297	0.001
l_{hbF}	0.81	NA	NA	NA	NA	NA
l_{hbR}	1.08	NA	NA	NA	NA	NA
l_P	1.050	0.001	1.050	0.001	1.050	0.001
l_R	0.297	0.001	0.265	0.001	0.297	0.001
l_{sp}	0.28	NA	NA	NA	NA	NA
l_{st}	0.49	NA	NA	NA	NA	NA
m_B	9.18	0.02	4.48	0.02	4.49	0.02
m_F	3.54	0.02	1.50	0.02	1.58	0.02
m_H	4.57	0.02	2.52	0.02	2.27	0.02
m_P	5.56	0.02	5.56	0.02	5.56	0.02
m_R	3.96	0.02	1.94	0.02	1.38	0.02
n_F	13.0	NA	14.0	NA	14.0	NA
n_R	13.0	NA	14.0	NA	14.0	NA
T^c_{B1}	1.676428	0.000003	1.632572	0.000004	1.639885	0.000006
T^c_{F1}	1.354974	0.000004	1.463519	0.000004	1.451154	0.000005
T^c_{H1}	1.628126	0.000005	1.422021	0.000002	1.392606	0.000002
T^c_{R1}	1.299370	0.000008	1.362063	0.000007	1.395046	0.000004
T^t_{B1}	2.26011	0.00001	1.291694	0.000003	1.26420	0.00001
T^t_{B2}	2.09595	0.00002	1.506534	0.000005	1.501279	0.000007
T^t_{B3}	1.92017	0.00001	1.367939	0.000004	1.492970	0.000005
T^t_{F1}	0.818258	0.000002	0.665696	0.000001	0.6232453	0.0000006
T^t_{H1}	1.6903	0.0001	0.826936	0.000002	0.776458	0.000001
T^t_{H2}	1.6440	0.0001	0.720503	0.000001	0.830610	0.000003
T^t_{H3}	1.21590	0.00002	0.3719856	0.0000003	0.5250995	0.0000005
T^t_{P1}	1.893993	0.000006	1.893993	0.000006	1.893993	0.000006
T^t_{R1}	0.823570	0.000001	0.6650523	0.0000008	0.622565	0.000001
w	1.101	0.002	1.070	0.002	0.989	0.002
w_{hb}	0.56	NA	NA	NA	NA	NA

Table 5.7: Raw measurements and their estimated uncertainty.

	Yellow		**Yellowrev**	
Variable	v	σ	v	σ
a_{B1}	0.220	0.003	0.220	0.003
a_{B2}	0.0	0.0	0.0	0.0
a_{B3}	-0.379	0.003	-0.379	0.003
a_{H1}	0.468	0.003	0.099	0.003

Continued on next page

Table 5.7 – continued from previous page

	Yellow		Yellowrev	
a_{H2}	0.396	0.003	0.445	0.003
a_{H3}	0.015	0.003	0.474	0.003
α_{B1}	139.5	0.2	139.5	0.2
α_{B2}	345.4	0.2	345.4	0.2
α_{B3}	215.9	0.2	215.9	0.2
α_{H1}	0.3	0.2	89.3	0.2
α_{H2}	32.0	0.2	33.5	0.2
α_{H3}	87.9	0.2	4.3	0.2
d_F	27.93	0.01	27.93	0.01
d_P	0.0300	0.0001	0.0300	0.0001
d_R	27.88	0.01	27.88	0.01
f	0.057	0.001	-0.057	0.001
g	9.81	0.01	9.81	0.01
γ	72.7	0.2	70.6	0.2
h_{bb}	0.276580359362	NA	0.276602031136	NA
λ_{st}	1.2653637077	NA	1.2653637077	NA
l_{cs}	0.45	NA	0.45	NA
l_F	0.304	0.001	0.304	0.001
l_{hbF}	0.7	NA	0.7	NA
l_{hbR}	1.145	NA	1.145	NA
l_P	1.050	0.001	1.050	0.001
l_R	0.302	0.001	0.302	0.001
l_{sp}	0.21	NA	0.21	NA
l_{st}	0.515	NA	0.515	NA
m_B	3.31	0.02	3.31	0.02
m_F	1.90	0.02	1.90	0.02
m_H	2.45	0.02	2.45	0.02
m_P	5.56	0.02	5.56	0.02
m_R	2.57	0.02	2.57	0.02
n_F	13.0	NA	13.0	NA
n_R	13.0	NA	13.0	NA
T^c_{B1}	1.71695	0.00001	1.71695	0.00001
T^c_{F1}	1.49847	0.00002	1.49847	0.00002
T^c_{H1}	1.518206	0.000008	1.528827	0.000006
T^c_{R1}	1.40931	0.00002	1.40931	0.00002
T^t_{B1}	1.19029	0.00002	1.19029	0.00002
T^t_{B2}	1.200785	0.000006	1.200785	0.000006
T^t_{B3}	1.282136	0.000008	1.282136	0.000008
T^t_{F1}	0.773040	0.000002	0.773040	0.000002
T^t_{H1}	1.012698	0.000003	0.4756557	0.0000009
T^t_{H2}	0.948609	0.000002	0.963826	0.000003
T^t_{H3}	0.4579289	0.0000006	1.019585	0.000003
T^t_{P1}	1.893993	0.000006	1.893993	0.000006
T^t_{R1}	0.784395	0.000001	0.784395	0.000001
w	1.089	0.002	0.985	0.002
w_{hb}	0.24	NA	0.24	NA

Table 5.8: Raw measurements and their estimated uncertainty.

	Rigid		**Rigidcl**		**Gyro**	
Variable	v	σ	v	σ	v	σ
a_{B1}	-0.521	0.001	-0.507	0.001	0.153	0.001
a_{B2}	-0.295	0.001	-0.244	0.001	-0.195	0.001
a_{B3}	0.518	0.001	0.510	0.001	-0.105	0.001
a_{B4}	0.140	0.001	0.149	0.001	0.192	0.001
a_{B5}	0.516	0.001	NA	NA	NA	NA
a_{G1}	-0.059	0.001	-0.059	0.001	NA	NA
a_{G2}	0.075	0.001	0.075	0.001	NA	NA
a_{G3}	-0.069	0.001	-0.069	0.001	NA	NA
a_{H1}	NA	NA	NA	NA	0.238	0.001
a_{H2}	NA	NA	NA	NA	0.287	0.001
a_{H3}	NA	NA	NA	NA	0.098	0.001
a_{H4}	NA	NA	NA	NA	-0.008	0.001
α_{B1}	233.0	0.1	228.2	0.1	134.1	0.1
α_{B2}	180.2	0.1	176.0	0.1	219.0	0.1
α_{B3}	55.7	0.1	54.4	0.1	192.8	0.1
α_{B4}	342.5	0.1	344.1	0.1	NA	NA
α_{B5}	51.8	0.1	NA	NA	NA	NA
α_{G1}	57.3	0.1	57.3	0.1	NA	NA
α_{G2}	224.4	0.1	224.4	0.1	NA	NA
α_{G3}	332.3	0.1	332.3	0.1	NA	NA
α_{H1}	NA	NA	NA	NA	323.5	0.1
α_{H2}	NA	NA	NA	NA	342.8	0.1
α_{H3}	NA	NA	NA	NA	292.5	0.1
α_{H4}	NA	NA	NA	NA	272.1	0.1
α_{S1}	252.6	0.1	252.6	0.1	NA	NA
α_{S2}	156.2	0.1	156.2	0.1	NA	NA
α_{S3}	127.6	0.1	127.6	0.1	NA	NA
α_{S4}	20.9	0.1	20.9	0.1	NA	NA
α_{S5}	301.0	0.1	301.0	0.1	NA	NA
a_{S1}	-0.092	0.001	-0.092	0.001	NA	NA
a_{S2}	-0.407	0.001	-0.407	0.001	NA	NA
a_{S3}	-0.296	0.001	-0.296	0.001	NA	NA
a_{S4}	0.386	0.001	0.386	0.001	NA	NA
a_{S5}	0.255	0.001	0.255	0.001	NA	NA
d	0.96338	0.00008	0.96338	0.00008	0.54134	0.00008
d_1	0.03705	0.00003	0.03705	0.00003	0.04574	0.00004
d_2	0.00980	0.00003	0.00980	0.00003	0.00945	0.00004
d_3	0.01005	0.00003	0.01005	0.00003	0.0	0.0
d_4	0.02855	0.00003	0.02855	0.00003	0.0	0.0
d_5	0.01001	0.00001	0.01001	0.00001	NA	NA
d_6	0.02217	0.00001	0.02217	0.00001	NA	NA
d_F	21.0846	0.0006	21.0846	0.0006	21.2782	0.0007
d_P	0.030103	0.000006	0.030103	0.000006	0.030103	0.000006
d_R	20.8934	0.0006	20.8934	0.0006	21.6868	0.0007
d_{s1}	0.1349375	NA	0.1349375	NA	NA	NA
d_{s3}	-0.3603625	NA	-0.3603625	NA	NA	NA
g	9.81	0.01	9.81	0.01	9.81	0.01

Continued on next page

Table 5.8 – continued from previous page

	Rigid		**Rigidcl**		**Gyro**	
h_1	0.91561	0.00003	0.91561	0.00003	0.56515	0.00008
h_2	0.10160	0.00001	0.10160	0.00001	0.03110	0.00008
h_3	0.06708	0.00004	0.06708	0.00004	0.09246	0.00008
h_4	0.12211	0.00006	0.12211	0.00006	0.0	0.0
h_5	0.08355	0.00006	0.08355	0.00006	0.0	0.0
h_6	0.15369	0.00001	0.15369	0.00001	NA	NA
h_7	0.14833	0.00001	0.14833	0.00001	NA	NA
h_{bb}	0.291	NA	0.291	NA	0.1905	NA
l	0.962	0.002	0.962	0.002	NA	NA
λ_{st}	1.267109037	NA	1.267109037	NA	1.23394778	NA
l_{cs}	0.423	NA	0.423	NA	0.2413	NA
l_F	0.29572	0.00008	0.29572	0.00008	0.10082	0.00008
l_{hbF}	0.90805	NA	0.90805	NA	0.6096	NA
l_{hbR}	1.0795	NA	1.0795	NA	0.67945	NA
l_P	0.836	0.001	0.836	0.001	0.83550	0.00008
l_R	0.28028	0.00008	0.28028	0.00008	0.093	0.001
l_{sp}	0.2032	NA	0.1524	NA	0.0381	NA
l_{st}	0.5476875	NA	0.5476875	NA	0.238125	NA
m_B	22.90	0.01	23.00	0.01	3.04	0.01
m_D	NA	NA	NA	NA	3.86	0.01
m_F	1.55	0.01	1.55	0.01	1.41	0.01
m_G	3.35	0.01	3.35	0.01	NA	NA
m_H	NA	NA	NA	NA	1.36	0.01
m_P	4.65	0.01	4.65	0.01	4.65	0.01
m_R	4.90	0.01	4.90	0.01	1.54	0.01
m_S	2.05	0.01	2.05	0.01	NA	NA
n_F	10.0	NA	10.0	NA	23.0	NA
n_R	10.0	NA	10.0	NA	23.0	NA
T^c_{B1}	1.88231	0.00009	1.86670	0.00004	1.1736	0.0001
T^c_{D1}	NA	NA	NA	NA	0.79623	0.00002
T^c_{F1}	1.43309	0.00002	1.43309	0.00002	0.88747	0.00001
T^c_{G1}	0.77267	0.00002	0.77267	0.00002	NA	NA
T^c_{H1}	NA	NA	NA	NA	1.288842	0.000006
T^c_{R1}	1.22757	0.00002	1.22757	0.00002	0.812587	0.000010
T^c_{S1}	1.47091	0.00003	1.47091	0.00003	NA	NA
T^t_{B1}	3.4229	0.0002	3.02521	0.00005	0.34685	0.00002
T^t_{B2}	2.70613	0.00002	2.55895	0.00003	0.382251	0.000008
T^t_{B3}	3.07592	0.00002	3.03205	0.00005	0.35672	0.00002
T^t_{B4}	2.46588	0.00005	2.41714	0.00004	NA	NA
T^t_{B5}	3.0804	0.0001	NA	NA	NA	NA
T^t_{D1}	NA	NA	NA	NA	0.216570	0.000004
T^t_{F1}	0.421157	0.000007	0.421157	0.000007	0.169795	0.000004
T^t_{G1}	0.448654	0.000008	0.448654	0.000008	NA	NA
T^t_{G2}	0.43545	0.00001	0.43545	0.00001	NA	NA
T^t_{G3}	0.41619	0.00001	0.41619	0.00001	NA	NA
T^t_{H1}	NA	NA	NA	NA	0.36097	0.00002
T^t_{H2}	NA	NA	NA	NA	0.394980	0.000001
T^t_{H3}	NA	NA	NA	NA	0.2254071	0.0000008
T^t_{H4}	NA	NA	NA	NA	0.209330	0.000001

Continued on next page

Table 5.8 – continued from previous page

	Rigid		**Rigidcl**		**Gyro**	
T^t_{P1}	0.956919	0.000002	0.956919	0.000002	0.956919	0.000002
T^t_{R1}	0.486888	0.000007	0.486888	0.000007	0.156524	0.000004
T^t_{S1}	0.1519	0.0002	0.1519	0.0002	NA	NA
T^t_{S2}	0.535664	0.000002	0.535664	0.000002	NA	NA
T^t_{S3}	0.438209	0.000006	0.438209	0.000006	NA	NA
T^t_{S4}	0.52994	0.00002	0.52994	0.00002	NA	NA
T^t_{S5}	0.372150	0.000005	0.372150	0.000005	NA	NA
w_{hb}	0.535	NA	0.535	NA	0.42275	NA
x_{cl}	0.1984375	NA	0.20955	NA	NA	NA
z_{cl}	-0.942975	NA	-0.9017	NA	NA	NA

5.6.2 Bicycle Benchmark Parameters

Table 5.9: Computed physical parameters and their estimated uncertainties.

	Browser		**Browserins**		**Stratos**	
Variable	v	σ	v	σ	v	σ
c	0.069	0.002	0.068	0.002	0.056	0.002
g	9.81	0.01	9.81	0.01	9.81	0.01
I_{Bxx}	0.530	0.002	1.045	0.005	0.373	0.002
I_{Bxz}	-0.116	0.001	-0.113	0.003	-0.0383	0.0004
I_{Byy}	1.316	0.004	2.403	0.007	0.717	0.003
I_{Bzz}	0.757	0.003	1.850	0.008	0.455	0.002
I_{Fxx}	0.0884	0.0004	0.0884	0.0004	0.0916	0.0004
I_{Fyy}	0.149	0.002	0.149	0.002	0.157	0.001
I_{Hxx}	0.253	0.001	0.253	0.001	0.1768	0.0008
I_{Hxz}	-0.0720	0.0008	-0.0720	0.0008	-0.0273	0.0006
I_{Hyy}	0.246	0.003	0.246	0.003	0.144	0.002
I_{Hzz}	0.0956	0.0007	0.0956	0.0007	0.0446	0.0003
I_{Rxx}	0.0904	0.0004	0.0904	0.0004	0.0939	0.0004
I_{Ryy}	0.152	0.001	0.152	0.001	0.154	0.001
λ	0.400	0.003	0.400	0.003	0.295	0.003
m_B	9.86	0.02	14.71	0.02	7.22	0.02
m_F	2.02	0.02	2.02	0.02	3.33	0.02
m_H	3.22	0.02	3.22	0.02	3.04	0.02
m_R	3.11	0.02	3.11	0.02	3.96	0.02
r_F	0.3435	0.0001	0.3426	0.0001	0.3400	0.0001
r_R	0.3410	0.0001	0.3408	0.0001	0.3385	0.0001
w	1.121	0.002	1.121	0.002	1.037	0.002
x_B	0.276	0.003	0.217	0.003	0.326	0.003
x_H	0.867	0.004	0.867	0.004	0.911	0.004
z_B	-0.538	0.003	-0.622	0.003	-0.483	0.003
z_H	-0.748	0.003	-0.747	0.003	-0.730	0.002

Table 5.10: Computed physical parameters and their estimated uncertainties.

	Crescendo		**Fisher**		**Pista**	
Variable	v	σ	v	σ	v	σ
c	0.083	0.002	0.072	0.002	0.062	0.002
g	9.81	0.01	9.81	0.01	9.81	0.01
I_{Bxx}	0.500	0.002	0.283	0.001	0.290	0.002
I_{Bxz}	-0.015	0.001	0.0559	0.0003	0.050	0.001
I_{Byy}	1.117	0.004	0.470	0.003	0.476	0.009
I_{Bzz}	0.739	0.003	0.268	0.001	0.249	0.001
I_{Fxx}	0.0954	0.0004	0.0631	0.0003	0.0553	0.0002
I_{Fyy}	0.166	0.001	0.106	0.001	0.106	0.001
I_{Hxx}	0.384	0.002	0.1147	0.0010	0.0980	0.0004
I_{Hxz}	-0.078	0.001	-0.018	0.001	-0.0044	0.0003
I_{Hyy}	0.363	0.004	0.100	0.004	0.069	0.002
I_{Hzz}	0.166	0.001	0.0226	0.0006	0.0396	0.0002
I_{Rxx}	0.0966	0.0004	0.0630	0.0003	0.0552	0.0002
I_{Ryy}	0.144	0.001	0.101	0.001	0.076	0.001
λ	0.367	0.003	0.330	0.003	0.276	0.003
m_B	9.18	0.02	4.48	0.02	4.49	0.02
m_F	3.54	0.02	1.50	0.02	1.58	0.02
m_H	4.57	0.02	2.52	0.02	2.27	0.02
m_R	3.96	0.02	1.94	0.02	1.38	0.02
r_F	0.3426	0.0001	0.3302	0.0001	0.3338	0.0001
r_R	0.3400	0.0001	0.3386	0.0001	0.3321	0.0001
w	1.101	0.002	1.070	0.002	0.989	0.002
x_B	0.312	0.003	0.367	0.002	0.38	0.02
x_H	0.907	0.005	0.960	0.006	0.906	0.005
z_B	-0.526	0.003	-0.499	0.003	-0.477	0.007
z_H	-0.803	0.003	-0.719	0.004	-0.732	0.002

Table 5.11: Computed physical parameters and their estimated uncertainties.

	Yellow		**Yellowrev**	
Variable	v	σ	v	σ
c	0.047	0.002	0.180	0.002
g	9.81	0.01	9.81	0.01
I_{Bxx}	0.2240	0.0009	0.2254	0.0009
I_{Bxz}	0.0182	0.0001	0.0179	0.0001
I_{Byy}	0.388	0.005	0.388	0.005
I_{Bzz}	0.2160	0.0009	0.2147	0.0009
I_{Fxx}	0.0852	0.0003	0.0852	0.0003
I_{Fyy}	0.147	0.002	0.147	0.002
I_{Hxx}	0.1452	0.0006	0.1475	0.0006
I_{Hxz}	-0.0194	0.0005	-0.0172	0.0005
I_{Hyy}	0.120	0.003	0.120	0.002
I_{Hzz}	0.0292	0.0003	0.0294	0.0004
I_{Rxx}	0.0877	0.0004	0.0877	0.0004
I_{Ryy}	0.149	0.001	0.149	0.001
λ	0.302	0.003	0.339	0.003
m_B	3.31	0.02	3.31	0.02
m_F	1.90	0.02	1.90	0.02
m_H	2.45	0.02	2.45	0.02
m_R	2.57	0.02	2.57	0.02
r_F	0.3419	0.0001	0.3419	0.0001
r_R	0.3414	0.0001	0.3414	0.0001
w	1.089	0.002	0.985	0.002
x_B	0.422	0.004	0.412	0.004
x_H	0.948	0.004	0.919	0.005
z_B	-0.603	0.004	-0.618	0.004
z_H	-0.788	0.002	-0.816	0.002

Table 5.12: Computed physical parameters and their estimated uncertainties.

	Rigid		**Rigidcl**		**Gyro**	
Variable	v	σ	v	σ	v	σ
c	0.0599	0.0001	0.0599	0.0001	0.0445	0.0002
g	9.81	0.01	9.81	0.01	9.81	0.01
I_{Bxx}	2.64	0.01	2.371	0.008	0.03848	0.00009
I_{Bxz}	0.654	0.003	0.531	0.002	0.00620	0.00003
I_{Byy}	4.28	0.01	4.17	0.01	0.0661	0.0007
I_{Bzz}	1.94	0.02	1.901	0.010	0.04120	0.00010
I_{Dxx}	NA	NA	NA	NA	0.00534	0.00001
I_{Dyy}	NA	NA	NA	NA	0.0086	0.0001
I_{Fxx}	0.0524	0.0002	0.0524	0.0002	0.00852	0.00002
I_{Fyy}	0.0984	0.0007	0.0984	0.0007	0.01345	0.00010
I_{Gxx}	0.0497	0.0002	0.0497	0.0002	NA	NA
I_{Gxz}	0.00494	0.00003	0.00494	0.00003	NA	NA
I_{Gyy}	0.0174	0.0002	0.0174	0.0002	NA	NA
I_{Gzz}	0.0622	0.0002	0.0622	0.0002	NA	NA
I_{Hxx}	0.344	0.003	0.344	0.003	0.0484	0.0002

Continued on next page

Table 5.12 – continued from previous page

	Rigid		**Rigidcl**		**Gyro**	
I_{Hxz}	-0.092	0.001	-0.092	0.001	-0.01014	0.00008
I_{Hyy}	0.340	0.004	0.340	0.004	0.0439	0.0005
I_{Hzz}	0.1031	0.0007	0.1031	0.0007	0.01469	0.00005
I_{Rxx}	0.0701	0.0002	0.0701	0.0002	0.00724	0.00002
I_{Ryy}	0.1293	0.0006	0.1293	0.0006	0.01021	0.00008
I_{Sxx}	0.0827	0.0003	0.0827	0.0003	NA	NA
I_{Sxz}	-0.0351	0.0001	-0.0351	0.0001	NA	NA
I_{Syy}	0.093	0.001	0.093	0.001	NA	NA
I_{Szz}	0.0229	0.0001	0.0229	0.0001	NA	NA
λ	0.3175	0.0003	0.3175	0.0003	0.293	0.001
m_B	22.90	0.01	23.00	0.01	3.04	0.01
m_D	NA	NA	NA	NA	2.45	0.01
m_F	1.55	0.01	1.55	0.01	1.41	0.01
m_G	3.35	0.01	3.35	0.01	NA	NA
m_H	5.40	0.01	5.40	0.01	1.36	0.01
m_R	4.90	0.01	4.90	0.01	1.54	0.01
m_S	2.05	0.01	2.05	0.01	NA	NA
r_F	0.335573	0.000009	0.335573	0.000009	0.147241	0.000005
r_R	0.332528	0.000009	0.332528	0.000009	0.150068	0.000005
w	1.0638	0.0002	1.0638	0.0002	0.54605	0.00008
x_B	0.335	0.007	0.319	0.002	0.229	0.001
x_{cl}	0.1984375	NA	0.20955	NA	NA	NA
x_G	0.773	0.002	0.773	0.002	NA	NA
x_H	0.818	0.001	0.818	0.001	0.4757	0.0009
x_S	0.8923	0.0008	0.8923	0.0008	NA	NA
z_B	-0.736	0.005	-0.731	0.002	-0.2693	0.0008
z_{cl}	-0.942975	NA	-0.9017	NA	NA	NA
z_G	-1.141	0.002	-1.141	0.002	NA	NA
z_H	-0.986	0.002	-0.986	0.002	-0.447	0.001
z_S	-0.733	0.002	-0.733	0.002	NA	NA

CHAPTER

SIX

PARAMETER STUDIES

6.1 Introduction

Investigation of the effects of changes in the model parameters is a natural place to start once the various bicycle models are available. For the bicycle designer, understanding how changing parameters affects the dynamic characteristics is something of a holy grail. If connections can be drawn from model parameters to such things as handle-ability, stability, and controllability, bicycle designs could be tuned with these things mind. In the aircraft design world correlations have been drawn from open loop dynamics to handling qualities. It is highly likely that open loop dynamics can be predictors of the handling of a bicycle, but there are large differences in aircraft, ground vehicles, and bicycles. The most glaring is the size of the rider with respect to the vehicle and the fact that the rider's biomechanics, which are not trivial, contribute to the open loop dynamics of the entire system.

The eigenmodes of the Whipple model and the stability regime are prime targets for initial parameter studies and there are many papers that deal with various aspects. An analytical view of the parameter relationships would provide the most encompassing conclusions, but the complicated form of the equations typically lead researchers to numerical studies. [VZ75] studies the effects of trail, front wheel moment of inertia, and rider position on the dynamics using Routh's criterion and a sensitivity study. [KMP+11] refines the work in [Pap87] which makes use of a compact analytical form of the linear equations of motion and Routh's stability criterion to analytically find instability the capsize mode. [FSR90] and [ASKL05] examine the effect on stable speed range of independently varying wheel rotational inertia and find that for their parameter values both the weave and capsize critical speeds decrease with increase in spin moment of inertia. [FSR90] also shows that as trail increases both the critical speeds and the stable speed range increases. This conclusion is counter intuitive, as some [Koo06] seem to believe that an increase in trail lowers the weave critical speed, thus making the bicycle more stable. [Ste09] examines experimentally and numerically the effects of the front end geometry (trail and headtube angle) on eigenvalues, with some similar results as [KSM08]. [TWB10] examines the derivatives of the critical speeds with respect to the benchmark parameters for a nominal parameter set. Tak's method allows one to quickly visualize the independent parameter change which affects the stable speed range the most for a given bicycle. Other examples of parameter studies include [Sha71], [Sha94], [CDL99], and [LLLW03] among many others.

Numerical parameters studies were the first thing I did once I had a working Whipple model [MH08] and I've explored some other studies over the years. The following sections provide some of the results and various small findings.

6.2 Geometric Variation

My first curiosities about bicycle handling arose when I was designing the frame geometry of a recumbent bicycle for my undergraduate senior design project and this geometric outlook seems to be continually the main interest among bicycle enthusiasts and designers. Many bicycle designers focus on geometry as the primary design criterion for handling, in particular the head tube angle and trail, *Figure 6.1*. But wheelbase, front wheel diameter, frame/wheel alignment, and the rider position which is dictated by handlebar geometry are considered too. A browse through

bicycle magazines and frame builder literature provide a wide range of opinions about how geometry affects the handling. For example, Tim Paterek, an expert frame builder, claims that the comfort zone for trail falls between 0.05 m and 0.065 m for most bicycles [Pat04a]. Craig Calfee is another prominent frame builder interested the effects of fork alignment on handling who wrote a small piece on bicycle geometry for the 2007 North American Handbuilt Bicycle show [Cal07]. He points out that minute misalignments in the fork geometry can cause undesirable handling. Finally, Jan Heine has written extensively in his Vintage Bicycle Quarterly about handling, with subjective and objective measures by experienced riders of the handling differences in real bicycles.

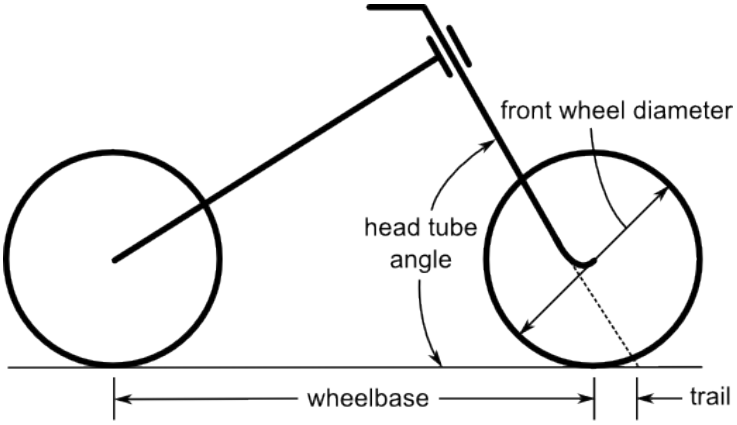

Figure 6.1: The essential geometry of a bicycle parameterized with variables typically of interest to bicycle designers.

But the reality is that little progress has been made to predict handling qualities from geometry using rigorous dynamic and control theory. Nonetheless parameter studies can still be done with the models we have available. The following results show how the stable speed range of the Whipple model linearized about the nominal configuration changes with respect to varying the essential geometry: trail, head tube angle, wheelbase, and front wheel diameter. Unlike in many other parameter studies, the physical changes associated with the rider's position and the bicycle's parameters other than the essential geometry are interdependent (e.g. adjusting the front wheel diameter changes the wheel's mass and moments of inertia together with the bicycle's frame geometry and adjusting the wheelbase causes the rider to reach further forward). It is important to point out that the parameter value combinations that result from independently varying the physical parameters do not necessarily equate to a realizable bicycle. For example, a wheel's spin moment of inertia is generally about two times the transverse moment of inertia, so varying those parameters independently is not that useful. The rider parameters are estimated using a method which was a slight precursor to the simple geometry method presented in Chapter *Physical Parameters*[1] and where based off of a 72 kg, 182 cm tall adult male. The rear frame and fork were modelled as a collection of uniform steel tubes and the wheels as simple tori. This allowed estimation of the inertial properties of a bicycle as a function of geometry. It assumed a normal diamond frame bicycle and the base geometry of the bicycle was measured from a 58 cm 1982 Schwinn LeTour steel road bike.

The stable speed range for the nominal configuration was between about 3.59 m/s and 4.88 m/s. Changes in the stable speed range were calculated by varying each parameter over a realistic range for a bicycle of this nature. Each figure shows a depiction of the maximal and minimal geometry configurations and the nominal stable speed range is shown with a vertical line.

At speeds greater than the capsize critical speed, the capsize mode is unstable with a slow time to double. Thus the instability can be assumed to be relatively easy to stabilize with a simple control, especially since the weave mode provides rapid roll damping. That implies that the stable speed range and capsize critical speed may be of less importance to actual stability, leaving the weave critical speed as the defining characteristic.

A slack head tube angle (< 72 degrees) has a higher weave critical speed than a larger head tube angle but the capsize critical speed varies very little with changing head tube angle, *Figure 6.2*. Slack head tube angles are found on many utility bicycles. I've observed from experience that these bicycles feel very unresponsive at low speeds and typically do not feel stable until moderate speeds are reached. The head tube angle results, *Figure 6.2* are in agreement with this

[1] The original method modeled the legs with a two cuboids instead of four cylinders.

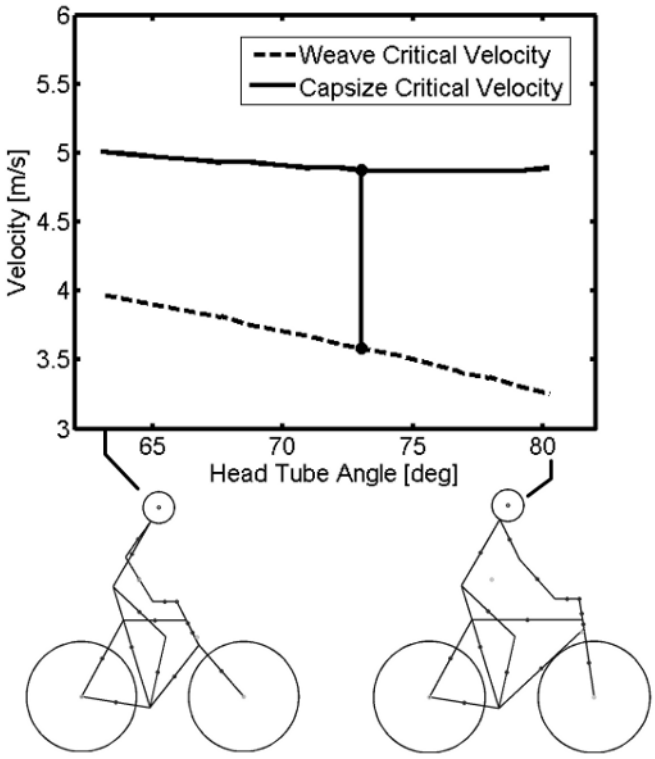

Figure 6.2: The change in stable speed range as a function of head tube angle.

anecdotal evidence insofar as the weave critical speed increases with decreasing head tube angle. The head tube angle results are interesting because the weave speed can be decreased using a steeper head tube angle without adversely affecting the capsize critical speed, thus simultaneously increasing the stable speed range and decreasing the weave speed. This is ideal if it is assumed that a low weave critical speed is beneficial for take off and a broad stable speed range is beneficial for cruising with little control input.

Trail is of particular interest, with many bicycle designers claiming that it is the most important parameter affecting handling qualities. As trail increases, the stable speed range broadens and the weave critical velocity increases, *Figure 6.3*. As trail approaches zero the stable speed range diminishes to zero. It is obvious that increasing trail will decrease the caster mode eigenvalue, but un-intuitively it increases the weave eigenvalue. The yellow bicycle and the silver bicycle [Koo06] both have their forks flipped for increase trail with the intent to make the bicycles stable at the speeds tested. According to the these results it does not seem that that is the case; it may have the opposite effect.

Long bicycles such as tandems and some recumbents are often hard to start and have slower response due to the diminished yaw control authority. As wheelbase increases, the size of the stable speed range stays roughly constant as both weave and capsize critical speeds increase linearly at the same rate, *Figure 6.4*. The weave critical speed increases as wheelbase increases which correlates with the difficulty in starting long wheelbase bicycles.

The weave critical speed decreases as front wheel diameter increases but the capsize critical speed decreases even faster so the size of the stable speed range also decreases, *Figure 6.5*. The results show that the weave critical speed decreases with a larger front wheel which provides stability at low speeds. This correlates with the findings for the flywheel bicycle presented in Chapter *Extensions of the Whipple Model*.

Here were presented some conclusions about the stability of the Whipple model and made the potential relationship of the critical speeds to geometry changes. This gives some idea of how one may begin connecting handling to the bicycle's dynamics.

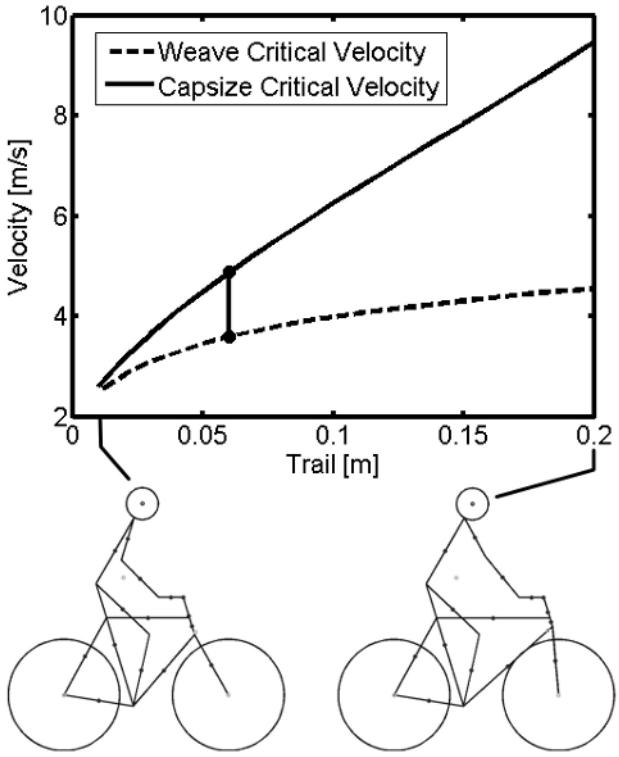

Figure 6.3: The change in stable speed range as a function of trail.

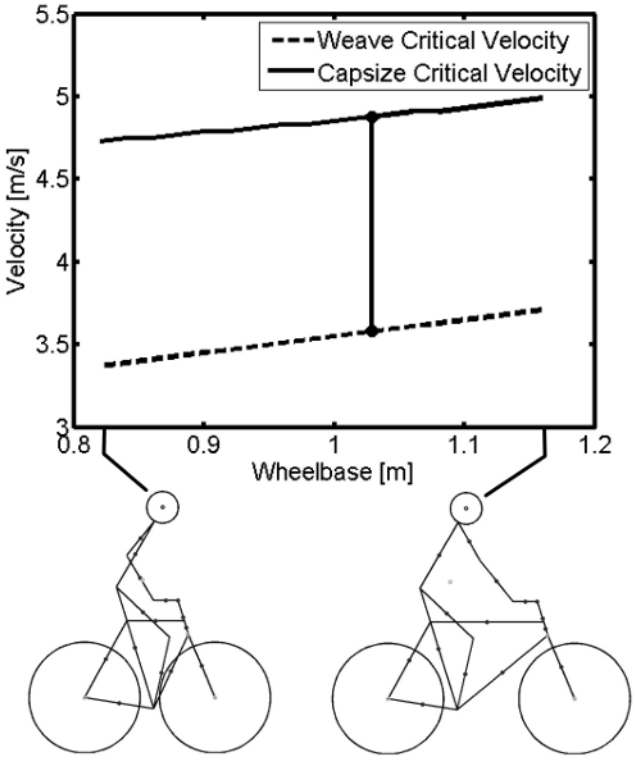

Figure 6.4: The change in stable speed range as a function of wheelbase.

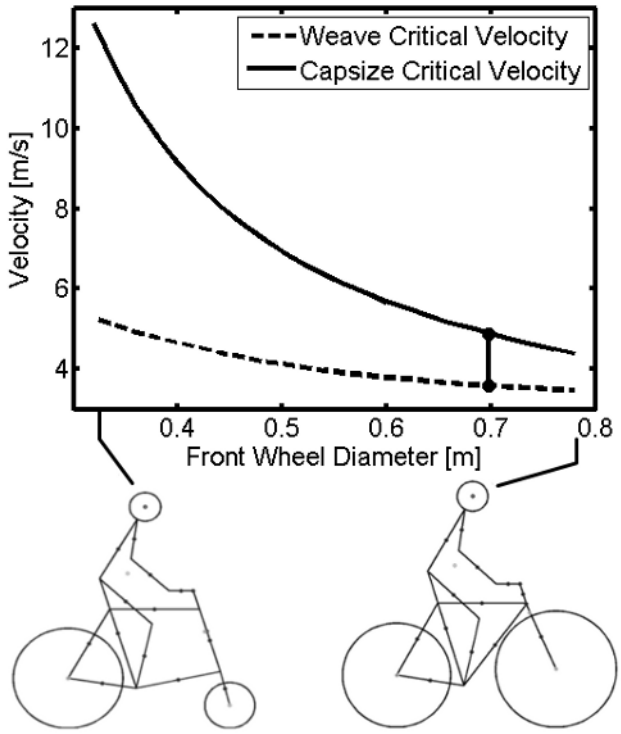

Figure 6.5: The change in stable speed range as a function of front wheel diameter.

6.3 Bicycle Comparison

I present the physical parameters of eleven bicycles in Chapter *Physical Parameters*. There is a variety of bicycles from commuter bicycles to road racing and mountain to a child's bicycle and some instrumented bicycles. Here I will present some comparisons of the linear dynamics of the different bicycles and try to make some conclusions about their dynamics. The "normal" diamond frame bicycle is very similar from bicycle to bicycle with very little variation in the essential geometry. More variation is seen in the mass and inertia.

6.3.1 Benchmark validity

The numerical values of the benchmark bicycle parameters in [MPRS07] are representative of a real bicycle but were chosen so that each parameter was guaranteed a detectable role in numerical studies. Figure *Figure 6.6* compares the eigenvalues of the benchmark bicycle with those of two ordinary bicycles, the Batavus Browser and Batavus Stratos including the same rider, Jason, seated on both bicycles. The eigenvalues are qualitatively similar, but the stable speed range of the benchmark bicycle is both lower and narrower than the other two. The benchmark weave frequency also diverts from the real bicycles at higher speeds, but other than that the benchmark parameters are most likely within realistic bounds for a normal style bicycle due to the similar dynamic behavior.

6.3.2 Rider-less bicycles

There are relatively few bicycles whose parameters have been measured exhaustively and accurately. *Figure 6.7* plots the effect of speed on the resulting eigenvalues of one such parameter set, labeled Silver, from [KSM08] and compares it to several of the rider-less bicycles I measured using almost identical techniques to Kooijman. Notice that all of the

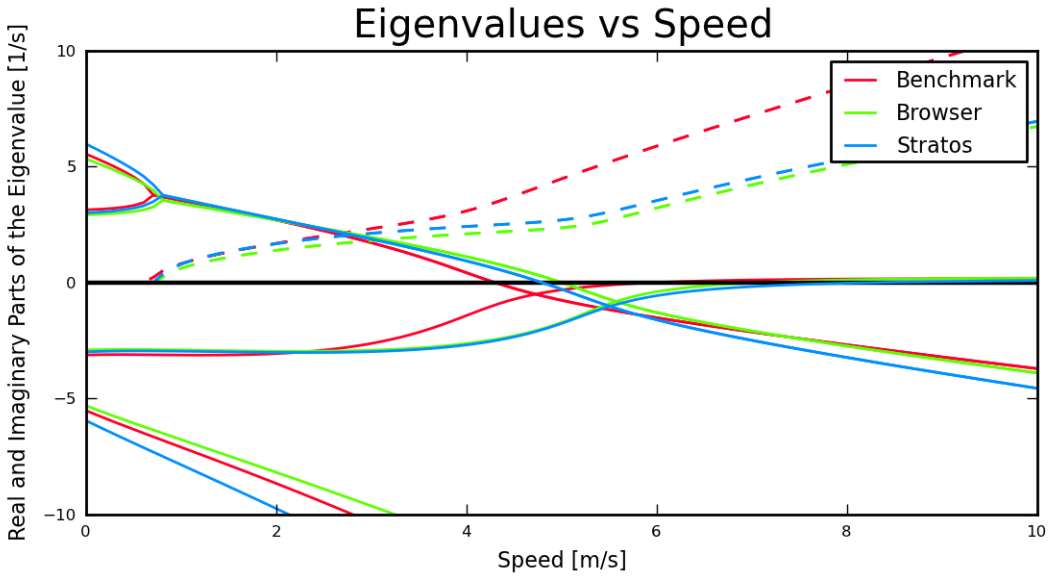

Figure 6.6: Real and imaginary parts of the eigenvalues as a function of speed for three bicycles including the benchmark bicycle from [MPRS07] and two bicycles (Browser and Stratos) and a rider (Jason) presented in Chapter *Physical Parameters*. Generated by `src/parameterstudy/bicycle_eig_compare.py`.

bicycles measured in Chapter *Physical Parameters* show a bifurcation in the caster and capsize modes at lower speeds which produces a second oscillatory mode. This bifurcation is not necessarily seen in the parameter sets with a rigid rider. Figures *6.8* and *6.9* show the eigenvector components for the two oscillatory modes for the Crescendo bicycle at 1.5 m/s. They turn out to be similar in that they are oscillatory in roll and steer, with steer being dominant in magnitude and the phase shifts are slightly larger for the weave mode. But the new mode is stable as opposed to the weave mode being unstable. The bicycles measured in [Ste09] and [ER11] both exhibit this mode, but Stevens' [Ste09] parameters are estimated from a CAD drawing, which may not be as accurate as more direct measurements. Steven's does show that this mode disappears with very steep or very slack head tube angles. The diagrams for very slack head angles more qualitatively resemble the Silver bicycle from [KSM08]. But it is still odd that the Silver bicycle is that different than all the other bicycles, with the only major difference being a flipped fork for more trail and a larger yaw and roll moment of inertia due to the outriggers.

6.3.3 Bicycles with riders

There are some potentially significant differences in the Whipple model dynamics between a riderless bicycle and a bicycle with a rider. *Figure 6.10* gives an example of how the eigenvalues change when a rider is added to the Stratos bicycle. The stable speed range broadens and the weave critical speed increases by more than 1 m/s. The second oscillatory mode disappears and the caster decays more rapidly. The weave bifurcation occurs at a lower speed. And finally the natural frequency of the weave mode for the rider and bike is much lower for speeds above 3 m/s. The changes in dynamics are large enough that conclusions made about bicycles without rigid riders don't necessarily extend to bicycles with rigid riders.

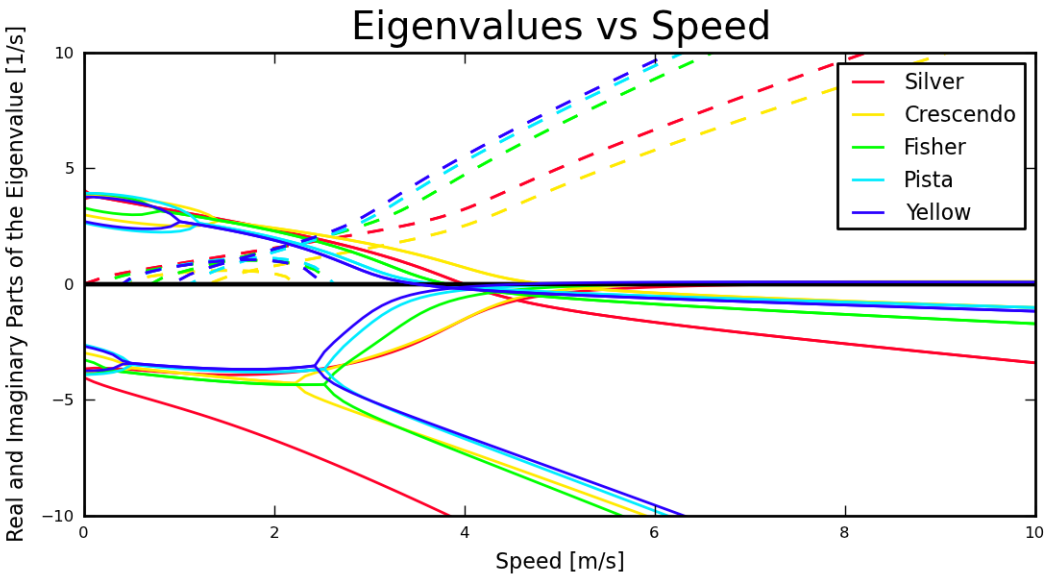

Figure 6.7: Real and imaginary parts of the eigenvalues as a function of speed for four bicycles including the silver bicycle from [KSM08] and three bicycles and riders presented in Chapter *Physical Parameters*. Generated by `src/parameterstudy/bicycle_eig_compare.py`.

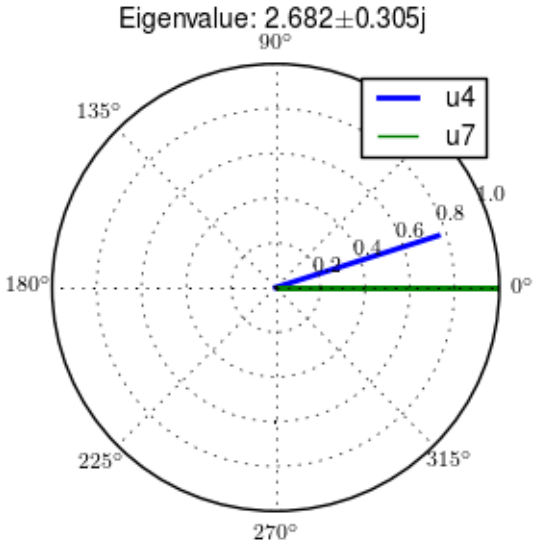

Figure 6.8: Eigenvector components for roll rate, u_4, and steer rate, u_9, for the Crescendo parameter values weave mode at 1.5 m/s. Generated by `src/parameterstudy/bicycle_eig_compare.py`.

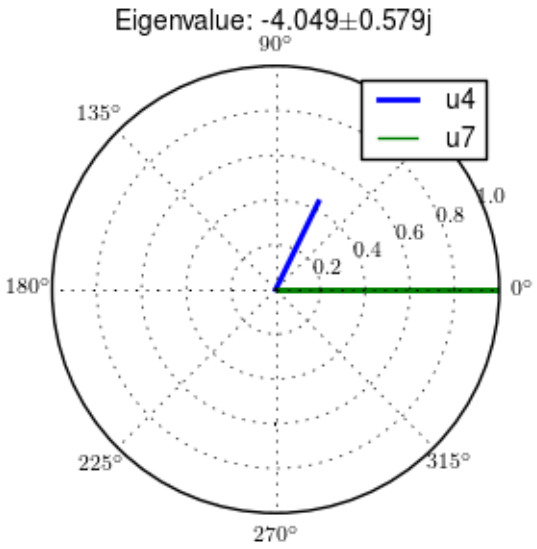

Figure 6.9: Eigenvector components for roll rate, u_4, and steer rate, u_9, for the Crescendo parameter values new mode at 1.5 m/s. Generated by `src/parameterstudy/bicycle_eig_compare.py`.

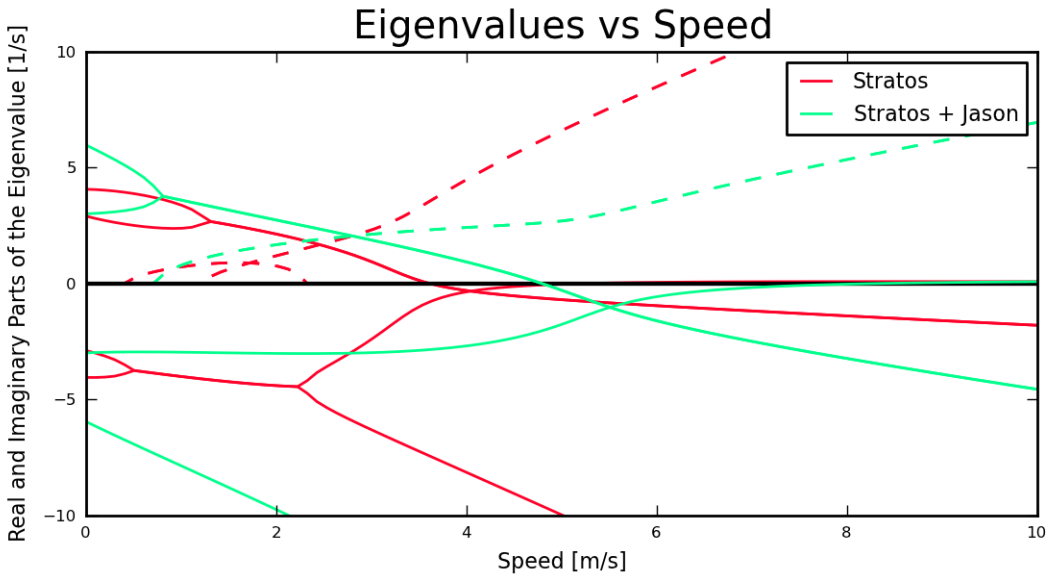

Figure 6.10: Real and imaginary parts of the eigenvalues with respect to speed for the Stratos bicycle with and without a rider. Generated by `src/parameterstudy/bicycle_eig_compare.py`.

6.3.4 Yellow bicycle

I measured the parameters of the "Yellow" bicycle at TU Delft, which was a replica of the Yellow bike from Cornell that demonstrates stability so well. I measured the bicycle in two configurations, one with the fork in the normal position and the second with the fork flipped 180 degrees about the steer axis which greatly increases trail. *Figure 6.11* plots the eigenvalues with respect to speed for the two yellow bicycle configurations and the Silver bicycle [KSM08] which also has a reversed fork and large trail. As was mentioned in the previous section the weave critical speed increases as the trail increases and this is clearly shown for the yellow bicycle with a reversed fork. But maybe more interestingly, the capsize critical speed increases dramatically with the reversed fork.

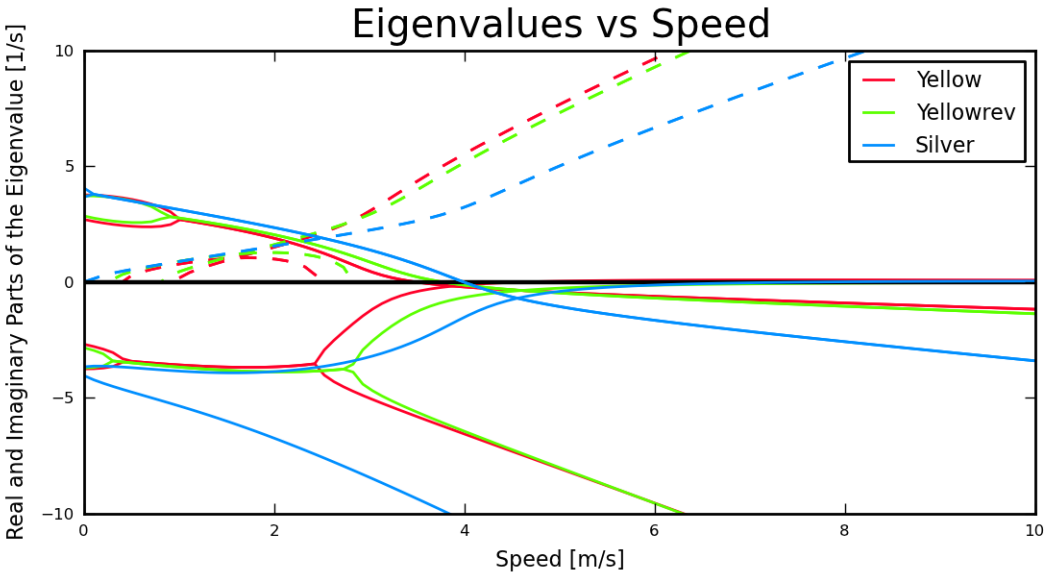

Figure 6.11: Real and imaginary parts of the eigenvalues respect to forward speed for the yellow bicycle in both configurations and the silver bicycle which also has a reversed fork. Generated by `src/parameterstudy/bicycle_eig_compare.py`.

6.3.5 Rear weight

Another fruitful comparison can be gathered from the Batavus Browser as we measured both the instrumented configuration and the factory version. The fundamental difference in the two configurations is that the instrumented version has a large weight atop the rear rack. Bicycle tourists are some of the first to mention the effects on handling due to weight on the front and rear racks of a bicycle, so this comparison examines that to some degree. *Figure 6.12* once again shows how the eigenvalues change with respect to speed for the two bicycles. The second bifurcation points for the second oscillatory mode are affected and the weave critical speed is slightly lower for the factory version. If a rider is added, *Figure 6.13*, shows that the added rear weight makes little difference in the linear dynamics.

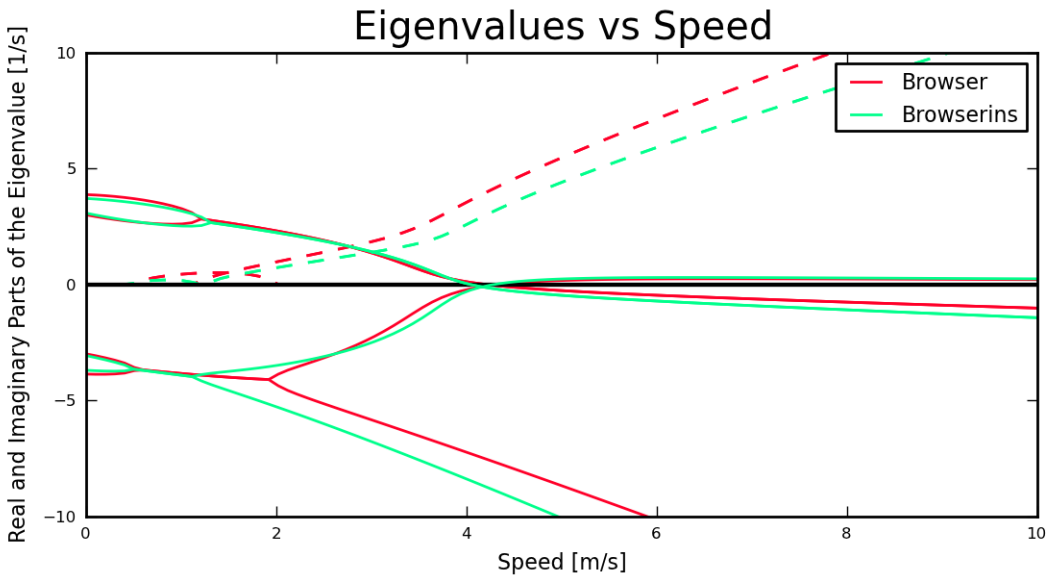

Figure 6.12: Real and imaginary parts of the eigenvalues with respect to forward speed for the factory Browser and the instrumented version which has a large weight on the rear rack. Generated by `src/parameterstudy/bicycle_eig_compare.py`.

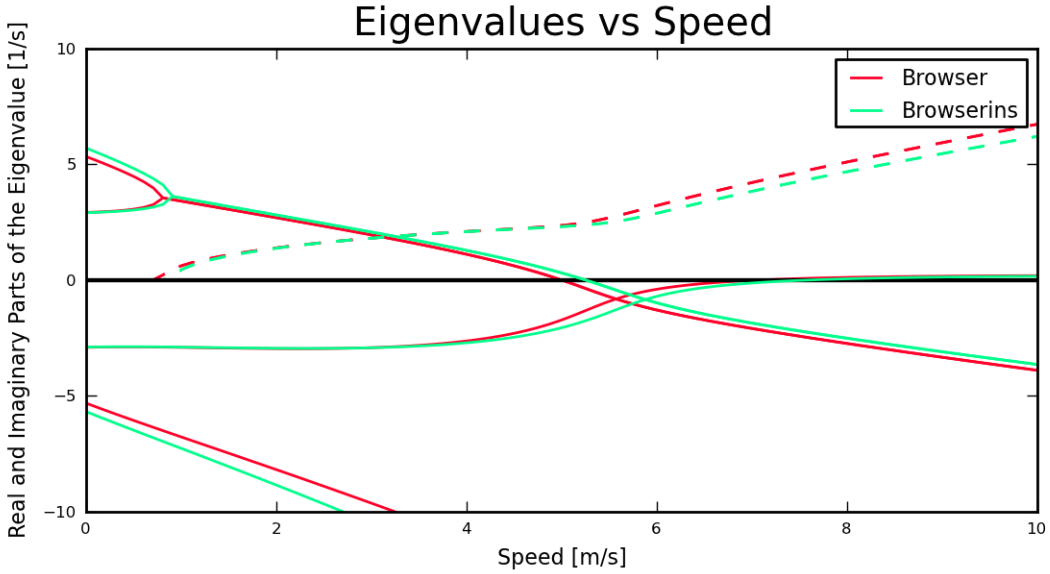

Figure 6.13: Real and imaginary parts of the eigenvalues with respect to forward speed for the factory Browser and the instrumented version which has a large weight on the rear rack and a rider. Generated by `src/parameterstudy/bicycle_eig_compare.py`.

6.4 Uncertainty

I had intended to calculate the uncertainty in the eigenvalue predictions based on the error propagation from the raw measurements, but I never quite figured it out. It would be interesting to draw error bars on the modes in the eigenvalue plots corresponding to the uncertainty values presented in Chapter *Physical Parameters*. It would be revealing with respect to the experiments that are done which try to estimate the eigenvalues of a stable bicycle [KSM08], [KS09], [Ste09], [ER10]. All of the these experiments, except for [KS09], plot a predicted eigenvalue for a speed range because it is difficult to maintain constant speed with an uncontrolled bicycle, but beyond that the uncertainty in the eigenvalue estimates is not reported. These could also be calculated with respect to the fit data. It would be interesting to account for the uncertainties in both methods of predicting the eigenvalues and then compare the model's ability to predict the data. Because the eigenvalues seem to be rather sensitive to changes in some parameters, this may be an important issue to address.

6.5 Frequency Response

The eigenvalues give a complete view of the linear system's open loop dynamics, but one can also examine the system's response to various inputs. The frequency response characterizes how the system responds to a sinusoidal input.

The transfer function from steer torque to the roll rate of a bicycle is particularly interesting because it captures the essential steering action needed to induce a turn. *Figure 6.14* shows the transfer function for Jason seated on the Browser for several different speeds. The speeds correspond to before the first weave bifurcation, unstable weave, stable speed range and unstable capsize. The roll rate amplitudes increase somewhat with speed, with the 6 m/s case showing larger output amplitudes than the more well damped 10 m/s one. The phase shows similarity between the higher two speeds and similarity between the lower two speeds where the phase is roughly the same for all speeds at high frequency. Both the magnitude and phase show differences at lower frequencies and seem to tend to the same response at higher frequencies.

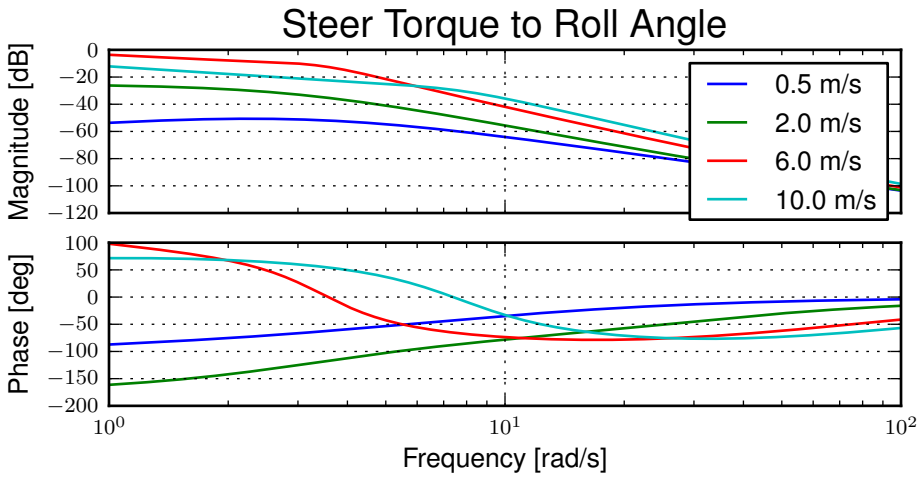

Figure 6.14: The steer torque to roll rate frequency response for various speeds.

Figure 6.15 shows the transfer function for the same rider (same configuration with respect to the rear wheel contact point) seated on a light weight bicycle, the Bianchi Pista, and very heavy bicycle, the Davis instrumented bicycle.

Notice that the light bicycle has an under-damped weave mode which is stable, while the heavy bikes weave mode is well damped and unstable. Once again, differences in the frequency response are less apparent at high frequencies.

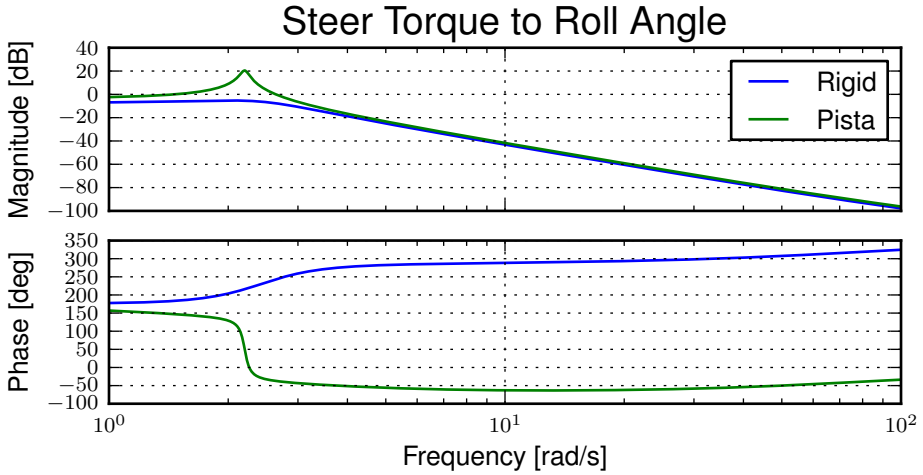

Figure 6.15: The steer torque to roll rate frequency response for a heavy and light bicycle, both with riders, at 5 m/s.

6.6 Conclusions

Parameter studies can allow one to explore the effects of design parameters on the system dynamics of particular bicycles. The eigenvalues provide a way to transform the parameters of a complex system into a minimum characteristic set of parameters that completely characterize the open loop (input ignorant) dynamics. And other characterizations such as the frequency response provide input/output behavior of the system's transfer functions. System stability, time to double/halve, natural frequency, and frequency responses are all important characteristics of the system. There are likely to be correlations from the open loop dynamics to handling, as has been demonstrated in the aircraft control literature, but currently correlations to bicycle handling are mostly speculative and anecdotal at this point.

For a basic diamond frame bicycle, large changes in parameters seem to be needed for large changes in the dynamics. Most bicycle design parameter values are such that the dynamic behavior is quite similar across designs and their differences may not be readily detectable by the human. [TWB10] shows that changes in only a few parameters can make a large difference in the stable speed range of the benchmark bicycle. Even if these changes are detectable by the rider, they are extremely adaptable to minor bicycle design variations in terms of the ability maneuver the bicycle, i.e. it takes little time to become comfortable with a different bicycle. This seems evident even with regards to changes in the front end geometry such as trail; countless debates have ensued over the effect of this parameter. Negative trail recumbents have been designed and the rider can learn to ride them, but they require a higher learning curve, see the Python Lowracer [Mag12] for an example. These bikes are difficult to learn but with practice they often be easily ridden with no hands. With this in mind, the open loop dynamics of most standard diamond frame bicycles don't really vary much, but this surely doesn't include tandems, large two wheel cargo bicycles, recumbent designs, etc. I've also shown that the differences in dynamics between a riderless bicycle one with a rigid rider can be significant. Parameter studies may let us find bicycle designs that don't fit the normal mold but may still have good handling, see [KMP+11] for some examples of exploring the extremes of the parameter space.

I've shown some qualitative comparisons for real and realistic bicycles. It is highly likely that the open loop weave eigenvalue and the critical speed (if there is one) correlate to what a rider feels when riding a bicycle, but this has yet to be proven with strong experimental evidence. Everyone can agree that balance is more difficult when starting up

than at cruising speed. The dynamics show that the system becomes more stable and more controllable (in the control system sense) as the speed increases. The weave eigenvalue and critical speed are currently as good indicators of stability one can get for normal bicycle designs.

CHAPTER

SEVEN

DELFT INSTRUMENTED BICYCLE

7.1 Preface

I had contacted the authors of [MPRS07] in the early winter of 2006 to try to get some tips on where to go with my master's thesis, which I wanted to do on the handling qualities of bicycles. I had previously come across Arend, Jaap, and Jim's conference paper [SMP04] on their benchmark Whipple model and used it to help me build and validate my first model earlier that year. Andy, Jim, and Arend all replied, Jim at great length as usual, and the seeds were sown for some future collaboration. Jim began flooding my inbox with years of thoughts on the handling of bicycles and it turned out that Arend had just applied for a big grant to fund two PhD students for bicycle handling research that was uncannily similar to what I was dreaming up myself. I hadn't decided to do my PhD at UC Davis quite yet and Arend's potential PhD slot was enticing (Jodi was slated for one). But I ended up finishing my masters the following spring and signing on for the PhD at Davis. That summer I started thinking about applying for a Fulbright grant to study somewhere. I contacted Arend again to see if he was interested in having me and he was excited. I told him I was going to do it and then put it off. A week shy of the deadline, I told Arend I didn't have time to do it. He encouraged me to apply anyway and I agreed to push through. I spent the next week putting together the proposal full time and after several drafts I sent it off. I didn't think about it much after that, but luck was on my side and I received the acceptance letter from the Fulbright commission the following spring. I was headed to the Netherlands for my first time living abroad. In the meantime Arend found a way to fund a PhD for Jodi so there was going to be some momentum and a teammate when I arrived.

When I arrived in Delft at the end of August in 2008 Jodi was working on several projects: a bicycle handling qualities review paper [KS11], the two mass skate bicycle [KMP+11], and an instrumented bicycle. I helped to some degree with all the projects, but primarily with setting up the instrumented bicycle and planning a set of experiments. This chapter details the work we did with the first instrumented bicycle. I've taken the text directly from our conference paper [KSM09] and gone through it with some updates, clarifications, and additions. Jodi and Arend were the primary writers of the paper. My contributions were more of the experimental design, performing the experiments, analyzing the data, discussing results and working on a visualization graphical interface that we never really used due to the inability to synchronize the video data we took with the sensor data.

7.2 Abstract

The purpose of this study is to identify human control actions in normal bicycling. The task under study is the stabilization of the mostly unstable lateral motion of the bicycle-rider system. We studied this by visual observation of the rider and measuring the vehicle motions. The observations show that very little upper-body lean occurs in normal riding and that stabilization is done primarily maintained by steering control actions. However, at very low forward speed a second control action was observed: knee movement. Moreover, the frequency of the control actions are all dominated by the pedaling frequency, while the amplitude of the steering motion increases rapidly with decreasing forward speed.

7.3 Introduction

Riding a bicycle is an acquired skill. At very low speeds the bicycle is very unstable and requires great attention by the rider. However, at moderate speed the bicycle is easy to stabilize, often with little conscious thought by the rider. These observations are corroborated by a stability analysis on a simple dynamical model of an uncontrolled bicycle [MPRS07] and some experiments [KSM08] and [KS09]. Although there is little established knowledge on how a person stabilizes a bicycle, two basic features are known: some uncontrolled riderless bicycles can balance themselves given some initial speed, and one can balance a forward moving bicycle by turning the front wheel in the direction of the undesired lean. But we all know that a rider on a bicycle not only moves the handlebars but also may make use of their upper body and other extremities. These rider body motions are even more profound when riding a motorcycle in extreme maneuvers [CL02].

The purpose of this study is to identify the major human control actions in normal bicycling focusing on the stabilization task.[1] We use the term "normal" to describe casual bicycling that requires minimal conscious control. The identification is done by visual observation of the rider and measurement of the motions of the instrumented bicycle, see *Figure 7.1*. In order to observe the human control actions a number of experiments were carried out. First, a typical town ride was performed to investigate what sort of actions take place during casual riding through an urban environment. After this, experiments were carried out in more controlled environment, a large treadmill (3×5 m), at various speeds. The same bicycle was used during all the experiments. The bicycle was ridden by two averagely skilled riders. Three riding cases were considered: normal bicycling, bicycle without pedaling (towing), and normal bicycling with lateral perturbations. These experiments were carried out to identify the upper body motions and the effect of the pedaling motion on the control. The rider was told to simply stabilize the bicycle and to generally ride in the longitudinal direction of the treadmill; no tracking task was set. Recorded data included the rigid body motions of the bicycle rear frame and the front assembly. The rider motion relative to the rear frame was recorded via video.

7.4 Instrumented Bicycle

A standard Dutch bicycle, 2008 Batavus Browser, was chosen for the experiments and is shown in *Figure 7.1*. This is a bicycle of conventional design, fitted with a 3-speed SRAM rear hub and coaster brakes. Some of the peripheral components were removed in order to be able to install measurement equipment and sensors (see *Table 7.1*). The bicycle was equipped with a 1/3" CCD color bullet-camera with 2.9mm (wide angle) lens. The camera was located at the front and directed towards the rider and rotated 90 degrees clockwise to get portrait aspect ratio. The video signal was recorded, via the AV-in port, on DV tape of a Sony Handycam located on the rear rack of the bicycle. The bullet camera was placed horizontally, approximately 65 cm in front of the handlebars and 1.2 m above the ground and held in place by a carbon-fiber boom connected to the down-tube of the rear frame, see *Figure 7.1*. This allowed us to view the rider's motion with respect to the bicycle frame.

Table 7.1: Sensors.

Measurement	Sensor Type	Manufacturer	Type	Specification
Yaw, roll, steer rates	MEMS Angular Rate	Silicon Sensing	CRS03	Full range output $\pm$ 100 deg/s
Steer angle	Potentiometer	Sakae	FPC40A	1 turn, conductive plastic, Servo mount
Forward speed	DC-motor	Maxon	2326-940-12-216-200	Graphite brush motor with a 5cm diameter disk on the shaft
Cadence	Reed relay and magnet			Kitchen magnet

[1] We took data for line tracking tasks also.

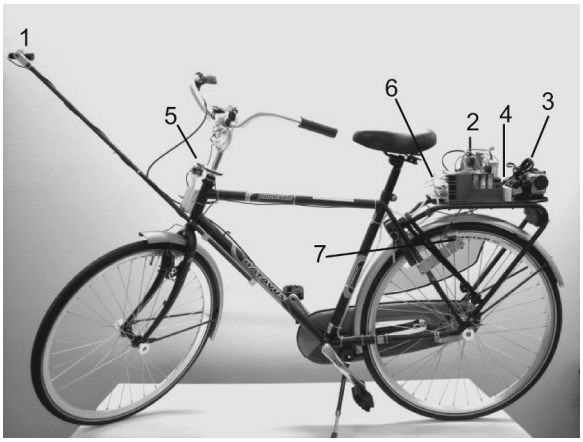

Figure 7.1: The instrumented bicycle with camera boom and video camera lens (1). On the rear rack the measurement computer (2), video camcorder (3) and battery packs (4) are positioned. Measured signals are the steer angle and steer-rate (5), rear frame lean- and yaw-rate (6) and forward speed (7).

We used a National Instruments CompactRIO (type CRIO-9014) computer for data collection. The CompactRIO was installed on the rear rack of the bicycle. It was fitted with a 32-channel, 16 bit analogue input module and a 4-channel, 16 bit analogue output module as well as a CRIO WLAN-MH1000 wireless modem by S.E.A. Datentechnik GmbH for a wireless connection with a "ground station" router, to which a laptop was connected. The measurement system is able to run autonomously once a measurement sequence is initiated. The CompactRIO was powered by a 11.1V, 1500 mAh Lithium Polymer battery which was also placed on the bicycle's rear rack.

The recorded signals were the body fixed roll, yaw, and steer rates, the steer angle, the rear wheel speed, and the pedaling cadence frequency. The angular rates were measured using 3 Silicon Sensing CRS03, single axis angular rate sensors with a rate range of $\pm$ 100 deg/s. The steer angle was measured using a potentiometer placed on the rear frame against the front of the head tube and connected via a belt and pulley pair. The angular rate sensors and the angular potentiometer were powered by a 4.8V, 2100 mAh Nickel Cadmium battery. The forward speed was measured by measuring the output voltage of a Maxon motor that was driven by the rear wheel. The cadence frequency was measured by a reed relay placed on the rear frame, and a magnet placed on the left crank-arm.

7.5 Town Ride Experiment

Our first basic experiment was a short, 15 minute ride around town. This experiment took place under normal riding conditions (dry weather, day-light, etc.), on roads familiar to the rider. The course covered included a round-a-bout, dedicated cycling paths, speed-bumps, pavement, normal tarmac roads, tight bends in a residential area and the rider had to stop at a number of traffic lights. There were no special precautions taken and the experiment was carried out amongst other traffic. From the recorded video and sensor data two main observations were made:

1. The video data showed that there was very little upper body lean relative to the rear frame during the entire ride. The small relative upper body lean that was noted appeared to simply be a result of pedaling. Only in the last few seconds prior to a sharp corner was an upper body lean angle observed, indicating that the lean was carried out because of a sudden heading change.

2. The recorded data, part of which is shown in *Figure 7.2*, clearly shows that only very small steering actions ($\pm$ 3 deg) are carried out during most of the experiment. Only when the forward speed has dropped, prior to making a corner, are large steer angles ($\pm$ 15 deg) seen.

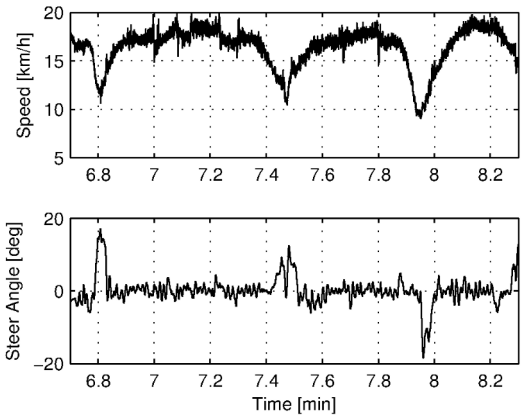

Figure 7.2: Data collected during a ride around town. The upper graph shows the speed the bicycle was traveling at; the lower the steering angle.

7.6 Treadmill Experiments

Riding a bicycle on the open road amongst normal traffic subjects the bicycle-rider system to many external disturbances such as side wind, traffic and road unevenness. To eliminate these disturbances a more controlled environment was selected to carry out further studies on human rider control for stabilization tasks. The experiments were carried out on a large (3×5 m) treadmill, shown in *Figure 7.3*. The dynamics of a riderless bicycle on a treadmill have been shown to be the same as for on flat level ground [KS09] for speeds between 4-6 m/s, so we make this assumption for the case with a rider too, albeit with caution.

Table 7.2: Rider information.

Rider	Weight [kg]	Height [cm]	Age
1	102	187	53
2	72	183	26

The experiments were carried out by two male, average ability riders of different age and build on the same bicycle. The saddle height was adjusted for each rider to ensure proper seating. The rider characteristics are given in *Table 7.2*. For both riders very similar results were found. The data and figures presented in this chapter were collected with rider 1.

Figure 7.3: Large treadmill, 3x5 m, max speed 35 km/h, courtesy of the Faculty of Human Movement Sciences, Vrije Universiteit, Amsterdam.

The uncontrolled dynamics of the bicycle rider system can potentially be described by the linearized model of the bicycle [MPRS07]. This model consists of four rigid bodies: the rear frame with rigid rider connected, the front

handlebar and fork assembly, and the two wheels. These are connected by ideal hinges and the wheels have idealized pure-rolling contact with level ground. [MKHS09] describes the method used to determine the model parameters for the instrumented bicycle-rider system[2]. These parameters are given in *Table 7.3* and the root locus of the system with respect to speed is depicted in *Figure 7.4*. At low speed, the dominant mode is the unstable oscillatory weave mode. This weave motion becomes stable around 18 km/h, the weave critical speed. At higher speeds, the non-oscillatory capsize motion becomes unstable but since its time to double so long it is considered to be very easy to control. With those assumptions, we assert that the instrumented bicycle rider system is in need of human stabilizing control below 18 km/h and is stable otherwise.

Table 7.3: Physical parameters of the Browser bicycle with rider one on board.

parameter	symbol	value for bicycle & rider
wheel base	w	1.12 m
trail	c	0.055 m
steer axis tilt ($\pi/2$ − head angle)	λ	0.375 rad
gravity	g	9.81 N kg $^{-1}$
rear wheel radius	r_{R}	0.342 m
rear wheel mass	m_{R}	3.12 kg
rear wheel mass moments of inertia	$(I_{\mathrm{R}xx}, I_{\mathrm{R}yy})$	(0.078, 0.156) kg m^2
rear body and frame mass position center of mass	$(x_{\mathrm{B}},\ z_{\mathrm{B}})$	(0.30, -1.08) m
rear body and frame mass	m_{B}	116 kg
rear body and frame mass moments of inertia	$\begin{bmatrix} I_{\mathrm{B}xx} & 0 & I_{\mathrm{B}xz} \\ 0 & I_{\mathrm{B}yy} & 0 \\ I_{\mathrm{B}xz} & 0 & I_{\mathrm{B}zz} \end{bmatrix}$	$\begin{bmatrix} 16.784 & 0 & -3.616 \\ 0 & I_{\mathrm{B}yy} & 0 \\ -3.616 & 0 & 6.035 \end{bmatrix}$ kg m^2
front handlebar and fork assembly position centrer of mass	$(x_{\mathrm{H}},\ z_{\mathrm{H}})$	(0.88, -0.78) m
front handlebar and fork assembly mass	m_{H}	4.35 kg
front handlebar and fork assembly mass moments of inertia	$\begin{bmatrix} I_{\mathrm{H}xx} & 0 & I_{\mathrm{H}xz} \\ 0 & I_{\mathrm{H}yy} & 0 \\ I_{\mathrm{H}xz} & 0 & I_{\mathrm{H}zz} \end{bmatrix}$	$\begin{bmatrix} 0.345 & 0 & -0.044 \\ 0 & I_{\mathrm{H}yy} & 0 \\ -0.044 & 0 & 0.065 \end{bmatrix}$ kg m^2
Front wheel radius	r_{F}	0.342 m
Front wheel mass	m_{F}	2.02 kg
Front wheel mass moments of inertia	$(I_{\mathrm{F}xx}, I_{\mathrm{F}yy})$	(0.081, 0.162) kg m^2

For safety reasons the riders were fitted with a harness that was connected to the ceiling via a long climbing rope. This ensured that should the rider fall over no contact with the moving part of the treadmill would be made. Also a retractable dog leash was connected between the front of the harness and the treadmill kill switch. This ensured that the treadmill would immediately come to a halt, should the bicycle go too far back, reducing the chance that the bicycle could go off the end of the treadmill.

Herein, three types of riding experiments are examined: normal bicycling, bicycle without pedaling (towing) and normal bicycling with lateral perturbations. The normal bicycling experiment was carried out to investigate what type of control actions a rider carries out to simply stabilize a bicycle. The towing experiment was carried out to remove the effects of the dominant pedaling motion, seen during the town-ride experiment, from the system. The bicycling with lateral perturbations was performed to investigate how the human rider recovers from a lateral impulsive force applied to the rear frame.

[2] The instrumented bicyle was measured less accurately at this time than what is presented in Chapter *Physical Parameters*, so the parameters are slightly different.

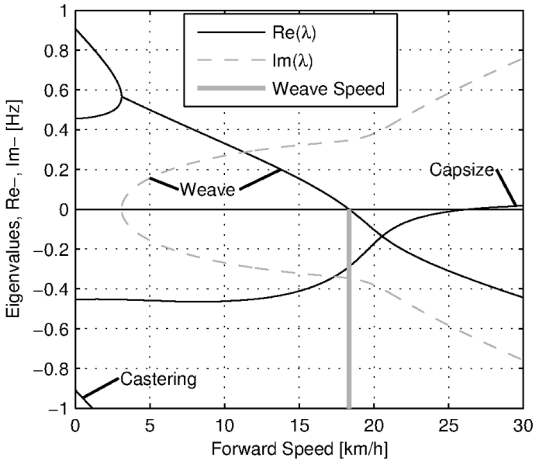

Figure 7.4: Eigenvalues for the linearized stability analysis of an uncontrolled bicycle-rider combination for the steady upright motion in the forward speed range of 0-30 km/h. Solid lines are real parts, dotted lines are imaginary parts. The bicycle is essentially stable from the weave speed, 18 km/h and above.

Each of the three experiments was carried out at 6 different speeds: 30, 25, 20, 15, 10 and 5 km/h. In total 36 experiments were performed. During the normal bicycling and bicycling with lateral perturbations experiments the rider pedalled normally and used first gear during the 5 and 10 km/h runs. Second gear was used in the 15 and 20 km/h runs and third gear was used during the 25 and 30 km/h runs. The cadence varied between 24 rpm at 5 km/h and 80 rpm at 30 km/h. During the towing series of experiments, the bicycle and rider were towed by a rope connected to the bicycle rear frame at the lower end of the head tube. The rider kept the pedals in the horizontal position during these experiments. The crank arm side that was placed forward was left to rider preference. During the lateral perturbations experiment the bicycle was perturbed by applying a lateral impulse to the rear frame. The impulse was applied by manually yanking a rope tied to the seat tube. The rider could not see the rope being actuated to ensure that the rider was unprepared, however, they knew the direction of the perturbation which was always a pull from the right.

The riders were instructed to stay on the treadmill and to generally ride in the longitudinal direction of the treadmill but not to concentrate on their exact position on the treadmill. We wanted the rider to focus on stabilization and maintaining heading and not to track lateral deviation. Sensor data was collected for 1 minute during each experiment at a 100Hz sample rate and the video data was collected simultaneously.

7.7 Normal Bicycling

Visual inspection of the video footage showed very little rider lean action during the experiment other than what resulted directly from the pedaling motion. During the low speed runs at 5 km/h, the rider's upper body was almost stationary, i.e. it could be considered to be rigidly attached to the rear frame. However at this speed the rider's knees showed significant lateral motion. This lateral knee motion can be seen in the video image in Figure *Figure 7.5*. A third observation was that the rider actuated the handlebars with higher amplitudes at lower speeds than at higher speeds.

This third observation is confirmed by the measured steer angle data. Figures *7.6* and *7.7* show the time history of the steer angle for the experiments carried out at 20 and 5 km/h, respectively. The standard deviation of the steer angle during the sixty seconds of measurement is also shown in the figures. At speeds above 20 km/h the average steer angle remains approximately constant. However the average magnitude of the steer angle grows by more than 500% when the speed is decreased from 20 km/h to 5 km/h. This increase in steer angle magnitude for the decreasing speeds is illustrated in Figure *Figure 7.8*. This jump in steering amplitude could be indicative of a threshold at which the system becomes harder to control, but there is no apparent connection to the open loop dynamics. For example, the change

Figure 7.5: Video still of normal pedaling at low speed (5 km/h) showing large lateral (left) knee motion and (right) steering action. The grey vertical line indicates the mid-plane of the bicycle. Note that there is little upper body lean.

in both the weave mode time to double and natural frequency is approximately the same between 5 and 10 km/h as between 10 and 15 km/h.

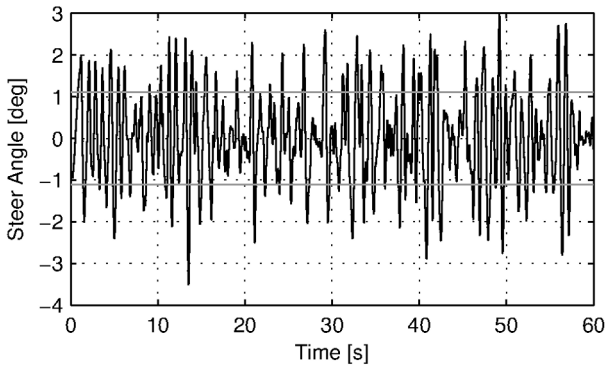

Figure 7.6: Steer angle time history plot for 20 km/h during normal bicycling. The standard deviation of the steer angle is shown in grey.

The frequency content of the steering signal for the different forward speeds is shown in *Figure 7.9*. The grey vertical dashed line indicates the rigid rider-bicycle weave frequency. We were not able to ascertain any connection between the dominate measured frequencies and the natural frequency of the weave mode. We had hypothesized that for speeds in the stable speed range, the optimal control frequency of the rider would correspond to the weave frequency, due to the fact that an uncontrolled bicycle-rider system recovers from perturbations at its natural frequency. The black vertical dashed line in each of the plots in Figure *Figure 7.9* indicates the measured pedaling frequency. The figure shows that during normal pedaling most of steering action takes place at, or around, the pedaling frequency, irrespective of the speed that the bicycle is moving. The pedaling frequency is especially dominant in the steering signal at the highest speeds where practically all of the steering takes place at the pedaling frequency.

Figure 7.10 plots the maximum steering amplitude versus speed. This maximum amplitude reduces with increasing speed and is similar in shape to the standard deviation plot in *Figure 7.8*.

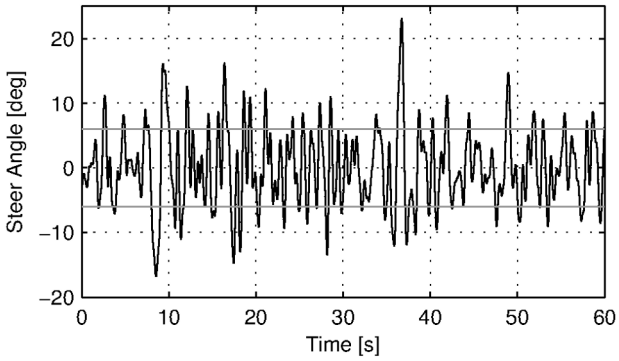

Figure 7.7: Steer angle time history plot for 5 km/h during normal bicycling. The standard deviation of the steer angle is shown in grey.

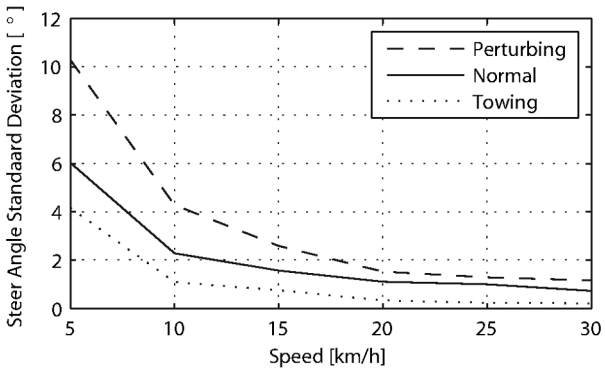

Figure 7.8: The standard deviation of the steer angle for the six different speeds for the three different experiments.

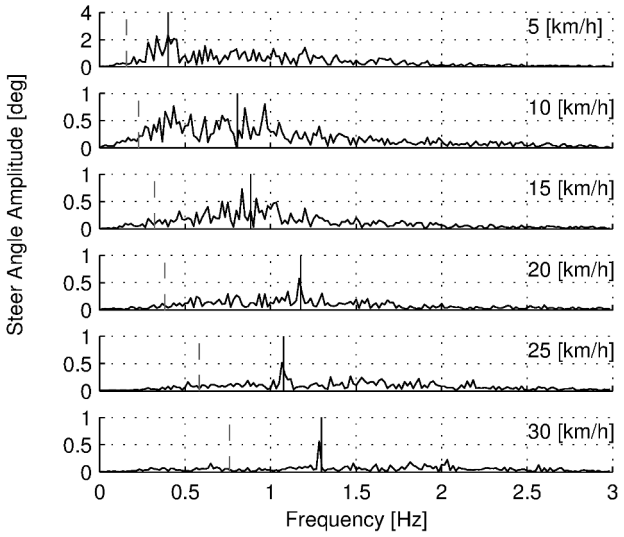

Figure 7.9: Steer angle amplitude plot for the six different speeds for normal pedaling experiment. Solid vertical line indicates the pedaling frequency. Dashed vertical grey line indicates the bicycle & rigid rider weave eigenfrequency.

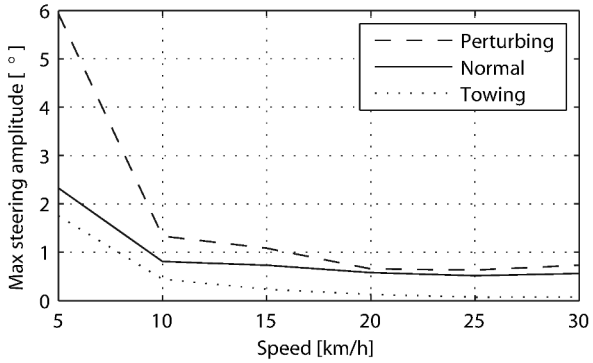

Figure 7.10: Maximum steering amplitude if the steering signal consisted of a single frequency for the three different experiments at the six different speeds.

7.8 Towing; no pedaling

Visual inspection of the video footage revealed, similar to the normal bicycling experiment, that little to no upper body leaning occurred at any of the measured speeds and that larger steer angles occurred at the slower speeds. However, unlike the normal bicycling experiment, no knee motion was noticed from visual inspection of the video footage at any of the speeds, other than small remnant motion as a result of slight steering deviations from straight ahead. The recorded steer angle data also confirmed that larger steer angles were made at decreasing speeds. *Figure 7.8* shows how the standard deviation of the steer angle reduces rapidly with increasing speed up to 20 km/h and from then on remains approximately constant. The figure also shows that the average steering amplitude at all speeds is lower than that for the pedaling case. The standard deviation is less than a degree for all speeds above 10km/h indicating that little to no steer action is required at higher speeds.

The steer angle frequency spectrum for each of the speeds is shown in *Figure 7.11*. It was once again expected that the rigid rider/bicycle weave frequency would be a dominant frequency in the frequency spectrum, especially with no pedaling. However there appears to be no connection with the open loop weave frequency even in the unstable speed range. In fact the frequency spectrum shows a wide range of frequencies of similar amplitude at all the speeds and none of the speeds seem to show any noticeable dominant frequencies.

7.9 Perturbing; pedaling

The video footage showed that, as a result of the lateral perturbation, the bicycle was pulled laterally away from under the rider causing the bicycle to lean over and in turn cause a short transient lean motion of the rider's upper body. The upper body appears to only lag behind the lower body and bicycle during this destabilizing part of the perturbation maneuver. During the subsequent recovery of the bicycle to the upright, straight ahead position, no body lean could be noted other than that as a result of the normal pedaling.

A second phenomenon observable in the video footage, as shown in *Figure 7.12*, is that at all speeds we observed a lateral knee motion during the short transient recovery process of the bicycle to the upright position. The lateral knee motion was very large during the 5 km/h measurement and much smaller at the higher speeds, but even at 30 km/h it is visible.

From the video footage we also concluded that the angle that the handlebars are turned during and after a perturbation decreased with increasing speed as can also be seen in the measured steer angle data as shown in *Figure 7.8*.

Figure 7.13 shows the frequency spectrum of the measured steer angle. Once again, for the higher speeds, the steer control action is carried out at the pedaling frequency. At the lower speeds (5 - 10 km/h) a wider frequency range is again present but the pedaling frequency is dominant. *Figure 7.10* shows the steering amplitude for the frequency with

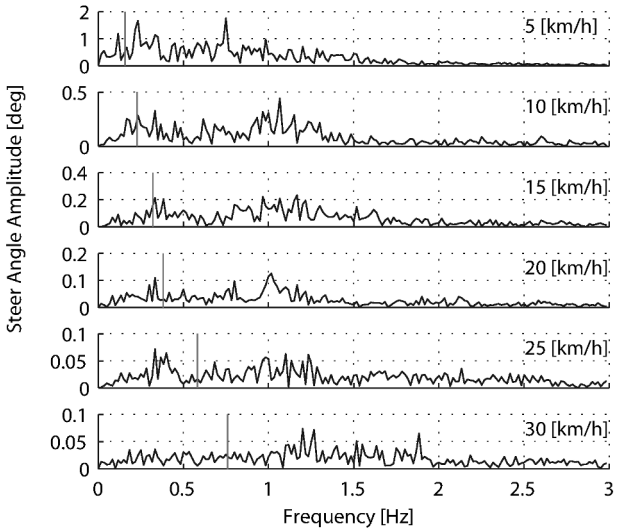

Figure 7.11: Steer angle amplitude plot for the six different speeds for the towing experiment. Vertical line indicates the bicycle & rigid rider eigenfrequency.

Figure 7.12: Video still directly after a perturbation (lateral force applied from the rider's right by a rope at the saddle tube) at 5 km/h. Vertical grey line indicates the bicycle mid-plane. Note the lateral right knee motion and steering action and the small upper body lean.

the maximum amplitude. Again the values for the highest speeds are similar to those of the standard deviation of the steer angle.

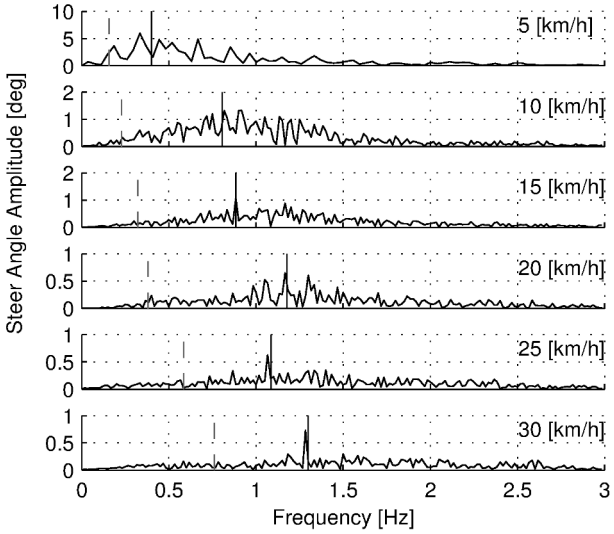

Figure 7.13: Steer angle amplitude plot for the six different speeds for perturbation experiment. Solid vertical line indicates the pedaling frequency. Dashed vertical grey line indicates the bicycle & rigid rider eigenfrequency.

Once again, the frequency spectrum shows no significant steering motion taking place at the rigid rider-bicycle weave natural frequency for any of the speeds.

7.10 Conclusion

The observations show that human stabilization control of the lateral motions of a bicycle during normal bicycling show little use of upper body lean, and that the primary control actions done through steering control. Only at very low forward speed is a potential second control action observed: knee movement. Moreover, this lateral knee motion seems to only occur while pedaling. The steering actions are dominated by the pedaling frequency while the amplitude of the steering motion increases rapidly with decreasing forward speed.

7.11 Appendix

The following sections details some extra information that was not conveyed in the papers [KS08], [KS09] and the modified version in the previous sections.

7.11.1 Experiments

As usual with the data deluge, we analyzed very little of the data. We recorded a total of 109 one-minute runs with two different riders. The previous sections detail only some analysis on runs from a single rider and did not include results from all of the experiments. As a result, the statistical significance of the presented analysis is somewhat weak. The following list details all of the experiments we performed:

- Normal pedaling at five speeds in which we started at the low speed, sped up to the highest and then sped down to the lowest giving twelve runs for each rider. (runs 1-6, 8-19, 101-106, 108-113)

- Normal pedaling starting at 5 km/h and decreasing speed until the rider could no longer balance with both riders. (runs 20, 21, 107, 114)
- Without pedaling (towed) at five speeds in which we either started at the low speed, sped up to the highest and then sped down to the lowest or did the opposite with both riders. (runs 22-27, 29-34, 115-120, 122-123, 126-131)
- Without pedaling starting at 5 km/h and decreasing speed until the rider could no longer balance with both riders. (runs 28, 121, 124, 125)
- Riderless weave stability test in which we increased the speed from 12 km/h to 25 km/h to try to detect the weave critical speed of the bicycle. We didn't have much luck getting the bicycle to stabilize at all.
- Lateral perturbation at six speeds for each rider. (runs 132-133)
- No hand balancing with pedaling for one rider. (runs 60-71)
- Lane changes for both riders at six speeds. (runs 160-165, 80-85)
- A single attempt at riding with eyes closed at 30 km/h[3]
- Line tracking at six speeds for one rider. (runs 90-96)

There is potentially considerable amount of findings and better statistical conclusions that can be made from the data.

7.11.2 Rate Gyros

We mounted three rate sensors to the bicycle to collectively measure the yaw rate, u_3, roll rate, u_4, and the steer rate, u_7. [4] We attached a rate gyro to the fork and handlebar assembly which measured the body fixed angular rate, u_{7s}, about the steer axis, $\hat{e}_3$. Another rate gyro was attached to the rear frame which measured the body-fixed angular rate, u_{3s}, about the axis approximately aligned with gravity, $s_\lambda \hat{c}_1 + c_\lambda \hat{c}_3$. Finally, a third rate gyro was mounted to measure the body fixed angular rate about a rearward pointing axis, $-c_\lambda \hat{c}_1 - s_\lambda \hat{c}_3$.[5] The desired rates are found from the measurments with

$$
\begin{aligned}
u_3 &= u_{3s} \\
u_4 &= -u_{4s} \\
u_7 &= u_{7s} + u_{4s}\sin(\lambda) - u_{3s}\cos(\lambda)
\end{aligned}
\tag{7.1}
$$

We did not analyze any of the data from the rate sensors on the bicycle, but some fruitful conclusions could be drawn such as confirming the dependence of yaw rate on the steer and roll rates which come from the nonholonomic constraints. Heading and wheel contact points can be estimated well for these tasks, as the rider always tends to "zero" heading and the drift from the sensor signal integration is quite linear, see Chapter *Davis Instrumented Bicycle* for details. A fairly complete kinematic state of the bicycle can be estimated, ignoring frame pitch.

7.11.3 Steer sensor design

The steer sensor, a simple rotary potentiometer, was mounted with a design that is fairly universal for different bicycle designs, *Figure 7.14*. It offers axial adjust ability and belt tension. The pulley diameters were chosen for +/- 45 degrees of steering angle corresponding to about +/- 168 degrees of potentiometer angle. I originally designed it with a cord type belt, but it was later switched to a timing belt due to our worry about it slipping. I'm not 100% that belt slip did not occur and this could affect the data we collected. Integrating the steer rate from the rate gyros or differentiating the potentiometer steer angle and comparing the results to the other sensor is a way to check. I examined one run and did not find belt slip.

[3] The closed eye attempt would have been successful if the treadmill had been infinitely wide, but the run was cut short due to the inevitable

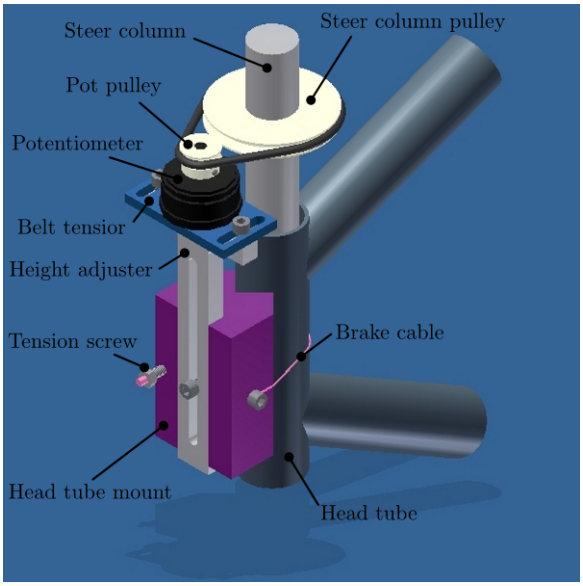

Figure 7.14: The original steer angle potentiometer and universal mount.

7.11.4 Data Visualization

Our original goal was to be able to visualize the motion by watching the video in slow motion or frame-by-frame along side a strip chart of the measured data. This requires some way to synchronize the video data with the sensor data. The Sony DCR-TV30E Handycam we used had a LANC output port that potentially provided an external signal that could be sampled by the data acquisition unit but we never quite figured it out. In the meantime though, I designed a graphical user interface in Matlab to interact with the data, *Figure 7.15*, giving the strip chart capabilities and video playback via the videoIO (http://sourceforge.net/projects/videoio/) package developed by Gerald Dalley. All would have worked out well, if we could have synchronized the video and sensor data, but we abandoned it and moved on to other things. I've made the source code and data available for download in case it is of use to anyone.

- Source code: https://github.com/moorepants/DelftBicycleDataViewer
- Data: http://mae.ucdavis.edu/~biosport/DelftBicycleDataViewerAndData.zip

7.11.5 Rider 2

Table 7.4 presents the parameters computed with the methods in [MKHS09] for the second rider, Jason, on the instrumented Batavus Browser. Only the rear frame and body parameters are different as the bicycle is identical. We only presented data in the previous analysis from runs in which Arend rode the bicycle.

lack of heading feedback the rider has available, causing the rider to drift to the edge of the treadmill.

[4] The ratiometric sensor voltages were actually measured, but converted to angular rates in real time by applying the conversion factors provided by the manufacturer's specification sheets. Thus, the angular rates are reported in the data sets.

[5] See Chapter *Bicycle Equations Of Motion* for the axes definitions.

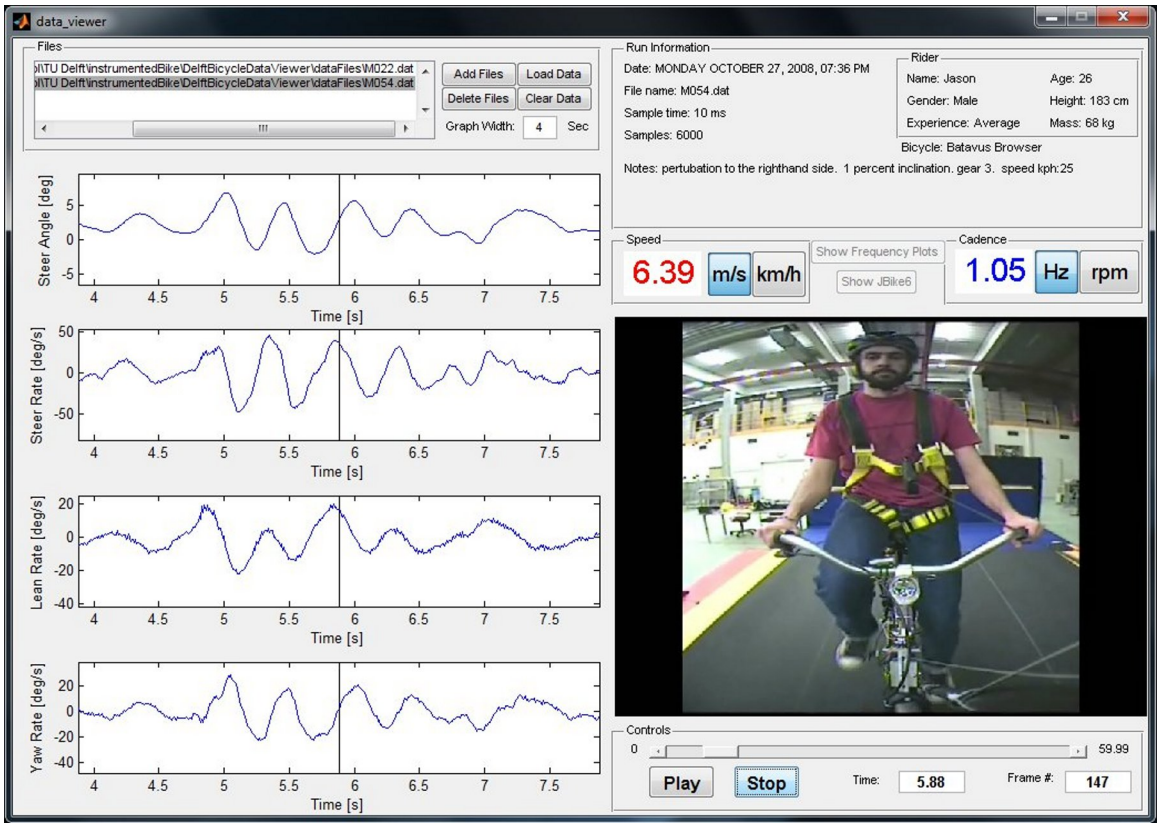

Figure 7.15: A screenshot of the GUI running on Windows 7. The strip chart advances along with the video. The user can scroll through the video and pause at select frames. The meta data for the run is displayed in the top right. The bicycle speed and the pedaling cadence are displayed as numerical values.

Table 7.4: Parameters of the second rider, Jason.

parameter	**symbol**	**value for bicycle & rider**
rear body and frame mass position center of mass	$(x_{\mathrm{B}},\ z_{\mathrm{B}})$	(0.28, -1.03) m
rear body and frame mass	m_{B}	86 kg
rear body and frame mass moments of inertia	$\begin{bmatrix} I_{\mathrm{B}xx} & 0 & I_{\mathrm{B}xz} \\ 0 & I_{\mathrm{B}yy} & 0 \\ I_{\mathrm{B}xz} & 0 & I_{\mathrm{B}zz} \end{bmatrix}$	$\begin{bmatrix} 11.89 & 0 & -2.13 \\ 0 & I_{\mathrm{B}yy} & 0 \\ -2.13 & 0 & 3.73 \end{bmatrix}$ kg m^2

CHAPTER

EIGHT

MOTION CAPTURE

8.1 Preface

Sometime during the winter of 2008, Arend proposed our next project while I was at Delft. I had told him that I wanted to have a project to call my own while I was there, that could be written up as a major portion of my dissertation and he proposed doing a motion study using principal components techniques in much the same fashion as [Tro02] had done with walking subjects. I think he'd formulated the idea in discussion with Andy Ruina, his longtime vacation buddy and colleague. I'd never heard of principal components (my statistics were and are still weak), so I started reading up on principal components and what Troje had done with walkers. I got a grasp of the technique and formulated a plan based on a bicyclist riding on the large treadmill we had access to and capturing their kinematics with a motion capture system. We went up for a preliminary test day to check out the motion capture system and meet Richard Casius who was the lab technician that knew the equipment. I was expecting he'd just show us the on/off button and make sure we didn't break anything, but he actually was there to run the system, help us figure it all out, and even do some post processing of the data. This was odd for me, as my experience in the U.S. was always that I had to do *everything* myself. Jodi was the rider for the preliminary tests. It went well and we felt confident that we'd get the kind of data we wanted. So we came back and started planning for three days of testing with three riders. Jodi and I were going to ride and my fixie friend, Victor, agreed to ride for us one day too. We had three successful days of testing. Jodi and I then began analyzing the data with him coding a visualization GUI that we'd devised and me processing the data using the PCA methods. Once we could *see* the data, we went through every run manually and coded each run for specific observations.

I got frustrated at this point, because we'd finally got to the results part and it seemed to me that Jodi and Arend were getting to do the majority of the analysis. I felt as if I'd put all my 100% effort into the work up to that point and because I had this notion of ownership of the final product it seemed as if my colleagues were getting to do the grand finale, whereas I wanted to be in control. We made it through it though, despite my discontent. Arend and Jodi didn't really understand my frustrations and deemed it a cultural difference. I didn't buy that then, but now reflecting I tend to agree. My upbringing and school training left me with little experience with *true* teamwork and I've had my eye on the PhD dissertation as some kind of embodiment of my personal understanding of *everything* that has to do with the subject I've been studying. I had never really seen it as a collection of many people's effort, the result being my orchestration of the collective ideas. These kinds of realizations reflect on what the heart the Fulbright grant is. I went into the grant thinking more about accomplishing the research goals that I proposed to do, but after the fact I realize that cultural understanding and personal interactions allowed me to grow as a person and realize the world in a more global sense than any of the research accomplishments did. That kind of foresight from the founders of grants like the Fulbright are invaluable to humanity as a whole. I wish every high school student or college student in the U.S. were required to study abroad. I think the political climate we see in the world would be positively affected in a great way.

Another tactic I that was new to me was sending in an abstract for a conference that really only talked about what we hoped to do, with the idea that it gives us a deadline to get something done. This worked in this case, but I can't say that it has been successful for me since. We first presented the results of this study at the ECCOMAS Multibody Dynamics conference in June of 2009 and I think it went pretty well [MKS09].

After the conference, the paper was selected to be published in the Multibody System Dynamics journal. I turned it down because Arend was more interested in publishing in the Journal of Biomechanics. In the meantime, I had been learning a lot about the open science movement and knew that our University currently had an agreement with Springer that the open access fee would be waived for all articles published by UCD affiliates and Multibody System Dynamics is a Springer journal. So I decided that would be the better choice, as journal titles seem like they are more and more irrelevant for my generation. We search for articles on the internet and read them regardless of where they are published, and the filtering of content quality is becoming an entirely different mechanism than it was for science in previous generations. I see the journal as a soon-to-be-lost relic. And hopefully, the closed peer review system may be consumed by collective quality control by the readers and appointed reviewers.

The work in this Chapter comes from two sources, the first is the peer reviewed Multibody System Dynamics article, [MKSH11], which I've copied verbatim albeit with some fixed errata. The second is an addendum to the results which was presented at the ISEA 2010 conference in Austria [MHP+10]. It is a lead in to looking at the data with some other statistical tools which I've had a growing interest in, but less than adequate understanding.

8.2 Experiment Design

We performed a wide range of maneuvers with three different riders at several speeds. The aim of this section is to provide a detailed description of the experiments and the accompanying data.

The experiments were performed in a controlled environment while the motion of the bicycle and rider were measured with an active motion capture system [Inc09]. The rider rode on a 3×5 meter treadmill, (*Figure 8.1*) capable of belt speeds up to 35 km/h. Three male riders [Victor, Jason, Jodi] of similar age [23, 26, 31 years] and build [height (1.84, 1.83, 1.76 m) and mass (74, 72, 72 kg)] participated as subjects. Each rode two different Dutch bicycles. Each rider performed all runs in one day in the same order (no randomization) and was instructed to bicycle comfortably at a constant speed in the range of 2 to 30 km/h for the duration of the run. There were at least 2 repetitions of each speed with each bicycle. A run was sampled at a frequency of 100 Hz for 60 seconds.

8.2.1 Equipment

All of the experiments were performed on a 3x5 m treadmilll at the the Vrije Universiteit over a three day period. The treadmill had a 1% incline to counter the rolling resistance. We used two bicycle donated by Batavus: the Browser and the Stratos Deluxe.

8.2.2 Manuevers

Normal For the "normal" bicycling task we instructed the riders to focus their sight into the distance and simply stabilize the bicycle and keep the heading generally pointing in the direction of the treadmill band velocity. Thus they were required to keep the bicycle roll angle and heading angle at zero. The rider pedaled during the experiment and was told to ride as if you were traveling down a straight empty road.

Towed The towed experiments were the same as the normal except that a rope was attached to the head tube of the bicycle and attached to the front railing of the treadmill. This allowed the rider to not have to pedal. The rider kept the cranks horizontal and was left to choose which foot he wanted forward. The rope could potentially have applied lateral forces to the frame if the rider drifted too much laterally, but we also held the rope taught and moved left and right to lessen the effect.

Line tracking The line tracking maneuver was the same at the normal maneuver except that the rider was instructed to keep his front wheel on a line we drew on the treadmill. This caused the rider to focus on not only stabilization but lateral deviation control.

No-hand We did some experiments with no hands riding (i.e. no steering control). The riders placed their hands on their hips and attempted to stabilize roll and yaw. Most of the these runs were with pedaling, but a few were taken with towing.

8.2.3 Data

The primary data was the three dimensional locations of the 31 markers for each run. We sampled at 100 hz, giving (31 markers)(3 coordinates)(100 hz)(60 seconds) = 558,000 data points per each one minute run. We collected data for 268 one minute runs and 3 shorter static measurements of the bicycles for a total of 271. The data for the first rider ended up somewhat corrupted. There are a lot of erratic value changes in the data. The basic motion is there though and clever filtering could clean the data for use.

We also collected data on the preliminary day with one rider and slightly different marker locations and we collected some data during a TV show filming of our work. We did not follow as strict protocols to the filmed experiments.

8.2.4 Source Code

The original data was processed with a series of Matlab scripts and then the resulting processed data files were viewed with a Matlab program.

The source code can be found at http://github.com/moorepants/MotionCapture.

8.3 Principal Component Analysis

8.3.1 Abstract

Recent observations of a bicyclist riding through town and on a treadmill show that the rider uses the upper body very little when performing normal maneuvers and that the bicyclist may, in fact, primarily use steering input for control. The observations also revealed that other motions such as lateral movement of the knees were used in low speed stabilization. In order to validate the hypothesis that there is little upper body motion during casual cycling, an in-depth motion capture analysis was performed on the bicycle and rider system.

We used motion capture technology to record the motion of three similar young adult male riders riding two different city bicycles on a treadmill. Each rider rode each bicycle while performing stability trials at speeds ranging from 2 km/h to 30 km/h: stabilizing while pedaling normally, stabilizing without pedaling, line tracking while pedaling, and stabilizing with no-hands. These tasks were chosen with the intent of examining differences in the kinematics at various speeds, the effects of pedaling on the system, upper body control motions and the differences in tracking and stabilization.

Principal component analysis was used to transform the data into a manageable set organized by the variance associated with the principal components. In this paper, these principal components were used to characterize distinct kinematic motions that occur during stabilization with and without pedaling. These motions were grouped on the basis of correlation and conclusions were drawn about which motions are candidates for stabilization-related control actions.

8.3.2 Introduction

Much progress has been made in understanding the rigid body dynamics of an uncontrolled bicycle ([MPRS07], [KSM08]) and various control schemes have been explored for tracking purposes ([PH08b], [SKM08], [Sha08]), but little is understood about how a bicyclist actually stabilizes a bicycle during normal riding. The bicycle and rider system is unique among vehicles in that the rider is from 80 to 90% of the total mass of the system, the system is laterally unstable, and the rider is flexibly coupled to the bicycle in such a way that many body motions can be used

as control inputs. Previous research into realistic bicycle control has focused on both steering and rider lean as control inputs, but there has been no experimental verification of which motions a rider actually uses for control. Recent observations of a bicyclist riding through town and on a treadmill [KSM09] show that the rider moves the upper body very little when performing normal maneuvers and that the bicyclist may, in fact, primarily use steering input for control. This corresponds well with the fact that control by leaning requires high gains compared to the gains required for steering when employing an optimal control strategy on a model ([PH08b], [SKM08], [Sha08]). The observations also revealed that the rider may use other control inputs such as drastic knee movements at low speeds. These conclusions were drawn by visually reviewing video data, so a more rigorous objective method of characterizing the dominant movements of the bicyclist while stabilizing a bicycle was needed. In order to validate the hypothesis that there is little upper body motion during normal cycling, motion capture techniques were used on the bicycle and rider system with the intent to use principal component analysis to identify the major motion patterns.

Principal component analysis has successfully been used with data collected from motion capture techniques to identify the dominant modes of motion of a person walking on a treadmill [Tro02] and to characterize different types of walking. We use similar methods for steady, normal bicycle riding on a treadmill. Cyclic motions, such as pedaling, are easily identified and separated from the other less cyclic control actions. Identifying the patterns of movement gives insight into which body movements are primarily used and are candidates for control inputs. This will be valuable for our overall research goals that include the design of a realistic biomechanical-based control system of a bicycle rider, among other things.

8.3.3 Experiments

To test our hypotheses, three riders performed a set of stability tasks in a controlled environment while the motion of the bicycle and rider were collected with a motion capture system. The tasks were performed on a 3×5 meter treadmill *Figure 8.1* capable of belt speeds up to 35 km/h. The treadmill was chosen because the envelope of space was suitable for the motion capture system and it eliminated any disturbances such as wind, rough ground, and obstacles. We chose three male riders of similar age [31, 23, 26 years], build [height (1.76, 1.84, 1.83 m) and mass (72, 74, 72 kg)]. We also used two different Dutch bicycles: a 2008 Batavus Browser with a 3 speed hub and a 2008 Batavus Stratos Deluxe with a 7 speed hub. The Browser is described by the manufacturer as "stable" and the Stratos Deluxe as "nervous."

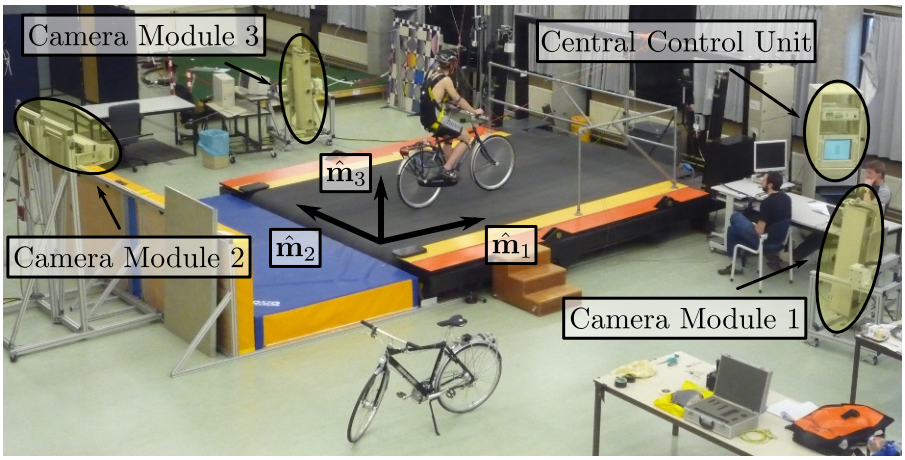

Figure 8.1: The 3×5 m treadmill at the Vrije Universiteit Amsterdam.

We made use of the Optotrak Certus Motion Capture System [Inc09] to record the motion of the bicycle and rider during the stability tasks. The system is based on active infrared emitting markers that are placed on the moving bodies and connected to a central control unit. Each marker emits a sequential infrared signal and the infrared pulses are captured by camera modules each containing three cameras. The accuracy of the three dimensional measurements is ± 0.15 mm [Inc09]. The system has no hardware based noise reduction. Wiring harnesses were built for both the rider and the bicycles to facilitate easy bicycle and rider exchange *Figure 8.2*.

Figure 8.2: Rider 1 and the Batavus Stratos Deluxe with marker positions. Body marker positions visible from the rear.

The marker coordinates were measured with respect to an inertial frame, $\mathbf{M}$, where the plane normal to $\hat{\mathbf{m}}_3$ is coplanar with the treadmill surface and $\hat{\mathbf{m}}_3$ is directed upward. We collected the three dimensional locations of 31 markers, 11 of which were located on the bicycle and 20 that mapped the rider *Figure 8.3*.

The markers were placed on the bicycle so that we could easily extract the rigid body motion (i.e. body orientations and locations) of the bicycle frame and fork. Four markers were attached to the fork and seven markers were attached to the rear frame. A marker was attached on the right and left sides of the center of each wheel, the seat stays, the ends of the handlebars, and the head tube. A single marker was also attached to the back of the seat post.

We recorded the locations of 20 points on the rider *Figure 8.3*: left and right sides of the helmet near the temple, back of the helmet, shoulders (greater tuberosity of the humerus), elbows (lateral epicondyle of the humerus), wrists (pisiform of the carpus), between the shoulder blades on the spine (T6 of the thoracic vertebrae), the tail bone (coccyx), midpoint on the spine between the coccyx and shoulder blades (L1 on the lumbar vertebrae), hips (greater trochanter of the femur), knees (lateral epicondyle of the femur), ankles (lateral malleolus of the fibula) and feet (proximal metatarsal joint). The body markers were not necessarily placed such that a complete rigid body model could easily be fit to the data. This was done to save setup and processing time because we only wanted a stick figure representation of the rider that allowed us to visually observe the dominant motions of the rider.

The stability tasks were designed such that the rider would ride at a constant speed within the range of 2 to 30 km/h. The bicyclists were told to maintain an upright straight-ahead course on the treadmill and to look into the distance, with exception of the line tracking task. The bicyclists were instructed to bicycle comfortably at the designated speed and data recording was started at random. In all cases the subject rode at the set speed until comfortable, then data was taken for 60 seconds at a 100 hertz sampling rate. Each test was performed on each bicycle with each rider. The following list describes the various tests:

Normal pedaling The subject was instructed to simply stabilize the bicycle while pedaling and keep the heading in approximately the forward direction. The speed started at 5 km/h and increased in 5 km/h increments up to 30 km/h. The speeds were then decreased in the same fashion to 5 km/h. From then on the speed was decreased

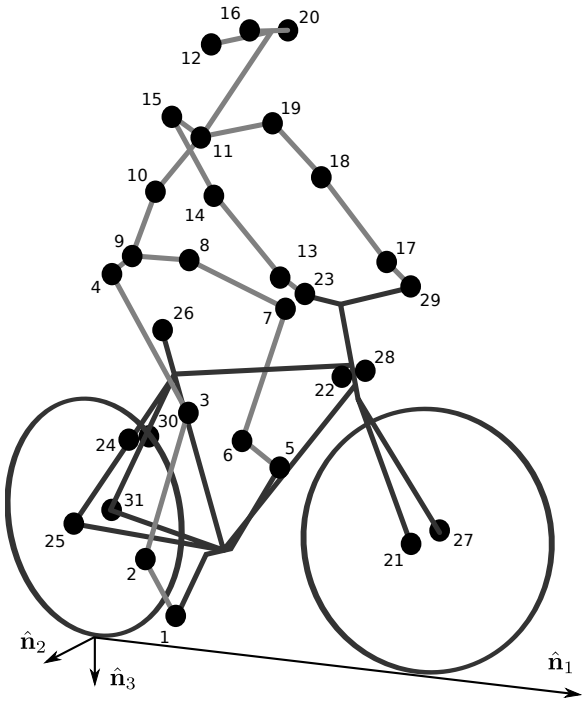

Figure 8.3: Schematic of the marker positions. The rider and bicycle are colored light gray and dark gray, respectively.

in 1 km/h increments until the subject was not able stabilize the bicycle any longer. Therefore, there were two sets of data for each speed and each bicycle except speeds below 5 km/h. Several additional runs were also performed with the rider pedaling using a different gear and thus a different cadence.

Without pedaling This was the same as the normal pedaling task except that a string was attached to the head tube of the bicycle such that the bicycle was fixed longitudinally relative to the treadmill and no pedaling was required. The rider kept the feet in the same position throughout the task.

No-hands The riders stabilized the bicycle without using steering for control. They were instructed to keep their hands on their hips while bicycling. The rider started at 30 km/h and decreased in 5 km/h increments through 20 km/h and thereafter the speeds were decreased in 1 or 2 km/h increments until the rider was not able to comfortably stabilize the bicycle.

Line tracking This was the same as normal pedaling except that the rider was instructed to track a line on the treadmill surface with the front wheel. A smaller subset of speeds was performed.

These tasks were designed with the intent to answer several questions:

1. What upper body motions are used while bicycling?
2. How does the system motion change with respect to changes in forward speed?
3. How does pedaling influence the control actions?
4. Can the open loop rigid body dynamics be detected in the controlled state?
5. What does the rider do differently to control the bicycle when riding no-hands?
6. Do different bicyclists perform similar motions while performing the same task?
7. Is there a difference in motion when stabilizing and trying to track a line?

Since there is no room to address all of these questions in this chapter, we focus on a single rider on the Browser bicycle and two of the tasks: normal pedaling and without pedaling. We were able to draw some conclusions on questions 1 through 4 with this smaller data set.

8.3.4 Open loop rigid body dynamics

One question we have is whether or not the eigenfrequencies of the weave motion for the uncontrolled system can be detected in the results from the stabilization tasks. In order to predict the uncontrolled (open loop) eigenvalues of the rigid rider system, the basic geometry, mass, center of gravity locations, and moments of inertia of the bicycle were measured. Also, the riders were measured and weighed such that the body segment geometry, mass, center of gravity locations, and moments of inertia could be estimated. The physical parameter estimation methods are described in [MKHS09]. This data was used to calculate eigenvalues and eigenvectors of the uncontrolled open loop system *Figure 8.4*.

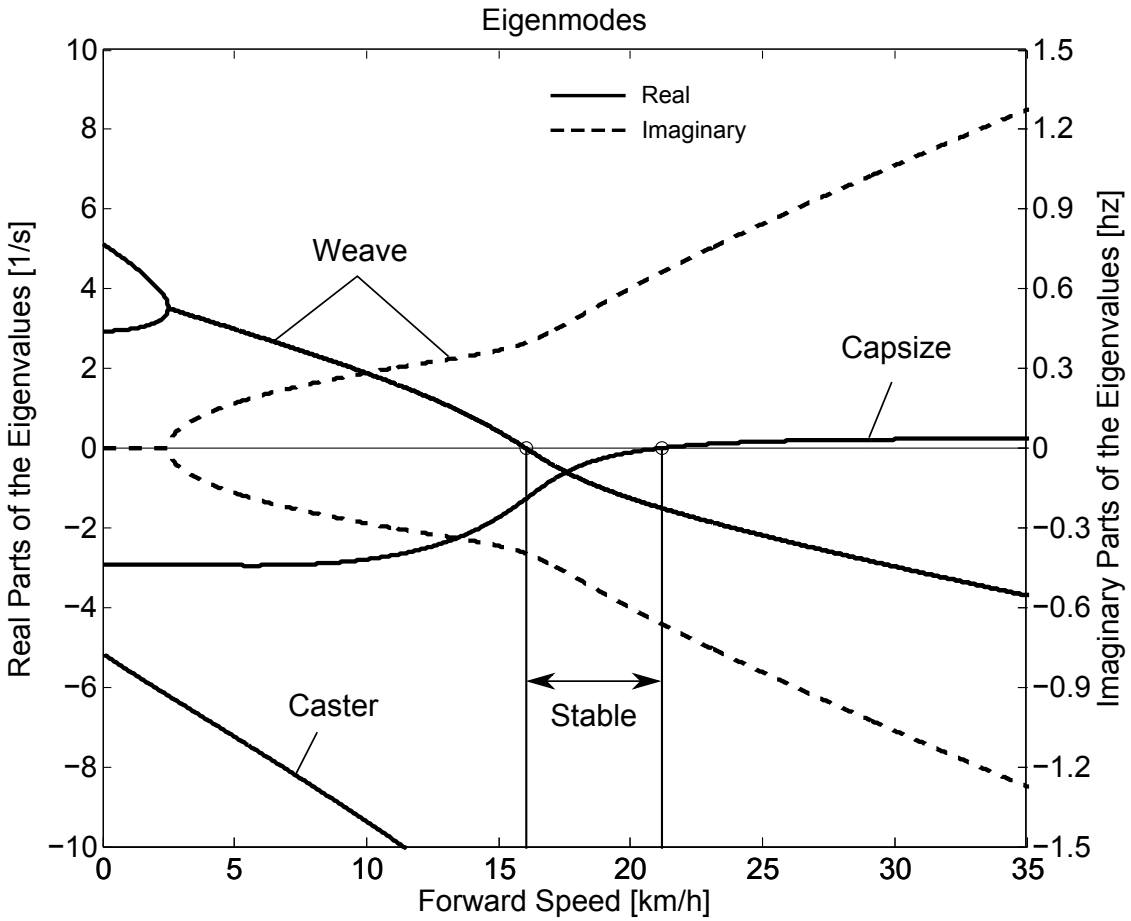

Figure 8.4: Eigenvalues of the Browser bicycle with the third rider rigidly attached as a function of speed. Note that the initially unstable weave motion becomes stable above 16 km/h, the weave speed.

8.3.5 Data processing

Missing markers

The Optotrak Certus Motion Capture System [Inc09] is based on the cameras' ability to detect the infrared light from the sensors so there are occasional gaps in the coordinate data due to the markers going out of view. We attempted to minimize this by careful marker and camera placement but were not able to totally eliminate the error. Any missing markers on the bicycle were reconstructed using the assumption that the bicycle is a rigid body. We had more than three markers on both the frame and fork, so if one marker location was not detected we used the relative location

of the remaining markers to reconstruct the missing marker. The gaps in the data of the markers on the human were repaired by fitting a cubic spline through the data. The spline estimated the marker coordinates during the gaps. We only used the splined data if the gaps were less than 10 time steps, or 0.1 sec; otherwise the trials were discarded.

Relative motion

We were interested in the analysis of three different marker combinations: the bicycle alone, the rider alone, and the bicycle and rider together. The motion of the bicycle and the bicycle-rider were calculated with reference to the $\mathbf{N}$ inertial frame[1] {The $\mathbf{N}$ frame is used instead of the $\mathbf{M}$ frame to be consistent with the vehicle coordinate standards used in [MPRS07] . See Section *Inertial frames and configuration variables* for the derivation.} and the motion of the rider was calculated with respect to the rear frame of the bicycle $\mathbf{B}$ *Figure 8.5*. These three marker combinations allowed us to differentiate more easily between rider specific and bicycle specific motions. Furthermore, six of the variables that describe the configuration of the bicycle in time were calculated to give insight into the rigid body dynamics. The configuration variables q_1 and q_2 locate the contact point of the rear wheel of the bicycle. The $\mathbf{B}$ frame captures the yaw (q_3) and roll (q_4) motions of the bicycle frame, the $\mathbf{D}$ frame is an intermediate frame that differs from $\mathbf{B}$ only by the bike's steer axis tilt (λ), and the $\mathbf{E}$ frame captures the steering angle (q_7) of the bicycle fork relative to the bicycle frame. The pitch of the bicycle frame (q_6) is assumed to be zero. Details of these calculations are shown in Section *Inertial frames and configuration variables*.

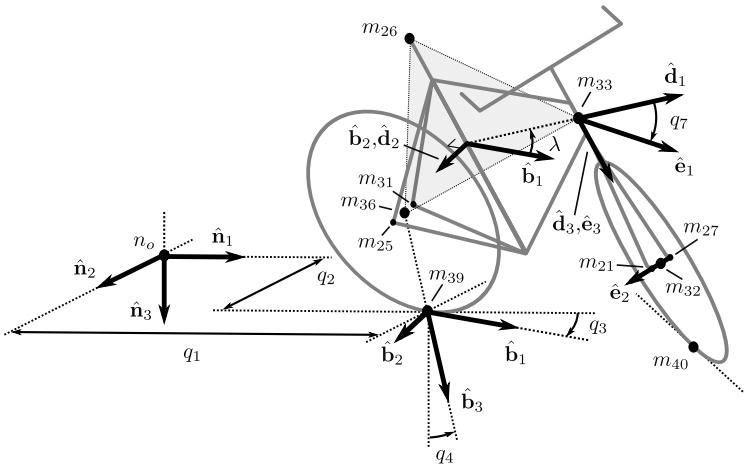

Figure 8.5: Diagram of the bicycle's inertial frame $\mathbf{N}$, rear frame $\mathbf{B}$, front frame $\mathbf{E}$ and configuration variables.

Principal Component Analysis

We used Principal Component Analysis, PCA, [Jol02] to extract and characterize the dominant motions of the system. Calculating the principal components effectively transforms the space of the data to a space that maximizes the variance of the data. The typical advantage of PCA is that the dimension of the system can be reduced while still retaining enough information to adequately describe the system. We are primarily interested in the way that PCA is able to extract linear components and rank them in order of variance from the mean position. If we assume that the components with the largest kinematic variance are motions that are the dominant motions used for control and propulsion (which in general is not necessarily true for dynamical systems) the comparison of these components for different riding conditions can give insight into what motions may be important for developing a biomechanical control model of the bicyclist.

The repaired data from the motion capture measurements contained the x, y, and z coordinates of each marker 1 through l at each time step $j = 1, 2, \ldots, n$. Each marker has three coordinates so there are a total of $m = 3l$

coordinates $i = 1, 2, \ldots, m$. The coordinates at each time step can be collected in vector $\mathbf{p}_j$.

$$\mathbf{p}_j^T = [x_{1j} \quad \ldots \quad x_{lj} \quad y_{1j} \quad \ldots \quad y_{lj} \quad z_{1j} \quad \ldots \quad z_{lj}] = [p_{1j} \quad p_{2j} \quad \ldots \quad p_{mj}]$$

We can organize these coordinate vectors into a matrix, $\mathbf{P}$, where the rows, i, map a single coordinate of a marker through n time steps.

$$\mathbf{P} = \begin{bmatrix} | & | & & | & & | \\ \mathbf{p}_1 & \mathbf{p}_2 & \ldots & \mathbf{p}_j & \ldots & \mathbf{p}_n \\ | & | & & | & & | \end{bmatrix}$$

The principal components were calculated for the three marker combinations as described earlier where $n = 60 \cdot 100 = 6000$ time steps. The number of rows of $\mathbf{P}$ were ($m = 3 \cdot 31 = 93$), ($m = 3 \cdot 11 = 33$) and ($m = 3 \cdot 20 = 60$) for the bicycle-rider, the bicycle alone and the rider alone, respectively.

One method of determining the principal components is to calculate the eigenvectors of the covariance matrix of the mean-subtracted data. We begin by calculating the mean $\mathbf{u}$ Equation (8.1) of the rows of $\mathbf{P}$ and subtracting it from each column of $\mathbf{P}$ to form the mean-subtracted data matrix $\bar{\mathbf{P}}$, Equation (8.3).

$$\mathbf{u} = \frac{1}{n} \sum_{j=1}^{n} \mathbf{p}_j \tag{8.1}$$

A vector of ones

$$\mathbf{h}^T = [h_1 \quad h_2 \quad \ldots \quad h_j \quad \ldots \quad h_n] \text{ where } h_j = 1 \text{ for all } j \tag{8.2}$$

allows us to subtract $\mathbf{u}$ from each column of $\mathbf{P}$,

$$\bar{\mathbf{P}} = \mathbf{P} - \mathbf{u}\mathbf{h}^T \tag{8.3}$$

The covariance matrix $\mathbf{C}$ of $\bar{\mathbf{P}}$ can then be calculated with Equation (8.4).

$$\mathbf{C} = \frac{1}{n-1} \bar{\mathbf{P}} \bar{\mathbf{P}}^T \tag{8.4}$$

Calculating the eigenvectors $\mathbf{v}_i$ and eigenvalues λ_i of the covariance matrix effectively transforms the space to one in which the variances are maximized and the covariances are zero. The eigenvectors are the principal components of the data set and the corresponding eigenvalues represent the variance of each principal component. The eigenvectors are ordered by decreasing eigenvalue where $\mathbf{v}_1$ is the eigenvector corresponding to the largest eigenvalue. The eigenvalues and eigenvectors are calculated by finding the independent solutions to Equation (8.5).

$$\mathbf{C}\mathbf{v}_i = \lambda_i \mathbf{v}_i \tag{8.5}$$

Each time step can now be represented as a linear combination of the principal components.

$$\mathbf{p}_j = \mathbf{u} + a_{1j}\mathbf{v}_1 + a_{2j}\mathbf{v}_2 + \ldots + a_{mj}\mathbf{v}_m \tag{8.6}$$

The coefficients a_{ij} can be solved for each time step j by reformulating Equation (8.6) and solving the system of linear equations.

$$\mathbf{P} - \mathbf{u}\mathbf{h}^T = \begin{bmatrix} | & | & & | \\ \mathbf{v}_1 & \mathbf{v}_2 & \ldots & \mathbf{v}_m \\ | & | & & | \end{bmatrix} \begin{bmatrix} a_{11} & \ldots & a_{1n} \\ \vdots & \ddots & \vdots \\ a_{m1} & \ldots & a_{mn} \end{bmatrix} = \mathbf{V}\mathbf{A} \tag{8.7}$$

$$\mathbf{A} = \mathbf{V}^{-1}(\mathbf{P} - \mathbf{u}\mathbf{h}^T)$$

With the principal components $\mathbf{v}_i$ being constant, the behavior in time is described by the coefficients a_{ij} where the discretization in time is indexed by j. The order of the system can be reduced by eliminating principal components that have little variance. We arbitrarily decided to examine the first $k = 10$ principal components knowing that the first

five would be based on the larger motions such as pedaling and that the remaining five may reveal some of the motions associated with control. The variance of each component, $\text{var}(\mathbf{a}_i) = \lambda_i$, is summed to determine the cumulative percentage of variance of the principal components, g_k.

$$g_k = 100 \frac{\sum_{i=1}^{k} \lambda_i}{\sum_{i=1}^{m} \lambda_i} \text{ where } 1 \leq k \leq m \tag{8.8}$$

Highly correlated data will show that even when $k << m$, g_k is close to 100%. Using 10 components g_{10} covers 100% ($\sigma = 2 \cdot 10^{-14}$ %) of the variation in the data for the bicycle, rider and bicycle-rider. The matrix $\mathbf{A}$ can then be reduced to a $k \times n$ matrix and eigenvectors corresponding to eigenvalues greater than λ_k can be eliminated.

Data Visualization

We developed a graphical user interface, "GUI", in Matlab that easily allows different trials to be compared with one another *Figure 8.6*. The program loads two different trials along with information on each trial. A graphical representation of the rider and bicycle are displayed in two adjacent screens and can be viewed from multiple perspectives. The animations of the runs can be played at different speeds, rewound and fast forwarded. The principal components are shown beside the corresponding animation display and combinations can be turned on and off for identification and comparison. Frequency and amplitude information for the temporal coefficients a_{ij} can also be displayed for comparison.

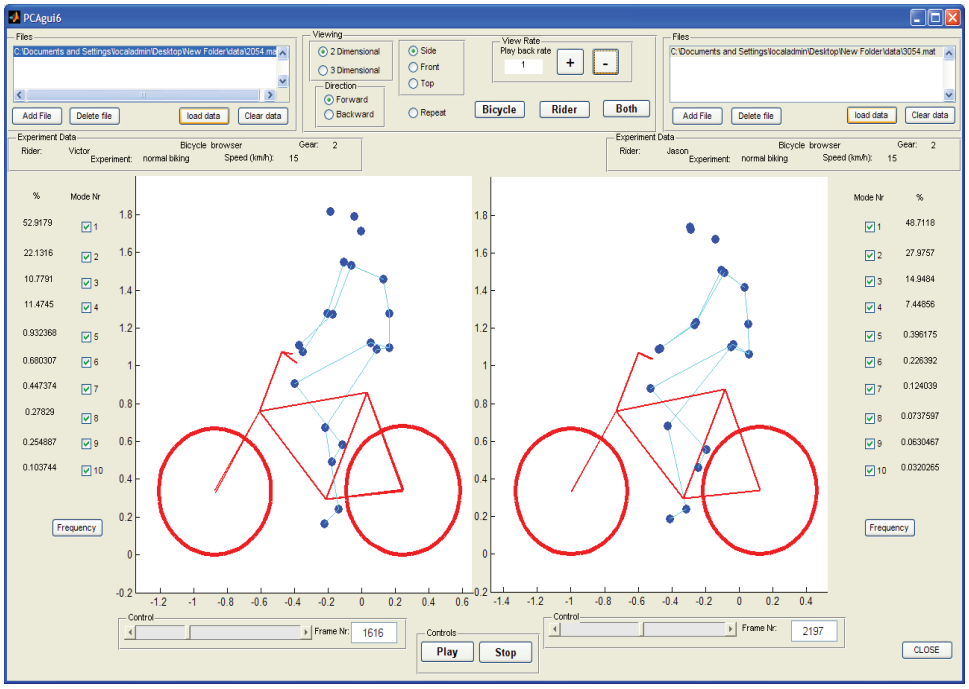

Figure 8.6: Screen shot of the Matlab graphical user interface (GUI) used to visualize principal components and compare between different components and trials.

8.3.6 Results

Motion identification

The reduced set of data provides two important pieces of information for the identification of motion: the principal components $\mathbf{v}_i$ and the corresponding coefficients a_{ij}. The principal components represent linear trajectories of the

markers and the coefficients show how the markers follow the trajectories with time. We began processing the data by reviewing each principal component of each trial in the GUI and noting what type of motion we saw *Table 8.1*. These descriptions were subjective because we grouped marker movement based on our preconceived understanding of rider and bicycle motion. Some of the components displayed motions that were not physically possible such as the upper leg stretching in length during the knee bounce. This is possible when examining a single component but when superimposed over the rest of the components the unrealistic motions are not present. Furthermore, for each component we examined amplitude and frequency content of the associated coefficients a_{ij} as shown in Figures *8.6* and *8.7* and noted the shape of the frequency spectrum and the frequencies at any distinct spikes.

Table 8.1: Example raw trial description for the bicycle and rider during normal pedaling at 10 km/h.

i	% Variance	Motion Description	Frequency Description
1	45.50	primarily longitudinal motion, some lateral	max amp = 0.6 m, most freq below 0.5 Hz, tiny spike at 1.6 Hz
2	29.39	primarily lateral motion, some longitudinal, small feet motion	max amp = 0.35 m, little spike at 0.8 Hz, most freq below 0.5 Hz
3	15.41	vertical pedaling, slight spine bend, hip/head/shoulder sway out of phase with pedaling	max amp = 0.27 m, large dominant spike at 0.8 Hz
4	8.27	horizontal pedaling, head/shoulder sway	large dominant spike at 0.8 Hz with 0.19 m amp
5	0.82	yaw, knees stay still	max amp = 0.04 m at 0.33 Hz, most freq below 1 Hz
6	0.27	erratic left-hand movement	max amp = 0.018 m, most freq below 2 Hz
7	0.21	steer, left-hand movement, slight roll	most freq below 2 Hz, spike at 0.33 Hz and 1.58 Hz
8	0.07	knee and head bounce	dominant spike at 1.58 Hz
9	0.04	lateral knee movement, head jiggle	spikes at 1.58 Hz and 2.37 Hz, most freq below 2.5 Hz
10	0.02	head and knee jiggle	spikes at 1.58 Hz and 3.17 Hz, most freq below 3.5 Hz

Several conclusions can be drawn from examining the coefficient data. First, some of the components are linked by the frequencies of the coefficients and describe an identifiable motion. The most obvious of these is that the vertical and horizontal pedaling components make up the circular pedaling motion. Both vary periodically and have a dominant frequency which is defined by the cadence. In the example trial, *Table 8.1*, the upper body motions are also linked to the pedaling. Components 8 and 9 both correspond to a frequency that is twice the pedaling frequency, which may be due to the forces created during each pedal stroke. Component 6 seems to be the result of a bad marker signal. Components 5 and 7 are interesting because they display motions of the bicycle that are not dominated by the pedaling frequency and may be candidate control motions. The percentage variance of each component gives an idea of the relative amplitude of the components. The descriptions of each trial were used to compile a list of motions that contribute to the principal components. These motions, illustrated in *Figure 8.9*, are:

Drift The bicycle and rider drift longitudinally and laterally on the surface of the treadmill. The motions are typically defined by two components that are not necessarily orthogonal or aligned with the inertial coordinate system. The motion is random and at low frequencies.

Steer Rotation of the front assembly with respect to the rear frame. The steering may appear linked to one of the pedaling components at the pedaling frequency or may be in one or more components sometimes combined with roll and/or yaw at more random frequencies.

Roll The bicycle and the rider roll with respect to the ground plane. Roll is typically linked with steer and/or yaw and often at the pedaling frequency.

Yaw The heading angle of the bicycle and rider change together with respect to the ground plane. This is typically

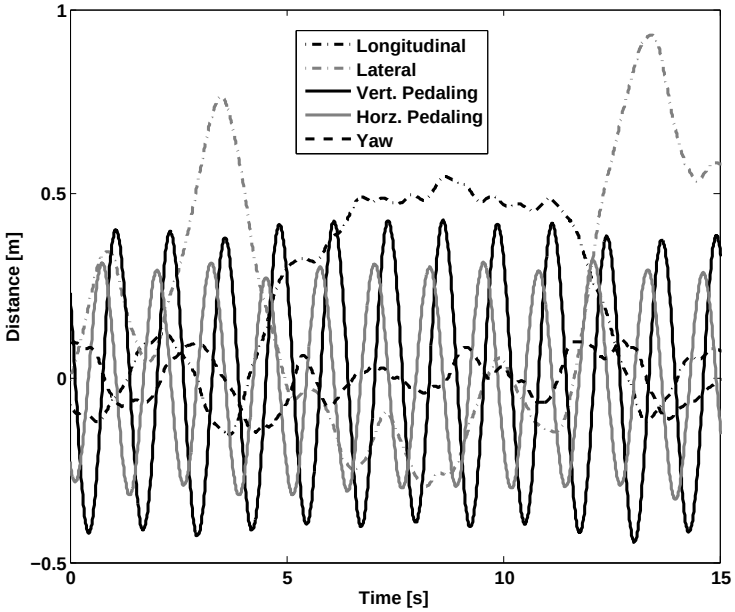

Figure 8.7: Coefficients a_{ij} versus time content of the first five principal components for normal pedaling at 10 km/h.

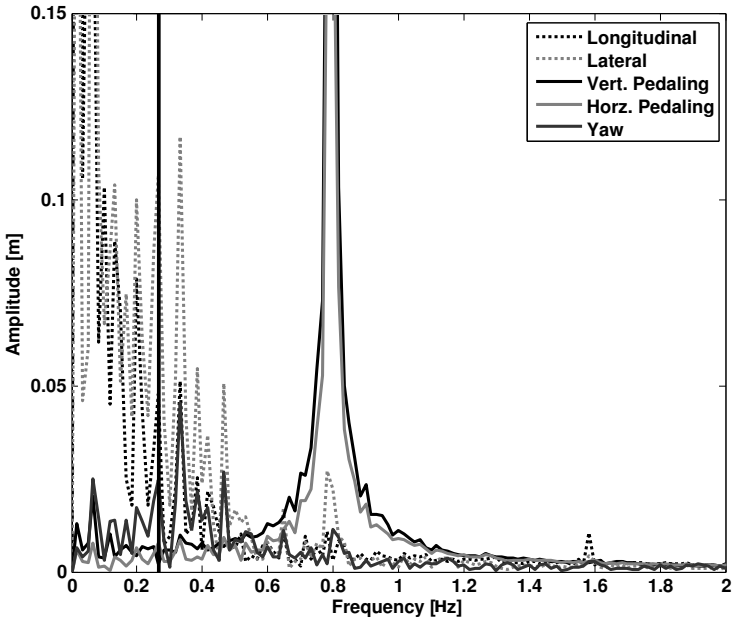

Figure 8.8: The frequency content of the first five principal components for normal pedaling at 10 km/h. The vertical black line represents the open loop weave frequency (0.28 Hz) determined from *Figure 8.4* at this forward speed. The pedaling frequency is about 0.8 Hz at this speed, see *Figure 8.10*.

linked with steer, roll and/or the drift.

Pedaling This motion is defined by two or more components, typically a vertical and horizontal motion of the feet, that show the feet rotating around the crank axle at a distinct frequency and the legs following suit.

Bend The spine bent laterally and was always connected with the vertical pedaling component.

Lean The upper body, shoulders and head lean laterally with respect to the rear frame and was always linked with the horizontal pedaling component.

Twist The shoulders rotate about the torso axis. This was linked to components that contained steering motions, both random and at the pedaling frequency.

Bounce The knee markers bounce up and down, the back straightens and the head nods at twice the pedaling frequency.

Knees The knees move laterally relative to the bicycle frame in both opposing directions and the same direction at random low frequencies.

Head Head twists and random head motions showed up often. These seemed to be due to the rider looking around randomly.

Motion Characterization

To identify how bicycling changes with speed it would be ideal to investigate how the amplitude of each component varies with speed. However, the analysis does not return the same set of components for each run so such a comparison is typically not possible. Therefore components were grouped into classes, where each class shows a specific physically relevant motion. The same total motion of the class can be described by one set of components in one trial and another, probably different, set of components in another trial. How the amplitudes of these classes vary among experiments can be used as a measure for how the rider and bicycle motion varies among trials.

To objectively identify which coefficients show the same type of motion and could therefore form a class, the frequency content of each of the time coefficients in a single trial was correlated to that of each of the other components in that trial. Next a minimum correlation value was set to determine which coefficients were correlated to each other. When the minimum was set at 0.9 only the coefficients making up the pedaling motion could be considered correlated. On the other hand when a minimum level of 0.7 was used practically every coefficient was correlated to each other. The only exception was the coefficient that displayed the bounce. Its maximum correlation with another coefficient was no higher than 0.4 for any of the tested speeds. The 0.8 level gave a number of distinct classes of components and thus this level was used to identify which coefficients were connected. Finally, the correlated coefficients were viewed simultaneously in the GUI enabling the determination of the motion class.

The correlated coefficients were used to form six different classes of motions, Table *Table 8.2*, each made up of combinations of the previously described motions in *Figure 8.9*.

Table 8.2: The six primary motion classes.

Class Name	Class Description
Drift	Drift
Pedaling	Pedaling, Bend, Lean, Twist, Steer-Yaw-Roll, Yaw
Bounce	Bounce
Knees	Knees
Other	Head and components that showed noise of some sort

In most cases, the correlated coefficients described a single class. However, in some cases, this was not the case and the coefficients were used to describe more than one class. An example is that at low speed the components containing the drift motions also contained large steer, yaw, and roll motions. Therefore, the motions were placed in both the Drift and the Steer-Yaw-Roll classes.

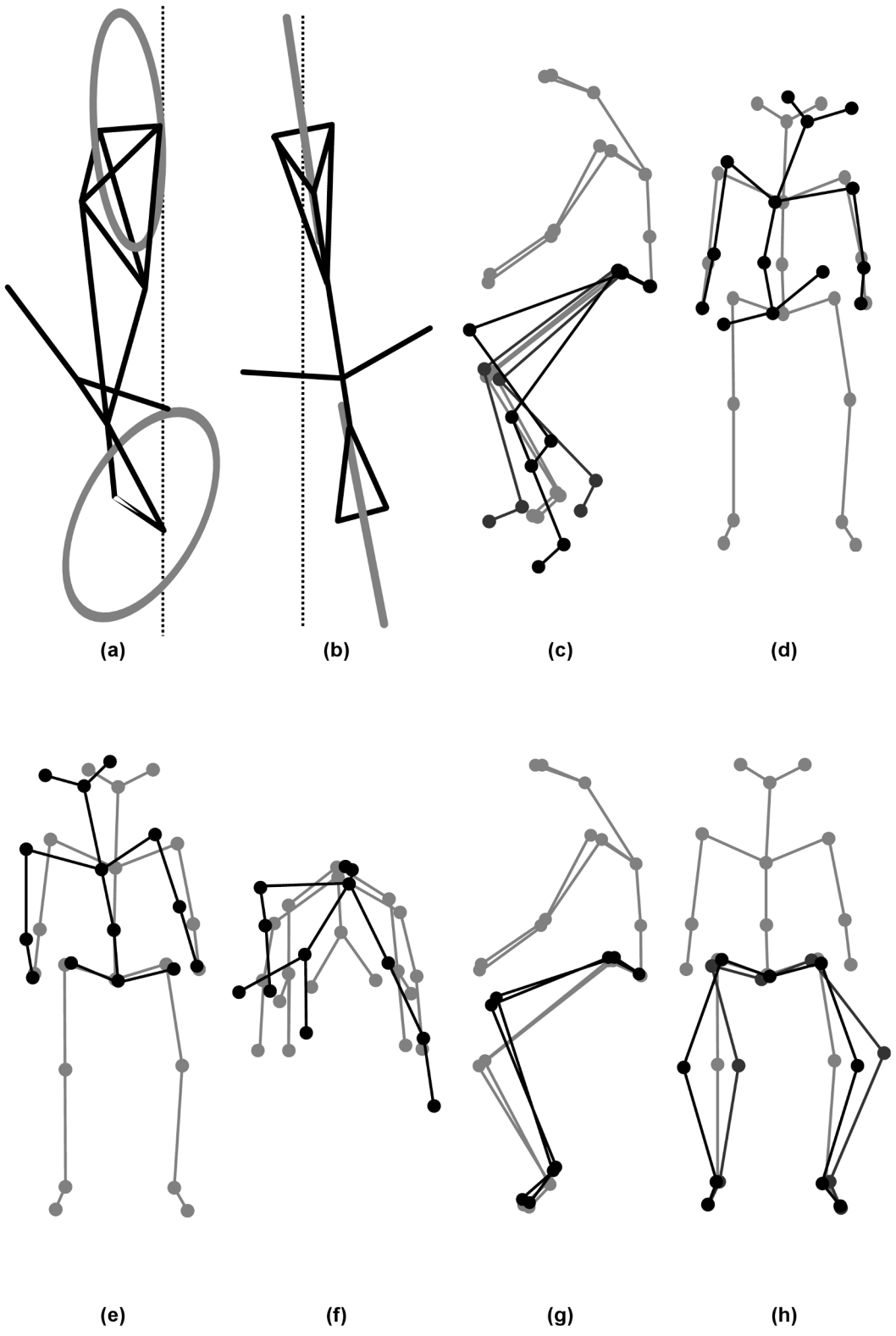

Figure 8.9: Diagrams of the common motions. (a) Top view of bicycle steer and roll, (b) bicycle yaw, (c) horizontal and vertical components of pedaling, (d) spine bend, (e) rider lean, (f) top view of rider twist, (g) knee bounce and (h) two lateral knee motions. All but pedaling (c) are exaggerated for clarity.

Since the rider was not instructed to hold a specific location on the treadmill the Drift class, which was usually the class with the largest amplitude, was not used in further analysis of the motion and neither was the 'Other' class. For each of the remaining classes, the percentages of variance of the remaining components were recalculated without the components placed in the Drift and the Other classes.

We also calculated various configuration variables from the bicycle marker locations (See Section *Inertial frames and configuration variables* independent of the PCA perspective for more specific motion characterizations. This allowed us to investigate the bicycle's configuration variable time histories and frequency content explicitly.

Characterization of motions during normal pedaling

Figure 10.10 shows how the relative percent variance of the four classes: Pedaling, Steer-Yaw-Roll, Bounce and Knees varies with speed for Rider 3 on the Batavus Browser bicycle. The percentage is the average of two runs at speeds 5 km/h and above. From the graph, it is clear that at 10 km/h and higher speeds practically all the motion that is taking place is the pedaling motion class. Below 10 km/h, the Steer-Yaw-Roll class becomes increasingly active and the relative percentage of the motion taking place in the pedaling class drops. Also, at speeds below 10 km/h the lateral knee motion (Knees) class percentage increases with decreasing speed. The increase is not as significant as that of the Steer-Yaw-Roll class (increase to roughly 5% at 2 km/h), but it is certainly visible. The spike at 4 km/h can be attributed to the fact that the classes may contain higher variance motions because the classification method is based on principal components that are not necessarily consistent between runs. The Bounce roughly remains constant at all speeds.

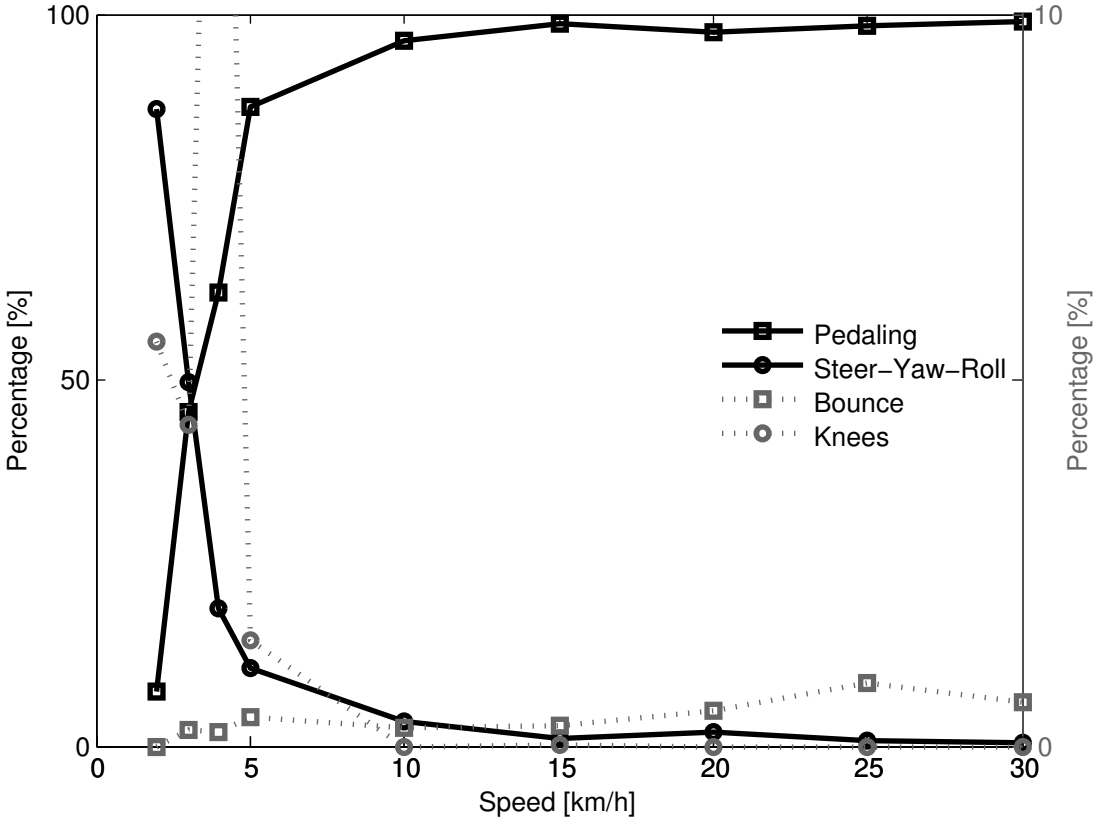

Figure 8.10: The relative percent variance of the four classes: Pedaling, Steer-Yaw-Roll, Bounce and Knees, at the different speeds when the Drift and Other classes were removed from the results for normal pedaling. The solid lines are scaled to 100% (left axis), the dotted lines are scaled to 10% (right axis).

The steer angle amplitude-frequency plot for each of the speeds calculated from the bicycle rigid body motions is

given in *Figure 8.11*. It clearly shows that the steering actions take place at or around the pedaling frequency for high and low speeds, respectively. It also shows that the amplitude of the steering angle increases by 5000% when the speed decreases from 30 km/h to 2 km/h. *Figure 8.11* also shows the open loop, rigid rider, weave eigenfrequency for each speed obtained from *Figure 8.4*. Apparently the open loop eigenfrequency is not a frequency at which the bicycle-rider operates.

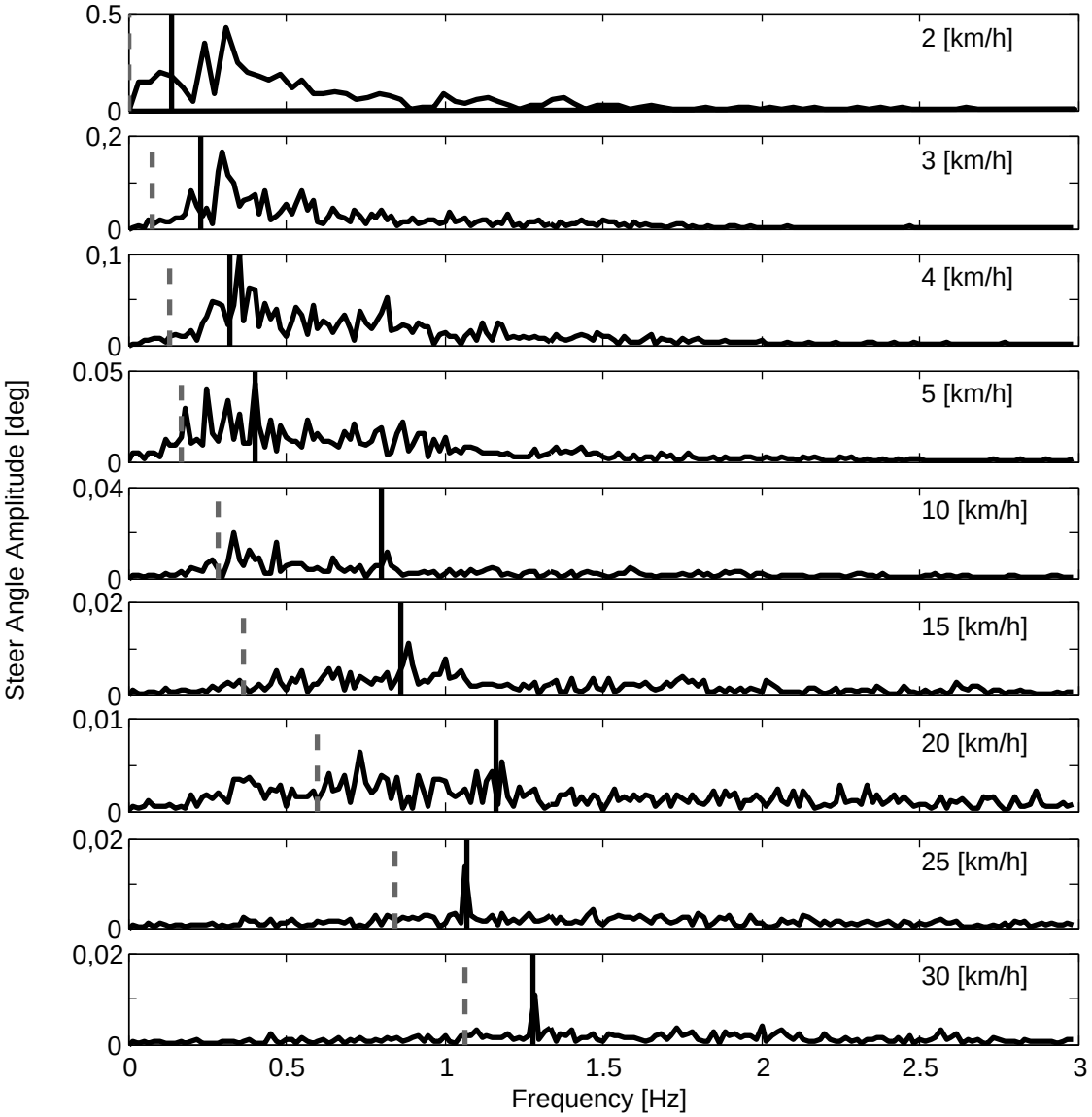

Figure 8.11: Steer angle amplitude plot for the nine different speeds for normal pedaling experiment. Solid vertical line indicates the pedaling frequency. Dashed vertical gray line indicates the bicycle-rigid rider open loop weave eigenfrequency from *Figure 8.4*.

8.3.7 Characterization of motions without pedaling

During normal pedaling, all motions, including the control tasks, are dominated by the pedaling motions. Therefore we also looked at the motions of bicycle-rider system without the influence of pedaling. *Figure 10.12* shows how the percent variance of by Steer-Yaw-Roll, Bounce and Knees varies with speed for Rider 3 on the Batavus Browser

bicycle without pedaling. Since the bicycle is towed and the riders feet remain in the same, constant, position relative to bicycle, there is no pedaling class present in analysis. Furthermore, no bend, lean or twist motions with high variance were detected during the experiments.

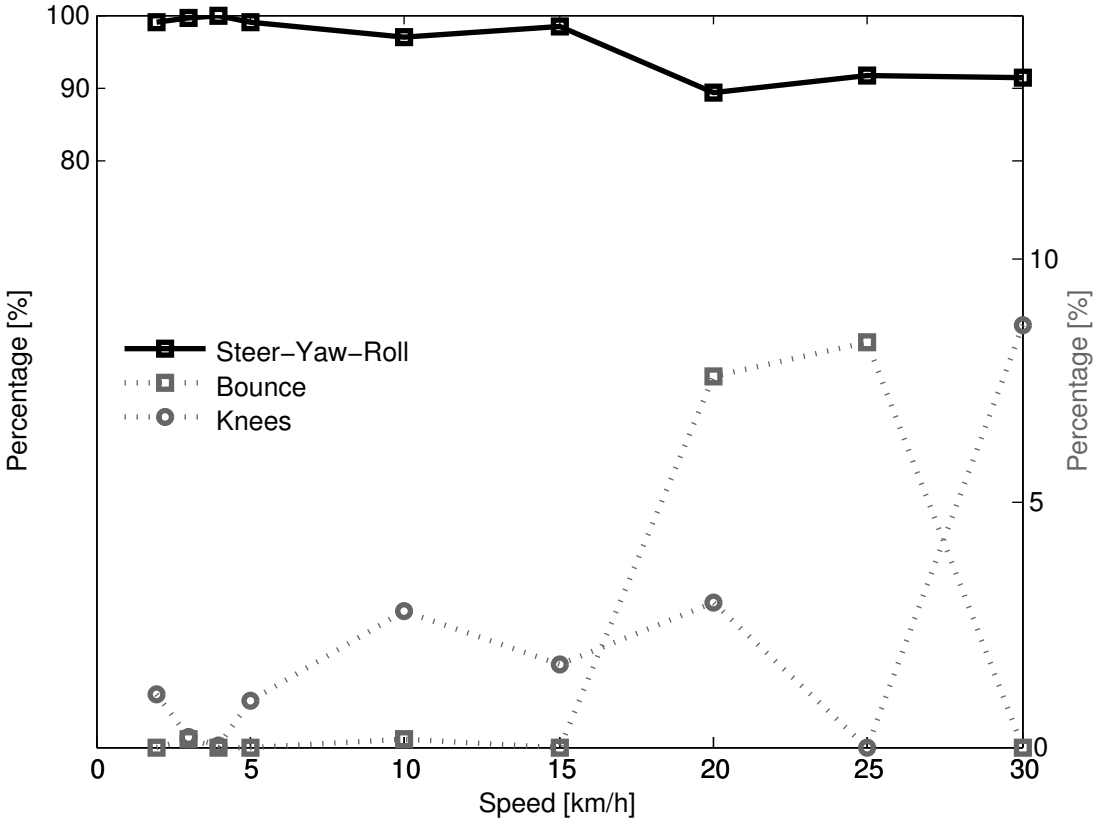

Figure 8.12: The percent variance of each of the three classes: Steer-Yaw-Roll, Bounce and Knees, at the speeds at which the Drift and Other classes were removed from the results for trials without pedaling. The solid lines are scaled to 100% (left axis), the dotted lines are scaled to 20% (right axis).

It is clear that at all speeds most motion takes place in the Steer-Yaw-Roll class. Also interesting is that unlike the normal pedaling situation, the Knee motion percentage does not increase at low speeds. This may mean that the lateral knee motion is connected to pedaling in some way. Like for the pedaling case, the Bounce and Knees classes may contain different principal components and a statistical approach to evaluate the percent variance of the classes would provide clearer results. Also note that as the bicycle becomes self stable above 16 km/h the total variance is tiny and thus any sort of random knee motion can be a relatively large motion.

Figure 8.13 shows the bicycle rigid body steer angle frequency-amplitude plot for different speeds. Compared to normal pedaling, the amplitudes are about half the size at the low speeds and one tenth the size at high speeds, indicating that smaller steering angles were made. The frequency content now also shows a much wider, flatter spectrum compared to normal pedaling. At 10 and 15 km/h, the frequency with the largest amplitude is near the open loop weave eigenfrequency. However, at the other speeds, this is not the case, once again indicating that the rigid body open loop weave eigenfrequency is not the frequency at which the bicycle is controlled.

8.4 Conclusions

The view provided by principal component analysis into bicycle-rider interaction, biomechanics and control has led us to several conclusions. During normal bicycling there are several dominant upper body motions: lean, bend, twist

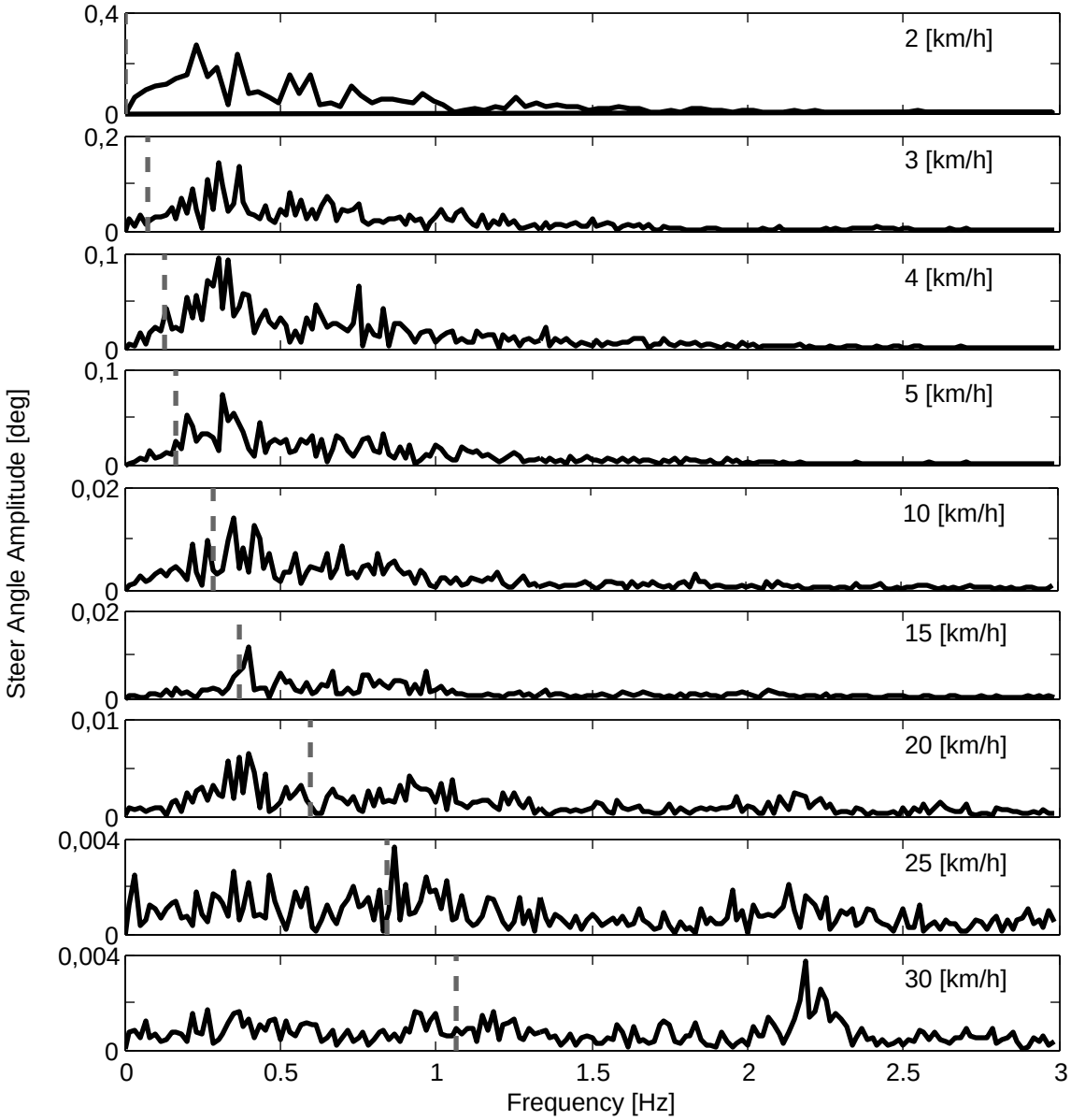

Figure 8.13: Steer angle amplitude plot for the nine different speeds for the tasks without pedaling. Dashed vertical grey line indicates the bicycle-rigid rider open loop weave eigenfrequency obtained from *Figure 8.4*.

and bounce, all of which seem to be linked to the pedaling motion. This is important for understanding which inputs are related to fundamental balance control and which are reactions to pedaling. We hypothesize that lateral control is mainly accomplished by steering since only upper body motion was observed at the pedaling frequency. If upper body motions are used for control then this control is carried out at the pedaling frequency. Considering variations of motion with respect to speed, we observed that there is a great deal of steering at low speeds but this decreases in magnitude as speed increases. This is generally true for all motions and shows that the bicycle-rider system becomes more stable at higher speeds with few detectable control actions. At low speeds additional lateral knee motions are observed which are probably more effective at augmenting steering control for lateral balance than upper body motions.

The bicycle model predicts that the weave mode is stable above about 16 km/h (4.4 m/s). Intuition might possibly lead one to believe that if the weave mode is already stable, that weave frequency might be relatively undisturbed by rider control actions and therefore present in the closed loop dynamics. However, we found no evidence of a distinct weave frequency in the steer angle time histories of any run. In fact the only distinct frequency that sometimes appeared was the pedaling frequency.

Principal component analysis provided a unique view into the control actions of a rider on a bicycle, but limitations in data reduction and motion grouping leave room for more objective statistical views into the motion of the bicycle-rider system.

8.5 Inertial frames and configuration variables

The transformation from marker coordinates to rigid body inertial frames and configuration variables shown in *Figure 8.5* is described here. A reference frame, $\mathbf{N}$, with origin n_o corresponding with the benchmark bicycle is defined with respect to the Optotrak reference frame, $\mathbf{M}$, Equation (8.9).

$$\mathbf{N} = \begin{bmatrix} \hat{\mathbf{n}}_1 \\ \hat{\mathbf{n}}_2 \\ \hat{\mathbf{n}}_3 \end{bmatrix} = \begin{bmatrix} 1 & 0 & 0 \\ 0 & -1 & 0 \\ 0 & 0 & -1 \end{bmatrix} \begin{bmatrix} \hat{\mathbf{m}}_1 \\ \hat{\mathbf{m}}_2 \\ \hat{\mathbf{m}}_3 \end{bmatrix} \tag{8.9}$$

Thirty-one marker locations were recorded and the vector to each is defined as $\mathbf{r}^{m_k/n_o}$ where $k = 1, 2, \ldots, l$ for the original markers and $k = l + 1, \ldots$ for any additional virtual markers. To calculate the reference frame attached to the rear bicycle we formed a frame center plane from the seat post marker, m_{26}, and two new additional virtual markers at the center of the rear wheel, m_{36}, and the center of the head tube, m_{33}. For example, the center of the rear wheel was calculated by Equation (8.10) where m_{25} and m_{31} are the left and right rear wheel markers.

$$\mathbf{r}^{m_{36}/n_o} = (\mathbf{r}^{m_{25}/n_o} + \mathbf{r}^{m_{31}/n_o})/2 \tag{8.10}$$

The normal vector to the plane through the rear wheel center, seat post and the head tube center is

$$\hat{\mathbf{b}}_2 = \frac{\mathbf{r}^{m_{36}/m_{26}} \times \mathbf{r}^{m_{33}/m_{26}}}{|\mathbf{r}^{m_{36}/m_{26}} \times \mathbf{r}^{m_{33}/m_{26}}|} \tag{8.11}$$

The heading vector of the rear frame is then $\hat{\mathbf{b}}_1 = \hat{\mathbf{b}}_2 \times \hat{\mathbf{n}}_3$ and $\hat{\mathbf{b}}_3 = \hat{\mathbf{b}}_1 \times \hat{\mathbf{b}}_2$ follows. These unit vectors define a reference frame that leans and yaws with the rear frame. We assumed that the rear frame pitch is negligible. The marker locations of the rider can now be expressed relative to the bicycle's inertial frame with reference to a point on the bicycle frame m_{36}. Equation (8.12) shows that the vector from any marker on the rider relative to m_{36} can be expressed in the bicycle reference frame, $\mathbf{B}$, rather than the inertial frame, $\mathbf{N}$. This formulation was used in the PCA of the rider-only markers to look specifically at rider motion relative to the bicycle. The subscripts, $\mathbf{N}$ and $\mathbf{B}$, in Equation (8.12) signify which reference frame the position vectors are expressed in.

$$\mathbf{r}_{\mathbf{B}}^{m_k/m_{36}} = (\mathbf{r}_{\mathbf{N}}^{m_k/m_{36}} \cdot \hat{\mathbf{b}}_1)\hat{\mathbf{b}}_1 + (\mathbf{r}_{\mathbf{N}}^{m_k/m_{36}} \cdot \hat{\mathbf{b}}_2)\hat{\mathbf{b}}_2 + (\mathbf{r}_{\mathbf{N}}^{m_k/m_{36}} \cdot \hat{\mathbf{b}}_3)\hat{\mathbf{b}}_3 \tag{8.12}$$

A reference frame $\mathbf{D}$ that is aligned with the steering axis of the rear frame can be formulated by rotation about the $\hat{\mathbf{b}}_2$ axis through the steer axis angle λ, which is measured for each bicycle [MKHS09].

$$\mathbf{D} = \begin{bmatrix} \hat{\mathbf{d}}_1 \\ \hat{\mathbf{d}}_2 \\ \hat{\mathbf{d}}_3 \end{bmatrix} = \begin{bmatrix} \cos\lambda & 0 & -\sin\lambda \\ 0 & 1 & 0 \\ \sin\lambda & 0 & \cos\lambda \end{bmatrix} \begin{bmatrix} \hat{\mathbf{b}}_1 \\ \hat{\mathbf{b}}_2 \\ \hat{\mathbf{b}}_3 \end{bmatrix} \tag{8.13}$$

The handlebar/fork inertial frame $\mathbf{E}$ is then calculated by defining $\hat{\mathbf{e}}_2$ to be aligned with the front wheel axle Equation (8.14).

$$\hat{\mathbf{e}}_2 = \frac{\mathbf{r}^{m_{21}/n_o} - \mathbf{r}^{m_{27}/n_o}}{|\mathbf{r}^{m_{21}/n_o} - \mathbf{r}^{m_{27}/n_o}|} \tag{8.14}$$

The handlebar/fork frame rotates around $\hat{\mathbf{d}}_3 = \hat{\mathbf{e}_3}$ and then $\hat{\mathbf{e}}_1 = \hat{\mathbf{e}}_3 \times \hat{\mathbf{e}}_2$. Equation (8.15) gives the instantaneous rear wheel radius which is used to formulate the vector to the rear wheel contact point Equation (8.16).

$$r_{\mathbf{R}} = -\frac{\mathbf{r}^{m_{36}/n_o} \cdot \hat{\mathbf{n}}_3}{\hat{\mathbf{b}}_3 \cdot \hat{\mathbf{n}}_3} \tag{8.15}$$

$$\mathbf{r}^{m_{39}/n_o} = \mathbf{r}^{m_{36}/n_o} + r_{\mathbf{R}}\hat{\mathbf{b}}_3 \tag{8.16}$$

This now allows us to calculate six of the eight configuration variables of the bicycle as a function of time (q_5 and q_8 are the rear and front wheel rotations, respectively).

$$\text{Distance to the ground contact point: } q_1 = \mathbf{r}^{m_{39}/n_o} \cdot \hat{\mathbf{n}}_1 \tag{8.17}$$

$$\text{Distance to the ground contact point: } q_2 = \mathbf{r}^{m_{39}/n_o} \cdot \hat{\mathbf{n}}_2 \tag{8.18}$$

$$\text{Yaw angle: } q_3 = \arccos\left(\hat{\mathbf{b}}_1 \cdot \hat{\mathbf{n}}_1\right) \tag{8.19}$$

$$\text{Roll angle: } q_4 = \arccos\left(\hat{\mathbf{b}}_3 \cdot \hat{\mathbf{n}}_3\right) \tag{8.20}$$

$$\text{Pitch angle: } q_6 = 0 \tag{8.21}$$

$$\text{Steer angle: } q_7 = \arccos\left(\hat{\mathbf{d}}_1 \cdot \hat{\mathbf{e}}_1\right) \tag{8.22}$$

8.6 Simple Statistics

8.6.1 Preface

Once again, we collected more data than we knew what to do with [MKSH11] and only looked at a subset of it from one rider. I took my first statistics class once I was back at Davis in the Fall of 2009 with the intention of learning better ways to analyze large data sets and make more over arching conclusions with the bicycle data. In the process, I learned about mixed effects models and that they seemed appropriate for our data sets and would potentially allow us

to see how the kinematic motions changed with respect to speeds, riders, maneuvers, etc. The first step in building a model like this is to identify the independent and dependent variables. The dependent variables can be broken up into continuous variables and factors. Speed constitutes the continuous variable, with riders, bicycles and maneuvers as the factors. The independent variables are trickier because we recorded time histories, so various statistics need to be chosen. These could be things like the results of the PCA analyses, but more concrete kinematic statistics potentially allow for more understanding. The PCA we did assumes nothing about the system being studied. For example, one statistic could be the standard deviation of various generalized coordinates. I never managed to get far with this as other things came up, but I at least started thinking about the relevant statistics. The following is a conference paper I submitted to the 2010 International Sports Engineering Association conference in which basic statistics of the time histories are chosen and some visualization of the statistics with respect to speed are shown. I primarily used this data to decide on sensor ranges when building the Davis instrumented bicycle presented in Chapter *Davis Instrumented Bicycle*, but I think that some better statistical models could be derived. I also only present some of the graphs here, but the source code can generate many more.

8.6.2 Abstract

An overview of bicycle and rider kinematic motions from a series of experimental treadmill tests is presented. The full kinematics of bicycles and riders were measured with an active motion capture system. Motion across speeds are compared graphically with box and whisker plots. Trends and ranges in amplitude are shown to characterize the system motion. This data will be used to develop a realistic biomechanical model and control model for the rider and for future experimental design.

8.6.3 Introduction

In the past decade, research has grown on single track vehicles culminating in the recently benchmarked bicycle model [MPRS07]. Two other recent papers ([ASKL05], [LS06]) have also presented overviews of current and historical research in bicycle dynamics and control. These review a plethora of dynamic models but little is known about which models are good at representing the actual system. Very little model-validation experimentation has been performed in the literature and many of the modeling assumptions, especially those regarding tire and rider dynamics, remain questionable. The most recent notable model-validation study is the verification of the benchmark model [KSM08]. Only a handful of other good experimental studies on bicycle dynamics exist. The work [VLS70a] performed some 40 years ago in the same halls as the Kooijman experiments [KSM08] included extensive efforts to validate a human control model using a bicycle simulator paired with statistical analysis. Also, around the same time as the first Delft experiments [VLS70a], a substantial study was done at Calspan and Schwinn [RM71].

With these studies providing some background, we have begun work to validate the kinematics of the bicycle and rider in a way that can facilitate the derivation of both dynamic models of the bike and rider and a rider control model. Our work began with an instrumented bicycle [KSM09] that was capable of measuring dynamics and collecting video of the rider's motion. We then used full body motion capture [MKS09] to quantitatively characterize the rider and bicycle kinematics. Principal component analysis was used to analyze the motion capture data but this proved to give less insight than expected. These initial efforts did show that the dominant motions for control are steering, that the rider's motions are small for normal bicycling tasks, and that pedaling motions are correlated with other rider motions. The present work examines the same motion capture data from [MKS09] with rigid body kinematics in mind and uses a statistical approach to identify trends with forward speed, a strong dependency of bicycle stability.

8.6.4 Experimental Design

The experiments were performed in a controlled environment while the motion of the bicycle and rider were measured with an active motion capture system [Inc09]. The rider rode on a 3×5 meter treadmill, (*Figure 8.1*) capable of belt speeds up to 35 km/h. Three male riders of similar age [23, 26, 31 years] and build [height (1.84, 1.83, 1.76 m) and mass (74, 72, 72 kg)] participated as subjects. Each rode two different Dutch bicycles. Each rider performed all runs in one day in the same order (no randomization) and was instructed to bicycle comfortably at a constant speed in the

range of 2 to 30 km/h for the duration of the run. There were at least 2 repetitions of each speed with each bicycle. A run was sampled at a frequency of 100 Hz for 60 seconds.

Bicycle markers were placed to easily extract the rigid body motion (i.e. body orientations and locations) of the frame and fork (*Figure 8.2*). Four markers were attached to the fork and seven to the rear frame. A marker was attached on the right and left sides of the center of each wheel, the seat stays, the ends of the handlebars, and the head tube. A single marker was also attached to the back of the seat post.

We recorded the locations of 20 points on the rider (*Figure 8.3*): left and right sides of the helmet near the temple, back of the helmet, shoulders (greater tuberosity of the humerus), elbows (lateral epicondyle of the humerus), wrists (pisiform of the carpus), between the shoulder blades on the spine (T6 of the thoracic vertebrae), the tail bone (coccyx), midpoint on the spine between the coccyx and shoulder blades (L1 on the lumbar vertebrae), hips (greater trochanter of the femur), knees (lateral epicondyle of the femur), ankles (lateral malleolus of the fibula) and feet (proximal metatarsal joint).

8.6.5 Data Processsing

Once marker data was repaired, we calculated several generalized coordinates. This provided a way to characterize the bicycle and rider as a system of rigid bodies which seems to give a clearer picture of the underlying control motions that the principal component analysis provided [MKS09]. The coordinates included bicycle yaw, roll and steer angles and the locations of the wheel ground contact points, and several coordinates to represent rider motion: the rider's lean and twist angles, lateral knee motion, and lateral tail bone motion, all relative to the bicycle frame plane of symmetry. The rider lean angle can be thought of as the angle of the rider's spine relative to the bicycle frame. The twist is the angle through which the torso rotates about the spine. The knee and butt motions are the relative lateral distances from the frame plane of symmetry for each marker. These are shown because we observed large lateral knee movement in video footage at low speeds [KSM09] that may be used for additional control. The butt motion is plotted to give an idea of how the seat can potentially be shifted under the torso to control roll angle. Figures *8.14*, *8.15*, *8.16*, and *8.17* show examples of the time histories of these coordinates.

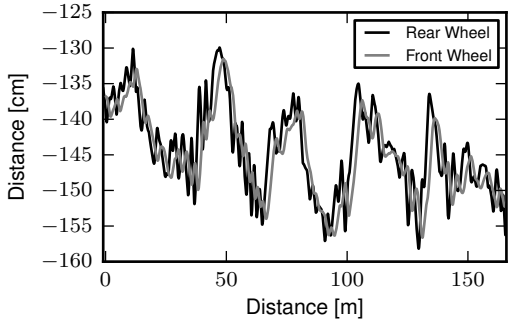

Figure 8.14: The positions of the front and rear wheel contact points throughout a single a normal biking run at 10 km/h.

The primary coordinates are presented in Section *Inertial frames and configuration variables*. The remaining are calculated as follows. The instantaneous front wheel radius is

$$r_{\mathbf{F}} = \frac{-\mathbf{r}^{m_{32}/n_o} \cdot \hat{n}_3}{\sin[\arccos(\hat{e}_2 \cdot \hat{n}_3)]} \tag{8.23}$$

The front wheel contact point is then

$$\mathbf{r}^{m_{40}/n_o} = \mathbf{r}^{m_{32}/n_o} + r_{\mathbf{F}} \frac{(\hat{e}_2 \times \hat{n}_3) \times \hat{e}_2}{|(\hat{e}_2 \times \hat{n}_3) \times \hat{e}_2|} \tag{8.24}$$

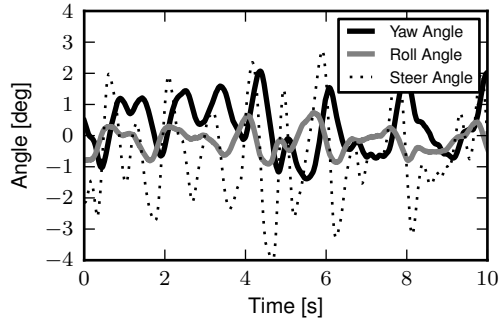

Figure 8.15: The bicycle yaw, roll and steer angles throughout a single a normal biking run at 10 km/h.

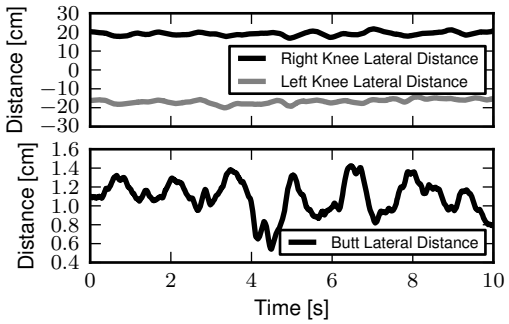

Figure 8.16: Lateral deviations of the knees and butt from the frame plane throughout a single normal biking run at 10 km/h.

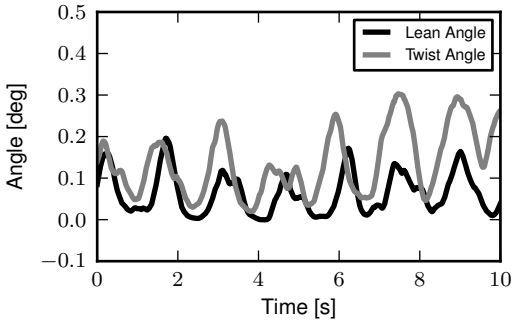

Figure 8.17: Rider lean and twist angles throughout a single normal biking run at 10 km/h.

The coordinates to the front wheel contact points are then found by a dot product with the lateral and longitudinal unit vectors in the ground plane

$$q_8 = \hat{n}_1 \cdot \mathbf{r}^{m_{40}/n_o} \tag{8.25}$$

$$q_9 = \hat{n}_2 \cdot \mathbf{r}^{m_{40}/n_o} \tag{8.26}$$

The lateral distance of the rider's knees to the bicycle frame are

$$q_{10} = \hat{b}_2 \cdot \mathbf{r}^{m_3/n_o} - \mathbf{r}^{m_{26}/n_o} \tag{8.27}$$

$$q_{11} = \hat{b}_2 \cdot \mathbf{r}^{m_7/n_o} - \mathbf{r}^{m_{26}/n_o} \tag{8.28}$$

Simarly, the tail bone's lateral deviation from the bicycle frame is

$$q_{12} = \hat{b}_2 \cdot \mathbf{r}^{m_9/n_o} - \mathbf{r}^{m_{26}/n_o} \tag{8.29}$$

I take the angle between a line running along the rider's back and the frame plane to be a measure of rider lean, *Figure 8.18*.

The rider's lean angle is then calculated by first finding the vector from the butt to the upper back

$$\mathbf{r}^{m_9/m_{11}} = \mathbf{r}^{m_{11}/n_o} - \mathbf{r}^{m_9/n_o} \tag{8.30}$$

projecting that vector into the plane normal to the roll axis

$$\mathbf{v} = \frac{\mathbf{r}^{m_9/m_{11}} - (\mathbf{r}^{m_9/m_{11}} \cdot \hat{b}_1)\hat{b}_1}{|\mathbf{r}^{m_9/m_{11}} - (\mathbf{r}^{m_9/m_{11}} \cdot \hat{b}_1)\hat{b}_1|} \tag{8.31}$$

and finally calculating the angle between the projected vector and the lateral symmetry plane

$$q_{12} = -(\mathbf{v} \cdot b_2) \arccos(-\mathbf{v} \cdot b_3) \tag{8.32}$$

The twist is the angle of the rider is calculated by creating a vector from one shoulder to the other

$$\mathbf{r}^{m_{19}/m_{15}} = \mathbf{r}^{m_{15}/n_o} - \mathbf{r}^{m_{19}/n_o} \tag{8.33}$$

and projecting it into the plane normal to the back line

$$\mathbf{w} = \frac{\mathbf{r}^{m_{19}/m_{15}} - (\mathbf{r}^{m_{19}/m_{15}} \cdot \mathbf{v})\mathbf{v}}{|\mathbf{r}^{m_{19}/m_{15}} - (\mathbf{r}^{m_{19}/m_{15}} \cdot \mathbf{v})\mathbf{v}|} \tag{8.34}$$

and finally computing the angle between it and a plane which is along the back line and perpendicular to the bicycle lateral plane of symmetry

$$q_{14} = -\mathbf{w} \cdot (\mathbf{r}^{m_9/m_{11}} \times (\hat{b}_1 \times \mathbf{v})) \arccos(\mathbf{w} \cdot (\hat{b}_1 \times \mathbf{v})) \tag{8.35}$$

8.6.6 Results

Direct examination of individual times series can be fruitful [Doy87], but it is hard to make generalizations that apply to more that one specific case. In our case, we have are nearly 3000 different time histories to examine with the coordinates we've chosen. Examining the frequency spectrum of each time history gives a different and sometimes more revealing view. For the runs in which the rider pedals, the pedaling frequency is often the dominant frequency, with little indication of other distinct frequencies [MKS09].

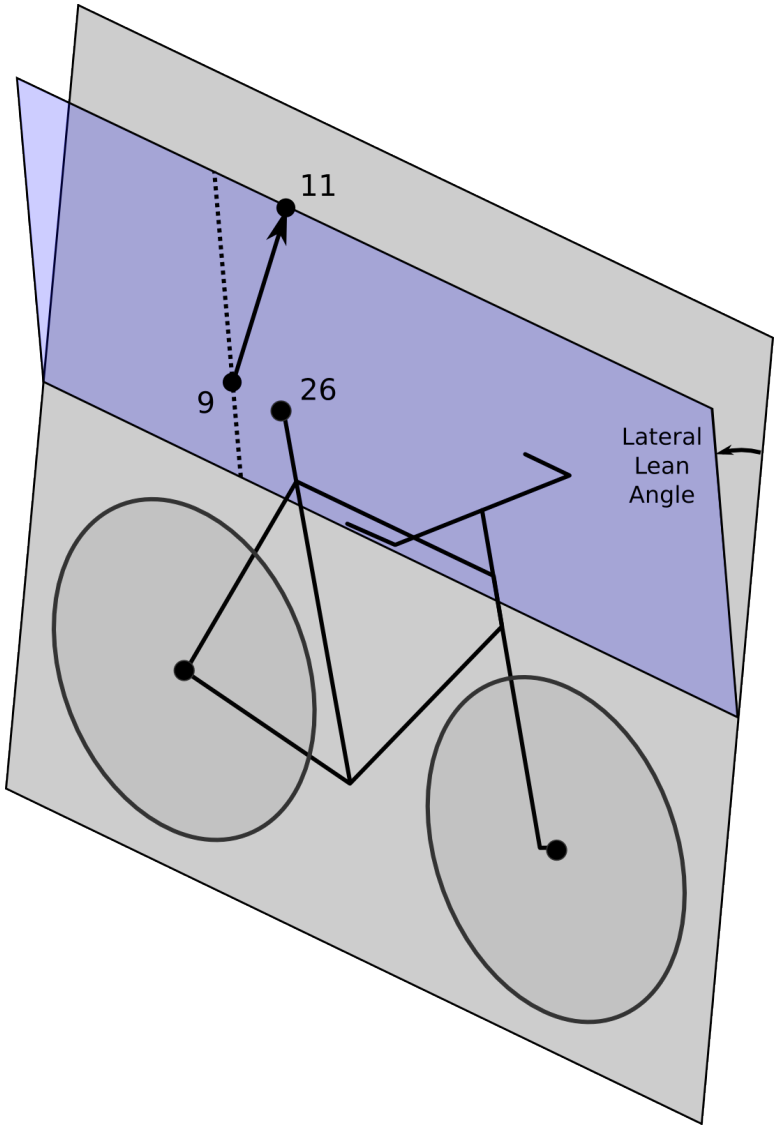

Figure 8.18: A depiction of the rider lean angle. It is independent of the rider's forward lean and point 9 can be out of the plane of the bicycle. It is the angle of the back vector projected into a plane normal to the roll axis.

A better way to visualize how the coordinates change with speed, for example, is to look at various statistics of the time histories. We grouped all of the runs together for combined data sets at each speed of between 48,000 and 72,000 points, depending on how many repetitions of runs were performed (i.e. between 8 and 12). These were then plotted as separate box plots for each speed and for each state. The box and whiskers charts plot a center line for the median of the data, a box that bounds the 25% and 75% quartiles, whiskers that encompass the data that falls within $1.5 \times (Q_{75} - Q_{25})$ and crosses for any outlier data points. Trends can be identified based on the spread and median of the data at each speed. An offset median shows that the distribution is skewed (e.g. steering more to the left than the right). The box and the whiskers encompass the vast majority of the data. The whiskers can be used to compare the coordinate excursions across speeds.

The yaw and steer plots show that the angles are small and tightly distributed at high speeds, but that below 10 km/h the spread begins to grow. It is also interesting that the yaw and steer graphs have very similar distributions. For a bicycle without a rider, there is a simple linear kinematic relationship such that yaw rate is only a function of steer rate and steer angle, which is the likely reason for the similarity in steer and yaw. The spread of the roll angle on the other hand stays fairly constant regardless of speed. The butt lateral distance has somewhat constant distributions across speeds and it is also apparent that the rider generally sits about one centimeter off the center plane of the bicycle. The lateral knee distances are interesting in the fact that spreads increase with lower speeds. We were able to visually detect large knee movements in the video data at low speeds and hypothesized about the role the knees could possibly play in control of the bicycle ([KSM09], [MKS09]). The rider lean angles are very small and do not show much change with speed. This continues to support our hypotheses that riders do not make use of leaning for control in normal bicycling. The rider twist angles show a little more spread at low speeds. This could be tied to the fact that you twist more when you steer more.

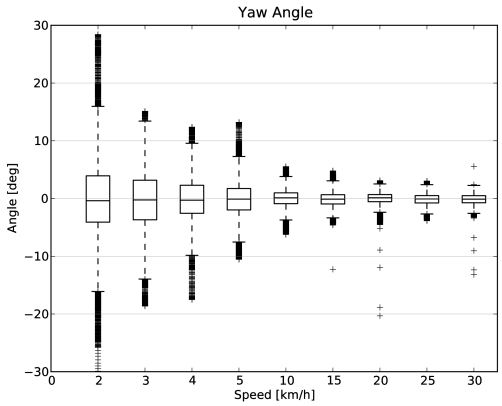

Figure 8.19: Box and whiskers plots of the yaw angle data from all riders and bicycles versus speed.

8.6.7 Conclusions

The box and whisker plots are a method of visualizing a more statistically valid view of the kinematics of the bicycle and rider during stabilization tasks. General trends in how states change with speed were shown and can be utilized for rider bicycle dynamic and control model design. This is only one of the first steps toward understanding how particular motions vary with speed, maneuvers, bicycles, riders, and even the correlations among the motions. The source code also computes statistics for the rates, accelerations, and frequency content of the coordinates. The numerical values presented also provide a framework for design of measurement techniques needed in experimental studies.

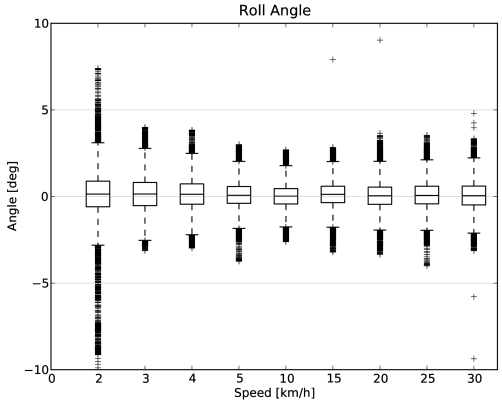

Figure 8.20: Box and whiskers plots of the roll angle data from all riders and bicycles versus speed.

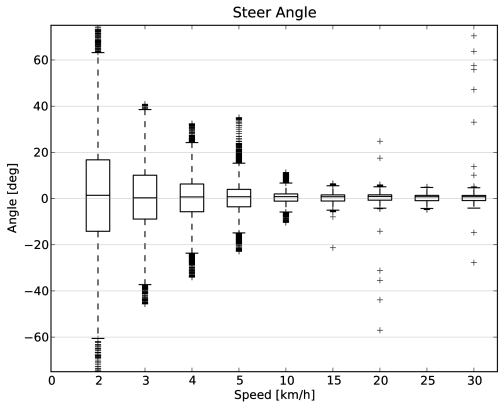

Figure 8.21: Box and whiskers plots of the steer angle data from all riders and bicycles versus speed.

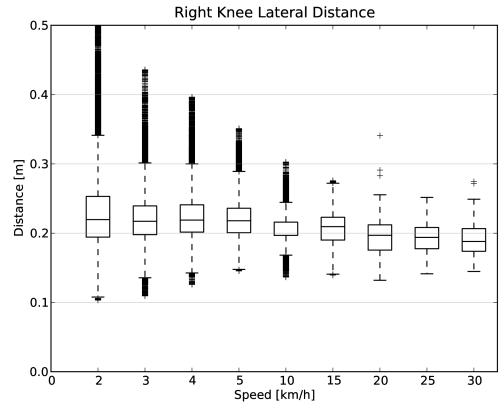

Figure 8.22: Box and whiskers plots of the right knee lateral distance data from all rider and bicycles versus speed.

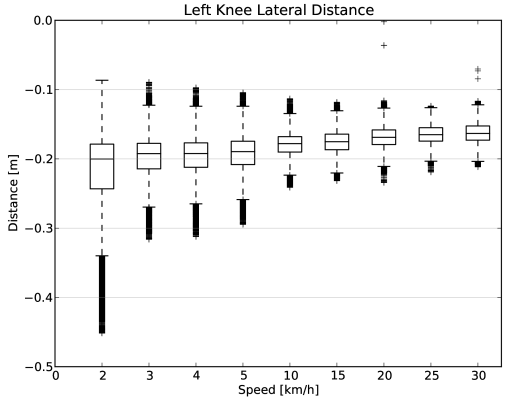

Figure 8.23: Box and whiskers plots of the left knee lateral distancee data from all riders and bicycles versus speed.

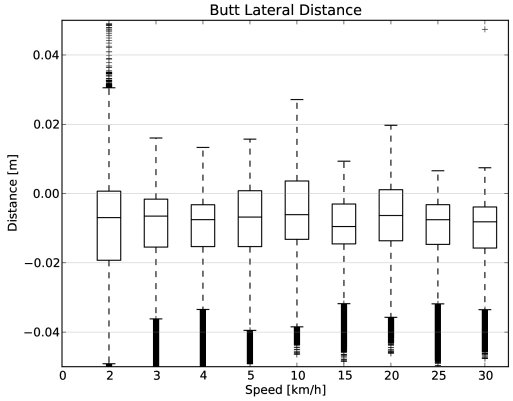

Figure 8.24: Box and whiskers plots of the butt lateral distance data from all riders and bicycles versus speed.

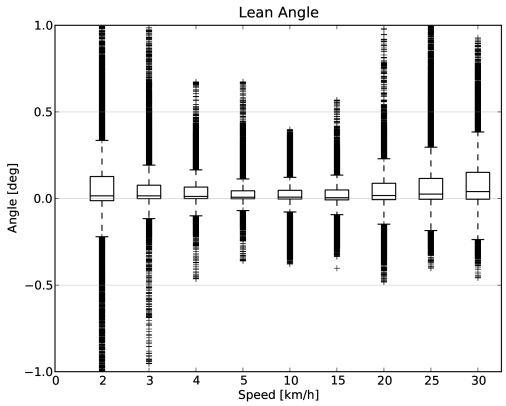

Figure 8.25: Box and whiskers plots of the lean angle data from all riders and bicycles versus speed.

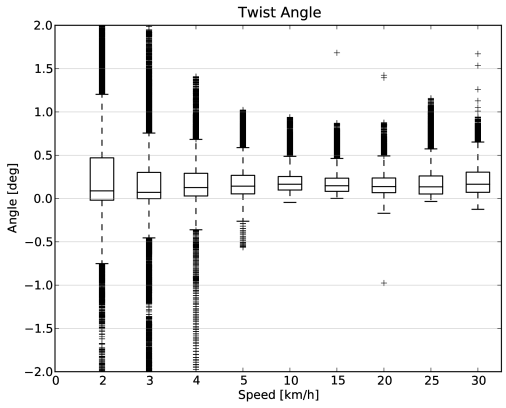

Figure 8.26: Box and whiskers plots of the twist angle data from all riders and bicycles versus speed.

8.7 Conclusions

The PCA data decomposes the motion into a collection of linear motions, with the dominant ones being exposed. We'd hoped that we would be able to apply a second PCA in much the same fashion as [Tro02] did with the walkers, but bicycling doesn't produce clean periodic motion like walking does. [Tro02] was able to apply the second PCA across second independent variables to characterize the change in motion with respect to the variables. We are most interested in dynamical changes with respect to speed for the bicycle-rider system, but also in how different bicycle designs affect the control and dynamics. Our attempt at tracking how the principal components changed with respect to speed, was somewhat flawed due to the difficulty in matching components from run to run. It correctly shows the increased motions at low speeds, but the information from the principal components became less and less relevant as we continued to work with it. This is what led me to transform the marker data into more concrete coordinates that have more meaning and connection to the kinematics we typically examine in the bicycle-rider system. I think the data set can provide some more concrete conclusions about how we balance a bicycle. Another thing that I thought about pursuing was making use of scaling with respect to mass in the principal component analysis. It is possible to applying weighting to the coordinates such that the principal components can be formulated with respect to a momentum-like quantity. This could reveal the motions that effect the dynamics rather than simply the primary kinematics.

CHAPTER

NINE

DAVIS INSTRUMENTED BICYCLE

9.1 Preface

At the beginning of 2009 I was in Delft working with Jodi and Arend on much of the work explained in the previous chapters. I was still also in contact with Mont and Luke back in Davis. Before I had come to Delft, Luke had mentioned the possibilities of applying for an NSF grant to fund the remainder of our bicycle dynamics projects. This was enticing, as there were few sources of grant funding over the years for in the Davis lab. We really needed some dedicated research time, as we spent the first few years taking teaching assistant positions which ate up most of our available research time outside of our classes. I fortunately got a Fulbright grant for the 2008 school year which gave me a year's stipend so that I could focus on research and on top of that Jodi's PhD budget helped fund the practical research costs in Delft and some of my conference trips. At the beginning of December 2008 Luke sent me an email with a renewed interest in applying for the NSF grant and Mont seemed to be on board. Mont also talked with Ron and got him interested. We spent the next two months writing our grant proposal using video conferencing and collaborative word processing to get it done. The basic idea was to pair Ron's manual control expertise with our bicycle dynamics expertise to study the dynamics, control and handling qualities of bicycles with the theoretical constructs supported by extensive experimentation. Our work paid off and we received the grant, albeit at a smaller amount than asked for so we had to cut back some of the scope (which Arend had correctly forecast of being too large!). This set us up for a two year study where we'd develop a manual control model, verify it and the basic bicycle dynamics with both an instrumented bicycle and a robotic bicycle, and wrap it up with some work on handling qualities predictions.

When I got back to Davis in September 2009 we started gearing up for the grant work that would start October 1st. I had to get my qualifying exam done in October and I also signed up for a Spanish class (which wasn't necessarily a good idea for the grant's sake). Luke also took some programming classes and this gave us a really slow start, as neither Luke or I realized that the scope of what we had to do didn't really allow any more time for classes. We got moving though and started to plan out the bicycle(s) we were going to build.

Our proposal called for two bicycles, but somehow Luke and I hatched a plan to build a single multi-purpose bicycle to "save money and time". Arend sent Danique over in January 2010 to do her internship with us. She was an excellent intern and made great progress on the custom data acquisition system we had envisioned. We decided to use a low level microprocessor, the Arduino, paired with with a set of digital sensors for data acquisition and control. During this time, Luke and I had our roughest moments working together which was mostly rooted in my frustrations with the progress of this bicycle design. I'd already built a bicycle with Jodi that did almost everything I needed and I felt like I was reinventing the wheel and wasting time with all this low level data acquisition work. Things eventually broke down after the stress boiled to the top and we sat down with Mont to figure out how to solve things. The conclusion was to split the bicycle back into two and each of us move forward more independently. I think this was the absolutely right move for me in terms of getting the project done as I planned and the stress immediately went away. But the part I'm still bothered about was my inability to work in a direct team with Luke when the pressure to get things done was high. I know that if we work together, the final product would be many times greater than our independent work because of our complimentary skill sets, but conflicting visions of the final product and the path to get there really put a wall between us. I'm continually learning how to do teamwork and probably always will be. I doubt it is one of my

strong points, as I always tend to want control. I hope that I can develop strong team environments for my students in the future.

Nevertheless, the instrumented bicycle moved forward. I was awarded an extra grant to cover my stipend for the summer of 2010 so we hired Gilbert, a new student in our lab, to help us out for the summer. Between me, Gilbert, and our undergraduate interns Mohammed, Stephen, Eric, and Chet we plowed through the bicycle construction through the summer pretty much putting the instrumented bicycle back on schedule for experimentation in the fall. But even with the summer push, it ended up taking me all fall quarter and some into the new year to get the bicycle in a working state and ready for the experimentation. This chapter discusses the design and operation of the Davis instrumented bicycle.

9.2 Introduction

This chapter details the design and implementation of an instrumented bicycle capable of accurately measuring the essential kinematics and kinetics associated with human control of the bicycle.

I had originally considered using motion capture for the kinematics as we had very successful results measuring the complete kinematic configuration of the bicycle and rider with motion capture techniques as explained in Chapter *Motion Capture*, but I no longer had access to a system as good as the one at the Vrije Universiteit. The systems available in Davis could capture the motion on the treadmill but were not especially not suited to capture the motion of the bicycle on the ground. With this in mind, we decided to expand upon the on board measurement techniques used in the Delft Instrumented bicycle as the basic design principle. This would allow the bicycle to collect data in a variety of environments. The most notable downside was inaccurate location tracking of the system. But we concluded that this wouldn't be detrimental to system identification and moved forward with the instrumentation.

The bicycle's primary design criteria were as follows:

- Sized for our intended riders: average adult males.
- Restrict the rider's biomechanical movement to more closely meet the Whipple model rigid rider assumption. This in turn also required the bicycle to be self propelled so that the rider does not have to move their legs to pedal.
- Accurately measure the rider's applied steering torque.
- Accurately measure the fundamental kinematics of the bicycle: three dimensional rates and orientations of the bicycle rear frame, front frame, and wheels.
- Accurately apply and measure a lateral disturbance force to the bicycle frame.

From early on, I intended to attempt some experiments with some constrained rider biomechanical motion, such as leaning, because the interplay of the various control inputs available to the rider, such as leaning, are a common theoretical research topic with little experimental backing. This led to secondary design criteria that as the project progressed were never fully implemented, but I'll discuss them for completeness. They are as follows:

- Restrict the rider's body motion to a limited set and measure the additional kinematics: hip roll, torso relative to hip lean, torso relative to hip twist, and lateral knee motions.
- Measure the additional reaction forces between the rider and bicycle: forces and moments in the seat post and forces at the foot pegs.

These criteria framed the subsequent design choices described herein.

9.3 Bicycle

We needed a bicycle that would allow for easy modification and various mounting points for sensors and data acquisition equipment. Our original requirements for a bicycle were as follows:

- Steel frame for easy modification and welding.
- Disc brake brackets for mounting the wheel speed encoders.
- 100mm front dropout spacing and 135mm rear dropout spacing.
- 1-1/8" thread-less headset to allow for easy modification.
- Cylindrical tubes for head, down, top, and seat tube (i.e. nothing non standard)
- Horizontal top tube for equipment mounting purposes.
- Threaded rack mount for instrumentation mounting.
- Accept 700c rims with high pressure tires.
- Frame size: 54-58cm for our intended riders.
- An electric hub motor for forward propulsion.

We ended up choosing a large size Surly 1x1 model, *Figure 9.1*. It is designed as a single-speed off-road bicycle for 26" wheels with fat tires, but can be setup with 700c higher pressure tires. The frame is constructed from butted 4130 CroMoly steel tubing. It has both front and rear cantilever brake mounts in addition to disc brake mounts. Otherwise it met all of our requirements. We purchased some standard components including 700c aluminum wheels with 23c Continental Gatorskin high pressure tires and basic handlebars and brakes.

Figure 9.1: The Surly 1x1 with 700c wheels and basic handlebars for upright seating. An Amped Bikes geared hub motor is shown installed along with the lead acid battery kit on the rear rack.

To allow the bicycle to be propelled without requiring the rider to pedal, we opted for a bicycle electric hub motor kit. Amped Bikes (http://www.ampedbikes.com) graciously donated both direct drive and geared kits which included the motors, controllers, throttle, and 36 volt lead acid batteries. I used the direct drive version on the instrumented bicycle. The lead acid batteries were very heavy so we purchased a light, ~2.8 kg, 36 volt lithium ion battery as a substitute to help decrease the bicycle weight. The kit comes with a motor controller with a rudimentary "cruise control". We needed some form of cruise control to allow the rider to set the speed during the experiment allowing them to focus their attention on lateral control as opposed to throttle control. The Amped Bike cruise control worked well for the experiments performed on the floor, but was more difficult to match the cruise control to the speed of the treadmill. Some sort of feedback control would alleviate the difficulties, but we made due. The exposed wires from the hub motor are also easily susceptible to damage. The bicycle fell over once, damaging the wires and shorting the Hall

effect sensors in the hub. I spent a couple of weeks repairing it[1]. Overall, the motor met our needs for constant speed propulsion and the single battery would last through an entire day of experimentation, but was susceptible to being easily damaged.

9.4 Rider Harnesses

The bicycle was designed to accommodate a range of allowable rider motions. I designed it with three modes in mind. First, the rider can simply have complete free rider biomechanical motion as they would when normally riding a bicycle. The second design was intended to restrict almost all of the rider's ability to move with respect to the bicycle frame to better mimic the rigid rider assumptions in many bicycle models. And third, a harness was designed to restrict the rider's movement to a particular subset of hypothesized dominant motions.

9.4.1 Rigid Rider

Rigid rider models are often employed in single track vehicle research but the rider has been rigidified very few times in experimental work. This is potentially problematic as the rigid rider assumption is a large one. [SVLB+73] made use of a rider brace in their bicycle simulator to prevent rider lean. [Eat73b] rigidified his motorcyclists' torso and performed several perturbation tests with the rider's hands off the handlebars! He found it difficult to identifying the linear modes of motion. [Doy87] comments on the utility of rigidifying the rider which was an example of his techniques to simplify the system, but he left the rider free to move in his experiments. Jim Papadopoulos has been a proponent of using recumbent bicycles in studies due to the natural rigidification of the rider. His thoughts and the difficulties we had in the studies from Chapters *Delft Instrumented Bicycle* and *Motion Capture* influenced my decision to restrict the rider's motion.

I constructed a harness such that the rider was rigidified as much as possible with respect to the rear frame, *Figure 9.2*. A medical back brace was used to rigidify the spine and hip motion. I then attached the brace to the bicycle frame via a stout adjustable arm.

I fashioned some knee straps with strong magnets taken from computer hard drives which would engage with a ferrous attachment plate on the frame so that the rider's legs would be rigid with respect to the rear frame, *Figure 9.3*. Chapters *Delft Instrumented Bicycle* and *Motion Capture* showed the rider tends to use lateral knee motions and we wanted to eliminate that as a confounding factor. The magnets were weak enough that the rider could remove his legs in an emergency.

These restrictions left the rider's arms and head free to move. The arm motion was required for controlling the bicycle, although one could imagine fixing the rider's arms and only allowing control with motion of their hands. The head probably should have been rigidified with respect to the body cast, but we didn't due to comfort reasons[2].

9.4.2 Restricted Motion

A second harness was partially developed to restrict the rider's motion to that described in *No Hands*. A back brace which left the hips free to move was used to keep the spine straight and a custom-molded hip brace was developed to hold securely to the pelvis, *Figure 9.4*. The plan was to attach the hip brace to the bicycle seat via a revolute joint in the roll direction which would allow the hips to *only* roll about the seat. The back brace would then be attached to the hip brace via a joint which would allow torso lean with respect to the hips. The feet would be attached to the foot pegs via clip-in pedals. Forces applied from the feet to the foot pegs would effectively allow the rider's hips to roll with respect to the bicycle frame (in reality because the rider is more massive and more inert, the bicycle frame would roll with respect to the inertial reference frame).

[1] See http://biosport.ucdavis.edu/blog/hub-motor-woes for repair details.

[2] Nonetheless, Jan had great plans for a halo-like ring with nails sticking through to the rider's scalp so that they couldn't move their head without excruciating pain; we just never got around to making it.

Figure 9.2: Jason strapped into the rigid rider harness. The arm allows for multiple degrees of adjustability to allow different riders and seating positions.

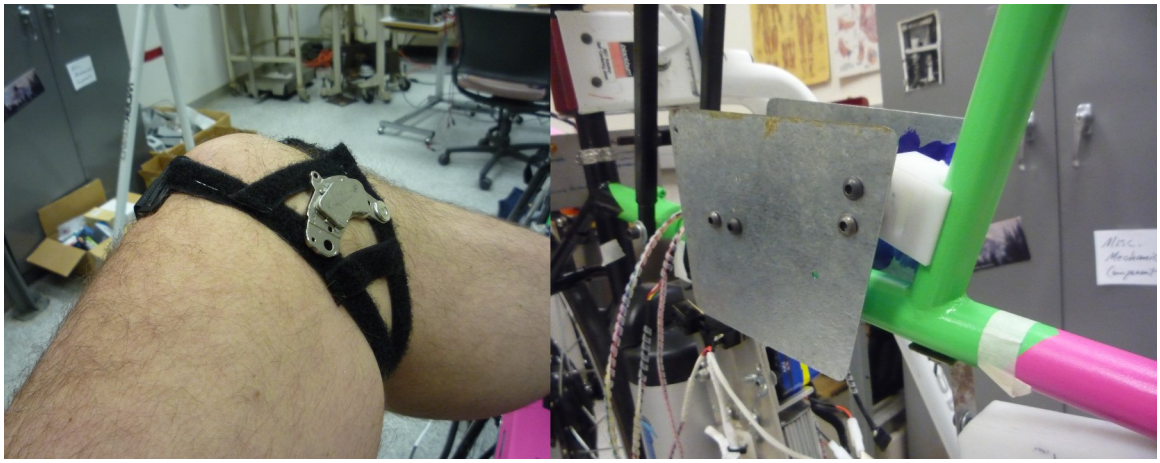

Figure 9.3: The left image shows the knee straps with hard drive magnets and the right image shows the knee attachment plates mounted to the top tube of the bicycle.

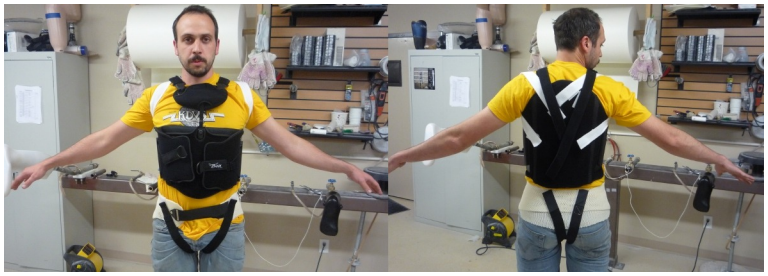

Figure 9.4: The hip and upper torso harnesses.

My hypothesis was that this harness would allow for the essential motion and torque application needed to effectively control the bicycle with no hands and would provide the next effective means of control to complement steer torque when riding with hands. This design was only partially finished, so the merits of it were never tested.

9.5 Orientations, Rates and Accelerations

The two most important states that describe the lateral dynamics of the bicycle are roll and steer (as defined in Chapter *Bicycle Equations Of Motion*). Ideally one would like to measure the angular orientation, angular rate, and angular accelerations of both the rear frame and the front frame. Sensors that allow direct, independent and accurate measurements of each are ideal, to avoid having to estimate measurements through differentiation, integration, or state estimators. The kinematics of each body need not be measured if they are connected to the rear fame via revolute joints, only measurement of the extra degree of freedom for each connected body relative to the rear frame is required. *Table 9.1* gives general ranges of bicycle kinematic motions from my previously collected data.

Table 9.1: Table of maximal measured values found in all experimental data taken in Chapter Motion Capture. The ranges were determined from 75 percentiles, the accuracy as a percentage of the range and the bandwidth as 75th percentile of the power in the signal.

Measurement	Range	Accuracy	Bandwidth
Roll Angle	± 8 deg	0.2 deg	45 hz
Roll Rate	± 30 deg/s	0.6 deg/s	40 hz
Roll Acceleration	$\pm 100 \frac{\text{deg}}{\text{s}}$	$2 \frac{\text{deg}}{\text{s}}$	25 hz
Steer Angle	± 65 deg	1 deg	45 hz
Steer Rate	± 150 deg	1.5 deg/s	35 hz
Steer Acceleration	$\pm 600 \frac{\text{deg}}{\text{s}}$	$12 \frac{\text{deg}}{\text{s}}$	30 hz

The yaw, roll, pitch and steer rates, are typically measured directly with rate gyros, which have been available for the later half of the 20th century. The direct measurement of angular accelerations has yet to mature [OV98], so numerical differentiation and filtering of the angular rates is often used. The angular accelerations can also be computed if the acceleration and location of multiple points are measured with accelerometers. Most all experimental work with bicycles and motorcycles provides good examples of employing these type of kinematic sensors.

9.5.1 Roll

The roll angle is typically the most difficult kinematic measurement due to the fact that both the bicycle translates with respect to the ground plane making mechanical measurement difficult and that the ground plane may not be normal to earth's gravitational field. Herein, we did not concern ourselves with the later because all of our experiments were on level ground. Integration of the easier roll rate measurement is an option, but definite initial conditions and some way to account for the drift due to integration are required, and not necessarily trivial. Past researchers have measured the roll angle with a variety of methods from trailers and third wheels to lasers and rate gyros with complementary state estimators.

[Doh53] used a trailer to measure roll angle. [KF59] and [Fu65] introduced one of the earliest direct roll angle measurements. They made use of a third wheel attached to one side of the motorcycle and measured the angle between the wheel mounting arm and the motorcycle frame. [Sin64] also used a third wheel after having little luck with accelerometers and rate gyros. He obtained decent measurements but abandoned the wheel because it was too large, dangerous and susceptible to vibration. [RM71] measured roll angle with a potentiometric free gyro with seemingly good results. Their data was captured with direct write recorders in a pace car. [Eat73b] used a third wheel and a potentiometer to measure roll angle on a motorcycle, but also had reliability issues. [VZ75] used a small trailer with two roller skate wheels and potentiometer to measure the roll angle on this robotic motorbike.

More modern techniques often focus around roll angle estimation. [BTS08], [BST09] developed a simple algorithm to remove the low frequency drift and only require yaw rate, roll rate and speed measurements to get peak roll estimation errors of 5 degrees, which were larger than we could accept. But their methods did allow for roll angle estimation on banked curves. Distance lasers have been used to directly measure the roll angle with respect to the ground but are particularly expensive [Eve10]. The roll angle can also be estimated with a state estimator such as a Kalman filter ([Gus02], [TJ10]). The plant in the Kalman filter can be general 3D motion of a rigid body or a model of the bicycle. Constraining the estimation with the use of a bicycle model as the plant could have drawbacks when using the resulting angle for model validation but can give potentially great results otherwise. These types of algorithms are implemented in many modern sensor packages and we decided to pursue one of these.

There is a class of sensors called Inertial Measurement Units (IMU) and/or Attitude Heading Reference Systems (AHRS) that have recently become very affordable and small enough to be appropriate for orientation and rate estimation due to the advent of MEMs rate gyros, accelerometers, magnetometers, and GPS technologies. An IMU can theoretically be rigidly affixed to each body of the system to give complete kinematic details of the motion of that body.

Inertial Measurement Units An inertial measurement unit typically measures three body fixed components of angular rate of a rigid body and the three dimensional acceleration of a single point.

Attitude Heading Reference System An attitude heading reference system measures what an IMU does but also often includes earth magnetic field measurements and/or GPS combined with a microprocessor and estimation algorithm to additionally provide orientation and/or location estimations.

Many of these systems were within our budget range so we scouted various companies (MemSense, Navionex, MotionNode, MicroPilot, Crossbow, VectorNav, Ch Robotics, etc.) to see what was offered[3]. We ended up choosing the VN-100 development board from a relatively new company called VectorNav (http://www.vectornav.com) due to price, on board orientation calculations, and the potential ease of collecting data via a typical RS-232 serial interface. My preferred software tools, Matlab and Python, both had good serial interface packages. We placed a single VN-100 on the rear frame to measure the angular orientations and rates along with the acceleration of a point on the rear frame. The VN-100 relies on additional magnetometer readings and an on-board proprietary algorithm based on a Kalman filter for computing the real time orientation about the three axes.

The VN-100 turned out to be a poor choice for our application in multiple ways, the second of which I'll talk about in a later section. The first is that the orientation estimations were very poor. I wanted *at least* accurate estimate of the roll angle of the bicycle. The VN-100 repeatedly was not able to provide this. VectorNav worked with me and tried offer various methods of tuning the VN-100 with state covariance weightings for the Kalman filter and also to tune out any static magnetic fields from the bicycle frame, but with no success. The issues were associated with both the wheel and front frame relative rotations to the rear frame, with could cause varying disturbances in the magnetic field. The hub motor also negatively affected the sensor readings and these may have been too great to tune out. I also realized that going with a proprietary generic estimator is a bad idea, especially when one has a good model of the dynamics of the rigid body that the sensor is attached to. In our case if the Kalman filter was programmable, we could tailor it with the bicycle model to improve the orientation estimation significantly. Also if the VN-100 could accept input signals, the filter could be tuned well too. After countless hours trying to tune their proprietary filter I gave up and went with a classic roll angle measurement design that I should have done in the beginning.

I designed a simple trailer, *Figure 9.5*, that was pulled behind the bicycle to measure roll angle with a potentiometer, much in the way the steer angle was measured. The trailer needed to be light such that it didn't adversely affect the lateral dynamics and be able to give a good estimate of the roll angle. All of our experiments were to be on smooth surfaces, so the vibration issues that on-road tests have seen were of little concern. I designed the trailer around two caster style polyurethane wheels (roller blade wheels). They were attached to a frame which attached via a revolute joint aligned with the roll axis to a yoke that attached at the axle of the rear wheel.

The potentiometer effectively measures the angle between the yoke and the main trailer frame[4]. For a direct mea-

[3] See our selection spreadsheet at https://docs.google.com/spreadsheet/pub?key=0Asn6BMg-bB_EdFJKVXFfeEgyMnpwR0JXNVlOYjg0Q0E&output=html

[4] As designed, the potentiometer measures exactly the angle between the yoke and the trailer frame. This is somewhat limiting as the full range of the potentiometer isn't utilized as was in the steering angle design. This effectively reduces the measured voltage range from the potentiometer, especially since the measured angles are often no more than 10 degrees. The NI USB-6218 has 16 bit resolution so it still adequatedly measures the data, but a step down gearing would improve the resolution of the roll measurement.

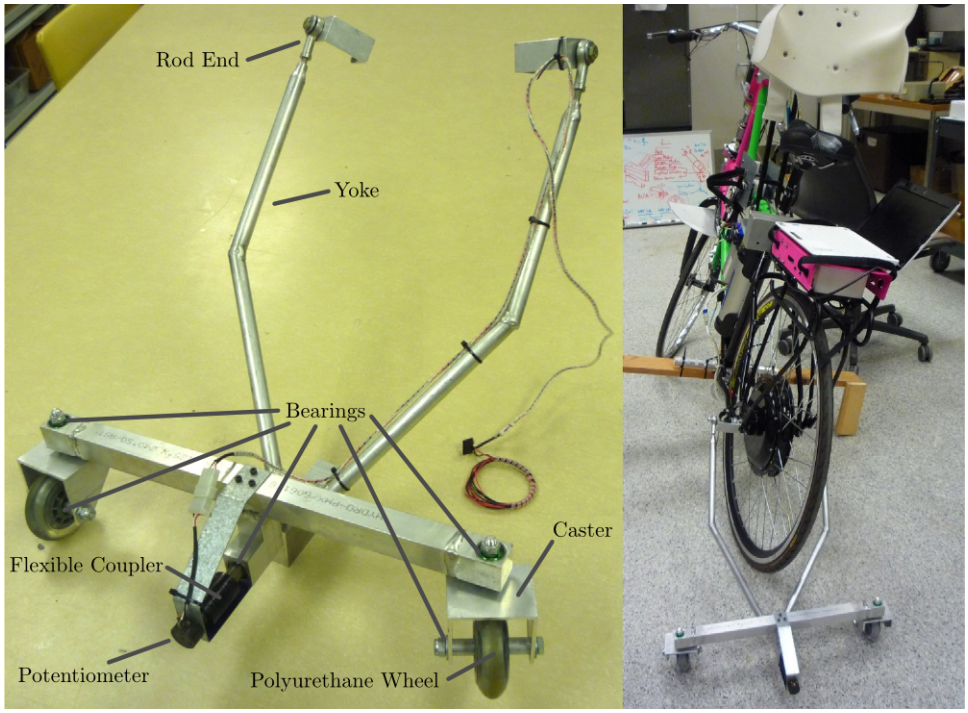

Figure 9.5: On the left is photo of the roll angle trailer with it's components annotated. The right photo shows it attached to the instrumented bicycle.

surement of the true roll angle of the bicycle, the trailer roll axis must lie in the ground plane, but this is physically impossible so it is preferable for the axis to be as close to the ground as possible. *Figure 9.6* shows how the yoke pitch angle and the trailer roll angle change as functions of the bicycle roll angle for various heights above the ground. Notice that the trailer roll angle is virtually identical to the bicycle roll angle for given heights.

9.5.2 Steer

The steer angle is easy to measure with either some form of write recorder, potentiometer, or encoder and has been accurately measured on many bicycle and motorcycle systems since the early 50's. Of the early methods, [Wil51] has a particularly interesting mechanical protractor design and [Doh53] makes use of a mechanical write recorder. Because the front frame is attached to the rear frame via a revolute joint only an additional single orientation and rate measurement is needed to measure the front frame motion. I used a similar design and setup as the Delft instrumented bicycle, *Figure 9.7*: a potentiometer for relative steering angle measurement and a single axis rate gyro for the body fixed angular rate of the front frame about the steer axis[5]. I modified the design with some minor improvements such as better tension adjustability and switching to a screw mount potentiometer.

9.5.3 Wheel Rate

As has been shown in previous chapters, bicycle dynamics are highly dependent on speed. This requires good estimation of the average speed for each constant speed run. I measured the rear wheel rate in the same fashion as on the Delft instrumented bicycle. We mounted a small DC permanent magnet motor (Globe Motors E-2120 without the encoder) to the rear frame in much the same way as a simple friction generator for a bicycle light *Figure 9.8*. A small

[5] The Silicon Sensing rate gyros had to be purchased in bulk but they offered samples. A single sample gyro cost upwards of $300 with half of the price required to ship a 1' x 1' x 1' giant box from Japan to California for a 1" x 1" x 1" sensor. I initially thought that this was worth it for the quality of the sensor, but I never saw any appreciable difference in the sensor quality as compare to the rate gyros on the VN-100 which can be purchased individually for less than $50.

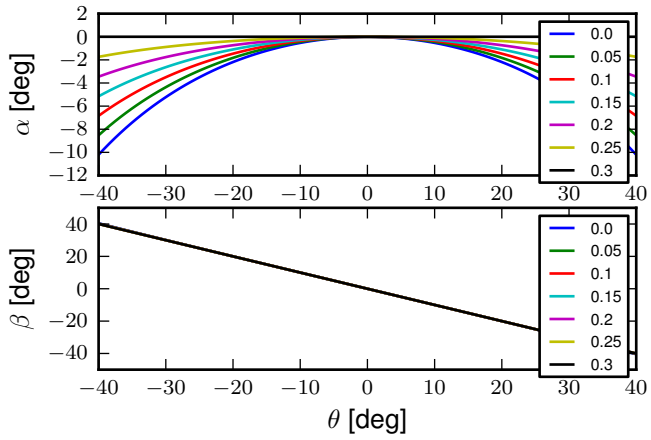

Figure 9.6: The yoke pitch angle α and the potentiometer angle β as a function of the bicycle roll angle θ for different for various joint heights h. The potentiometer angle is highly linear with respect to the roll angle. Generated by `src/davisbicycle/roll_angle_trailer.py`

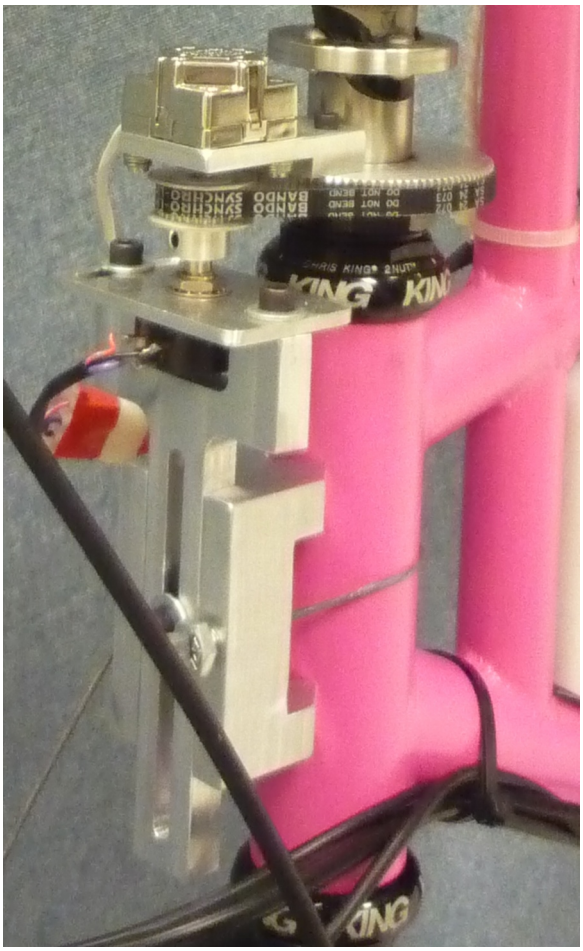

Figure 9.7: The steer angle and steer rate sensors.

knurled aluminum disc on the motor shaft engaged the sidewall of the tire which is radius r_c from the wheel hub. r_c was slightly different for runs 0 to 226 than for run numbers greater than 226 because it was remounted for better tangential disc to tire contact.

$$r_c = \begin{cases} 0.333m & \text{if the run number is} \leq 226 \\ 0.320m & \text{if the run number is} > 226 \end{cases} \tag{9.1}$$

The voltage of DC motors is linearly proportional to the angular speed of the disc. The disc diameter, $r_d = 0.029$ m, was chosen such that 0 to 10 volts would correspond to approximately 0 to 30 mph.

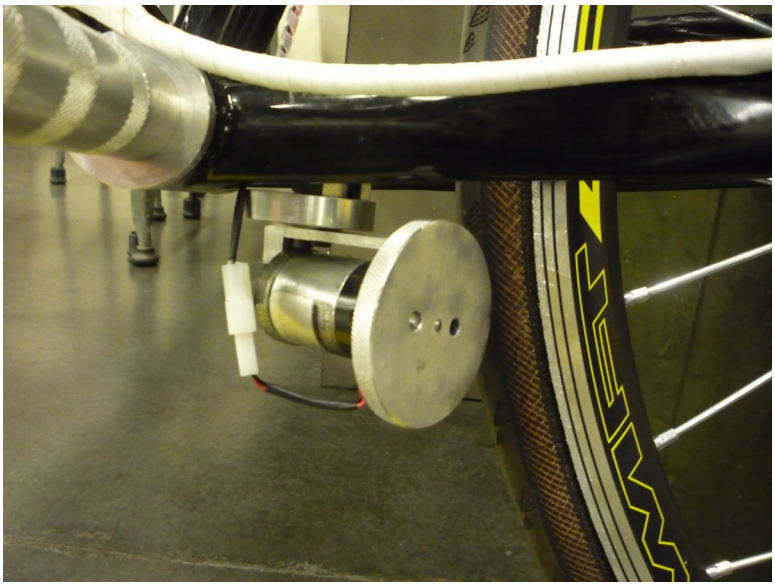

Figure 9.8: The wheel rate sensor mounted just below the bottom bracket. The original configuration is pictured where the velocity of the contact point was not quite in the plane of the disc. We later remounted it so that the motor disc contacted the tire casing tangential to the linear velocity at the contact point.

9.5.4 Sensors

Table 9.2 gives the characteristics of the final choice in sensors.

Table 9.2: Final Kinematic Sensors, *Accuracies reported with respect to the calibrated and filtered output.

Measurements	Range	Accuracy	Sensor
Roll Angle	$\pm 42.5°$ (pot $340° \pm 5°$ with 1:4 gear reduction)		Single turn potentiometer (ETI Systems SP22F)
Steer Angle	pot $340° \pm 5°$		Single turn potentiometer (ETI Systems SP22F)
Yaw Rate, Roll Rate, Pitch Rate	± 500 deg/s, ± 500 deg/s, ± 500 deg/s	$< \pm 0.06$ deg/s (bias stability)*	VN-100 (Invensense IDG500 and ISZ500)
Front frame fixed angular rate about the steer axis	± 200 deg/s	See manufacturer's spec sheet	Single axis rate gyro (Silicon Sensing CRS03-04S)
Rear wheel rate	0 - 40 rad/s		Globe Motors E-2120 DC Motor without the encoder
Rear frame 3D point acceleration	± 2 g	x/y :math‘<2‘ mg, z < 3 mg (bias stability)	VN-100 (Analog Devices ADXL325)

The VN-100 was mounted to the rear frame with its factory X axis aligned with $\hat{c}_1$, Y axis aligned with the $-\hat{c}_3$, and Z axis aligned with $\hat{c}_2$ as described in Chapter *Bicycle Equations Of Motion*. I made use of the VN-100's ability to output it's measurements with respect to a different reference frame than the factory frame and aligned the X, Y and Z axes with the $\hat{c}_1$, $\hat{c}_2$ and $\hat{c}_3$ axes, respectively. This pre-output rotation matrix was recorded in the meta data for each run. The steer rate gyro was attached such that its axis was aligned with $\hat{e}_3$.

The yaw, roll and pitch rates as defined in Chapter *Bicycle Equations Of Motion* are computed from the measured body fixed rear frame rates $\omega_{x,y,z}$, the measured roll angle q_4 and the steer axis tilt λ

$$\begin{aligned} u_3 &= \frac{\omega_x \sin(\lambda) - \omega_z \cos(\lambda)}{\cos(q_4)} \\ u_4 &= \omega_x \cos(\lambda) + \omega_z \sin(\lambda) \\ u_5 &= \omega_y + \omega_x \sin(\lambda)\tan(q_4) - \omega_z \cos(\lambda)\tan(q_4) \end{aligned} \tag{9.2}$$

The steer rate is found by subtracting the body fixed rear frame rate, ω_z from the body fixed front frame rate, ω_{ff_z}

$$u_7 = \omega_{ff_z} - \omega_z \tag{9.3}$$

The yaw angle, q_3, can be estimated by integrating the yaw rate, u_3. The result is affected by drift but for runs that are centered around zero, this drift can be removed by subtracting the resulting line from a linear regression on the drifted data. The resulting yaw angle can be used to compute estimates for the rear wheel contact velocities: u_1 and u_2 by making use of the measured rear wheel rate, u_6.

$$\begin{aligned} u_1 &= -u_6 r_R \cos(q_3) \\ u_2 &= -u_6 r_R \sin(q_3) \end{aligned} \tag{9.4}$$

The rear wheel contact rates can also be integrated and the linear drift subtracted out to find the position from an arbitrary initial condition. I also make use of the lengthy non-linear relationships for the front wheel contact points as a function of the rear wheel contact points, steer, roll, and pitch to compute the front wheel track. See the `BicycleDataProcessor` source code for these details.

9.6 Kinetics

A human is able to use contact forces and body movements to control the bicycle. The forces applied by the rider's hands to the handlebars are the most obvious and most effective method of controlling the bicycle [6]. But the rider also can impart forces through the seat and the foot pegs. If the rider is controlling the bicycle without touching the handlebar, these would be the only locations of rider to bicycle contact. For a complete dynamic picture of the rider's control inputs, all of the essential forces and moments at the rider/bicycle interface's need be measured. In the case of the rigidified rider, the steering torque is sufficient for characterizing the control inputs.

For the sake of perturbing the closed loop bicycle/rider system, we also needed to measure and externally apply force or torque. We opted for a simple lateral force perturbation.

9.6.1 Lateral Perturbation Force

I was introduced to the idea of external lateral force perturbations from some of my first email exchanges with Arend and when I was in Delft we did several experiments with lateral perturbations [KSM09]. We applied the impulsive type of perturbations without measuring the applied force assuming they could be modeled as impulses. There are also many other past attempts at exciting the system. [RM71] on the other hand attached a calibrated rocket to the handlebars of a riderless bicycle to give a known step input to steer torque. [Eat73b] had the motorcycle rider tap the

[6] [Wei72] shows that large rider lean angles are required to give similar capabilities as steer control. [Sha08] shows that the use of steer torque control is always the more optimal choice than rider lean torque control for optimal control based on path deviation error and control power. [MKSH11] experimentally shows that the steering angle magnitudes are much larger than other rider body movements.

handlebars to apply an impulse and also drop weights from the side of the motorcycle to apply a roll torque. [DFT12] similarly had the motorcycle rider apply impulsive forces to the handlebars to excite the weave mode. [DL11] discusses several methods of applying a roll torque to the bicycle including a mass swing, a mass slider, a rope, and laterally accelerating the ground. His designs are intended to apply an oscillatory roll torque to facilitate system identification in the frequency domain[7].

We weren't able to come up with a clever way of perturbing the system with a harmonic input and frankly I did not think a great deal about the perturbation methods, so I simply attached a 100 lb force load cell (Interface SSM-100) in line with a rope attached to the underside of the bicycle seat. We intended to apply impulsive lateral forces to the bicycle rear frame. This worked for the first round of experiments, but only provided a negative lateral force as it could only be pulled. After the first experiment attempts, we solved this by attaching the load cell in line with a push/pull stick which was attached to the seat via a ball joint, *Figure 9.9*. The ball joint prevented any external moments from being applied to the bicycle and the force to be in a mostly lateral direction.

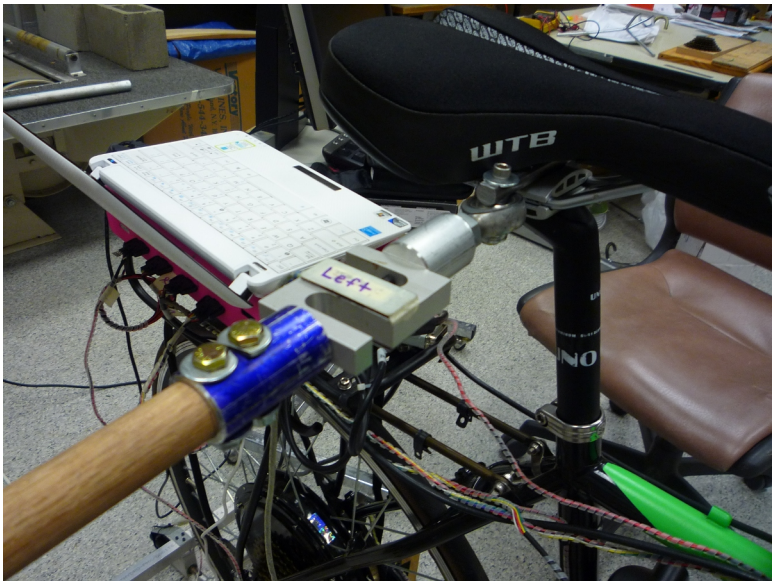

Figure 9.9: The lateral force stick attached to the underside of the seat. A rod end was used at the connection to prevent moments from being applied to the rear frame.

We were also concerned with the rider predicting the lateral perturbations. Ideally the rider shouldn't be able to predict the instant or the direction of the upcoming perturbation. The rider wore a helmet with a blinder on the side of the lateral force stick so that they could not see the movements of the stick or the person operating the stick. And secondly, we wrote a simple program which randomly instructed the perturber when and in which direction to apply the force for the treadmill experiments. During the runs in the gymnasium, we retained the blinder and provided the perturber with a series of random push/pull sequences before each run. The operator applied as many perturbations as possible over the length of the track, which didn't give much unpredictability in the time of perturbation. *Figure 9.10* gives an example perturbation measurement during a treadmill run.

9.6.2 Seat Post

As already mentioned, I had intended to measure the forces at all of the rider/bicycle interfaces. Cal Stone [Sto90] developed a seat post which was capable of measuring five components of force in the seat post with an array of strain gauges. I was going to add a strain gage bridge for the remaining unmeasured component, torque about the seat axis, to complete the force measurements and use the seat post in combination with the flexible rider harness. The seat post

[7] A sum of sines would be ideal, see [DL11] for some ideas on other types of inputs. It has been shown that a sum of sines can provide a non-predictable signal to the human [MK74].

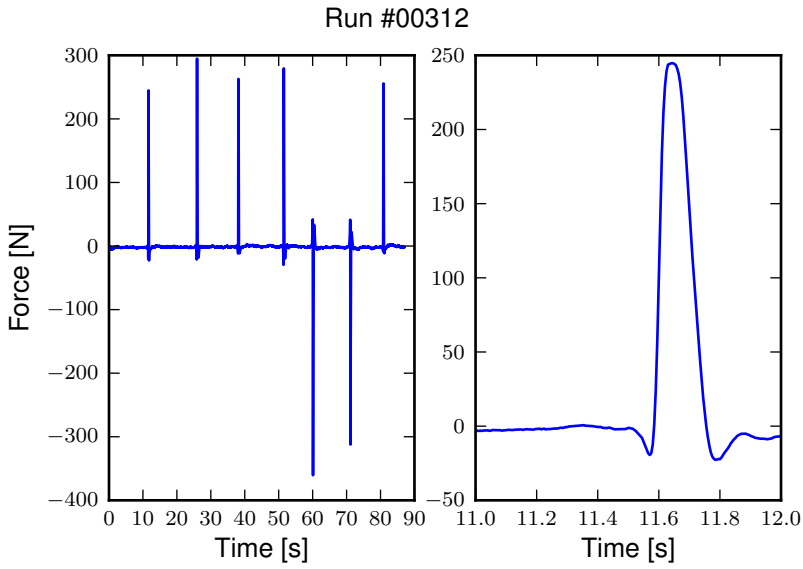

Figure 9.10: The left figure shows an example of a lateral perturbation sequence during a treadmill run. The right figure shows the profile of a perturbation over one second.

was originally instrumented by simply gluing strain gage bridges onto a stock seat post and carefully calibrating the sensor for a variety of loading combinations. The accuracy of the seat post force measurements was not all that high due to the small strains seen along the outer wall of the seat post. In a way, the use of the seat post was more because of the convenience of having access to it than obtaining the actual kinetics involved when using the flexible rider harness. Gilbert and I spent a lot of time figuring out how to use and calibrate the seat post and associated equipment. Fortunately, a copy of Cal's research notes were found that helped decipher most of the work. We even got in touch with Cal and he provided additional information. But as time constraints weighed in, we had to abandon the effort.

9.6.3 Foot Pegs

Gilbert designed a set of foot pegs such that clip-less bicycle pedals could be screwed into the ends providing secure attachment of the feet but allowing easier detachment, *Figure 9.11*. Each foot peg was fit with two strain gage bridges to measure the downward force applied by the rider's feet. These were also abandoned due to time constraints.

9.6.4 Steer Torque

A rider applies forces to the handlebars that cause the front frame to rotate relative to the bicycle frame. These forces can be lumped into an effective steer torque. Steer torque is the most effective natural input to control a bicycle and the input that the human most often utilizes. [RL72] explicitly differentiates steer torque based control from steer angle as opposed to [VLS69] which hypothesized that steer angle was the controlled input. [Wei72] demonstrates that steer angle control input has poor gain and phase margins as compared to steer torque control input. [WZT79] shows that a no hand lane change is much less "precise and efficient" as to one done with steer torque control. [Sha08] shows that steer torque is always the optimal control input when the cost function is based on control power. Accurately measuring the applied steer torque can provide rich data with which to understand the bicycle dynamics and the validity of the underlying models. But steer torque is one of the more difficult variables to properly measure. The required steering torque for controlling a bicycle in normal maneuvers is of relatively low magnitude, typically less than 5 Nm. This small torque can be swamped by the other potentially large forces a rider may apply to the bicycle's handlebars. These small torque magnitudes require a well designed load cell to give accurate measurements.

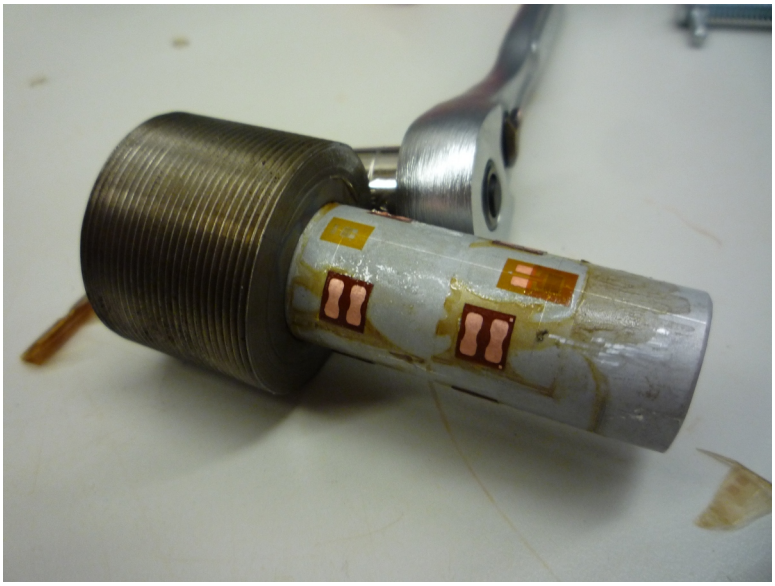

Figure 9.11: One of the foot pegs after the strain gages were applied. The 7075 aluminum peg was press fit into the bottom bracket insert made from 1018 steel.

There are very few published studies that measure or attempt to measure steer torque on a bicycle or lightweight single track vehicles and these measurements typically do not match the results of the analytical models. There have been more attempts at measuring the steer torque on motorcycles.

Bicycle Experiments

[DL97] David de Lorenzo instrumented a bicycle which could measure pedal, handlebar, and hub forces to characterize the in-plane structural loads during downhill mountain biking. The handlebar forces were measured with a handlebar sensitive to x (pointing forward and parallel to the ground) and z (pointing upwards, perpendicular to the ground) axis forces on both the left and right sides of the handlebar. Net torque about any vector in the fork plane of symmetry can be calculated from the applied forces. Figure 3d in the paper shows a single plot of steering torque with maximums around 7 Nm. The stem extension torque (representing the torque from pushing down and up on the handlebars) reaches 15 Nm, which is about twice the maximum steer torque shown. The calibration details lead me to believe that the crosstalk from the all of the forces and moments on the handlebars gives a very low accuracy for the reported torques, probably in the ± 1 to 3 Nm range.

[JD98] They don't measure steer torque explicitly but attempt to predict the contributions to the torques acting on the front frame based on orientation, rate and acceleration data taken while riding a bicycle with no-hands. They show a single graph with torques under ± 2.5 Nm acting on the front frame about the steer axis.

[CBAS03] This is a report about a design project at UCSB to develop and implement a steer torque measurement device on a bicycle. The experiments and measurements seem to be one of a kind for bicycles up to that point in time. They begin with doing some basic experiments by attaching a torque wrench to a bicycle and made left at right turns at speeds from 0 to 13 m/s (0 to 30mph). The torques were found to be under 5 Nm except for the 13 m/s trial which read about 20 Nm. They designed a pretty nice compact torque measurement setup by mounting the handlebars on bearings and using a linear force transducer to connect the handlebars to the steer tube, *Figure 9.12*, which reduced the effects of other moments and forces acting on the steer tube. It seems that downward forces applied to the handlebars could possibly still be transmitted to the load cell. The design does allow one to choose the lever arm for the load cell, thus giving some choice to amplify the force signal. They set it up to measure from 0 to 84 Nm with a Model SM Series S-type load cell from Interface with a 670 Newton range. This range is quite large with respect to the torque values found in the first experiments. They self calibrated the sensor with with a set of pulleys and cables to apply a pure torque to the handlebars. They

measured the torque during two different maneuver types: a sharp turn at various angles and steady turns on various diameter circles, both at 10 mph (4.5 m/s). The rider maintained constant speed through visual feedback of a speedometer. The signals were very noisy and Cheng filters the data with a moving average. He was not able to identify any countersteering. Cheng claimed the rider turns the handle bars right to initiate a right turn, which is counter to what models and other experiments predict. For the sharp turns the highest reported torque is about 10 Nm, for the steady turning they report the highest average torque as 1 Nm.

[ASKL05] Åström et al. talks briefly about the steer torque measurement system constructed for the UCSB instrumented bicycle but with little extra information. He does include a nice photo of the apparatus, *Figure 9.12*.

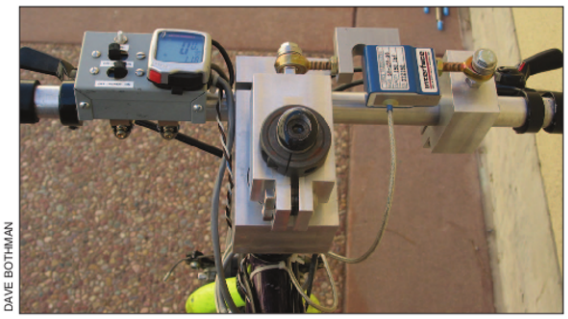

Figure 16. *The handlebar of the instrumented UCSB bicycle. Steer torque is measured using a strain gauge on the right. The box on the left contains a display for speed and switches for data logging.*

Figure 9.12: Cheng's design, from [ASKL05].

[IM06] They construct a bicycle with a steer motor and controller which treats the rider's additional input as an additive input instead of a disturbance. The rider's steer torque contribution is estimated from the motor torque and the handlebar and motor moments of inertia. Little detail is given to properly assess the design, but measuring steer torque by motor current may be effective. They are one of the few studies that takes into account some of the inertial effects of the handlebar.

[CP10] He designed a custom torque sensor that fit inside a bicycle steer tube. He mostly removed the crosstalk effects due to an axial load on the sensor, but the design still seems very likely susceptible to bending moments on the steer tube. He also didn't account for the dynamic inertial affects of the handlebar and fork/wheel which are above and below the sensor, but this is most likely inconsequential for steady turns. His measured steer torques for steady turns never exceeded 2.4 Nm. He wasn't able to predict steer torque well with his bicycle model and only points to the fact that the sensor was 90% oversized for an explanation of the poor results.

[VDO11] Designs a steer torque sensor for a bicycle which has a range of about ± 7.5 Nm. He was acutely aware of crosstalk issues with respect to the other forces applied to the handlebars and tried to design accordingly, but found that his design was still very susceptible to handlebar loads. He modifies the device to eventually get more reliable readings. He also didn't account for the inertial effects of the front frame. He had test subjects ride the bicycle around town so the data is difficult to interpret.

Motorcycle Experiments

[Wil51] Wilson-Jones beautiful treatise on single track vehicle dynamics may document the first steer torque measurements ever done. He constructed an mechanical analog torsion bar that provided the instantaneous steer torque readings to the motorcycle driver via a head tube mounted protractor. He used this to gage torques in turns.

[Kon55] Kondo's work is the first electrical measurement of steer torque that I've come across. He does not give great detail of the sensor and shows only one plot of steer torque and steer angle from experimental measurements. The units for the steering force are in kilograms and I'm not completely sure what was being measured. My poor understanding is limited by the light translations with which I got help.

[Fu65] Measures steering torque in steady turns but the resulting data is not published in this paper. He refers to it as future work in the review section. He claims agreement with [KF59] of which he was a co-author, but I wasn't able find this paper.

[Eat73b] Eaton attached a torque bar with strain gages to the top of the motorcycle handlebar, *Figure 9.13* and had the rider control the motorcycle with one hand to get a measure of steering torque. The steer torque sensor design was very simplistic, but he found good agree with his motorcycle model when identifying the motorcycle from the steer torque input and roll angle output. The motorcycle steer torque measurements are probably more forgiving as the steer torques are of a much higher average magnitude. For his roll stabilization tasks (i.e. straight riding) he measured maximum values of steer torques of 3.4 Nm for speeds of 15 to 30 mph.

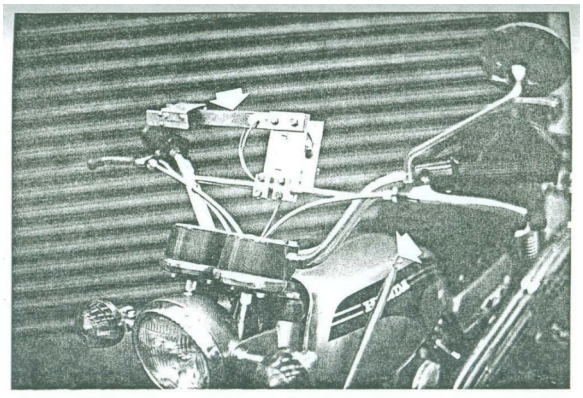

Figure 5.1 Steering torque bar and throttle control (arrows).

Figure 9.13: Eaton's simple bar torque sensor.

[WZT79] Weir et al. designed a modular torque sensor which could be affixed to multiple motorcycles, *Figure 9.14*. The range was +/- 70 Nm with 1% accuracy and >10 Hz dynamic range. The crosstalk due to the other moments on the steer was removed by utilizing two thrust bearings. It included stops to prevent sensor overload protection and weighed 14 Newtons. They comment that the handlebars are significantly rigid for their purposes. They comment that the range is too large for small amplitude inputs used in steady turning and straight running and that more sensitivity would be needed to measure these accurately. Weir used this to measure steer torques for several motorcycles at various speeds (>10 m/s) for steady turning and lane change maneuvers. Steady turning produced torques in the range of -10 to 30 Nm and the lane change produced -20 to 55 Nm.

[SH88] They measure steer torque on four motorcycles during high speed lane changes. No detail of the steering torque measurement system is given but they show the time traces of steer torque for some of the maneuvers which vary between -20 and 20 Nm. The time traces have little visible human remnant or noise, which is questionable.

[TMH00] The abstract for this paper indicates steer torque measurements on a motorcycle, but I haven't located the paper. I include the citation for completeness.

[BDL00] Same description of the transducer as [BBCL03].

[BBCL03] Biral et al. designed a custom steer torque measurement system for a motorcycle using a cantilever beam, *Figure 9.15*. The handlebars were mounted on a bearing similar in idea to [WZT79] but the steering torque load is transmitted through a thin cantilever beam which engages the fork. The design is such that other handlebar forces will not influence the torque measurement. It includes stops in case the beam breaks. They report

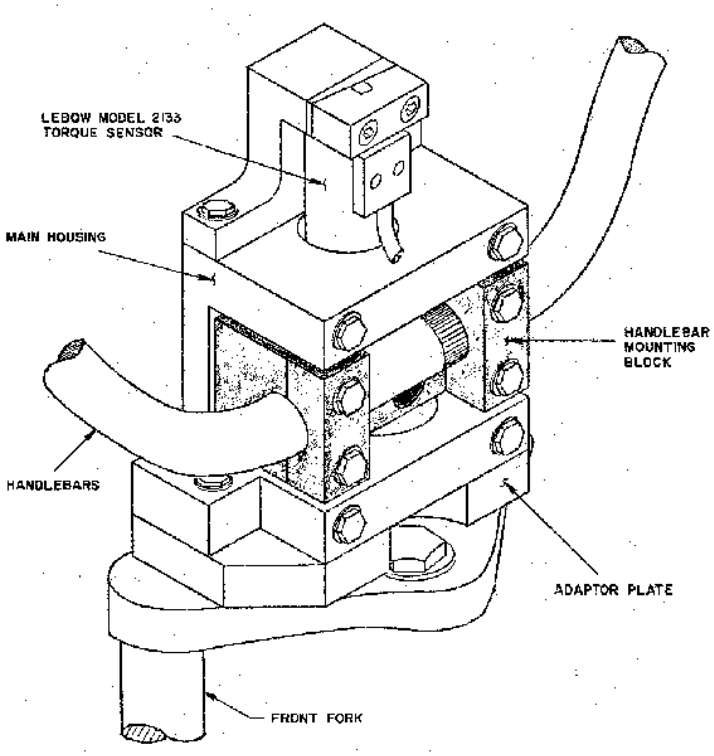

Figure 151. Steer Torque Sensing Assembly

Figure 9.14: The steer torque measurement design from [WZT79]. The adaptor plate allowed one to attached the main housing to a variety of motorcycle forks. The handlebar mounting block "floated" on a set of thrust bearings that resisted all forces applied to the handlebars except the moment about the steer axis. The Lebow torque sensor resisted the moment about the steering axis to give a pure torque measurement.

experimental values for torque that match their model predictions very well. The measure torques from -20 to 20 Nm for a slalom maneuver at 40 m/s.

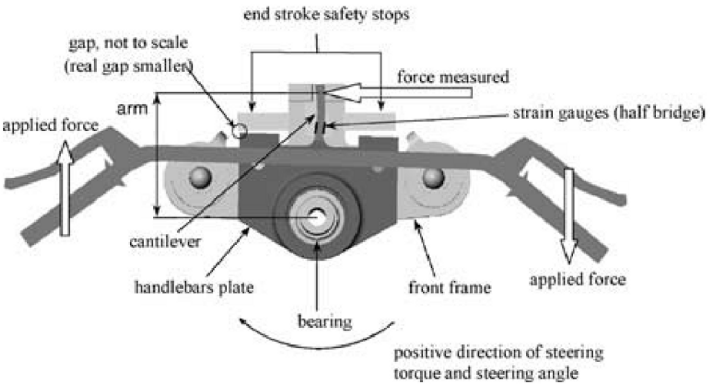

Figure 9.15: The cantilever beam design taken from [BBCL03].

[Jam02], [Jam05] James measures steer torque on an off-road motorcycle by attaching a lightweight secondary handlebar connected to the primary handlebar via a load cell. In the second paper he has a single wheel trailer attached to the vehicle.

[CMMR06] They measure steer torque on a scooter during a lane change and turning to compare with their model. No detail is given on how steer torque is measured, so I can't comment on the quality of the measurement but they report values of -15 to 40 Nm on a couple of graphs. The paper is extremely poor and makes false conclusions.

[Eve10] He mounts two axis load cells at the handlebar grips to measure the forces on the grip. This puts the sensor right at the human/machine interface thus negating the need to worry about the inertial effects of the front frame. For his obstacle maneuver tests the maximum steer torques were no greater than 40 Nm.

[TJ10] Measured motorcycle steer torque in steady turns and slalom maneuvers. The torques in the two time history graphs are less than 20 Nm.

Bicycle Models

[LS06] Limebeer and Sharp show a graph of a steer torque pre-filter (i.e. torque generated for roll control) output to command a ~40 degree roll angle for the benchmark bicycle model. The torques are in the realm of -0.5 to 2.5 Nm.

[Sha07b] Sharp uses the benchmark bicycle model and an LQR controller with preview to follow a randomly generated path that has about 2 meter lateral deviations. The bicycle is traveling at 10 m/s and the steer torque ranges from about -15 to 15 Nm. Medium control reduces the torques to under ± 10 Nm. Straight line to circle path maneuvers show torques ranging from -0.5 to 0.5 Nm for loose control and -2.5 to 2.5 for medium control.

[CH08] They model a recumbent bicycle with the Whipple model and additional rotating legs. The bicycle is stabilized in roll from 5 to 30 m/s requiring up to ± 8 Nm of steering torque, which is a function of the leg oscillation frequency.

[Sha08] Sharp used the benchmark bicycle model and an LQR controller with preview to make a bicycle track a 4 meter lane change at 6 m/s. During this maneuver, the steer toque ranged from about -1 to 1 Nm. He also showed a very fine steer torque variation in the range of 0 to 0.0025 Nm about 10 meters before the start of the lane change.

[PH09] Peterson and Hubbard show the steady turning required steering torques for the benchmark bicycle on page 7. The torques for lean angles from 0 to 10 degrees and steer from 0 to 45 degrees are under 3 Nm.

Motorcycle Models

[Sha71] Reports steady state motorcycle steering torques for 10 degree banking turns in the range of -25 Nm to 2.35 Nm for speeds 10 ft/s to 160 ft/s.

[CDL99] Studies steady turning of a motorcycle model with toroidal tires and tires as force generators. For slower speed steady turns, the model predicts steering torques up to 10 Nm.

[TSSF06] They stabilize a motorcycle model at roll angle up to 30 degrees with -5 to 7.5 Nm of steer torque.

[Sha07a] Sharp uses a multi-degree of freedom motorcycle model and an LQR controller with preview to control a motorcycle moving at 30 m/s through a 4 meter lane change and a 250 meter S-turn. For the lane change he gets torques ranging from about -20 Nm to 55 Nm for a more aggressive control and -4 to 6 Nm for less aggressive control. The S-turn gives torques from -40 Nm to 70 Nm with a sharp peak in torque in the middle of the S-turn.

[CLP07] They study steady turning of motorcycles and show a plot that predicts steer torques in the range of -3 to 10 Nm for lateral accelerations from 0 to 11 m/s^2 and speeds from 5 to 50 m/s.

[MN07] Their steer controller for Sharps four degree of freedom motorcycle model shows a -50 nm maximum steer torque for a commanded roll angle of 20 degrees.

Steering torque has been measured in relatively few instances of bicycle experiments and not many more for motorcycles. Of these, very few of the designs may actually measure a pure rider applied steer torque. This is more consequential for bicycles than motorcycles because the small torques used in typical bicycle control are certainly less than 10 Nm with the majority less than 5 Nm. [VDO11], in particular, showed how sensitive the torque measurements are to other handlebar loads. Also, most of these designs measure the torque somewhere between the rider hands and the ground contact point. This is a physically ideal way to measure the steer torque, but no one has accounted for the dynamic inertial effects of the front frame above or below the sensor. [Eve10] may be the only design which mitigates this issue. I'll show later in this chapter that for maneuvers that require large steer angular accelerations, that this is a significant additive effect.

With these previous works in mind, I wanted to develop a very accurate steer torque measurement system for our bicycle. If one is interested in extracting the "pure torque" applied by the rider to control the bicycle for model validation purposes, it is critical to take care of several important details.

Another thing to note is the differences in magnitudes of steer torques in the bicycle models as compared to the bicycle experiments. The steer torque used to control the various models presented are much lower than the measured values. This implies that there may be some missing components of torque in the models, especially with respect to tire interactions with the ground.

I started by taking some crude steer torque measurements myself, similar to the first method presented by [CBAS03], as I hadn't found Cheng's paper or any of the post 2008 references yet. Secondly, I address the issue of the potential loads acting on the steer tube other than steer torque. And finally, I show the calculations to account for the inertial effects of the front frame.

Torque Wrench Experiments

Following in Cheng's footsteps, we decided to do some experiments with an accurate torque wrench to get an idea of the maximum torques we would see in our experiments. We designed a simple attachment to the steer tube that allowed easy connection of various torque wrenches, *Figure 9.16*. A helmet camera was mounted to the bicycle such that it could view the torque wrench, handlebars and speedometer relative to the bicycle frame, *Figure 9.17*. The torque wrench (CDI Torque Products 751LDIN) had a range from 1.7 to 8.5 Nm and a $\pm 2\%$ accuracy of full scale (± 0.17 Nm) for static measurements, *Figure 9.18*. The bicycle speed was maintained by an electric hub motor (i.e. no pedaling) with a crude power based cruise control, but speeds remaining fairly constant.

We recorded video data for two riders performing seven different maneuvers: straight run into tracking a half circle of radius 6 and 10 meters, tracking a straight line, 2 meter lane change, slalom with 3 meter spacing, and steady circle

Figure 9.16: The mounting bracket for the torque wrenches. The lower portion clamps to a 1 1/8" steer tube and the upper portion clamps of a 1/4" socket end.

Figure 9.17: The dial indicator face of the torque wrench which reads out in inch pounds and newton meters.

Figure 9.18: The complete setup with the frame mounted helmet camera.

tracking of radius 5 and 10 meters. I viewed the videos and noted the maximum and minimum torques for each run. I ignored obviously high torque readings from accelerations due to riding over bumps.

The single comma separated data file includes the run number that corresponds to the video number, the rider's estimate of the speed after the run in miles per hour, the maximum reading from the torque needle after the run in inch-lbs, the rider's name, the maneuver, the minimum speed seen on the video footage in miles per hour, the maximum speed seen on the video footage in miles per hour, the maximum torque seen on the video footage in inch-lbs, the minimum torque seen on the video footage in Nm, and the rotation sense for each run (+ for clockwise [right turn] and - for counter clockwise [left turn]). The videos, data file and R source code are archived at http://www.archive.org/details/BicycleSteerTorqueExperiment01 .

The primary goal was to determine the maximum torques we will see for the types of maneuvers we are interested in. The histogram, *Figure 9.19*, shows that we never recorded any torques higher than 5 Nm and table *Table 9.3* gives the maximum and minimum torques for each maneuver. *Figure 9.20* shows all of the recorded torques as a function of speed. There may be an underlying dependency on speed, i.e. that the maximum torques decrease as speed decreases.

Table 9.3: Maximum and minimum torques values for the different maneuvers.

Maneuver	Maximum Torque	Minimum Torque
Steady Circle (r = 10m)	3.4	-2.4
Steady Circle (r = 5m)	2.4	-2.2
Half Circle (r = 10m)	3.8	-3.2
Half Circle (r = 6m)	3.4	-5.0
Lane Change (2m)	2.9	-2.6
Line Tracking	2.6	-3.4
Slalom	4.5	-4.8

This set of experiments enforces the previously cited experimental findings that steer torques in bicycle control are typically very small. Ideally our sensor's range should be somewhere around ± 8 to 10 Nm.

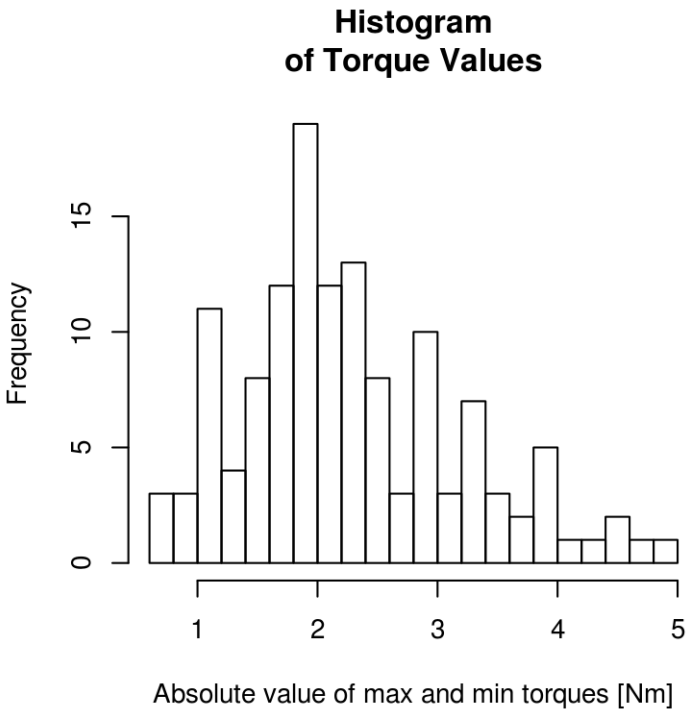

Figure 9.19: A histogram of the maximum recorded torques for all runs. The median is around 2 Nm with torques measured up to 5 Nm. Generated by `src/davisbicycle/torque-wrench.R`.

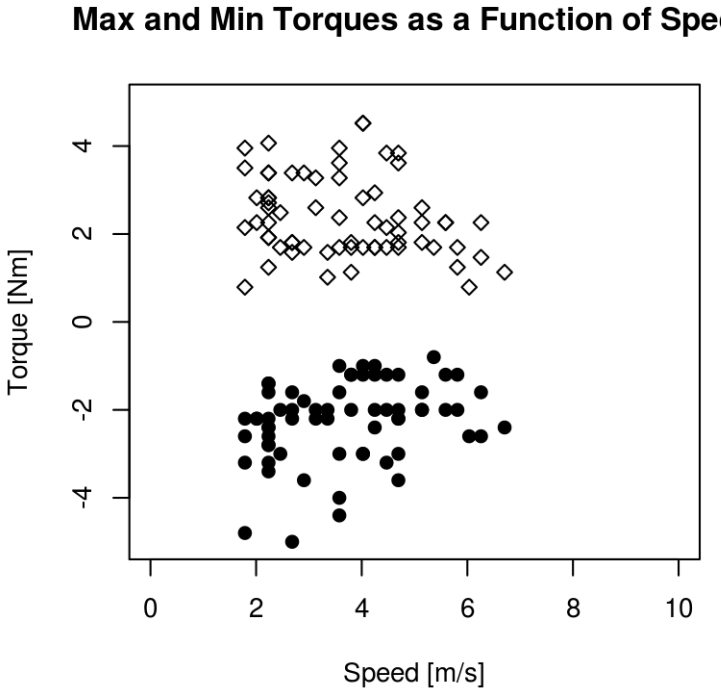

Figure 9.20: The maximum torques as for each run as a function of speed. Generated by `src/davisbicycle/torque-wrench.R`.

Forces on the steer tube

Measuring the steer torque is not trivial. This is because various models predict torques ranging in the 0-2 Nm (0-1.5 ft lbs) range with signal variations and reversals requiring ± 0.01 Nm (0.01 ft lbs) in measurement accuracy. The range and accuracy are easily measured with modern torque sensors, but the fact that large moments can be applied to the fork and handlebars by the ground and/or rider introduces the problem of crosstalk. The forces and moments applied to the fork will corrupt the relatively small torque measurements as they can be hundreds of times larger in magnitude. With this in mind, we seek a way to isolate the torque measurement to eliminate or minimize the crosstalk and get good, noiseless, accurate readings.

One of the simplest ways to measure steer torque may be to apply a strain gauge bridge primarily sensitive in torque to the steer tube of the fork. This method and others would require that the cross sensitivity of the bridge to other loads in the steer tube to be negligible. For example, [DL97] effectively did this with his handlebar design but used several other bridges to measure additional moments and forces in handlebar assembly and calibrated the set of bridges together to help eliminate the crosstalk. The measured steer torques are less than 10 Nm and the loads due to the applied forces at the wheel contact, headset bearings and handlebars can potentially be orders of magnitude greater. [VDO11] clearly experienced the difficultly in removing the cross talk from a steer torque sensor and few studies have explicitly addressed this.

Assuming we may want to measure steer torque somewhere between the handlebars and fork crown, a simple static analysis can be performed to gage the relative magnitudes of loads in the steer tube. The bicycle steer tube has various other forces acting on it. For the most basic case, the ground contact force at the front wheel puts the fork into bending and compression. Likewise the person can apply forces to the handlebars which also put the steer tube into bending and compression. *Figure 9.21* shows the free body diagram for a bicycle statically loaded.

The forces and moments acting on the fork can be isolated algebraically and the fork modeled as a basic beam supported by the headset bearings (points C and D) and the forces/moments due to the ground reaction force and force

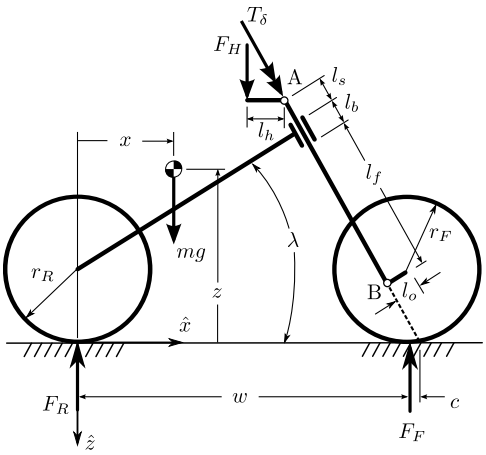

Figure 9.21: The free body diagram allows for an external steering torque, independent downward forces on each handlebar, the ground reaction forces and a force acting on the mass of the bicycle and rider due to vertical acceleration. The vertical acceleration is simply due to gravity when static, but can be thought of as a multiple of the acceleration due to gravity for dynamic purposes.

applied to the handlebars were calculated and applied to points A and B, *Figure 9.22*.

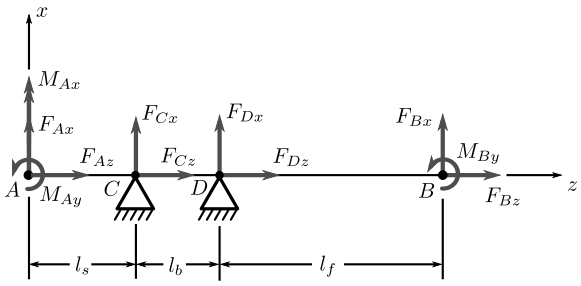

Figure 9.22: The free body diagram of the fork under the loads shown in *Figure 9.21*. The headset bearings at C and D are assumed to not resist moments.

The following graph, *Figure 9.23*, shows what the shear and bending moment diagrams for a 2g vertical acceleration and ~200 N force on one handlebar grip look like both from the side and the front of the bike.

This graph shows that the bending moments and shear stresses can be of much larger magnitude than the steer torques. Misalignment of strain gages and the resulting sensor crosstalk are magnified by the differences in loads and need to be carefully accounted for. If the cross talk strains due to the bending moments are even 1% of the of the total strain due to the moments, that can still corrupt the steer torque measurement.

This analysis also predicts that if no loads are placed on the handlebars the entire portion of the steer tube/stem above the headset has no bending moments and no shear stress. This could be the ideal place for a torque sensor, if one can eliminate the transfer of forces applied by the handlebars to the steer tube.

This lead me through several design ideas but ultimately to a design that isolates the steer torque sensor from the handlebar and fork loads with a zero backlash telescoping double universal joint. The idea solidified after thinking about an upside down tall bike I had created several years before. This bicycle's tall handlebar, to reach the high rider, was attached to the bicycle stem at the headset by a horizontal revolute joint which prevented the rider from applying a fore/aft moment to the handlebar extension, but the rider could still apply steer torques. My design exploited this odd feature by using a universal joint which could only transmit a torque about it's primary axis. The telescoping degree of freedom was added after Gilbert explained its necessity, *Figure 9.24*.

I attached the universal joint to a Futek 150 in-lb ($\pm$17 Nm) TFF350 torque sensor for accurate torque measurements.

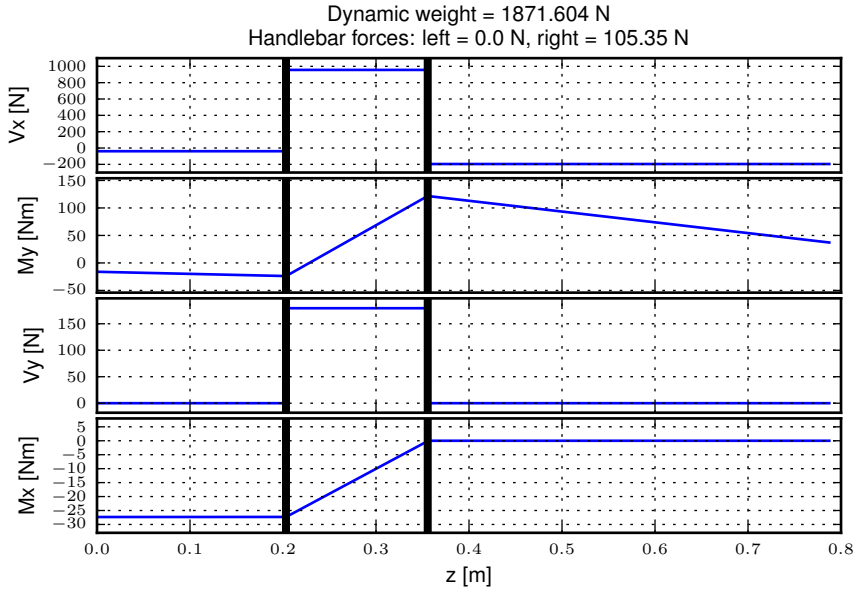

Figure 9.23: The shear and bending diagrams of the fork under a 2g acceleration and a right side handlebar load. The vertical black lines represent the headset bearing locations. Generated by `src/davisbicycle/fork_load.py`.

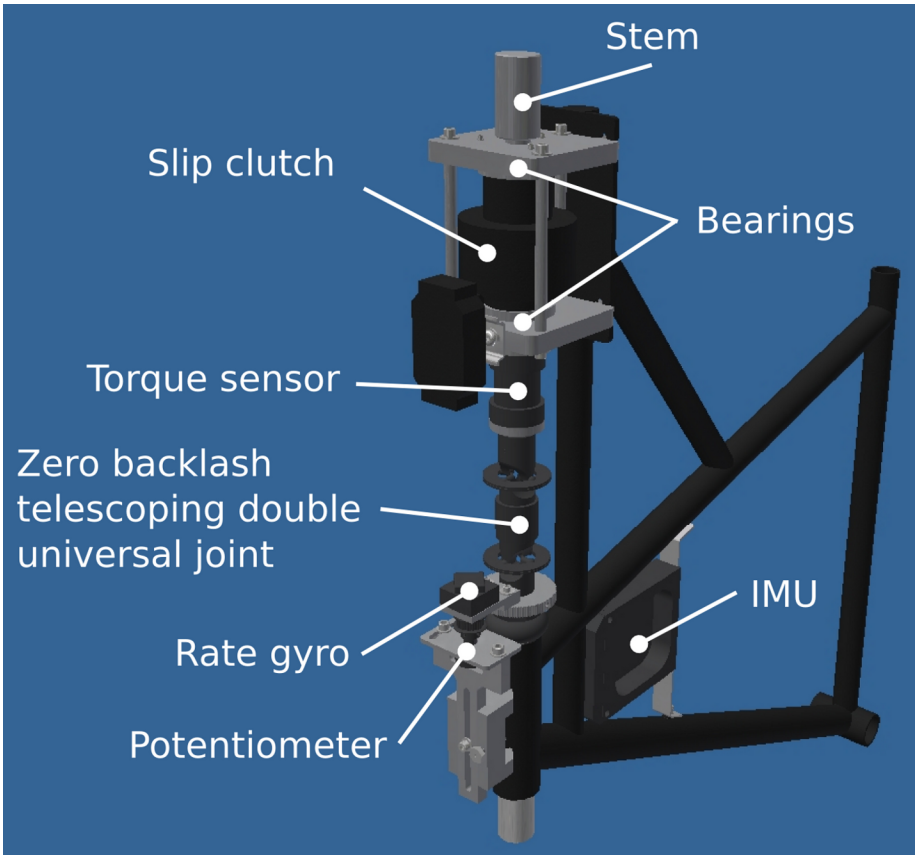

Figure 9.24: The final steer torque design. The steer torque sensor is mounted atop the universal joint such that the only load component which can be transferred through the sensor is an axial torque.

The torque sensor overloads at 150% of the rated output (i.e. 22.5 Nm), so some care was needed to protect the sensor from overload and to prevent the rider from losing steer control if the sensor were to break. I found a "slip" clutch distributed by Stock Drive Products (http://www.sdp-si.com) (SDP). It turned out that the device was the Torq-Tender manufactured by Zero-Max Inc. (http://www.zero-max.com), but as usual practice SDP doesn't readily provide that information. This particularly expensive torque overload protection turned into a major headache. SDP lists the rated torques but with no indication of the operating speed the torques are measured at. It turns out they are with respect to an 1800 rpm operating speed. My rates were rather low, I purchased a much larger torque sensor than I needed. It was rather painful trying to get them to change the springs around the Christmas holidays and check the torque rating at zero rotational speed. The second issue had to do with it not actually being a slip clutch. I wanted the torque protection to slip at a given torque (just under overload of the sensor). The friction based slipping would still allow the rider to control the bicycle, but SDP mistakenly called them "slip clutches" when in fact they are more like binary torque limiters and transfer little to no torque after the limit is reached, so the rider would most likely crash if the torque limiter broke loose. Thirdly, there was play in the torque limiter. I used shim material to take up much of the play, but there remained some backlash. I ultimately locked the slip clutch and relied on careful attendance of the bicycle and the fact that the rider was unlikely to ever apply greater than 22.5 Nm of torque. The runs 0-226 may have a tiny bit of play in the torque limiter and for runs greater than 226 the limiter was locked.

Steer Dynamics

The final design was setup to exclusively measure the torque in the steer tube along the steer axis, but this measured torque, T_M, is not the same as the input torque used for our bicycle models, (i.e. T_δ). The steer torque in the model is defined as the torque between the front frame and the rear frame about the steer axis. If the torque sensor measures the steering torque anywhere but at the interface of the human's hands and the front frame, one must account for the inertial effects of the front frame. As far as I can tell, no one who has measured steer torque on a single track vehicle has accounted for these effects. There is a relationship from T_M to T_δ that requires one to know, at a minimum, the friction in the steer axis bearings above the torque sensor (this is potentially both viscous and Coulomb) and the inertial characteristics of the front frame above the torque sensor[8].

In our case, we measured the torque in the steering column, T_M, from a sensor that is mounted between the handlebars and the fork. The sensor was also mounted between two sets of bearings: the headset and the slip clutch bearings. We are interested in knowing the torque applied about the steer axis by the rider's contact forces to the handlebars, T_δ.

A free body diagram can be drawn of the upper portion of the handlebar/fork assembly, where the lower portion is cut at the steer torque sensor, *Figure 9.25*. The torques acting on the handlebar about the steer axis are the measured torque, T_M, the rider applied steer torque, T_δ, and the friction from the upper bearing set, T_U, which can be described by Coulomb, T_{U_F}, and viscous friction, T_{U_V}.

We measure the angular rate of the bicycle frame, B, with three rate gyros

$$^N\bar{\omega}^B = w_{b1}\hat{b}_1 + w_{b2}\hat{b}_2 + w_{b3}\hat{b}_3 \tag{9.5}$$

The handlebar, G, is connected to the bicycle frame, B, by a revolute joint that rotates through the steering angle, δ, and we measure the body fixed angular rate of the handlebar, w_{h3} about the steer axis directly with a rate gyro. The angular velocity of the handlebar can be written as follows

$$^N\bar{\omega}^G = (w_{b1}c_\delta + w_{b2}s_\delta)\hat{g}_1 + (-w_{b1}s_\delta + w_{b2}c_\delta)\hat{g}_2 + w_{h3}\hat{g}_3 \tag{9.6}$$

The steer rate, $\dot{\delta}$, can be computed by subtracting the angular rate of the bicycle frame about the steer axis from the angular rate of the handlebar about the steer axis.

$$\dot{\delta} = w_{h3} - w_{b3} \tag{9.7}$$

Now define a point, s, on the steer axis closest to the center of mass of the handlebar, g_o.

$$\bar{r}^{g_o/s} = d\hat{g}_1 \tag{9.8}$$

[8] The elasticity of the steer column may also be a factor.

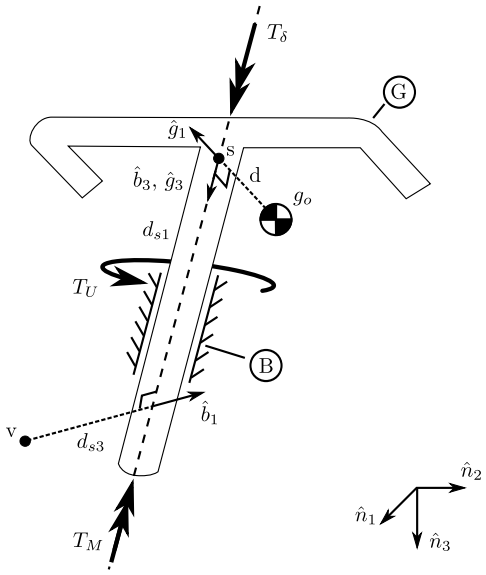

Figure 9.25: A free body diagram of the handlebar with all of the torques acting on it about the steer axis. The rear frame, B, is at an arbitrary orientation with respect to the Newtonian reference frame.

We also measure the acceleration of a point, v, on the bicycle frame.

$$^N\bar{a}^v = a_{v1}\hat{b}_1 + a_{v2}\hat{b}_2 + a_{v3}\hat{b}_3 \tag{9.9}$$

The location of point v is known with respect to s

$$\bar{r}^{s/v} = d_{s1}\hat{b}_1 + d_{s3}\hat{b}_3 \tag{9.10}$$

$^N\bar{a}^{g_o}$ can now be calculated using the two point theorem for acceleration [KL85] twice starting at the point v

$$^N\bar{a}^s = {}^N\bar{a}^v + {}^N\dot{\bar{\omega}}^B \times \bar{r}^{s/v} + {}^N\bar{\omega}^B \times ({}^N\bar{\omega}^B \times \bar{r}^{s/v}) \tag{9.11}$$

$$^N\bar{a}^{g_o} = {}^N\bar{a}^s + {}^N\dot{\bar{\omega}}^G \times \bar{r}^{g_o/s} + {}^N\bar{\omega}^G \times ({}^N\bar{\omega}^G \times \bar{r}^{g_o/s}) \tag{9.12}$$

The angular momentum of the handlebar about its center of mass is

$$^N\bar{H}^{G/g_o} = I^{G/g_o} \cdot {}^N\bar{\omega}^G \tag{9.13}$$

where I^{G/g_o} is the inertia dyadic with reference to the center of mass which exhibits symmetry about the 1-3 plane.

Now, the dynamic equations of motion of the handlebar can be written: the sum of the torques on the handlebar about point s is equal to the derivative of the angular momentum of G in N about g_o plus the cross product of the vector from s to g_o with the mass times the acceleration of g_o in N [Mer75]

$$\sum \bar{T}^{G/s} = {}^N\dot{\bar{H}}^{G/g_o} + \bar{r}^{g_o/s} \times m_G\, {}^N\bar{a}^{g_o} \tag{9.14}$$

We are only interested in the components of the previous equation in which the steer torque appears, so only the torques about the steer axis are examined.

$$\sum T_3^{G/s} = T_\delta - T_U - T_M = \left({}^N\dot{\bar{H}}^{G/g_o} + \bar{r}^{g_o/s} \times m_G\, {}^N\bar{a}^{g_o}\right) \cdot \hat{g}_3 \tag{9.15}$$

And T_δ can be written as

$$\begin{aligned} T_\delta =& I_{G_{22}}\left[(-w_{b1}s_\delta + w_{b2}c_\delta)\,c_\delta + w_{b2}s_\delta\right] + I_{G_{33}}\dot{w}_{g3} + \\ & I_{G_{31}}\left[(-w_{g3}+w_{b3})w_{b1}s_\delta + (-w_{b3}+w_{g3})w_{b2}c_\delta + s_\delta\dot{w}_{b2} + c_\delta\dot{w}_{b1}\right] + \\ & \left[I_{G_{11}}(w_{b1}c_\delta + w_{b2}s_\delta) + I_{G_{31}}w_{g3}\right]\left[-w_{b1}s_\delta + w_{b2}c_\delta\right] + \\ & dm_G\left[d(-w_{b1}s_\delta + w_{b2}c_\delta)(w_{b1}c_\delta + w_{b2}s_\delta) + d\dot{w}_{g3}\right] - \\ & dm_G\left[-d_{s1}w_{b2}^2 + d_{s3}\dot{w}_{b2} - (d_{s1}w_{b3} - d_{s3}w_{b1})w_{b3} + a_{v1}\right]s_\delta + \\ & dm_G\left[d_{s1}w_{b1}w_{b2} + d_{s1}\dot{w}_{b3} + d_{s3}w_{b2}w_{b3} - d_{s3}\dot{w}_{b1} + a_{v2}\right]c_\delta + \\ & T_U + T_M \end{aligned} \tag{9.16}$$

The expression for steer torque can be linearized by assuming that the steer and pitch angles are small, to see the dominant terms around the point of linearization.

$$T_\delta = T_M + T_U + (I_{G_{33}} + d^2m_G)\dot{w}_{g3} + (I_{G_{31}} - dd_{s3}m_G)\dot{w}_{b1} + dd_{s1}m_G\dot{w}_{b3} + dm_Ga_{v2} \tag{9.17}$$

All of the terms in T_δ are measured by the on-board sensors or are previously estimated physical parameters except for the upper bearing frictional torque, T_U. We estimated this torque contribution through experiments described in the following sections.

Bearing Friction

The torque sensor is mounted between two sets of bearings. The upper set are tapered roller bearings and the lower are typical bicycle headset bearings. Each are preloaded a nominal amount during installation. We assume that the rotary friction due to each bearing set can be described as the sum of viscous and Coulomb friction. The Coulomb friction can be described as a piecewise function of the steering rate, (9.18), and viscous friction as a function linear in the steer rate, (9.19).

$$T_{Bc} = t_B\,\mathrm{sgn}(\dot{\delta}) = \begin{cases} t_B & \text{if } \dot{\delta} > 0 \\ 0 & \text{if } \dot{\delta} = 0 \\ -t_B & \text{if } \dot{\delta} < 0 \end{cases} \tag{9.18}$$

$$T_{Bv} = c_B\dot{\delta} \tag{9.19}$$

The total friction due to all of the bearings is

$$T_B = T_{Bc} + T_{Bv} \tag{9.20}$$

To estimate t_B and c_B, we set up the bicycle such that the steer axis was vertical, the front wheel was off the ground, and the rear frame was rigidly fixed in inertial space. We then attached two springs of stiffness k each to the handlebars such that the force from the springs acted on a lever arm, l, relative to the steer axis, *Figure 9.26*.

This configuration allowed us to apply small perturbations to the handlebars and measure the dampened vibrations in the steer angle, steer rate, and steer torque. For the first set of trials the sensors were mounted as they normally are, with the steer angle and rate measurements taken just above the headset and the steer torque measured between the upper and lower bearing sets. We also took data for a second set of trials with the steer rate sensor mounted to the top of the steer column in case the steer column to account for any torsional flexibility.

The equations of motion governing the system are

$$I_{HF}\ddot{\delta} + c_B\dot{\delta} + t_B\,\mathrm{sgn}(\dot{\delta}) + 2kl^2\delta = 0 \tag{9.21}$$

The length of the lever arm was 0.231 meters. The spring stiffness was estimated by suspending an 11.4 kg mass from one of the spring and letting it oscillate while measuring its vertical acceleration via an accelerometer. A grey box identification routine was used to estimate the spring stiffness for three trials. We found the average spring stiffness

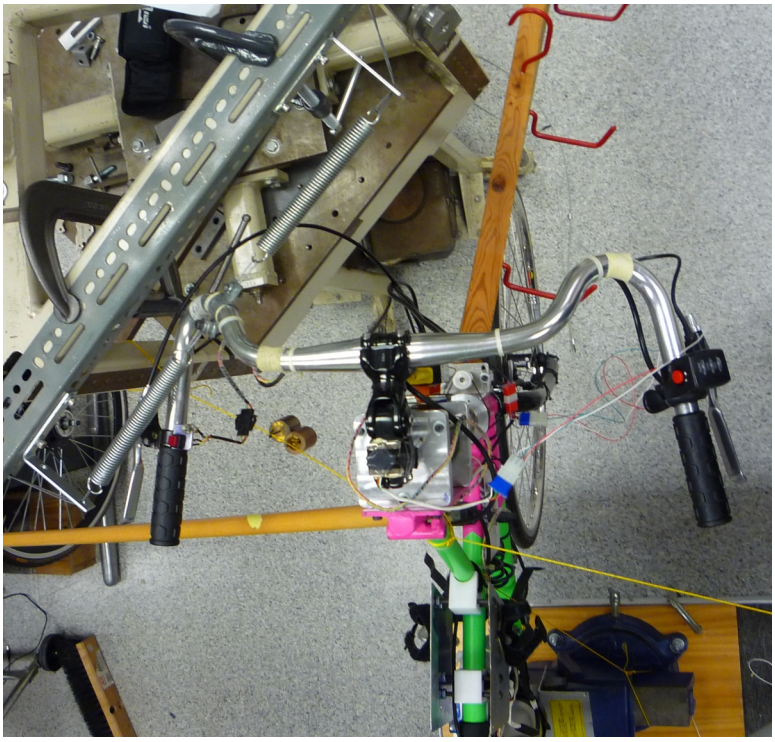

Figure 9.26: An overhead view of the steer friction experimental setup. The steer axis of the bicycle is vertical and the bicycle frame is secured such that it is rigid with respect to the earth. The wheel was isolated from rotation relative to the fork. Two springs in series were attached to the handlebars.

to be 904.7 ± 0.6 N/m. The inertia of the handlebar, fork, and front wheel about the steer axis, I_{HF}, was computed based on the measurements described in Chapter *Physical Parameters* and found to be $0.1297 + / - 0.0005\ kg \cdot m^2$[9].

The friction coefficients are found with a non-linear grey box identification based on the measured steer angle over 15 trials (runs 209-223) where the steering assembly was perturbed from equilibrium. The resulting viscous coefficient is $c_B = 0.34 \pm 0.04\ N \cdot m \cdot s^2$ and the Coulomb coefficient is $t_B = 0.15 \pm 0.05\ N \cdot m$.

To calculate the applied steer torque, T_δ, we need an estimate of the upper bearing friction, T_U. A simple assumption is that the friction in the upper bearings equals the friction in the lower bearings, $T_U = T_B/2$, but for some of the trials we measured the torque between the bearings, the steer angle just above the lower bearings and the steer rate above the upper bearings. This information allows the estimation of the upper and lower bearing friction independently. The equations of motion of the assembly above the torque sensor are

$$I_G\ddot{\delta}_U + c_U\dot{\delta} + t_U \operatorname{sgn}(\dot{\delta}) + 2kl^2\delta = -T_m \tag{9.22}$$

The friction coefficients of the upper bearings can be estimated by treating the measured torque as an input and the measured steer rate as the output in a non-linear grey box formulation. The moment of inertia, I_G, of the handlebars about the steer axis, i.e. the portion above the torque sensor, is computed from the physical parameter measurement described in Chapter *Physical Parameters* and is $0.0656 \pm 0.0003\ kg \cdot m^2$.

Assuming I_G, k, and l as fixed parameters gave poor fits (around 50% of the data variability was accounted for by the model), and thus most likely poor estimates of the friction coefficients. The viscous coefficient was found to be $c_U = 0.6 \pm 0.1$ and the Coulomb friction as $t_U = 4.0E-8 \pm 7E-8$. These results are questionable. From the previous excellent estimates of I_{HF}, I would have not expected our I_G number to be a poor estimate, but this leaves either our precomputed value of I_G or the measure torque T_m as the most likely candidates to being incorrect. If I_G

[9] If I_{HF} is left as a free parameter, along with c_B and t_B, the mean of I_HF over 15 trials is identified to be 0.1269 ± 0.0008. This good agreement lends confidence to the methods in Chapter *Physical Parameters*.

is a free parameter the identification produces outputs that fit the data well, but I_G is different than what was found with other techniques, $I_G = 0.0955 \pm 0.0005$. The fits for the 7 trials rose to over 87% of the variability explained by the model and the viscous friction was $c_U = 0.38 \pm 0.06$ and the Coulomb $t_U = 0.08 \pm 0.06$. The same can be done to compute the lower bearing friction, but the fits were very poor. The results of finding the upper bearing and lower bearing friction are inconclusive. So the assumption that the upper friction is half of the total friction is used to compute the actual steer torque.

It is also worth noting that the bearings are under load when a rider is seated on the bicycle and that we didn't measure the friction under that loading of the bicycle and rider's weight.

Rider Applied Torque

With decent estimates of the torque due to upper bearing friction the actual rider applied steering torque, T_δ, can be computed using Equation (9.16). *Figure 9.27* gives a breakdown of the torque components found in Equation (9.16) in a typical run. The frictional torques are broken into the viscous and Coulomb parts and the dynamic torques are broken into the terms due to the change in angular momentum and the terms due to the acceleration terms. Notice that up to 2 Nm of additional torque is required for the rider to overcome the friction and inertia of the front assembly and that the majority of that torque is due to the inertial effects. This extra torque may be negligible in motorcycle dynamics, but must be accounted for when studying the much lighter bicycle.

9.6.5 Strain Gauge Amplification

All of the load cells (lateral force, steer torque, seat post and foot pegs) required analog amplification of the millivolt bridge signals to bring them up to a level measurable by the NI USB-6218 which had a maximum input range of ± 10 volts at 16 bit. I purchased the Futek CSG-110 strain gage amplifier for the torque sensor and had the sensor factory-calibrated in tandem with the amplifier for a ± 10 volt output. Cal Stone [Sto90] had developed a custom amplifier for his seat post and handlebars which could amplify up to fourteen bridge signals. Because I was intending to make use of the seat post, the amplifier box was used for all the other strain gages. I did not make use of the seat post and foot pegs, so the amplifier was only used for the lateral force load cell. I used the amplifier box as it was except for changing the first stage analog amplifier resistor to 16.5k ohm for a ± 100 lbs range of the lateral force load cell. Cal Stone's thesis, his research notes, and the system electrical diagram (http://biosport.ucdavis.edu/research-projects/bicycle/instrumented-bicycle/electrical-diagram/) give the details of the circuit designs.

9.7 Calibration

All of the analog sensors I used require some sort of calibration that can be used to develop a relationship between the measured voltage from the sensor and the physical phenomenon that is being measured. I self-calibrated some sensors, had one calibrated at the factory, and used the reported manufacturer specifications for others. The calibration data that is not presented below is stored in the main trial database.

9.7.1 Potentiometers

I calibrated the steer angle sensor by inserting a custom protractor into the steer tube of the fork, *Figure 9.28* and measuring the voltage of the potentiometer output at a series of distinct angles. This calibration was done anytime the timing belt or pulleys were disengaged and before each experimentation session.

The roll angle potentiometer was calibrated by measuring the bicycle frame's absolute roll angle with a digital level and recording the voltage output for a sweep of angles, *Figure 9.29*. I also took static measurements each day of experiments so that the roll angle could be computed from the accelerometer's output in case the bias in the roll angle calibration was poor.

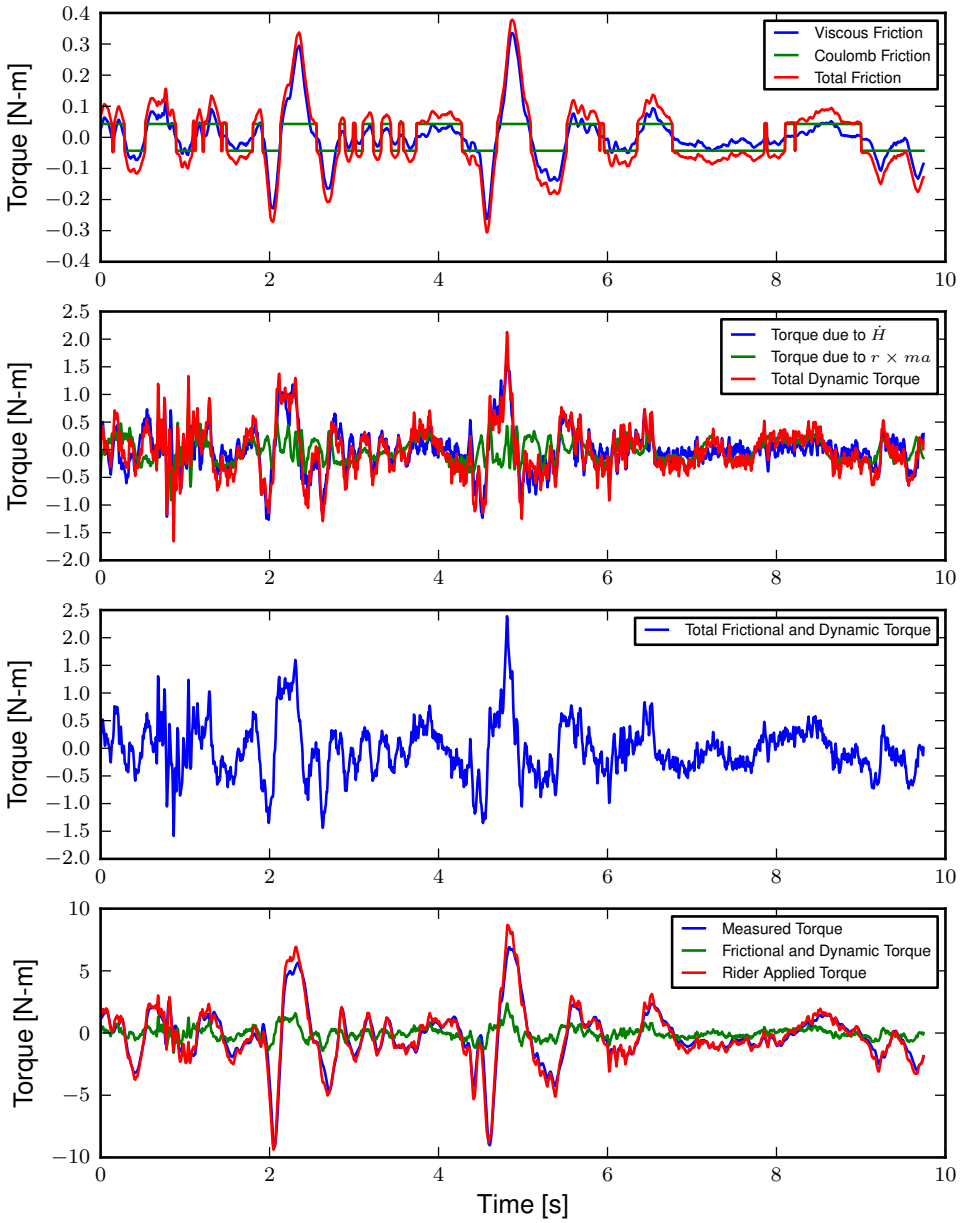

Figure 9.27: This is a plot of the steer torque components for run #700. The top plot shows the additive viscous and Coulomb friction. The total bearing friction during the run is less 0.3 Nm. The second plot shows the torque the rider must apply to overcome the handlebar inertia. The dominant term is the $I_{G_{33}} w_{b3}$ and during the peak accelerations the additive torque is up to 1.5 Nm for this run. The third plot shows the total additive torque which is up to 2 Nm. And finally the last plot shows the difference in the measured torque and the rider applied torque. There are large differences, especially at the peaks. Generated by `src/davisbicycle/steer_torque_components.py`.

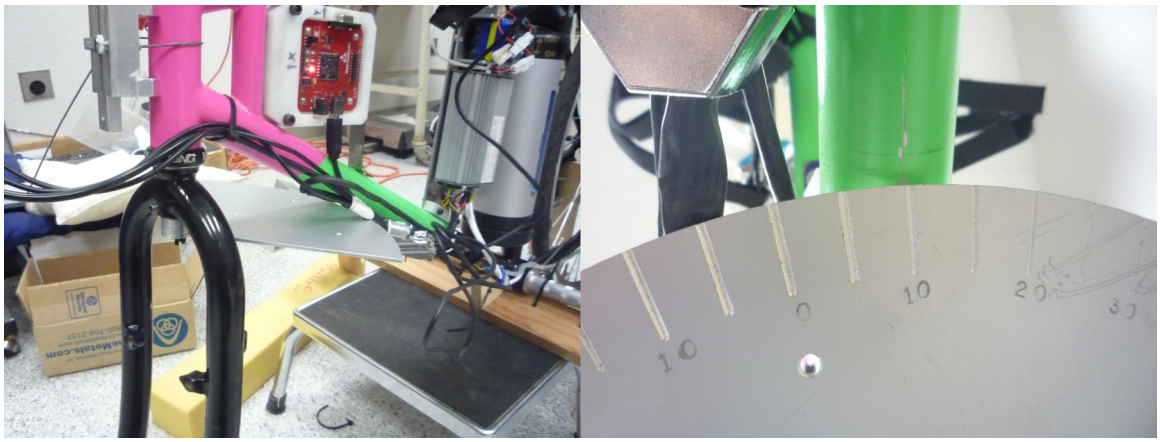

Figure 9.28: The left image shows the protractor mounted in the fork. It is pinned in place with a roll pin for precise alignment with the front brake mounting hole. The right image shows the underside of the protractor with the engraved angles at every five degrees and the scribe line on the center of the down tube.

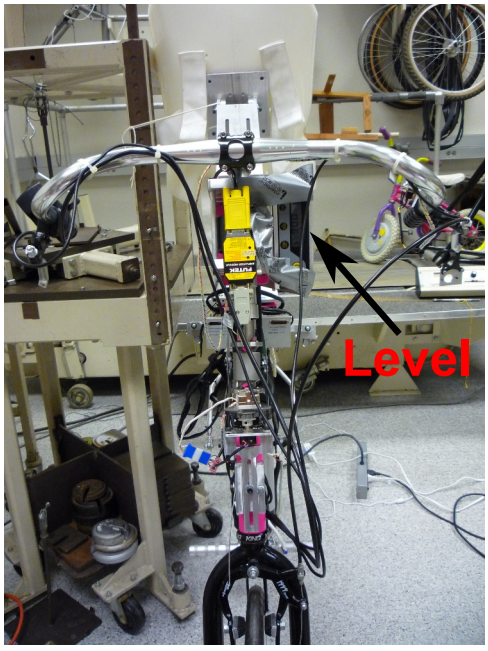

Figure 9.29: The bicycle during a roll angle calibration. The digital level is taped to the side of the steer column and the bicycle is set at various roll angles while the roll angle potentiometer is sampled.

For both cases the potentiometer's output voltage is ratiometric (i.e. scales with respect to the supply voltage V_s) with respect to the supply voltage V_s and the potentiometer angle δ can be computed given the average calibration supply voltage V_c, the slope m, and intercept of the calibration curve b relating voltage to the angle. Depending on the calibration, the angle could be the rotation angle of the potentiometer as in the case of the roll angle measurement or the actual steer angle in the case of the steer angle due to the gearing from the steer tube[10]. For example

$$\delta = \frac{V_c}{V_s} mV + b \tag{9.23}$$

9.7.2 Rate Gyros and Accelerometers

The analog accelerometers and rate gyros typically have specifications for the sensitivity and the zero bias z, where both are ratiometric. The sensitivity gives the linear relationship of the output voltage for a given acceleration or rate. The zero bias is the output voltage of the sensor for zero acceleration or rate for a given supply voltage. For example

$$\dot{\delta}_m = m\left(V - \frac{V_s}{V_c} z\right)$$

9.7.3 Wheel Rate

We measured rear wheel angular speed with the same technique used with the Delft instrumented bicycle. We mounted a small DC motor such that a knurled roller wheel attached to its shaft rolled against the rear tire. The voltage of of a DC motor has a linear relationship with the rotational speed of the motor. To generate a calibration curve, we used an AMETEK 1726 Digital Tachometer to measure the rotational speed in rpm and digital multimeter to measure the voltage for a sweep of motor rotational speeds. *Table 9.4* gives the calibration data and *Figure 9.30* shows the results of a linear regression through the data.

Table 9.4: DC Tachometer Calibration Data

RPM	Voltage
42.5	0.094
62.0	0.1385
89.0	0.199
132.0	0.291
185.0	0.406
271.5	0.595
391.0	0.857
569.0	1.252
855.0	1.879
1243.0	2.738
1785.0	3.91
2588.0	5.67

The relationship from motor rotational speed to voltage is $mV + b$ with the slope and intercept of the rpm to voltage curve determined by regression; $m = 456.3862 \frac{\text{rpm}}{\text{volt}}$ and $b = -1.2846$ rpm, respectively. We then attached a small disc to the motor shaft such that the disc rubs against the rotating tire. The disc diameter was chosen such that the motor would output 0 to 10 volts for a bicycle forward speed range of about 0 to 13.4 m/s (0 to 30 mph). The rotational speed of the rear wheel as a function of voltage can be written as a linear relationship

$$\dot{\theta}_R = s_f(mV + b)\frac{r_d}{r_c} \tag{9.24}$$

[10] It slipped my mind to add a step-up gear for the roll angle measurement, leaving the output voltage range small with respect to the roll angle range. Ideally, the potentiometer should rotate its full rotation for a desired roll angle range.

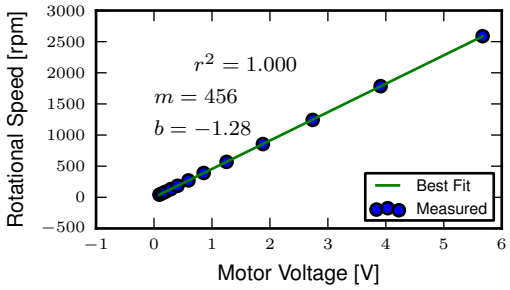

Figure 9.30: The best fit line through the wheel speed motor calibration data presented in *Table 9.4*. Generated by `src/davisbicycle/calibration_fits.py`.

where r_d is the radius of the generator disc and r_c is distance from the rear wheel center to the disc/tire contact point and $s_f = \frac{2\pi}{60}$ is a scaling factor from rpm to radians per second. $r_d = 0.028985$ m and $r_c = 0.333375$ m when the generator was first attached (runs 0 to 226) and $r_c = 0.3199511$ m after the generator was remounted (runs 227 to end). The relationship between the rear wheel rate as a function of voltage can more generally be rewritten as

$$\dot{\theta}_R = m_R V + b_R$$

where $m_R = \frac{s_f m r_d}{r_c}$ and $b_R = \frac{s_f b r_d}{r_c}$. The nominal forward speed of the bicycle can also be computed

$$v = \dot{\theta}_R r_R$$

9.7.4 Lateral Force

The lateral force was calibrated by applying a series of compressive and tensile loads to the load cell and measuring the amplified voltage output, *Figure 9.31*. Before calibrations, the amplifier offset voltage potentiometer was set to about 2.5 V and the nulling potentiometer adjusted so that the voltage was zero for the no load case.

$$F = \frac{V_c}{V_s}(mV + b)$$

9.7.5 Steer Torque

The steer torque sensor was calibrated at the factory in tandem with the amplifier and Futek supplies a certified calibration document with the calibration data. The CSG-110 amplifier supplies constant 10 Vdc to excite the strain gauge bridge. I did not measure this voltage because the maximum voltage for the NI USB-6218 is 10 V, so no ratiometric scaling was used. As long as the battery supplied 12+ V to the CSG-110, this would not be an issue. Tables *9.5* and *9.6* give the factory reported data and *Figure 9.32* shows the regression results.

$$T_\delta = mV + b$$

Figure 9.31: The load cell under a compressive static loading during the calibration procedure, with Jan looking on.

Table 9.5: Factory Calibration Data
Clock Wise Torque

Load (in-lb)	Output (Vdc)
0	0.000
30	1.998
60	3.993
90	5.997
120	7.994
150	9.997
0	0.002

Table 9.6: Factory Calibration Data
Counter Clockwise Torque

Load (in-lb)	Output (Vdc)
0	0.000
30	-1.995
60	-3.994
90	-5.989
120	-7.986
150	-9.986
0	0.002

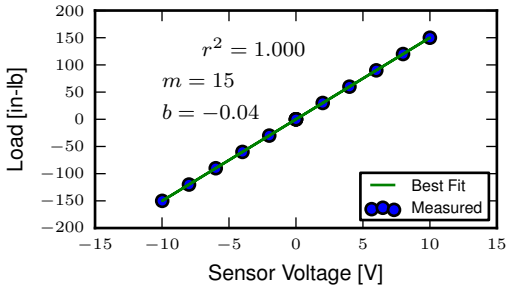

Figure 9.32: The best fit line through the steer torque sensor calibration data presented in Tables *9.5* and *9.6*. Generated by `src/davisbicycle/calibration_fits.py`.

9.7.6 Calbration Software

I wrote a simple program that collects the data for the self calibrations and generates a generic calibration file with a standard format for the various sensors. The files for the data from the manufacturer-supplied calibration data were manually constructed. All of the files are then parsed and collected into a single calibration table in the main database. When converting raw voltage signals to engineering units, the calibration coefficients are applied with respect to the calibration date (i.e. the calibration coefficients are selected with respect to the date up to and nearest the date of the run). The programs can be found in the tools directory in `BicycleDAQ` and in `BicycleDataProcessor`.

9.8 Software

9.8.1 Data Acquisition

Both the VectorNav VN-100 and the NI USB-6218 were connected to a small ASUS EEEPC netbook which was mounted on the rear rack of the bicycle, *Figure 9.33*. The devices were controlled and the data logged using Matlab. I interacted with the VN-100 with Matlab's Serial I/O toolbox and the NI USB-6218 with the Data Acquisition Toolbox. A custom program written within Matlab's Graphical User Interface framework was designed to allow the user to set meta data before each run, arm the system, and view the raw data signals after the run, *Figure 9.34*. The general features are as follows:

- Automatically increments run numbers
- Sets meta data: rider, environment, speed, maneuver, notes
- Initializes the system
- Views raw data time history traces
- Loads previous runs, view the time traces, edit the meta data and re-save
- Saves output as a Matlab mat file
- Converts the run and calibration mat files to HDF5 format
- Collects calibration data

Due to the time synchronization issue talked about below we were limited to a single trigger setup, versus a multiple trigger for repeated runs. (i.e. we had to stop after every run to re-initialize the devices, versus allowing the rider to trigger a series of runs in a row without having to stop).

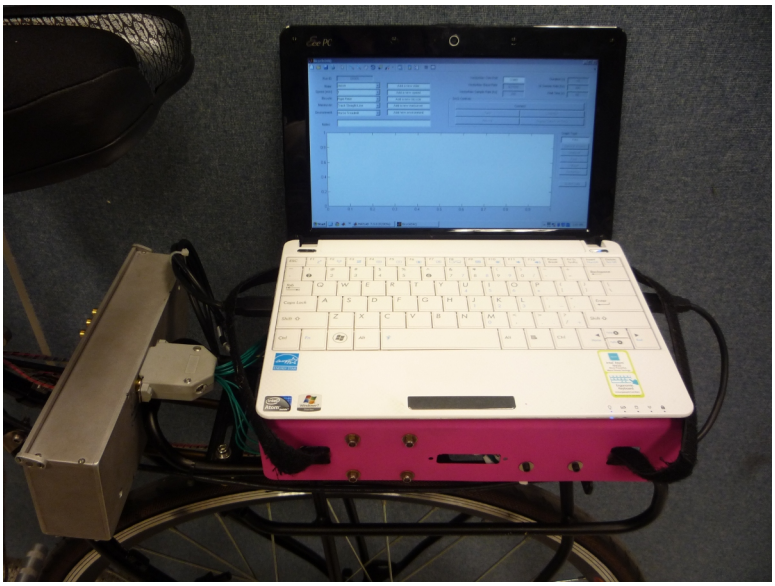

Figure 9.33: The laptop mounted to the rear rack.

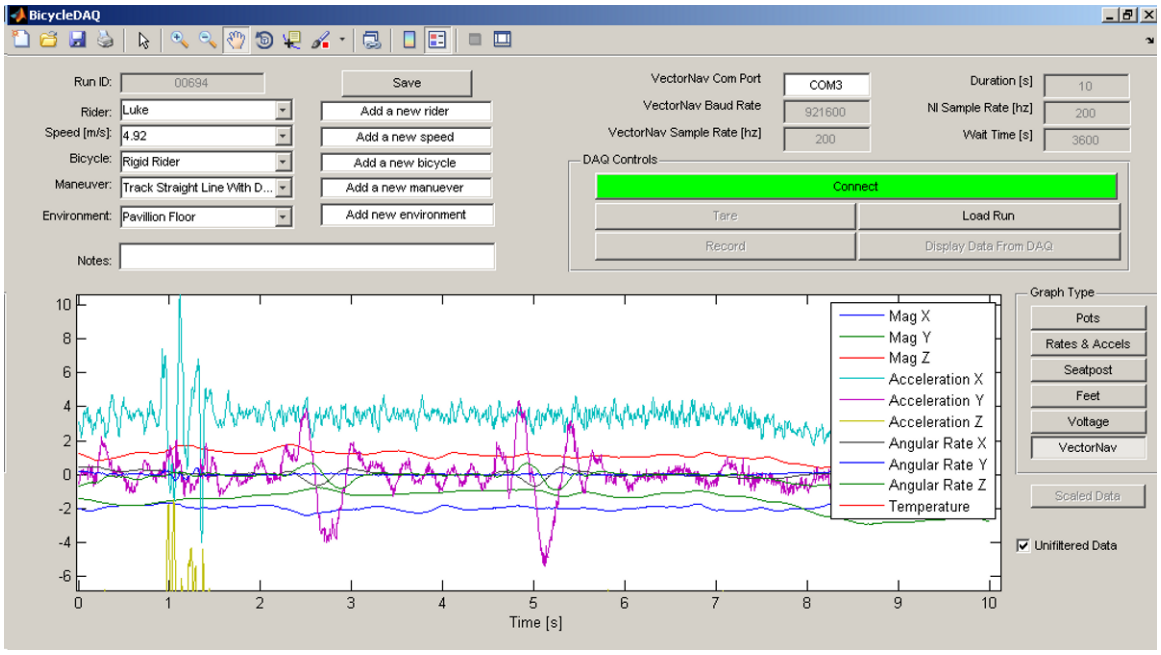

Figure 9.34: A screenshot of the software running under Matlab 7.8.0 (2009a) on Windows XP .

The source code for the software is available in a Github repository https://github.com/moorepants/BicycleDAQ, including some tools for initial post-processing of the collected data.

9.8.2 Time Synchronization

When we originally chose to use the VectorNav VN-100 and the NI USB-6218 with a netbook PC, we had convinced ourselves that they would all work together seamlessly. The manufacturers of each device seemed to think so and their disconnected knowledge helped convince us too. This turned out to be very wrong. The main issue, which seems to rear its head often in data acquisition, is time synchronization of all the hardware involved. A PC running a typical operating system is not capable of detailed and strict time management of processes. This is certainly true of collecting serial data from two independent devices. My intention was to collect data from both the VN-100 and the USB-6218 simultaneously with the Matlab Serial I/O and Data acquisition toolboxes, hopefully triggering the initial collection of data from the two devices simultaneously or by reading the VN-100 serial data through the USB-6218.

The simultaneous triggering was hampered primarily by the VN-100's asynchronous data transfer and no apparent ways to either start it with a trigger or by recording some signal from it through the USB-6218. It may be possible to read serial data through the USB-6218, but I did not figure it out. It very well may have been missing the features to do so, or that Matlab didn't have a robust enough interaction with the USB-6218 to do so. I struggled quite a bit with this unforeseen issue and we started devising solutions to measure an identical event with both the VN-100 and the USB-6218 and to synchronize the signals afterwards. [VDO11] had to use a similar technique. We would need to select a sensor which was also on the VN-100 and then excite the two sensors with the same event. Ideally this event would be a step input to both sensors. We tried rate gyros and accelerometers but couldn't come up with an adequate event, until we mentioned the problem to Ron and he immediately suggested just riding over a bump! This was the ticket. We ended up attaching an additional three axis accelerometer to the VN-100 development board which would read the same vertical component of acceleration and constructing a bump for the bicycle to travel over at the beginning of each run. This provided us with two signals which could be synchronized in time.

Bump

The accelerometers had a ± 3 g range, so we needed a bump which would provide vertical accelerations within that range for speeds from 1 to 7 m/s. For a sinusoidal shaped bump, the vertical acceleration for a given speed can easily be computed. The height of a bump as a function of time is

$$y(t) = \frac{h}{2}\left[1 - \cos\left(\frac{2\pi v}{L}t\right)\right] \tag{9.25}$$

where the maximum bump height is h, v is the forward speed and L is the length of the bump. The acceleration

$$\frac{d^2y(t)}{dt^2} = 2h\left(\frac{\pi v}{L}\right)^2 \cos\left(\frac{2\pi v}{L}t\right)$$

Because the cosine varies from -1 to 1, the maximum acceleration due to the bump and acceleration due to gravity is

$$a = 2h\left(\frac{\pi v}{L}\right)^2 + g$$

The maximum height of a 1 meter long bump and forward speed of 7 m/s to give a 3 g acceleration is

$$h = \frac{a - g}{2}\left(\frac{L}{\pi v}\right)^2 = \frac{3(9.81\text{ m/s}) - 9.81\text{ m/s}}{2}\left(\frac{1\text{ m}}{\pi(7\text{ m/s})}\right)^2 = 0.020\text{ m}$$

I fashioned a very low sinusoidal bump from wood that we laid on the track on the floor at the beginning of the track, *Figure 9.35* and also launched under the bicycle on the treadmill. The bump launching is somewhat amusing and we had to construct a "bump catcher" so that the bump didn't fly off the back of the treadmill and hurt anyone or anything, *Figure 9.36*.

Figure 9.35: The sinusoidal profile of the finished bump.

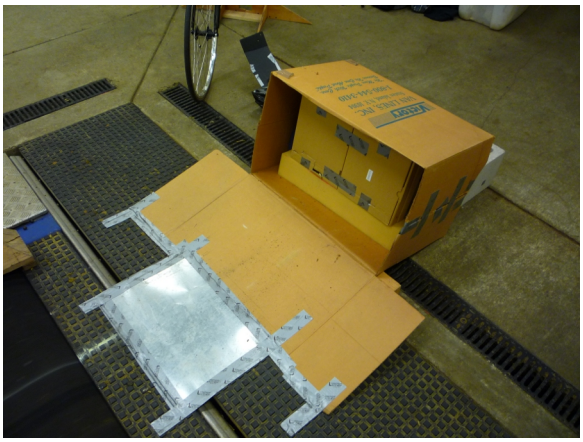

Figure 9.36: The high precision bump catcher.

9.8.3 Signal Synchronization

The bump provides the event and the acceleration output of the tandem accelerometers logs the event. The time shift between the two signals can be computed by minimizing the least squares error of one signal minus the other signal which has been interpolated at the sample times of the first signal. *Figure 9.37* shows the two independent recorded events.

The basic algorithm for computing the error between the two signals is:

1. Shift the NI signal some time τ.
2. Truncate both signals around the common data.
3. Interpolate the NI signal at the VN time samples.
4. Compute the sum of squares of the VN signal minus the interpolated NI signal.

Using this formulation, then minimize the error with respect to τ. The minimization requires a good guess, as the minimizing function has local minima. I use both the location of the max values in the signals and finding the minimal value of the error as a function of a fixed number of τ values to get good guesses. See the `BicycleDataProcessor` source code for the details. The computed time shift is used to shift and truncate all of the signals as in *Figure 9.38*.

9.8.4 Data Processing

To handle processing the large amount of data, I developed an object oriented program, BicycleDataProcessor (https://github.com/moorepants/BicycleDataProcessor), in Python that interacts with an HDF5 database containing the data. The program makes use of PyTables (http://www.pytables.org) for database interaction and the SciPy/NumPy (http://www.scipy.org) matplotlib (http://matplotlib.sourceforge.net) stack for computation and plotting. The program is structured around three classes:

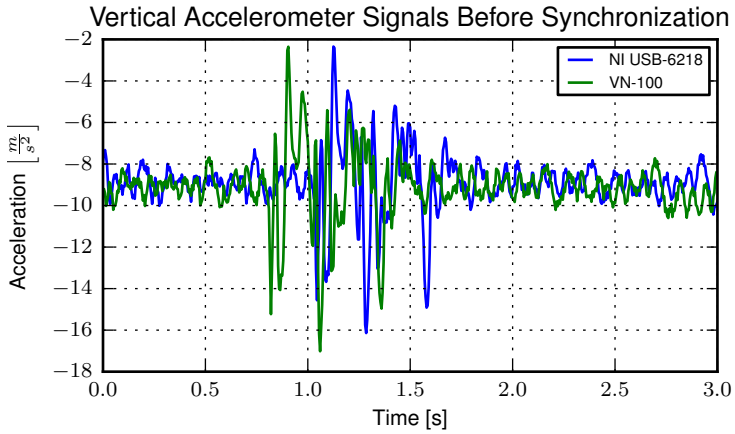

Figure 9.37: This plot shows the accelerometer signals collected by both the NI USB-6218 and the VN-100 for a typical run. The spikes in acceleration are due to the bicycle traversing the bump. The NI signal starts about a third of a second before the VN signal. Generated by `src/davisbicycle/time_sync.py`.

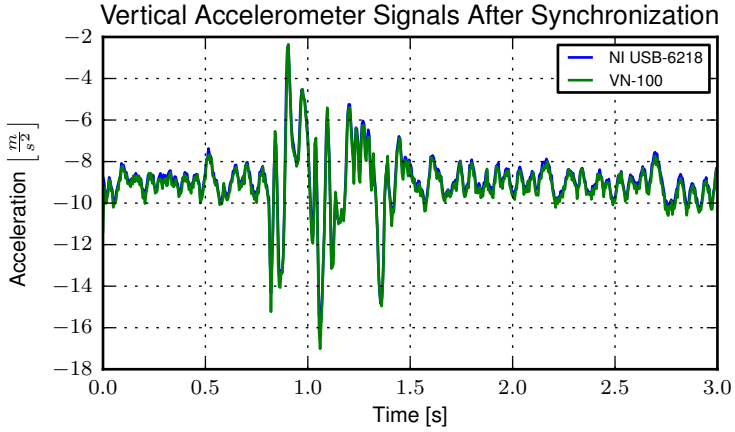

Figure 9.38: This plot shows the same accelerometer signals shown in the previous figure after finding the optimal time shift. Generated by `src/davisbicycle/time_sync.py`.

Signal This is a subclass of the NumPy ndarray. It tracks a 1 dimensional time series along with its units. There are basic methods for typical signal processing such as differentiation, filtering, and frequency spectrum.

RawSignal This a subclass of Signal for the raw signals. The attributes are populated from the database. In addition to the Signal methods, it has the ability to scale the signal based on calibration data.

Sensor This class contains calibration data for particular sensors and has methods to extract the correct calibration constants based on calibration date.

Run This is the primary class which stores the meta data and signal data for a specific run. It has methods to process the raw data into more meaningful time series that are useful for analyzing the bicycle dynamics. There are also methods for plotting and exporting the data.

The data collection and initial processing follows this pattern:

1. Collect data during a run via the BicycleDAQ software. This stores the metadata and raw signal data for each run in a Matlab mat file.
2. Build the complete HDF5 database with BicycleDataProcessor by importing all of the run and calibration data files.
3. Load runs from the database and manipulate them for further processing such as plotting.

This approach works well and allows for easy querying of the 700+ runs for further data analysis. The processed data can be exported to generic file formats or as ones compatible with Matlab. This example gives the basics of loading a run and plotting the processed data in *Figure 9.39*:

```
import bicycledataprocessor as bdp
dataset = bdp.DataSet()
trial = bdp.Run('00699', dataset, filterFreq=40.)
fig = trial.plot('PullForce', '2289*RollAngle', '1448*SteerAngle', '32*SteerTorque')
fig.show()
```

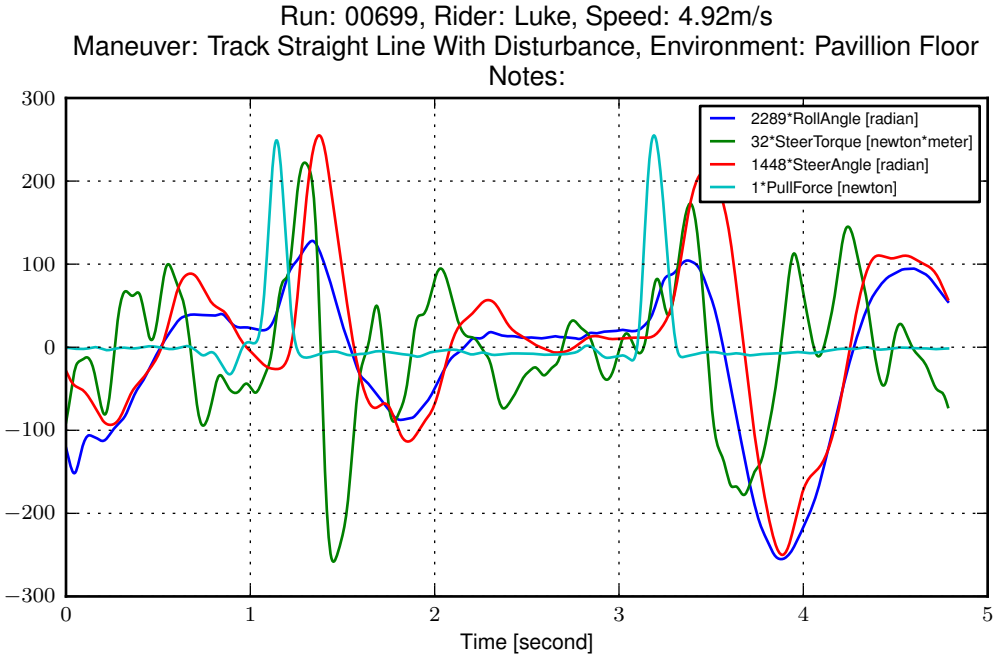

Figure 9.39: The resulting output of a basic plot command for a run.

9.9 Conclusion

In this chapter I gave a detailed description of the Davis instrumented bicycle with the hope that enough information is present for someone to make use of the bicycle and/or recreate one (of course with improvements). The bicycle served us well in terms of the kinematic and kinetic data we were interested in collecting.

Some recommendations for improvements are as follows:

- Power the entire system from the hub motor battery to reduce the number of batteries.
- The steering universal joint needs keyways instead of set screws for a more solid connection.
- Get rid of the VN-100 and replace with two analog rate gyros for yaw and roll. This would take away the time synchronization issue. The newer versions of the VN-100 offer more capabilities including synchronization signals, so that could be looked into, but overall it is still a poor (and expensive) choice for this application.
- Add some gearing to the roll angle measurement for better resolution, and develop a more accurate calibration scheme, perhaps by making use of the on-board accelerometers.
- Do away with the torque limiter. Another solution for safeguarding the sensor and rider in case of failure is needed.

CHAPTER

TEN

CONTROL

10.1 Introduction

I have shown that a basic bicycle model can exhibit stability when linearized about the nominal configuration for a range of speeds, Chapter *Bicycle Equations Of Motion*. Stability is a strong function of the parameters of the bicycle and it turns out that standard bicycle designs, typically exhibit a speed dependent stability and the bicycle becomes stable at some speed threshold, Chapter *Parameter Studies*. Based on the damping of the weave mode, one may also even claim that the bicycle becomes *more* stable as speed increases, neglecting the very slow, easily controllable capsize instability. I've also shown that stability can be enhanced or decreased by extending the Whipple model with a flywheel or rider degrees of freedom, Chapter *Extensions of the Whipple Model*. In Chapter *Motion Capture*, I've examined the kinematics of the rider to see if the rider's motion during a control task has any correlation to the kinematics of the Whipple model and identified the dominant rider motions during stabilization.

As far as roll stability is concerned, it is highly probable that a human must implement active control at *all* times while balancing. I conclude this because the bicycle's roll angle responds to the human's postural control. But the stability exhibited of the almost-always-present weave mode may alleviate the need for primary roll control provided by the rider. And even if the bicycle-rider system is open loop unstable at a given speed, the question arises of *how* instable is it or *how* controllable is it. Classic controllability is simply a binary test to determine whether or not it is possible for a system to be controlled, whereas there must be some measure variable measure of controllability that is more relevant to the proposed questions. [SPC01] studies how parameter changes affect controllability, and comes up with rideability index. [SK10a] and [SMK12] also determine the controllability of several bicycle models and uses modal controllability as a continuous measure of the controllability. The pole locations of an open loop system can also give a general sense of the degree of its controllability, with roots in the far right plane likely being difficult to stabilize.

One can work with different bicycle models (simple/complex [or low/high order] and linear/non-linear), different control structures, and different ways to identify the optimal numerical values for the controller. For a given order model, most control structures allow one to place the closed loop poles in the desired location. Controllers designed for low order or linear models are even likely to work with higher order models and non-linear models. But the control structure design provides different views into the feedback mechanisms at work. For the human controller, these structures may or may not correspond well to the human's physiological and neurological system. The human has to choose his control actions to balance the requirements for robustness and performance.

The bicycle-rider system presents both a theoretical and experimentally rich dynamical system for control studies. It is very tractable in the sense that most people are familiar with controlling a bicycle and that it is a *simple* machine which is readily available for experimental use. Additionally, control of the bicycle is not necessarily trivial due to it's complex dynamics and thus it provides a good platform for testing many control strategies. Past control studies tend to be framed in two different but overlapping frameworks. The first is to simply control a bicycle (model or real) with any control algorithms and mechanisms available. Both the simple roll stabilization task and more complex path tracking tasks have been examined. The results show that bicycles are readily controllable by a variety of means, from a simple steer in the direction of the rate of fall to full state feedback with preview of future path variations. Depending on the sensing and actuation methods chosen these controllers range in their resemblance to how a human may actually control a bicycle. This leads into a second framework in which the researcher is explicitly trying to determine the how

a human balances and controls a bicycle. Basic understanding of the limited sensory input and actuation available to a human give constraints on what control structures are adopted. Both frameworks are motivated by many things such as a desire to implement automatic control, improving simulation for vehicle design, handling qualities inquiries, control system testing, etc.

The intention of the work presented in this dissertation falls in the second framework, where we are most concerned with identifying the human controller. The first part of this chapter gives an overview of other non-human based single track vehicle control efforts, followed by some simple control examples. I follow this with a review on human based control design and finish up with some addendum material to our paper [HMH12] which details the controller design we developed to represent the human.

10.2 Ideal Control Models

Many studies exist on the control of a single track vehicles. The following provides a light review of much of the literature which focus on *ideal* controllers for single track vehicles. Here I use the word ideal to simply label control design which is not explicitly focused on the human operator control. I've split the review of control models into two sections. The first are about controllers which have actually been implemented, or attempted to be implemented, on robotic vehicles. The second are theoretic controllers that weren't necessarily introduced to identify the human control system. The following section details efforts that explicitly concern controllers that mimic or try to understand the human controller.

Figure 10.1 shows a histogram by year of the all the references I've collected in the course of this project. It is interesting to note the explosion in the early seventies that probably coincides with the bicycle boom and the digital computer age. We've also had a boom in the last decade, with research interests growing. This may coincide with the microcontroller advances and potentially some from the growth in bicycling.

10.2.1 Robot Control

[VZ75] van Zytveld was one of the first to explore the automatic stabilization of the single track vehicle that was not explicitly in the human control framework, although he did chose feedback variables that he believed a human rider could sense. He attempted to control a robot bicycle with only a leaning rider (inverted pendulum) through proportional and derivative feedback of rider lean angle and bicycle roll angle. He made use of a linear model with a rider lean degree of freedom which is fundamentally the same as the one presented in Chapter *Extensions of the Whipple Model*. His controller worked on paper, but he wasn't able to ever balance the robot bicycle, with the suspected problems being the limitations of the hardware he used.

[Nag83] They constructed a robot bicycle which balanced and tracked itself by feeding back lateral deviation at a previewed time and the current roll angle. He was successful at stabilizing his robot. The bicycle model was much simpler than the Whipple model but it gave good agreement between experiment and the model predictions, with the exception of counter-steer predictions.

[RP85], [RP86] Ruijs and Pacejka developed a robotic motorcycle to study the effect of road irregularities (i.e. cat eyes), is this dangerous. The experiments were thought to be to dangerous for a human rider thus the robot was developed. They used a simple control scheme based on gain scheduling as a function of speed. Below the weave speed was lean rate was fed back and above the weave speed lean angle was fed back. Additionally, little bit of steer damping was included. The machine worked as was able to maintain stability during the experiments.

[BL99] They developed a digital fuzzy controller to stabilize a remote controlled bicycle robot. They do not seem to demonstrate the robot actually balancing, but only bench tests of the sensors and actuators.

[Gal00] He designed a robot balancing bicycle which controls a gimbaled gyroscope to apply a restoring torque with respect to the sensed roll angle, but was not successful at balancing the real robot.

[MKT+01], [MKT+03], [KMBU04], [KKBM05], [MBU+06], [SKK+07] These papers, among others, detail work on a Honda motorcycle robot, with the controller modeled after a human. The video demonstrations of this

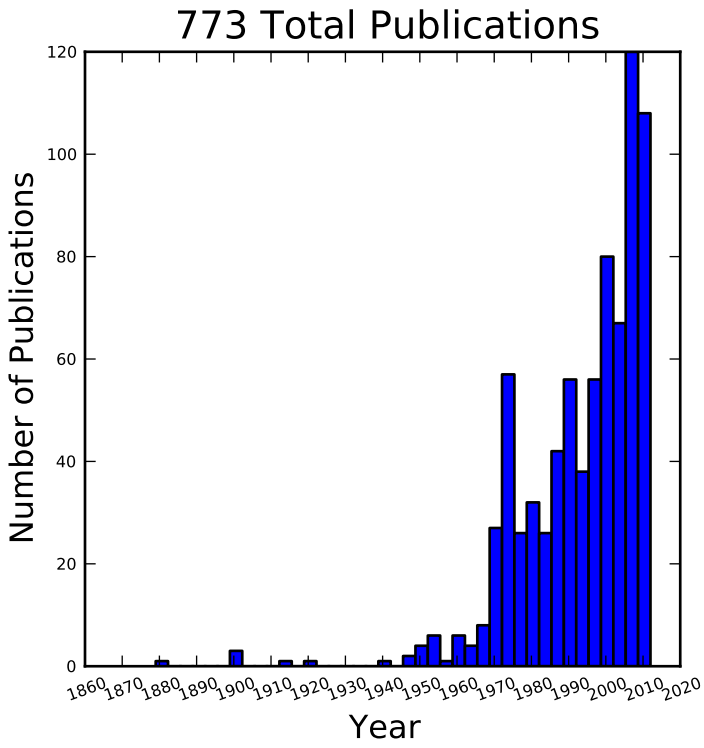

Figure 10.1: Histogram of my reference database on single track vehicle dynamics, controls, and handling. There are probably 50 or so titles that don't technically belong, but barring those this gives a good idea of the growth in single track vehicle dynamics research. Generated by `src/control/publication_histogram.py`.

vehicle indicate that it may be the most manually realistically controlled robot there is, not to mention that it seems to work really well. Most of these papers are in Japanese and I've had trouble finding others, so I cannot comment on all the details.

[TM04] They successfully balances a bicycle on rollers with a PD roll angle to steer angle controller with a disturbance observer.

[INM05] They use PD control on the bicycle roll angle to control steer angle and rider lean angle. The controller is implemented on a bicycle robot, which is able to balance on rollers.

[IM06] They use the same model base as [INM05] except they now add a human torque estimator, so that the controller will not treat the human's applied steer torque as a disturbance if the controller is activated while a rider is also trying to control the bicycle. They show some crude experimental results, which I assume are of a rider controlling the bicycle with and without the automatic controller activated. Their human torque accounting is based on an estimation of the human torque from the steer motor torque, rather than explicitly measuring the human's torque input.

[YUS06] They implement a controller modified from the one presented in [YU05] with an additional H_∞ controller. They show successful roll stabilization of a robot scooter in which they only implement the roll stabilization control.

[Mur09] The Murata Manufacturing company designed a bicycle robot to demonstrate the utility of their sensors which debuted in 2006 [Mur09]. There is little published detail on the control techniques but they seem to primarily make use of a roll rate gyro with steering and a gyro actuator. They also have other sensors such as ultrasonic sensors for obstacle detection. They demonstrate stability at zero speed, reverse and forward speeds, stopping for obstacles, and tracking a narrow s-curve in their video material. There are no published papers detailing the control system.

[Tau07] This is a Japanese Master's thesis on acrobatic bike robot that may be able to do a wheelie. I was not able to find this paper but have included it for completeness.

[MY07] They use the same vehicle and control model as in [YUS06] and a new two degree of freedom "rider" pendulum. They demonstrate roll stability of the robot at exactly zero forward and speeds up to 2 m/s.

[TP08] Thanh designs a controller with H_2/H_∞ techniques and applies it successfully to a bicycle robot which uses a flywheel for stabilization. He compares it to a PD controller and a genetic algorithm and shows that it is more robust.

[Mut10] Mutsaerts designed a Lego NXT bicycle robot with a simple proportional steer into the direction of roll rate controller and demonstrated (http://youtu.be/VxiOy4QzD7I) bicycle roll stability in crude turns and straight ahead running.

[Bic11] In 2011 the first BicyRobo Thailand student competition (http://bicyrobo.ait.ac.th/) occurred and many videos on the internet demonstrate the successful design of some teams. The full-size bicycle robots have roll stability and even path following. One video demonstrates students riding the robot bicycle and simultaneously applying manual steer torques.

[Yam11] The videos http://www.youtube.com/watch?v=mT3vfSQePcs and http://ai2001.ifdef.jp/ demonstrate an impressive remote controlled mini robot bicycle that is similar in nature to the [BL99] design with remote control. He uses a commercially available bipedal robot seated on a small bicycle. A gyro detects the roll rate and he uses a PID controller to apply the correct steering for roll stabilization. Remote control is employed to control the heading.

Other relevant papers that I either could not find, translate, or find time to read include [BFG+98], [SS00], [SUK+00], [Mur02], [OMUS02], [MW04], [MT06], [Sup06], [SL07], [TM09], [Bre10], [CALR10], [KY11]. I have included them here for completeness.

The limited success of most of the bicycle robots demonstrates that the actual implementation of single track vehicle control is not trivial. Some robots could demonstrate basic roll stability and some are even capable of path tracking but many didn't quite work either. The Murata Boy robot is impressive in its abilities but it uses control outside of what

humans are capable of. The motorcycle robot by Kageyama et al. is probably the most successful demonstration of a full sized vehicle with control of only steering. The vehicle dynamic models and control methodologies are varied, implying that many techniques may be applicable.

10.2.2 Theoretic Control Models

It is far easier to develop theoretic control models than taking them as far as implementation. There are many more successfully designed models on paper than implemented. This section details some of the modeling efforts.

[For92] He studied the robust stabilization of the wobble mode in motorcycles.

[Get94], [GM95], [Get95] He uses a simple bicycle model that exhibits non-minimum phase behavior and is able to track roll angle and forward velocity using proportional and derivative control. One year later, Getz adds path tracking to his model.

[KO96] He uses a neural network model to balance a two wheeled vehicle.

[CHA96] They use the same simple bicycle model and tracking variables as [Nag83], but controlled it with linear quadratic regulator.

[Yav97] and [Yav98] They study path tracking of a simple bicycle model using some kind of generalized control structure, with a bicycle model similar to [GM95].

[Sha01] They stabilize the roll angle of a motorcycle with a PID controller which operates on the error in roll angle to provide a steer torque. The gains for the controller are chosen by trial and error. The gains are difficult to find for low-speed, high-roll-angle scenarios.

[STW02] They use a simple bicycle model to build a roll rate feedback controller for a high speed recumbent bicycle. They use proportional feedback of the roll rate to control the steer angle.

[LH02] They develop a control model based on something akin to sliding mode control to stabilize the bicycle and track a path.

[CE03] Chidzonga uses the simple point mass bicycle model with a load sharing controller to demonstrate a track stand around zero forward speed. (Although the balancing might have just been due to a miracle from Jesus.)

[Kar04] Karnopp uses a very simple bicycle model and basic proportional control to demonstrate the counter steering require to balance the bicycle. He also examines rear steered bicycles.

[YU05] They set up a linear trajectory tracking control model and non-linear stabilization control by controlling steer torque, rider lean torque, and rear wheel torque. They demonstrate the control in a simulation of a bicycle jump maneuver.

[NM05b] This follows the [TM04] and [INM05] work, but adds velocity tracking.

[HAP05] He makes use of the [CL02] motorcycle model with a eight body rider biomechanical model. He stabilizes the bodies and tracks a path using LQR control.

[ASKL05] They apply simple proportional control of a point mass type bicycle model to stabilize the roll angle with a steer angle input.

[SN06] They stabilize a simple bicycle model using fuzzy control rules to provide a desired roll correction based on the current steer and roll angles. The simulations show stability but with very erratic control that seems like it would be poor for a real controller.

[LS06] They implement a PD controller on roll rate to stabilize the Whipple bicycle model outside the stable speed range.

[FMPM06] A simple point mass bicycle is stabilized with steer angle using three methods: a classical lead/lag compensator design, Ackerman pole placement, and LQR optimal control.

[Sha07b] He develops a path tracking controller for the benchmark bicycle [MPRS07] based on full state feedback and optimal control (LQR). He explores tight to loose control and shows how the gains vary with speed. He also include a preview model of which the tight control needs 2.5s of preview and the loose control needs at least 12.5 s. It is interesting to note that he found little change in computed gains for 20% variations in the various model parameters, leading him to conclude that the rider would be robust to various bicycle designs. His controllers show good performance for randomly generated paths.

[Sha07a] Here Sharp extends his LQR control method with preview from [Sha07b] to the motorcycle with the addition of rider lean torque control. He says that the objective was to develop a control scheme that *somewhat* represents a rider and which is simple and effective. His controller inputs are the rider's upper-body absolute and relative lean angles and the path tracking error. He claims that riders control the motorcycle at the weave frequency at high speeds. He is able to successfully stabilize and track a path and determine optimal preview gains. He also finds that the rider lean torque control is relatively ineffective and, even with high weighting in the LQR formulation, the steer torque input dominates the optimal solution.

[Sha08] Sharp applies his LQR based preview model control model from [Sha07a] to the benchmark bicycle. His findings are somewhat similar. His bicycle model is 6th order (he includes heading and path deviation) and he sets up the optimal control problem on full state feedback including varying numbers of path preview points. The bicycle tracks a path well and he shows high, medium, and low authority control by changing the LQR weightings. In general the bicycle roll angle and rate gains are the largest, with rider lean gains following, and steer related gains being the smallest. His leaning rider is initially stabilized by a passive spring and damper, and he finds that the lean torque control is minor when paired with steer torque control. Lean torque alone requires very high gains.

[MN07] Marumo and Nagai design both a PD controller with respect to roll angle and an LQR controller with full state feedback to stabilize the roll of Sharp's basic motorcycle model through steer torque. The intention is to have a steer-by-wire system so the rider can specify the desired roll angle with something like a joystick, thus alleviating the need for the human to learn to counter steer. They include an additional torque to the controller output computed from the steady state inverse steer torque to roll angle transfer function.

[CC07] Chidzonga expands on the work in [CC07] by once again managing a track stand with a load sharing control scheme.

[PH08b] Peterson designs a yaw rate and rear wheel speed tracking controller based on full state feedback and LQR control. He uses a non-linear Whipple like model with rider lean torque as the only control input. His simulation required 30 Nm of rider lean torque for a 0.3 rad/sec and 1 rad/sec step in yaw rate and rear wheel rate respectively.

[KM08] They stabilize a bicycle model with only a leaning "rider" pendulum actuator and track a path.

[Con09] Connors adds moving legs to the Whipple bicycle model and uses parameters to simulate a low slung recumbent bicycle. He designs an LQR full state feedback controller to stabilize the bicycle.

The following papers were either not found, not translated, or I did not read them, but they all have single track vehicle control: [NII97], [Che00], [PHH01], [FB03], [KN03], [NM05a], [Sac06], [Bje06], [CD06].

Variations on PID control of steer angle or steer torque with feedback of the roll angle are the most popular controller designs, many them being successful. LQR types follow close behind. H_∞ and other more modern control designs make up the rest. It is clear that roll stabilization and command is the critical task and must be conquered before path tracking can be employed. The steer torque is generally chosen as the primary input with just cause and rider leaning is also used in some models.

10.3 Basic Control

It turns out that the Whipple bicycle model can be stabilized with simple feedback of roll angle or roll rate, with the combination of both working in most cases. [Mut10] in fact demonstrates the simple roll rate feedback stabilization with a small robotic bicycle. But these are not necessarily good controllers, and certainly not controllers which mimic

the human. Regardless, their simplicity allows one to demonstrate some of the interesting system dynamics. Take for example Charlie riding on the Rigidcl bicycle at 7 m/s. The linear Whipple model about the nominal configuration gives the steer torque and roll torque inputs to roll and steer angle outputs transfer functions as

$$
\begin{aligned}
\left(\frac{\phi}{T_\phi}\right)_b(s) &= \frac{0.0095052(s+26.32)(s+16.78)}{(s+22.28)(s+0.5872)(s^2+2.801s+11.24)} \\
\left(\frac{\delta}{T_\phi}\right)_b(s) &= \frac{-0.094941(s-3.744)(s+2.729)}{(s+22.28)(s+0.5872)(s^2+2.801s+11.24)} \\
\left(\frac{\phi}{T_\delta}\right)_b(s) &= \frac{-0.094941(s+107.8)(s+20.83)}{(s+22.28)(s+0.5872)(s^2+2.801s+11.24)} \\
\left(\frac{\delta}{T_\delta}\right)_b(s) &= \frac{5.5445(s+2.934)(s-2.934)}{(s+22.28)(s+0.5872)(s^2+2.801s+11.24)}
\end{aligned}
\tag{10.1}
$$

The denominators of the transfer functions show that we have three stable modes, as expected. The numerators are potentially more interesting. Note that the steer torque to steer angle and the roll torque to steer angle transfer functions both have a single right half plane zero. This single right half plane zero means that the steer angle response from either input will exhibit an initial undershoot for a given steer torque input [HB07]. This phenomenon can be demonstrated by examining the step response of the two transfer functions with right half plane zeros *Figure 10.2*.

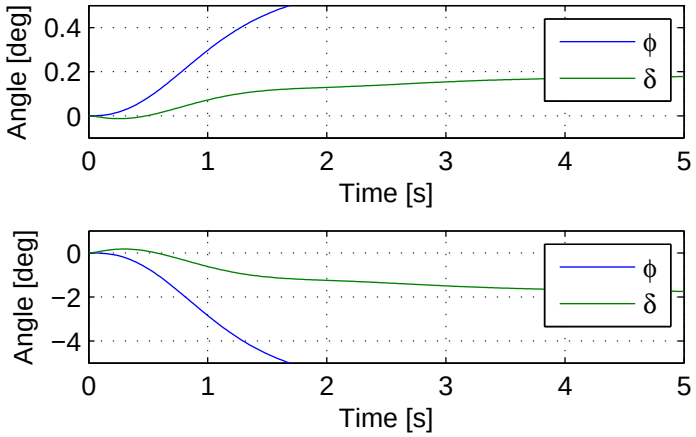

Figure 10.2: The upper graph shows the roll and steer angle time histories for a step response to roll torque to the Whipple model linearized about the nominal configuration. The lower graph input is for a step input to steer torque. The parameter values are taken from the rider Charlie on the Rigicl bicycle and the speed is 7 m/s which is within the stable speed range. Generated by `src/control/control.m`.

As expected we see initial undershoot in the steer angle for both cases. In this case, the initial undershoot initially departs in the asymptotic direction, but reverses and settles to a negative steer angle. This is easily demonstrated on a real bicycle by placing one's flat open palms on the handlebar grips. By applying a torque intending to turn the handlebars in the positive direction, the handlebars initially go in the correct direction, but once the frame rolls in the negative direction, the steering angle reverses and puts the bicycle into a steady turn in the negative direction.

If we examine the change in the transfer function zeros as a function of forward speed *Figure 10.3*, we see that both the steer angle transfer functions in Equation (10.1) always have a right half plane zero. And for $\frac{\delta}{T_\delta}(s)$, the zeros do not change with respect to speed. It is also interesting to note that below about 2 m/s the roll torque to roll angle transfer function has a right half plane zero. For roll torque, this would mean that at low speeds a positive roll torque step input (e.g. a gust of wind[1]) would cause a positive roll angle initial overshoot with the roll angle settling to a negative value

[1] A gust of wind does not impart a pure roll torque. The wind acts on both the front and rear frames and the rider. Pure roll torques that map to the input described in Chapter *Bicycle Equations Of Motion* are not necessarily observable in nature.

at steady state[2].

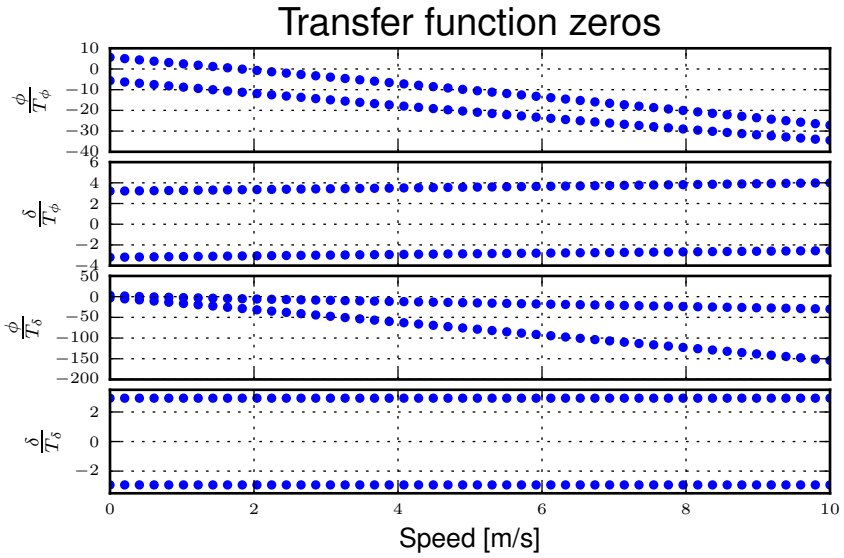

Figure 10.3: The zeros of the steer torque to roll and steer angle transfer functions. Generated by `src/control/zero_wrt_speed.py`.

The zeros can be computed analytically with respect to the canonical form presented in [MPRS07].

$$\mathbf{M} = \begin{bmatrix} m_{\phi\phi} & m_{\phi\delta} \\ m_{\delta\phi} & m_{\delta\delta} \end{bmatrix} \tag{10.2}$$

$$\mathbf{C}_1 = \begin{bmatrix} 0 & c_{1\phi\delta} \\ c_{1\delta\phi} & c_{1\delta\delta} \end{bmatrix}$$

$$\mathbf{K}_0 = \begin{bmatrix} k_{0\phi\phi} & k_{0\phi\delta} \\ k_{0\delta\phi} & k_{0\delta\delta} \end{bmatrix}$$

$$\mathbf{K}_2 = \begin{bmatrix} 0 & k_{2\phi\delta} \\ 0 & k_{2\delta\delta} \end{bmatrix}$$

The state, input and output matrices follow

$$\mathbf{A} = \begin{bmatrix} \mathbf{0}_{2\times2} & \mathbf{I}_2 \\ -\mathbf{M}^{-1}(g\mathbf{K}_0 + v^2\mathbf{K}_2) & -\mathbf{M}^{-1}v\mathbf{C}_1 \end{bmatrix}$$

$$\mathbf{B} = \begin{bmatrix} \mathbf{0}_{2\times2} \\ \mathbf{M}^{-1} \end{bmatrix}$$

$$\mathbf{C} = \begin{bmatrix} 1 & 0 & 0 & 0 \\ 0 & 1 & 0 & 0 \end{bmatrix}$$

The numerators of the transfer functions from the inputs to the outputs are computed with

$$\mathbf{C}\,\mathrm{adj}(s\mathbf{I}_4 - \mathbf{A})\mathbf{B} = \mathbf{0}_{4\times4} \tag{10.3}$$

Limiting the solution to only the steer torque input and solving for the roots of the polynomials, the zeros are found

$$s_\phi = -\frac{c_{1\phi\delta}v}{2m_{\phi\delta}} - \frac{\sqrt{c_{1\phi\delta}^2v^2 - 4gk_{0\phi\delta}m_{\phi\delta} - 4k_{2\phi\delta}m_{\phi\delta}v^2}}{2m_{\phi\delta}} \tag{10.4}$$

[2] I've often felt like I fall into the wind on my bicycle and this could confirm it at least for low speeds, but it may be tied more to phenomena associated with the rider's biomechanical degrees of freedom.

$$s_\delta = \pm\sqrt{-\frac{gk_{0\phi\phi}}{m_{\phi\phi}}} \tag{10.5}$$

Substituting the benchmark parameters in for the coefficients in Equation (10.5) which are the zeros of $\left(\frac{\delta}{T_\delta}\right)_b(s)$ show that they are simply a function of the total potential energy of the system divided by the roll moment of inertia with respect to the center of mass.

$$s_\delta = \pm\sqrt{-\frac{gm_T z_T}{I_{Txx}}}$$

This right half plane zero is important for understanding how to control a bicycle. Controlling by steer torque leads to unintuitive behavior of the bicycle, which the rider must learn.

10.3.1 Counter Steering

Countersteering is the colloquial term used to describe the non-minimum phase behavior demonstrated in the previous section. Motorcycle driving instructors are keenly aware of this and teach their students to steer into the obstacle that they want to go around.

[LS06] and [Sha08] explain that the term countersteering is used for two potentially conflicting ideas. They examine the effects of the right half plane zero of a simplified point mass model in much the same way as [ASKL05]. Sharp and Limebeer show that both the steer torque to steer angle and steer torque to lateral deviation have right half plane zeros and Åström develops a *steer angle* to roll angle transfer function that has a right half plane zero. The Whipple model matches the [LS06] interpretation, i.e. that the right half plane zero is in the steer torque to steer angle transfer function.

The first and most common definition of countersteer is:

> To initiate a turn, steer torque is applied in the opposite direction you want to turn which then causes the steer angle to initially depart in the opposite direction of the turn, but after the vehicle rolls the steer angle reverses into the direction of the turn.

The second definition, also clarified by [CLP07], regards the sign of the steer torque in steady turns:

> The applied steer torque may reverse sign with respect to the steer angle to maintain steady turn. This is generally true at high speeds.

The step response to steer torque at a stable speed shows that for a given roll angle departure the natural stability enforces that steer angle must initially depart in the opposite direction, *Figure 10.2*. In the case of roll torque input, a positive roll torque causes a positive roll angle but an initially negative steer angle. Afterwards the bicycle settles into a positive steady turn with respect to yaw. For the steer torque input, a positive steer torque causes an initially positive steer angle which in turn cause a negative roll angle. The bicycle settles into a negative steady turn.

To see this phenomenon outside of the stable speed range some form of control is needed to make simulations stable. Below the weave critical speed, the bicycle can generally be stabilized by a simple feedback gain on roll rate. Note that this gain must be negative, giving positive feedback. This implies that we apply steer torque in the same sense as the rate of fall[3]. *Figure 10.4* shows the response to a commanded steer torque below the weave speed under simple control. The countersteering in the steer angle is evident.

And above the capsize critical speed, the bicycle can be stabilized by a simple feedback gain on roll angle which also must be negative. *Figure 10.5* shows the countering steering required above the stable speed range.

For steer torque control inputs countersteering amounts to this: to get the bicycle into a positive turn, one must initially apply a negative steer torque to cause an initially negative steer angle and a positive roll angle. The steer angle exhibits

[3] The system can be stabilized by negative roll angle feedback at speeds close to the weave critical speed.

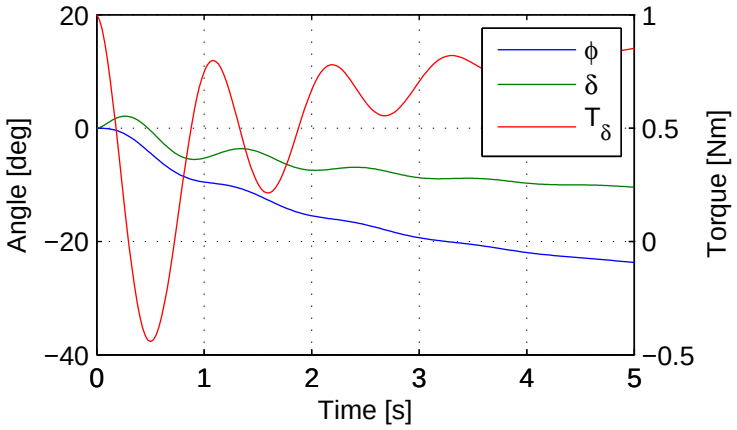

Figure 10.4: The step response to a commanded steer torque at 5.0 m/s which is below the weave speed. The gain is set to -5. Generated by `src/control/control.m`.

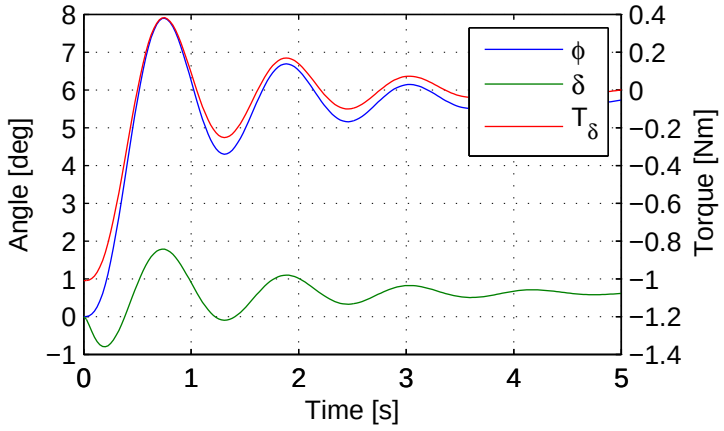

Figure 10.5: The step response to a commanded roll angle at 10 m/s which is above the capsize speed. The gain is set to -10.1. Generated by `src/control/control.m`.

initial undershoot due to the right half plane zero and settles to a positive angle at steady state. This is the case for at least all speeds above very slow speeds where the steer torque to roll angle transfer function has a right half plane zero.

10.4 Human Operator Control

There are few studies focusing explicitly on human control of a bicycle or motorcycle with the intent of identifying the human controller or controlling the vehicle with a human-like controller. The majority of the studies of this nature happened in the early seventies when manual control theories were relatively new. The following details the efforts that I've come across in my research.

10.4.1 van Lunteren and Stassen

van Lunteren and Stassen did some the earliest work on the subject at Delft University of Technology. They were primarily interested in identifying the human control system in the bicycle riding task. Their studies spanned several years in the late 60's and early 70's. [VLS67], [VLS69], [VLS70a], [VLS70b], [SVLB+73], [VLS73] uses a bicycle roll angle feedback with PID control that drives the rider's lean angle and steer angle. The bicycle model they employ is quite simple (it models their simulator more than a real bicycle) and does not exhibit proper coupling in steer and roll. The model also utilizes angle inputs as opposed to input torques. Their control structure was chosen in part because of equipment limitations but they cite recent manual control models [MGK67a] as being preferable. Nonetheless the research was ground breaking at the time and quite impressive, with real time system identification in a manually controlled electromechanical system. They concluded using roll angle input was more reflexive and that the control using steer angle was more cerebral based on identified time delays. They further developed their system to include a visual tracking outer loop. [DL11] develops a more up-to-date model with the same type of structure as van Lunteren and Stassen, in which he feeds back roll angle and steer angle, and drives steer torque with PID controllers. He also points out a sign error in van Lunteren and Stassen's work.

10.4.2 CALSPAN

The CALSPAN group developed a controller for their bicycle and motorcycle research that parallels the Delft work except they made use of the latest bicycle and motorcycle models with steer torque and learn torques as plant inputs [RL72]. The specifically point out the advantages of choosing the inputs to be torques and cite the Delft group's misguided assumptions. They design a PID controller with time delays for both steer torque and rider lean torque control to stabilize the inner roll loop. The outer loops consist of the previewed error in the desired path at several future time steps. This error is weighted to calculate a cumulative error which is then multiplied by a gain to compute an adjustment to the commanded roll angle. They show simulations of both good roll stabilization and slalom path tracking which they compare to video footage of an actual bicycle rider.

10.4.3 Weir and Zellner

Weir worked with McRuer on some manual control papers prior to his PhD thesis [Wei72], where he employed the crossover model together with a motorcycle model which is based on Sharp's early motorcycle model [Sha71] to evaluate the controller used by humans. This is the first complete attempt at analyzing the rider-motorcycle control system. Weir determined that roll angle feedback combined with a basic human model and a simple gain controlling steer torque was the most descriptive control mechanism. In particular, he showed how steer angle control was poor and he even examined rider lean angle control using a pseudo rider lean model similar to [HMH12]. Rider lean could successfully control the system, but required large lean angles. He also worked with multiple loop closures and found that roll angle fed back to control steer torque, with heading and lateral deviation fed back to control rider lean angle presented the best control strategy for the human rider. He only did his studies at a single high speed with a motorcycle model which only required stabilization of the capsize mode. It is highly likely that these control strategies could vary

with speed, especially at low speed where the weave mode is the dominant instability. Weir and Zellner went on to complete several more important studies involving manual control of the motorcycle [WZ78], [WZ79], including a detailed technical report for the U.S. Department of Transportation [WZT79] in which much experimental work was done verifying their mathematical models.

10.4.4 Eaton

Eaton's PhD thesis builds off of Weir's work and is primarily focused on validating the Weir models with experiments [Eat73b]. He pairs the successful motorcycle model develop by Sharp [Sha71] with Weir's McRuer-style manual control models that were based on the crossover model with time delays. He focused on the inner loop roll stabilization tasks. His model uses roll angle feedback and the controller compensates for roll angle error. He eliminates body lean control as an option to simplify things.

10.4.5 Aoki

For completeness, [Aok79] should be included, although I have not had time to study his work. It looks promising with both a human control model and experimental validation.

10.4.6 Doyle

A recently uncovered study by Doyle ([Doy87], [Doy88]), thanks to Google's book scanning endeavors and Jim Papadopoulos's persistence in searching, presents a slow speed view for bicycle control in much contrast to the Weir studies, not only because of the speed and vehicle differences, but because it is examined from the view of a psychologist. We engineers are quick to model the human sensory and actuation system, with little understanding of the intricacies of the human brain. Doyle's treatise gives a refreshing look from outside the engineering box. Doyle's control model is fundamentally a sequential loop closure with the inner most loop being roll control and the outer two being heading and path deviation. He says that the outer loops are highly dependent on the inner loop. For the inner loop he determines that continuously feeding back both roll acceleration, with integral and proportional gains adjusted by the human as the crossover model dictates, will stabilize the bicycle at non-intended roll angles. To control roll angle, he claims that we do not do this in a continuous way but rather that we apply discrete pulses when the roll angle meets a threshold. The continuous portion of this model has similar form to the one developed by Weir which in turn resembles our model detailed in the next section.

10.4.7 Wu and Liu

I'll mention briefly some efforts modeling the human with fuzzy control. I have little understanding of fuzzy control but [Clo94] says that fuzzy control methodologies fundamentally let one translate linguistic rules from an expert in controlling the particular system into a control logic algorithm. [TS83] discussed developing fuzzy control rules from the human operator's actions. This somewhat parallels how the PID controller was developed based on a ship helmsman's decision structure [Wik12c]. It seems to certainly be valuable for conscious control efforts, but may have deficiencies when trying to determine the control strategy of unconscious control. But a combination of fuzzy logic and crossover type control may prove useful in describing the human control system. Liu and Wu have done extensive work applying fuzzy control to single track vehicles ([LW93], [WL94], [WL95], [WL96a], [WL96d], [WL96b], [WL96c]).

10.4.8 Mammar

[MEH05] developed a motorcycle control scheme based on a motorcycle dynamics model similar to Sharp's work with steer torque and rider lean angle as the model inputs. He includes a human model with four elements: a simple second order neuromuscular model similar to that of [HMH12], a time delay, gain, and a first order lead filter representing a mental workload model. His control elements include a roll angle feedback gain, a reference signal pre-filter, and

a compensator with proportional, integral, and lead control terms. The proportional term in the compensator is the only speed dependent term. They select the numerical values for the control elements using H_∞ loop shaping for robustness. They finally show simulation results with good performance with regard to disturbance rejection and roll tracking.

10.4.9 de Lange

More recently, [DL11] wrote his master's thesis on identifying the human controller in the bicycle-rider system. He employed a controller which fed back roll angle and steer angle with PID plus second derivative control and time delays to command steer torque through a neuromuscular model filter to the Whipple model. The model is similar in flavor to van Lunteren and Stassen's, but more up-to-date and uses more feedback loops. He chose eight gains plus time delays and attempted to identify which loops were not important from the experimental data presented in the next Chapter *System Identification*. He finds that the critical feedback variables for a stable model were roll angle, roll rate, steering rate, and the integral of the steer angle, claiming the last one is proportional to heading and thus the rider controls heading with steer. He also finds the time delays generally destabilize his model and he removes them.

10.4.10 Hess

Finally, we've developed a control model with Ron Hess [HMH12] that is used later this dissertation for human operator identification. The following section gives a brief synopsis, but one should refer to the published paper for more detail.

10.4.11 Conclusion

A single track vehicle can be stabilized and controlled by a variety of means. Controllers based on simplified dynamical models can potentially control more advanced linear and nonlinear models and/or real systems (i.e. steer into the fall). The roll stabilization is the critical task, as path following can't occur without roll control authority. Few people have demonstrated robust control of a *real* system which stabilizes in roll at a variety of speeds. Even fewer have added path tracking abilities. It doesn't seem like anyone has stabilized a robotic bicycle with a controller that has the limitations of a human built in.

10.5 Hess Manual Control Model

Many control model architectures can be used to attempt to identify the human control system while riding the bicycle. We are limited by the type of sensory information a human rider can sense, the human's processing delays, and the bandwidth and physical limitations of the human's actuators. The human operator has been modeled with simple models like the crossover model, to more complex neuromuscular dynamics, and even fuzzy and optimal control; [Hes97] provides a good overview. Some of the controllers are essentially equivalent placing the closed loop poles in the same place, but make use of different techniques to get to the end result. [DL11] notes that all feedback controllers can be mapped to a common structure. The models may also be different in complexity. But in general, finding the simplest mathematical model capable of capturing the desired dynamics is a good goal. With this in mind, my advisor Ron Hess developed a controller based on the Whipple bicycle model and his previous successful multi-loop human operator models. We present the control model and the loop closure procedure for selecting the five model gains in [HMH12]. This model is fundamentally similar in nature to Weir's work and is built on the same foundations such as that of McRuer et al. ([MGK67a] [MGK67b]). We similarly found steer angle based control to be troublesome and had success across a broad range of speeds and selection of bicycles with steer torque control. We also employed a similar method of evaluating rider lean control without introducing an extra degree of freedom. It also resembles the work of [Doy87] with the inner loop structure dedicated to roll stabilization and the outer loops to high cognitive control in heading and path tracking.

10.5.1 Basics of manual control theory

Manual control, or human operator control, was primarily birthed from control engineers after World War II. The requirements for machine designs in which humans were the principal control element, such as artillery guns and aircraft, led to human control modeling. Work by [Tus47] theorized early on that human control systems could be modeled similarly to automatic feedback systems. Tustin's work was followed by years of theoretical and experimental work by McRuer and his group to understand the control system of aircraft pilots.

McRuer's group found out that humans adjust their control such that the combined human and plant dynamics behave with desirable closed loop dynamics in many types of tracking tasks. This phenomenon can be captured by a variety of theoretical control structures from simple dynamics to complex neuromuscular models [Hes97]. Fortunately, the simpler models can often capture much of the essential dynamics in human-machine systems such as our bicycle-rider system. In particular, we make use of the crossover model [MK74] to structure our controller design. The reason for this is multi-fold. It allows us to use a simple system which has been applied to numerous man-machine systems with good results.

The basic idea of the crossover model is that, when the human is paired with the plant which she is trying to control, the combined open loop transfer function conforms to the dictates of a sound control system design around the crossover frequency [Hes97]. The form of this transfer function for many control tasks remarkably takes the form

$$G_{human}G_{plant}(s) = \frac{\omega_c e^{-\tau_e s}}{s} \tag{10.6}$$

The model is governed by only two parameters: the cross over frequency, ω_c and the effective time delay, τ_e. The simplicity of this model and its ability to describe many human in the loop systems is what makes it so powerful.

The model is capable of describing the dynamics of the human at various crossover frequencies and various performance levels. The majority of the model's experimental validation efforts have been based around laboratory and vehicle control tasks where good performance was required (i.e. skilled subjects).

We also focus only on compensatory control structures where the human closes loops based on output error. This is a simplification as humans are also able to to take advantage of pursuit and preview based control.

10.5.2 Model Description

The control structure was designed to meet these requirements:

1. Roll stabilization is the primary task, with path following in the outer loops. The system should be stable in roll before closing the path following loops.
2. The input to the bicycle and rider biomechanic model is steer torque.
3. The neuromuscular mode of the closed system should have a natural frequency around 10 rad/s to match laboratory tracking tasks of a human operator.
4. The system should be simple. In our case only simple gains are needed to stabilize the system and close all the loops.
5. We should see evidence of the crossover model in the open loop roll, heading, and lateral deviation loops.

The multi-loop model we use is constructed with a sequential loop closure technique that sets the model up to follow the dictates of the crossover model. The three inner loops manage the roll stabilization task and the outer two loops manage the path following. We include a simple second order model of the human's open-loop neuromuscular dynamics which produces a steer torque from the steer angle error.

$$G_{nm}(s) = \frac{\omega_{nm}^2}{s^2 + 2\zeta_{nm}\omega_{nm}s + \omega_{nm}} \tag{10.7}$$

The neuromuscular parameters, ζ_{nm} and ω_{nm}, were chosen as 0.707 and 30 rad/s, respectively, such that the innermost loops gave a typical response for a human operator.

The bicycle is modeled using the Whipple model linearized about the nominal configuration with the primary control input being steer torque. The inner loops are closed with sequential gains starting with the proprioceptive steer angle loop, followed by the vestibular roll rate loop, and the visual roll angle loop[4], *Figure 10.6*. The steer angle loop in essence captures the force/feel or haptic feedback we use while interacting with the handlebars. The need for this loop is readily apparent when trying to control a bicycle simulation with a joystick or steering wheel with no haptic feedback as demonstrated in [DL11]; the difficultly level is high without it. We found that this proprioceptive loop was essential for stabilization and closed loop performance, unlike typical aircraft control models. The outer loops are also visual: heading and lateral path deviation, *Figure 10.7*.

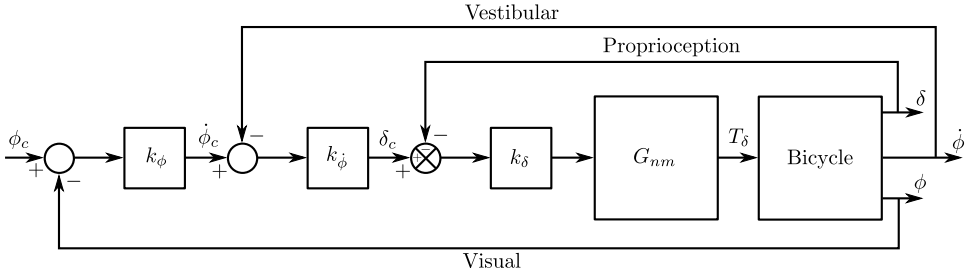

Figure 10.6: The inner loop structure of the control system with steer angle δ, roll rate $\dot{\phi}$, and roll angle ϕ feedback loops.

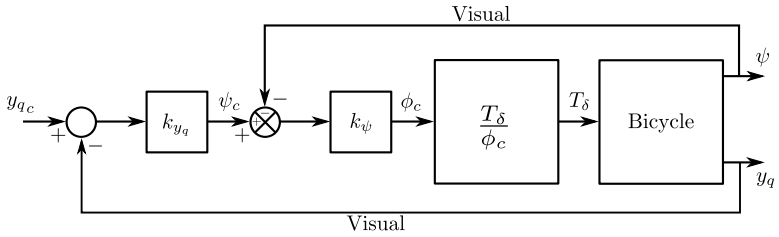

Figure 10.7: The outer loop structure of the control system with the inner loops closed. The heading ψ and front wheel lateral deviation y_q are fed back.

The control structure is simply a function of five gains, which the human "chooses" such that the dictates of the crossover model are met to get good overall system performance. The two inner-most loop gains are chosen such that all of the oscillatory roots of the roll rate closed loop have at least a 0.15 damping ratio. The three outer loop gains are chosen such that the system has a -20 dB slope around crossover. The crossover frequencies are selected sequentially such that the next is half the value of the previous.

Traditionally, sequential loop closure methods are performed on a case by case basis and involve some subjectiveness in applying the design rules of thumb. This is time consuming and error prone when you have to find the gains for many systems such as our bicycles and riders at various speeds. The technique described in [HMH12] can be automated to alleviate this. The following gives the details for developing the gain selection routine.

The roll angle closed loop should be stable, as stability in roll is critical for the path tracking in the outer two loops. To get there, the closure of the proprioceptive and vestibular loops must push the poles to a favorable spot for application of the crossover model on the roll angle loop. To do this, the first two loop closures require that all of the oscillatory modes have a minimum damping ratio of 0.15 and natural frequency around 10 rad/s. We first use the proprioceptive gain, k_δ to push the poles originating at the bicycle weave eigenvalue to a higher frequency with about 0.55 damping ratio. The choice of this gain is somewhat arbitrary, but it needs to set the weave mode pole such that it has a small enough damping ratio to allow the roll rate loop to further push it to a damping ratio of 0.15. In [HMH12] we make

[4] [Doy88] notes that his riders can balance even while blindfolded. This is even true for people who've been blind since birth. So the roll angle dectection, must necessarily not be all visually based. Indeed, in aircraft flight control, the so-called vestibular "tilt-cue" (the human's ability to effectively sense roll angle, ϕ) is a well-known phenonmenon, e.g., [JMJ78].

both loops have a 0.15 damping ratio, but that is not necessary and may not be what the human does. The closed loop transfer function for the steer loop is

$$G_{\delta c}(s) = \frac{\delta}{\delta_c}(s) = \frac{G_{\delta o}(s)}{1 + G_{\delta o}(s)} \tag{10.8}$$

where

$$G_{\delta o}(s) = k_\delta G_{nm} \left(\frac{\delta}{T_\delta} \right)_b (s) \tag{10.9}$$

A numerical example of Charlie on the Rigidcl bicycle at 5 m/s gives numerical values for the open steer angle loop

$$G_{\delta o}(s)|_{k_\delta = 1} = \frac{4990.0342(s + 2.934)(s - 2.934)}{(s + 17.08)(s + 2.56)(s^2 - 1.306s + 5.18)(s^2 + 43.02s + 900)} \tag{10.10}$$

The characteristic equation is 6th order and the caster, capsize, and neuromuscular modes are all stable whereas the weave mode is unstable. The first loop closure will drive the unstable weave pole out to a higher frequency and mid-range damping ratio.

To set the damping ratio multiple approaches can be taken. Here I'll show a Bode design approach and a root locus based design. For the Bode design we select a gain that creates a damped neuromuscular peak near 10 rad/s, *Figure 10.8*. For this bicycle and speed, a gain of ~17.5 will set the inner loop as desired.

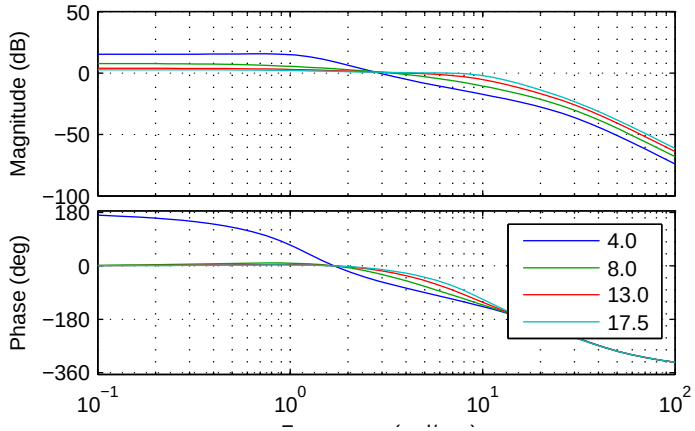

Figure 10.8: The Bode plots of the closed steer loop with various gains. Notice how the higher gains start to increase the bandwidth by pushing the neuromuscular pole closer to a frequency typical of human operator and plant dynamics [HMH12]. Generated by `src/control/choose_gains.m`.

By plotting the root locus of the closed loop poles as a function of k_δ the desired gain can also easily be picked off on a root locus diagram, *Figure 10.9*. The root locus of the steer closed loop poles as a function of k_δ gives an idea where we can push the poles for the next loop closure. Notice that the poles associated with the weave mode at $k_\delta = 0$ are pushed into the stable regime and back out again, crossing the 0.55 damping ratio line twice. There is a range of gains between about 4.0 and 17.5 which cause all of the oscillatory modes to have at least 0.55 damping ratio. This is very clear when plotting the damping ratio versus gain in *Figure 10.10*. The best choice typically is to set the gain such that the pole is at the highest frequency allowable with minimum damping, to give typically observed human operator behavior. This will set up the bandwidth of the subsequent loops to be high enough for good system performance.

With the loop closed at $k_\delta = 17.48$ the transfer function takes the form

$$G_{\delta c}(s) = \frac{87225.7974(s + 2.934)(s - 2.934)}{(s + 3.175)(s - 1.767)(s^2 + 10.86s + 97.55)(s^2 + 48.48s + 998.8)} \tag{10.11}$$

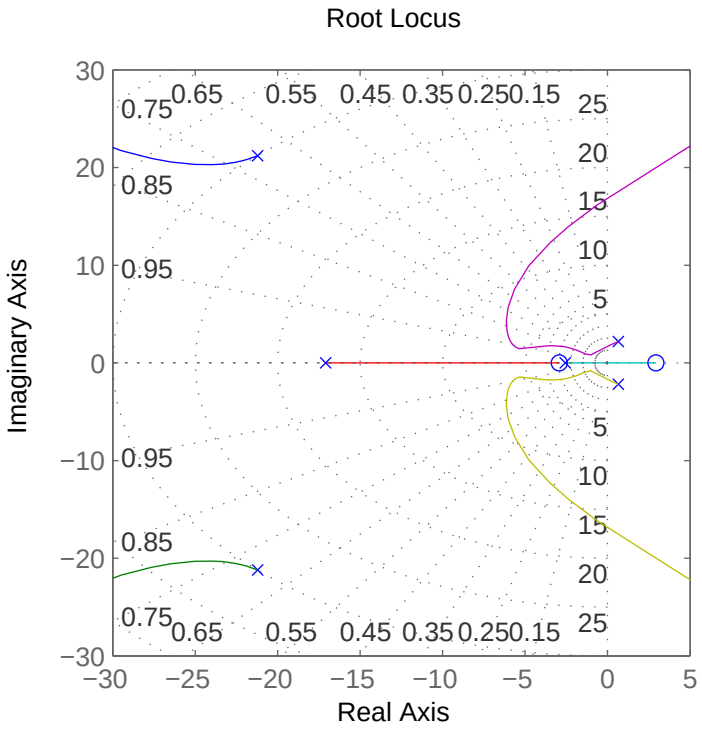

Figure 10.9: The root locus of the steer closed loop poles versus k_δ plotted from 0 to ∞. Generated by `src/control/choose_gains.m`.

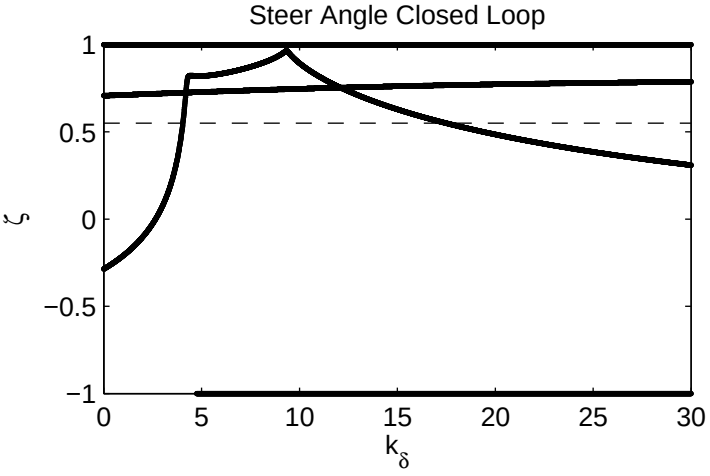

Figure 10.10: The damping ratio of all the poles as a function of gain. Note that there are gains such that all the roots are stable and the damping ratio is at least 0.55, although inner loop stability is not a requirement for total system stability. Generated by `src/control/choose_gains.m`.

Notice the single unstable pole at $s = 1.767$. The roll rate loop closure transfer function now takes the form

$$G_{\dot{\phi}c}(s) = \frac{\dot{\phi}}{\dot{\phi}_c}(s) = \frac{G_{\dot{\phi}o}(s)}{1 + G_{\dot{\phi}o}(s)} \tag{10.12}$$

where

$$G_{\dot{\phi}o}(s) = k_{\dot{\phi}} k_\delta G_{nm}(s) \left(\frac{\dot{\phi}}{T_\delta} \right)_b (s)[1 - G_{\delta c}(s)] \tag{10.13}$$

The roll rate loop gain, $k_{\dot{\phi}}$, is now chosen such that the neuromuscular mode has a minimum damping ratio of 0.15 and frequency is around 10 rad/s. From Figures *10.11* and *10.12* we see that we need to set the roll rate gain to a negative values, about -0.44. Since the bicycle with steer control exhibits non-minimum phase behavior, we need to introduce a positive feedback on roll rate. So it turns out that with a small negative gain we can maintain the neuromuscular mode behavior but introduce the required sign change for stability. This gives the desired 10 dB peaking in the Bode diagram, *Figure 10.13*.

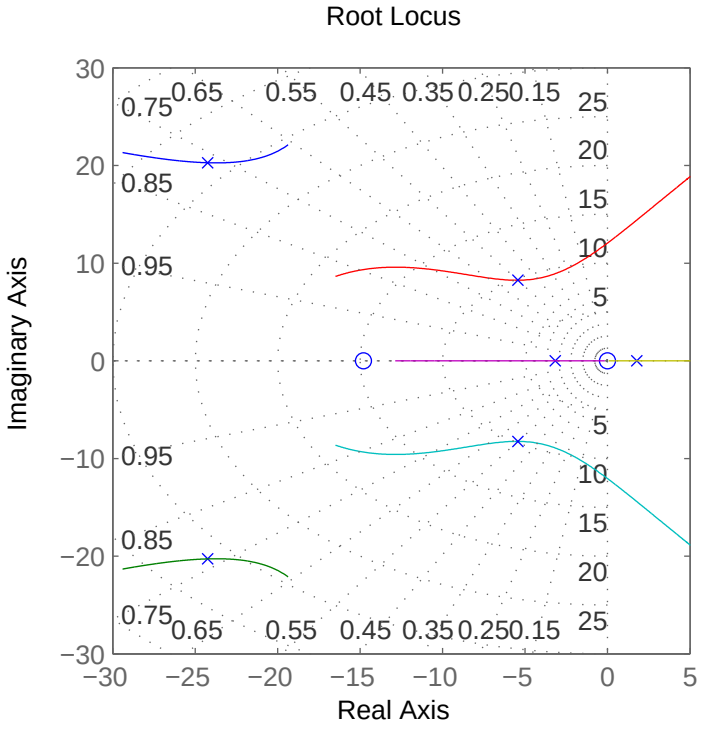

Figure 10.11: The root locus of the roll rate closed loop for gains $k_{\dot{\phi}}$ from -4 to 2. Generated by `src/control/choose_gains.m`.

Notice that the closed roll rate loop does not have any right half plane zeros and there is a single unstable pole.

$$G_{\dot{\phi}c} = \frac{657.1919s(s + 77.09)(s + 14.79)}{(s + 8.106)(s - 0.6015)(s^2 + 3.121s + 107.6)(s^2 + 50.13s + 1042)} \tag{10.14}$$

The bicycle-rider system is similar enough in nature for speeds above 2 m/s that this loop closure seems to always work. We've had some trouble stabilizing the model at speeds below 2 m/s, with the choice of k_δ an important factor in the ability to stabilize at low speeds. [DL11] reported difficulties stabilizing his system below about 2 m/s too. We've found that relaxing the 10 dB peak requirement on the inner most loop such that the neuromuscular mode is more damped, will allow for successive closure and a stable system for lower speeds. But as we all know, the bicycle

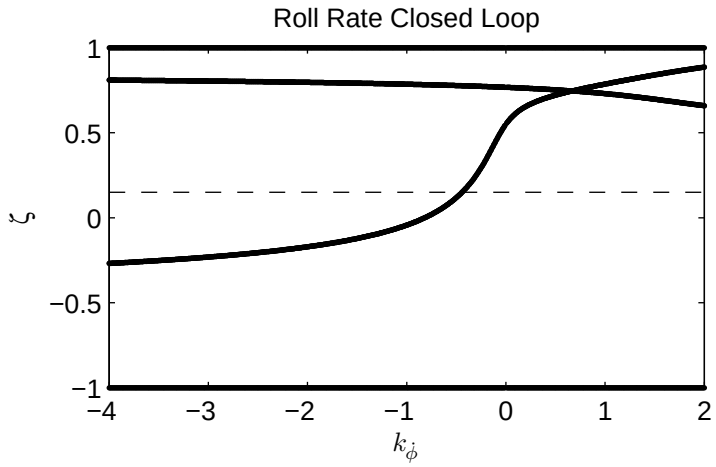

Figure 10.12: The damping ratio of all roots of the roll rate closed loop as a function of gain $k_{\dot{\phi}}$. Generated by `src/control/choose_gains.m`.

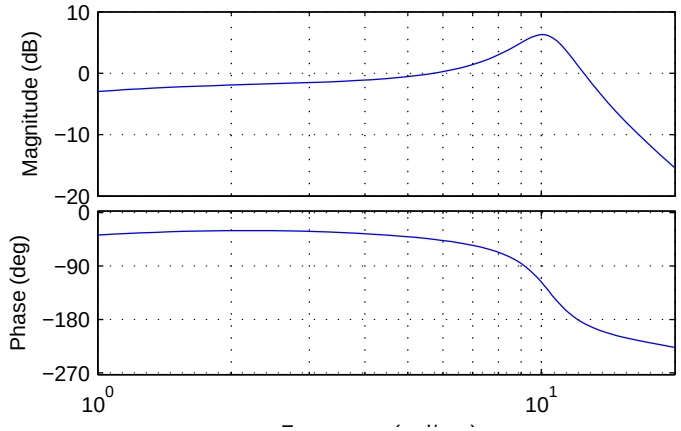

Figure 10.13: The Bode plot of the roll rate closed loop. The neuromuscular mode peaks with a 10 dB magnitude. Generated by `src/control/choose_gains.m`.

is very difficult for a human to balance at extremely low speeds. The fast time constants compounded with human neuro processing delays makes this true. There are slow bicycle riding competitions that take advantage of this fact to test the balancing skill of the rider.

With the roll rate loop closed, the final three loops can be closed by setting the gain such that the crossover frequency of the roll loop is 2 rad/s and the outer loops crossover at half the previous frequency. This is easily set by measuring the gain of transfer function at the desired crossover frequency and realizing that a change in gain will raise or lower the gain curve.

$$G_{\phi c}(s) = \frac{\phi}{\phi_c}(s) = \frac{G_{\phi o}(s)}{1 + G_{\phi o}(s)} \tag{10.15}$$

where

$$G_{\phi o}(s) = k_\phi k_{\dot{\phi}} k_\delta G_{nm}(s) \left(\frac{\phi}{T_\delta}\right)_b (s)[1 - G_{\dot{\phi} c}(s)][1 - G_{\delta c}(s)] \tag{10.16}$$

$$k_\phi = \frac{1}{|G_{\phi o}(2j)|} \tag{10.17}$$

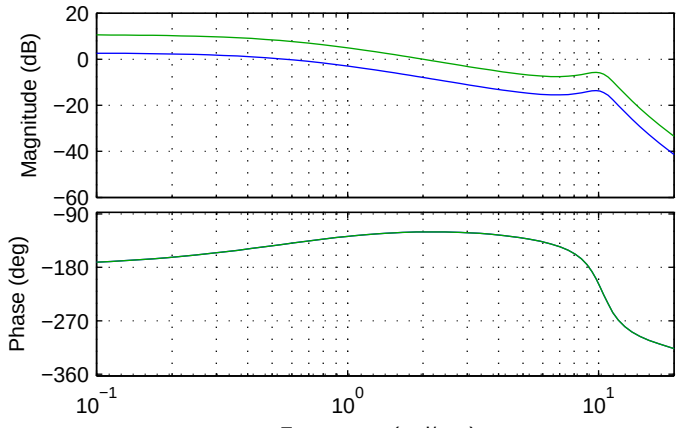

Figure 10.14: The open loop frequency response for the roll angle loop. Blue is gain of unity and the green line uses the gain to give desired crossover. Generated by `src/control/choose_gains.m`.

As can be surmised from the Bode diagram, *Figure 10.14* we've now stabilized the system in roll by forcing the system to behave like the crossover model around the crossover frequency, 2 rad/s. We can now command the roll angle, *Figure 10.15*.

$$G_{\phi c}(s) = \frac{1639.4234(s + 77.09)(s + 14.79)}{(s + 6.881)(s + 1.982)(s^2 + 1.864s + 93.21)(s^2 + 50.03s + 1041)} \tag{10.18}$$

It is important to note that this system is a Type 0 system and thus exhibits steady error as seen in *Figure 10.15*. If we were only concerned with roll stabilization, a low frequency integrator would be needed to remove the steady state error. This was not included in the model design, because the integrator is not needed if the heading loop is closed around the system. The remaining loops are closed using the rule of thumb [Hes97] of crossing over at half the previous inner loop's crossover frequency.

$$G_{\psi c}(s) = \frac{\psi}{\psi_c}(s) = \frac{G_{\psi o}(s)}{1 + G_{\psi o}(s)} \tag{10.19}$$

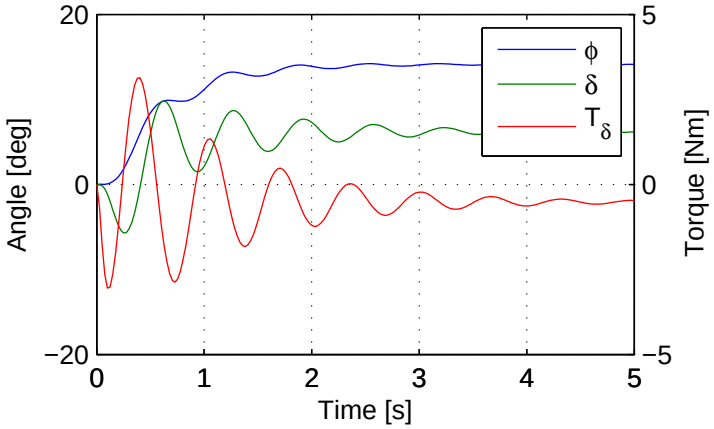

Figure 10.15: The response of the system for a commanded roll angle of 10 degrees. Notice the initial counter steering and the steady state error in the roll angle. This simulation also demonstrates the steady state negative torque needed for a positive turn. Generated by `src/control/choose_gains.m`.

where

$$G_{\psi o}(s) = k_\psi k_\phi k_{\dot{\phi}} k_\delta G_{nm}(s) \left(\frac{\psi}{T_\delta}\right)_b (s)[1 - G_{\phi c}(s)][1 - G_{\dot{\phi} c}(s)][1 - G_{\delta c}(s)] \tag{10.20}$$

$$k_\psi = \frac{1}{|G_{\psi o}(1j)|} \tag{10.21}$$

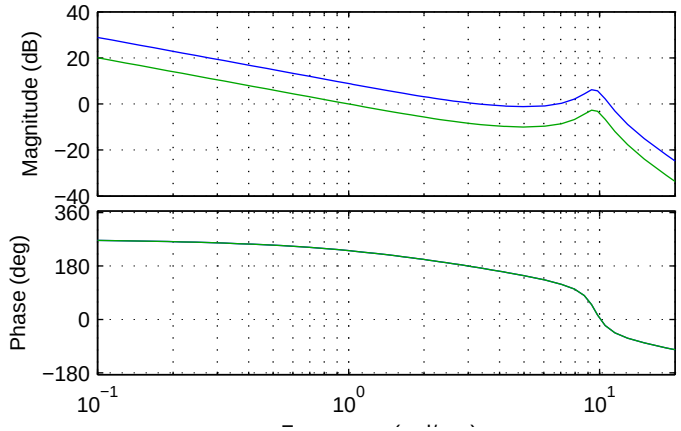

Figure 10.16: The open loop frequency response for the yaw angle loop. Blue is gain of unity and the green line uses the gain to give desired crossover. Generated by `src/control/choose_gains.m`.

$$G_{y_q c}(s) = \frac{y_q}{y_{q_c}}(s) = \frac{G_{y_q o}(s)}{1 + G_{y_q o}(s)} \tag{10.22}$$

where

$$G_{y_q o}(s) = k_{y_q} k_\psi k_\phi k_{\dot{\phi}} k_\delta G_{nm}(s) \left(\frac{y_q}{T_\delta}\right)_b (s)[1 - G_{\psi c}(s)][1 - G_{\phi c}(s)][1 - G_{\dot{\phi} c}(s)][1 - G_{\delta c}(s)] \tag{10.23}$$

$$k_{y_q} = \frac{1}{|G_{y_q o}(0.5j)|} \tag{10.24}$$

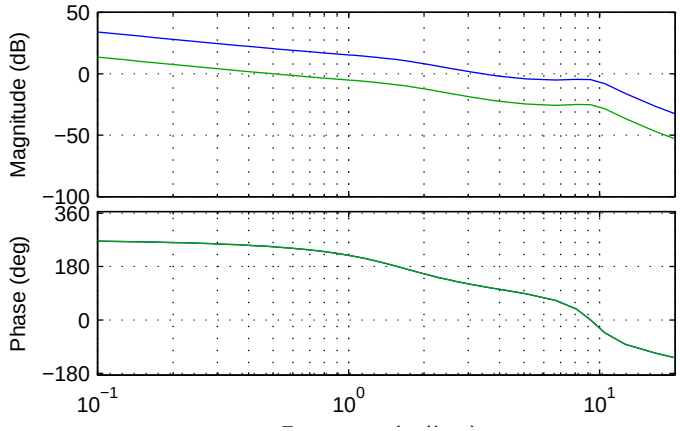

Figure 10.17: The open loop frequency response for the front wheel lateral deviation loop. Blue is gain of unity and the green line uses the gain to give desired crossover. Generated by `src/control/choose_gains.m`.

At this point all the loops are closed and the bicycle can track a given path with good performance. The closed loop system bandwidth is approximately equal to the open loop crossover frequency of the lateral deviation loop. *Figure 10.18* shows the system response to a step commanded input to lateral deviation.

The gains can be computed across a relevant speed range for the bicycle. We developed an algorithm for automatically selecting the appropriate gains for difference physical parameter values and at different speeds. *Figure 10.19* shows how the gains vary with respect to speed for a particular bicycle and rider. Notice that at higher speeds the gains change somewhat linearly, but at speeds below 3 m/s there is non-linear variation. These gains give stable systems which are capable of the lane change maneuver but, due to the difficulties in selecting the gains with the rules above, the algorithm may be making poor choices, especially for $k_{\dot{\phi}}$, at very low speeds.

We automated this method based on the Bode design guidelines. The gain choices for proper neuromuscular peaks in the inner most loops require good initial guesses, as there are often multiple solutions. The correct solution puts the neuromuscular natural frequency at a typical value for human operators.

10.5.3 Software

We designed a software suite in Matlab to implement the automated gain selected for various bicycles, riders, and speeds. The software was constructed around a Simulink version of the model described above and offers this functionality:

1. It generates the state space form of the linear Whipple model for any parameter sets and speeds. The outputs include all eight of the configuration variables and their derivatives reported in Chapter *Bicycle Equations Of Motion* with the addition of the front contact point. This includes the lateral force input described in Chapter *Extensions of the Whipple Model*.
2. It generates the state space form of the closed loops system as a function of the bicycle-rider parameters, the speed, the five gains and the neuromuscular frequency.

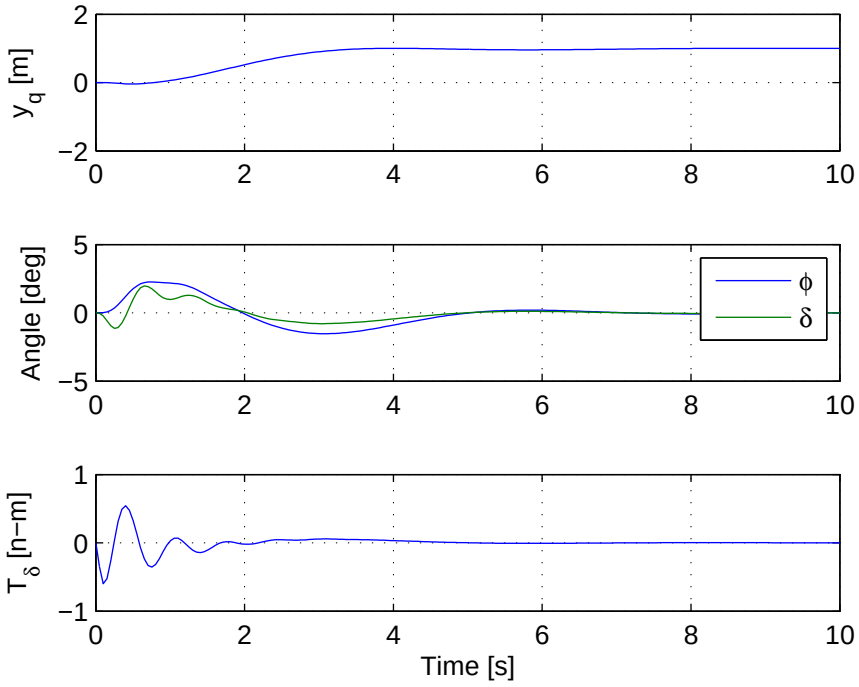

Figure 10.18: The step response to a commanded lateral path deviation. Notice that for the positive rightward turn, the steer torque and steer angle are negative to initiate the positive turn. Generated by `src/control/choose_gains.m`.

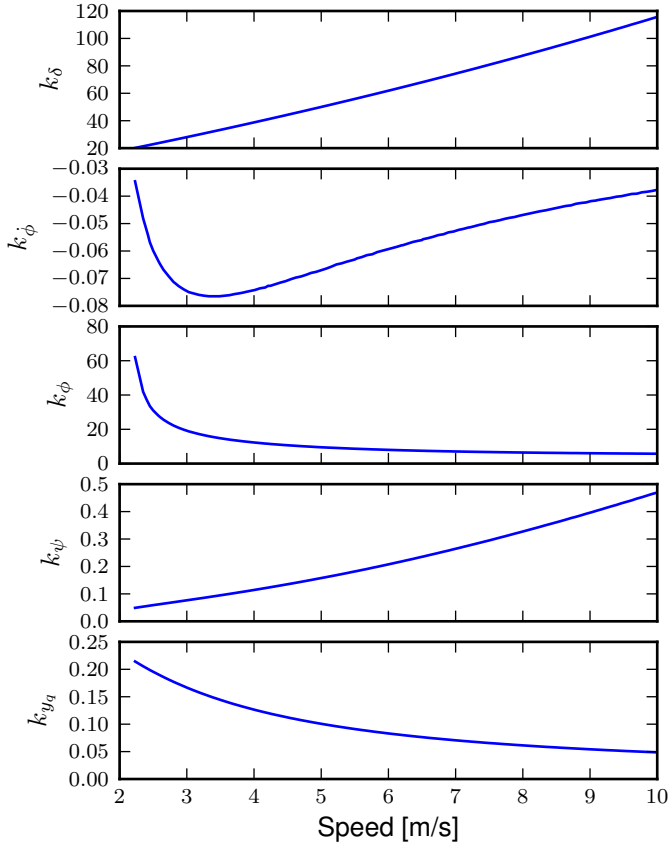

Figure 10.19: The auto computed gains as a function of speed for the Whipple model with the parameter values from the Davis instrumented bicycle with Jason as the rider. These gains were computed with the method in [HMH12]. Generated by `src/davisbicycle/plot_gains.py`.

3. It computes the gains with the sequential loop closure guidelines described above for any give bicycle-rider and speed. (Very low speeds may require some manual tweaking.) The open and closed loop transfer functions for each loop can be returned and or plotted. It can also do this for roll torque as the input as described in [HMH12].
4. It simulates the system performing a single or double lane change with a given or computed set of gains and plots the results.
5. It computes the lateral force input transfer functions.
6. It computes the handling quality metric described in [HMH12].
7. It plots the gains versus speed.

The software was used to generate most of the results and plots in [HMH12] and the source code for doing so is included. The source can be downloaded at https://github.com/moorepants/HumanControl.

10.6 Notation

T_δ Steer torque.

T_ϕ Roll torque.

M, C_1, K_0, K_2 The velocity and gravity independent canonical matrices of the Whipple model.

$\mathbf{0}_{n\times n}$ An $n \times n$ matrix of zeros.

$\mathbf{I}_n$ An $n \times n$ identity matrix.

v Forward speed.

g Acceleration due to gravity.

$\mathbf{A}, \mathbf{B}, \mathbf{C}$ The state, input, and output matrices.

s The Laplace variable.

s_ϕ, s_δ Roots of the steer torque to roll angle and steer torque to steer angle transfer functions.

m_T The total mass of the bicycle-rider system.

z_T The height of the center of mass of the total bicycle-rider system.

I_{Txx} The moment of inertia of the bicycle-rider system about the longitudinal axis.

$G_{nm}(s)$ The neuromuscular transfer function.

ζ_{nm} The neuromuscular damping ratio.

ω_{nm} The neuromuscular natural frequency.

$k_{\delta,\dot{\phi},\phi,\psi,y_q}$ The controller loop gains.

x_p, y_p Rear wheel contact point.

x_q, y_q Front wheel contact point.

ψ Yaw angle.

ϕ Roll angle.

δ Steer angle.

$G_{xo}(s)$ The open loop transfer function of loop x.

$G_{xc}(s)$ The closed loop transfer function of loop x.

CHAPTER

ELEVEN

SYSTEM IDENTIFICATION

11.1 Preface

I started to think about system identification when I arrived at Delft and the discussions began with Arend and Jodi. I hadn't much clue about the formal field and theory of system identification. My first look at it was when Arend presented me with a light introduction by Ljung, so I credit Arend and his cohorts for the ideas that have been implemented in this chapter. We talked about it here and there but never really put together a solid experimental plan to do anything about it. Karl Åström visited us in Delft in late 2008 and we talked some with him about system identification of the bicycle. I mainly recall him focusing on how to excite the system in a very controlled manner with an oscillating mass on the bicycle. Some of these ideas propagated through Arend to Peter and can be seen in the final sections of his thesis [DL11]. Many of these ideas influenced our NSF proposal and ultimately the final portion of what I was to do for my dissertation work.

Once I had gotten back to Davis we now had the resources available from NSF funding to make something happen. My goal had basically formalized into creating a instrumented bicycle to be controlled by a person that was capable of measuring all of the kinematics and kinetics involved in regulated control tasks. We also originally had hoped to be able to vary the dynamics of the bicycle, but the reduced funding nixed that idea. It took some time into the project to really understand what we might be able to accomplish with that but it finally materialized into validating Ron's theoretic control model which is discussed in [HMH12] and Chapter *Control* with data collected via the instrumented bicycle. After our first experiments, over a year into the project timeline it became apparent that simple tasks with measured lateral perturbations would provide the best chance of validating his model. Unfortunately, I had not thought a great deal about how to provide and measure these lateral perturbations but the manually excited perturbations seemed to do the trick.

We ran a lot of preliminary system identification analyses on the first set of trial data, but it quickly became apparent that we had little understanding of the subject. The early analyses did give confidence that the data was of good enough quality to do something with, but our goal of identifying the parameters of the controller were still far from our reach.

We performed the final set of experiments around August and September of 2011 to get a large sample of data for the final analyses. The NSF grant was to end at the end of September and I still had to figure out how to analyze all of the data, not to mention write up a ton of work for my dissertation. We ended up extending the NSF grant another year (as seems to be typical with these things). I look back to our original proposal and in hindsight the scope was way too large (accurately predicted by Arend). We nixed the handling qualities parts when the funding was lowered, but I now see that what we hoped to do really took another 6-12 months longer than we had intended.

The final analyses have forced me to figure out what system identification is all about and I've learned a great deal rapidly and much on my own. At this stage we weren't able to find any local experts on the subject to help us along but I've gotten some great insight from both the single track vehicle dynamics email list and from personal communication with Karl Åström. I still feel very weak in the subject but it is more clear how difficult identifying complex systems is, especially trying to nail down physical parameters.

As many doctoral students probably hope when starting their long trek to the PhD, I hoped for some grand findings to arise from this work. But I've been humbled a lot in that quest. I present here the work I've done with regards to

identifying the bicycle and rider system with what I think are good results, but I hope that it can be a guide for others to see some of the difficulties in executing this kind of analysis with some ideas to better structure it.

11.2 Introduction

The work presented in this Chapter is intended to be the icing on the cake that takes into account all of the theory presented in the previous chapters and evaluates it with a large set of data taken with the instrumented bicycle described in Chapter *Davis Instrumented Bicycle*. It is also the overarching deliverable I was responsible for under the NSF grant. This chapter details system identification of a bicycle and rider system. It is broken in two main parts, the first goal being to identify the passive bicycle rider system and the second to identify the active portion, i.e. the rider's control system. The literature review gives an introduction to other's efforts in both these analyses with respect to single track vehicles.

Two important concepts need to be mentioned briefly before proceeding. The first is a review of the terms used to categorize model structures in the system identification field: white box, black box, and grey box. System identification is the process of identifying a model that best predicts a particular input/output relationship. If we develop a model entirely from first principles[1], e.g. using Newton's laws to describe the motion of an object, when all of the parameters and states are known then this is called a white box model because we know everything about it a priori. The second case, the black box model, describes a model in which one only knows the structure, i.e. order, of the underlying equations but all the coefficients are unknown. Finally, the grey box model falls in between the first two in that one may have more knowledge of the structure of the coefficients based on first principles, e.g. one may know that some model coefficients are zero or that the model may be parameterized by some known and some unknown physical characteristics.

The second concept regards the notion of process and measurement noise in a dynamic system. Dynamic systems have states that evolve dynamically through time, but a real system has elements that are not purely deterministic which are typically called noise. The noise can be broken up into the process noise, the noise due to errors in, or random inputs into, the model, and the measurement noise, the noise due to errors in the measurements. The ability to characterize these two types of noise plays a large role in the accurate identification of dynamic systems.

11.3 Literature

There is a rich history of bicycle and motorcycle mathematical model development. This has been able to explain many of the more dynamically fascinating phenomena, from countersteering and stability to speedman's wobble and gyroscopic effects. But the amount of experimental validation of these idealized models pales in comparison, with the motorcycle experimentation outdistancing that done with bicycles.

Basic bicycle and motorcycle identification is typically done on data collected by exciting the vehicle through force/torque perturbations in either roll or steer. These experiments can be done when the bicycle is under closed loop control or when the bicycle is stable, the former being a requirement for speeds outside of the stable speed range. But, the mode excitation methods are limited to the frequency band around that mode of motion. Manual excitation under closed loop control gives better excitation bandwidth and a pairing with modern system identification techniques can provide richer models.

11.3.1 Passive Vehicle and Rider Identification

Identification of passive, open loop vehicle-rider models is more prevalent than the identification of the controller. It is indeed a requirement to have a very good vehicle model before attempting to identify the control system a human employs while controlling the system. The bicycle and motorcycle are excellent choices for manual control experiment

[1] First principles here means any modeling techniques that use fundamental "known" building blocks to create a dynamic model. These buildling blocks can include items such as Newton's laws of motion, the laws of thermodynamics, friction and contact models, electrical components, etc.

design due to the fact that they are relatively economical systems that require a broad range of human control skills to stabilize and direct the vehicle, but they have the disadvantage that first principles models are somewhat more difficult to develop and have smaller pool of prior research as say cars or aircraft. The approaches to identifying the passive model include mode excitation techniques to system identification under more general inputs.

CALSPAN

The earliest comprehensive bicycle model validation began at CALSPAN in the late 60's. This included several revolutionary studies, in one of which they made use of a rocket to apply know step torques to an uncontrolled riderless bicycle. In another, simulations of slalom maneuvers were visually compared with video footage [RM71].

Eaton

David Eaton's work ([Eat73b], [Eat73a], [ES73]) may be the closest example to the work presented in this chapter. He did his PhD work at the University of Michigan under the Highway Safety Research Institute. His dissertation focused on the experimental validation of the motorcycle modeling work of [Sha71] and the human controller modeling work of [Wei72]. He did this with two sets of experiments: 1) identification of the uncontrolled dynamics of the motorcycle under perturbations, and 2) identification of the rider controller during roll stabilization tasks. The latter of which will be discussed in the next section.

His initial experiments were aimed at validating and identifying the passive motorcycle system. During these experiments, his subjects road a motorcycle with their bodies rigidly braced to the frame and hands-free at speeds of 15, 30, and 45 mph (6.7, 13.4, and 20.1 m/s) along side a pace car which recorded the output from roll angle, roll rate, and steer angle sensors. The brace and open loop response allowed rigid rider modeling assumptions to be used. Weights were dropped from one side of the motorcycle to induce a step roll torque and the rider used a single pulse in steering torque to the handlebars to right the motorcycle in roll after the drop. These experiments were impressively dangerous and would be hard pressed for approval by the Institutional Review Board if done today, but well designed for the typical modeling assumptions. The resulting time histories of the measured system outputs were compared to simulations of Sharp's model [Sha71] augmented with a variety of tire models of Eaton's design. He found good agreement between the experiments and the models for higher speeds, but felt that a more complex tire model was needed to predict the wobble mode in slower speed runs.

The second set of experiments were more tame. The three riders simply balanced the motorcycle on a straight path at two speeds, 15 mph and 30 mph, for a total of 38 runs. He added a steer torque transducer bar above the handlebars. The rider controlled the motorcycle with one hand and the rider applied torque was recorded along with the other signals. No perturbations were necessary, as the rider's natural control actions excited the system in a wide enough bandwidth. From this data he was able to identify the motorcycle steer torque to roll angle transfer function through the spectral densities of the measured signals (by dividing the cross spectrum of the roll angle and steer torque signal by the power spectrum of the steer torque). The identified transfer functions show good agreement with the augmented Sharp motorcycle model at the 30 mph speeds, but less so for the 15 mph runs.

His generated frequency responses from the second experiments provided an empirical model, while the simulation comparisons from the first experiments were validation rather than identification.

Weir, Zellner, Teper

Weir, Zellner, and Teper performed an extensive experimental study on motorcycle handling qualities for the U.S. National Highway Traffic Safety Administration in the late 70's, [WZT79]. This was a follow up to both the CALSPAN studies and [Tag75], both under or related to the same Administration. There is little to no explicit system identification in the study but some important elements are there. In terms of the passive model identification, they present steady state comparisons of their experimental data to their models with varying degrees of qualitative agreement and generally good ability to predict the conditions at which sign reversals in torque are needed to maintain a steady turn. They also compare single lane change simulations of a controlled vehicle to their measured data by visual inspection.

They unfortunately admit that adjusting the first principles models to better fit their measured data was outside the scope of the project. But this gives some early examples of model evaluation with respect to good quality data.

James

Stephen James published a study in 2002 [Jam02] in which he attempted to identify the linear dynamics of an off-road motorcycle. He measured steering torque, steer angle, speed, roll rate, and yaw rate with his subjects manually exciting the vehicle through steer torque during runs at various speeds on a straight single lane road. He made use of black box ARX SIMO identification routines of 6th and 7th order (his and others motorcycles models are usually 10th+ order) to tease out the weave and wobble eigenvalues. He compares the identified eigenvalues, eigenvectors and frequency responses to his motorcycle model and claims good fits based on visual interpretation of the plots. The agreement is questionable due to the lack of statistics in the model comparisons and little validation of his first principles model which assumes a rigid rider. The study does show that there is the possibility of identification of multiple modes of motion with simple manual excitation of the handlebars. He also used these techniques to identify the same motorbike with a single wheel trailer in [Jam05].

Biral et al.

[BBCL03] performed a nice study to identify motorcycle dynamics under an oscillatory steer torque input. They measured steer torque, roll rate, steer angle, and yaw rate with an instrumented motorcycle. They performed slalom maneuvers at speeds from 2 to 30 m/s at three sets of cone spacings in the slalom course. The resulting time histories were close to ideal sinusoids. They used curve fitting to find amplitude and phase relationships among the measured signals. The results were plotted on Bode plots for comparison to the frequency response of several first principles models. The models predict the experimental data and their motorcycle model is shown to do a better job than other models from literature. This claim is only based on visual inspection. I would say this technique and others like it are more of an ad hoc method of system identification of the vehicle dynamics because they rely heavily on very specific input and output characteristics, but nevertheless seems to be effective. Making use of formal system identification techniques could potentially give more reliable results and the ability to better characterize the uncertainty in the predictions.

Kooijman

Jodi Kooijman has worked on experimental validation of the benchmark bicycle [MPRS07] linear equations of motion for a riderless bicycle [Koo06], [KSM08], [KS09]. His instrumented bicycle measured the steer angle, forward speed, roll rate, and yaw rate. Due to the fact that the bicycle can be stable at certain speeds he was able to launch the bicycle in and around the stable speed range and perturb the bicycle with a lateral unmeasured impulse and record the stable decay in the steer, roll, and yaw rates. The post perturbation time histories of the measured signals provided nice decaying oscillations and curves could be fit to find both the time decay constant and frequency of oscillation. These were then compared to the predicted weave response based on the first principle model numerically populated with measured physical parameters of the bicycle. He found good prediction abilities of the weave mode between 4 and 6 m/s. The "goodness" of fit were gaged by visual inspection with no uncertainty estimates in the models or the results from the dynamic measurements. The method was not able to predict the heavily damped caster mode nor the capsize mode. He also demonstrated that the measured dynamics were the same when the experiments were performed on a treadmill.

In [KMP+11], Jodi constructed a bicycle with very unusual physical characteristics including negative trail and canceled angular momentum of the wheels. He performed similar experiments to his Master's thesis work. They show the comparison of a single stable experiment in which yaw and roll rates were measured and compared to the predictions of the benchmark bicycle.

[Ste09] and [ER11] both perform experiments similar to Kooijman's with similar results, although Steven's results vary in the ability of the model to predict the data for various configurations of his adjustable bicycle.

These also fall into the ad hoc system identification techniques that take advantage of the stability at certain speeds and very specific output characteristics. The variability in reproducibility in the studies from other researchers should be noted.

Chen and Doa

[CD10] develop a first principles non-linear bicycle model with a fuzzy controller and use it to generate stable simulations for various speeds. They then do an output error grey box identification on the resulting data with respect to the non-zero and non-unity entries of the state, input and output matrices (i.e. just the entries of the acceleration equations). The identification is done for a discrete number of speeds in the range 1 to 15 m/s. The eigenvalues are calculated of the resulting identified, speed-dependent A matrices and the root locus plotted versus speed.

The resulting eigenvalues seem to behave like the benchmark bicycle but the capsize mode is shown to go unstable briefly at a speed lower than the stable speed range. They did not attempt to characterize or identify the process noise even though they generated the data with a known model with known input noise. Also their non-linear bicycle equations of motion [CD06] were never validated against any other accepted models. Both of these could potentially explain the discrepancies in their identification. Their identification procedure does show that it may be possible to get good estimates of a linear model of the vehicle alone from noisy data regardless of the controller which stabilizes the vehicle.

Doria

In [DFT12] experiments are performed where a motorcycle rider excites the steering with a pulse and lets the motorcycle oscillate while the rider keeps his hands on the handlebars (as opposed to Eaton's hands-free experiments). The resulting dynamical measurements are nice decaying sinusoidal-like motions and the authors fit optimal curves to the data. They identify the time constants, and frequency and phase information to construct the eigenvalues and eigenvectors of the excited mode. The empirically derived eigenvectors show some resemblance to the model's predictions.

11.3.2 Controller Identification

van Lunteren and Stassen

At Delft University of Technology in the Man-Machines research group, Drs. van Lunteren and Stassen began work in 1962 to identify the human controller for a normal population of subjects and report on their work into the early 70's ([VLS67], [VLS69], [Sta69], [VLS70a], [VLS70b], [VLS70c], [VLS73], [SVLB+73]). They chose a bicycle simulator as the plant because it was a common task that average people could do and their studies could focus on a wider population of individuals as compared to most previous work based around trained pilots. The bicycle simulator did not capture all of the essential dynamics of a real bicycle as it's operation was based on only the simplified roll dynamics of Whipple's model, but nonetheless offered a similarly complex roll stabilization control task as a normal bicycle would. The simulator was controlled by both the steering angle and the rider's lean angle, both of which are questionable inputs as have been pointed out as early as [RL72].

They assumed the rider's control actions can be described by a PID controller with time delays on each feedback variable and mention that this controller was chosen instead of a McRuer style controller primarily due to limitations of their computational equipment. The error in the roll angle is fed into two PID controllers each with a time delay: one to output the corrective steer angle and the other to output the corrective lean angle. They introduce a remnant term for each control action and the external disturbances to the bicycle model.

The identification goal was to find the six gains and two time delays in which the controller performed as a human would. The preferred method was a real time estimation routine due to the speed of computations and reasonable agreement their correlation method. The results indicated that the subjects used no integral control (i.e. only position and rate feedback). They could identify within a bandwidth of about 2 Hz and noticed that when the system was undisturbed there was a 0.5 Hz dominant frequency in the rider's control actions. The rate feedback was more dominant

in generating the lean control input than it was for the steer control input. Also, they found the time delay for lean to be larger than the steer time delay and postulate that the steer action is a result of cerebral activity while the lean is more of a reflexive pattern. Another finding resulting from analysis of Nyquist plots of different riders' identified control actions showed that riders chose different control actions. They attribute this to the roll stabilization being a sub-critical task (i.e. a more difficult task may force different riders to adopt similar control behavior). They also investigated the effects of drugs, such as alcohol, on the riders control behavior. They found correlations from drug dose to time delays and the error in the control actions. Their later studies introduced better identification methods and they found discrepancies in the identified time delays of the later work as compared to the previous work. For example, the steer control time delay was originally found to be around 1.5 seconds and the improved methods found the delay to be around 0.7 seconds. The discrepancy was attributed to the bias due to remnant in their early work. They also introduced a visual tracking task into the simulator but had difficulties in getting reliable transfer function identification as compared to the roll stabilization transfer functions which improved in quality due to longer trials of 35 minutes.

The methods developed in their studies are excellent and thorough examples of early parameter identification in human control tasks. The simpler plant dynamics were most likely beneficial in reducing the uncertainty in the identified parameters, but the choice of angles as inputs instead forces of torques may not be a realistic enough model of the human's actuation.

Eaton

After feeling confident in his motorcycle identification results, Eaton made use of the Wingrove-Edwards ([WE68], [WEC69], [Win71], [Edw72]) method in tandem with an impulse identification to identify the human controller. The remnant element was large with respect to the torque that was linearly correlated with the roll angle, but the human control element was identified with a simple gain and time delay for most of the high speed runs. The time delay identification of about 0.3 seconds was very repeatable across all runs. Furthermore, he demonstrated that the crossover model was evident in the resulting closed loop rider-motorcycle transfer functions.

Eaton is one of very few who have identified the rider controller during actual single track vehicle tests with confidence in the underlying passive rider-vehicle model. This study has influenced the work in this chapter in many ways.

Doyle

A recently uncovered study on the manual control of a bicycle from a psychologist's perspective has some very non-traditional techniques and outlooks for the understanding of the control system employed while balancing a bicycle [Doy87]. Anthony Doyle's paper [Doy88] on his thesis topic opens with "The old saw says that once learned it is never forgotten, but what exactly is learned has been by no means clear." This reflection points to the great complexity behind balancing a bicycle, such an easily gained skill. He chooses to study the bicycle over a simpler task partially due to the fact that the rider has little freedom in effective control strategies and partially because it is a skill many people can do.

His goal was to determine how much of the rider's control actions can be accounted for without involving higher cerebral functions. He mentions the Weir and Zellner work and the fact that its focus is on motorcycles at high speed, and questions whether the control employed for their system is simply a different version of the one employed on a bicycle at low speed or whether they are different control methodologies altogether.

He was aware of the inherent stability that bicycles can provide and constructs an instrumented bicycle where the head angle, trail, and front wheel gyro effects are eliminated so that "all steer movements are a result of the human's control". He also mentions, but doesn't use, a body brace to eliminate unnecessary body movements and he blindfolds his subjects so that their sensory information is limited to proprioception and vestibular cues. He mentions the arm and upper body movements and how it is difficult to tease out the deliberate movements versus the passive dynamics of the body. With the instrumented bicycle he conducts low speed steady turn and balancing tasks and measures speed, roll rate, and steer angle.

Along with the experimental data, he developed a bicycle and rider model with accompanying controller. The derivation of the bicycle model is questionable due to the non-traditional methods, but he does end up with a model which behaves like a bicycle including speed dependent stability. He is aware of the need to roll the bicycle frame in the direction of the desired turn for directional control and how counter-steering plays a roll in this. This concept leads to the primary inner loop being chosen as roll control and his control structure resembles that of Weir's work in terms of sequential loops. He cites the crossover model and is aware that humans can adjust their gains as needed for good performance. The controller is traditional in most senses and follows the patterns by McRuer, Weir, and Eaton, but he adds in the ability to add discrete pulses to the roll angle. He feeds back roll acceleration and integrates it to get roll angular velocity. This is basically a continuous PD control on roll rate. But his non-continuous addition to the controller is based on a fuzzy logic-like rule "Make a pulse against the lean whenever it gets bigger that 1.6 degrees."

It seems like he gets somewhat close matches to the experimental traces from his control model simulations without the discrete pulses, but then adds in pulses (single or multiple) to the steering so that the traces matches more closely. His identification technique and criterion is focused around a detailed examination of the patterns in the time histories in a very qualitative way.

His results focus on the evidence for intermittent control and finds the traditional gains to be inversely proportional to speed. He claims the balancing part of the control system is done primarily in the lower cortex.

To me, Doyle's work emphasizes the need for close collaboration between psychologists and control engineers to formalize the theory for human balance. His intermittent control theory may be valid, but due to the unusual model development, simulation and analysis techniques it is hard to gauge whether the need for intermittent control was simply an artifact of poor vehicle modeling. His insight into the human control theory is very enlightening and his ways of wording bring the theory outside the traditional control framework for an expansion in understanding.

Lange

Peter de Lange's recent Master thesis work [DL11] focused on identifying the rider controller from the data that he helped us collect while interning at our lab. He used the Whipple bicycle model, a simplified second order representation of the human's neuromuscular dynamics (natural frequency 2.17 rad/s and damping ratio of 1.414[2]) and a PID like controller with a 0.03 second time delay. The controller structure had gains proportional to the integral of the angle, the angle, the angular rate and the angular acceleration for roll and steer. The control task was defined as simple roll stabilization (i.e. track a roll angle of zero degrees), even though the data was collected during heading and roll tracking tasks.

He used a four step process for identifying the rider controller 1) he "removed" the human remnant by averaging the time histories over several individual perturbations, 2) he identified a high order finite impulse response model (only a function of previous inputs) for the lateral force to steer angle SISO pair (lateral perturbation force input and steer angle as output) 3) low pass filtered the resulting responses, and 4) he identified the rider controller parameters with a grey box model using the filtered FIR simulation results as the base data. The grey box model was parameterized with eight gains and a time delay. He was able to identify the gains, but the time delay always gave a resulting unstable model, so he dropped it. Furthermore, all of the gains were not necessary for good model predictions so he eliminated the unnecessary gains systematically to find the critical feedback elements. These turned out to be the gains for roll angle, roll rate, steer rate, and the integral of the steer angle. The first three are as one may expect and he concludes that the steer angle integral could be equated to yaw angle feedback since they are proportional in the linear sense.

Peter's approach hinges on the averaging process in step one. The human remnant is large relative to the measurements and averaging potentially removes data that isn't necessarily noise. This averaging is atypical, as process noise models are usually employed to account for these variations in the data. Using a model such as ARMAX instead of the two step averaging and FIR model would potentially allow one to identify the underlying linear model without removing potentially valid data in the time history averaging process. Or all of the steps could be combined into a state space grey box formulation with a process noise model, for a more direct route to identifying the free parameters. But these methods have their difficulties and will be described later in the Chapter.

[2] This overdamped low bandwidth neuromuscular model is very different than what we assumed and ultimately identified.

11.3.3 Conclusion

The literature provides many examples of first principle models for both the open loop vehicle-rider system dynamics and the rider's control, but often proving that those models are good predictors of real physical phenomena is difficult. The previous examples presented above have various similarities that influence the methods I've chosen to use to identify the vehicle and the rider.

Open loop identification The purpose of the open loop identification is to identify the passive vehicle and rider dynamics. This includes the force and kinematic relationships of the bicycle or motorcycle and, if a rider is present, the passive dynamics of the rider's body motion. Their are two basic approaches that have been used in literature.

Mode Excitation This involves identifying particular modes of motion by forcing the system such that those modes are excited. The input to the vehicle is typically limited to a narrow bandwidth. The forcing can be generated manually from human control, by external perturbations, or as a result of the maneuver. The techniques are best at identifying sustained oscillatory modes. Decaying oscillations are fit to the data to extract time constant, frequency, and phase shift for various input-output combinations. These techniques generally give good repeatable results, but are limited to identifying single modes and require many experiments to get a spread in frequency content and vehicle speed. These methods are also limited to identifying open loop dynamics.

Excitation Many modes of a model can be simultaneously excited if proper inputs to the vehicle are chosen, giving the opportunity to identify more complete dynamic models. Frequency sweeps, white noise, and sum of sines are good candidates for a broad input spectrum. And it turns out that the remnant associated with human control and or deliberate random manual excitation can provide a wide bandwidth input spectrum as shown in [Eat73b] and [Jam02] for adequate system identification of many modes including the higher frequency wobble mode. Modern system identification techniques can be used to find models and identify physical parameters.

Rider Control Identification (closed loop, active) Few have attempted to identify the rider as a control element in the bicycle or motorcycle system. The large array of potential control actions from a unconstrained rider is extremely difficult to measure, especially when both the forces and kinematics are keys to proper identification. Typically limits are put on how the rider can actuate the system and in some cases limits are put on the rider's ability to sense the system. This is somewhat critical so that the system is much more tractable. Similar to the open loop excitation techniques, a broad frequency spectrum provides better data to work for identification purposes. [DL11] has a good overview of excitation ideas.

The open loop dynamics are in some sense much easier to model with first principles, as the theory is much more mature. On the other hand, the theoretical constructs of the control system of the human is relatively in its infancy, so having the advantage of strongly validated first principles is much weaker than say in the field of mechanics. Most researchers' approaches have been modeled from the manual control work lead by authors such as Tustin and McRuer in the 50's and 60's. When mapped to the bicycle, the primary control loop is taken as roll stabilization and roll command authority, with the secondary loops being heading and tracking. Both sequential loop controller designs and the popular PID controllers have been used as a structure for gain and delay parameter identification in the control loops.

Accurate parameter identification relies on accurate characterization of the system process noise and in the case of a human rider, the process noise is often comparable in magnitude and frequency to the control actions themselves. Techniques that treat the controller as a quasi-linear structure, in which the noise is modeled as white and Gaussian and characterized by the portion of the output not linearly correlated to the input (i.e. remnant), have been popular in the past. [Eat73b] took care to account for this and found that the crossover model was a good predictor of human control action. A proper treatment of the noise by other researchers is typically little to none and justly so as it is not necessarily easy to deal with small signal-to-noise ratios in the linear control framework. Modern system identification techniques offer some ability to model process noise with ARMAX types of implementations and state space formulations benefiting from the integration with Kalman filters. As will be discussed in the following sections, model identification works fairly well but parameter identification such as those for control gains becomes increasingly difficult with larger noise.

11.4 Experimental Design

Our main experimental designs were focused around reasonable ways to excite the rider/bicycle system with the goal of identifying the parameters of the rider control system. I started by simply repeating some of the perturbation experiments from Chapters *Delft Instrumented Bicycle* and *Motion Capture*, but included and measured the lateral perturbation force and the steer torque which were critical measurements for realistic input/output relationships that the previous studies lacked. We also attempted single lane change maneuvers because we'd been using a lane change as our objective criterion in our simulations [HMH12] and they had been used successfully used in the literature. It turned out that we were able to get reasonable results with preliminary system identification with the lateral perturbation runs and did not pursue the lane change maneuvers beyond the preliminary efforts. The lane changes were especially difficult on the narrow treadmill.

11.4.1 Riders

We chose three riders: Charlie, Jason, and Luke of similar age: 34, 28-29, 32, mass: 79, 84, 84 kg and bicycling ability although Luke has more technical mountain biking skill than the other two riders. A wide range of skill levels were outside the scope of the project and we preferred riders with good proficiency as it has been shown that it increases repeatability of results in tasks such as these [WZT79]. The seat height and harness were set in the same position for Charlie and Luke and in a different position for Jason. The inertia of the rear frame was measured for both configurations (thus the "Rigidcl" and "Rigid" bicycles) in Chapter *Physical Parameters*.

11.4.2 Environments

We performed the experiments in two different environments: on a treadmill and in a large gymnasium.

Treadmill

Dr. James Jones at the veterinary school at here at Davis graciously let us use their horse treadmill (Graber Ag Kagra Mustang 2200) during their downtime, *Figure 11.1*. The treadmill is 1 meter wider and 5 meters long and has a speed range from 0.5 m/s to 17 m/s. This was only a third of the width treadmill at Vrije Universiteit in Amsterdam, but after some practice runs we felt that narrow lane changes and the lateral perturbations could be successfully performed. We used the treadmill because the environment was very controllable, in particular with regard to fixed constant speeds, and it offered the ability to do very long run durations within a broad speed range. Potentially both the side railings and the belt side curbs added to rider's lack of lateral movement space and changed the riders' control strategy.

Pavilion

The bicycle was designed in such a way that all of the data collection equipment was on board and was suitable for data collection in a free environment. After lengthy bureaucratic negotiations, we were able to make use of the UCD pavilion floor for the experiments, *Figure 11.2*. The floor was made of a stiff rubber[3] and provided a rectangular, wind-free space of about 100' by 180' (30 m by 55 m). We rode around the perimeter to build up speed and did our maneuvers on a straight section about 100 feet (30 m) long. We were not able to travel at speeds higher than about 7 m/s as the tires would slip in the final turn into the test section (this seemed to be due to the dust on the floor). This indoor environment provided a wind free area which was more akin to the environment bicyclists normally ride in than did the treadmill.

[3] The floor is a product called "pulastic" which is manufactured by Robbins Sport Surfaces (http://www.robbinsfloor.com).

Figure 11.1: Sideview of the horse treadmill while Luke was riding the bicycle.

Figure 11.2: Overhead view of the pavilion floor during a perturbation run.

11.4.3 Maneuvers

Our choice of maneuvers was primarily guided by our previous experiments and the search for an optimal way to externally excite the system. We also made sure to perform sets of experiments that would act as a control without deliberate disturbances. The following list details the meaning of the maneuver labels in the dataset.

System Test This is a generic label for data collected during various system tests that should not be used for general analysis. This was primarily used to check that all sensors were working before each set of experiments.

Balance The rider is instructed to simply balance the bicycle and keep a relatively constant heading. They were instructed to focus on a point of their choosing in the far distance. There was an open door in front of the treadmill which allowed the rider to look to a point outside across the street. In the pavilion, the rider looked into the rafters of the building or at the furthest wall. We may have given slightly different instructions to the riders and Charlie did not understand the instructions exactly during some of the earlier runs, but nonetheless these can be analyzed with a control model that only has the roll and heading loops closed and maybe even with only the roll loop closed. We had a line taped to the pavilion floor during these runs that was still in the periphery of the rider's vision. This may have affected their heading control even though they were instructed to ignore it.

Balance With Disturbance Same as 'Balance' except that a lateral force perturbation is applied just under the seat of the bicycle. The rider wore a face shield on the side of the perturber so no visual cues were available to predict the perturbation time or direction. On the treadmill, we sample for 60 to 90 seconds with five to eleven perturbations per run. On the pavilion floor we were able to apply only two to four perturbations per run due to the length of the track. In the early runs (< 204), the lateral force was applied only in the negative direction (to the left) and the perturber decided when to apply the perturbations. For the later runs (> 203), we applied a random sequence of positive and negative perturbations that was unknown to the rider. On the treadmill, the rider signaled when they felt stable and the perturbation was applied at a random time between 0 and 1 second based on a simple computer program. On the pavilion floor, we simply applied the perturbations randomly but as soon as the rider felt stable so that we could get in as many as possible during each run.

Track Straight Line The rider was instructed to focus on a straight line that was marked on the ground and he attempted to keep the front wheel on the line. The line of sight from the rider's eyes to the line on the ground was essentially tangent the top of the front wheel. In the pavilion, the line could be seen up to 100 feet ahead, so there was greater peripheral view of the line. On the treadmill, there was from 0.5 to 1.5 meters of preview line available.

Track Straight Line With Disturbance Same as "Track Straight Line" except that a lateral perturbation force is applied to the seat of the bicycle. This was done in the same fashion as described in "Balance With Disturbance".

Lane Change The rider attempted to track a line in similar fashion as the "Track Straight Line" maneuver except that the line was a single lane change. On the pavilion floor, the line was taped on the ground and the rider was instructed to do whatever felt best to stay on the line *Figure 11.3*. They could use full preview looking ahead, focus on the front wheel and line, or a combination of both. We also tried some lane changes on the treadmill but the lack of preview of the line made it especially difficult. We were able to manage it by marking a count down on the belt so that the rider new when the lane change would arrive. The rider also knew the direction of lane change beforehand for all the scenarios.

Blind With Disturbance We did a run or two for each rider on the pavilion floor with the rider's eyes closed to attempt to completely open the heading loop. In hindsight, blind tests would be preferable when identifying the rider control system so that only inner roll stabilization loop need be analyzed.

Static Calibration We took a short duration sample of the sensors' signals while no rider was on the bicycle and the bicycle was fixed as close as possible to vertical in roll before each set of runs. The static accelerometer readings could theoretically give the roll and pitch angles of the bicycle frame and be used to account for the bias in the roll angle measurements.

I only focus on the Balance and Track Straight Line maneuvers with and without disturbances in the following analyses and they will be referred to as Heading Tracking and Lateral Deviation Tracking in the text (as opposed to the labels

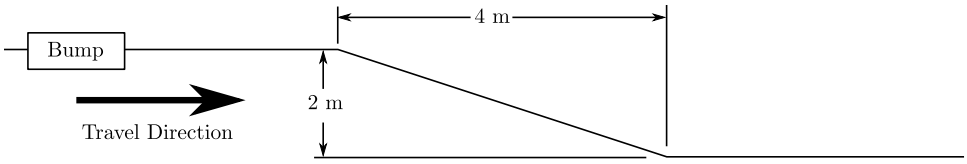

Figure 11.3: The dimensions of the single lane change on the pavilion floor for runs 115-139.

in the database).

Heading Tracking The rider was instructed to simply balance the bicycle and keep a relatively constant heading while focusing their vision at a point in the far distance.

Lateral Deviation Tracking The rider was instructed to focus on a straight line that was marked on the ground and to attempt to keep the front wheel on the line.

Both tasks were performed with and without the application of a manually applied lateral perturbation force just below the seat. The forces were applied randomly in direction and time.

11.5 Data

The experimental data was collected on seven different days. The first few days were mostly trials to test the equipment, procedures and different maneuvers. The data from the trial days is valid data and we ended up using it in our analysis. The tires were pumped to 100 psi at the start of each day.

February 4 2011 Runs 103-109 These were the first trials on the treadmill for preliminary testing. Only Jason rode. We performed lateral deviation tracking with disturbances. The bike fell over, broke and we had to cut it short.

February 28, 2011 Run 115-170 These were the first trials in the pavilion. Jason was the only rider. We tried lane changes (115-139), lateral deviation tracking with disturbances (140-157), and a mixture of heading tracking and lateral deviation tracking with no disturbances (158-170). I noted that the slip clutch backlash seemed to be larger than the previous day with a guess of about 1 degree.

March 9, 2011 Runs 180-204 This was the second go at the treadmill, still just testing things. Jason was the only rider. We did heading and lateral deviation tracking with disturbances and some lane changes. The lane changes were 0.25 m wide left and right maneuvers back and forth among two lines on the treadmill at 2 m long segments. Countdown markers to give an idea when the lane change started were necessary due to the rider's limited preview distance. We did the highest speed during any subsequent trials at 9 m/s. The 9 m/s runs generated a large amount of noise in the lateral force channel. The treadmill elevation was set at 0.1% upwards incline (because it was stuck).

August 30, 2011 Runs 235-291 Jason and Luke rode and performed heading and lateral deviation tasks with and without perturbations at three speeds on the treadmill.

September 6, 2011 Runs 295-318 Charlie performed heading and lateral deviation tasks with and without perturbations on the treadmill.

September 9, 2011 Runs 325-536 Luke, Charlie and Jason performed heading and lateral deviation tracking tasks on the Pavilion floor with and without perturbations. Most of Luke and Charlie's runs were corrupt due to the time synchronization issues.

September 21, 2011 Runs 538-706 Luke and Charlie repeated the runs from September 9th. And we added a couple of blind runs for each of them.

The meta data and raw time history data for each run and all sensor calibration data were stored in individual Matlab mat files on the data acquisition computer using the BicycleDAQ (https://github.com/moorepants/BicycleDAQ) software. The run files and calibration files are automatically numbered in sequence with a five digit number; one

sequence for runs and one for calibrations. These mat files were then parsed and merged into a uniform, organized, and complete single HDF5 database that could be accessed by a number of programs and languages for fast data queries. I made use of PyTables (http://www.pytables.org) for writing and reading from the database. The software BicycleDataProcessor (http://github.com/moorepants/BicycleDataProcessor) was designed as an interface to the data in the database. In particular, it is able to load the raw data from individual runs, process it, and present it for easy manipulation and viewing.

The database is initially structured with three top-level tables and nodes containing the time histories of the sensors for each run. The run table has a row for each run and the columns store each piece of meta data, including the corruption coding described below. The signal table has a row for each raw and processed signal type and the classification information for each. The calibration table has a row for each calibration which provides information about the sensor and the data collected in the calibration.

We recorded a large set of meta data for each run to help with parsing during analyses. We also video recorded all of the runs (minus a few video mishaps). I coded each run based on the notes, data quality, and viewing the video for potential or definite corrupted data with the following five codes.

Corrupt If the data is completely unusable due to time synchronization issues or others then this is set to true.

Warning Runs with a warning flag are questionable and potentially not usable.

Knee The rider's knees would sometimes de-clip from the frame during a perturbation. This potentially invalidates the rigid rider assumption. An array of 15 boolean values, one for each perturbation in the run, are stored for each run and each true value in the array represents an individual perturbation where a knee disengaged with the bicycle.

Handlebar On the treadmill the bicycle handlebars occasionally contacted the side railings. Each perturbation during the run in which this happened was recorded.

Trailer On the treadmill the roll trailer occasionally contacted the side of the treadmill. Each perturbation during the run which this happened was recorded.

We ultimately collected 600+ runs that were potentially usable for analysis. *Figure 11.4* gives a breakdown of the runs by rider, environment, maneuvers, and speed bins.

The processed data provides filtered signals that correspond to the coordinates and speeds outlined in our models, Chapters *Bicycle Equations Of Motion* and *Extensions of the Whipple Model*. We were even able to estimate the path of the wheel contact points on the ground. The quality of the data is high with little to no missing data and complete descriptions of the dynamic state through time. Figures *11.5* and *11.6* give examples of the processed data for the two environments.

11.6 System Identification

My primary goal in the following analyses of all the collected data is to identify the manual control system employed the rider. I will approach this in a similar fashion to [Eat73b] and attempt to identify the plant, i.e. the open loop bicycle and rider dynamics, first followed by an identification of the control system. The question arises as to what the plant and controller consist of. In this case, I consider the plant to include the passive or open loop model of the bicycle combined with the rider's biomechanics and the controller to be the some makeup of the human brain which takes sensory inputs, has time delays, and sends outputs for muscular control.

This two part process was not originally thought to be needed and I started with the identification of the control system assuming the Whipple model would be adequate for the open loop dynamics. But my preliminary attempts at identifying the controller with the Whipple model in place showed that the plant always under-predicted the steer torque needed for a given measured trajectory. This lead me into the exploration of the validity of the Whipple model.

There is actually very little experimental validation of the open loop dynamics of the bicycle, with [Koo06] being one of the better studies. But his study was limited to a riderless bicycle in a narrow speed range where the bicycle was stable. Taking the validity of first principles models like this for granted can potentially lead to inaccurate conclusions.

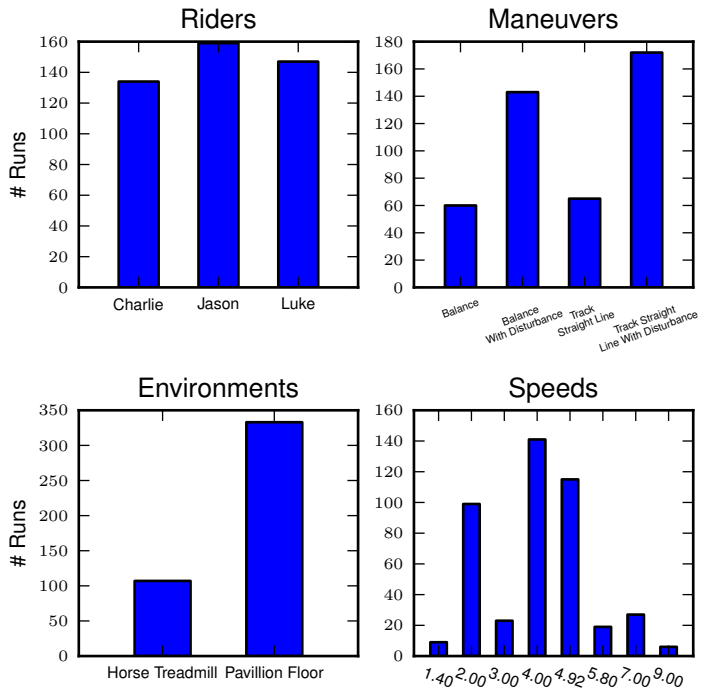

Figure 11.4: Four bar charts showing the number of runs that are potentially usable for model identification. These include runs from the treadmill and pavilion, one of the four primary maneuvers, and were not corrupt. Generated by `src/systemidentification/data_histograms/py`.

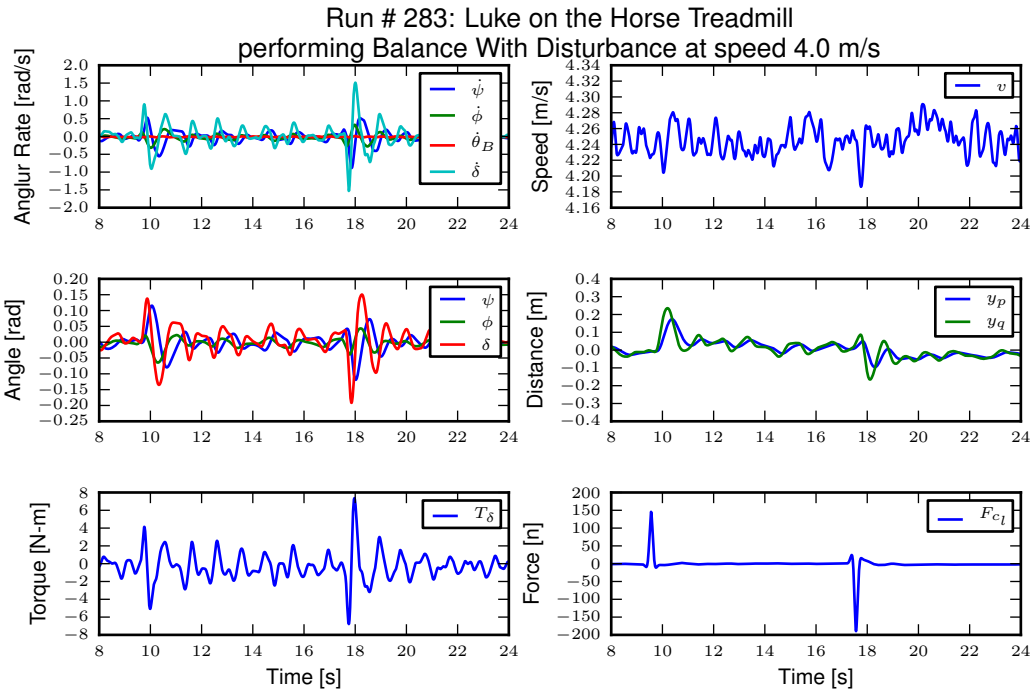

Figure 11.5: The time histories of the computed signals for a typical treadmill run after processing and filtering. Only a portion of the 90 second run is shown for clarity. Generated by `src/systemidentification/run_time_history.py`.

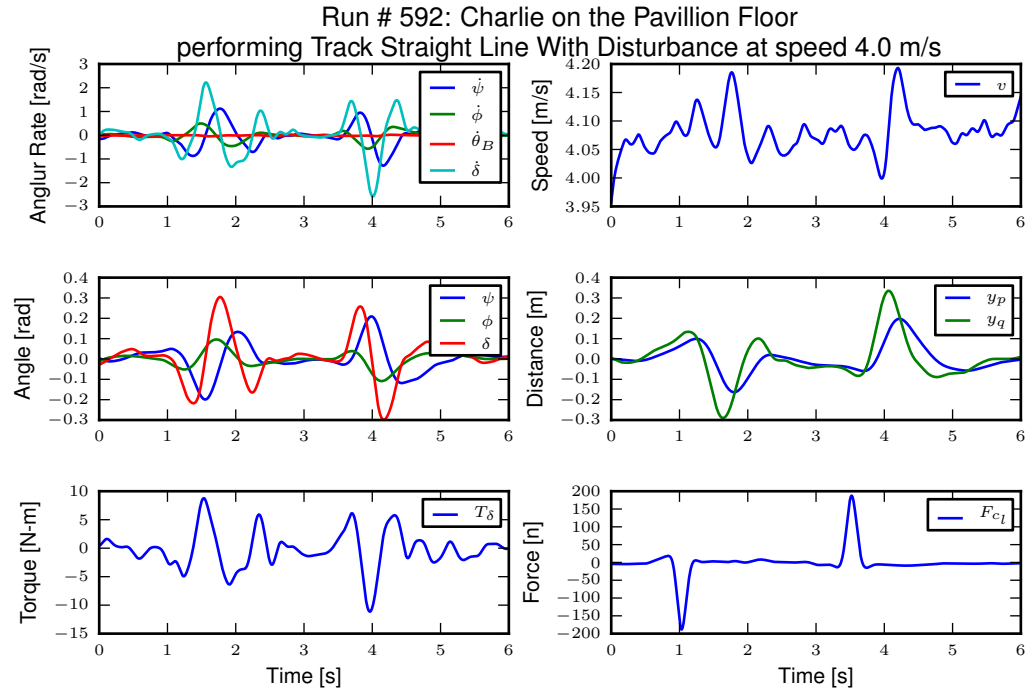

Figure 11.6: The time histories of the computed signals for a typical pavilion run after processing and filtering. Generated by `src/systemidentification/run_time_history.py`.

In our case, it resulted in erroneous early estimations of the controller parameters. As pointed out by many, in particular the motorcycle researchers, there is very good reason to question some of assumptions. The main questionable assumption being knife-edge no side-slip wheels, especially when under a rider's weight. And secondly, the rider's biomechanics have much more influence and coupling to the bicycle than the motorcycle, which must be accounted for.

After a model for the open loop system is derived I identify parameters in the control structure described in [HMH12] and in Chapter *Control*. We've shown that this control structure is robust for a range of speeds and lends itself to the dictates of the crossover model which is built upon strong experimental evidence in human operator modeling. I make use of multi-input multi-output grey box state space identification techniques to arrive at the optimal parameters for the measured data.

Before I proceed, it is important to emphasize the difference in identifying a model that best predicts the data and identifying physical parameters in a model structure that cause the predictions to best fit the measured data. In the first case, it is somewhat easy to fit a model to input and output data. By increasing the order of the model and thus the number of free parameters one can theoretically fit every data point. This is most evident in the over-fitting of a linear trend with that of a higher order polynomial. It still often takes human intuition and reasoning to limit the order of the system to something that represents the true relationships between the variables. But even in this case, the individual meaning of the resulting identified parameters of a black box system may have little apparent connection to the known first principles laws we are familiar with and trust. In dynamics, we often want to know how well our first principles models predict the measured motion and secondly we'd like the ability to identify parameters, particularly ones we are uncertain of in the first principles models, from the measured data. Accurately identifying model parameters is much more difficult task, because noises, both process and measurement, have to be accounted for to get repeatable and accurate estimates of the parameters. I have had good success with finding models that predict the data but little success with explicit and accurate parameter identification in the following analyses. There is great room for improvement in the parameter identification if the noise issues are better managed.

11.7 Bicycle Model Validity

The open loop dynamics of the bicycle-rider system can be described using many models, see [ASKL05], [LS06], and [MPRS07] for good overviews. The benchmarked Whipple model [MPRS07] provides a somewhat minimalistic model in a manageable analytic framework which is capable of describing the essential dynamics such as speed dependent stability, steer and roll coupling, and non-minimum phase behavior. I use this model as the standard base model to work with, as the fidelity of simpler models are generally not adequate. The model is 4th order with roll angle, steer angle, roll rate and steer rate typically selected as the independent states and with roll and steer torque as inputs. I neglect the roll torque input and in its place extend the model to include a lateral force acting at a point on the frame to provide a new input, accurately modelling imposed lateral perturbations (see Chapter *Extensions of the Whipple Model* for the details). I also examine a second candidate model which adds inertial effects of the rider's arms to the Whipple model, also in Chapter *Extensions of the Whipple Model*. This model was designed to more accurately account for the fact that the riders were free to move their arms with the front frame of the bicycle. This model is similar in fashion to the upright rider in [SK10a], but with slightly different joint definitions. Constraints are chosen so that no additional degrees of freedom are added, keeping the system both tractable and comparable to the benchmarked Whipple model.

I make the assumptions that the model is (1) linear and (2) has two degrees of freedom. The best model for a given set of data is constrained by those two assumptions. The implications of this is that even if the model predicts the outputs from the measured inputs it may not reflect realistic parameter values in a first principles sense because all real systems have infinite order. Secondly, the identified model may not map to the assumption we make in first principles derivations about things such as joints, friction, inertia, etc. There may exist higher order models which both fit the output data well and better map parameter values to first principle constructs. For example, a bicycle model with side slip at each wheel will be sixth order and if the regression to find the best model has extra degrees of freedom in the two additional equations, the optimal solution may be such that the numerical values of the equation coefficients map more closely to the first principle parameters. For example, it may be possible to make a fourth order model behave similarly to a sixth order model with "correct" first principles parameters by choosing unrealistic parameter

values. But if the primary goal is the control identification, rather than understanding the quality of our first principles derivations, the model of lowest order that still fits the data well is completely suited for the task.

I estimated the physical parameters of the first principles models with the techniques described in Chapter *Physical Parameters*. The bicycle was measured to get accurate estimates of the parameters used in the benchmark bicycle. Each rider's inertial properties were estimated using Yeadon's [Yea90b] method which allowed easy extraction of body segment parameters for more complicated rider biomechanic models such as the inclusion of moving arms as described above. The parameter computation is handled with two custom open source software packages [Dem11] and [MKSH11].

11.7.1 State Space Realization

During all of the experiments there are two measured external (or exogenous) inputs: the steer torque and the lateral force. Both inputs are generated manually, the first from the rider and the second from the person applying the pulsive perturbation. The outputs can be any subset of the measured kinematical variables or combinations thereof. The problem can then be formulated as follows: given the inputs and outputs of the system and some system structure, what model parameters give the best prediction of the output given the measured input. This a classic system identification problem.

Method

For this analysis, I limit the inputs to steer torque and lateral force and the outputs to roll angle, steer angle, roll rate, and steer rate. The ideal fourth order system can be described with the following continuous state space description

$$
\begin{aligned}
\dot{x}(t) &= \mathbf{F}x(t) + \mathbf{G}u(t) \\
\begin{bmatrix} \dot{\phi} \\ \dot{\delta} \\ \ddot{\phi} \\ \ddot{\delta} \end{bmatrix} &= \begin{bmatrix} 0 & 0 & 1 & 0 \\ 0 & 0 & 0 & 1 \\ a_{\ddot{\phi}\phi} & a_{\ddot{\phi}\delta} & a_{\ddot{\phi}\dot{\phi}} & a_{\ddot{\phi}\dot{\delta}} \\ a_{\ddot{\delta}\phi} & a_{\ddot{\delta}\delta} & a_{\ddot{\delta}\dot{\phi}} & a_{\ddot{\delta}\dot{\delta}} \end{bmatrix} \begin{bmatrix} \phi \\ \delta \\ \dot{\phi} \\ \dot{\delta} \end{bmatrix} + \begin{bmatrix} 0 & 0 \\ 0 & 0 \\ b_{\ddot{\phi}T_\delta} & b_{\ddot{\phi}F_{c_l}} \\ b_{\ddot{\delta}T_\delta} & b_{\ddot{\delta}F_{c_l}} \end{bmatrix} \begin{bmatrix} T_\delta \\ F \end{bmatrix} \\
\eta(t) &= \mathbf{H}x(t)
\end{aligned}
\tag{11.1}
$$

where $\eta(t)$ are the outputs and $\mathbf{H}$ is the identity matrix.

Assuming that this model structure can adequately capture the dynamics of interest of the bicycle-rider system, our goal is to accurately identify the unknown parameters θ which are made up of the unspecified entries in the $\mathbf{F}$ and $\mathbf{G}$ matrices. To do this one needs to recognize that this continuous formulation is not compatible with noisy discrete data. The following difference equation can be assumed if we sample the continuous system at $t = kT$, $k = 1, 2, \ldots$, with T being the sample period and making the assumption that the variables are constant over the sample period (i.e. zero order hold).

$$
\begin{aligned}
x(kT + T) &= \mathbf{A}(\theta)x(kT) + \mathbf{B}(\theta)u(kT) + w(kT) \\
y(kT) &= \mathbf{C}(\theta)x(kT) + v(kT)
\end{aligned}
\tag{11.2}
$$

The additional terms w and v represent the process and measurement noise vectors, respectively, which are assumed to be sequences of white Gaussian noise with zero mean and some covariance. By making use of the Kalman filter, Equation (11.2) can be transformed such that the optimal estimate of the states, $\hat{x}$, with respect to the process and measurement noise covariance are utilized, see [Lju98].

$$
\begin{aligned}
\hat{x}(kT + T, \theta) &= \mathbf{A}(\theta)\hat{x}(kT) + \mathbf{B}(\theta)u(kT) + \mathbf{K}(\theta)e(kT) \\
y(kT) &= \mathbf{C}(\theta)\hat{x}(kT) + e(kT)
\end{aligned}
\tag{11.3}
$$

where $\mathbf{K}$ is the Kalman gain matrix. $\mathbf{K}$ is a function of $\mathbf{A}(\theta)$, $\mathbf{C}(\theta)$ and the covariance and cross covariance of the process and measurement noises, but it can also be directly parameterized by θ. With that, this equation is called

the *directly parameterized innovations form* [Lju98] and the entries of the four matrices in equation (11.3) can be estimated directly.

The $\mathbf{A}$ and $\mathbf{B}$ matrices are related to $\mathbf{F}$ and $\mathbf{G}$ by

$$\mathbf{A}(\theta) = e^{\mathbf{F}(\theta)T} \tag{11.4}$$
$$\mathbf{B}(\theta) = \int_{\tau=0}^{T} e^{\mathbf{F}(\theta)\tau}\mathbf{G}(\theta)d\tau$$

where T is the sampling period. With a linear assumption $\mathbf{A}$ and $\mathbf{B}$ can even be directly estimated in discrete form by

$$\mathbf{A}(\theta) = \mathbf{I} + \mathbf{F}(\theta)T \tag{11.5}$$
$$\mathbf{B}(\theta) = \int_{\tau=0}^{T} (\mathbf{I} + \mathbf{F}(\theta)\tau)\mathbf{G}(\theta)d\tau$$

The one step ahead predictor for the innovations form is

$$\hat{y}(t|\theta) = \mathbf{C}(\theta)\left[q\mathbf{I} - \mathbf{A}(\theta) + \mathbf{K}(\theta)\right]^{-1}\left[\mathbf{B}(\theta)u(t) + \mathbf{K}(\theta)y(t)\right] \tag{11.6}$$

where q is the forward shift operator ($qu(t) = u(t+1)$) [Lju98]. The predictor is a vector of length p where each entry is a ratio of polynomials in q. These are transfer functions in q from the previous inputs and outputs to the current output. In general, the coefficients of q are non-linear functions of the parameters θ.

We can now construct the cost function, which will enable the computation of the parameters which give the best fit using optimization methods. We'd like to minimize the error in the predicted output with respect to the measured output at each time step. First form Y_N which is a $pN \times 1$ vector containing all of the current outputs at time kT.

$$Y_N = \left[y_1(1)\ldots y_p(1)\ldots y_1(N)\ldots y_p(N)\right]^T \tag{11.7}$$

where p is the number of outputs and N is the number of samples. Then organize the predictor vector, $\hat{Y}_N(\theta)$, the one step ahead prediction of Y_N given $y(s)$ and $u(s)$ where $s \leq t-1$

$$\hat{Y}_N = \left[\hat{y}_1(1)\ldots\hat{y}_1(1)\ldots\hat{y}_p(N)\ldots\hat{y}_p(N)\right]^T \tag{11.8}$$

The cost function is then the norm of the difference of Y_N and $\hat{Y}_N(\theta)$ for all k.

$$V_N(\theta) = \frac{1}{pN}||Y_N - \hat{Y}_N(\theta)|| \tag{11.9}$$

The value of θ which minimizes the cost function is the best prediction

$$\hat{\theta}_N = \underset{x}{\operatorname{argmax}} V_N(\theta, Z^N) \tag{11.10}$$

where Z^N is the set of all the measured inputs and outputs.

In general, the minimization problem is not trivial and may be susceptible to many of the issues associated with optimization including local minima. The number of unknown parameters in the $\mathbf{K}$ matrix is a function of the number of states and the number of outputs, in our case in $\mathbf{R}^{4\times4}$ which more than doubles the number of unknowns present in the $\mathbf{A}$ and $\mathbf{B}$ matrices. It is thus critical to reduce the number of unknown parameters to have a higher chance of finding the global minimum of the cost function. The accuracy of the system parameters depends on the ability to estimate the $\mathbf{K}$ matrix along with the other parameters.

Before identification I further processed all of the signals that were generally symmetric about zero by subtracting the means over time. For some of the pavilion runs, this may have actually introduced a small bias, as the short duration runs with unbalanced perturbations may not have zero mean.

I made use of the Matlab System Identification Toolbox for the identification of the parameters θ in each run of this model structure. In particular, a structured *idss* object was built with the initial guesses of the unknown parameters based on the Whipple model and the initial guesses for the initial conditions and the Kalman gain matrix being equal to zero. All of my attempts at identifying the Kalman gain matrix were plagued by local minima.

Results

It turns out that finding a model that meets the criterion is not too difficult when the output error form is considered ($\mathbf{K} = 0$). This model may be able to explain the data well, but the parameter estimation is potentially poor because the parameters in the state and input matrices are adjusted such that the results fit both the true trajectories *and* the noise. Global minima in the search routine are quickly found when the number of parameters is between 10 and 14. When the $\mathbf{K}$ matrix is added the number of unknown parameters increases by 16 and the global minimum becomes more difficult to find and I was rarely able, if ever, to find the global minimum for the general problem, even when reducing the number of outputs to one.

Figure 11.7 shows typical example input and output data for a single run (#596) with both steer torque and lateral force as inputs. The plot compares the simulation response of the input to the measured response. Notice that the identified model predicts the trajectory extremely well. Similar results are found for the majority of the runs. The Whipple model predicts the trajectory directions but the magnitudes are large, meaning that for a given trajectory, the Whipple model requires less torque than that measured. The Whipple model with the arm inertial effects does a better job than the basic Whipple model, but still has some magnitude differences with respect to the identified model. It also has a harder time predicting the roll angle than both the identified model and the Whipple model.

The identified models are almost always unstable due to the high weave critical speed and, even though the measured inputs stabilize the true system, they will not necessarily stabilize the models. This poses an issue when gauging the model quality by the percentage variance of the output data explained by the model. A model that blows up during the simulation may not necessarily be a bad model, but it will return a very small percent variance and lose its ability to be compared by that criterion. [BBCL03] and [TJ10] both are able to run feed-forward simulations of their motorcycle models with the measured steering torque. They both are dealing with high speed motorcycles which typically only have a slightly unstable capsize mode. [TJ10] uses a controller to compensate the torque for unbounded errors so that the simulation doesn't blow up. The method I use here is to choose short duration portions of the runs for simulation and search for the best set of initial conditions to keep the model stable during the duration. This generally works but there are ultimately some incomparable runs due to this issue.

I use this structured state space output error identification procedure for a collection of experiments ($n = 368$) over a range of speeds between about 1 and 9 m/s. Figures *11.8* and *11.9* plot the identified coefficients of the dynamical equations of motion (i.e. the bottom two rows of the $\mathbf{F}$ and $\mathbf{G}$ matrices) as a function of speed for all of the experiments using box plots. Both the Whipple (green) and arm (red) model predictions are superimposed for comparison. The first notable thing is that the coefficients seem to generally have large variance, especially as the speed increases. Secondly, the roll acceleration, $\ddot{\phi}$, equation seems to be better predicted by the two models and the data has less spread at the lower speeds, barring the $\dot{\phi}$ coefficient which has large spread and no apparent relationship with speed for both equations. The roll equation also seems to have less spread in the experimental data. For example, the $a_{\ddot{\phi}\delta}$ coefficient appears to be very tight and the first principles models predict it very well. The constant, linear, and quadratic trends in the coefficients are somewhat visible in the data but the variance in the coefficients clouds it. This variability in the coefficient predictions depends on many things including data quality, the ability to identify a process noise model, speed being constant during the run, choice of unknown coefficients, and more. With all of these improved, detailed regression models may be able to reveal the true trends[4]. Nonetheless, these graphs reveal several important things:

- The identified models predict the data well with most having mean predicted variance of the four outputs above 70% (but this is tightly coupled to run duration, i.e. longer runs have more room for model error).
- Some of the coefficients are well predicted by the Whipple model and can be fixed from first principles calculations, notably: $a_{\ddot{\phi}\phi}$, $a_{\ddot{\phi}\delta}$ and $b_{\ddot{\delta}T_\delta}$ and maybe even $a_{\ddot{\delta}\delta}$.
- The roll rate coefficients are highly variable with poor prediction by the models. Deficiencies in the first principles models are likely.
- Either the higher speed runs are outliers, or the behavior of the system changes more rapidly with speeds above 5 m/s or so.

[4] I spent some time trying to regress models to each of the speed dependent coefficients in the state space model by assuming either a constant, linear, or quadratic line. I tried simple regression techniques and also some mixed effects techniques to obviate the fact that some of the speed bins had many more runs than others. This method may be used to generate a speed independent model based on all of the runs, but needs more work.

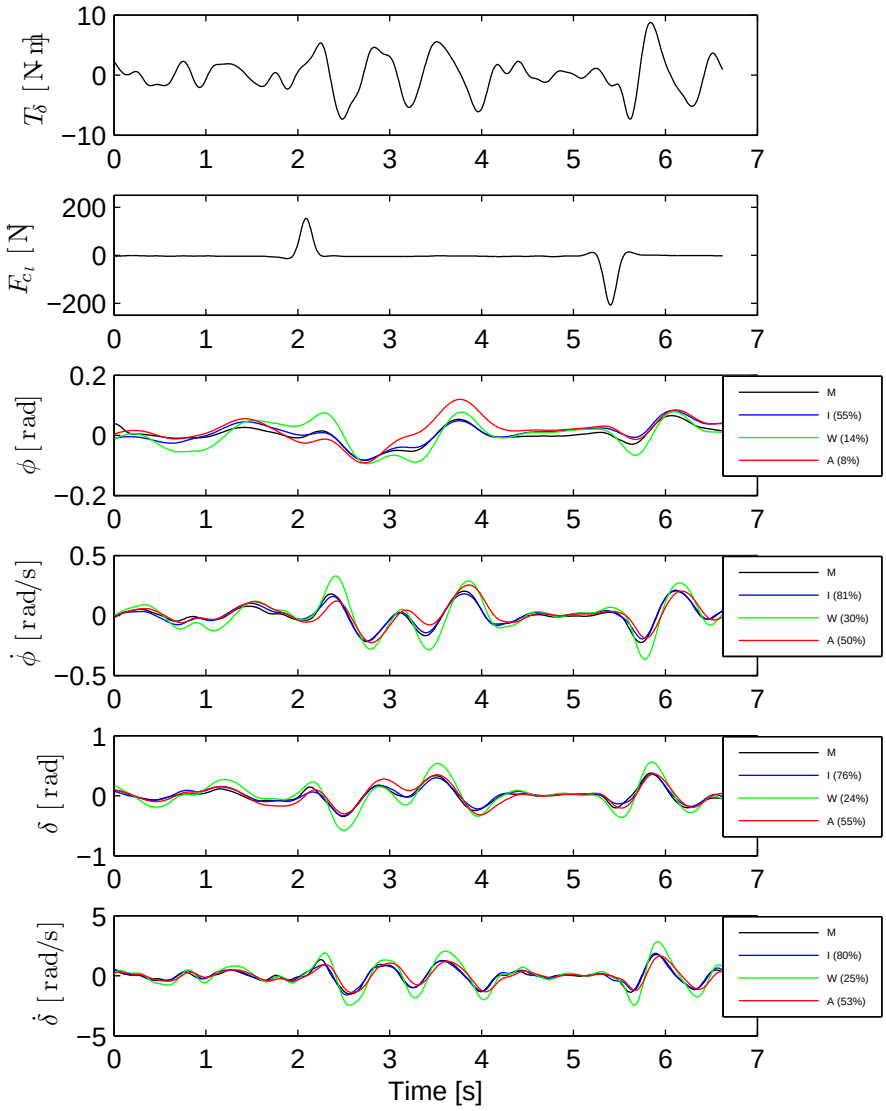

Figure 11.7: Example results for the identification of a single run (#596). The experimentally measured steer torque and lateral force are shown in the top two graphs. All of the signals were filtered with a 2nd order 15 hertz low pass Butterworth filter. The remaining four graphs show the simulation results for the Whipple model (W), Whipple model with the arm inertia (A), and the identified model for that run (I) plotted with the measured data (M). The percentages give the percent of variance explained by each model.

- Some coefficients spread around zero giving inconsistent signs and others give opposite signs from those the first principles models expect.

Figure 11.10 gives another view of the resulting data. It is a frequency response plot at the mean speed for a set of runs. The blue lines give the mean and one standard deviation bounds of the magnitude and phase of the system transfer function $\frac{\phi}{T_\delta}(s)$ for the set of runs. Even though the spread in the identified parameters seems high in Figures *11.8* and *11.9*, the Bode plot shows that the identified system frequency response is not as variable, especially in magnitude. It is also apparent that the experimental magnitude mean has a -5 to -10 dB offset across the frequency range shown with respect to the Whipple model, although the Whipple model does fall within one standard deviation of the mean. This correlates with the amplitude differences in the trajectories shown in *Figure 11.7*. Notice that the arm model has little to no offset between 2 and 10 rad/s, thus the better amplitude matching. The frequency response may give a better indication of the overall identified model quality.

Conclusion

I have shown that a fourth order structured state space model is both adequate for describing the motion of the bicycle under manual control in a speed range from approximately 1.5 m/s to 9 m/s. The fact that higher order models may not be necessary for bicycle dynamic description is an important finding. More robust models of single track vehicles are typically higher than 4th order, with degrees of freedom associated with tire slip, frame flexibilities, and rider biomechanics. These findings suggest that the more complex models may be overkill for many modeling purposes. The data subsequently also reveals that fourth order archetypal first principles models are not robust enough to fully describe the dynamics. The deficiencies are most likely due to un-modeled effects, with the knife-edge, no side-slip wheel contact assumptions being the most probable candidate. Un-modeled rider biomechanics such as passive arm stiffness and damping and head motion may play a role too. The uncertainty in the estimates of the physical parameters from Chapter *Physical Parameters* is not large enough to explain the difference between the identified coefficient identification and their predictions from first principles. It is likely that something as simple as a "static" tire scrub torque is needed to improve the fidelity of the first principles derivations, but that doesn't preclude that the additional of a tire slip model might also improve the models.

11.7.2 Canonical Identification

One issue I faced with the state space realization was dealing with multiple experiments. Ideally I had hoped to identify a linear model that was a function of speed with respect to all or various subsets of the experiments. It is possible to concatenate runs, but discontinuities in the data potentially disrupt the identification. There is also the possibility of designing a cost function that gives the error in all the outputs across all of the runs simultaneously instead of on a per run basis. Both my recently obtained knowledge in system identification and the constraints of the methods available in the Matlab System Identification toolbox were limiting factors in these two approaches. But, Karl Åström suggested doing the system identification with respect to the second order form of the equations of motion. This would allow one to use both simple least squares for the solution and the ability to compute models from large sets of runs. This section deals with this approach.

Model structure

The identification of the linear dynamics of the bicycle can be formulated with respect to the benchmark canonical form realized in [MPRS07], Equation (11.11). If the time varying quantities in the equations are all known at each time step, the coefficients of the linear equations can be estimated given enough time steps.

$$\mathbf{M}\ddot{q} + v\mathbf{C}_1\dot{q} + [g\mathbf{K}_0 + v^2\mathbf{K}_2]q = T \tag{11.11}$$

where the time-varying states roll and steer are collected in the vector $q = [\phi \quad \delta]^T$ and the time varying inputs roll torque and steer torque are collected in the vector $T = [T_\phi \quad T_\delta]^T$. This equation assumes that the velocity is constant with respect to time as the model was linearized about a constant velocity equilibrium, but the velocity can also potentially be treated as a time varying parameter if the acceleration is negligible. I extend the equations to

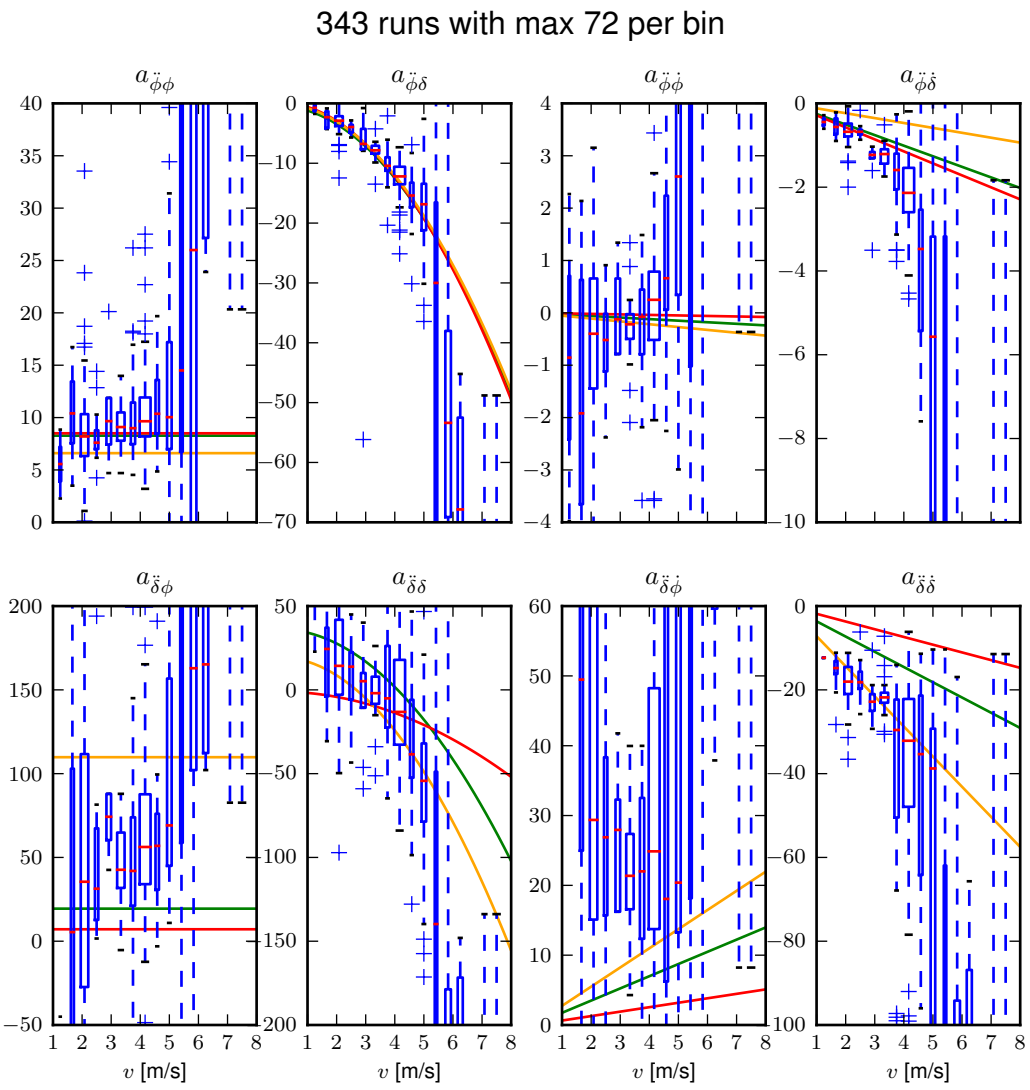

Figure 11.8: State coefficients of the linear dynamical equations of motion plotted as a function of speed. Each box plot represents the distribution of that parameter for a small range of speeds, i.e. speed bin. The width of the box is proportional to the total duration of the runs in that speed bin. The green line is the Whipple model and the red line is the arm model. Only experiments with a mean fit percentage greater than zero are shown. The orange line is the model identified with the canonical method using runs done by Luke in the pavilion which is presented and discussed in the next section. Generated by `src/systemidentification/coefficient_box_plot.py`.

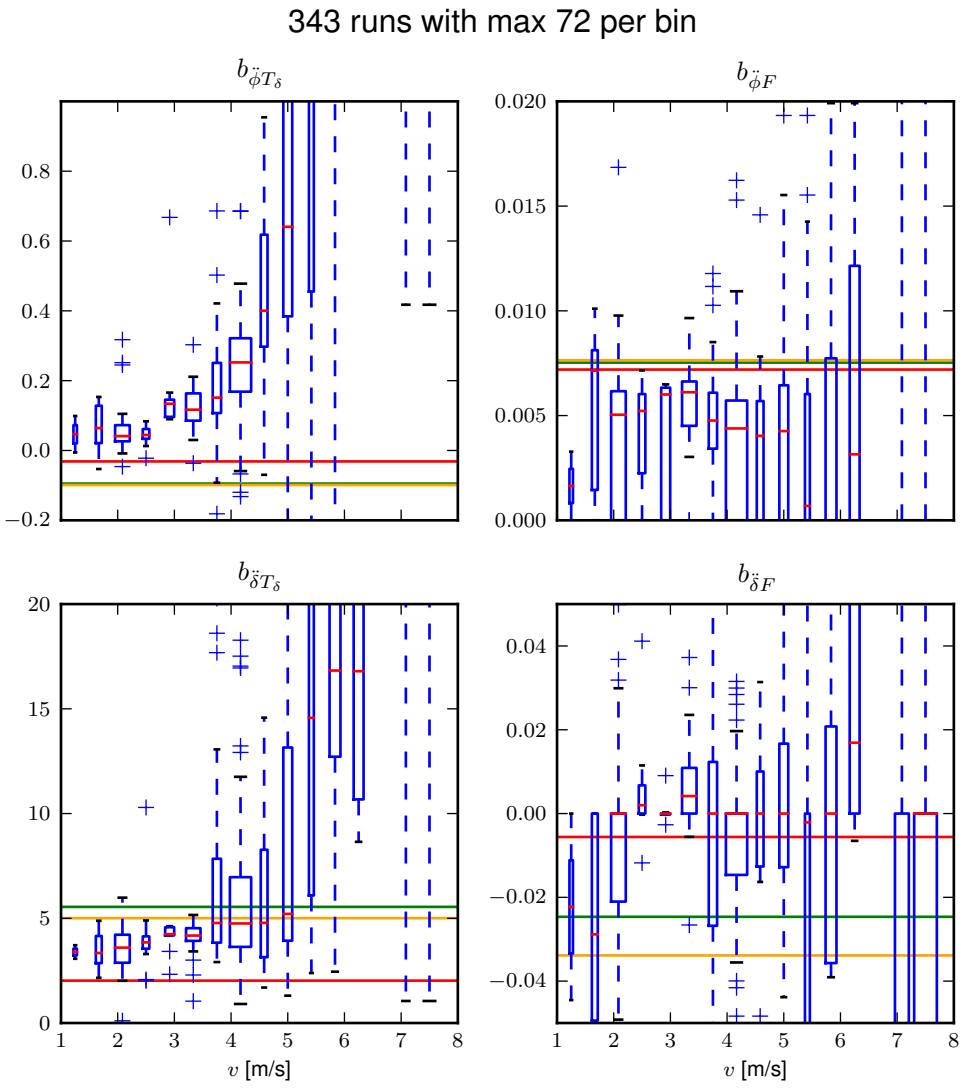

Figure 11.9: Input coefficients of the linear dynamical equations of motion plotted as a function of speed. Each box plot represents the distribution of that parameter for a small range of speeds, i.e. speed bin. The width of the box is proportional to the total duration of the runs in that speed bin. The green line is the Whipple model and the red line is the arm model. Only experiments with a mean fit percentage greater than zero are shown. The orange line is the model identified with the canonical method using runs done by Luke in the pavilion which is presented and discussed in the next section. Generated by `src/systemidentification/coefficient_box_plot.py`.

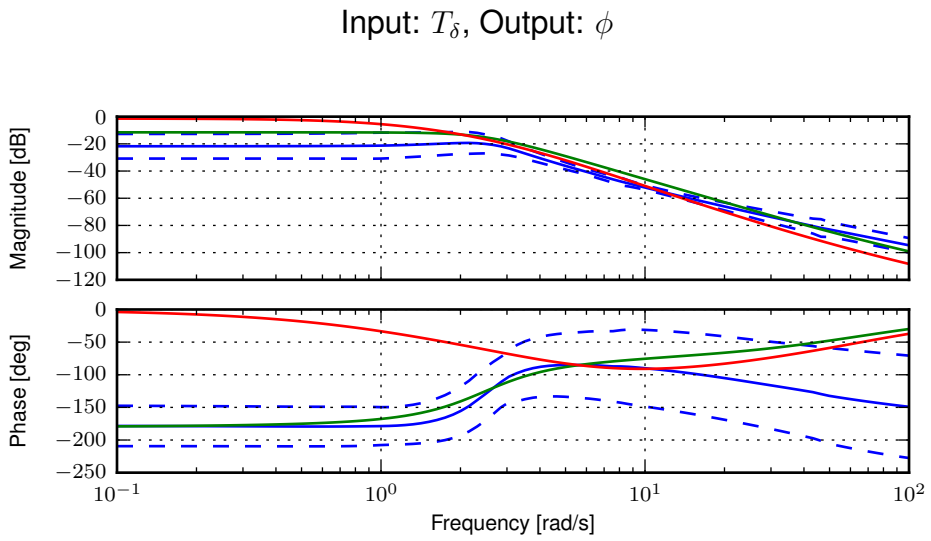

Figure 11.10: Frequency response of steer torque to roll angle for a set of runs at 4.0 ± 0.3 m/s. The solid blue line is the mean from the identified runs and is bounded by the standard deviation, the dotted blue lines. The green line is the Whipple model and the red line is for the model which accounted for the arm inertial effects.

properly account for the lateral perturbation force, F, which was the actual input we delivered during the experiments. It contributes to both the roll torque and steer torque equations.

$$\mathbf{M}\ddot{q} + v\mathbf{C}_1\dot{q} + [g\mathbf{K}_0 + v^2\mathbf{K}_2]q = T + HF \tag{11.12}$$

where $H = [H_{\phi F} \quad H_{\delta F}]^T$ is a vector describing the linear contribution of the lateral force to the roll and steer torque equations. $H_{\phi F}$ is approximately the distance from the ground to the force application point. $H_{\delta F}$ is a distance that is a function of the bicycle geometry (trail, wheelbase) and the longitudinal location of the force application point. For our normal geometry bicycles, including the one used in the experiments, $H_{\delta F} << H_{\phi F}$. I estimate H for each rider/bicycle from geometrical measurements and the state space form of the linear equations of motion calculated in Chapter *Extensions of the Whipple Model*.

$$\dot{x} = \mathbf{A}x + \mathbf{B}u \tag{11.13}$$

where $x = [\phi \quad \delta \quad \dot{\phi} \quad \dot{\delta}]^T$ and $u = [F \quad T_\phi \quad T_\delta]^T$. The state and input matrices can be partitioned.

$$\mathbf{A} = \begin{bmatrix} 0 & \mathbf{I} \\ \mathbf{A}_l & \mathbf{A}_r \end{bmatrix} \tag{11.14}$$

$$\mathbf{B} = \begin{bmatrix} 0 & 0 \\ \mathbf{B}_F & \mathbf{B}_T \end{bmatrix} \tag{11.15}$$

where $\mathbf{A}_l$ and $\mathbf{A}_r$ are the 2 x 2 sub-matrices corresponding to the states and their derivatives, respectively. $\mathbf{B}_F$ and $\mathbf{B}_T$ are the 2 x 1 and 2 x 2 sub-matrices corresponding to the lateral force and the torques, respectively. The benchmark canonical form can now be written as

$$\mathbf{B}_T^{-1}[\ddot{q} - \mathbf{A}_r\dot{q} - \mathbf{A}_l q] = T + \mathbf{B}_T^{-1}\mathbf{B}_F F \tag{11.16}$$

where

$$\begin{aligned} \mathbf{M} &= \mathbf{B}_T^{-1} \\ v\mathbf{C}_1 &= -\mathbf{B}_T^{-1}\mathbf{A}_r \\ [g\mathbf{K}_0 + v^2\mathbf{K}_2] &= -\mathbf{B}_T^{-1}\mathbf{A}_l \\ H &= \mathbf{B}_T^{-1}\mathbf{B}_F \end{aligned} \tag{11.17}$$

Table 11.1: The location of the lateral force point for each rider.

Rider	H
Charlie	$[0.902 \quad 0.011]^T$ m
Jason	$[0.943 \quad 0.011]^T$ m
Luke	$[0.902 \quad 0.011]^T$ m

The location of the lateral force application point is the same for Charlie and Luke because they used the same seat height. The force was applied just below the seat, which was adjustable in height for different riders.

Data processing

Chapter *Davis Instrumented Bicycle* details how each of the signals were measured and processed. For the following analysis, all of the signals were filtered with a second order low pass Butterworth filter at 15 Hz. The roll and steer accelerations were computed by numerically differentiating the roll and steer rate signals with a central differencing method except for the end points being handled by forward and backward differencing. The mean was subtracted from all the signals except the lateral force.

Identification

A simple analytic identification problem can be formulated from the canonical form. If we have good measurements of q, their first and second derivatives, forward speed v, and the inputs T_δ and F, the entries in $\mathbf{M}$, $\mathbf{C}_1$, $\mathbf{K}_0$, $\mathbf{K}_2$, and H can be identified by forming two simple regressions, i.e. one for each equation in the canonical form. I use the instantaneous speed at each time step rather than the mean over a run to improve accuracy with respect to the speed parameter as it has some variability.

The roll and steer equation each can be put into a simple linear form

$$\mathbf{\Gamma}\Theta = Y \tag{11.18}$$

where Θ is a vector of the unknown coefficients and $\mathbf{\Gamma}$ and Y are made up of the inputs and outputs measured during a run. Θ can be all or a subset of the entries in the canonical matrices. If there are N samples in a run and we desire to find M entries in the equation, then $\mathbf{\Gamma}$ is an $N \times M$ matrix and Y is an $N \times 1$ vector. The Moore-Penrose pseudo inverse can be employed to solve for Θ analytically. The estimate of the unknown parameters is then

$$\hat{\Theta} = [\mathbf{\Gamma}^T\mathbf{\Gamma}]^{-1}\mathbf{\Gamma}^T Y \tag{11.19}$$

For example, if we fix the mass terms in the steer torque equation and let the rest be free the linear equation is

$$\begin{bmatrix} v(1)\dot{\phi}(1) & v(1)\dot{\delta}(1) & g\phi(1) & g\delta(1) & v(1)^2\phi(1) & v(1)^2\delta(1) & -F(1) \\ \vdots & \vdots & \vdots & \vdots & \vdots & \vdots & \vdots \\ v(N)\dot{\phi}(N) & v(N)\dot{\delta}(N) & g\phi(N) & g\delta(N) & v(N)^2\phi(N) & v(N)^2\delta(N) & -F(N) \end{bmatrix} \begin{bmatrix} C_{1\delta\phi} \\ C_{1\delta\delta} \\ K_{0\delta\phi} \\ K_{0\delta\delta} \\ K_{2\delta\phi} \\ K_{2\delta\delta} \\ H_{\delta F} \end{bmatrix} = \begin{bmatrix} T_\delta(1) - M_{\delta\phi}\ddot{\phi}(1) - M_{\delta\delta}\ddot{\delta}(1) \\ \vdots \\ T_\delta(N) - M_{\delta\phi}\ddot{\phi}(N) - M_{\delta\delta}\ddot{\delta}(N) \end{bmatrix} \tag{11.20}$$

The error in the fit is

$$\epsilon = \hat{Y} - Y = \mathbf{\Gamma}\hat{\Theta} - Y \tag{11.21}$$

The covariance of Θ, Equation (11.23), of the parameter estimations can be computed with respect to the error.

$$\sigma^2 = \frac{\epsilon^T \epsilon}{N - d} \tag{11.22}$$

$$\mathbf{U} = \sigma^2(\mathbf{\Gamma}^T\mathbf{\Gamma})^{-1} \tag{11.23}$$

Equations (11.19), (11.21), (11.22), and (11.23) can be solved for each run individually, a portion of a run, or a set of runs. Secondly, all of the parameters in the canonical matrices need not be estimated. The analytical benchmark bicycle model [MPRS07] gives a good idea of which entries in the matrices we may be more certain about from our physical parameters measurements in Chapter *Physical Parameters*. I went through the benchmark formulation and fixed the parameters based on these rules, keeping in mind that even little numbers can have large effects to the resulting dynamics:

- If the parameter is greatly affected by trail, leave it free.
- If the parameter is greatly affected by the front assembly moments and products of inertia, leave it free.
- If the parameter is identically equal to zero, fix it.

The reasoning for these assumptions are:

- Trail is difficult to measure and be certain about, especially since the bicycle tire deforms and creates a variable shaped tire contact patch which depends on the tires properties, pressure, and the configuration of the bicycle. The true trail is what is typically called pneumatic trail and gives the location in the tire patch at which the resultant contact force acts.
- The front frame moments and products of inertia play a large role in the steer dynamics and I'm not as confident in the estimation of these due to the fact that our apparatus was more suited to the estimate the inertial properties of the rear frame than the front.
- The zero entries in the velocity dependent stiffness and damping matrices that correspond to the roll angle and rate are assumed to hold from first principles.

For the roll equation this leaves $M_{\phi\delta}$, $C_{1\phi\delta}$, and $K_{0\phi\delta}$ as free parameters, and for the steer equation this leaves $M_{\delta\phi}$, $M_{\delta\delta}$, $C_{1\delta\phi}$, $C_{1\delta\delta}$, $K_{0\delta\phi}$, $K_{0\delta\delta}$, $K_{2\delta\delta}$, and $H_{\delta F}$ as free parameters.

I start by identifying the three coefficients of the roll equation for the given data. This choice is due to there being

more certainty in the roll equation estimates from first principles because there are fewer unknown parameters.

$$\begin{bmatrix} \ddot{\delta}(1) & v(1)\dot{\delta}(1) & g\delta(1) \\ \vdots & \vdots & \vdots \\ \ddot{\delta}(N) & v(N)\dot{\delta}(N) & g\delta(N) \end{bmatrix} \begin{bmatrix} M_{\phi\delta} \\ C_{1\phi\delta} \\ K_{0\phi\delta} \end{bmatrix}$$
$$= \begin{bmatrix} H_{\phi F}F(1) - M_{\phi\phi}\ddot{\phi}(1) - C_{1\phi\phi}v(1)\dot{\phi}(1) - K_{0\phi\phi}g\phi(1) - K_{2\phi\phi}v(1)^2\phi(1) - K_{2\phi\delta}v(1)^2\delta(1) \\ \vdots \\ H_{\phi F}F(N) - M_{\phi\phi}\ddot{\phi}(N) - C_{N\phi\phi}v(N)\dot{\phi}(N) - K_{0\phi\phi}g\phi(N) - K_{2\phi\phi}v(N)^2\phi(N) - K_{2\phi\delta}v(N)^2\delta(N) \end{bmatrix} \tag{11.24}$$

I then enforce the assumptions that $M_{\phi\delta} = M_{\delta\phi}$ and $K_{0\phi\delta} = K_{0\delta\phi}$ to fix these values in the steer equation to the ones identified in the roll equation, leaving fewer free parameters in the steer equation[5]. This symmetry is enforced to coincide with the theory and choice of coordinates. Finally, I identify the remaining steer equation coefficients with

$$\begin{bmatrix} \ddot{\delta}(1) & v(1)\dot{\phi}(1) & v(1)\dot{\delta}(1) & g\phi(1) & v(1)^2\delta(1) & -F(1) \\ \vdots & \vdots & \vdots & \vdots & \vdots & \vdots \\ \ddot{\delta}(N) & v(N)\dot{\phi}(N) & v(N)\dot{\delta}(N) & g\phi(N) & v(N)^2\delta(N) & -F(N) \end{bmatrix} \begin{bmatrix} M_{\delta\delta} \\ C_{1\delta\phi} \\ C_{1\delta\delta} \\ K_{0\delta\phi} \\ K_{2\delta\delta} \\ H_{\delta F} \end{bmatrix}$$
$$= \begin{bmatrix} T_\delta(1) - M_{\delta\phi}\ddot{\phi}(1) - K_{0\delta\delta}g\delta(1) - K_{2\delta\phi}v(1)^2\phi(1) \\ \vdots \\ T_\delta(N) - M_{\delta\phi}\ddot{\phi}(N) - K_{0\delta\delta}g\delta(N) - K_{2\delta\phi}v(N)^2\phi(N) \end{bmatrix} \tag{11.25}$$

Results

I selected data for three riders on the same bicycle, performing two maneuvers, in two different environments. There is little reason to believe the dynamics of the passive system should vary much with respect to different maneuvers, but there is potentially variation across riders due to the differences in their inertial properties and there may be variation across environments because of the differences in the wheel to floor interaction. I opted to compute the best fit model across series of runs to benefit from the large dataset. This leaves these four scenarios:

- All riders in both environments, one data set
- All riders in each environment, two data sets
- Each rider in both environments, three data sets
- Each rider in each environment, six data sets

[5] It is also possible to solve the roll and steer equations simultaneously and enforce the symmetry, which is probably a better idea.

Table 11.2: The number of runs and time samples in each data subset.

Rider	Environment	Number of runs	Number of time samples, N
(C)harlie	(H)orse treadmill	24	267773
(C)harlie	(P)avilion	87	118700
(C)harlie	(A)ll	111	386473
(J)ason	(H)orse treadmill	57	804995
(J)ason	(P)avilion	93	112582
(J)ason	(A)ll	150	917577
(L)uke	(H)orse treadmill	25	272719
(L)uke	(P)avilion	88	125878
(L)uke	(A)ll	113	398597
(A)ll	(H)orse treadmill	106	1345487
(A)ll	(P)avilion	268	357160
(A)ll	(A)ll	374	1702647

A total of 12 different models can be derived from this perspective.

All riders in both environments

This section details the example results for one subset of data. Here I make the assumption that the best fit model doesn't vary much across riders or environments. The assumption that the passive model of the bicycle and rider are similar with respect to rider can be justified by recognizing that the Whipple model predicts little difference in the dynamics with respect to the three bicycle/rider combinations. On the other hand, I have little reason to believe the environments are the same except that both floors are made of a rubber like material. I calculated the best fit over 374 runs giving about 142 minutes of data sampled at 200 Hz, $N = 1720647$.

The eigenvalues as a function of speed of the identified model can be compared to those of the Whipple and arm models, see Section *Rider Arms* in Chapter *Extensions of the Whipple Model*. *Figure 11.11* shows the root locus of the three models. The oscillatory weave mode exists in all three models, with it always being stable in the arm model but being unstable at lower speeds in the other two models. The identified model's oscillatory weave mode is unstable over most of the shown speed range. Above 3 m/s or so, the Whipple model's oscillatory weave mode diverges from the identified model to different asymptotes. The arm model weave mode diverges somewhere in between. Note that the arm model has an unstable real mode for all speeds. *Figure 11.12* gives a different view of the root locus allowing one to more easily compare the real parts of the eigenvalues. The imaginary parts of the weave mode have similar curvature with respect to speed for all the models, with the identified model having about 1 rad/s larger frequency of oscillation for all speeds. The identified model does have a stable speed range where the Whipple model under predicts the weave critical speed by almost 2 m/s. The identified caster mode is much faster than the one predicted by the Whipple model which is somewhat counterintuitive because tire scrub torques would probably tend to slow the caster mode. Although, the pneumatic trail and the rider's arm inertia could play a larger role that expected. Furthermore, the caster mode may not be well identified because the experiments were not design to specifically excite it.

The identification process is based on identifying the input/output relationships among measured variables. The frequency response provides a view into these relationships. Figures *11.13* to *11.16* give a picture of how the first principles models compare to the identified model with respect to frequency response from a roll torque input. The frequency band from 1 rad/s to 12 rad/s is of most concern as it bounds a reasonable range that the human may be able to operate within.

The roll torque to roll angle response *Figure 11.13* shows that at 2 m/s (solid lines) the response of the Whipple model and the identified model are practically identical across the frequency range shown. On the other hand, the arm model predicts the high frequency (> 4 rad/s) behavior really well, but the magnitude is as great as 50 dB larger and the phase off by 180 degrees at lower frequencies. At 4 m/s the Whipple model still predicts the phase well, but the magnitudes do not match below 100 rad/s with 10 dB difference at lower frequencies. At this speed the arm model matches the identified model as low as 3.5 rad/s but the low frequency phase still being 180 degrees off. The magnitude of the

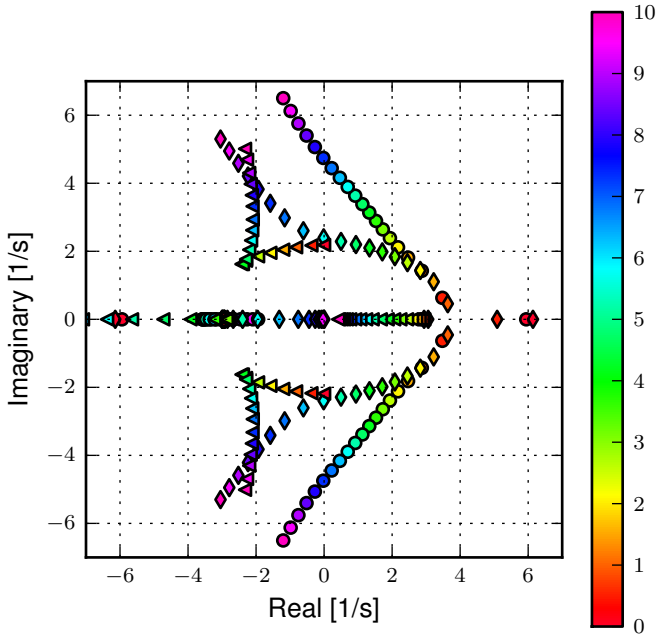

Figure 11.11: Root locus of the identified model (circle), the Whipple model (diamond), and the arm model (triangle) with respect to speed in m/s. Generated by *src/systemidentification/canonical_plots.py*.

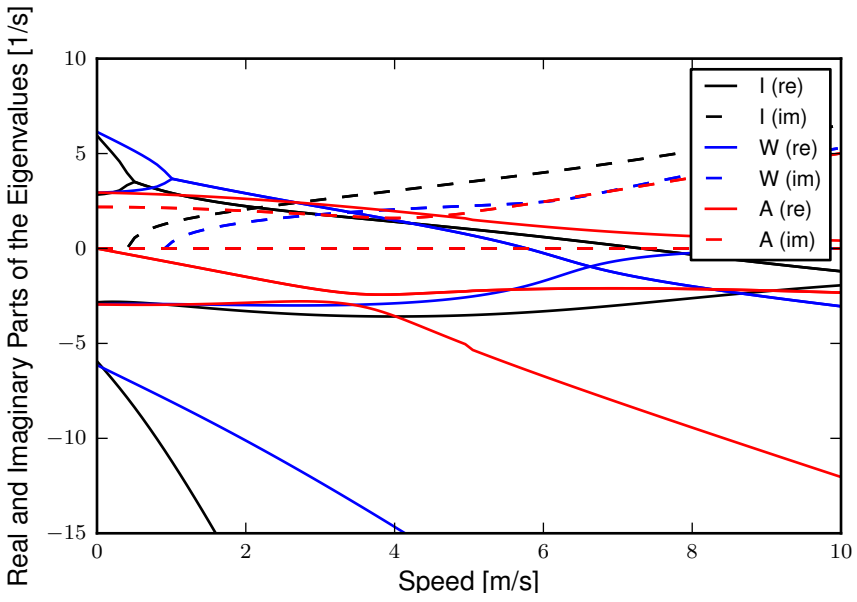

Figure 11.12: Real and imaginary parts of the eigenvalues as a function of speed for model (I)dentified from all runs, the (W)hipple model and the (A)rm model. Generated by *src/systemidentification/canonical_plots.py*.

identified model stays quite constant among the 4, 6, and 9 m/s models. As the speed increases the Whipple and arm models are less predictive of the identified model at low frequencies, but tend to match out past 4 rad/s or so.

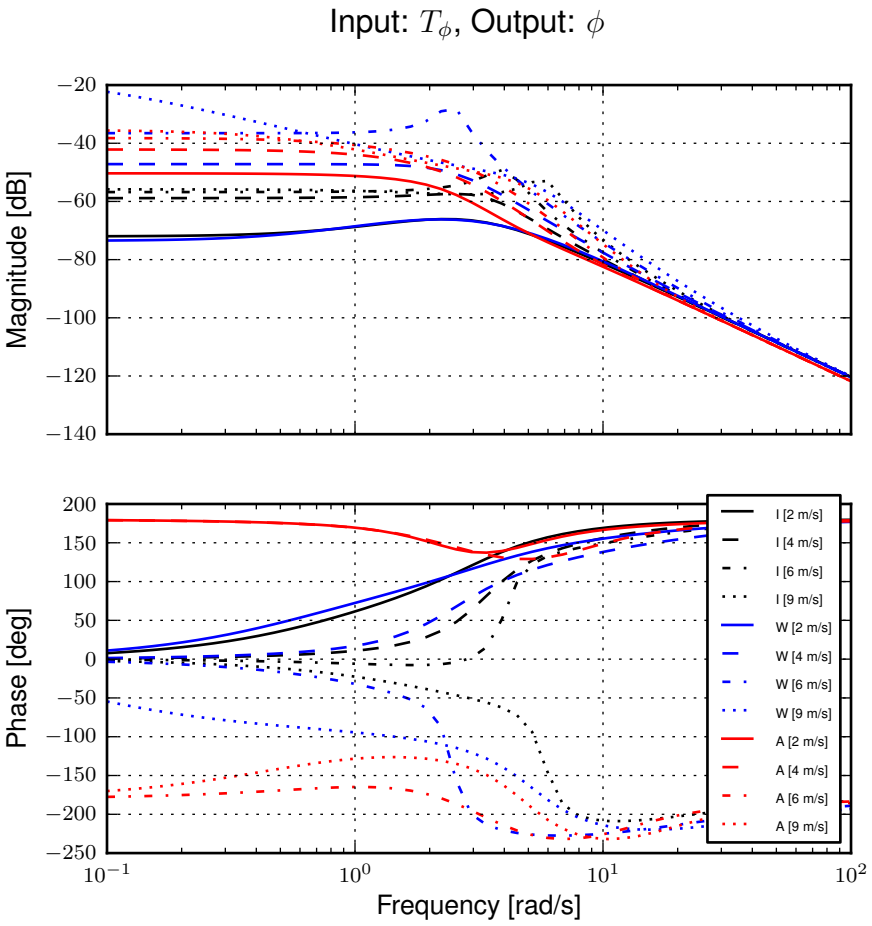

Figure 11.13: $\frac{\phi}{T_\phi}$ frequency response of the three models, (I)dentified, (W)hipple, and (A)rm, at four speeds (2, 4, 6, and 9 m/s). The color indicates the model and the line type indicates the speed. Generated by *src/systemidentification/canonical_plots.py*.

Figure 11.14 shows the steer angle response with respect to the roll torque. Once again the Whipple model is almost identical to the identified model at the lowest speed, 2 m/s. The arm model has about a +5 dB offset at low frequencies and a -10 dB offset at high frequencies with the models only being similar just around 4 rad/s. At 9 m/s the Whipple model has similar magnitude and phase above 7 rad/s whereas the low frequency shows that the Whipple model has up to +30 dB magnitude difference with respect to the identified model. The arm model behaves in much the same way at 9 m/s.

The steer torque to roll angle transfer function, *Figure 11.15* may be the most important to model accurately as it is the primary method of controlling the bicycle's direction, i.e. commanding roll allows one to command yaw. At 2 m/s the Whipple model magnitude matches at lower frequencies (< 4 rad/s) better and the arm model better at higher frequencies (> 4 rad/s). A 4 m/s and above the magnitude of identified varies little with speed, which contrasts the stronger speed dependence of the first principles models. The low frequency behavior of the identified model is not well predicted by the Whipple and arm models at the three highest speeds but about about 3 rad/s the arm model shows better magnitude matches than the Whipple model.

The steer torque to steer angle frequency response, *Figure 11.16*, shows that at speeds above 2 m/s the first principle

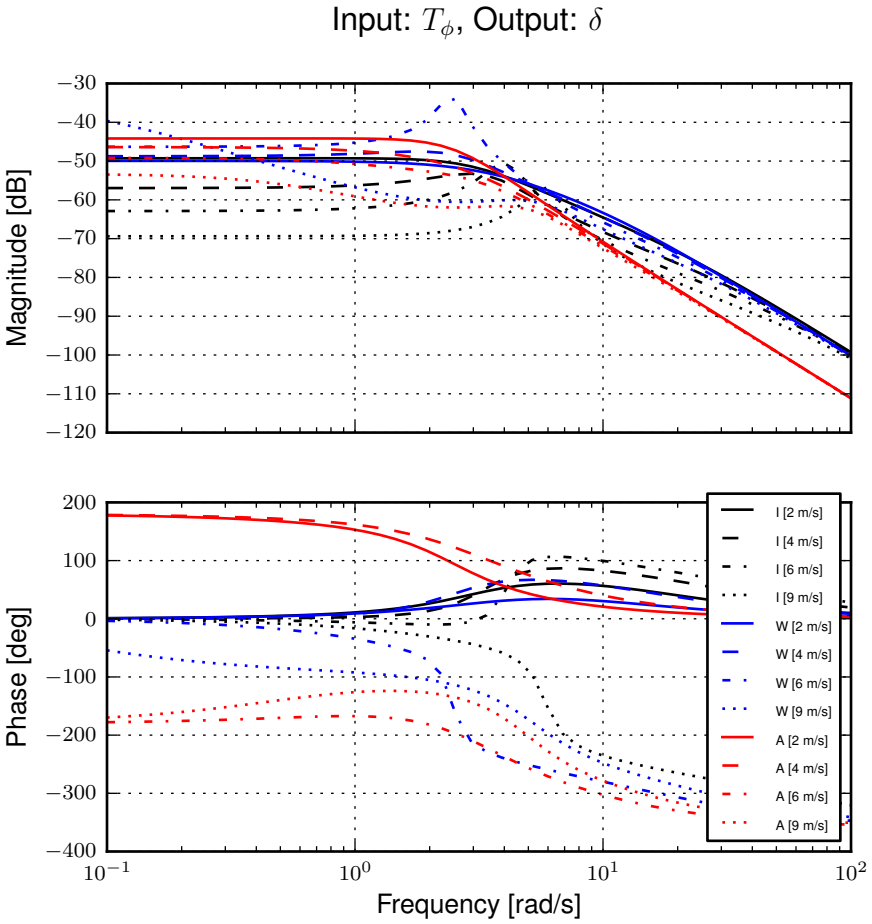

Figure 11.14: $\frac{\delta}{T_\phi}$ frequency response of the three models, (I)dentified, (W)hipple, and (A)rm, at four speeds (2, 4, 6, and 9 m/s). The color indicates the model and the line type indicates the speed. Generated by *src/systemidentification/canonical_plots.py*.

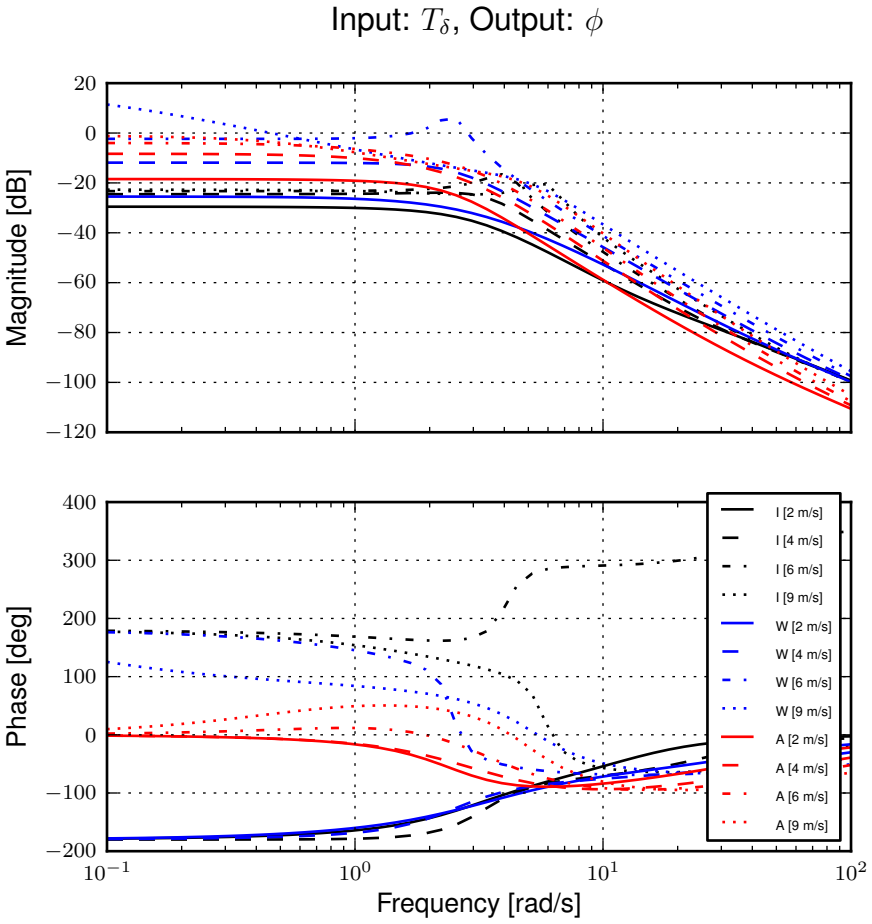

Figure 11.15: Frequency response of the three models, (I)dentified, (W)hipple, and (A)rm, at four speeds (2, 4, 6, and 9 m/s). The color indicates the model and the line type indicates the speed. Generated by *src/systemidentification/canonical_plots.py*.

models do not predict the response well at low frequencies. The response changes more drastically with respect to speed for the first principles models than for the identified model.

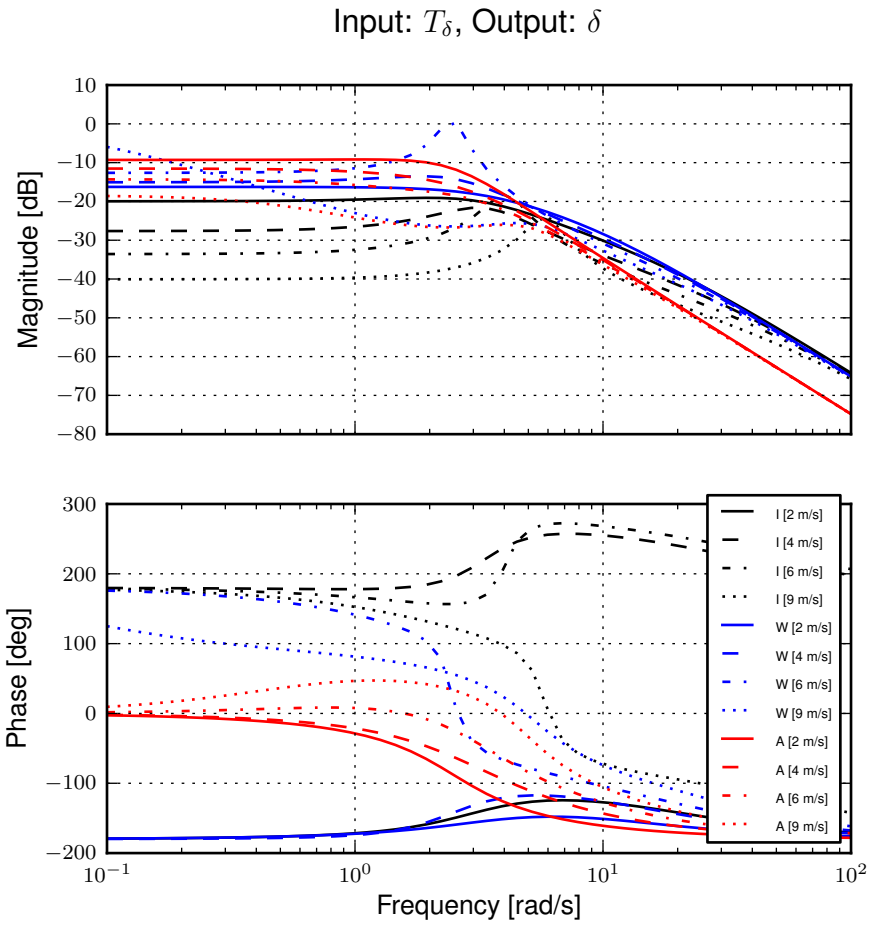

Figure 11.16: Frequency response of the three models at four speeds. The color indicates the model and the line type indicates the speed. Generated by *src/systemidentification/canonical_plots.py*.

Comparison of identified models

Tables *11.3*, *11.4*, and *11.5* present the identified canonical coefficient values from all twelve of the chosen data subsets. The variances of the coefficient estimates with respect to how well the model fits the data in the steer equation are quite low except for the $H_{\delta F}$ parameter. The low variance is partially due to the large datasets but also due to the quality of the resulting fits. The $H_{\delta F}$ is highly dependent on the trail which is expected to be difficult to identify. The coefficient estimates are not all repeatable among the data subsets. In particular $C_{1\delta\phi}$ and $H_{\delta F}$ have the largest relative variance among the models (> 62%). $M_{\delta\delta}$, $C_{1\phi\delta}$, $C_{1\delta\delta}$, and $K_{2\delta\delta}$ are the most consistent among the models (< 18%) with the remaining coefficients falling somewhere in between. This is odd because these data sets are not independent of one another where some are subsets of the others but once again the identification procedure does not explicitly account for process noise and the coefficient estimates reflect this. A sensitivity study for each coefficient with respect to the various physical parameters could help reveal which parameters less likely fit into the Whipple model mold.

Table 11.3: Identified coefficients of the benchmark bicycle model for various sets of data. The first column indicates which rider's runs were used: (C)harlie, (J)ason, (L)uke or (A)ll. The second column indicates which environment's runs were used: (P)avilion Floor, (H)orse Treadmill, or (A)ll. The remaining columns give the resulting numerical value of the identified parameter, its standard deviation with respect to the model fit, and the percent difference with respect to the value predicted by the Whipple model. Table generated by src/systemidentification/canonical_tables.py.

		$M_{\phi\delta}$			$C_{1\phi\delta}$			$K_{0\phi\delta}$		
R	E	Value	σ	% Diff	Value	σ	% Diff	Value	σ	% Diff
A	H	1.659	0.010	-27.6%	21.35	0.02	-49.3%	-5.29	0.06	123.2%
C	H	3.36	0.02	54.4%	20.05	0.04	-49.8%	-0.1	0.1	-96.5%
L	P	2.56	0.03	13.2%	33.53	0.05	-19.5%	-4.53	0.10	91.7%
J	P	2.53	0.02	3.7%	30.04	0.05	-32.7%	-1.82	0.10	-26.7%
C	A	3.75	0.02	72.6%	21.19	0.05	-47.0%	-1.9	0.1	-16.5%
L	H	1.82	0.02	-19.5%	19.18	0.04	-53.9%	-6.84	0.10	189.8%
A	A	2.284	0.008	-0.3%	23.94	0.02	-43.1%	-3.92	0.04	65.4%
J	H	0.95	0.01	-61.0%	22.21	0.02	-50.3%	-7.13	0.08	187.5%
L	A	2.19	0.02	-3.1%	25.94	0.03	-37.7%	-5.37	0.07	127.4%
A	P	3.02	0.02	31.7%	28.64	0.04	-31.9%	-2.93	0.08	23.8%
J	A	1.70	0.01	-30.4%	24.26	0.02	-45.7%	-3.97	0.06	60.2%
C	P	4.15	0.05	90.8%	22.3	0.1	-44.1%	-3.4	0.3	48.6%

Table 11.4: Identified coefficients of the benchmark bicycle model for various sets of data. The first column indicates which rider's runs were used: (C)harlie, (J)ason, (L)uke or (A)ll. The second column indicates which environment's runs were used: (P)avilion Floor, (H)orse Treadmill, or (A)ll. The remaining columns give the resulting numerical value of the identified parameter, its standard deviation with respect to the model fit, and the percent difference with respect to the value predicted by the Whipple model. Table generated by src/systemidentification/canonical_tables.py.

		$M_{\delta\delta}$			$C_{1\delta\phi}$			$C_{1\delta\delta}$		
R	E	Value	σ	% Diff	Value	σ	% Diff	Value	σ	% Diff
A	H	0.2088	0.0003	-5.3%	-0.891	0.002	183.0%	1.5982	0.0008	14.8%
C	H	0.1435	0.0007	-34.0%	-0.881	0.006	179.6%	1.601	0.002	19.5%
L	P	0.2505	0.0009	14.2%	-0.549	0.009	74.2%	2.100	0.003	52.6%
J	P	0.1786	0.0007	-20.4%	-1.09	0.01	246.6%	1.915	0.002	31.0%
C	A	0.1760	0.0008	-19.1%	-0.380	0.008	20.7%	1.675	0.002	25.0%
L	H	0.2336	0.0007	6.5%	-1.058	0.005	235.8%	1.726	0.002	25.5%
A	A	0.2000	0.0003	-9.2%	-0.888	0.002	182.0%	1.7337	0.0008	24.5%
J	H	0.2500	0.0005	11.5%	-0.849	0.003	169.6%	1.545	0.001	5.7%
L	A	0.2385	0.0006	8.7%	-1.053	0.004	234.4%	1.943	0.002	41.3%
A	P	0.1949	0.0006	-11.6%	-0.236	0.007	-24.9%	1.872	0.002	34.4%
J	A	0.2012	0.0003	-10.2%	-0.953	0.002	202.4%	1.6592	0.0009	13.5%
C	P	0.220	0.002	1.3%	0.84	0.02	-366.5%	1.702	0.005	27.0%

Table 11.5: Identified coefficients of the benchmark bicycle model for various sets of data. The first column indicates which rider's runs were used: (C)harlie, (J)ason, (L)uke or (A)ll. The second column indicates which environment's runs were used: (P)avilion Floor, (H)orse Treadmill, or (A)ll. The remaining columns give the resulting numerical value of the identified parameter, its standard deviation with respect to the model fit, and the percent difference with respect to the value predicted by the Whipple model. Table generated by src/systemidentification/canonical_tables.py.

		$K_{0\delta\delta}$			$K_{2\delta\delta}$			$H_{\delta F}$		
R	E	Value	σ	% Diff	Value	σ	% Diff	Value	σ	% Diff
A	H	-0.6055	0.0003	-18.1%	2.182	0.002	-0.7%	0.0064	0.0008	-41.5%
C	H	-1.2406	0.0007	75.5%	2.563	0.006	21.9%	0.020	0.002	77.1%
L	P	-0.4889	0.0009	-33.7%	2.603	0.009	18.9%	0.011	0.003	-1.3%
J	P	-0.6561	0.0007	-15.3%	1.99	0.01	-13.2%	0.007	0.002	-30.2%
C	A	-0.9017	0.0008	27.6%	2.763	0.008	31.4%	0.018	0.002	59.1%
L	H	-0.3181	0.0007	-56.8%	2.508	0.005	14.5%	0.006	0.002	-44.1%
A	A	-0.6678	0.0003	-9.7%	2.340	0.002	6.5%	0.0086	0.0008	-21.8%
J	H	-0.3579	0.0005	-53.8%	1.968	0.003	-14.3%	-0.000	0.001	-100.9%
L	A	-0.4614	0.0006	-37.4%	2.524	0.004	15.2%	0.008	0.002	-31.0%
A	P	-0.6003	0.0006	-18.8%	2.469	0.007	12.4%	0.013	0.002	17.7%
J	A	-0.6207	0.0003	-19.8%	1.996	0.002	-13.1%	0.0047	0.0009	-55.7%
C	P	-0.288	0.002	-59.3%	2.81	0.02	33.8%	0.020	0.005	79.9%

It is interesting to note that $C_{1\delta\phi}$ deviates quite significantly from the Whipple model prediction. This term depends on the wheel radii, wheel rotational inertia, wheelbase, steer axis tilt, and trail. All of these but trail are easily measured so it is tempting to solve for trail given $C_{1\delta\phi}$ and the other measured parameters described in [MPRS07].

$$c = -\frac{w(C_{1\delta\phi} + S_F \cos\lambda)}{S_T \cos\lambda} \tag{11.26}$$

The results for each data subset are given in *Table 11.6*. On average the values are extremely unrealistic when compared to the measured geometric trail of $c = 0.0599$ meters. This may imply that including the effects of pneumatic trail would not be enough to improve the predictive capabilities of the Whipple model. It also points to the potentially erroneous assumptions made in this identification effort such as the order of the system and which parameters are fixed. Even thought the model is quite adequate for describing the measured motion, it lacks the complexness to identify the precise deficients in the first principles assumptions.

Table 11.6: The trail computed from the identified and the measured physical parameters.

R-E	**A-H**	**C-H**	**L-P**	**J-P**	**C-A**	**L-H**	**A-A**	**J-H**	**L-A**	**A-P**	**J-A**	**C-P**
c [m]	1.006	0.989	0.443	1.335	0.167	1.279	1.001	0.937	1.272	-0.069	1.107	-1.835

The measurement errors, model structure and order dictate how well the models can predict the input-output behavior of each run or even each perturbation. The ideal goal is to select one or a small set of models that do a good job at predicting the measured behavior for each run. The previous section's state space methods have already shown that the Whipple and arm models may not provide adequate predictions.

Figures *11.17*, *11.18*, and *11.19* plot the steer torque to roll angle frequency response for three speeds: 2 m/s, 5.5 m/s and 9.0 m/s for each of the models in Tables *11.3*, *11.4*, and *11.5*. At the lowest speed, all of the models have a similar frequency response, especially in the frequency band between about 1 an 20 rad/s. At 5.5 m/s the models are similar at a higher bandwidth, 4 to 30 rad/s, and at 9.0 m/s even higher, 10 to 50 rad/s. Notice that the frequency band where the models are most similar shifts to higher frequencies at higher speeds. The model derived from all of the data (all rider and all runs), gives an average model and if this model is significantly better at predicting the measured behavior of the Whipple and arm models, it may be a good general candidate model for this bicycle.

The predictive capability and quality of a given model can be quantified by an assortment of criterion and methods. I've made use of two criterion to judge the quality of these models with respect to given data. The first is to simulate the system given the measured inputs. This method works well when the open loop system is stable, but if it is unstable

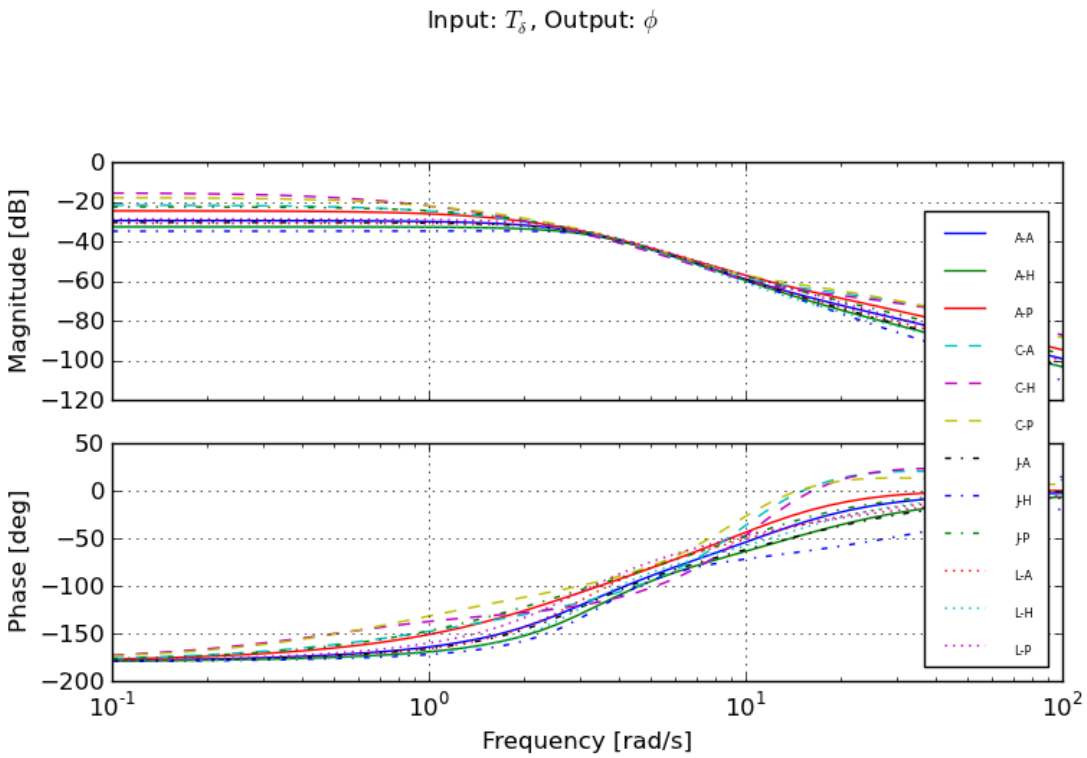

Figure 11.17: Steer torque to roll angle frequency responses at 2.0 m/s for all the identified models in Tables *11.3*, *11.4*, and *11.5*.

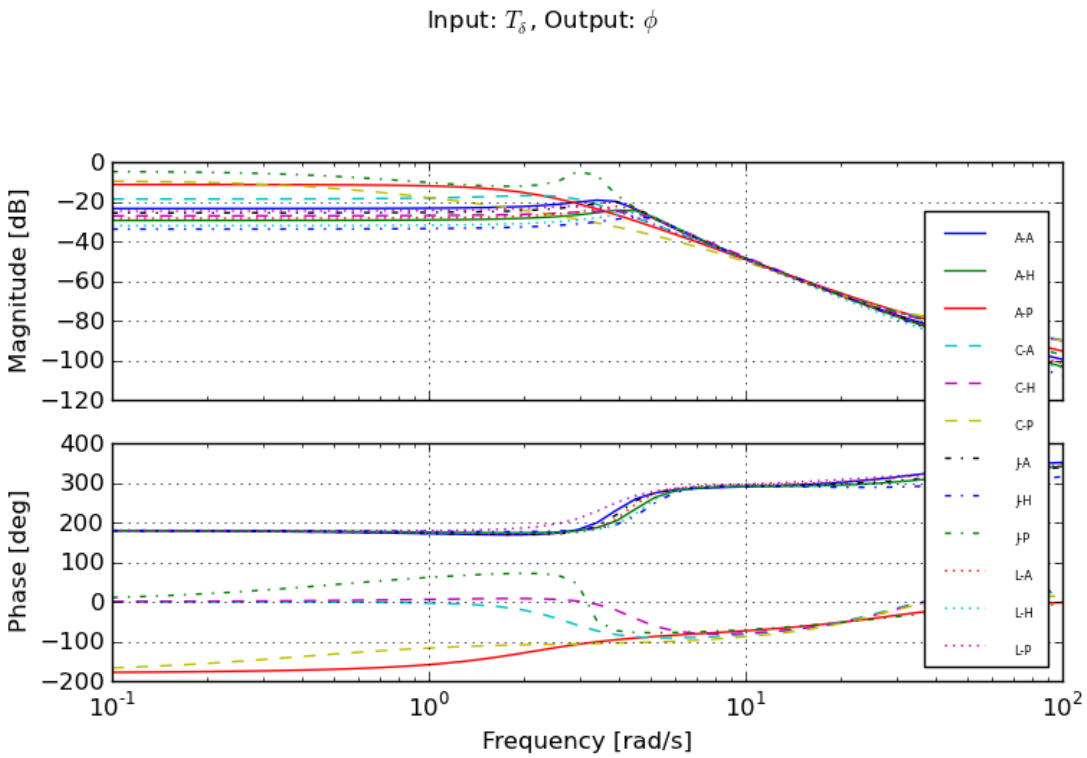

Figure 11.18: Steer torque to roll angle frequency responses at 5.5 m/s for all the identified models in Tables *11.3*, *11.4*, and *11.5*.

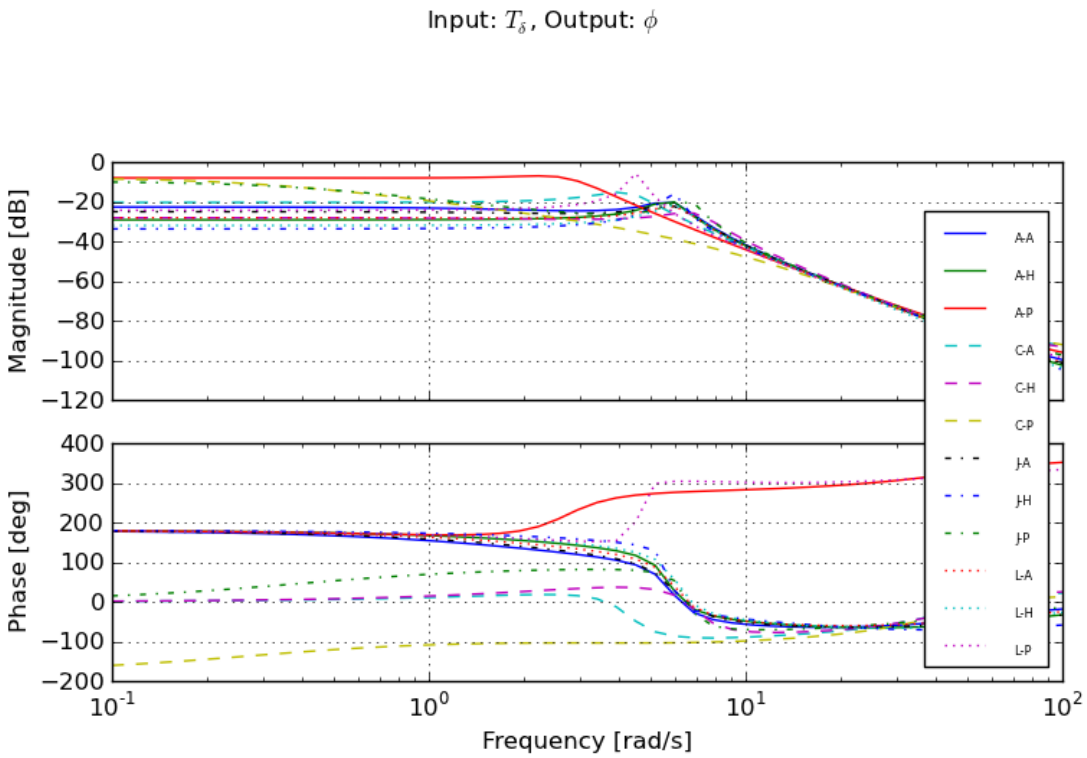

Figure 11.19: Steer torque to roll angle frequency responses at 9.0 m/s for all the identified models in Tables *11.3*, *11.4*, and *11.5*.

as so in the case of this bicycle, it may be difficult to simulate. Searching for initial conditions that give rise to a stable model for the duration of the run or simulating by weighting the future error less may relieve the instability issues. Another option is to see how well the inputs are predicted given the measured outputs. The canonical form of the equations lend themselves to this and only two inputs per run need be checked.

The predicted torques on the system are

$$y_p = \mathbf{M}\ddot{q} + v\mathbf{C}_1\dot{q} + [g\mathbf{K}_0 + v^2\mathbf{K}_2]q \tag{11.27}$$

and the measured torques as

$$y_m = T + HF \tag{11.28}$$

y_p and y_m can be computed for each run along with the *variance accounted for* (VAF), by the model for both the total roll torque and the steer torque

$$\text{VAF} = 1 - \frac{||y_p - y_m||}{||y_m - \bar{y}_m||} \tag{11.29}$$

I compute the VAF for each of the 374 runs used in the canonical identification outlined in Equation (11.29) using each of the 12 identified models and both the Whipple and Arm models. This percentage can be used as a criterion with which to judge the ability of one model versus another to predict the measurement. I then take the median of the VAF over each of the 12 sets of runs, Tables *11.7* and *11.8*. The results give an idea of how well the various models are able to predict the data for all of the runs in a given set.

Table 11.7: Median VAF for the roll equation of various models (rows) for all runs in each data subset (columns).

	A-A	**A-H**	**A-P**	**C-A**	**C-H**	**C-P**	**J-A**	**J-H**	**J-P**	**L-A**	**L-H**	**L-P**
A-A	-11.9%	-39.5%	-8.5%	-28.9%	-20.4%	-30.2%	-30.5%	-71.9%	-21.9%	9.0%	5.4%	9.0%
A-H	-19.3%	-43.4%	-16.9%	-35.8%	-27.7%	-38.6%	-37.4%	-85.0%	-26.9%	0.5%	-2.1%	0.5%
A-P	-3.6%	-31.8%	2.1%	-19.4%	-19.4%	-19.8%	-22.7%	-55.3%	-11.8%	20.3%	11.1%	20.5%
C-A	-14.8%	-50.3%	-11.1%	-26.8%	-31.1%	-26.8%	-34.9%	-83.1%	-22.5%	3.0%	-5.7%	3.5%
C-H	-17.2%	-49.6%	-13.9%	-31.8%	-31.9%	-31.8%	-35.8%	-76.0%	-24.5%	-0.3%	-8.1%	-0.2%
C-P	-13.4%	-51.7%	-8.8%	-22.5%	-31.2%	-22.5%	-36.1%	-91.0%	-21.3%	6.0%	-4.5%	6.9%
J-A	-13.9%	-38.0%	-9.6%	-31.6%	-20.6%	-33.8%	-31.0%	-67.6%	-23.4%	7.5%	5.8%	7.6%
J-H	-21.1%	-43.9%	-17.5%	-39.8%	-27.5%	-41.7%	-38.6%	-81.7%	-28.5%	0.5%	-0.0%	0.6%
J-P	-2.5%	-27.5%	3.0%	-18.2%	-18.2%	-18.6%	-20.1%	-43.1%	-10.3%	21.0%	12.9%	21.1%
L-A	-9.9%	-29.4%	-5.2%	-26.0%	-18.5%	-28.1%	-27.4%	-64.3%	-19.5%	13.2%	9.4%	13.3%
L-H	-26.1%	-53.4%	-23.1%	-39.4%	-37.5%	-42.5%	-41.8%	-77.0%	-31.6%	-8.2%	-12.1%	-7.8%
L-P	-0.3%	-29.7%	8.2%	-20.8%	-31.3%	-20.8%	-25.9%	-35.8%	-16.8%	22.5%	11.0%	22.6%
Whipple	-10.8%	-37.5%	-3.1%	-28.5%	-37.4%	-28.5%	-44.2%	-67.5%	-35.9%	17.6%	17.8%	16.2%
Arm	-11.6%	-36.4%	-4.1%	-27.8%	-36.2%	-27.8%	-46.0%	-64.1%	-32.9%	15.8%	13.6%	16.9%

Table 11.8: Mean VAF for the steer equation of various models (rows) for all runs in each data subset (columns).

	A-A	**A-H**	**A-P**	**C-A**	**C-H**	**C-P**	**J-A**	**J-H**	**J-P**	**L-A**	**L-H**	**L-P**
A-A	59.4%	56.8%	60.0%	60.6%	49.7%	61.2%	58.7%	60.1%	58.4%	59.3%	56.2%	60.3%
A-H	53.4%	53.4%	53.4%	53.5%	46.8%	54.2%	55.7%	58.1%	55.3%	51.8%	51.7%	51.8%
A-P	63.1%	58.1%	64.3%	64.0%	54.4%	65.8%	57.5%	57.9%	57.4%	65.3%	59.7%	66.8%
C-A	49.4%	44.9%	50.2%	50.9%	42.9%	51.6%	48.0%	45.1%	49.0%	49.4%	46.1%	50.2%
C-H	47.5%	47.3%	47.7%	47.1%	45.5%	47.2%	50.0%	50.5%	49.3%	47.0%	45.3%	47.0%
C-P	44.1%	41.6%	45.2%	46.9%	41.6%	48.4%	40.5%	39.9%	40.7%	43.9%	43.3%	45.1%
J-A	60.2%	58.1%	60.9%	59.9%	51.4%	61.8%	59.6%	63.1%	59.1%	60.5%	57.7%	60.9%
J-H	46.1%	50.3%	45.5%	42.1%	41.8%	42.3%	50.8%	53.4%	49.5%	44.9%	46.9%	42.9%
J-P	64.5%	60.5%	65.1%	62.9%	57.7%	64.6%	61.5%	62.2%	60.8%	67.8%	63.6%	69.0%
L-A	58.4%	57.8%	58.6%	56.8%	51.1%	57.8%	57.0%	59.6%	55.2%	60.3%	60.1%	61.2%
L-H	47.2%	49.8%	47.0%	46.5%	43.4%	46.7%	49.9%	52.4%	48.9%	46.7%	47.8%	46.6%
L-P	61.7%	59.5%	62.9%	60.2%	50.0%	62.7%	54.3%	60.6%	52.8%	68.2%	63.0%	70.0%
Whipple	55.3%	51.0%	56.4%	56.1%	48.7%	58.4%	55.4%	55.5%	55.4%	53.0%	49.5%	55.7%
Arm	28.0%	18.6%	30.3%	36.2%	18.9%	37.4%	17.6%	20.4%	12.6%	29.3%	15.9%	34.2%

Tables *11.7* and *11.8* give the median for each set of runs in each column for each model given in the row for roll and steer respectively. The maximum VAF in the column gives a measure of the best model for predicting each individual run in that set of runs. Intuitively, I would expect that the diagonal of the upper 12 rows would be the maximum in

each column due to the fact that that model was derived from that set of runs, but that is not always the case. I believe that this can be explained by the fact that there are more outlier runs in some sets. These outliers have enough effect in the resulting regressions, that the models generated from sets of runs with fewer outliers are able to predict the data better.

The models are able to predict the steer torque much better than the roll torque. The roll torque should be zero in all of the runs without disturbances but the roll equations do not predict a zero value. This is also reflected in the negative median values of all the runs with disturbances in much of *Table 11.7*. We fixed six of the nine parameters in the roll equation to those of the Whipple model and fixed three of the nine parameters in the steer equation. These extra degrees of freedom can partially explain why the steer predictions are better than the roll predictions. The model for the roll torque is more susceptible to the noise in the rate and angle measurements and has consequences of +/- 50 Nm variation in the predicted roll torques. These are unfortunately comparable in magnitude to the measured roll torques due to the lateral perturbations. But *Table 11.7* can still be used to gage which models are better with reference to each other. The values in *Table 11.7* are only generated from the runs with disturbances, as a relative measure of quality to zero is hard to make.

Tables *11.7* and *11.8* reveal:

- The arm model is poor at predicting the steer torque.
- The models derived from Charlie's runs are poorer at predicting the inputs.
- The Whipple model is not too bad at predicting steer torque, but on average about 10% worse than the best models.
- The models identified from the pavilion runs are generally the best (with exception of Charlie's). The ones generated from Luke and Jason's runs are typically the best at predicting both steer torque and roll torque, with Luke's giving better roll torque predictions.
- The roll torque is poorly predicted by all models when it is supposed to be zero. This raises implications in the validity of the roll equation and the potential need for tire slip models.

It may seem odd that a model identified from the subset of runs of one rider in one environment is the best at predicting the runs on a individual basis, but the uncertainty and error in both the data and the model structures don't dictate that this can't be. Keep in mind that all of the frequency responses of all 12 models shown in Figures *11.17*, *11.18*, and *11.19* are probably bounded in the uncertainty of the predicted responses and each can be considered a "good" model, even including the Whipple model.

The second method of evaluating the quality of the identified models is to simulate the model with the measured inputs and compare the predicted outputs with the measured outputs with a similar VAF criterion. I simulated all 14 models with the inputs from the 374 runs and computed the VAF explained by the model for each output. Since the models are typically unstable at all of the speeds we tested, I searched for the set of initial conditions which minimizes the VAF for all outputs. For the majority of runs and models, this is sufficient to find a stable simulation for the duration of the run. However, this is not always the case. For long duration runs I select a random 20 second section of the data to simulate, reducing the likelihood that the simulation blows up due to the model's instability. Finally, I ignore any outputs VAFs that are less than -100 percent as they are most likely due to unstable simulations. *Table 11.9* presents the median percent variance accounted for across all runs for each model and each output. The best model seems to be the one generated from the data with Luke on the Pavilion Floor once again, but these results differ from the previous otherwise.

- For all outputs other than roll angle, the arm model is better than the Whipple model.
- The models from Charlie's data fare much better than the input comparisons and are better than some of Jason's.
- The model identified from the data with Jason on the Pavilion floor is very poor in roll angle prediction as opposed to being a good choice from the input comparison results.
- All of the identified models are better predictors than the first principles models.

Table 11.9: The median VAF in the simulation output variables.

	phi	delta	phiDot	deltaDot
AA	28.6%	61.8%	51.8%	65.2%
CH	18.6%	57.2%	52.6%	62.2%
LA	29.4%	59.8%	52.9%	67.9%
AH	24.1%	57.4%	43.1%	64.2%
CA	14.9%	54.5%	51.7%	59.8%
JP	-3.4%	35.4%	34.1%	61.7%
LH	24.3%	57.7%	46.1%	65.7%
AP	29.7%	58.9%	60.6%	63.2%
JH	22.8%	53.6%	42.0%	62.8%
LP	38.2%	62.8%	60.9%	68.4%
CP	19.0%	46.0%	42.0%	47.1%
JA	27.9%	61.0%	49.4%	65.9%
Whipple	-21.0%	10.3%	5.8%	12.2%
Arm	-33.1%	19.6%	29.7%	33.1%

The mean percent variance across the outputs can be computed and the models ranked by the mean, *Table 11.10*. The best model seems to be LP and the AA is also a pretty good predictor. Notice that the Whipple model is poorer than the arm model.

Table 11.10: The mean of the median VAF in the simulation output variables presented in Table 11.9.

Model	L-P	A-P	L-A	A-A	J-A	L-H	C-H
Mean	57.6%	53.1%	52.5%	51.8%	51.1%	48.5%	47.7%
Model	A-H	J-H	C-A	C-P	J-P	Arm	Whipple
Mean	47.2%	45.3%	45.2%	38.5%	31.9%	12.3%	1.8%

The orange lines in Figures *11.8* and *11.9* correspond to the L-P model which allows comparison of the results of the canonical identification process with those of the state space identified models. The L-P model seems be better at fitting the data, especially in the steer acceleration equation, but the large variance in the state space coefficients is still a problem. This lends more confidence that that the L-P model is a better model choice than the Whipple or the arm model.

Discussion

Canonical identification The canonical realization, Section *Canonical Identification*, is a good method for identifying a model for data from multiple runs. It relies on quality measurements of the coordinates, rates, and accelerations. I use numerical differentiation of the rates to get the accelerations instead of direct measurements and the angles are not perfectly related to the rates through differentiation because they were measured from different sensors. The noise in the measurements and whether the measurements are accurately the derivatives of one another have bearing on the results. It is possible to identify all of the entries in the canonical matrices, but it is likely some of those are easily predicted from first principles so I fix them to the Whipple model predictions if that is the case. This leaves the roll equation mostly known and the steer equation mostly unknown and the results reflect better fits with respect to steer than roll as a result. This formulation does not explicitly account for process noise, so it may be be susceptible to similar accuracy errors as the state space formulation is. The advantage in this method is the ability to use large sets of data for the calculations. It is extremely surprising that a model from a small subset of the data is better at predicting all of the runs on an individual basis.

Input comparison The input prediction comparisons do not predict the roll torque well at all. It seems that the roll torque equation magnifies the noise in the coordinate, rate, and acceleration measurements such that the resulting noise in the roll torque is equivalent in magnitude to the roll perturbations. But the roll perturbations

do seem to clearly be present in the predictions. This results in difficultly comparing the quality of the resulting models with respect to the roll equation. This also points to the potential deficiencies in the Whipple roll torque equation and these large magnitude roll torques may also be due to inaccurate modeling of the tire dynamics.

Output comparison The output comparison (simulations) give more reasonable results because all four outputs generally fit well across runs given the measured inputs. It is surprising that the ranking of model prediction ability is different for the input comparisons than the output comparisons, but the fact that the model identified from Luke's pavilion runs is the best from both comparisons, at least gives credence to its further adoption. The first principles models are dead last in the ranking and the model identified from Jason's pavilion runs is surprisingly poor due to poor roll angle prediction.

Whipple model The input comparisons show that the Whipple model is relatively reasonable at predicting the data but the output comparisons make it out to be much poorer. The Whipple model is clearly the worst at explaining the variance in the steer angle, roll rate, and steer rate outputs and is second to worst in roll angle. Also contrary to the Whipple model predictions, the weave mode of all identified models is unstable until at least 8-9 m/s or so. The caster mode is also typically much faster in the identified models. This implies that the real system does not benefit from open loop stability at all during most normal speed bicycling and that the rider is always responsible for stabilizing the vehicle. This may explain why none of the riders ever felt comfortable enough to try hands-free riding while strapped into the harness.

Arm model I had hypothesized that the arm model would better predict the measured motion because it more accurately modeled the fact that we allowed the rider full use of his arms to control the steering and that the arms effectively added to the front frame inertia. This was validated with respect to the output simulation comparisons. They predict that the arm model is much better than the Whipple model for most of the output variables. But this is in contrast to the input comparison predictions which were the opposite, with the Whipple being much better than the arm model. More work is needed to verify which model is better and why the results differ at all.

Rider biomechanics may mot be modeled The models identified from Charlie's runs are different than those of Jason and Luke. The models from Charlie's runs do not predict the runs very well, even including the subset of Charlie's data. I'm not sure if the rider's arm stiffness can affect these results or how much the different riders can effect this if we are only searching for the passive bicycle-rider model. The other potential explanation is that there are too many outliers in Charlie's runs. This could have something to do with the runs that had time synchronization issues.

Predicting derivatives The roll angle is more poorly predicted than the other variables. The steer angle and steer rate are better predicted than the roll angle and roll rate. In the output comparisons I enforce that the roll rate is the derivative of the roll and the same for the steer variables. The poorer prediction of roll angle is probably due to noise and error in the independent measurements of these variables. I toyed with complementary filters to try to combine the angle and rate measurements in a way that filtered and enforced the derivative relationship between the measured variables, but did not have much luck improving the results. It may be better to focus on one each of the roll and steer variables for minimization purposes. It is well known that fitting models with many fewer inputs to outputs is difficult and the fewer outputs reduces the number of noise terms to estimate.

Conclusion

The best candidate model for the measured system is the model identified from the data subset with rider Luke and the pavilion floor. I find no reason to use different models for each rider or environment as this model does a better job at predicting than the other models derived from matching subsets. I will use the model identified from the set of runs with Luke on the pavilion floor as the base bicycle model for identifying the controller for all the runs in the following section of this Chapter. I could use the individual bicycle identifications for each run, but using a model derived from a set of runs has the advantage that it will be less affected by the lack of identifying the process noise explicitly.

Suggestions for improving the results.

- Fit to MISO models instead of MIMO for simplification.

- Fix at least the $a_{\phi\delta}$ coefficient and make the noise with respect to the kinematical equations equal to zero giving 11-13 total parameters to fit.
- Use model reduction techniques to combine many MISO and SISO models for a given run.
- Use better initial guess techniques and try global optimizers to get to the best solution.

11.8 Rider Controller Identification

Now that I have a reasonable estimate of the plant, the rider control system can be identified. There are many control structures that exist that may explain the data. If the feedback and input variables are the same for two different control structures, they can be mapped to each other and are essentially equivalent. Much of the difference in control structures such as PID, sequential loop closure, LQR are the physical interpretations of the gains, delays, and other parameters. Here, I limit the control structure to the one developed in [HMH12] and Chapter *Control*. With this structure, I will have the ability to compare the results with the theoretical hypothesis we developed.

11.8.1 Grey Box Models

The block diagram of the control structure described in Chapter *Control* is shown again in Figures *11.20* and *11.21*. The closed loop system can be written in state space form, which will be used with a state space identification procedure as defined in Section *State Space Realization*. I'll develop forms for pure heading tracking and lateral deviation tracking.

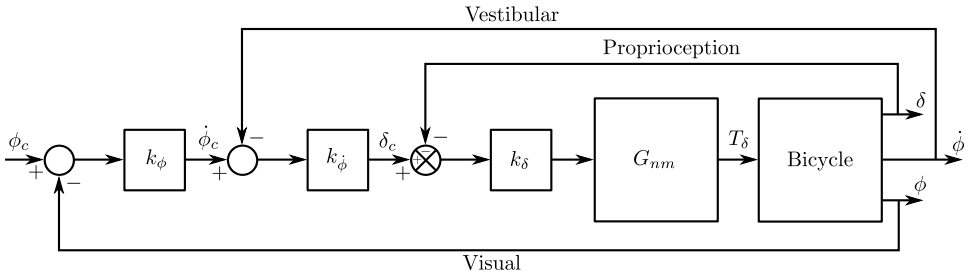

Figure 11.20: The inner loop structure of the control system which feeds back steer angle δ, roll rate $\dot{\phi}$, and roll angle ϕ.

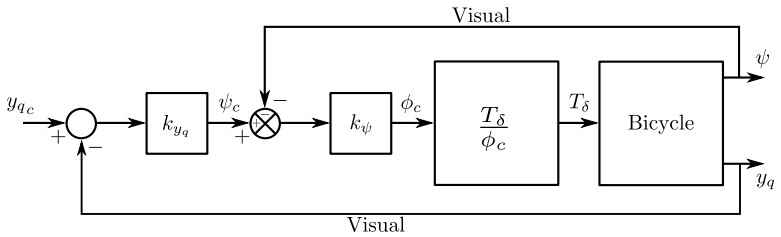

Figure 11.21: The outer loop structure of the control system with the inner loops closed which feeds back the heading ψ and the front wheel lateral deviation y_q.

The bicycle block for lateral deviation tracking has states $x_b = \begin{bmatrix} \phi & \delta & \dot{\phi} & \dot{\delta} & \psi & y_p \end{bmatrix}^T$, inputs $u_b = [T_\delta \quad F]^T$, and

outputs $y_b = \begin{bmatrix}\delta & \phi & \dot{\phi} & \psi & y_q\end{bmatrix}^T$. The state, input, and output matrices are follows

$$\mathbf{A}_b = \begin{bmatrix} 0 & 0 & 1 & 0 & 0 & 0 \\ 0 & 0 & 0 & 1 & 0 & 0 \\ a_{b\ddot{\phi}\phi} & a_{b\ddot{\phi}\delta} & a_{b\ddot{\phi}\dot{\phi}} & a_{b\ddot{\phi}\dot{\delta}} & 0 & 0 \\ a_{b\ddot{\delta}\phi} & a_{b\ddot{\delta}\delta} & a_{b\ddot{\delta}\dot{\phi}} & a_{b\ddot{\delta}\dot{\delta}} & 0 & 0 \\ 0 & a_{b\dot{\psi}\delta} & 0 & a_{b\dot{\psi}\dot{\delta}} & 0 & 0 \\ 0 & 0 & 0 & 0 & a_{b\dot{y}_p\psi} & 0 \end{bmatrix} \tag{11.30}$$

$$\mathbf{B}_b = \begin{bmatrix} B_{bT_\delta} & B_{bF} \end{bmatrix} = \begin{bmatrix} 0 & 0 \\ 0 & 0 \\ b_{b\ddot{\phi}T_\delta} & b_{b\ddot{\phi}F} \\ b_{b\ddot{\delta}T_\delta} & b_{b\ddot{\delta}F} \\ 0 & 0 \\ 0 & 0 \end{bmatrix}$$

$$\mathbf{C}_b = \begin{bmatrix} 0 & 1 & 0 & 0 & 0 & 0 \\ 1 & 0 & 0 & 0 & 0 & 0 \\ 0 & 0 & 1 & 0 & 0 & 0 \\ 0 & 0 & 0 & 0 & 1 & 0 \\ 0 & 1 & 0 & 0 & c_{by_q\psi} & c_{by_q y_p} \end{bmatrix}$$

The neuromuscular block is described by the transfer function

$$G_{nm}(s) = \frac{\omega_{nm}^2}{s^2 + 2\zeta_{nm}\omega_{nm}s + \omega_{nm}} \tag{11.31}$$

which can be written in state space form with the states $x_{nm} = \begin{bmatrix}T_\delta & \dot{T}_\delta\end{bmatrix}^T$, input $u_{nm} = U_{nm}$ and output $y_{nm} = T_\delta$.

$$\mathbf{A}_{nm} = \begin{bmatrix} 0 & 1 \\ -\omega^2 & -2\zeta\omega \end{bmatrix} \tag{11.32}$$

$$B_{nm} = \begin{bmatrix} 0 \\ \omega^2 \end{bmatrix}$$

$$\mathbf{C}_{nm} = \begin{bmatrix} 1 & 0 \end{bmatrix}$$

The combined plant (rider neuromuscular model and bicycle) has states $x_p = \begin{bmatrix}\phi & \delta & \dot{\phi} & \dot{\delta} & \psi & y_p & T_\delta & \dot{T}_\delta\end{bmatrix}^T$, inputs $u_p = [F \quad U_{nm}]^T$, and outputs $y_p = \begin{bmatrix}\delta & \phi & \dot{\phi} & \psi & y_q\end{bmatrix}^T$. The state, input, and output matrices of the plant are

$$\mathbf{A}_p = \begin{bmatrix} \mathbf{A}_b & B_{bT_\delta} & 0_{6\times1} \\ \mathbf{0}_{2\times6} & \mathbf{A}_{nm} & \end{bmatrix} \tag{11.33}$$

$$\mathbf{B}_p = \begin{bmatrix} B_{bF} & 0_{6\times1} \\ 0_{2\times1} & B_{nm} \end{bmatrix}$$

$$\mathbf{C}_p = \begin{bmatrix} \mathbf{C}_b & \mathbf{0}_{5\times2} \end{bmatrix}$$

The sequential loop closure rationale dictates that the commanded output variables are

$$\psi_c = k_{y_q}(y_{q_c} - y_q)$$
$$\phi_c = k_\psi(\psi_c - \psi)$$
$$\dot{\phi}_c = k_\phi(\phi_c - \phi)$$
$$\delta_c = k_{\dot{\phi}}(\dot{\phi}_c - \dot{\phi})$$

and the input to the neuromuscular block as a function of the desired path is

$$U_{nm} = k_\delta(\delta_c - \delta)$$

The input to the neuromuscular block can be written in linear form as

$$U_{nm} = \begin{bmatrix} -k_\delta k_\phi k_{\dot\phi} k_\psi \\ -k_\delta k_\phi k_{\dot\phi} \\ -k_\delta \\ -k_\delta k_{\dot\phi} \\ -k_\delta k_\phi k_{\dot\phi} k_\psi k_{y_q} \\ k_\delta k_\phi k_{\dot\phi} k_\psi k_{y_q} \end{bmatrix}^T \begin{bmatrix} \psi \\ \phi \\ \delta \\ \dot\phi \\ y_q \\ y_c \end{bmatrix}$$

The closed loop state space for lateral deviation tracking can be formed by inserting the controller output U_{nm} into the plant dynamics $(\mathbf{A}_p, \mathbf{B}_p)$ to rearrange the plant state space to be a function of the desired path and the lateral force, $u_l = [F \quad y_{qc}]^T$. The closed loop system $(\mathbf{A}_p, \mathbf{B}_p)$ takes the same form as the plant system with the exception of the steer torque acceleration equation, which is now a function of the controller gains, the neuromuscular parameters, and the desired path of the front wheel contact point. The new entries to the system matrices are

$$x_l = \begin{bmatrix} \phi & \delta & \dot\phi & \dot\delta & \psi & y_p & T_\delta & \dot T_\delta \end{bmatrix}^T \tag{11.34}$$

$$u_l = [F \quad y_{qc}]^T$$

$$\mathbf{A}_l = \begin{bmatrix} 0 & 0 & 1 & 0 & 0 & 0 & 0 & 0 \\ 0 & 0 & 0 & 1 & 0 & 0 & 0 & 0 \\ a_{b\ddot\phi\phi} & a_{b\ddot\phi\delta} & a_{b\ddot\phi\dot\phi} & a_{b\ddot\phi\dot\delta} & 0 & 0 & 0 & 0 \\ a_{b\ddot\delta\phi} & a_{b\ddot\delta\delta} & a_{b\ddot\delta\dot\phi} & a_{b\ddot\delta\dot\delta} & 0 & 0 & 0 & 0 \\ 0 & a_{b\dot\psi\delta} & 0 & a_{b\dot\psi\delta} & 0 & 0 & 0 & 0 \\ 0 & 0 & 0 & 0 & a_{b\dot y_p\psi} & 0 & 0 & 0 \\ 0 & 0 & 0 & 0 & 0 & 0 & 0 & 1 \\ -\omega^2 k_\delta k_{\dot\phi} k_\phi & -\omega^2 k_\delta (1 + c_{by_q\delta} k_{\dot\phi} k_\phi k_\psi k_{y_q}) & -\omega^2 k_\delta k_{\dot\phi} & 0 & -\omega^2 k_\delta k_{\dot\phi} k_\phi k_\psi (1 + c_{by_q\psi} k_{y_q}) & -\omega^2 k_\delta k_{\dot\phi} k_\phi k_\psi k_{y_q} & -\omega^2 & -2\omega\zeta \end{bmatrix}$$

$$\mathbf{B}_l = \begin{bmatrix} 0 & 0 \\ 0 & 0 \\ b_{b\ddot\phi F} & 0 \\ b_{b\ddot\delta F} & 0 \\ 0 & 0 \\ 0 & 0 \\ 0 & \omega^2 k_\delta k_{\dot\phi} k_\phi k_\psi k_{y_q} \end{bmatrix}$$

The output matrix, $\mathbf{C}_l$, can be constructed to provide any desired outputs, which I choose to be a subset of the outputs we measured during the experiments such as steer angle, roll rate, steer torque, etc.

Given that the bicycle model, $(\mathbf{A}_b, \mathbf{B}_b, \mathbf{C}_b)$, is known, the closed loop analytical state space representation is parameterized by seven parameters: the five controller gains and the two neuromuscular parameters. The model is eighth order with two inputs.

Notice that the controller is unlike a state or output feedback model in the sense that the gains only appear in a single row in the A and B matrices. This reflects some of the inherent limitations the human system has for sensing and actuation. Output feedback systems often require an observer so that full estimated state feedback can be used. This model assumes that the rider does not have that ability. They are only able to sense noisy outputs and adjust their torque compensation within the bandwidth limits of the neuromuscular system based on five simple gains.

I also make use of a second closed loop model which is essentially the same, but the outer lateral deviation tracking

loop is removed and tracking a commanded heading remains. This model is seventh order with two inputs.

$$x_h = \begin{bmatrix} \phi & \delta & \dot{\phi} & \dot{\delta} & \psi & T_\delta & \dot{T}_\delta \end{bmatrix}^T \tag{11.35}$$

$$u_h = \begin{bmatrix} F & \psi_c \end{bmatrix}^T$$

$$\mathbf{A}_h = \begin{bmatrix} 0 & 0 & 1 & 0 & 0 & 0 & 0 \\ 0 & 0 & 0 & 1 & 0 & 0 & 0 \\ a_{b\ddot{\phi}\phi} & a_{b\ddot{\phi}\delta} & a_{b\ddot{\phi}\dot{\phi}} & a_{b\ddot{\phi}\dot{\delta}} & 0 & 0 & 0 \\ a_{b\ddot{\delta}\phi} & a_{b\ddot{\delta}\delta} & a_{b\ddot{\delta}\dot{\phi}} & a_{b\ddot{\delta}\dot{\delta}} & 0 & 0 & 0 \\ 0 & a_{b\dot{\psi}\delta} & 0 & a_{b\dot{\psi}\dot{\delta}} & 0 & 0 & 0 \\ 0 & 0 & 0 & 0 & 0 & 0 & 1 \\ -\omega^2 k_\delta k_{\dot{\phi}} k_\phi & -\omega^2 k_\delta & -\omega^2 k_\delta k_{\dot{\phi}} & 0 & -\omega^2 k_\delta k_\phi k_{\dot{\phi}} k_\psi & -\omega^2 & -2\omega\zeta \end{bmatrix}$$

$$\mathbf{B}_h = \begin{bmatrix} 0 & 0 \\ 0 & 0 \\ b_{b\ddot{\phi}F} & 0 \\ b_{b\ddot{\delta}F} & 0 \\ 0 & 0 \\ 0 & 0 \\ 0 & \omega^2 k_\delta k_\phi k_{\dot{\phi}} k_\psi \end{bmatrix}$$

The numerical values from the model derived from Luke's runs in the pavilion were used to populate the bicycle state space entries, $(\mathbf{A}_b, \mathbf{B}_b), \mathbf{C}_b)$, except for the entries in the heading and lateral deviation acceleration equations which were calculated with the Whipple model. This has the consequence that those entries are developed with potentially erroneous geometric values such as trail.

11.8.2 Data

Only the runs with lateral disturbances are suitable for identifying the rider controller. I used the subset of 262 valid disturbance runs for the following analysis. This subset included runs from all three riders, both environments, and both the lateral deviation and heading tracking maneuvers. All signals had their means subtracted except for the lateral force.

11.8.3 Identification

In the following analyses the Kalman gain matrix is assumed to be equal to zero and the model takes on an output error form. This was required to bring the number of parameters to a reasonable size and provide a chance at finding the optimal solution.

Through trial and error with many different approaches to identification, I found that finding the optimal solution was not a trivial problem. The SIMO problem with full noise estimation has a minimum of 15 parameters. This problem is fraught with local minima. Even the assumption of an output error structure and the reduction of the parameter space to seven, doesn't escape the difficulty of finding the true minimum. To have a decent chance at finding a good solution, I opted to identify only the SISO system with the lateral force as the input and the steering angle as the output. The choice of steer angle as the sole output is for much the same reason as in [DL11], i.e. the steer angle is a very good quality measurement and together with steer torque reflects the rider's contribution to the system dynamics as a reaction to the lateral force.

I used the prediction error method [Lju98] to find the optimal parameters for each run. A good solution required good initial parameter guesses for which I used a combination of stable starting guesses from the loop closure technique described in Chapter *Control* and recursively used random guesses from previous good and bad solutions as starting points, eventually homing in on the optimal solutions.

The criterion for a good model was based on the variance accounted for in the measurement output. The mean VAF for all the identified runs is 62 ± 12 percent, and considering the large relative human remnant, fits above 30% are

still relatively good. I ensured stability in the identified models and no issues associated with unstable simulations corrupting the model quality criteria were present.

It turned out that the identified parameters for the SISO model not only predicted the steer angle, but when extra outputs are added it predicts them well too. The resulting parameters from the SISO model can then be used as initial guesses for the SIMO formulation to check multiple outputs. The identification process followed these steps:

1. Process, filter and detrend the data.
2. Construct the SISO (Input: F, Output: δ) grey box state space model.
3. Identify the five gains and the neuromuscular frequency for the lateral force and steer angle data using a variety of initial parameter guesses.
4. Construct the SIMO grey box state space model.
5. Identify the six parameters as before using the result of the SISO identification as the initial parameter guess for the SIMO system.

The results in Figures *11.22* and *11.23* give typical examples of the model's ability to predict the measured data in two different runs, one on the treadmill and one on the gymnasium floor, respectively. Notice that the human's remnant is relatively large when the input is zero, especially in the treadmill run. The model is able to predict the human's initial control response to the external input and lumps the remnant into the output error. This response is very repeatable across riders and runs. The model considers the remnant as output error during the non perturbed portions of the run. Notice that the steer torque is well predicted around the perturbation. Previous identifications with the Whipple model predicted much lower torque magnitudes and much different parameters. Including the identified bicycle model from Section *Canonical Identification* proved to give much better control predictions.

11.8.4 Results

I computed the optimal five gains and neuromuscular frequency[6] for all 262 runs and recorded the VAF of the steer angle output explained by the model for each run along with the identified parameters.

The first set of quantities of interest are the identified parameters themselves. As I've already mentioned in the previous section, identifying the parameters accurately is a function of the number of free parameters, which parameters are free, and the quality of the noise model. In my case, our noise model is an output error structure and may contribute to much more spread in the identified parameters. *Figure 11.24* gives an idea of how the six identified parameters vary with speed. As shown in Chapter *Control* the theory predicts that the gains are mostly linear above about 2 m/s and that the neuromuscular frequency is a constant parameter with respect to the human operator.

Figure 11.24 gives these insights:

- The gains increase with speed with k_ϕ and k_{y_q} having small slopes.
- The low speed runs have much more spread. This is probably due to the fact that the human remnant is relatively large at these speeds and the model attempts to fit the noise rather than casting it as output error.
- The ~9 m/s runs have poorer data quality than other runs due to the treadmill interference in the measurement electronics, thus the spread is large.
- The neuromuscular frequency stays relatively constant just below 30 rad/s, barring the higher variability in the low speed runs.
- The gains may be reasonably characterized with simple linear relationships.

[6] The nueromuscaulr damping ratio was fixed to 0.707 as per [MM71]. The uniqueness of the identifiablity of the parameters is questionable if this is not fixed, as wildly different solutions for the neuromuscular frequency were often found if the damping ratio was left free.

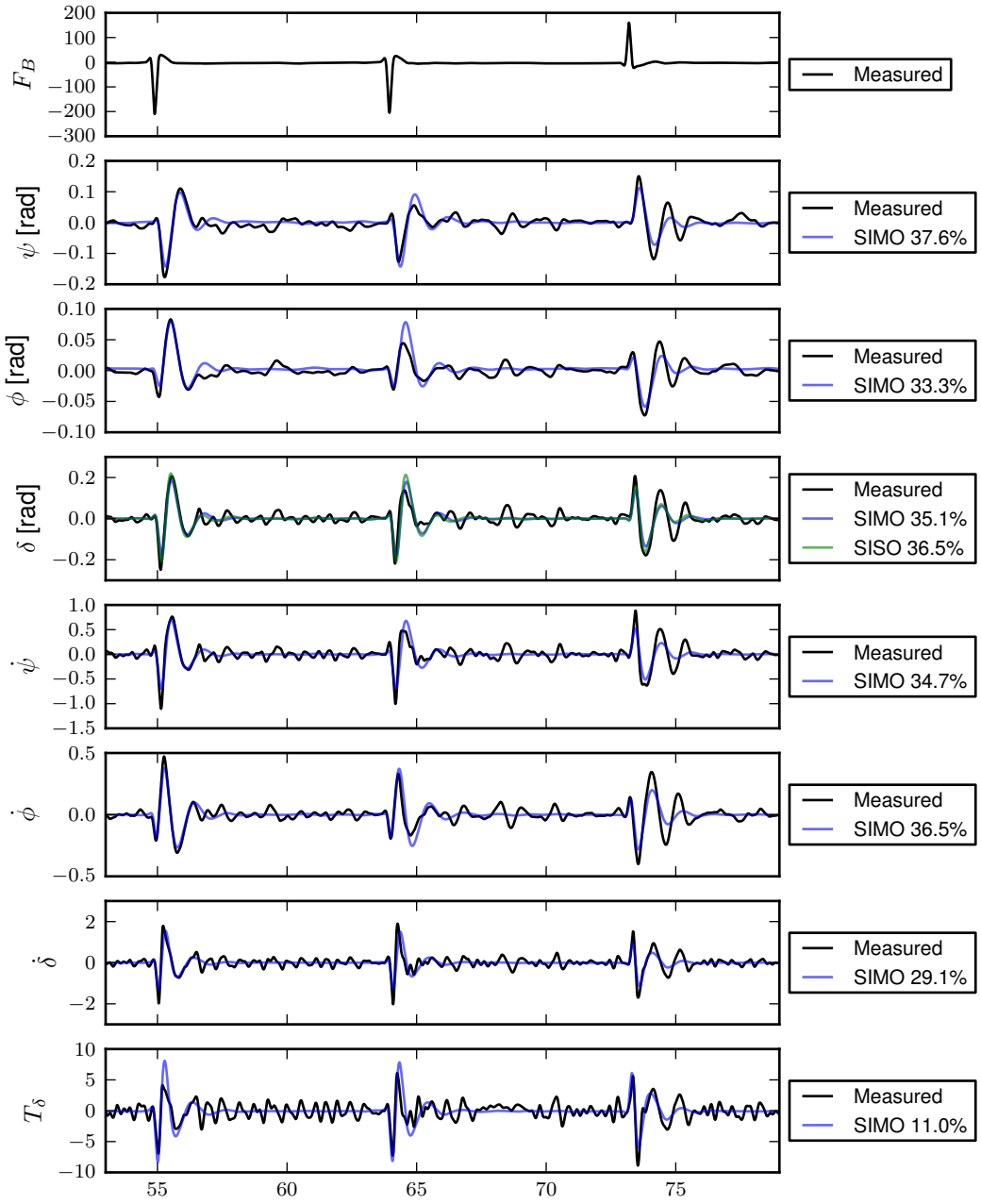

Figure 11.22: Simulation of an identified model derived from the inputs and outputs (SIMO) of one of Charlie's treadmill runs #288 (4.23 m/s) validated against the data from run #289 (4.22 m/s). The black line is the processed and filtered (low pass 15 Hz) measured data, the blue line is the simulation from the identified SIMO model and the green line is the identified SISO model. Generated by *src/systemidentification/rider_id_model_quality_plot.py*.

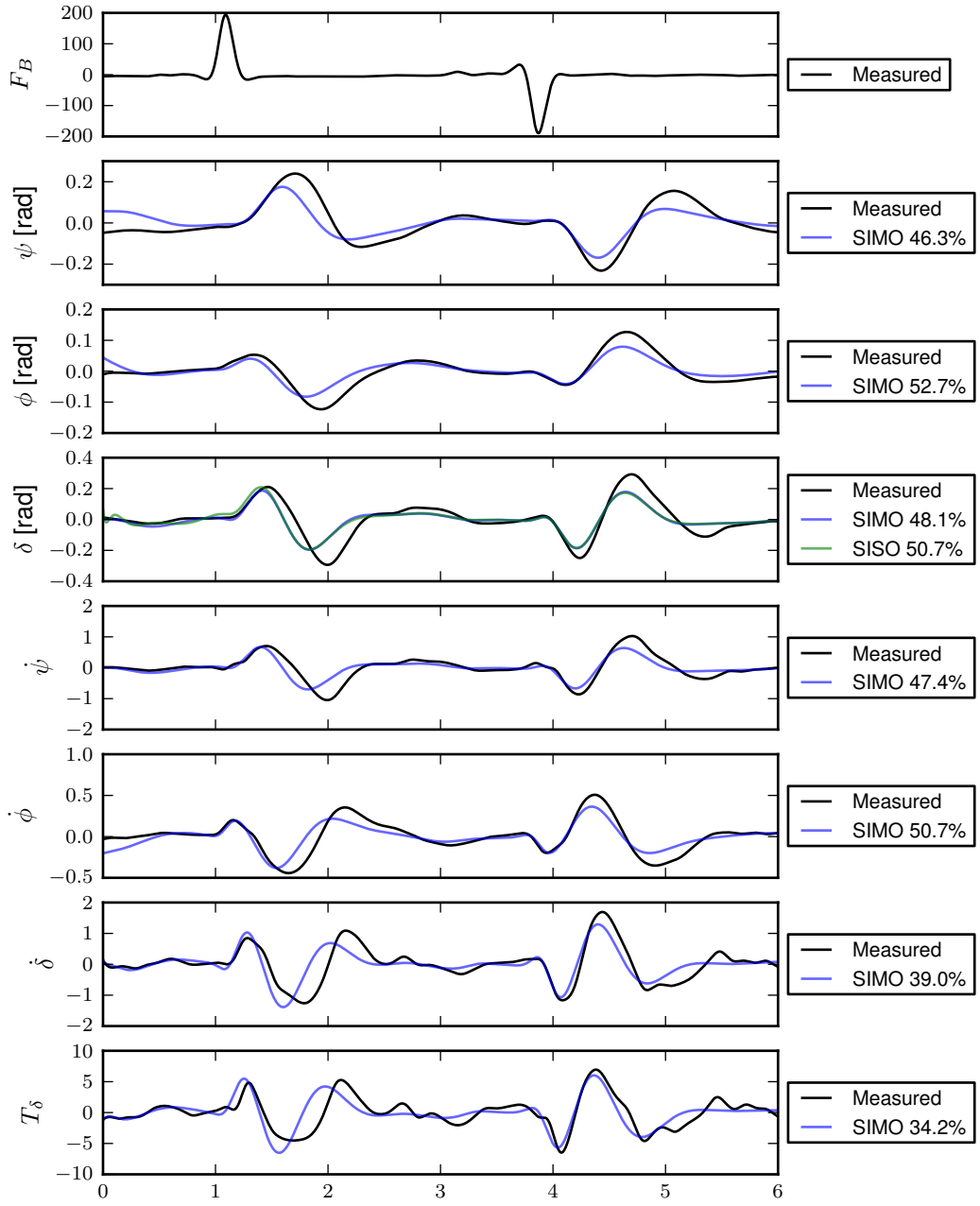

Figure 11.23: Simulation of an identified model derived from the inputs and outputs (SIMO) of one of Luke's pavilion runs #657 (3.99 m/s) validated against the data from run #658 (3.74 m/s). The black line is the processed and filtered (low pass 15 Hz) measured data, the blue line is the simulation from the identified SIMO model, and the green line is the identified SISO model. Generated by *src/systemidentification/rider_id_model_quality_plot.py*.

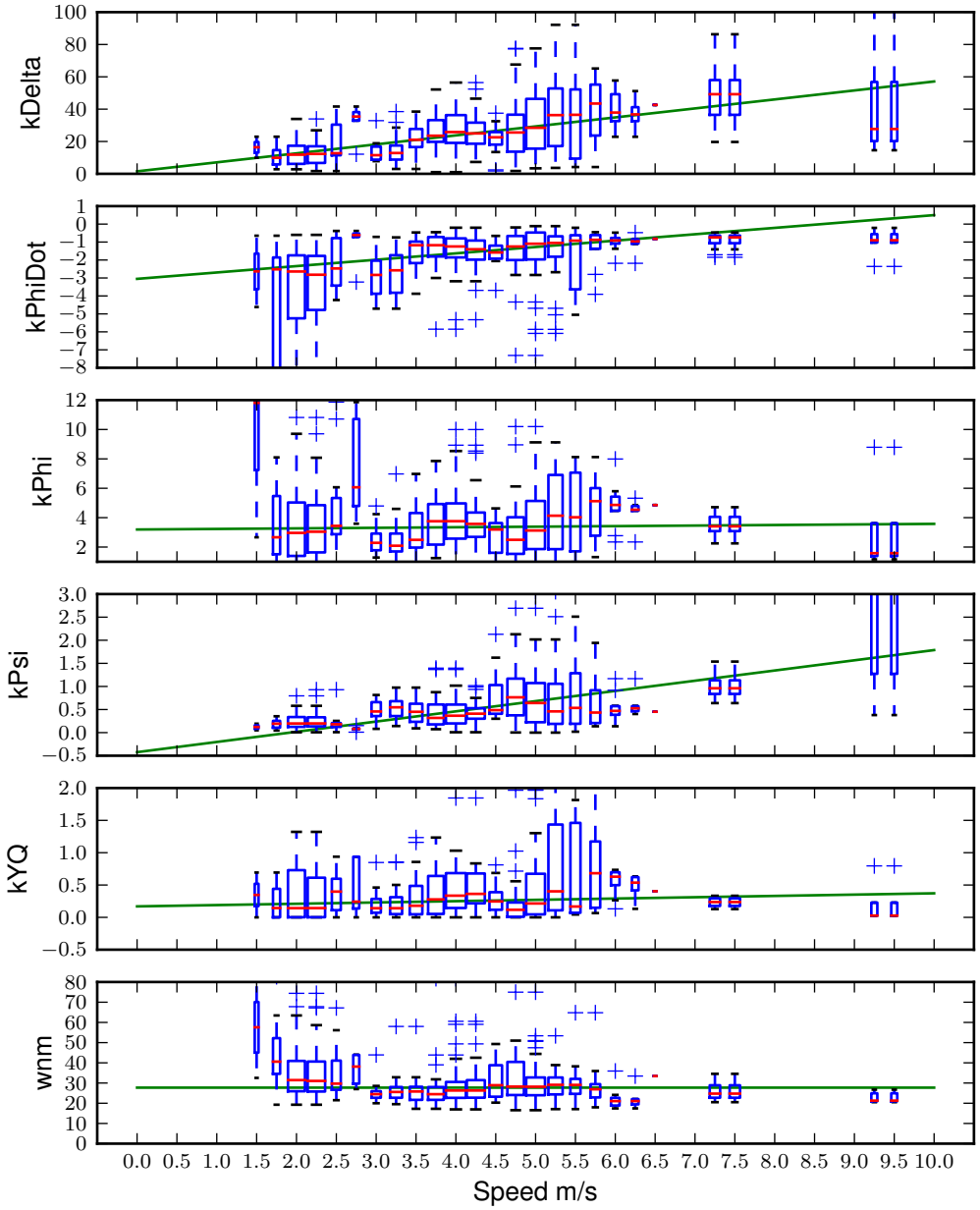

Figure 11.24: Each of the five identified parameters as a function of speed. The parameter values are grouped into 0.5 m/s speed bins and box plots showing their distributions are given for each speed bin. The red line gives the median of the speed bin, the box bounds the quartiles, and the whisker is 1.5 times the inner quartile range. The width of the boxes are proportional to the square root of the number of runs in the bin. The green line gives the linear fit to the median values which are weighted with respect to the inverse of the standard deviation of each speed bin. The neuromuscular frequency is the best constant that fits the data. Generated by *src/systemidentification/control_parameters_vs_speed_plots.py*.

Loop Shaping

The values of the parameters are difficult to directly compare with the ones found by the loop shaping technique described in Chapter *Control* due to some of the educated guesses about the rider's internal control choices. But it is possible to evaluate the same loops' frequency responses in an effort to understand how the rider chooses the gains.

Figure 11.25 shows the frequency response of the closed inner-most loop for a particular speed bin. The theory presented in [HMH12] and Chapter *Control* postulates that the rider chooses a gain such that the damping ratio of the high frequency neuromuscular peak around 10 rad/s and about gives a 10 dB peak ($\zeta = 0.15$). *Figure 11.25* shows that there may be a more heavily damped neuromuscular peak, but the large variability in the lower frequencies indicates that the rider's choice is not so constant. This may be explained by the fact that it is more critical for the roll rate loop to exhibit the neuromuscular peaking and the differences in the three rider's behavior. I've previously shown in Chapter *Control* that there are not necessarily unique gains in the first two loops to achieve the correct peaking in the roll rate loop.

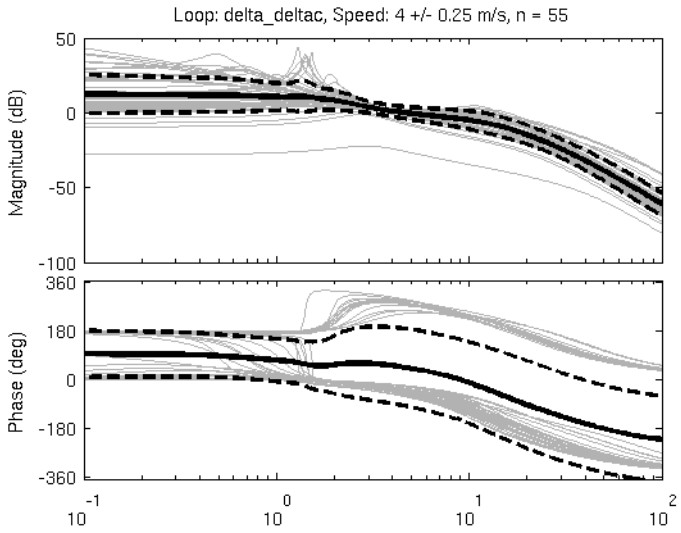

Figure 11.25: Frequency responses of the closed steer angle loop around 4 m/s. The grey lines plot the response of each individual run in the speed bin while the solid black lines give the mean gain and phase bounded by the dotted black lines which indicate one standard deviation.

Figure 11.26 shows the frequency response of the closed roll rate loop $\frac{\dot{\phi}}{\dot{\phi}_c}(s)$. As was just pointed out, the theory is that this loop, which completes the inner control loop, must exhibit this typical neuromuscular peaking seen in human-machine control tasks. The mean magnitude plots indicates that this is the case and that the riders do choose their steer and roll rate gains such that the inner loops exhibit the typical response.

Our theory for the selection of the remaining three gains suggests that the loops follow the dictates of the crossover model (i.e. 20 db slope around crossover) and that the crossover frequencies start at 2 and each successive loop is closed at half the previous crossover frequency such that the roll angle, heading and lateral deviation loops are closed in that order. Figures *11.27*, *11.28*, and *11.29* show the empirically derived frequency responses for the remaining loops.

The median crossover frequencies for this 4 m/s speed bin are $\omega_{\phi c} = 3.66$, $\omega_{\psi c} = 0.98$, and $\omega_{y_q c} = 1.06$. This indicates that the rider is more aggressive than our theory predicts with the higher roll crossover frequency in the roll angle loop. Also, the riders do not crossover at half the previous frequency, with the two outer loops crossing over at about the same frequency indicating that the lateral deviation tracking is more pertinent to the rider than the theory suggests. This may be partially due to the narrowness of the treadmill which constitutes 80% of the data.

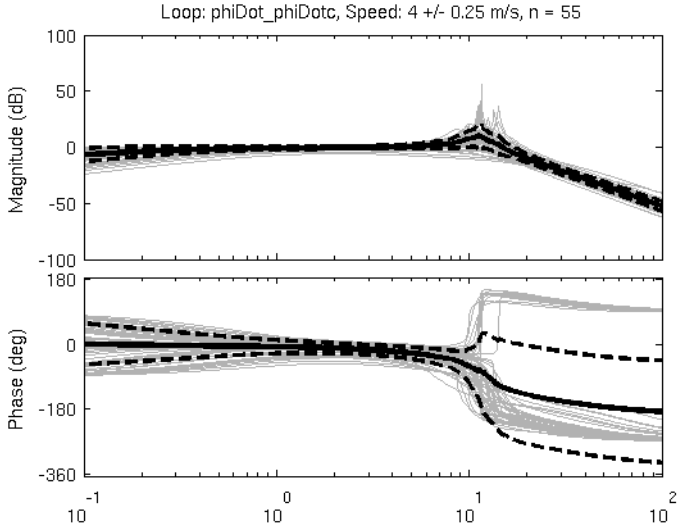

Figure 11.26: Frequency responses of the closed roll rate loop around 4 m/s. The grey lines plot the response of each individual run in the speed bin while the solid black line give the mean gain and phase bounded by the dotted black lines which indicate the one sigma standard deviation.

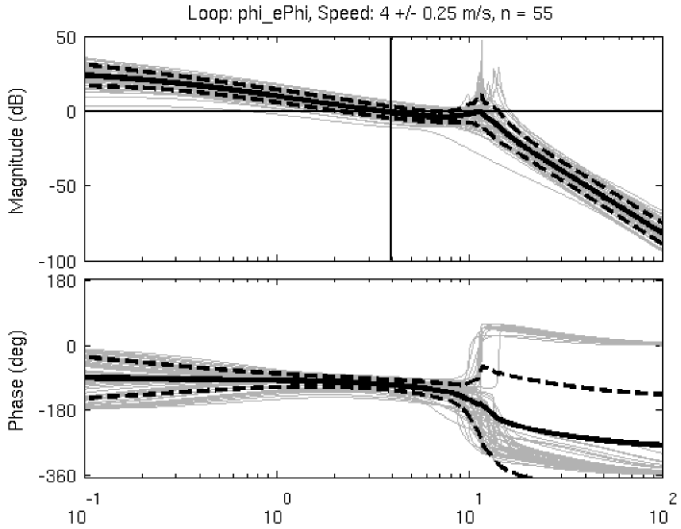

Figure 11.27: Frequency responses of the open roll angle loop around 4 m/s. The grey lines plot the response of each individual run in the speed bin while the solid blacks line give the mean gain and phase bounded by the dotted black lines which indicate one standard deviation.

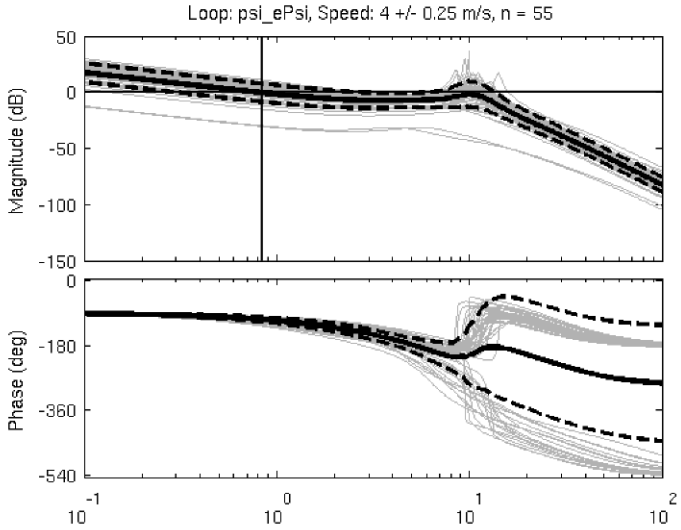

Figure 11.28: Frequency responses of the open heading loop around 4 m/s. The grey lines plot the response of each individual run in the speed bin while the solid blacks line give the mean gain and phase bounded by the dotted black lines which indicate one standard deviation.

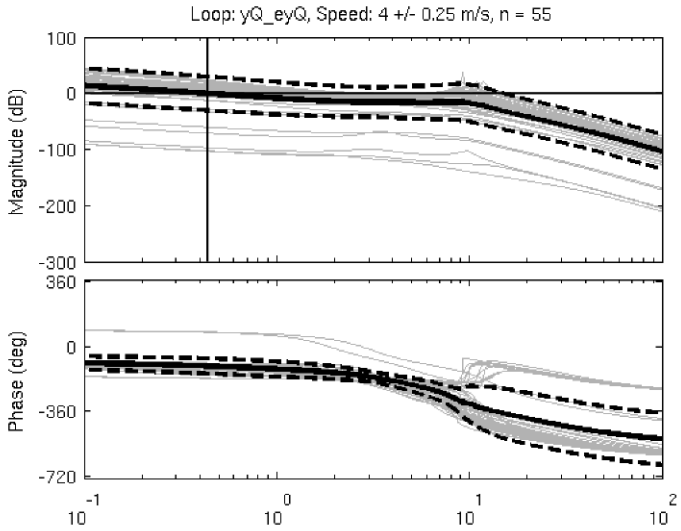

Figure 11.29: Frequency responses of the open lateral deviation loop around 4 m/s. The grey lines plot the response of each individual run in the speed bin while the solid black lines give the mean gain and phase bounded by the dotted black lines which indicate one standard deviation.

Our hypothesis is that the crossover frequencies are constant with respect to speed, so the distribution of the crossover frequencies for all runs should have a tight distribution regardless of speed. Secondly, we postulated that the rider crosses over the roll angle loop around 2 rad/s. *Figure 11.30* shows the distribution of the crossover frequencies for each loop where the median values of the crossover frequencies are $w_{\phi c} = 3.31$, $w_{\psi c} = 1.20$, and $w_{y_q c} = 0.98$, all with somewhat large standard deviations.

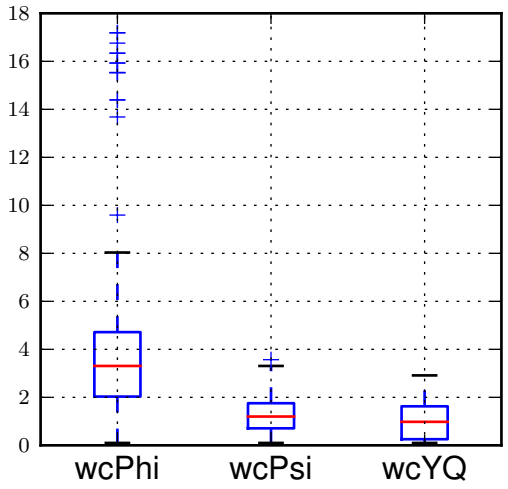

Figure 11.30: Median crossover frequencies in rad/s for the open outer loops for all runs at all speeds.

If the medians are any indication of the true crossover frequency the rider is more aggressive than predicted and the two outer loop crossover frequencies are much closer in value than predicted. The one-half rule of thumb does seem to hold for the inner two loops.

Full System Response

Once the loops are all closed the system output response to the two inputs F_B and y_{qc} can be examined. Given a commanded input y_{qc}, the tracking performance can be gauged by the closed loop Bode plot $\frac{y_q}{y_{qc}}(s)$ given in *Figure 11.31*. Notice that in general, the response is well behaved with a 0 dB magnitude out to about 10 rad/s, all poles are stable and the phase lag increases gradually with frequency.

Similarly, the system's response to the lateral disturbance force *Figure 11.32* is favorable for all the identified models and shows good disturbance rejection.

The reader may note that some of the Bode plots among Figures *11.25-11.29* indicate instability in that amplitude and phase characteristics synonymous with quadratic poles with small, positive damping ratios are in evidence. For example, one can see the evidence of such poles around 1-2 rad/s in *Figure 11.25* and 10 rad/s in *Figure 11.26*. It should be emphasized that these Bode plots represent either (1) open-loop transfer functions, or (2) inner, closed loop transfer functions. Hence, they do not imply final, outer closed loop instabilities. Indeed, the Bode plots of the outer-most, closed loop transfer function of *Figure 11.31* (lateral deviation) do not indicate any such quadratic poles with small positive damping ratios. The gain selection procedure in Chapter *Control* attempted to insure stability at least by closing of the roll angle loop, but these plots show that may not always be required for adequate performance for the complete system.

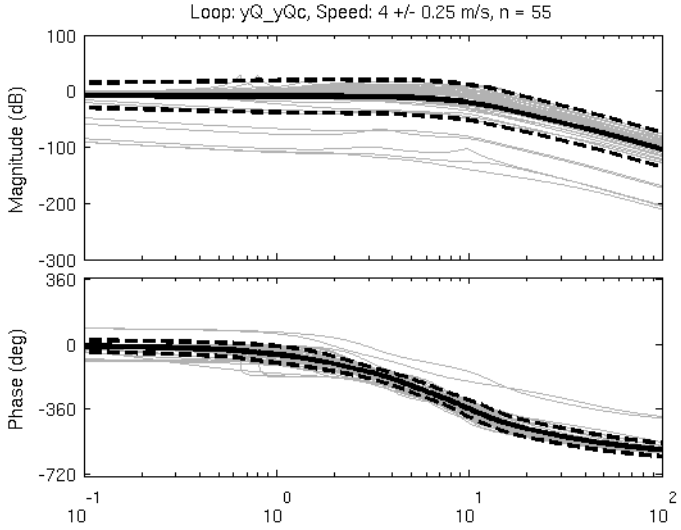

Figure 11.31: Frequency responses of the closed loop system lateral deviation tracking response around 4 m/s. The grey lines plot the response of each individual run in the speed bin while the solid black lines give the mean gain and phase bounded by the dotted black lines which indicate one standard deviation.

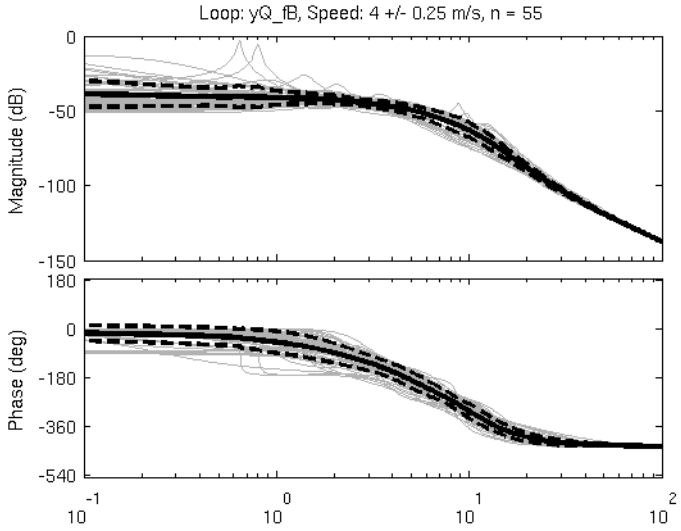

Figure 11.32: Frequency responses of the closed loop system disturbance rejection response around 4 m/s. The grey lines plot the response of each individual run in the speed bin while the solid black lines give the mean gain and phase bounded by the dotted black lines which indicate one standard deviation.

11.8.5 Conclusion

I have shown that a simple rider controller can be identified from the collected data given that the plant model of the bicycle/rider system is properly chosen, in my case identified separately from the same data. In addition these basic conclusion arise:

- The fundamental, remnant-free, control response of the rider under lateral perturbations can be described reasonably well by the simple five gain sequential loop closure and an eighth order closed loop system. No time delays are needed and the continuous formulation is adequate for good prediction.
- The identified gains seem to exhibit linear trends with respect to speed as predicted by theory and the identified neuromuscular frequency seems to be constant with a median around the theoretical prediction of 30 rad/s.
- The identified parameters show resemblance to the patterns in the theoretical loop closure techniques, especially in that the rider selects their gains such that the closed roll rate loop exhibits a 10 dB peak around 10-11 rad/s and that the riders cross over the outer three loops in the predicted order.
- The crossover frequencies of the three outer loops are relatively constant with respect to speed and point to a speed independence of system response bandwidth selection among riders in this task.
- The parameters do not seem to be uniquely identified if the neuromuscular damping ratio is included as a free parameter.

All of these conclusions are based on a preliminary statistical view of the data. I believe the spread in the results can be tightened up significantly with further data processing and the use of both simple and more complex statistical methods. In my view, the data set still has a lot more tell with further analysis but it has also revealed the need for further simplified experiments. The following are some thoughts on improving the analysis:

Improving the bicycle model. To have any hope of identifying a realistic and accurate controller, the plant must have a very good representative model. The bicycle is an excellent platform for testing the human's control system due to it's low speed instability and the fact that non-trivial control is needed to stabilize and direct the non-minimum phase system, but the first principles models for bicycle/rider biomechanics are not yet adequate or descriptive enough to describe the plant. This is mostly due to poor understanding of the tire to ground interaction and the rider's complicated coupling to the bicycle frames in which the rider is free to use more than one actuation for control. But, as has been shown here, system identification can be used to develop a realistic plant model for specific bicycles and even small variations in riders. A data driven model is currently the best choice until the first principles models are able to catch up and may, in fact, be able to provide more robust models due to the inherent complexity of describing all of the system with first principles.

Estimating the process noise matrix. The better one can estimate the process noise in the system, the more accurate the parameter predictions will get. In all of my attempts I had little success in ever estimating the optimal model when some or all of the process noise parameters were free. For the controller portion, the process noise is not awfully different in magnitudes than the rider's control actions with respect to the disturbance and it is very apparent in the low speed runs. This type of noise is much more difficult to properly account for. The parameter estimates from the output error structures used in this study are susceptible to the model fitting the noise and the control actions as opposed to just the control actions. The identifications fortunately were able to fit the control actions and not the noise and this is much more apparent and true in the treadmill runs. It may be possible to develop estimates of the process and measurement noise covariance matrices from the undisturbed runs where the human's remnant is the dominant source of variability in the outputs.

Fixing the neuromuscular model. The results give some indication that the neuromuscular model is an appropriate choice. The gain identification could possibly be improved by fixing both the neuromuscular frequency and damping ratio, and only estimating the gains. In general, the more parameters you can be confident about via first principles, the more the identified parameters may be able to tell you about the system with higher certainty.

Removing outliers. A more systematic approach to the removal of outlier data using criteria from the resulting fit variance, parameters, and frequency responses would help tighten up the data. The outliers are quite apparent in the data I've shown and a detailed look at why they are outliers may allow many of them to be removed.

Mixed effects modeling. There are statistical methods available that can account for all of the factors and repeated experiments. One such method is mixed effects or multilevel modeling. I explored the use of these in a preliminary fashion but need more time to understand the methods so that I apply them correctly. This would provide models based on the many factors in the experiments and give stronger comparisons with respect to them, such as variations among riders and environments.

First Principles Checks There are potentially some simpler checks that can be run with respect to the first principles models. For example, the Whipple equations of motion can be formulated with no nonholonomic lateral and longitudinal wheel constraints leaving only unknown tire forces. The data I've collected, in particular the lateral accelerations and roll, yaw, steer angles and rates, can be used to calculate the in-ground-plane forces at the tire contact points. If these forces aren't the same as the nonholonomic constraints predict, then tire slip must be occurring. This validation and others can be performed with the data set I've collected, potentially answering some important questions.

If I had unlimited time, I would work on these ideas more thoroughly. I hope to be able to explore the data in more detail with better methodologies and ideas in the future, but that may or may not happen. Fortunately the data is available if others would like to try out different methods, plant models, bicycle models, etc. and my methods, software, and methodologies are hopefully detailed enough for reuse.

BIBLIOGRAPHY

[Aok79] Akira Aoki. Experimental study on motorcycle steering performance. *Society of Automotive Engineers*, February 1979. SAE Paper 790265.

[BMCP07] Pradipta Basu-Mandal, Anindya Chatterjee, and Jim M. Papadopoulos. Hands-free circular motions of a benchmark bicycle. *Proceedings of the Royal Society A: Mathematical, Physical and Engineering Sciences*, 463(2084):1983–2003, August 2007.

[BL99] S. Berriah and G. Lachiver. Control of equilibrium and trajectory of a remotely controlled bicycle. In *Engineering Solutions for the Next Millennium. 1999 IEEE Canadian Conference on Electrical and Computer Engineering*. 1999.

[BFG+98] A. V. Beznos, A. M. Formal'sky, E. V. Gurfinkel, D. Jicharev, A. V. Lensky, K. V. Savitsky, and L.S. Tchesalin. Control of autonomous motion of two-wheel bicycle with gyroscopic stabilization. In *Proceedings of the 1998 IEEE International Conference on Robotics and Automation*, 2670–2675. Leuven, Belgium, 1998.

[Bic11] BicyRobo. Bicyrobo thailand championship. World Wide Web, 2011. http://bicyrobo.ait.ac.th/.

[BBCL03] F. Biral, D. Bortoluzzi, V. Cossalter, and M. Lio. Experimental study of motorcycle transfer functions for evaluating handling. *Vehicle System Dynamics: International Journal of Vehicle Mechanics and Mobility*, 39(1):1–25, 2003.

[Bje06] L. Bjermeland. Modeling, simulation and control system design for an autonomous bicycle. Master's thesis, Norges Teknisk-Naturvitenskapelige Universitet, 2006.

[BST09] I. Boniolo, S. M. Savaresi, and M. Tanelli. Roll angle estimation in two-wheeled vehicles. *IET Control Theory and Applications*, 3(1):20–32, January 2009.

[BTS08] I. Boniolo, M. Tanelli, and S.M. Savaresi. Roll angle estimation in two-wheeled vehicles. In *17th IEEE International Conference on Control Applications, Part of 2008 IEEE Multi-conference on Systems and Control*, 31–36. San Antonio, Texas, USA, September 2008.

[BDL00] D. Bortoluzzi, A. Doria, and R. Lot. Experimental investigation and simulation of motorcycle turning performance. In *3rd International Motorcycle Conference*. 2000.

[Bre10] Snorre Eskeland Brekke. Autonomous bicycle. Master's thesis, Norwegian University of Science and Technology, 2010.

[CP10] S. M. Cain and N. C. Perkins. Comparison of a bicycle steady-state turning model to experimental data. In *Bicycle and Motorcycle Dynamics 2010 Symposium on the Dynamics and Control of Single Track Vehicles*. Delft, Netherlands, October 2010. TU Delft.

[Cal07] Craig Calfee. Geometry of bike handling. North American Hand Built Bicycle Show Program, 2007.

[CMMR06] R. Capitani, G. Masi, A. Meneghin, and D. Rosti. Handling analysis of a two-wheeled vehicle using MSC.ADAMS/motorcycle. *Vehicle System Dynamics: International Journal of Vehicle Mechanics and Mobility*, 44:698–707, 2006.

[CALR10] V. Cerone, D. Andreo, M. Larsson, and D. Regruto. Stabilization of a riderless bicycle [Applications of control]. *Control Systems, IEEE*, 30(5):23 –32, October 2010.

[CCM+75] R. F. Chandler, C. E. Clauser, J. T. McConville, H. M. Reynolds, and J. W. Young. Investigation of inertial properties of the human body. Technical Report AMRL TR 74-137, Wright-Patterson Air Force Base, Ohio, 1975. NTIS No. AD-A016 485.

[CD06] Chih-Keng Chen and Thanh-Son Dao. Fuzzy control for equilibrium and roll-angle tracking of an unmanned bicycle. *Multibody System Dynamics*, 15:321–346, 2006.

[CD10] Chih-Keng Chen and Trung-Kien Dao. A study of bicycle dynamics via system identification. In *2010 International Symposium on Computer Communication Control and Automation (3CA)*, volume 2, 204–207. May 2010.

[Che00] Ping Ho Chen. A scheme of fuzzy training and learning applied to elebike control system. In *Ninth IEEE International Conference on Fuzzy Systems*. 2000.

[CBAS03] Kok Y. Cheng, David Bothman, and Karl J. Åström. Bicycle torque sensor experiment. Technical Report, University of California, Santa Barbara, 2003.

[CC07] R.F. Chidzonga and E. Chikuni. Stabilizing a bicycle below critical speed. In *AFRICON 2007*, 1–7. September 2007.

[CE03] Richard. F. Chidzonga and Eduard Eitelberg. Controlling velocity and steering for bicycle stabilization. In *First African Control Conference*. Cape Town, South Africa, December 2003.

[CMY69] C. E. Clauser, J. T. McConville, and J. W. Young. Weight, volume and center of mass of segments of the human body. Technical Report AMRL TR 69-70, Wright-Patterson Air Force Base, Ohio, 1969. NTIS No. AD-710 622.

[Clo94] Chad Cloud. Teaching kids how to ride a bike [fuzzy control]. In *Proceedings of the First International Joint Conference of the North American Fuzzy Information Processing Society Biannual Conference. The Industrial Fuzzy Control and Intelligent Systems Conference, and the NASA Joint Technology Workshop on Neural Networks and Fuzzy Logic. NAFIPS/IFIS/NASA '94.*, 175–176. December 1994.

[CHA96] S. O. Cloyd, M. Hubbard, and L. W. Alaways. A control scheme for an opposed recumbent tandem human-powered bicycle. *Journal of Applied Biomechanics*, 212(4):480–492, November 1996.

[Con09] Brendan Connors. Modeling and stability analysis of a recumbent bicycle with oscillating leg masses. Master's thesis, University of California, Davis, 2009.

[CH08] Brendan Connors and Mont Hubbard. Modelling and stability analysis of a recumbent bicycle with oscillating leg masses. In Margaret Estivalet and Pierre Brisson, editors, *The Engineering of Sport 7*, volume 1, 677–685. ISEA, Springer Paris, August 2008.

[CL02] V. Cossalter and R. Lot. A motorcycle multi-body model for real time simulations based on the natural coordinates approach. *Vehicle System Dynamics*, 37(6):423–447, 2002.

[CLP07] V. Cossalter, R. Lot, and M. Peretto. Steady turning of motorcycles. *Proceedings of the Institution of Mechanical Engineers, Part D: Journal of Automobile Engineering*, 221:1343–1356, 2007.

[CDL99] Vittore Cossalter, Alberto Doria, and Roberto Lot. Steady turning of two-wheeled vehicles. *Vehicle System Dynamics*, 31(3):157–181, 1999.

[DL11] Peter de Lange. Rider identification in bicycling: A preliminary analysis. Master's thesis, Delft University of Technology, 2011.

[DLH96] D. S. de Lorenzo and Mont Hubbard. Dynamic bicycle stability of a flexibly coupled rider. Internal report UC Davis, 1996.

[DL97] David S. de Lorenzo. Quantification of structural loading during off-road cycling. Master's thesis, Univeristy of California, Davis, 1997.

[Dem11] Christopher Dembia. *Yeadon: A Python Library For Human Inertia Estimation*. 2011. http://pypi.python.org/pypi/yeadon/.

[Dem55] W. T. Dempster. Space requirements of the seated operator, geometrical, kinematic and mechanical aspects of the body with special reference to the limbs. Technical Report WADC 55-159, Wright-Patterson AFB, Ohio, 1955.

[DFT12] A. Doria, M. Formentini, and M. Tognazzo. Experimental and numerical analysis of rider motion in weave conditions. *Vehicle System Dynamics*, 2012.

[Doy88] A. J. R. Doyle. The essential human contribution to bicycle riding. *Training, Human Decision Making and Control*, pages 351–370, 1988.

[Doy87] Anthony John Redfern Doyle. *The Skill of Bicycle Riding*. PhD thesis, Department of Psychology, University of Sheffield, 1987.

[Doh53] E. Döhring. *Über die Stabilität und die Lenkkräfte von Einspurfahrzeugen*. PhD thesis, Technical University Braunschweig, Germany, 1953.

[Doh55] E. Döhring. Stability of single-track vehicles. *Forschung Ing.-Wes.*, 21(2):50–62, 1955. Translated by J. Lotsof, March 1957.

[Eat73a] David J. Eaton. An experimental study of the motorcycle roll stabilization task. In *Proceedings of the Ninth Annual Conference on Manual Control*, 233–234. May 1973.

[Eat73b] David J. Eaton. *Man-Machine Dynamics in the Stabilization of Single-Track Vehicles*. PhD thesis, University of Michigan, 1973.

[ES73] David J. Eaton and Leonard Segel. Lateral dynamics of the uncontrolled motorcycle. In *Second International Congress on Automotive Safety*. San Francisco, CA, USA, July 1973.

[Edw72] Frederick G. Edwards. Determination of pilot and vehicle describing functions from the gemini-10 mission. Technical Report, NASA Ames Research Center, 1972.

[ER10] J.L. Escalona and A.M. Recuero. A bicycle model for education in machine dynamics and real-time interactive simulation. In *Proceedings of Bicycle and Motorcycle Dynamics 2010, A Symposium on the Dynamics and Control of Single Track Vehicles*. Delft, The Netherlands, October 2010.

[ER11] José Escalona and Antonio Recuero. A bicycle model for education in multibody dynamics and real-time interactive simulation. *Multibody System Dynamics*, pages 1–20, 2011.

[Eve10] M. V. C. Evertse. Rider analysis using a fully instrumented motorcycle. Master's thesis, Delft University of Technology, 2010.

[FMPM06] Chad Findlay, Jason Keith Moore, and Claudia Perez-Maldonado. SISO control of a bicycle-rider system. MAE 272 Report 2, Winter 2006, 2006.

[For92] F.A. Forouhar. *Robust stabilization of high-speed oscillations in single track vehicles by feedback control of gyroscopic moments of crankshaft and engine inertia*. PhD thesis, University of California, Berkeley, 1992.

[FSR90] G. Franke, W. Suhr, and F. Rieß. An advanced model of bicycle dynamics. *European Journal of Physics*, 11(2):116–121, 1990.

[FB03] Ruggero Frezza and Alessandro Beghi. Simulating a motorcycle driver. In Wei Kang, Carlos Borges, and Mingqing Xiao, editors, *New Trends in Nonlinear Dynamics and Control and their Applications*, volume 295 of Lecture Notes in Control and Information Sciences, pages 175–186. Springer Berlin / Heidelberg, 2003.

[Fu65] Hiroyasu Fu. Fundamental characteristics of single-track vehicles in steady turning. *JSME Bulletin*, 9(34):284–293, 1965.

[Gal00] Jason Matthew Gallaspy. Gyroscopic stabilization of an unmanned bicycle. Master's thesis, Auburn University, Auburn, Alabama, USA, 2000.

[Get94] Neil H. Getz. Control of balance for a nonlinear nonholonomic non-minimum phase model of a bicycle. In *American Control Conference*, volume 1, 148–151. Baltimore, MD, June–July 1994. AACC.

[Get95] Neil H. Getz. Internal equilibrium control of a bicycle. In *Proceedings of the 34th IEEE Conference on Decision and Control (Cat. No.95CH35803)*, volume 4, 4285–4287. New York, NY, USA, December 1995. IEEE Control Syst. Soc, IEEE. Proceedings of 1995 34th IEEE Conference on Decision and Control, 13-15 December 1995, New Orleans, LA, USA.

[GM95] Neil H. Getz and Jerrold E. Marsden. Control for an autonomous bicycle, paper 525473. In *International Conference on Robotics and Automation*, volume 2, 1397–1402. Nagoya, Aichi, Japan, May 1995. IEEE.

[GWS05] I. W. Griffiths, J. Watkins, and D. Sharpe. Measuring the moment of inertia of the human body by a rotating platform method. *American Journal of Physics*, 73(1):85–92, 2005.

[Gus02] Fredrik Gustafsson. Methods for estimating the roll angle and pitch angle of a two-wheeled vehicle system and a computer program to perform the methods. 2002.

[Han88] Richard Scott Hand. Comparison and stability analysis of linearized equations of motion for a basic bicycle model. Master's thesis, Cornell University, Ithaca, New York, May 1988.

[Hes97] R. A. Hess. *Handbook of Human Factors and Ergonomics*., chapter Feedback Control Models: Manual Control and Tracking, pages 1249–1294. number 38. Wiley, New York, Second edition, 1997.

[HMH12] Ronald Hess, Jason K. Moore, and Mont Hubbard. Modeling the manually controlled bicycle. *IEEE Transactions on Systems, Man, and Cybernetics - Part A: Systems and Humans*, 42(3):545–557, 2012.

[HB07] Jesse B. Hoagg and Dennis S. Bernstein. Nonminimum-phase zeros: much to do about nothing. *IEEE Control Systems Magazine*, 27:45–57, June 2007.

[HAP05] Kevin Huyge, Jorge Ambrósio, and Manuel Pereira. A control strategy for the dynamics of a motorcycle. In *ENOC*. Eindhoven, Netherlands, August 2005.

[Inc09] Northern Digital Incorporated. Optotrak certus motion capture system. 2009. http://www.ndigital.com/.

[IM06] K. Iuchi and T. Murakami. An approach to fusion control of stabilization control and human input in electric bicycle. In *32nd Annual Conference on IEEE Industrial Electronics*, 3211–3216. Paris, France, 2006.

[INM05] K. Iuchi, H. Niki, and T. Murakami. Attitude control of bicycle motion by steering angle and variable cog control. In *Industrial Electronics Society, 2005. IECON 2005. 31st Annual Conference of IEEE*, 6. November 2005.

[JD98] A. W. Jackson and M. Dragovan. An experimental investigation of bicycle dynamics. Unpublished report, 1998.

[Jam05] Stephen R James. Lateral dynamics of motorcycles towing single-wheeled trailers. *Vehicle System Dynamics: International Journal of Vehicle Mechanics and Mobility*, 43(8):581–599, 2005.

[Jam02] Stephen R. James. Lateral dynamics of an offroad motorcycle by system identification. *Vehicle System Dynamics*, 38(1):1–22, July 2002.

[JMJ78] H. R. Jex, R. E. Magdaleno, and A. M. Junker. Roll tracking of g-vector tilt and various types of motion washout. In *Fourteenth Annual Conference on Manual Control*, 463–502. University of Southern California, April 1978.

[Jol02] I.T. Jolliffe. *Principal Component Analysis*. Springer Series in Statistics. Springer, New York, 2nd edition, 2002.

[Jon70] David E. H. Jones. The stability of the bicycle. *Physics Today*, 23(4):34–40, 1970.

[KO96] I. Kageyama and Y. Owada. An analysis of a riding control algorithm for two wheeled vehicles with a neural network modeling. *Vehicle System Dynamics*, 25:317–326, 1996.

[KMBU04] Ichiro Kageyama, Shun'ichi Miyagishi, Masayuki Baba, and Hajime Uchiyama. Construction of rider robot for motorcycle. *Journal of the Society of Automotive Engineers of Japan*, 58:67–73, 2004.

[KF59] Katumi Kageyama and Hiroyasu Fu. Experiments on control characteristics of a motor-cycle in steady turning, especially on the effects of lean in and lean out. *Jour. SAE Japan*, 13(10):41–45, 1959. 596009.

[KN03] Yutaka Kamata and Hidekazu Nishimura. System identification and attitude control of motorcycle by computer-aided dynamics analysis. *JSAE Review*, 24(4):411 – 416, 2003.

[KL00] T. R. Kane and D. A Levinson. *Dynamics Online: Theory and Implementation with AUTOLEV*. Online Dynamics, Inc., Sunnyvale, CA, 2000.

[Kan75] Thomas R. Kane. Fundamental kinematical relationships for single-track vehicles. *International Journal for Mechanical Sciences*, 17:499–504, 1975.

[Kan77a] Thomas R. Kane. Kinematical implications of side slip for single-track vehicles. *Society of Automotive Engineers*, February 1977. SAE Paper 770056.

[Kan77b] Thomas R. Kane. Steady turning of single-track vehicles. In *International Automotive Engineering Congress and Exposition*, number 770057. Detroit, MI, February–March 1977. SAE.

[Kan78] Thomas R. Kane. The effect of frame flexibility on high speed weave of motorcycles. In *SAE Paper 780306*, 33–40. SAE, 1978.

[KL85] Thomas R. Kane and David A. Levinson. *Dynamics: Theory and Applications*. McGraw Hill, New York, NY, 1985.

[Kar04] Dean Karnopp. *Vehicle Stability*. Marcel Dekker, Inc., 2004.

[KAN88] T. Katayama, A. Aoki, and T. Nishimi. Control behaviour of motorcycle riders. *Vehicle System Dynamics*, 17:211–229, 1988.

[KM08] Lychek Keo and Yamakita Masaki. Trajectory control for an autonomous bicycle with balancer, paper 4601741. In *International Conference on Advanced Intelligent Mechatronics*, 676–681. Xi'an, China, July 2008. IEEE/ASME.

[KY11] Lychek Keo and Masaki Yamakita. Control of an autonomous electric bicycle with both steering and balancer controls. *Advanced Robotics*, 25:1–22, January 2011.

[Koe83] C. Koenen. *The dynamic behaviour of a motorcycle when running straight ahead and when cornering*. PhD thesis, Delft University of Technology, 1983.

[Kon55] M. Kondo. Experimental study on the stability and control of single-track vehicles. *JSME*, 58(442):827–833, 1955.

[Koo06] J. D. G. Kooijman. Experimental validation of a model for the motion of an uncontrolled bicycle. Master's thesis, Delft University of Technology, 2006.

[KMP+11] J. D. G. Kooijman, J. P. Meijaard, Jim M. Papadopoulos, Andy Ruina, and A. L. Schwab. A bicycle can be self-stable without gyroscopic or caster effects. *Science*, 332(6027):339–342, 2011.

[KS08] J. D. G. Kooijman and A. L. Schwab. Some observations on human control of a bicycle. In I. Zobory, editor, *11th mini Conference on Vehicle System Dynamics, Identification and Anomalies (VSDIA2008), Budapest, Hungary*, 8. Budapest University of Technology and Economincs, November 2008.

[KS09] J. D. G. Kooijman and A. L. Schwab. Experimental validation of the lateral dynamics of a bicycle on a treadmill. In *Proceedings of the ASME 2009 International Design Engineering Technical Conferences & Computers and Information in Engineering Conference, IDETC/CIE 2009*, number DETC2009-86965. 2009.

[KS11] J. D. G. Kooijman and A. L. Schwab. A review on handling aspects in bicycle and motorcycle control. In *Proceedings of the ASME 2011 International Design Engineering Technical Conferences & Computers and Information in Engineering Conference. IDETC/CIE*, number DETC2011-47963. Washington, DC, USA, August 2011.

[KSM08] J. D. G. Kooijman, A. L. Schwab, and J. P. Meijaard. Experimental validation of a model of an uncontrolled bicycle. *Multibody System Dynamics*, 19:115–132, May 2008.

[KSM09] J. D. G. Kooijman, A. L. Schwab, and Jason K. Moore. Some observations on human control of a bicycle. In *Proceedings of the ASME 2009 International Design and Engineering Technical Conferences & Computers and Information in Engineering Conference*. 2009.

[KKBM05] Takeyuki Kuriyama, Ichiro Kageyama, Masayuki Baba, and Shunichi Miyagishi. 2102 control system design and construction of rider robot for two-wheel vehicle. *The Transportation and Logistics Conference*, 14:207–210, 2005.

[LLLW03] Hsien-Chung Lai, Jing-Sin Liu, D. T. Lee, and Li-Sheng Wang. Design parameters study on the stability and perception of riding comfort of the electrical motorcycles under rider leaning. *Mechatronics*, 13(1):49 – 76, 2003.

[Leb10] Eric O. Lebigot. *Uncertainties: a Python package for calculations with uncertainties*. 2010. http://pypi.python.org/pypi/uncertainties/.

[LH02] Sangduck Lee and Woonchul Ham. Self stabilizing strategy in tracking control of unmanned electric bicycle with mass balance, paper 1041594. In *International Conference on Intelligent Robots and Systems*, volume 3, 2200–2205. Lausanne, Switzerland, September–October 2002. IEEE/RSJ.

[LS06] David J.N. Limebeer and Robert S. Sharp. Bicycles, motorcycles, and models. *IEEE Control Systems Magazine*, 26(5):34–61, October 2006.

[LW93] T.S. Liu and J.C. Wu. A model for a rider-motorcycle system using fuzzy control. *Systems, Man and Cybernetics, IEEE Transactions on*, 23(1):267–276, January 1993.

[Lju98] Lennart Ljung. *System Identification: Theory for the User*. Prentice Hall, 1998.

[MM71] R. E. Magdaleno and D. T. McRuer. Experimental validation and analytical elaboration for models of the pilot's neuromuscular subsystem in tracking tasks. Technical Report CR-1757, NASA, April 1971.

[Mag12] Jürgen Mages. Python lowracer. World Wide Web, August 2012. [Online; accessed 10-Aug-2012] http://www.python-lowracer.de/.

[MEH05] S. Mammar, S. Espie, and C. Honvo. Motorcycle modelling and roll motion stabilization by rider leaning and steering torque. In *Proceedings of the 2005 IEEE Conference on Control Applications, Toronto Canada, August 28-31, 2005*, 1421–1426. 2005.

[MK79] Guy K. Man and Thomas R. Kane. Steady turning of two-wheeled vehicles, paper 790187. In *Dynamics of Wheeled Recreational Vehicles*, 55–75. Detroit, MI, February–March 1979. SAE.

[MN07] Y. Marumo and M. Nagai. Steering control of motorcycles using steer-by-wire system. *Vehicle System Dynamics: International Journal of Vehicle Mechanics and Mobility*, 45(5):445–458, 2007.

[MK74] D. T. McRuer and E. S. Krendel. Mathematical models of human pilot behavior. Technical Report STI-P-146, Systems Technology, Inc., Hawthorne, CA, USA, 1974. AGARD AG 188.

[MGK67a] Duane T. McRuer, Dunstan Graham, and Ezra S. Krendel. Manual control of single-loop systems: part i. *Journal of the Franklin Institute*, 283(1):1 – 29, 1967.

[MGK67b] Duane T. McRuer, Dunstan Graham, and Ezra S. Krendel. Manual control of single-loop systems: part ii. *Journal of the Franklin Institute*, 283(2):145 – 168, 1967.

[MPRS07] J. P. Meijaard, Jim M. Papadopoulos, Andy Ruina, and A. L. Schwab. Linearized dynamics equations for the balance and steer of a bicycle: A benchmark and review. *Proceedings of the Royal Society A: Mathematical, Physical and Engineering Sciences*, 463(2084):1955–1982, August 2007.

[Mer75] J.L. Meriam. *Dynamics*. Wiley, 1975.

[MT06] B. Michini and S. Torrez. Autonomous stability control of a moving bicycle. MIT Report, 2006.

[MK96] Paul Mitiguy and Thomas R. Kane. Motion variables leading to efficient equations of motion. *The International Journal of Robotics Research*, 15(5):522–532, 1996.

[MBU+06] Shun'ichi Miyagishi, Masayuki Baba, Hajime Uchiyama, Ichiro Kageyama, and Takeyuki Kuriyama. Construction of rider robot proto2 for motorcycles. In *Proceedings. JSAE Annual Congress*. 2006.

[MKT+01] Shunichi Miyagishi, Ichiro Kageyama, Kouhei Takama, Masayuki Baba, and Hajime Uchiyama. 1411 a study on a rider robot for two wheeled vehicle. *The Transportation and Logistics Conference*, 10:125–128, 2001.

[MKT+03] Shunichi Miyagishi, Ichiro Kageyama, Kouhei Takama, Masayuki Baba, and Hajime Uchiyama. Study on construction of a rider robot for two-wheeled vehicle. *JSAE Review*, 24(3):321 – 326, 2003.

[MKS09] J. K. Moore, J. D. G. Kooijman, and A. L. Schwab. Rider motion identification during normal bicycling by means of principal component analysis. In K. Arczewski and M. Wojtyra J. Frączek, editors, *Multibody Dynamics 2009, ECCOMAS Thematic Conference*. Warsaw, Poland, June-July 2009.

[MH08] Jason Moore and Mont Hubbard. Parametric study of bicycle stability. In Margaret Estivalet and Pierre Brisson, editors, *The Engineering of Sport 7*, volume 2. International Sports Engineering Association, Springer Paris, 2008.

[Moo06] Jason K. Moore. Low speed bicycle stability: Effects of geometric parameters. For course MAE 223, UC Davis, Winter 2006, August 2006.

[Moo11] Jason K. Moore. *BicycleParameters: A Python library for bicycle parameter estimation and analysis*. 2011. http://pypi.python.org/pypi/BicycleParameters.

[MHP+10] Jason K. Moore, Mont Hubbard, Dale L. Peterson, A. L. Schwab, and J. D. G. Kooijman. An accurate method of measuring and comparing a bicycle's physical parameters. In *Bicycle and Motorcycle Dynamics: Symposium on the Dynamics and Control of Single Track Vehicles*. Delft, Netherlands, October 2010.

[MHS+10] Jason K. Moore, Mont Hubbard, A. L. Schwab, J. D. G. Kooijman, and Dale L. Peterson. Statistics of bicycle rider motion. *Procedia Engineering*, 2(2):2937–2942, 2010. The Engineering of Sport 8 - Engineering Emotion.

[MKHS09] Jason K. Moore, J. D. G. Kooijman, Mont Hubbard, and A. L. Schwab. A method for estimating physical properties of a combined bicycle and rider. In *Proceedings of the ASME 2009 International Design Engineering Technical Conferences & Computers and Information in Engineering Conference, IDETC/CIE 2009*. San Diego, CA, USA, August–September 2009. ASME.

[MKSH11] Jason K. Moore, J. D. G. Kooijman, A. L. Schwab, and Mont Hubbard. Rider motion identification during normal bicycling by means of principal component analysis. *Multibody System Dynamics*, 25:225–244, 2011.

[MPH07] Jason K. Moore, Dale L. Peterson, and Mont Hubbard. Influence of rider dynamics on the whipple bicycle model. In *11th International Symposium on Computer Simulation in Biomechanics*. Tainan, Taiwan, June 2007. ISB.

[MW04] Christopher M. Muhich and Christopher D. Wagner. Design of a bicycle stabilizer. Technical Report, University of Notre Dame, 2004.

[Mur02] D. Muraoka. Stable running control of autonomous bicycle robot. Master's thesis, Keio University, 2002. in Japanese.

[Mur09] Murata. Murata boy. Http://www.murataboy.com/, 2009.

[MY07] Akihiro Murayama and Masaki Yamakita. Development of autonomous bike robot with balancer, paper 4601741. In *Annual Conference*, 1048–1052. Kagawa, Japan, September 2007. SICE.

[Mut10] J. T. M. Mutsaerts. Lego NXTbike-GS bicycle with active stability. Youtube.com, May 2010. http://youtu.be/o7nSQ2ycGX4.

[Nag83] M. Nagai. Analysis of rider and single-track-vehicle system; its application to computer-controlled bicycles. *Automatica*, 19(6):737–740, 1983.

[NII97] Y. Nakano, H. Iwasaki, and S. Iwane. Stabilizing control of un-manned bicycle with piezoelectric microgyroscope. In *Proceeding of SICE Conference*, volume 40, 343–344. 1997. in Japanese.

[NM05a] H. Niki and T. Murakami. An approach to self stabilization of bicycle motion by handle controller. *IEEJ Transactions on Industry Applications*, 125-D(8):779–785, 2005.

[NM05b] Hiroshi Niki and Toshiyuki Murakami. An approach to stable standing motion of electric bicycle. In *Proceedings of 2005 CACS Automatic Control Conference*. Tainan, Taiwan, November 2005.

[OMUS02] Yusuke Oda, Masayuki Miyamoto, Kei Uchiyama, and Gou Shimizu. Study on the autonomous run by integrated control of bicycle. In *JSME 11th Conference of Transportation and Logistics Division No.02-50*. December 2002.

[OV98] S. J. Ovaska and S. Valiviita. Angular acceleration measurement: A review. In *Proc. IEEE IMTC/98 Instrumentation and Measurement Technology Conf*, volume 2, 875–880. 1998.

[Pac06] H.B. Pacejka. *Tire and vehicle dynamics*. SAE-R. SAE International, 2006.

[Pap87] Jim M. Papadopoulos. Bicycle steering dynamics and self-stability: A summary report on work in progress. Cornell Report, 1987.

[PHH01] Ingyu Park, Sangchul Han, and Woonchul Ham. Control algorithm for stabilization of attitute of unmanned electric bicycle. In *The Proceedings of 2001 INCOM*. Wien, Austria, 2001.

[PKP99] S. J Park, C.B. Kim, and S. C. Park. Anthropometric and biomechanical characteristics on body segments of Koreans. *Applied Human Sciences*, 18(3):91–9, May 1999.

[Pat04a] Tim Paterek. *The Paterek Manual For Bicycle Frame Builders*. Henry James Bicycles, Inc., 2004.

[Pat04b] W. B. Patterson. *The Lords of the Chainring*. W. B. Patterson, 2004.

[PH08a] Dale L. Peterson and Mont Hubbard. Analysis of the holonomic constraint in the Whipple bicycle model, paper 267. In *The Engineering of Sport 7*, volume 2, 623–631. Biarritz, France, June 2008. ISEA, Springer.

[PH08b] Dale L. Peterson and Mont Hubbard. Yaw rate and velocity tracking control of a hands-free bicycle. In *International Mechanical Engineering Congress and Exposition*. Boston, October 2008. ASME.

[PH09] Dale L. Peterson and Mont Hubbard. General steady turning of a benchmark bicycle model. In *Proceedings of IDETC/MSNDC 2009 the ASME 2009 International Design Engineering Technical Conferences & 7th International Conference on Multibody Systems, Nonlinear Dynamics, and Control*, number DETC2009/MSNDC-86145. 2009.

[PMFH10] Dale L. Peterson, Jason K. Moore, Danique Fintelman, and Mont Hubbard. Low-power, modular, wireless dynamic measurement of bicycle motion. *Procedia Engineering*, 2(2):2949–2954, 2010. The Engineering of Sport 8 - Engineering Emotion.

[Psi79] Mark Psiaki. Bicycle stability: a mathematical and numerical analysis. Master's thesis, Princeton University, Princeton, NJ, 1979.

[Rol73] R. D. Roland. Simulation study of motorcycle stability at high speed. In *Second International Congress on Automotive Safety*. San Francisco, July 1973.

[RR73] R. D. Roland and R. S. Rice. Bicycle dynamics, ride guidance modeling and disturbance response. Calspan Report ZS-5157-K-1, Calspan Corporation, April 1973. prepared for the Schwinn Bicycle Company.

[RL72] R.D. Roland and J.P. Lynch. Bicycle dynamics tire characteristics and rider modeling. Calspan Report YA-3063-K-2, Cornell Aeronautical Labaratory, Inc., Buffalo, NY, USA, March 1972. prepared for the Schwinn Bicycle Company.

[RP85] P. A. Ruijs and H. B. Pacejka. Research in lateral dynamics of motorcycles. *Vehicle System Dynamics*, 14(1–3):149–152, 1985.

[RP86] P.A.J. Ruijs and H.B. Pacejka. Recent research in lateral dynamics of motorcycles. In *Procedings of 9th IAVSD Symposium on The Dynamics Of Vehicles on roads and on tracks, Sweden June 24-28 1985*, volume supplement to Vehicle System Dynamics, Volume 15, 467–480. 1986.

[Sac06] Alessandro Saccon. *Maneuver Regulation of Nonlinear Systems: The Challenge of Motorcycle Control*. PhD thesis, Universitá Delgi Studi Di Padova, 2006.

[Say90] Michael William Sayers. *Symbolic Computer Methods to Automatically Formulate Vehicle Simulation Codes*. PhD thesis, The University of Michigan, 1990.

[SK10a] A. L. Schwab and J. D. G. Kooijman. Controllability of a bicycle. In *5th Asian Conference on Multibody Dynamics 2010*. Kyoto, Japan, August 2010.

[SK10b] A. L. Schwab and J. D. G. Kooijman. Lateral dynamics of a bicycle with passive rider model. In *The 1st Joint International Conference on Multibody System Dynamics*. Lappeenranta, Finland, May 2010.

[SKM08] A. L. Schwab, J. D. G. Kooijman, and J. P. Meijaard. Some recent developments in bicycle dynamics and control. In A. K. Belyaev and D. A. Indeitsev, editors, *Fourth European Conference on Structural Control (4ECSC)*, 695–702. Institute of Problems in Mechanical Engineering, Russian Academy of Sciences, 2008.

[SMK12] A. L. Schwab, J. P. Meijaard, and J. D.G. Kooijman. Lateral dynamics of a bicycle with a passive rider model: stability and controllability. *Vehicle System Dynamics*, 2012.

[SMP04] A. L. Schwab, J. P. Meijaard, and J. M. Papadopoulos. Benchmark results on the linearized equations of motion of an uncontrolled bicycle. In *Proceedings of The Second Asian Conference on Multibody Dynamics*. August 2004.

[SPC01] K. A. Seffen, G. T. Parks, and P. J. Clarkson. Observations on the controllability of motion of two-wheelers. In *Proceedings of the Institute of Mechincal Engineers*, volume 215. 2001.

[SN06] Himanshu Dutt Sharma and UmaShankar N. A fuzzy controller design for an autonomous bicycle system. In *Engineering of Intelligent Systems, 2006 IEEE International Conference on*, 1–6. Islamabad, April 2006.

[SEL04] R. S. Sharp, Simos Evangelou, and David J. N. Limebeer. Advances in the modelling of motorcycle dynamics. *Multibody Sytem Dynamics*, 12(3):251–283, 2004.

[Sha97] R.S. Sharp. The measurement of mass and inertial properties of vehicles and components. In *Automotive Vehicle Technologies, Autotech 1997, Mech. Eng. Publ.*, 209–217. Bury St Edmunds, 1997.

[Sha71] Robin S. Sharp. Stability and control of motorcycles. *Journal of Mechanical Engineering Science*, 13(5):316–329, 1971.

[Sha75] Robin S. Sharp. The dynamics of single track vehicles. *Vehicle System Dynamics: International Journal of Vehicle Mechanics and Mobility*, 5(1):67–77, 1975.

[Sha94] Robin S. Sharp. Vibrational modes of motorcycles and their design parameter sensitivities. In *Proc. Int Conf. Vehicle NVH Refinement*, 3–5. Birmingham, May 1994.

[Sha01] Robin S. Sharp. Stability, control and steering responses of motorcycles. *Vehicle System Dynamics*, 35(4–5):291–318, March 2001.

[Sha07a] Robin S. Sharp. Motorcycle steering control by road preview. *Journal of Dynamic Systems, Measurement, and Control*, 129(4):373–382, 2007.

[Sha07b] Robin S. Sharp. Optimal stabilization and path-following controls for a bicycle. *Proceedings of the Institution of Mechanical Engineers – Part C – Journal of Mechanical Engineering Science*, 221(4):415–427, April 2007.

[Sha08] Robin S. Sharp. On the stability and control of the bicycle. *Applied Mechanics Reviews*, 61(6):24, November 2008.

[SL01] Robin S. Sharp and David J. N. Limebeer. A motorcycle model for stability and control analysis. *Multibody Syst. Dyn.*, 6(2):123–142, 2001.

[SLG99] Robin S. Sharp, David J. N. Limebeer, and M. Gani. A motorcycle model for stability and control analysis. In *Proc. Euromech Colloquium 404, Advances Computational Multibody Dynamics*, 287–312. 1999.

[SG71] D. V. Singh and V. K. Goel. Stability of Rajdoot scooter. Technical Report, SAE, 1971. SAE Paper 710273.

[Sin64] Digvijai Singh. *Advanced Concepts of the Stability of Two-Wheeled Vehicles: Application of Mathematical Analysis to Actual Vehicles*. PhD thesis, University of Wisconsin, June 1964.

[SS00] Pitikhate Sooraksa and U. Sritheerawirojana. A bicycle robot: part 1 modeling and control. In *Proceedings of the 17th ISARC*, 1–5. Taipei, Taiwan, 2000.

[SUK+00] Pitikhate Sooraksa, T. Uthairat, S. Kaopratum, U. Sritheerawirojana, and V. Monyakul. A bicycle robot: part 2 system implementation. In *Proceedings of the 17th ISARC, Taipei, Taiwan*. 2000.

[SVLB+73] H. G. Stassen, A. van Lunteren, P.L. Brinkman, W.C.J. Moolenaar, J.S.M.J. van Dieten, A. J. de Ron, M. F. W. Dubois, H. A. Udo de Haes, J. J. Kok, and W. Veldhuyzen. Progress report January 1970 until January 1973 of the Man-Machine Systems Group. Technical Report, Delft University of Technology, 1973.

[Sta69] H.G. Stassen. The polarity coincidence correlation technique - a useful tool in the analysis of human-operator dynamics. *Man-Machine Systems, IEEE Transactions on*, 10(1):34–39, March 1969.

[Ste09] David Stevens. The stability and handling characteristics of bicycles. Master's thesis, The University of New South Wales, 2009.

[Sto90] Cal Kent Stone. Rider/bicycle interaction loads during seated and standing treadmill cycling. Master's thesis, University of California, Davis, 1990.

[SH88] Masamori Sugizaki and Akira Hasegawa. Experimental analysis of transient response in motorcycle-rider systems. *Society of Automotive Engineers*, November 1988. SAE Paper 881783.

[Sup06] S. Suprapto. Development of a gyroscopic unmanned bicycle. Master's thesis, AIT, Thailand, 2006.

[STW02] Shashikanth Suryanarayanan, Masayoshi Tomizuka, and Matt Weaver. System dynamics and control of bicycles at high speeds. In *Proceedings of the 2002 American Control Conference (IEEE Cat. No.CH37301)*, volume 2, 845–850. Danvers, MA, USA, May 2002. American Autom. Control Council; IFAC; SICE, American Automatic Control Council.

[SKK+07] Yoshitada Suzuki, Ichiro Kageyama, Yukiyo Kuriyagawa, Masayuki Baba, and Shunichi Miyagishi. 4311 study on construction of rider robot for two-wheel vehicle. *JSME Annual Meeting*, 2007(7):357–358, 2007. in Japanese.

[SL07] Audun Sølvberg. Cyberbike. Master's thesis, Norwegian University of Science and Technology, 2007.

[Tag75] M. Taguchi. A preliminary test report on the controllability and stability of experimental safety motorcycle. In *Second International Motorcycle Safety Conference*. Washington, D. C., USA, December 1975.

[TWB10] Tae-Oh Tak, Jong-Sung Won, and Gwang-Yeol Baek. Design sensitivity analysis of bicycle stability and experimental validation. In *Proceedings of Bicycle and Motorcycle Dynamics 2010: Symposium on the Dynamics and Control of Single Track Vehicles*. 2010.

[TS83] T. Takagi and M. Sugeno. Derivation of fuzzy control rules from human operator's control actions. In *IFAC Symposium on Fuzzy Information, Knowledge Representation and Decision Analysis*, 55–60. Marseilles, France, July 1983.

[TM04] Y. Tanaka and T. Murakami. Self sustaining bicycle robot with steering controller. In *The 8th IEEE International Workshop on Advanced Motion Control, 2004. AMC '04*, 193–197. March 2004.

[TM09] Y. Tanaka and T. Murakami. A study on straight-line tracking and posture control in electric bicycle. *Industrial Electronics, IEEE Transactions on*, 56(1):159–168, January 2009.

[TSSF06] Mara Tanelli, Francesco Schiavo, Sergio M. Savaresi, and Gianni Ferretti. Object-oriented multibody motorcycle modelling for control systems prototyping. In *Proc. IEEE Computer Aided Control System Design*

IEEE International Conference on Control Applications IEEE International Symposium on Intelligent Control, 2695–2700. 2006.

[TMH00] Sekine Taro, Okano Michiharu, and Nagae Hiroyasu. Analysis of motorcycle's behavior in the pylon course slalom. Experimental study on the pylon course slalom of motorcycles. In *JSAE Annual Congress*, volume 58-00. 2000.

[Tau07] A. Taura. Realization of acrobatic motions by bike robot with balancer. Master's thesis, Tokyo Institute of Techinology, 2007.

[TJ10] A. P. Teerhuis and S. T. H. Jansen. Motorcycle state estimation for lateral dynamics. In *Bicycle and Motorcycle Dynamics 2010, Symposium on the Dynamics and Control of Single Track Vehicles*. 2010.

[TP08] Bui Trung Thanh and Manukid Parnichkun. Balancing control of bicyrobo by particle swarm optimization-based structure-specified mixed $h_2/h_\infty $. *International Journal of Advanced Robotic Systems*, 5(4):187–195, 2008.

[TY48] S. Timoshenko and D. H Young. *Advanced dynamics*. McGraw-Hill, New York, 1948.

[Tro02] N. F. Troje. Decomposing biological motion: A framework for analysis and synthesis of human gait patterns. *Journal of Vision*, 2(5):371–387, September 2002.

[Tus47] A. Tustin. The nature of the operator's response in manual control and its implications for controller design. *Journal of the Institution of Electrical Engineers - Part IIA: Automatic Regulators and Servo Mechanisms*, 94:190–206, 1947.

[VDO11] J. H. van den Ouden. Inventory of bicycle motion for the design of a bicycle simulator. Master's thesis, Delft University of Technology, 2011.

[VLS67] A. van Lunteren and H. G. Stassen. Investigations on the characteristics of a human operator stabilizing a bicycle model. In *International Symposium on Ergonomics in Machine Design*. Prague, 1967.

[VLS69] A. van Lunteren and H. G. Stassen. On-line parameter estimation of the human transfer in a man-bicycle system. In *Technical sessions, 4th congress of IFAC*, number 70.3, 41–55. Warsaw, Poland, June 1969.

[VLS70a] A. van Lunteren and H. G. Stassen. Investigations on the bicycle simulator. Chapter III of Annual Report 1969 of the Man-Machine Systems Group WTHD21, Delft University of Technology, Laboratory for Measurement and Control, 1970.

[VLS70b] A. van Lunteren and H. G. Stassen. On the influence of drugs on the behavior of a bicycle rider. In *Sixth Annual Conference on Manual Control*. Wright-Patterson AFB, Ohio, 1970.

[VLS70c] A. van Lunteren and H. G. Stassen. On the variance of the bicycle rider's behavior. In *Procedings of the 6th Annual Conference on Manual Control*. Wright-Patterson AFB, Ohio, April 1970.

[VLS73] A. van Lunteren and H. G. Stassen. Parameter estimation in linear models of the human operator in a closed loop with application of deterministic test signals. In *Proceedings of the 9th Annual Conference on Manual Control*. May 1973.

[VZ75] P. van Zytveld. *A Method for the Automatic Stabilization of an Unmanned Bicycle*. PhD thesis, Stanford University, 1975.

[War06] L. Ward. Gyrobike: Preventing scraped knees. *Popular Mechanics*, November 2006.

[WZ79] D.H. Weir and J. W. Zellner. Experimental investigation of the transient behavior of motorcycles. In *SAE Technical Paper Series*. 1979. SAE Paper 790266.

[Wei72] David H. Weir. *Motorcycle Handling Dynamics and Rider Control and the Effect of Design Configuration on Response and Performance*. PhD thesis, University of California Los Angeles, Los Angeles, CA, 1972.

[WZ78] David H. Weir and John W. Zellner. Lateral-directional motorcycle dynamics and rider control. Technical Report 780304, SAE, 1978.

[WZT79] David H. Weir, John W. Zellner, and Gar Teper. Motorcycle handling. Technical Report Volume II, U.S. Department of Transportation National Highway Traffic Safety Administration and Systems Technology, Inc., Washington, D.C., May 1979.

[Whi99] Francis J. W. Whipple. The stability of the motion of a bicycle. *Quarterly Journal of Pure and Applied Mathematics*, 30:312–348, 1899.

[WW82] Frank Rowland Whitt and David Gordon Wilson. *Bicycling Science*. MIT Press, 1982.

[Wik12a] Wikipedia. Gyro monrail — Wikipedia, the free encyclopedia. 2012. [Online; accessed 25-May-2012].

[Wik12b] Wikipedia. Gyrocar — Wikipedia, the free encyclopedia. 2012. [Online; accessed 25-May-2012].

[Wik12c] Wikipedia. PID controller — Wikipedia, the free encyclopedia. 2012. [Online; accessed 7-June-2012].

[WP04] D. G. Wilson and Jim Papadopoulos. *Bicycling Science*. MIT Press, 3rd edition, 2004.

[Wil51] R. A. Wilson-Jones. Steering and stability of single-track vehicles. In *Proceedings of the Institute of Mechanical Engineers (Auto Div)*, 191–199. 1951. Part 4.

[Win71] R.C. Wingrove. *Comparison of methods for identifying pilot describing functions from closed-loop operating records*. NASA technical note. National Aeronautics and Space Administration, 1971.

[WE68] R.C. Wingrove and F.G. Edwards. Measurement of pilot describing functions from flight test data with an example from gemini x. *Man-Machine Systems, IEEE Transactions on*, 9(3):49 –55, sept. 1968.

[WEC69] R.C. Wingrove, F.G. Edwards, and Ames Research Center. *A technique for identifying pilot describing functions from routine flight-test records*. NASA technical note. National Aeronautics and Space Administration, 1969.

[WL94] J. C. Wu and T. S. Liu. Fuzzy model of rider control for a motorcycle undergoing lane change. *International Journal of Vehicle Design*, 15(1–2):27–44, 1994.

[WL95] J. C. Wu and T. S. Liu. Fuzzy control of rider-motorcycle system using genetic algorithm and auto-tuning. *Mechatronics*, 5(4):441–455, June 1995.

[WL96a] J. C. Wu and T. S. Liu. A sliding-mode approach to fuzzy control design. *IEEE Transactions on Control Systems Technology*, 4(2):141–151, 1996.

[WL96b] J. C. Wu and T. S. Liu. Stabilization control for rider-motorcycle model in Hamiltonian form. *Vehicle System Dynamics*, 26(6):431–448, December 1996.

[WL96c] J. C. Wu and T. S. Liu. Stabilization control of non-holonomic systems with application to rider-motorcycle systems. *International Journal of Systems Science*, 27(11):1165–1175, 1996.

[WL96d] J.C. Wu and T.S. Liu. Fuzzy control stabilization with applications to motorcycle control. *IEEE Trans. Syst., Man, Cybern.*, 26(6):836–847, 1996.

[Yam11] Yamaguchi. Biped robot riding a bicycle. World Wide Web, November 2011. http://ai2001.ifdef.jp/.

[YUS06] M. Yamakita, A. Utano, and K. Sekiguchi. Experimental study of automatic control of bicycle with balancer. In *Intelligent Robots and Systems, 2006 IEEE/RSJ International Conference on*, 5606–5611. October 2006.

[YU05] Masaki Yamakita and Atsuo Utano. Automatic control of bicycles with a balancer, paper 1511181. In *International Conference on Advanced Intelligent Mechatronics*, 1245–1250. Monterey, CA, July 2005. IEEE/ASME.

[Yav97] Y. Yavin. Navigation and control of the motion of a riderless bicycle by using a simplified dynamic model. *Mathematical and Computer Modeling*, 25:67–74, 1997.

[Yav98] Y. Yavin. Navigation and control of the motion of a riderless bicycle. *Computer Methods in Applied Mechanics and Engineering*, 160:193–202, 1998.

[Yea90a] M. R. Yeadon. The simulation of aerial movement-ii. A mathematical inertia model of the human body. *Journal of Biomechanics*, 23:67–74, 1990.

[Yea90b] M. R. Yeadon. The simulation of aerial movement–i. the determination of orientation angles from film data. *Journal of Biomechanics*, 23(1):59 – 66, 1990.

[ZS83] V. Zatsiorsky and V. Seluyanov. The mass and inertia characteristics of the main segments of the human body. In H. Matsui and K. Kobayashi, editors, *Biomechanics VIII-B*, 1152–l 159. Illinois, 1983. Human Kinetic.

[ZSC90] V. Zatsiorsky, V. Seluyanov, and L. Chugunova. In vivo body segment inertial parameters determination using a gamma-scanner method. In N. Berme and A. Cappozzo, editors, *Biomechanics of Human Movement: Applications in Rehabilitation, Sports and Ergonomics*, 186–202. Ohio, 1990. Bertec.

[RM71] R. Douglas Roland Jr. and Daniel E. Massing. A digital computer simulation of bicycle dynamics. Calspan Report YA-3063-K-1, Cornell Aeronautical Laboratory, Inc., Buffalo, NY, 14221, June 1971. Prepared for Schwinn Bicycle Company, Chicago, IL 60639.

[ASKL05] Karl J. Åström, Richard E. Klein, and Anders Lennartsson. Bicycle dynamics and control. *IEEE Control Systems Magazine*, 25(4):26–47, August 2005.